Mixed-Mode Partition Theories for One-Dimensional Fracture

by

Christopher M. Harvey

DOCTORAL THESIS

Submitted in partial fulfilment of the
requirements for the award of

Doctor of Philosophy

of Loughborough University

March 2012

Dedicated to my parents

Catherine and Martin Harvey

and to the memory of

my grandmother Sheila Donaldson

Abstract

Many practical cases of fracture can be considered as one-dimensional, that is, propagating in one dimension and characterised by opening (mode I) and shearing (mode II) action only with no tearing (mode III) action. A double cantilever beam (DCB) represents the most fundamental one-dimensional fracture problem. There has however been considerable confusion in calculating its mixed-mode energy release rate (ERR) partition. In this work, new and completely analytical mixed-mode partition theories are developed for one-dimensional fractures in isotropic homogeneous and laminated composite DCBs, based on linear elastic fracture mechanics (LEFM) and using the Euler and Timoshenko beam theories. They are extended to isotropic homogeneous and laminated composite straight beam structures and isotropic homogeneous plates based on the Kirchhoff-Love and Mindlin-Reissner plate theories. They are also extended to non-rigid elastic interfaces for isotropic homogeneous DCBs. A new approach is used, based on orthogonal pure fracture modes.

Two sets of orthogonal pairs of pure modes are found. They are distinct from each other in the present Euler beam and Kirchhoff-Love plate partition theories and coincide on the first set in the present Timoshenko beam and Mindlin-Reissner plate partition theories. After the two sets of pure modes are shown to be unique and orthogonal, they are used to partition mixed modes. Interaction is found between the mode I and mode II modes of the first set in the present Euler beam and Kirchhoff-Love plate partition theories. This alters the ERR partition but does not affect the total ERR. There is no interaction in the present Timoshenko beam or Mindlin-Reissner plate partition theories.

The theories distinguish between local and global ERR partitions. Local pureness is defined with respect to the crack tip. Global pureness is defined with respect to the entire region mechanically affected by the crack. It is shown that the global ERR partition using any of the present partition theories or two-dimensional elasticity is given by the present Euler beam or Kirchhoff-Love plate partition theories.

The present partition theories are extensively validated using the finite element method (FEM). The present beam and plate partition theories are in excellent agreement with results from the corresponding FEM simulations. Approximate 'averaged partition rules' are also established, based on the average of the two present beam or plate partition theories. They give close approximations to the partitions from two-dimensional elasticity.

The propagation of mixed-mode interlaminar fractures in laminated composite beams is investigated using experimental results from the literature and various partition theories. The present Euler beam partition theory offers the best and most simple explanation for all the experimental observations. It is in excellent agreement with the linear failure locus and is significantly closer than other partition theories. It is concluded that its excellent performance is either due to the failure of materials generally being based on global partitions or due to the through-thickness shear effect being negligibly small for the specimens tested.

The present partition theories provide an excellent tool for studying interfacial fracture and delamination. They are readily applicable to a wide-range of engineering structures and will be a valuable analytical tool for many practical applications.

Acknowledgements

I am sincerely grateful to my supervisor, Dr. Simon Wang. He inspired me to undertake a PhD in the first place and furthermore, has been my inspiration throughout. I thank him for his friendship, guidance, support and all the expertise he has shared with me. I also thank him for his encouragement to do as well as I possibly can.

Dr. Paul Cunningham has freely offered his expertise on experimental matters throughout. Although in the end, time did not allow for full experimental investigations in addition to the theoretical and numerical work, thanks to his time and guidance, there are now experimental apparatus, preliminary results and plans in place for testing in the near future.

The final months of my PhD have been particularly stressful, with postdoctoral research applications, applications for a lectureship, a particularly short deadline for the completion of this thesis, work for publications, and a lot of uncertainty regarding my future, all occurring together. Simon really helped during this time. Simon and Paul in particular have spent a great deal of time helping with and writing postdoctoral research applications. Dr. Martin Passmore and Tom Carslake have worked hard to recruit me as a lecturer in the Department of Aeronautical and Automotive Engineering. Many other people in the university have also been involved with these applications and I am very grateful to all of them. It is with great enthusiasm and anticipation that I now look forward to working with Simon and other staff in the department as a lecturer.

The Department of Aeronautical and Automotive Engineering provided me with funding for the duration of my PhD. Without that, none of this would have been possible. I am also very grateful to Simon and the department for the provision of funding to attend conferences, technical meetings, lectures and a summer school on fracture.

A very helpful discussion regarding this work was had with Prof. John Hutchinson of Harvard University. He also gave permission for a figure from his work to be reproduced. Some interesting discussions were also had with Prof. Gordon Williams of Imperial College London. I am very grateful to both of these people.

My PhD examiners, Prof. Shuguang Li of Nottingham University and Prof. Vadim Silberschmidt of Loughborough University, also deserve special thanks. They both made valuable recommendations for the improvement of this thesis. They both also provided crucial assistance in the securing of a lectureship for me at Loughborough University. I am extremely grateful to them.

Of course, I must thank my parents, who have made me what I am—I used not to even like maths, but Mum made me do extra every evening after school! In particular, without their kindness during the final month (including making cakes and sandwiches for my lunch), I would not have finished writing this thesis in time.

Finally, I thank my God who has supplied every need of mine according to his glorious riches in Christ Jesus.

Contents

Figures

Tables

Symbols

a length of fracture

A effective extensional stiffness of beam

A_{ij} laminate extensional stiffness coefficient

b width of beam

B effective coupling stiffness of beam

B_{ij} laminate coupling stiffness coefficient

C_{ij} material stiffness coefficient

$\{d\}$ nodal displacements vector

D effective bending stiffness of beam

D_{ij} laminate bending stiffness coefficient

D_{op}, D_{sh} relative opening and shearing displacements

$[\overline{E}]$ effective elastic modulus matrix

E_i Young's modulus along i-axis

F_n, F_s resultant interface normal and shear forces

F_{nB}, F_{sB} crack tip normal and shear forces

F_{nBP} crack tip normal force due to shearing

$F_{nB\theta_1}$ crack tip normal force due to mode $\{\varphi_{\theta_1}\}$

G, G_I, G_{II} total, mode I and mode II energy release rates

G_c, G_{Ic}, G_{IIc} total, mode I and mode II critical energy release rates

G_P mode I energy release rate due to shearing

$G_{\theta_i}, G_{\beta_i}$ energy release rates due to mode $\{\varphi_{\theta_i}\}$ and mode $\{\varphi_{\beta_i}\}$

h thickness of beam

H effective shearing stiffness of beam

I_{ii} second moment of area around i-axis

$[k]$ stiffness matrix for finite element

K, K_I, K_{II} total, mode I and mode II stress intensity factors

K_c, K_{Ic}, K_{IIc} total, mode I and mode II critical stress intensity factors

k_s interface spring stiffness

M_{1B}, M_{2B}, M_B crack tip bending moments on upper, lower and intact beams

M_{xx}, M_{yy}, M_{xy} moment resultants on plate element

$[N]$ shape function matrix

N_{1B}, N_{2B}, N_B crack tip axial forces on upper, lower and intact beams

N_{1Be} crack tip equivalent axial force on upper beam

N_{xx}, N_{yy}, N_{xy} in-plane force resultants on plate element

P_{1B}, P_{2B}, P_B crack tip shear forces on upper, lower and intact beams

P_c point contact force

Q_{ij} reduced stiffness coefficient for lamina

$\overline{Q}_{ij}$ transformed reduced stiffness coefficient for lamina

Q_x, Q_y transverse force resultants on plate element

$\{r\}$ nodal loads vector

R radius of axisymmetric plate

S cross-sectional area

S_{ij} material compliance coefficient

u displacement in direction of x- or r-axis

U strain energy

v displacement in direction of y-axis

w displacement in direction of z-axis

Greek

α_{φ_i} mixed-mode partition coefficient for mode $\{\varphi_i\}$

β_i, β_i' pure mode II load relationships

γ thickness ratio h_2/h_1; surface energy

γ_{ij} engineering shear strain in ij-plane

Δa length of crack influence region

$\Delta G_{\varphi_i\varphi_j}$ energy release rate interaction between modes $\{\varphi_i\}$ and $\{\varphi_j\}$

ε_{ij} component of strain at point

θ_i, θ_i' pure mode I load relationships

κ shear correction factor

μ_{ij} shear modulus in ij-plane

ν_{ij} Poisson's ratio

Π potential energy

$\{\overline{\sigma}\}$ effective stress vector

σ_{ii} normal stress along i-axis

σ_n normal stress in crack influence region

τ_{ij} shear stress in ij-plane

τ_n shear stress in crack influence region

$\{\varphi_{\theta_i}\}, \{\varphi_{\beta_i}\}$ mode vectors for the ith pure mode I mode and the ith pure mode II mode in the first set

$\{\varphi_{\theta_i'}\}, \{\varphi_{\beta_i'}\}$ mode vectors for the ith pure mode I mode and the ith pure mode II mode in the second set

ψ rotation of normal to mid-surface of beam about y-axis

Subscripts

$1, 2, \ldots, i$ upper beam, lower beam, ..., ith beam

A quantity at limit of region of crack influence

B quantity at crack tip

I, II, III fracture mode I, II and III

Abbreviations

COH2D4 cohesive four node quadrilateral

DCB double cantilever beam

ENF end-notched flexure

ELS end-loaded split

ERR energy release rate

FEM finite element method

FRMM fixed ratio mixed-mode

FSDT first-order shear deformation theory

LEFM linear elastic fracture mechanics

MMB mixed-mode bending

PEEK polyether ether ketone

PMMA poly(methyl methacrylate)

QUAD4 four node quadrilateral

UD unidirectional

VCCT virtual crack closure technique

VRMM variable ratio mixed-mode

XFEM extended finite element method

Mixed-Mode Partition Theories for One-Dimensional Fracture

Domini sui esse intelligat ubique invenerit veritatem

—Augustine of Hippo, De Doctrina Christiana
Lib. II, C. XVIII

Chapter 1

Mixed-mode partitioning

Contents

1.1 Introduction

In brittle isotropic homogeneous materials, it is well known that cracks propagate in pure mode I (opening) conditions (Cotterell and Rice 1980, Gold'stein and Salganik 1974). The direction of propagation is determined by the need to maintain these conditions. This is known as the 'criterion of local symmetry'. When a mixed-mode fracture in such a material becomes critical, it tends to kink by an angle into a direction such that the advancing crack tip is a mode I fracture.

However, in cases where cracks exist on interfaces between materials, cracks are often constrained to propagate along these interfaces because they represent a plane of weakness. In interface cracking, since mixed-mode cracks propagating along an interface cannot kink into a mode I fracture, they therefore generally propagate as a mixed-mode fracture and can even propagate as a pure mode II (sliding) fracture. Materials generally have a different fracture toughness in each mode. Fracture toughness is the property which describes the ability of a material containing a crack to resist fracture. Therefore, in the case of mixed-mode propagation, the total fracture toughness is load-dependent and is not an intrinsic material property. Because of this, the fracture mode partition, that is the proportion of each fracture mode, plays a key role in the propagation of fractures and therefore also in the development of crack propagation criteria. To predict whether a crack will propagate or not, calculating the fracture mode partition is essential.

Many modern materials are layered and therefore contain interfaces. The structural performance of these materials often depends on the interfaces. Composite materials are examples of such materials. They are formed by combining two or more materials on a macroscopic scale. The result should be that they have better engineering properties than

conventional materials. There are three common types of composite material: (1) fibrous composites, in which fibres are embedded in a matrix material; (2) particulate composites, in which macro size particles are embedded in a matrix material; and (3) laminated composites, which are made up of layers of different materials, potentially including other composites.

The focus of this thesis is on laminated composites and, in particular, on laminated fibre-reinforced composites. Laminated composites consist of layers of at least two different materials, which have been bonded together. Lamination allows the best properties of constituent layers to be combined to form a more useful material. Properties such as strength, stiffness, low weight, etc. can be emphasised by lamination.

Bimetals are an example of a laminated composite. By combining two metals with different coefficients of thermal expansion, the laminate will warp or bend under a temperature change. They are well suited for use in temperature-measuring devices. Another example is in clad metals, where one metal is clad or sheathed with a different metal to optimise certain properties. A high-strength aluminium alloy covered with a layer of corrosion-resistant aluminium alloy combines the corrosion resistance of one alloy, which is usually relatively weak, with another alloy, which is high-strength but does not resist corrosion well. The result is a new material with both high strength and corrosion resistance. The idea of clad metals has been extended to laminated glass. Safety glass is a layer of polyvinyl butryal sandwiched between two layers of ordinary window glass. The ordinary glass is brittle and can break into many sharp-edged pieces but is also durable. The plastic is very tough and very flexible but is also susceptible to scratching. By combining the two materials, each material protects the other and the result is glass with vastly improved properties.

Laminated fibre-reinforced composites on the other hand combine layers of fibrous composites into laminates. The layers are bonded together with the fibres of each layer typically oriented in different directions in order to give the laminate different strength and stiffness in different directions. In doing this, the composite material can be tailored to the specific design requirements of the structural element being built. There are many examples of applications for fibre-reinforced composites, including aircraft wing panels and body sections, boat hulls, tennis rackets, golf club shafts, etc.

Currently, almost every aerospace company is developing products made with fibre-reinforced composites. There are a great many advantages to using these materials. Modern commercial aircraft contain very high percentages of composites and consequently very large weight savings, with all the associated benefits, are being realised. Weight-savings as high as 40% are possible, however in the aerospace industry currently, this value is closer to about 20% (Jones 1999). The impact on jet engine performance is also very substantial. With various metal alloys, thrust-to-weight ratios of 5 to 1 are achieved. With fibre-reinforced plastics, ratios on the order of 40 to 1 appear possible (Jones 1999). However, the full potential of these materials is not currently being met because of one major

obstacle and that is the tendency of these structures to delaminate when they are highly strained. This can occur during use or manufacture.

Delamination is both the most severe and prevalent failure mechanism of laminated composites. When it occurs there is a significant reduction in stiffness and load-carrying capacity. A further consideration is the propagation of delamination, which can cause the whole structure to fail. Since laminated composites are now being used in many complex and demanding applications, a thorough understanding of delamination and delamination propagation is important. This is also necessary in order to achieve the maximum benefit from these materials.

Historically, both stress-based methods and fracture mechanics methods have been used to investigate delamination. There are drawbacks to both of these approaches. Due to the stress singularities at the ends of discontinuous plies, the stress-based methods are highly dependent on mesh size, or in the case of average or point stress criteria, they involve certain characteristic lengths which do no have a very strong theoretical foundation. Fracture mechanics on the other hand relies on the assumption of an initial defect or crack length.

The strength of any material is related to its flaws that are always present. This is especially true of composite materials. Therefore the mechanics of fracture including crack propagation are fundamental in the design analysis of composite structures. Fracture mechanics criteria are a part of every metal aeroplane design. This step was made by the US Air Force as a result of fracture and fatigue problems on F-111, C5-A, Electra, etc. A great deal of attention is now being given to similar fracture mechanics criteria for composite materials.

In this thesis, the fracture mechanics approach is used and delaminations are simply referred to as 'fractures' or 'cracks' in order to keep consistency with the description of fracture mechanics.

Fracture mechanics uses solid mechanics to calculate the 'driving force' on a crack and experimental solid mechanics to characterise the material's resistance to failure. As pointed out above, it is generally true that resistance of a material to failure is dependent on the fracture mode. It is therefore of extreme importance that a mixed mode can be partitioned into contributions from each pure mode in order to be able to make predictions about crack growth. There has been significant confusion for many years on this issue.

Many practical cases of fracture can be considered as one-dimensional, that is, propagating in one dimension and characterised by opening and shearing action only, with no tearing. Study of one-dimensional fracture is very important, since it provides insight into and understanding of the mechanics. One-dimensional fracture has attracted the attention of several eminent researchers and many theories have been put forward. However the problem is still not completely understood due to the many difficulties and complications.

The aims of this thesis are to: (1) clear up the confusion surrounding the fracture mode partition of one-dimensional mixed fracture modes; (2) reveal the underlying mechanics

of the fracture mode partition; (3) to derive new and completely analytical mixed-mode partition theories with a clear physical basis and mechanical interpretation; and (4) to validate the new theories against numerical simulations and published data from experimental investigations.

Various parts of this thesis have been reported on several occasions. The full journal papers are Wang and Harvey (2012*c*), Wang and Harvey (2012*a*), Harvey and Wang (2012*c*), Wang, Harvey and Guan (2012) and Harvey and Wang (2012*a*). Further publications from this work are in preparation in Harvey, Wang and Cunningham (2012) and Harvey and Wang (2012*b*). Some early journal papers are given by Harvey and Wang (2012*d*) and Wang and Harvey (2011*a*). Finally, the conference papers are Wang and Harvey (2012*b*), Wang and Harvey (2011*b*), Wang and Harvey (2010), Harvey and Wang (in press), Wang and Harvey (2009).

The problem of calculating the mode partition of a mixed-mode fracture has been studied extensively using varied approaches. Broadly the work can be categorised as analytical, numerical or experimental. In the remainder of this chapter (Chapter 1), a review is given of the main work in each of these categories. Further detailed comments will also be made on the relevant literature at appropriate points in the thesis. The structure of the rest of the thesis is as follows:

Chapter 2 The essential background theory is presented, concerning the two major theoretical disciplines which contribute to this work: (1) composite laminated plate theory; and (2) linear elastic fracture mechanics (LEFM).

Chapter 3 The role of the finite element method (FEM) in this work is explained and concepts from LEFM are implemented. Elements, which are used for numerical modelling in later chapters, are derived.

Chapter 4 The most fundamental one-dimensional fracture problem is considered: one-dimensional fracture in layered isotropic homogeneous double cantilever beams (DCBs). Completely new, analytical theories for mixed-mode partitioning are presented. The theories are validated using the FEM.

Chapter 5 The work of Chapter 4 is extended to one-dimensional delamination in laminated fibre-reinforced composite DCBs. Completely new, analytical theories for mixed-mode partitioning are presented. The theories are validated using the FEM.

Chapter 6 The theories presented in Chapter 4 and Chapter 5 are used to solve one-dimensional fracture problems in layered isotropic homogeneous and laminated fibre-reinforced composite straight beam structures. Layered isotropic homogeneous axisymmetric plates are also considered. Analytical results are compared against numerical results from the FEM.

Chapter 7 The propagation of mixed-mode interlaminar fracture is investigated using existing experimental results from published literature and the various competing partition theories, including the present ones. Assessments are made of the predictive power of each theory.

Chapter 8 The work of Chapter 4 is extended to one-dimensional fracture in layered isotropic homogeneous DCBs with non-rigid elastic interfaces. The theories are validated using the FEM.

Chapter 9 Finally, conclusions are made regarding the findings of the research and the progress which has been made. Some important work that remains to be done is outlined.

1.2 Analytical theories

Theoretical studies of fractures in layered materials have been mainly carried out by adopting LEFM to deal with the singularity at the crack tip. Unlike in homogeneous bodies, for which the stress field around the crack tip is well-established (Williams 1957), interfacial cracks have caused some considerable difficulties when using two- or three-dimensional LEFM. These are: (1) the mismatch of material properties across the interface generally causes *mixed* fracture modes; (2) the singular field is not square-root singular (as it is in homogeneous bodies) but takes a new form; (3) both the stress fields and the relative displacements between the surfaces of the crack around the crack tip show an oscillatory singularity (Williams 1959, England 1965); and (4) the faces of the crack interpenetrate. Clearly this is a wrong prediction and there is a 'gap' in the theory, which needs to be bridged before it can confidently be applied to important, practical problems. It is for this reason that the theories for interfacial cracks between dissimilar media have not yet entered into the realm considered to be 'classical physics' as the theories for cracks in isotropic homogenous media have.

Since determining the mode partition of mixed-mode fractures is often essential, there have been many attempts to circumvent the above problems. Reviews of these attempts are included in this section. Note that the fundamental background theory to the fracture mechanics on this subject can be found in Chapter 2.

One approach has been to use beam or plate theory instead of elasticity theory. In many cases, this is preferable anyway, especially when working with delaminations in laminated composites. In his pioneering work, Williams (1988) considered isotropic homogeneous beams with a crack at a specified distance from the top or bottom surface. He suggested some conditions for obtaining pure mode I and pure mode II fractures, namely, that a pure mode II fracture is obtained when the curvature at the crack tip in the two arms (i.e. the beams above and below the crack) is the same; and that a pure mode I fracture requires the crack tip bending moments to be equal and opposite. The basis for suggesting these conditions is not clear from the paper. Since the opening displacement produces mode I

and the sliding displacement produces mode II, it may be that the underlying justification was to do with zeroing relative displacements between the surfaces at the crack tip. If this is the case however, the pure mode I condition breaks down for arms of different thicknesses. Williams also attempted to partition the total energy release rate (ERR) by decomposing a mixed mode into a superposition of pure modes.

There are some well-documented problems with Williams's (1988) theory. Shim and Hong (1993) reported that their FEM simulations disagreed with Williams's partition when the two arms have different thicknesses. Zhang and Wang (2009) also noted this in their work. Hutchinson and Suo (1992) said that Williams's work contains 'conceptual errors'.

Whereas Williams's (1988) work offered a completely analytical, closed-form partition theory, several other pieces of work have used a semi-analytical approach, which combines an analytical method to calculate the total ERR, but which finds the mode partition using results from the numerical solution of a two-dimensional continuum problem.

In fact, Schapery and Davidson (1990) claimed that classical plate theory alone (or indeed classical beam theory—the original terminology of each paper is maintained in this review even though in most cases, the theory used is more accurately termed 'beam theory') 'does not provide quite enough information to obtain a decomposition of ERR into its opening and shearing mode components'. Their partition is based on classical plate theory, so in order to proceed without 'enough information', they non-dimensionalised the problem and solved it numerically using the FEM and boundary conditions for some example cases. The cases which they considered were cracked isotropic homogeneous plates with equal and then different thickness arms. Both the total ERR and the partitions were then found to be in good agreement with the results from the FEM using four node quadrilateral (QUAD4) elements. It is noteworthy that classical plate theory provided a value for the total ERR which was very close to that from two-dimensional elasticity. Also noteworthy is that Schapery and Davidson's (1990) theory does not predict the same pure modes as Williams's (1988) theory. It should however agree well with the partition theory of Suo and Hutchinson (1990), Suo (1990) and Hutchinson and Suo (1992).

Suo and Hutchinson's (1990) approach was similar to Schapery and Davidson's (1990). It is also based on classical plate theory for an isotropic homogeneous material except for the aspects which determine the mode partition of a mixed mode. Instead of using the FEM to determine the partition, as Schapery and Davidson did, Suo and Hutchinson used integral equation methods to obtain a linear elasticity solution for the crack tip region. Hutchinson, Mear and Rice (1987) and Rice (1988) had previously introduced a complex stress intensity factor $K = K_I + iK_{II}$, where K_I and K_{II} are mode I and mode II stress intensity factors and $i = \sqrt{-1}$. These are classical stress intensity factors and are based on the near-tip stress field of an interface crack being square-root singular. By 'square-root singular' it is meant that the stress is related to $r^{-1/2}$ (r being the radial distance from the crack front). The interpenetration of surfaces, predicted by these equations in the—usually small—region around the crack tip was considered irrelevant (Hutchinson et al. 1987, Rice

1988). Returning to Suo and Hutchinson's (1990) work, they found that this complex stress intensity factor can be written in terms of a single dimensionless real scalar function, which is itself a function of three parameters. For an isotropic homogeneous material however, the number of parameters reduces to one only. Suo and Hutchinson approximated this one-parameter function numerically by rigorously solving the crack integral equations for one loading case. The mode partition could then be found for other cases.

Thus the problem might appear to be solved, however Charalambides, Kinloch, Wang and Williams (1992) pointed out a number of potential limitations to Suo and Hutchinson's (1990) partition theory (and others similar to it). First, there are the well-known problems associated with two- and three-dimensional LEFM (listed above). In particular, Charalambides et al. discussed the reliance of stress intensity considerations on a square-root singular field, when according to Williams (1959), the field is not of this form unless the materials of the two arms have identical elastic constants. Therefore, Suo and Hutchinson's (1990) approach can only strictly be applicable to isotropic homogeneous materials. In bimaterial cases, the elastic mismatch parameter must be assumed sufficiently small. In addition, Charalambides et al. questioned whether any singular field is dominant in nature, which it must be if it is to dominate the damage and hence the failure mechanism. Therefore Charalambides et al. advocated using ERR instead, which they termed the 'global approach'.

Sheinman and Kardomateas (1997) extended Suo and Hutchinson's (1990) partition theory to general non-homogeneous laminated composites. They derived the total ERR using classical lamination theory and the J-integral for a one-dimensional model of plane stress, plane strain and cylindrical bending. For the decomposition, they used results from Suo and Hutchinson's (1990) linear elasticity solution for the crack tip region and assumed equivalent orthotropic properties through the laminate thickness. In particular, a relationship between the total ERR and the mode I and mode II stress intensity factors was used. This relationship is rooted in the original work of Sih, Paris and Irwin (1965). Comparing this expression with the one for total ERR, derived from classical lamination theory, gave expressions for the two stress intensity factors. As expected, for isotropic homogeneous materials, these expressions reduce to Suo and Hutchinson's ones. Again, this partition theory relies on there being a square-root singular stress field at the crack tip, which is far from certain. In Sih et al.'s work, they dealt with cracks in rectilinearly anisotropic bodies and found that the elastic stress singularity is always square-root singular. However, they used theories of anisotropic elasticity, which work on a macroscopic scale and 'smear out' the mechanical properties of the materials. Therefore the crack is actually modelled as being in a continuum that behaves orthotropically and not as a crack on an interface between two different orthotropic materials. In such smearing techniques, the effects of ply stacking-sequence are ignored completely, which causes errors. Therefore the application of Sih et al.'s relationship for ERR in terms of the mode I and mode II stress intensity factors is not strictly valid for delaminations in laminated composites.

On the subject of the applicability of a square-root singular stress field to interface cracks between dissimilar solids, Rice (1988) completed a re-examination of LEFM in this area to shed light on some of the complicating factors. He argued that although elasticity solutions for interfacial cracks predict interpenetration of the crack surfaces near the tip (Williams 1959), this is not a reason to reject them. He contended that whilst these predictions mean that the solutions must be wrong in detail, on the scale of the contact zone, they still provide a proper characterising parameter for the crack tip region. Specifically, he noted the validity of the square-root singular stress field and the complex stress intensity factor for cases of small-scale non-linear material behaviour and/or small-scale contact zones at the crack tip. These are obviously arguments in favour of using Suo and Hutchinson's (1990) approach for delaminated laminates. Rice (1988) also suggested some new types of stress intensity factor for interfacial cracks between dissimilar media. These of course do not carry the same classical physical interpretations which identify singular fields in a homogenous body.

Similar work to Sheinman and Kardomateas's (1997) and Suo and Hutchinson's (1990) was also carried out by Wang and Qiao (2004). Wang and Qiao modelled an interface crack between two shear deformable elastic layers with different material properties. They used plates based on first-order shear deformation theory (FSDT) to calculate the total ERR. In the same way as Sheinman and Kardomateas (1997), for the mode decomposition they used Sih et al.'s (1965) relationship between the mode I and mode II stress intensity factors and the total ERR. This method therefore also assumes a square-root singular stress field so the respective arguments of Rice (1988) and Charalambides et al. (1992) need to be weighed up. In addition, they too assumed equivalent orthotropic behaviour to convert the problem of a delaminating beam into an equivalent homogenous problem with orthotropic behaviour. The same potential problems with this apply, as described above.

The work of Zou, Reid, Soden and Li (2001) shed light on the problem of the oscillatory behaviour involved in two- or three-dimensional LEFM. Unlike in the above models, they divided the laminate into sublaminates in both the delaminated and the undelaminated regions and modelled them using FSDT plates. Using lamination theory eliminated both the stress singularity and the oscillatory behaviour. Instead, the interfacial singularity at the crack tip was reflected in a stress resultant discontinuity across the crack tip. Using this approach, they found that the virtual crack closure technique (VCCT) could then be used to obtain the individual components of ERR, which are both well-defined according to their classical definitions and converge to definite values as the magnitude of the virtual delamination extension reduces. Zou et al.'s (2001) theory does not provide a general closed-form analytical solution. It requires knowledge of crack tip resultant forces and the displacements of the delaminated laminate surfaces behind the crack tip. This information can be found through the FEM or by other means. They argued that this improved the generality of their approach since, provided that the resultant forces and displacements

are known, the partition of ERR is calculable for any crack, including in laminates with multiple delaminations.

Zou, Reid, Li and Soden (2002) extended this initial piece of work by reformulating the expressions for the total ERR and its mode I, II and III components to require knowledge of the stress resultants and the *derivatives* of relative displacement between the delamination surfaces *at* the crack tip (as opposed to the relative displacements behind the crack tip). They did this because they realised that the original formulation, which is based on the VCCT, placed strict requirements on meshes at the crack tip when the FEM is used to obtain the necessary information, for example requiring elements at the crack tip to be orthogonal to the delamination front and having elements the same size immediately ahead of and behind the crack tip. The total ERR was partitioned by identifying the components in the expression due to opening, sliding and tearing action. These of course give rise to the mode I, II and III ERRs respectively.

To demonstrate that their theory can provide the ERR partition without necessarily requiring FEM simulations, Zou et al. (2002) calculated analytically the stress resultants and the derivatives of relative displacement at the crack tip for an isotropic homogenous DCB, with the upper and lower arms modelled with one sub-laminate each. They used FSDT plate theory to do this. The resulting partitions drift away from Suo and Hutchinson's (1990) theory as the ratio of the upper and lower thicknesses move away from unity. More complex cases with multiple delaminations were solved using the FEM.

Bruno and Greco (2001) also derived an analytical theory for partitioning ERR for delaminations in laminates based on classical plates. For the case of isotropic homogenous DCBs modelled with two sublaminates, this theory gives the same partition as Zou et al.'s (2002) theory. This implies that there is a problem with at least one of the theories since Zou et al. used FSDT plates whereas Bruno and Greco used classical plate theory (with no shear deformation). The effect of through-thickness shear has been shown to have significant effects on the partition (Zou et al. 2001, Zou et al. 2002, Wang and Qiao 2004, and several others). The two theories can't therefore give the same partition and both be correct.

Bruno and Greco's (2001) theory sets out to model the same configuration as Wang and Qiao (2004), however Wang and Qiao used the 'local approach' based on stress intensity factors, as proposed by Suo and Hutchinson (1990), whereas Bruno and Greco used energy considerations and ERR, which is sometimes called the 'global approach'.

Bruno and Greco (2001) derived a laminated plate method where the adhesion between layers is modelled by means of a linear interface acting in the opening and sliding failure mode directions. The crack tip stress resultants are recovered when the stiffness of the interface approaches infinity. Similarly, the ERR components are calculated by means of the interface stiffness as it approaches infinity, along with the relative displacements at the crack tip. First Bruno and Greco derived the governing equations for their structural model. By assuming a two-layer plate system, they reduced the problem to an algebraic

eigenvalue one, which they solved numerically. They also obtained analytical some solutions. One was for a symmetrical two-layer plate with the same mechanical and geometric characteristics for each layer. Unsurprisingly this solution is the same as the one obtained by Williams (1988) and also given by most other subsequent partition theories (the one point of universal agreement for all partition theories seems to be for isotropic homogenous DCBs with equal thickness upper and lower arms). In another solution, they derived an analytical ERR partition for general two-layer plates without restrictions on their mechanical and geometrical characteristics. They did this by decomposing the general loading case into a 'first ineffective', which does not produce ERR, and an equivalent stress system. The ERR partition is then recovered by decomposing the equivalent force system in such a way that the total ERR does not contain any mixed-product terms between the mode I and mode II stress resultants. The sum of the mixed-product terms between these stress resultants is therefore forced to be zero. A clear explanation for this assumption is not given. It is this particular analytical partition for classical beams that agrees with Zou et al.'s (2002) theory for FSDT plates (see above).

Luo and Tong's (2009) theory is similar to Bruno and Greco's (2001). Both are for classical beams bonded with a linear interface but in this case, the mode I and mode II ERRs are obtained by letting the adhesive thickness approach zero (as opposed to letting the interface stiffnesses approach infinity). After deriving the governing differential equations for laminated beams bonded with thick adhesive, Luo and Tong partitioned the total ERR by equating the energy required for the crack to propagate a length in the adhesive to the work done by a crack-tip force to close the relative opening and sliding displacements over that propagated crack length—a crack closure integral (Irwin 1958). They were then able to derive completely analytical, closed-form solutions for the ERR partition for layered isotropic homogeneous structures with different thickness arms, subject to axial forces and bending moments.

Now some more recent work is commented on. Diaz, Caron and Ehrlacher (2007) used an approach, which they called the M4-5N (Multi-particle Model of Multi-layered Materials with five kinematic fields per layer for an N-layer laminate) model. It is similar to Zou et al.'s (2001) approach since both model each lamina with a FSDT plate. Also neither model sets out to provide completely analytical, closed-form solutions but instead to derive expressions for the ERRs in terms of quantities, which can be determined by other means, for example by using the FEM. Zou et al. (2001) required the crack tip stress resultants and the relative displacements behind the crack tip. Zou et al. (2002) required the crack tip stress resultants and the derivatives of the relative displacements at the crack tip. Diaz et al. (2007) required knowledge of the crack tip stresses. Their approach was to first derive the ERR partitions using the VCCT. The relative displacements were then written in terms of the stresses and substituted into the expressions for the ERR components. This resulted in expressions for the ERR components which are quadratic functions of the interfacial stresses only. No assumed initial flaw length was therefore required. Diaz et al.

argued that this is an important result because these expressions are therefore valid for delamination onset as well as growth.

It is apparent that most analytical modelling has used LEFM. Most engineering materials show some non-linear elastic and inelastic behaviour under operating conditions that involve large loads. This may be especially true at crack tips where stress singularities exist. When a significant region around a crack tip has undergone plastic deformation, other approaches can be used. Cohesive zone modelling is one of these techniques and recently there has been a surge of interest in it.

Nguyen and Levy (2009) used a cohesive zone modelling approach that allowed them to model delamination propagation without considering the ERR partition. They developed an exact theory of interfacial debonding for laminated composites comprised of a number of layers and bonded with non-linear, decohesive interfaces. First they derived a Fourier series solution for a single plate subject to an arbitrary loading on its surfaces. A hyperelastic constitutive relation was used to describe the normal and tangential force-separation behaviour of the interfaces between layers. At some given separation, the interface no longer transmitted any force and this represented a delamination. Nguyen and Levy then constructed the integral equations that govern the interfacial separation for bilayers and multi-layer laminates. These analytical equations were solved numerically. Nguyen and Levy's model can be used to calculate ERR partition (by examining the area under the stress-displacement graph in each direction for the interface) although it was unnecessary for them to do this since they were considering only interfacial slip and peel.

Ouyang and Li (2009) developed a cohesive zone model to model the interface shear fracture of the end-notched flexure (ENF) test (see §1.4.1), which is a pure mode II test used to calculate the mode II fracture toughness. They modelled the specimen as two classical beams bonded with an arbitrary non-linear cohesive interface. They derived exact expressions for the mode II fracture toughness using the J-integral. To validate their model, they assumed an exponential type cohesive law (with two parameters) and calibrated it against test data by adjusting the values of interface shear strength and mode II fracture toughness. Solutions for the resulting equations then closely followed the experimental data and Ouyang and Li were able conclude from their results that the mode II fracture toughness is either independent of or very weakly dependent on crack length.

1.3 Numerical techniques and investigations

1.3.1 Approaches to modelling interface delamination

When numerically modelling interface cracking, there are two different approaches: (1) direct application of fracture mechanics; and (2) interface modelling, which indirectly introduces fracture mechanics by assigning constitutive laws to an interface.

First, the most commonly used techniques which fall under the former approach are briefly described here. Krueger (2002) gives a review of these techniques. Irwin (1958)

originally contended that if a crack extends by a small amount, the energy absorbed in the process is equal to the work required to close the crack to its original length. This is what is known as the 'crack closure integral'. The crack closure technique, sometimes called the 'two-step VCCT', is a form of this method, often employed numerically, which examines the displacements before and after a small crack extension in order to calculate the ERR. Rybicki and Kanninen (1977) developed a modified form of this method, the VCCT, in which they say that if the crack extension is small, then the relative displacements behind the new crack tip will be approximately the same as those behind the original crack tip. Therefore only one simulation is needed instead of two. They derived the mode I and mode II ERRs by considering the work done by the normal and shear stresses at the crack tip on the relative opening and sliding displacements respectively. The relative displacements were obtained using the FEM with QUAD4 elements and the forces at the crack tip were obtained by placing very stiff spring elements in the finite element mesh between the nodes on either side of the crack tip. They ran two sets of FEM simulations: the first modelled a DCB specimen with upper and lower arms of different thicknesses which were subject to equal and opposite loads; the second modelled a finite-width strip containing a central crack and subject to uniform opening stress. The results from the FEM simulations for the mode I ERRs agreed well with reference solutions (Kanninen 1973, Fedderson 1967) when converted into stress intensity factors. Raju (1987) extended the work of Rybicki and Kanninen (1977) to calculate ERRs for higher order and singular finite elements.

Rice (1968) developed a concept known as the J-integral. The J-integral is an energetic contour path integral (called J) around a crack. It is equal to the ERR for a crack in a body under monotonic loading. Rice showed that that the J-integral around a crack is independent of the path.

The crack extension technique can also provide an efficient FEM calculation of the total ERR, by considering the energy difference between two successive crack-tip locations. Normally this requires two separate finite element runs with slightly different crack lengths. By adopting the virtual crack extension technique (Hellen 1975) the ERR can be calculated with the FEM solution of the original crack geometry and the additional analysis of a few elements with perturbed nodal locations as a result of virtual crack extension. Because of its computational efficiency, the virtual crack extension technique has been widely used in the FEM evaluation of total ERRs for two- and three-dimensional cracks. Modifications of the method exist to allow for mode separation.

Another commonly-used method is the stiffness derivative (Parks 1974), which is based on evaluating the change in the stiffness matrix due to crack extension. It is a technique developed for the FEM. It requires only one full analysis but the approach is complex. This method does not provide the modal components of ERR but only the total ERR.

The most common of these approaches is the VCCT. It does however require that stress field, when a crack is perturbed, is self-similar. Therefore very small elements at the crack front are required and they must also be orthogonal to it, which can cause problems

when curved crack fronts develop due to spatially varying ERRs. In addition, as in all fracture mechanics, it is necessary to assume an initial flaw. Some of these problems can be overcome with interface modelling. In this approach, interface elements are embedded at potential delamination sites. This is the second of the two approaches listed above.

Interface modelling assumes that a resin-rich interface layer exists between laminae and that delamination occurs within this interface layer. Micrographs reveal that such a layer does exist and that delamination does normally occur preferentially within it.

The most simple and convenient interface model uses spring elements. They are available in many FEM programs, so no new formulation of finite elements is required. Cui and Wisnom (1993) used point springs to model the interface layer. They assumed a zero thickness interface, so duplicate nodes along the interface were joined by these springs. Therefore, for each pair of nodes, two independent springs were used to connect them: a spring tangential to the interface, which carries a force equal to the integration of the through-thickness shear stress over the element length; and a spring normal to the interface, which carries a force equal to the integration of the interface normal stress over the element length. They assumed that the interface was perfectly rigid until failure, by using a very large spring stiffness, which precluded any significant displacements.

The fundamental idea of the interface model is to introduce a failure criterion and to let the computer program decide where and when a delamination initiates and how it propagates. This can be achieved by a load incrementing scheme. Cui and Wisnom (1993) used an assumed force-displacement relationship, in which the springs behave linearly up until an elastic displacement limit, which is extremely small due to the high initial stiffness. Then the springs yield and constant spring force behaviour is assumed up until a critical displacement, when the spring stiffness is zeroed. The critical ERR, that is, the fracture toughness, is available directly from the area under this force-displacement curve. The length of failed springs represents the fracture length and the yielding springs ahead of the delamination front represent the plastic zone. Cui and Wisnom modelled two specimens: a three-point bending specimen without any fracture and a cut-ply specimen in tension. They found that their predictions from this method for delamination onset and delamination propagation were in agreement with experimental results.

Interface modelling does not necessarily mean that fracture mechanics is only indirectly involved. Zhang and Wang (2009) and Wang and Zhang (2009) employed a simple variation of the interface spring model in conjunction with the finite strip method (as opposed to the FEM) to model mixed-mode failure in post-buckling. Their interface springs were very stiff and completely linear, so did not yield. The length of the plastic zone was therefore zero. The ERR partition was calculated using the VCCT. To model mixed-mode failure, they used a linear mixed-mode failure criterion based on ERR (see §1.4.3), which requires knowledge of the critical ERR for each mode. They obtained excellent agreement with complex experimental post-buckling results, which exhibited both stable and unstable delamination propagation and the snap-through phenomenon (Kutlu and Chang 1995).

Mi, Crisfield, Davies and Hellweg (1998) described another type of interface modelling, using zero thickness interface elements embedded between eight node quadrilateral elements. They formulated the interface element based on a material model defined in terms of tensile strength, cracking strain and maximum strain. The area under this stress-strain curve is equal to the critical ERR. They also assumed that with reversing strains, the material unloads directly towards to the origin. Because their damage model was based on strains, they indirectly involved fracture mechanics by calculating the damage model parameters such that a failure criterion from fracture mechanics was satisfied. They used two failure criteria, which were the linear interaction relationship for mixed-mode failure (see §1.4.3) and a generalised power law variation of it. The scalar damage parameter, which in basic terms varies from 0 to 1 and quantifies the degree from damage, was determined by these means, using concepts from fracture mechanics. The model provided excellent agreement with the DCB, ENF and mixed-mode bending (MMB) tests using the FEM and plane-strain elements.

This kind of interface modelling is called 'damage mechanics' (rather than 'fracture mechanics'), although the mechanical damage behaviour of the interface can be modelled with the indirect introduction of fracture mechanics in a combined approach. Deriving interface damage models for finite elements is complex. Alfano and Crisfield (2001) laid down the framework for a general damage mechanics theory for delamination. Most later work is about deriving new interface elements with different damage laws and different finite element formulations and applying these elements to practical problems. The most important of these works are now briefly described. Some early work was carried out by Petrossian and Wisnom (1998). Qiu, Crisfield and Alfano (2001) developed a one-dimensional interface element for the simulation of mixed-mode delamination with buckling. Chen (2002) applied one-dimensional interface elements to the delamination of sandwich panels. Camanho, Davila and de Moura (2003) developed a zero-thickness interface element, which can predict delamination onset and growth under mixed-mode loading between solid finite elements. Wagner and Balzani (2008) simulated delamination in stringer-stiffened, fibre-reinforced composite shells using an interface elements based on standard hexahedral solid elements. Pinho, Iannucci and Robinson (2006) implemented a three-dimensional interface element in the widely-used industrial FEM software LS-Dyna, which demonstrated how interface modelling can ease the computational burden of predicting the onset and propagation of delamination.

Meo and Thieulot (2005) modelled a DCB test using four different approaches: the first used interfacial decohesion elements with a bilinear stress-strain law; the second used non-linear interface springs with the same law to describe its mechanical behaviour; the third used solid elements to represent the matrix, which were eliminated when the ERR exceeded the critical value. In the fourth approach, the interface was modelled with ties, where coincident nodes were tied together until the maximum interlaminar stresses were reached. This choice of failure criterion for the latter approach meant that it did not

perform very well. The first three approaches, which were rooted in the fracture mechanics concept of failure when the ERR exceeds a critical value, all gave very similar results though, which closely agreed with experimental results.

Finally, there is another relatively recent development in the modelling of fracture propagation: the extended finite element method (XFEM). One of the most awkward problems when modelling fracture propagation is that remeshing tends to be required near the crack tip as the crack grows. This is because the accurate application of fracture mechanics to the FEM places some strict requirements on the mesh that are not necessarily maintained as the crack grows. Remeshing is onerous and requires projection of variables between the different meshes and causes difficulties during post-processing, for example, when a variable at a spatial point is monitored. The XFEM is one solution to these difficulties. In Belytschko and Black's (1999) original implementation, discontinuous displacement functions are added to standard polynomial displacement functions. This provides a new set of displacement functions, known as 'enrichment functions', that include crack opening displacements. Elements can therefore be intersected by a crack and don't need to conform to the fracture surfaces. Belytschko and Black (1999) first derived XFEM for LEFM. Zi and Belytschko (2003) developed the original theory with a new formulation for elements containing crack tips. Comparisons with reference solutions showed excellent agreement.

XFEM has been extended for many applications, including three-dimensional crack propagation, arbitrary branched and intersecting cracks, etc. Of particular interest is the very recent extension to delamination in orthotropic bimaterial composites. Ashari and Mohammadi (2011) completed the early research into this. New bimaterial orthotropic crack-tip enrichment functions were extracted from the analytical LEFM solution for the region around an interfacial crack tip. This released the finite elements from the usual constraints of both needing to conform to fracture surfaces and the boundaries between materials.

1.3.2 Energy release rate and mode partition

Since the focus of this review is on determining ERR partition, no further detailed review into the different approaches to modelling delamination is given. Instead attention is now given to ground-breaking numerical work on determining ERR partition.

The difficulties, when modelling cracks between dissimilar materials with two- or three-dimensional LEFM, are not restricted to analytical approaches only. Because resin layers are very thin and several elements would be needed through the thickness to begin to resolve them, FEM meshes can become very large, containing large numbers of elements and nodes. Although detailed FEM simulations of laminates should certainly model these resin layers, it is often desirable to neglect them and instead assume that delamination occurs at a discrete interface between neighbouring plies.

O'Brien, Johnston, Raju, Morris and Simmonds (1987) modelled an edge-delaminated laminated composite with this kind of 'bare' interface using the FEM. They studied the

convergence of ERRs for various size delamination tip elements. They ran simulations using hybrid singular elements, which are designed to capture to singular stress field around the crack tip, and also with eight node quadrilateral elements. In both cases, the total ERR agreed extremely well with value from laminated plate theory. With the hybrid singular elements, they found that if the ratio of element size at the delamination front Δa to the ply thickness h was between $0.18 < \Delta a/h < 0.55$, then individual the individual components of ERR were constant within this range. However for $\Delta a/h < 0.18$ and $\Delta a/h > 0.55$, varying components of ERR were obtained; they were not constant. First, for $\Delta a/h < 0.18$, O'Brien et al. attributed this behaviour to the fact that the elements neighbouring the crack tip would also be subject to the singular stress field along with the crack tip element, and thus, the crack tip element would be too small. Second, for $\Delta a/h > 0.55$, they attributed this behaviour to the crack tip element being too large and capturing both the singular and far-field components, which the singular element is unable to handle. They therefore concluded that singular elements should only be used in the range $0.18 < \Delta a/h < 0.55$. Also, for the case of eight node quadrilaterals, since they obtained good agreement with the hybrid singular elements for $\Delta a/h < 0.25$, they recommended this as a good choice of element size.

Raju, Crews Jr. and Aminpour (1988) investigated the same problem further using a quasi three-dimensional FEM and the VCCT to calculate the ERRs. They also found that the components of ERR did not converge as the size of the delamination tip element decreased, but that the total ERR converged well. From their numerical studies, they found that the non-convergence of the individual components of ERR is due to the oscillatory part of the stress singularity. Furthermore, they found that when materials are chosen such that the oscillatory component of the singularity is zero, the modal contributions do converge. This is also in agreement with continuum analyses, which say that when the oscillatory component is not present, the stress field is square-root singular and the ERR components are then well-defined. Raju et al. therefore concluded that the non-convergent behaviour of the individual components is due to the oscillatory singularity at the crack tip, which the two- and three-dimensional FEM inevitably captures.

Zou et al.'s (2001) analytical work has already been discussed but it is worth mentioning again briefly here because it has numerical implications. They re-analysed the 'bare' interface laminate by numerically solving analytical equations, which model a laminate as a stack of sublaminates, each based on FSDT plate theory. They found that by modelling an assembly of sublaminates, which can accommodate a stress resultant across a crack tip in order to reflect the crack-tip stress singularity, the oscillatory effects can be avoided. Other numerical work which models laminates in the same way, can therefore expect the same result. This explains the excellent performance of Wang and Zhang's (2009) model (discussed in §1.3.1), which used this kind of model in conjunction with the finite strip method.

Use of plates and interface elements in the FEM eliminates some of the difficulties in obtaining converged ERR partitions (see §1.3.1). Bruno, Greco and Lonetti (2003) assessed the reliability of plates and interface elements in deriving mode partition for laminated composites. To do this, they made comparisons between the accuracy of fracture mode partitions obtained by plate and interface elements and those obtained using a local continuum approach. They also aimed to highlight the differences between the two common analytical approaches to determining mode partition, namely elasticity theory and plate theory. Bruno et al. modelled multilayer FSDT plates, bonded with variable stiffness interface elements, which were based on fracture mechanics. The ERR was obtained by means of the VCCT. They further showed that this approach circumvents the classic oscillatory problem and leads to a well-defined ERR partition. The most notable finding however was that by using multiple layers of FSDT plates, the numerical ERR partitions approach those given by Suo and Hutchinson's (1990) analytical theory, which is based on two-dimensional elasticity. This implies that the partition theories based on elasticity are in fact differentiated from plate partition theories only by modelling differently the effects of through-thickness shear on ERR decomposition. Furthermore, it implies that the assumption of Hutchinson et al. (1987) and Rice (1988), that the interpenetration of surfaces predicted by elasticity solutions in the region around the crack tip is irrelevant, is indeed valid because partitions from the FEM using FSDT plates with an interface model, for which interpenetration of cracked surfaces is not an issue, agree with analytical partitions from elasticity theory.

In §1.2, the combined analytical-numerical approach to mixed-mode partitioning was discussed. In this approach, the ERR partition is calculated analytically based on the global loading at the crack tip. The crack tip can therefore be considered in isolation with loads applied at the boundaries of an 'influence region'. These loads are determined by means of another—usually numerical—method. The analytical aspects of this have been considered in detail already. On the numerical front, there is therefore an opportunity to embed the analytical mode partition theory into a crack tip finite element or simply just to run FEM simulations using a relatively coarse finite element mesh in order to obtain global loads for use in an analytical partition theory. The loading on the crack tip element is determined by the FEM, and the ERR partition is determined by the loading on the crack tip element in conjunction with the analytical partition theory. This crack tip element approach is significantly more efficient because highly refined finite element meshes are no longer required in the vicinity of the crack tip. Also, it eliminates the inaccuracies in calculating the mixed-mode partition (provided that the partition theory in use is correct).

Note that sometimes 'crack tip element approach' refers to the analytical task of determining the ERR as a function of globally applied loads because it is based on the concept of a crack tip embedded inside an elemental body. This has already been discussed in §1.2 although it wasn't referred to by this name. As pointed out, crack tip elements in the

FEM, and the crack tip element approach to analytical modelling are intertwined, however it is the use of crack tip elements with the FEM that is discussed here.

Davidson, Hu and Schapery (1995) derived some equations for a crack tip element based on elasticity theory, following the same approach as Schapery and Davidson (1990) in their semi-analytical approach (see §1.2). Davidson, Hu and Yan (1996) demonstrated the efficiency and accuracy of this approach by applying it to a number of cases, including beams with multiple fractures in post-buckling, free-edge delamination and three-dimensional beams with fractures. In cases where the near-tip field would be oscillatory, they assumed a condition that removed it. ERR partitions from the crack tip element were mostly in good agreement with results from highly refined two- and three-dimensional finite element meshes. Later, Davidson, Yu and Hu (2000) refined the original model to correct some of the deficiencies for three-dimensional crack tip elements, using a method based on plate theory to determine the ERR partitions.

Obtaining the mode partition numerically by means of crack tip elements is convenient and computationally efficient but it relies on accurate analytical mixed-mode partition theories. Since the technique neither develops analytical partition theories nor numerically implements concepts from fracture mechanics, this approach is given no more attention here.

1.4 Experimental test methods and results

1.4.1 Test methods

Interlaminar fracture has been investigated experimentally for many years. As a result, a number of test methods have been developed. Some have been been written down in standards by various standardisation organisations. A brief review is given here of the most common test methods for characterising interlaminar fracture experimentally.

Strawley, Jones and Gross (1964) developed an experimental technique to measure critical ERR for a material. The method they described is for—what are in effect—DCBs, although it can easily be extended to other specimens. A DCB is a beam specimen with a mid-plane crack at one end. Two opposing forces are applied at the free end, as shown in Fig. 1.1 (a). They determined the compliance of multiple DCB specimens with different crack lengths by measuring the displacements of the two opposing forces. The compliance of an individual specimen is easily found by measuring the slope of the linear part of the load-displacement curve, as shown in Fig. 1.1 (b). The resulting compliances for each specimen can then be plotted on a crack length-compliance curve, as shown in Fig. 1.1 (c). To evaluate the critical ERR for a given specimen with a known crack length, the rate of change of compliance with crack length needs to be known. This is can be found from the crack length-compliance curve in Fig. 1.1 (c). The critical ERR can then be calculated using simple mathematical relations, which are based on the critical ERR being the rate of change of strain energy with increase in crack area.

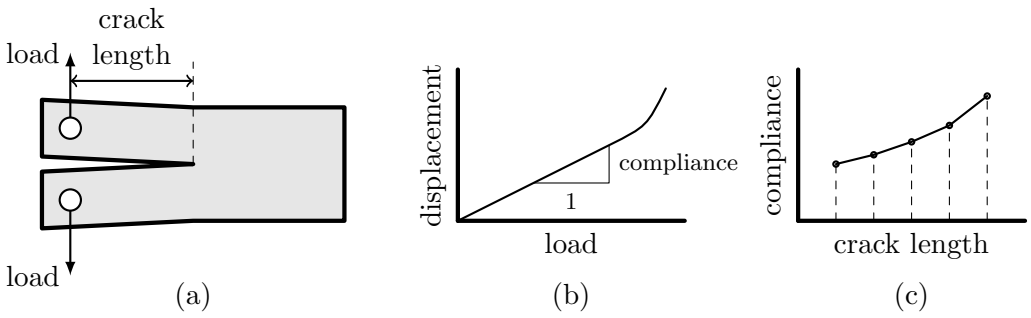

Figure 1.1: (a) DCB specimen. (b) Typical load-displacement curve for a DCB. (c) Typical crack length-compliance curve from multiple DCBs.

The type of experiment is important (Kundu 2008). It affects the exact form of the mathematical relations for critical ERR. In a fixed-force experiment, the load is continuously increased until the crack begins to propagate and the applied load does not change during crack propagation. The critical ERR is then calculated from the compliance-crack length derivative and this critical load. Since the compliance increases with crack length, once the crack starts to propagate, the specimen fails.

In a fixed-grip experiment, the specimen is subjected to a specified displacement, which is continuously increased until the crack begins to propagate (at the critical crack opening displacement). After propagating a small distance, the crack stops. In this case, the critical ERR is calculated from the compliance-crack length derivative and the critical crack opening displacement with its corresponding compliance.

The critical ERR can be also determined from just one DCB specimen by using beam theory to derive the compliance-crack length derivative, shown in Fig. 1.1 (c), for a given specimen geometry (Kundu 2008). The critical ERR is then calculated in the way described above with the critical load or the crack opening displacement, depending of the type of experiment.

Comprehensive reviews of some standard test methods are given by Martin (1991) and Davies, Blackman and Brunner (1998). Hashemi, Kinloch and Williams (1990) applied Williams's (1988) analytical partition theory to the four most common standard test methods: the DCB test for mode I testing; the ENF test and end-loaded split (ELS) test for mode II testing; and the MMB test for mixed-mode testing. As well as presenting analytical formulae for use by other researchers, they also aimed to identify and eliminate the many difficulties in the literature, which, in parallel with the analytical and numerical problems, have contributed to the confusion regarding mixed-mode partitioning. It is worth noting that because the cracks in these specimens are generally located at the mid-plane, Williams's (1988) beam partition theory has worked well for the beam theory data reduction (see §1.2 for further discussion on the applicability and limitations of Williams's analytical partition theory). These four most common test methods are now briefly reviewed.

Double cantilever beam test

The DCB test is widely used to measure the mode I interlaminar fracture toughness of laminated composites. The current standard test method is given by the ASTM (2007e3). According to the standard, the DCB specimen, shown in Fig. 1.1 (a), consists of a uniform thickness laminate with a non-adhesive insert placed at the mid-plane at one end before curing. This insert simulates the delamination. The standard test is limited to laminated composites consisting of unidirectional (UD) carbon fibre and glass fibre with brittle single-phase polymeric matrices. The specimen dimensions should be at least 125 mm long, between 20 and 25 mm wide and normally between 3 and 5 mm thick (ASTM 2007e3). A 24 ply DCB typically gives satisfactory measurements of mode I fracture toughness without the need for geometric non-linearity corrections (Martin 1991). The test can of course also be applied to specimen configurations other than those specified, but the standard reflects current understanding and experience from round-robin testing (O'Brien and Martin 1993).

The test is carried out by opening the free ends of the DCB. Opening forces are applied to the DCB specimen by means of hinges or loading blocks. The displacement of each free end is controlled and the load, displacement and crack length are recorded. To measure the crack length (which is the sum of the initial crack length and the distance the crack has growth), gradations can be marked on the specimen edge from the centre of the loading pin. The mode I fracture toughness is then calculated either by using the compliance calibration method or the modified beam theory method, which are described above.

The DCB test has been used on composites since the 1960s, however the original ASTM standard was not approved until 1994 despite only one specimen geometry being used (the DCB) and the data analysis being reasonably straightforward. The reason that it took so long to develop a standard is that were some experimental complications. In particular, one major obstacle to standardisation came in the 1980s with the observation that UD specimens are strongly affected by fibre bridging and multiple cracks, which occur as a crack moves above and below bundles of fibres (Davies et al. 1998). These phenomena are rarely seen in more realistic, non-UD laminates. Also, it was found that when bridging and multiple cracking occur, fracture resistance curves (R-curves), which plot mode I fracture toughness against crack length, are no longer intrinsic material properties but instead depend on the specimen stiffness (Davies et al. 1998).

Other complications included whether to calculate the fracture toughness based on crack initiation or propagation. Several values for the initiation fracture toughness can be determined from the experimental load-displacement curve and then there are also the propagation values (ASTM 2007e3). Together these form the R-curve, which ideally would reveal a single characteristic fracture toughness for a given material. Unfortunately it is not always so. With propagation, the result is affected by the above problems of bridging and multiple cracking. The focus therefore then shifted to initiation fracture toughness. This resulted in a debate on the type of initial defect to be used and its thickness, since it was observed that the fracture toughness decreased as starter film thickness was decreased

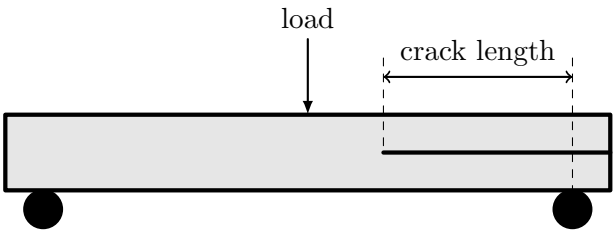

Figure 1.2: ENF mode II test configuration.

until below a certain thickness a constant value was measured. After several round robins, including the one documented by O'Brien and Martin (1993), a maximum film thickness of 13 µm was arrived at (ASTM 2007e3) because below the threshold value of 15 µm, the measured fracture toughness was observed to be independent of thickness.

Once the type of defect had been fixed, another issue was then how to determine when initiation occurs. There are a number of initiation fracture toughnesses: The first is calculated at the point where the load-displacement relationship deviates from linearity. The second value is based on the recorded load and displacement for the first point at which delamination is visually observed to grow. The final value is calculated at the point where the compliance has changed by 5%, which typically corresponds to about 1 mm of crack growth for the specimens defined in the ASTM (2007e3) standard (Davies et al. 1998).

End-notched flexure test

The ENF test is commonly used to measure the mode II interlaminar fracture toughness of laminated composites. There is currently no widely-used standard for mode II testing, although a Japanese standard does exist (JIS 2008). The ENF specimen configuration is similar to that of the DCB test: it is UD and has a non-adhesive insert, placed at the mid-plane at one end prior to curing. The specimen rests on two roller supports, which allow it to rotate freely, and it is loaded at the mid-span. It is therefore in a three-point bending configuration. Load and displacement is measured. The ENF test is shown in Fig. 1.2

The most common method for reducing the ENF test data for the mode II fracture toughness is with a beam theory expression. Carlsson, Gillespie and Trethewey (1986) presented solutions for the compliance and the ERR of an ENF specimen. This mode II test is however also complicated by a number of factors, which include unstable propagation and friction effects. The unstable propagation means that fracture toughness must be determined based on the point of delamination initiation. In the same way as for the DCB test, there are different ways to do this. Visually observing the point of initiation is difficult because the delaminated surfaces are being pressed together and because, as mentioned, initiation is immediately followed with unstable propagation. Therefore the initiation fracture toughness may be calculated using the loads and displacements at one of the following: the point that corresponds to the maximum load (at which unstable

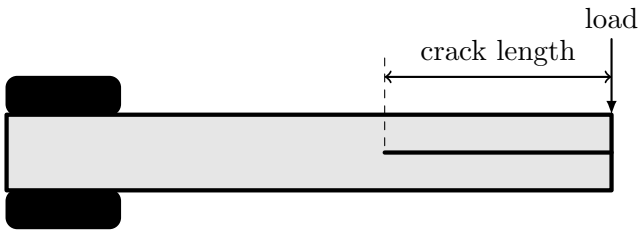

Figure 1.3: ELS mode II test configuration.

delamination growth occurs); the point of deviation from linearity of the load-displacement curve; or the point where the compliance has increased by 5% from its initial value.

Improvements to the original beam theory expression for fracture toughness by Carlsson, Gillespie and Trethewey (1986) were offered by Carlsson, Gillespie and Pipes (1986) and Zhou and He (1994) to account for shear deformation, which can potentially have a significant effect since the specimen must be thick enough to avoid substantial geometric non-linearity effects. In doing this, Carlsson, Gillespie and Pipes (1986) assumed zero rotation at the specimen centre. Zhou and He (1994) pointed out that this was an 'unreasonable assumption' and easily seen to be incorrect from photographs. They presented a more general method, which models the specimen as two cantilever beams, one of which is a DCB. They were both supported at the point of zero rotation, which was not constrained to lie at the mid-span.

End-loaded split test

Another common method to measure mode II interlaminar fracture toughness is the ELS test (Corletto 1986, Hashemi et al. 1990). The ELS test configuration is shown in Fig. 1.3. It has a very similar configuration to the ENF test. It is rigidly clamped at the intact end and loaded at the other cracked end. Both arms are bent in the same sense with the load shared to give the same deflection. The advantage of this test is that once the deformation has reached 55% of the length of the specimen, the propagation becomes stable (Martin 1991). Therefore, any R-curve effect may be determined in one loading sequence.

Mixed-mode bending test

Delaminations in laminated composites do not often occur in pure modes but instead tend to be combinations of all three modes. Since there is no reason for the fracture toughness of each mode to be the same, it is important to devise testing methods to: (1) determine the fracture toughness in different pure modes (which is the purpose of the tests described above); and (2) determine the fracture toughness in mixed modes. The mixed-mode fracture toughness is often described by means of a 'mixed-mode failure criterion'. Many such criteria have been suggested and some are discussed in §1.4.3. A number of different tests have been designed to produce mixed modes. Most of these tests

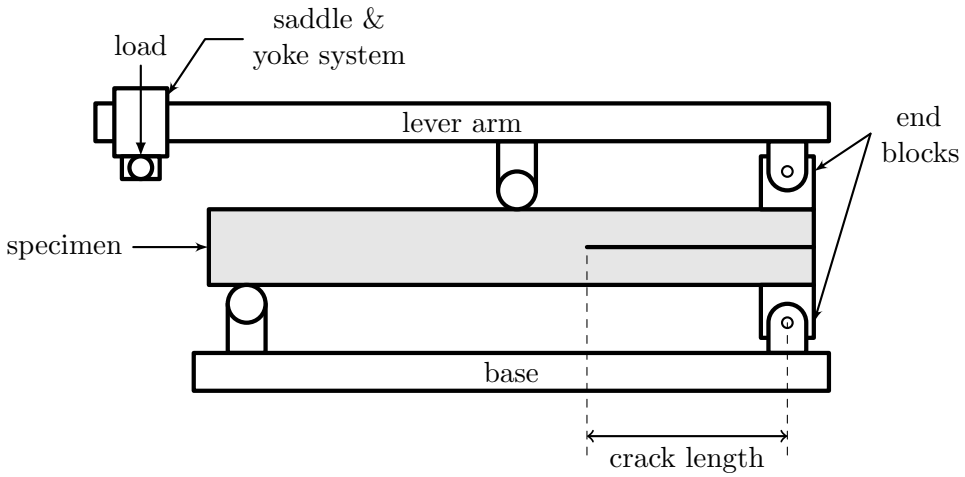

Figure 1.4: MMB test configuration.

focus on mixed mode I and II fractures. One of these tests, which has received a lot of attention, is the MMB test, which is shown in Fig. 1.4.

Reeder and Crews Jr. (1990) developed this test by combining DCB mode I loading with ENF mode II loading on a split UD laminate. This was achieved by adding an opening-mode load to a mid-span loaded ENF specimen. A loading lever with a fulcrum at the mid-span applied the opening load at the delaminated end of the specimen and achieved the requisite loading. Reeder and Crews Jr. (1990) analysed the test using two methods to calculate the mode I and mode II ERRs: (1) the FEM with eight node quadrilateral elements and the VCCT; and (2) Williams's (1988) analytical partition theory based on Euler beam theory. This partition theory assumes that opposite crack tip bending moments produce pure mode I and that equal curvature in the two arms at the crack tip produces pure mode II. As discussed in §1.2, these seem to be good assumptions when the arms have equal thickness, which is the case for the MMB test. Reeder and Crews Jr. (1990) found good agreement between the two analyses. They also found that the MMB test could produce a wide range of mode I to mode II ERR ratios by varying the load position on the lever.

Reeder and J. H. Crews (1991) made modifications to the original test to reduce non-linearities. They found that the errors in the ERRs when calculated using the linear theory could be as large as 30%. Because of the complexity involved in using a non-linear analysis to analyse the MMB data, they instead redesigned the apparatus to minimise the non-linearity. With the redesigned apparatus, loads were applied through a 'saddle' attached to the lever with free-rotating joint just above the mid-plane of the test specimen. They found that the redesigned apparatus had geometry non-linearity errors of less than 3%.

In comparison to other mixed-mode tests, the MMB test has two distinct advantages: (1) the same specimen geometry can be used for both mode I and mode II tests; and (2) the mixed mode ratio can easily be varied over the whole range from pure mode I to

pure mode II. As a result, this test method is the only one seriously being considered for standardisation (Davies et al. 1998).

1.4.2 Mixed-mode failure tests

Since this work is concerned with the partition of mixed-mode fractures, experimental results from various mixed-mode tests are now reviewed.

Hashemi, Kinloch and Williams (1991) carried out extensive experimental investigations to establish which out of Williams's (1988) partition theory (referred to as the 'global approach' in their work) and Suo and Hutchinson's (1990) partition theory (referred to as the 'local approach') is the most appropriate for partitioning mixed modes in laminated composites. They used a variety of test methods, including variations on some of the test methods described in §1.4.1, in order to obtain mixed modes. These were the asymmetric DCB and ELS tests, so-called because the specimens used in these tests had fractures away from the mid-plane. Williams's (1988) partition theory predicts pure mode I and II for equal and opposite moments and equal curvatures respectively whilst Suo and Hutchinson's (1990) partition theory predicts mixed modes. The two analytical partition theories are clearly quite different. Hashemi et al. (1991) compared experimental measurements of the total critical ERR with the values predicted by the two theories.

Further comparisons between the two analytical theories were made by using two new tests, which they called the variable ratio mixed-mode (VRMM) test and the fixed ratio mixed-mode (FRMM) test. In the VRMM test, a specimen with a mid-plane crack at one end is hinged at both ends by its top surface, and the upper arm is loaded upwards at a specified location. The mode partition is changed by moving the point of load application. Since the crack is at the mid-plane, the two partition theories (the local and global partition theories) gave same partition (see §1.2). The FRMM test on the other hand consisted of an asymmetric DCB specimen with an opening load applied to one arm only. The two analytical theories gave different partitions for this test.

Hashemi et al.'s (1991) approach to compare the two theories was to experimentally measure the critical ERR by measuring the load and displacement at the identified point of initiation and/or propagation and to partition this ERR into mode I and mode II components using the two theories. Results were then plotted on a graph of mode I versus mode II ERR, which gave a failure locus for each partition theory. Since the failure locus is considered to be an intrinsic material property, it was expected that the results from both the VRMM and FRMM tests should lie on the same curve. Hashemi et al. observed that Williams's (1988) partition of the FRMM test data produced approximately the same failure locus as the partition of the VRMM test data (for which both partition theories give the same partition). However, Suo and Hutchinson's (1990) partition of the FRMM test data produced a very different failure locus to the one from the VRMM data. Hashemi et al. therefore concluded that the global partition given by Williams's (1988) partition theory is the right one.

Given the findings reviewed in §1.2, it is possible to make some additional comments on the experimental data in Hashemi et al.'s (1991) work. It is known from FEM simulations that Williams's (1988) global partition theory is correct when the crack lies at the mid-plane, but does not work when the arms have different thickness. Since the specimens in the VRMM test have arms of equal thickness, this implies that the ERR partitions from the VRMM data, calculated using Williams's (1988) global partition theory, should be correct. The plots of mode I versus mode II ERR for the VRMM data show a very strong linear relationship in the failure locus, however all these data points are concentrated over only half the full range of ERR partitions. On the other hand, the global partition of the FRMM test data must be treated as questionable because the crack does not lie at the mid-plane in this test. The failure locus from this data shows a marked curve over the full range. Hashemi et al. may have been able to incorrectly conclude that the same failure locus is given by both tests if the global partition is used simply because over the comparable regions, the two sets of data are close, even though the range of the VRMM data is not large enough to give the complete picture.

Charalambides et al. (1992) presented the results from a very similar investigation to the one carried out by Hashemi et al. (1991). They also observed the curve in the failure locus when using Williams's (1988) global partition theory to partition the experimentally measured critical ERR. Under the assumption that the global partition is the correct one, they suggested a general criterion for fracture under mixed-mode loading, which fits the observed curve. They did this by assuming that mixed-mode fractures are controlled by mode I but that there is a secondary sliding component to the critical ERR due to some mechanical effect, such as surface roughness. Three experimental observations were required fit the curve to a set of data.

Charalambides et al. (1992) also made some comparisons with spalling data from the work of Thouless, Evans, Ashby and Hutchinson (1987). Spalling is where cracks occur very close to the surface. They carried out experiments on glass and poly(methyl methacrylate) (PMMA), by loading the spall axially at a specified distance from the free surface. They discovered some trends in crack location, crack propagation load and in the onset of spalling. In particular, they observed that as the cracks propagated, they stabilised at a constant distance from the free surface. Under the assumption that in an isotropic homogeneous material, the crack propagates in such a way as to maintain pure mode I conditions at the crack tip (Cotterell and Rice 1980, Gold'stein and Salganik 1974), they used Suo and Hutchinson's (1990) partition theory to predict the stabilised crack depth and the crack propagation load. They made comparisons between the predicted and experimentally measured values. They noted 'appreciable discrepancies'. Charalambides et al. (1992) were unable to get better agreement using Williams's (1988) partition theory without postulating an additional sliding component to the mode II ERR due to fracture surface roughness.

Kinloch, Wang, Williams and Yayla (1993) continued the work of Hashemi et al. (1991) by comparing the failure loci obtained from multiple different mixed-mode fracture tests and Williams's (1988) partition theory. They also included data from the modified MMB test (Reeder and J. H. Crews 1991). In the work, they made further comparisons with Suo and Hutchinson's (1990) partition theory and concluded that Williams's (1988) partition theory gave better results. Finally, they also fitted the mixed-mode failure criterion, suggested by Charalambides et al. (1992), to each set of data and found that all the failure loci could be described by this criterion.

Thouless (1990) experimentally investigated the fracture of an interface under mixed-mode loading. He bonded different thickness glass slides together with a thin adhesive layer and loaded the cracked end with equal and opposite shear forces. He analytically calculated the total ERR using beam theory and the ERR partition using Suo and Hutchinson's (1990) partition theory, based on two-dimensional elasticity. He found that when the specimens were viewed as being elastically homogeneous entities with a plane of weakness, a correlation could be observed between the apparent fracture toughness of the interface and the degree of mixed-mode loading. However, he also examined scanning-electron micrographs of the cracked surfaces and observed that the correlation could be attributed in part to a subtle change in the actual failure mechanism, namely, that in pure mode I conditions, the crack propagated entirely within the interface layer, but that in pure mode II conditions, the crack propagated towards the adhesive/glass interface.

Benzeggagh and Kenane (1996) carried out MMB tests on UD glass/epoxy laminated composites to investigate mixed-mode failure criteria for crack initiation and growth. For initiation, they measured the critical ERR using the compliance method (described in §1.4.1) and observed a different R-curve for different mixed-mode ratios. The higher the proportion of mode II ERR was, the greater was the value of the total critical ERR. For propagation, they defined two new quantities: an 'effective crack length' and a 'total fracture resistance', which is a different quantity to the total critical ERR. The effective crack length was calculated by means of the displacement and load at any point after the crack had begun to grow. They used an empirical relationship between the compliance and the effective crack length (observed from the initiation data) and from this derived the total fracture resistance. The total fracture resistance increased with crack length up to a plateau. The total fracture resistance was taken to be this plateaued value. Benzeggagh and Kenane then assessed the performance of a semi-empirical failure criterion. They were able to get good agreement between the experimental results and the criterion by selecting suitable values for the empirical parameters. Of particular note is the linear relationship they found between the mode ratio and the total fracture toughness.

1.4.3 Empirical failure loci

Failure criteria have so far been mentioned a few times. It is worth briefly commenting on some of the main important work in this area. The idea of failure criteria is rooted

in fracture mechanics. When a surface is created, there is a disruption of intermolecular bonds and the surface energy quantifies this. Surface energy is the excess energy per unit area at the surface compared to the bulk of the material. Surfaces must be in a higher state of energy than the bulk of a material because otherwise there would be a driving force for surfaces to be created (to find a more favourable, lower energy state) and then only surfaces would exist, which clearly isn't the case. As a crack grows, the energy that must be supplied to it must be balanced by the amount of energy dissipated due to the formation of new surfaces and other dissipative processes, such as plasticity. When the elastic energy released due to a potential increment of crack growth outweighs the demand for surface energy for the same crack growth, the introduction of a crack will lead to its propagation (Ewalds and Wanhill 1984).

When the critical ERR is reached, a crack will propagate. For cracks in isotropic homogeneous bodies, cracks tend to kink by an angle into a direction so that the advancing crack tip is a pure mode I fracture (Cotterell and Rice 1980, Gold'stein and Salganik 1974). After an experiment to measure the mode I fracture toughness, this simple criterion can be used with relative confidence. However, in cases where cracks exist on interfaces between materials, cracks are often constrained to propagate along these interfaces because they represent a plane of weakness. In interface cracking, since mixed-mode cracks propagating along an interface cannot kink into a mode I fracture, they therefore generally propagate as a mixed-mode fracture and can even propagate as a pure mode II fracture. Materials generally have a different fracture toughness in each mode. Therefore, in the case of mixed-mode propagation, the total fracture toughness is load-dependent and is not an intrinsic material property. The critical ERR is therefore a function of the mode partition and many failure criteria exist which attempt to describe the relationship between the mode partition and the critical ERR.

To the author's knowledge, no mathematical solution with a sound theoretical basis exists for a general failure criterion. Therefore, any existing failure criterion must be empirical. Many different failure criteria have been suggested for mixed-mode fracture toughness. Reeder (1992) gave a comprehensive review of them, however there remains plenty of uncertainty and confusion on the subject. This can be attributed to a number of reasons, including the many difficulties on all three of the analytical, numerical and experimental fronts, different failure responses in different materials, and criteria sometimes being based on inconsistent sets of toughness data (from different tests).

As discussed in §1.4.1, a number of different tests are required to measure pure mode fracture toughness and it is unclear what effect the different test configurations have on the measured failure response. Reeder and Crews Jr. (1990) developed the MMB test, which allows almost any combination of mode I and mode II loading to be tested with the same specimen configuration, thereby avoiding these inconsistencies.

Four simple failure criteria are shown in Fig. 1.5 in which the fracture toughness is represented by means of the ERR. The mode I and II components of ERR are denoted

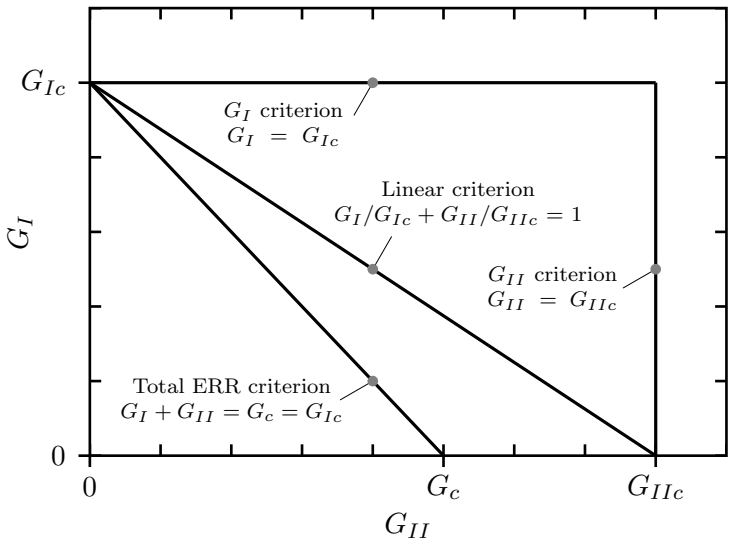

Figure 1.5: Mixed-mode fracture toughness diagrams for simple failure criteria.

by G_I and G_{II} respectively. The critical values of the mode I, II and the total ERR are denoted by G_{Ic}, G_{IIc} and G_c respectively. The simplest failure criteria assume that the mode I component, the mode II component or the total fracture toughness will stay constant as the mixed-mode ratio changes. The first of these criteria, the 'G_I criterion' in Fig. 1.5, assumes that only the mode I component of loading controls delamination growth and that therefore the mode II fracture toughness is infinite. The second, the 'G_{II} criterion' in Fig. 1.5, assumes the opposite. The third, the 'Total ERR criterion' in Fig. 1.5, assumes that a crack will extend if the total ERR reaches some critical value. It is therefore independent of the mode partition. The mode I and mode II fracture toughness are known to be quite different for most materials. The simplest criterion which allows for the effect of mixed-mode partition is the 'Linear criterion' in Fig. 1.5, which normalises each component of ERR against its critical pure-mode value. If the sum of these normalised components reaches 1, then the crack propagates. As shown, the failure locus is a straight line connecting the pure mode I and mode II fracture toughnesses.

Reeder (1992) used the MMB test to review the many different delamination criteria for a brittle epoxy composite, a toughened epoxy composite, and a thermoplastic composite. They also examined the fracture surfaces and observed that a change in failure mechanism may take place as the ratio of mode I to mode II ERR reaches unity. They therefore developed a new bilinear failure criterion. The responses of the two epoxy composites were best modelled with this new bilinear failure criterion. The failure response of the thermoplastic composites could be modelled well with both the bilinear criterion and a simple linear failure criterion.

The linear failure criterion is perhaps the one most often used in the literature. In addition there is plenty of data that either strongly supports the criterion or suggests criteria that are close to it.

Kutlu and Chang (1995) modelled graphite/epoxy composite panels containing multiple through-the-width delaminations. The panels were subjected to compression all the way through to the post-buckling region. Kutlu and Chang used the linear failure criterion in conjunction with the FEM and obtained excellent agreement with the experimental results, which exhibited complex behaviour, including both stable and unstable delamination propagation and the snap-through phenomenon. They compared load, displacement, strain, end-shortening and delamination length. Later Wang and Zhang (2009) using the finite strip method, and Harvey (2009) and Harvey and Wang (2012*d*) using the FEM, duplicated these results and the same linear failure criterion.

Other work that supports the linear failure criterion is given by Wu and Reuter Jr. (1965), Sanford and Stonesifer (1970), Jurf and Pipes (1982) and Donaldson (1985). Work which suggests failure criteria that are close to the linear one include Wu (1967), McKinney (1972) and Yoon and Hong (1990). Many other pieces of work fall into both categories.

As stated above, many other empirical failure criteria exist. Readers are directed to Reeder (1992) for a comprehensive review.

1.5 Conclusion

To the author's knowledge, all the significant work on the subject of mixed-mode partitioning has been reviewed. Analytical, numerical and experimental work has been considered. On each of these fronts, there have been significant difficulties and confusion. Since progress on one front is directly linked to progress on another, this has contributed to the fact that what appears to be a simple problem in LEFM—to partition the ERR for an interfacial crack into mode I and mode II components—has still not been completely understood and solved.

The findings from the literature are now briefly summarised. There are two main analytical approaches to mode partitioning: (1) a local approach based on an assumed square-root singular stress field at the crack tip; and (2) a global approach based on ERR. Under most circumstances, they give different partitions. Suo and Hutchinson's (1990) partition theory is the main theory in the first category and Williams's (1988) partition theory is the main one in the second category. Suo and Hutchinson claimed that Williams's theory contains 'conceptual errors'. Charalambides et al. claimed that Suo and Hutchinson's theory incorrectly assumes a dominant and square-root singular crack-tip field. Neither approach appears to provide universally good predictions of experimental results. Schapery and Davidson (1990) claimed that the problem cannot be solved using beam or plate theory.

Numerical work has been complicated by the presence of an oscillatory stress singularity at the crack tip, as predicted by two- and three-dimensional elasticity. This led to difficulties in obtaining converged values for the individual components of ERR. Modelling fractures using the FEM requires large numbers of elements in the crack tip region, which is

computationally expensive. Also, use of different types of finite element can give different ERR partitions.

Experimentally, only the total critical ERR can be measured. To partition the ERR, a mixed-mode partition theory has to be used, which may or may not be correct—there are many to choose from. There are also a large number of empirically observed failure criteria. There is no sound theoretical basis for any of them.

It is therefore concluded that there is great scope for research in the area of mixed-mode partitioning. The aims of this thesis are to: (1) clear up the confusion surrounding the fracture mode partition of one-dimensional mixed fracture modes; (2) reveal the underlying mechanics of the fracture mode partition; (3) to derive new and completely analytical mixed-mode partition theories with a clear physical basis and mechanical interpretation; and (4) to validate the new theories against numerical simulations and published data from experimental investigations.

To achieve these aims, three disciplines in structural mechanics will be combined: (1) fracture mechanics; (2) composite laminated plate theory; and (3) the FEM. The principles from these three disciplines that are essential for this thesis are presented in Chapters 2 and 3.

In Chapter 4, the most fundamental one-dimensional fracture problem is considered: one-dimensional fracture in layered isotropic homogeneous DCBs. Solving this problem, which has already caused considerable problems, will 'pave the way' for more complex problems and indeed, the work in Chapter 4 underpins the more complicated and elaborate theoretical development in the following chapters.

In Chapter 5, the degree of complexity is increased by considering one-dimensional delamination in laminated fibre-reinforced composite DCBs. The theories from Chapters 4 and 5 are then applied to more complex structures: layered isotropic homogeneous straight beam and plate structures and laminated fibre-reinforced composite straight beam structures.

Validation will be achieved by means of: (1) the FEM; and (2) comparisons with existing experimental results from published literature. By simultaneously approaching the problem of mixed-mode partitioning from all three fronts (analytical, numerical and experimental), the currently existing difficulties and confusion on each front, which have been described in this chapter, will be clarified and solved.

Experimental validation is the subject of Chapter 7. One-dimensional fracture in layered isotropic homogeneous DCBs with non-rigid elastic interfaces are considered in Chapter 8. Finally, conclusions are made in Chapter 9.

Chapter 2

Essential background theory

Contents

2.1 Introduction

The analytical modelling of delamination in laminated composites is governed by two main theoretical disciplines: (1) the mechanics of laminated composite plates and shells; and (2) fracture mechanics. In this chapter, the concepts from each of these disciplines (which are fundamental in the following chapters) are presented. Reddy (2004) and Jones (1999) are the main references for §2.2. Kundu (2008), Suo (2010) and Zehnder (2007) are the main references for §2.3.

2.2 Laminated composite materials

2.2.1 Basic concepts and terminology

Laminated composite materials consist of layers of at least two different materials that are bonded together. The fundamental building block of a laminated composite is called a 'lamina' or 'ply'. A lamina is a layer of material that can itself be composite, and can be flat, or curved as in a shell. Composite laminae are made up of individual materials referred to as constituent materials. There are two categories of constituent materials: matrix and reinforcement. At least one of each type is required. Typically, the matrix supports, protects and provides a means of distributing load among, and transmitting load between, the reinforcement materials; and the reinforcement imparts its mechanical and

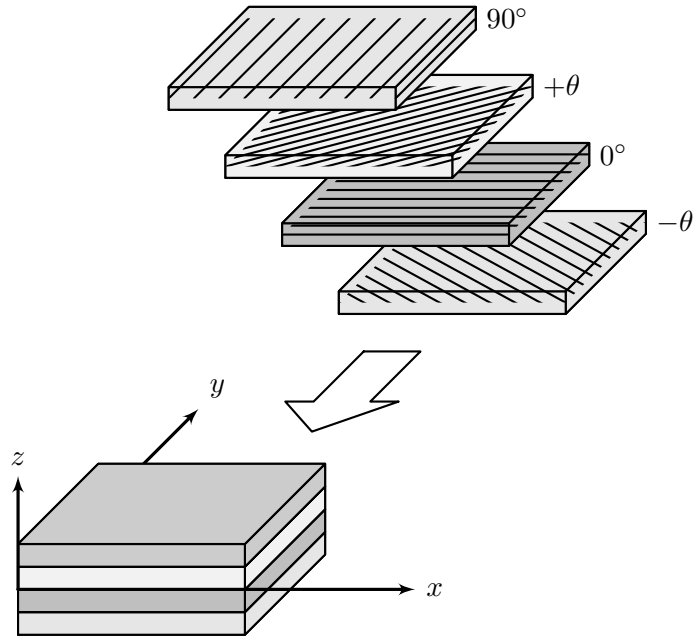

Figure 2.1: A laminate made up of UD laminae with different fibre orientations.

physical properties to enhance the overall material properties. Note however that some modern composite material can surely be found for which its constituent materials defy these prescriptive definitions.

Fibre-reinforced laminae consist of reinforcing fibres embedded in a matrix material. The matrix is typically metallic, ceramic or polymeric. The fibres can be continuous or discontinuous, and UD, bidirectional, woven or randomly distributed. The mechanism of load transfer is the shearing stress developed in the matrix and this is what prevents fibres from being pulled out once they have broken. This is clearly illustrated in whisker-reinforced composite laminae. In these materials, the fibres are short and randomly distributed, but by shear stress being transferred between the fibres through the matrix, the material is able to carry loads above the inherent matrix strength. Otherwise, this would not be possible.

A laminate is a stack of laminae, which have been arranged and oriented to achieve the desired thickness and stiffness characteristics. The layers of the laminate are usually bonded together by the same matrix material that is used in the individual laminae. This means that some of the matrix material in a lamina coats the surfaces and is used to bond it to adjacent lamina without adding more matrix material.

UD fibre-reinforced laminae have very high strength and modulus in the direction of the fibres, but have relatively low strength and modulus in the direction transverse to the fibres. They can be stacked so that the fibres in each lamina are oriented in the same or different directions, as shown in Fig. 2.1. The sequence of various orientations is termed the 'stacking sequence' or 'lay-up'. The difference in the mechanical properties of a lamina in different directions give designers the flexibility to tailor the stiffness and strength of a laminate to match structural requirements by choosing an appropriate lay-up.

In this work, it is fibre-reinforced laminated composites that are emphasised. Therefore the concepts derived in this section are applicable mainly to this type of material. These concepts however are often applicable to other forms of composite material, with some fairly obvious modifications.

Laminates made up of fibre-reinforced laminae suffer from a number of failure modes. On a local scale, there is fibre fracture and matrix cracking. Also, the mismatch of material properties between matrix and fibre may cause fibre debonding to take place. On a global scale there is ply splitting. Also, because of the mismatch of material properties between layers, the shear stresses produced between layers may cause delamination, that is, fracture at lamina interfaces. In this work, it is the delamination failure mode that is under consideration.

2.2.2 Constitutive equations of a lamina

In formulating the constitutive equations of a lamina, it is assumed that: (1) the lamina is a continuum, that is, no gaps exist in the material; and (2) it behaves linear elastically.

The first assumption means that it is only the macromechanical behaviour of a lamina that is considered. Although composite materials are inherently heterogeneous (meaning that the material properties are a function of position) on a microscopic scale, macroscopic material properties can nevertheless be derived from a weighted average of the material properties of its constituent materials (the fibre, the matrix and any voids). The composite material can then be assumed homogeneous (material properties are independent of position). Fibre-matrix debonding and fibre breakage are not resolved in such a formulation. For this, a micromechanical approach would be needed.

The second assumption implies that the generalised Hooke's law is valid. Constitutive equations characterise a material by its reaction to an applied load. Materials for which the constitutive behaviour is only a function of the current state of deformation are known as 'elastic'. If infinitesimal deformation is assumed then the equations of the generally non-linear elasticity theory become linearised, meaning that the relationships between the stresses and strains are linear. The linear elastic constitutive equations for infinitesimal deformation are referred to as the 'generalised Hooke's law'.

According to Cauchy, the stress at any point in a continuum is completely defined by nine component stresses: three orthogonal normal stresses and six orthogonal shear stresses. Fig. 2.2 shows the notation used for these stresses in Cartesian rectangular coordinates. Similarly, for strain at a point in a continuum, there are three orthogonal normal strains and six orthogonal shear strains. The stresses and strains at a point can both be expressed as second order tensors, as shown by the matrices in Eq. (2.1).

$$\left[\sigma\right] = \begin{bmatrix} \sigma_{11} & \tau_{12} & \tau_{13} \\ \tau_{12} & \sigma_{22} & \tau_{23} \\ \tau_{13} & \tau_{23} & \sigma_{33} \end{bmatrix} \quad \text{and} \quad \left[\varepsilon\right] = \begin{bmatrix} \varepsilon_{11} & \varepsilon_{12} & \varepsilon_{13} \\ \varepsilon_{12} & \varepsilon_{22} & \varepsilon_{23} \\ \varepsilon_{13} & \varepsilon_{23} & \varepsilon_{33} \end{bmatrix} \tag{2.1}$$

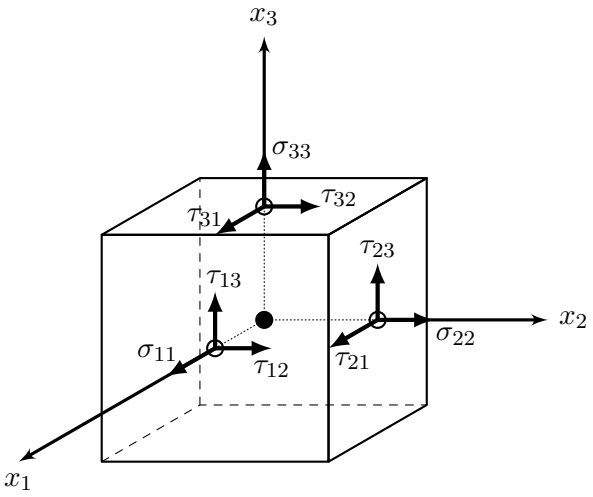

Figure 2.2: Notation for the stress components in Cartesian rectangular coordinates.

In Eq. (2.1), static equilibrium is assumed, making the stress tensor symmetric. The strain tensor is already symmetric by definition. Therefore the number of orthogonal shear stresses and strains reduces to three each, as shown. Now, for a completely anisotropic material, Hooke's law can be written in terms of 21 independent material stiffness coefficients

$$\begin{Bmatrix} \sigma_{11} \\ \sigma_{22} \\ \sigma_{33} \\ \tau_{23} \\ \tau_{13} \\ \tau_{12} \end{Bmatrix} = \begin{bmatrix} C_{11} & C_{12} & C_{13} & C_{14} & C_{15} & C_{16} \\ C_{12} & C_{22} & C_{23} & C_{24} & C_{25} & C_{26} \\ C_{13} & C_{23} & C_{33} & C_{34} & C_{35} & C_{36} \\ C_{14} & C_{24} & C_{34} & C_{44} & C_{45} & C_{46} \\ C_{15} & C_{25} & C_{35} & C_{45} & C_{55} & C_{56} \\ C_{16} & C_{26} & C_{36} & C_{46} & C_{56} & C_{66} \end{bmatrix} \begin{Bmatrix} \varepsilon_{11} \\ \varepsilon_{22} \\ \varepsilon_{33} \\ \gamma_{23} \\ \gamma_{13} \\ \gamma_{12} \end{Bmatrix} \tag{2.2}$$

where γ_{ij} are the engineering shear strains, equal to $2\varepsilon_{ij}$ and $\Big[C\Big]$ is the stiffness matrix. It is assumed that the stress-strain relationships in Eq. (2.2) are invertible. The compliance matrix is the inverse of the stiffness matrix, i.e. $\Big[S\Big] = \Big[C\Big]^{-1}$.

$$\begin{Bmatrix} \varepsilon_{11} \\ \varepsilon_{22} \\ \varepsilon_{33} \\ \gamma_{23} \\ \gamma_{13} \\ \gamma_{12} \end{Bmatrix} = \begin{bmatrix} S_{11} & S_{12} & S_{13} & S_{14} & S_{15} & S_{16} \\ S_{12} & S_{22} & S_{23} & S_{24} & S_{25} & S_{26} \\ S_{13} & S_{23} & S_{33} & S_{34} & S_{35} & S_{36} \\ S_{14} & S_{24} & S_{34} & S_{44} & S_{45} & S_{46} \\ S_{15} & S_{25} & S_{35} & S_{45} & S_{55} & S_{56} \\ S_{16} & S_{26} & S_{36} & S_{46} & S_{56} & S_{66} \end{bmatrix} \begin{Bmatrix} \sigma_{11} \\ \sigma_{22} \\ \sigma_{33} \\ \tau_{23} \\ \tau_{13} \\ \tau_{12} \end{Bmatrix} \tag{2.3}$$

When three mutually orthogonal planes of material symmetry exist, the number of elastic coefficients drops to nine. Such materials are called 'orthotropic'. The stress-strain

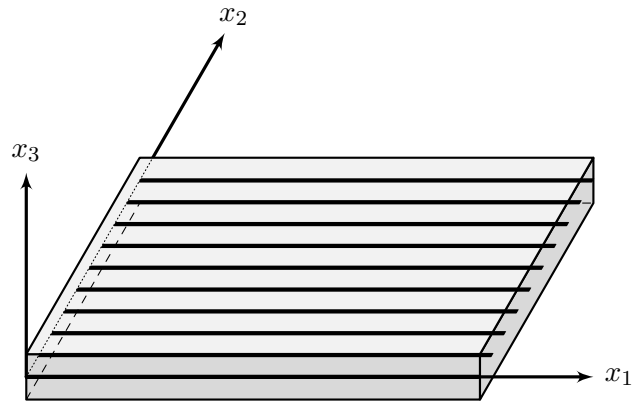

Figure 2.3: The principal material coordinate system (x_1, x_2, x_3) for a UD fibre-reinforced lamina.

relationships for orthotropic materials take the form

$$\begin{Bmatrix} \sigma_{11} \\ \sigma_{22} \\ \sigma_{33} \\ \tau_{23} \\ \tau_{13} \\ \tau_{12} \end{Bmatrix} = \begin{bmatrix} C_{11} & C_{12} & C_{13} & 0 & 0 & 0 \\ C_{12} & C_{22} & C_{23} & 0 & 0 & 0 \\ C_{13} & C_{23} & C_{33} & 0 & 0 & 0 \\ 0 & 0 & 0 & C_{44} & 0 & 0 \\ 0 & 0 & 0 & 0 & C_{55} & 0 \\ 0 & 0 & 0 & 0 & 0 & C_{66} \end{bmatrix} \begin{Bmatrix} \varepsilon_{11} \\ \varepsilon_{22} \\ \varepsilon_{33} \\ \gamma_{23} \\ \gamma_{13} \\ \gamma_{12} \end{Bmatrix} \tag{2.4}$$

and the strain-stress relationships are given by

$$\begin{Bmatrix} \varepsilon_{11} \\ \varepsilon_{22} \\ \varepsilon_{33} \\ \gamma_{23} \\ \gamma_{13} \\ \gamma_{12} \end{Bmatrix} = \begin{bmatrix} S_{11} & S_{12} & S_{13} & 0 & 0 & 0 \\ S_{12} & S_{22} & S_{23} & 0 & 0 & 0 \\ S_{13} & S_{23} & S_{33} & 0 & 0 & 0 \\ 0 & 0 & 0 & S_{44} & 0 & 0 \\ 0 & 0 & 0 & 0 & S_{55} & 0 \\ 0 & 0 & 0 & 0 & 0 & S_{66} \end{bmatrix} \begin{Bmatrix} \sigma_{11} \\ \sigma_{22} \\ \sigma_{33} \\ \tau_{23} \\ \tau_{13} \\ \tau_{12} \end{Bmatrix} \tag{2.5}$$

UD fibre-reinforced laminae are treated as orthotropic materials. The principal material coordinate axis x_1 is taken to be parallel to the fibre; the x_2 axis is perpendicular to the fibre direction in the plane of the lamina; and the x_3 axis is perpendicular to the plane of the lamina, as shown in Fig. 2.3. The material properties are typically determined experimentally using appropriate test specimens made from the material. To characterise a UD lamina, the required engineering parameters are the Young's moduli in the 1, 2 and 3 material directions, denoted by E_1, E_2 and E_3 respectively; the shear moduli in the 2-3, 1-3 and 1-2 planes, denoted by μ_{23}, μ_{13} and μ_{12} respectively; and the Poisson's ratios ν_{23}, ν_{13} and ν_{12}. The Poisson's ratio ν_{ij} is defined as the ratio of the transverse strain in the jth direction to the axial strain in the ith direction when stressed in the ith direction. The

compliance matrix in Eq. (2.5) therefore becomes

$$\Big[S\Big] = \begin{bmatrix} \frac{1}{E_1} & -\frac{\nu_{21}}{E_2} & -\frac{\nu_{31}}{E_3} & 0 & 0 & 0 \\ -\frac{\nu_{12}}{E_1} & \frac{1}{E_3} & -\frac{\nu_{32}}{E_3} & 0 & 0 & 0 \\ -\frac{\nu_{13}}{E_1} & -\frac{\nu_{23}}{E_2} & \frac{1}{E_3} & 0 & 0 & 0 \\ 0 & 0 & 0 & \frac{1}{\mu_{23}} & 0 & 0 \\ 0 & 0 & 0 & 0 & \frac{1}{\mu_{13}} & 0 \\ 0 & 0 & 0 & 0 & 0 & \frac{1}{\mu_{12}} \end{bmatrix} \tag{2.6}$$

for a UD fibre-reinforced lamina. Finally, since the compliance matrix $\Big[S\Big]$ is symmetric, this implies that the following reciprocal relationships hold:

$$\frac{\nu_{21}}{E_2} = \frac{\nu_{12}}{E_1}; \quad \frac{\nu_{31}}{E_3} = \frac{\nu_{13}}{E_1} \quad \text{and} \quad \frac{\nu_{32}}{E_3} = \frac{\nu_{23}}{E_2} \tag{2.7}$$

2.2.3 Transformation of stresses and strains

Since fibre-reinforced laminated composites have several laminae, each with a different orientation of its principal material coordinate system, the principal material coordinate system does not generally coincide with the coordinate system of the laminate (the global coordinate system). Therefore, the stresses and strains in the principal material coordinate system of each lamina must be transformed to the corresponding quantities in the global coordinate system.

Let (x, y, z) denote the global coordinate system and let (x_1, x_2, x_3) denote the principal material coordinate system for a lamina. The x_3 axis is parallel to the z-axis; the x_1-axis lies in the plane of the lamina and is oriented at an angle of $+\theta$ counterclockwise to the x-axis, as shown in Fig. 2.4. A material point in the global coordinate system (x, y, z) is transformed into the principal material coordinate system of a lamina (x_1, x_2, x_3) by

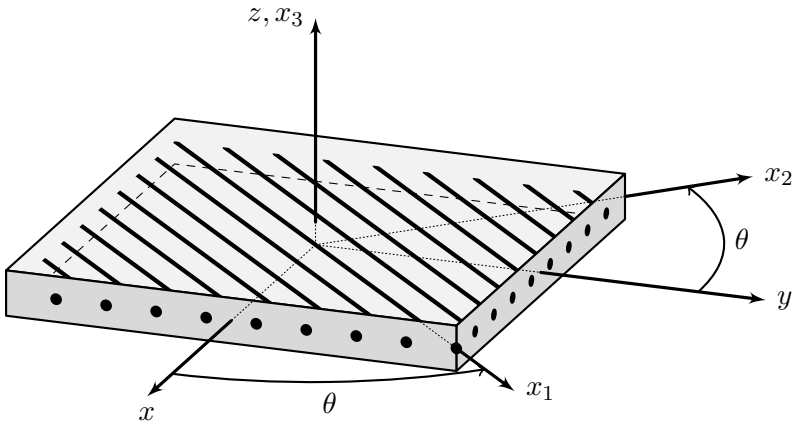

Figure 2.4: The principal material coordinate system (x, y, z) and the global coordinate system (x_1, x_2, x_3) for a UD fibre-reinforced lamina.

means of the $\left[L\right]$ matrix as follows:

$$\begin{Bmatrix} x_1 \\ x_2 \\ x_3 \end{Bmatrix} = \begin{bmatrix} \cos\theta & \sin\theta & 0 \\ -\sin\theta & \cos\theta & 0 \\ 0 & 0 & 1 \end{bmatrix} \begin{Bmatrix} x \\ y \\ z \end{Bmatrix} = \left[L\right] \begin{Bmatrix} x \\ y \\ z \end{Bmatrix} \tag{2.8}$$

The inverse of Eq. (2.8) is

$$\begin{Bmatrix} x \\ y \\ z \end{Bmatrix} = \begin{bmatrix} \cos\theta & -\sin\theta & 0 \\ \sin\theta & \cos\theta & 0 \\ 0 & 0 & 1 \end{bmatrix} \begin{Bmatrix} x_1 \\ x_2 \\ x_3 \end{Bmatrix} = \left[L\right]^T \begin{Bmatrix} x_1 \\ x_2 \\ x_3 \end{Bmatrix} \tag{2.9}$$

Note that the inverse of $\left[L\right]$ is equal to its transpose: $\left[L\right]^{-1} = \left[L\right]^T$. These transformation relationships are also valid for vectors in the two coordinate systems.

Now, consider the stress transformation. Let $\left[\sigma\right]_g$ and $\left[\sigma\right]_m$ be the stress tensors at a point in the global and principal material coordinate systems respectively. They are given by

$$\left[\sigma\right]_g = \begin{bmatrix} \sigma_{xx} & \tau_{xy} & \tau_{xz} \\ \tau_{xy} & \sigma_{yy} & \tau_{yz} \\ \tau_{xz} & \tau_{yz} & \tau_{zz} \end{bmatrix} \quad \text{and} \quad \left[\sigma\right]_m = \begin{bmatrix} \sigma_{11} & \tau_{12} & \tau_{13} \\ \tau_{12} & \sigma_{22} & \tau_{23} \\ \tau_{13} & \tau_{23} & \sigma_{33} \end{bmatrix} \tag{2.10}$$

A component of stress can be considered to be a force acting on a unit normal area. Therefore, for the transformation of a stress component, both the direction of the force and the area it acts on need to be transformed, that is, there are two transformations. The resulting relationships between $\left[\sigma\right]_g$ and $\left[\sigma\right]_m$ are

$$\left[\sigma\right]_m = \left[L\right]\left[\sigma\right]_g\left[L\right]^T \quad \text{and} \quad \left[\sigma\right]_g = \left[L\right]^T\left[\sigma\right]_m\left[L\right] \tag{2.11}$$

Carrying out the matrix multiplications in Eq. (2.11) and rearranging the equations gives

$$\begin{Bmatrix} \sigma_{xx} \\ \sigma_{yy} \\ \sigma_{zz} \\ \tau_{yz} \\ \tau_{xz} \\ \tau_{xy} \end{Bmatrix} = \begin{bmatrix} \cos^2\theta & \sin^2\theta & 0 & 0 & 0 & -\sin 2\theta \\ \sin^2\theta & \cos^2\theta & 0 & 0 & 0 & \sin 2\theta \\ 0 & 0 & 1 & 0 & 0 & 0 \\ 0 & 0 & 0 & \cos\theta & \sin\theta & 0 \\ 0 & 0 & 0 & -\sin\theta & \cos\theta & 0 \\ \sin\theta\cos\theta & -\sin\theta\cos\theta & 0 & 0 & 0 & \cos^2\theta - \sin^2\theta \end{bmatrix} \begin{Bmatrix} \sigma_{11} \\ \sigma_{22} \\ \sigma_{33} \\ \tau_{23} \\ \tau_{13} \\ \tau_{12} \end{Bmatrix} \tag{2.12}$$

or

$$\left\{\sigma\right\}_g = \left[T\right]\left\{\sigma\right\}_m \tag{2.13}$$

The inverse relationship is

$$\left\{\sigma\right\}_m = \left[R\right]\left\{\sigma\right\}_g \tag{2.14}$$

where

$$\Big[R\Big] = \begin{bmatrix} \cos^2\theta & \sin^2\theta & 0 & 0 & 0 & \sin 2\theta \\ \sin^2\theta & \cos^2\theta & 0 & 0 & 0 & -\sin 2\theta \\ 0 & 0 & 1 & 0 & 0 & 0 \\ 0 & 0 & 0 & \cos\theta & -\sin\theta & 0 \\ 0 & 0 & 0 & \sin\theta & \cos\theta & 0 \\ -\sin\theta\cos\theta & \sin\theta\cos\theta & 0 & 0 & 0 & \cos^2\theta - \sin^2\theta \end{bmatrix} \tag{2.15}$$

Now, consider the strain transformation. Let $\Big[\varepsilon\Big]_g$ and $\Big[\varepsilon\Big]_m$ be the strain tensors at a point in the global and principal material coordinate systems respectively. They are given by

$$\Big[\varepsilon\Big]_g = \begin{bmatrix} \varepsilon_{xx} & \varepsilon_{xy} & \varepsilon_{xz} \\ \varepsilon_{xy} & \varepsilon_{yy} & \varepsilon_{yz} \\ \varepsilon_{xz} & \varepsilon_{yz} & \varepsilon_{zz} \end{bmatrix} \quad \text{and} \quad \Big[\varepsilon\Big]_m = \begin{bmatrix} \varepsilon_{11} & \varepsilon_{12} & \varepsilon_{13} \\ \varepsilon_{12} & \varepsilon_{22} & \varepsilon_{23} \\ \varepsilon_{13} & \varepsilon_{23} & \varepsilon_{33} \end{bmatrix} \tag{2.16}$$

Eq. (2.11) is also valid for strain transformations.

$$\Big[\varepsilon\Big]_m = \Big[L\Big]\Big[\varepsilon\Big]_g\Big[L\Big]^T \quad \text{and} \quad \Big[\varepsilon\Big]_g = \Big[L\Big]^T\Big[\varepsilon\Big]_m\Big[L\Big] \tag{2.17}$$

Carrying out the matrix multiplications in Eq. (2.17) and rearranging the equations gives

$$\begin{Bmatrix} \varepsilon_{xx} \\ \varepsilon_{yy} \\ \varepsilon_{zz} \\ \gamma_{yz} \\ \gamma_{xz} \\ \gamma_{xy} \end{Bmatrix} = \begin{bmatrix} \cos^2\theta & \sin^2\theta & 0 & 0 & 0 & -\sin\theta\cos\theta \\ \sin^2\theta & \cos^2\theta & 0 & 0 & 0 & \sin\theta\cos\theta \\ 0 & 0 & 1 & 0 & 0 & 0 \\ 0 & 0 & 0 & \cos\theta & \sin\theta & 0 \\ 0 & 0 & 0 & -\sin\theta & \cos\theta & 0 \\ \sin 2\theta & -\sin 2\theta & 0 & 0 & 0 & \cos^2\theta - \sin^2\theta \end{bmatrix} \begin{Bmatrix} \varepsilon_{11} \\ \varepsilon_{22} \\ \varepsilon_{33} \\ \gamma_{23} \\ \gamma_{13} \\ \gamma_{12} \end{Bmatrix} \tag{2.18}$$

or

$$\Big\{\varepsilon\Big\}_g = \Big[R\Big]^T\Big\{\varepsilon\Big\}_m \tag{2.19}$$

Recall that $\gamma_{ij} = 2\varepsilon_{ij}$. Similarly $\gamma_{yz} = 2\varepsilon_{yz}$, etc. The inverse relationship is

$$\Big\{\varepsilon\Big\}_m = \Big[T\Big]^T\Big\{\varepsilon\Big\}_g \tag{2.20}$$

Note that in contrast to in Eqs. (2.13) and (2.14), $\Big[T\Big]$ and $\Big[R\Big]$ in Eqs. (2.19) and (2.20) are transposed.

Finally in this section, it remains to derive the transformed stress-strain and strain-stress relationships for a lamina. Let

$$\Big\{\sigma\Big\}_g = \Big[\overline{C}\Big]\Big\{\varepsilon\Big\}_g \quad \text{and} \quad \Big\{\varepsilon\Big\}_g = \Big[\overline{S}\Big]\Big\{\sigma\Big\}_g \tag{2.21}$$

where $\left[\overline{C}\right]$ is the transformed stiffness matrix and $\left[\overline{S}\right]$ is the transformed compliance matrix. They can be derived as follows:

$$\left\{\sigma\right\}_g = \left[T\right]\left\{\sigma\right\}_m = \left[T\right]\left[C\right]\left\{\varepsilon\right\}_m = \left[T\right]\left[C\right]\left[T\right]^T\left\{\varepsilon\right\}_g = \left[\overline{C}\right]\left\{\varepsilon\right\}_g \tag{2.22}$$

$$\left\{\varepsilon\right\}_g = \left[R\right]^T\left\{\varepsilon\right\}_m = \left[R\right]^T\left[S\right]\left\{\sigma\right\}_m = \left[R\right]^T\left[S\right]\left[R\right]\left\{\sigma\right\}_g = \left[\overline{S}\right]\left\{\sigma\right\}_g \tag{2.23}$$

Therefore

$$\left[\overline{C}\right] = \left[T\right]\left[C\right]\left[T\right]^T \quad \text{and} \quad \left[\overline{S}\right] = \left[R\right]^T\left[S\right]\left[R\right] \tag{2.24}$$

For an orthotropic material, the material stiffness matrix in Eq. (2.4) transforms to

$$\left[\overline{C}\right] = \begin{bmatrix} \overline{C}_{11} & \overline{C}_{12} & \overline{C}_{13} & 0 & 0 & \overline{C}_{16} \\ \overline{C}_{12} & \overline{C}_{22} & \overline{C}_{23} & 0 & 0 & \overline{C}_{26} \\ \overline{C}_{13} & \overline{C}_{23} & \overline{C}_{33} & 0 & 0 & \overline{C}_{36} \\ 0 & 0 & 0 & \overline{C}_{44} & \overline{C}_{45} & 0 \\ 0 & 0 & 0 & \overline{C}_{45} & \overline{C}_{55} & 0 \\ \overline{C}_{16} & \overline{C}_{26} & \overline{C}_{36} & 0 & 0 & \overline{C}_{66} \end{bmatrix} \tag{2.25}$$

Similarly, the material compliance matrix for an orthotropic material, given in Eq. (2.5), is transformed to

$$\left[\overline{S}\right] = \begin{bmatrix} \overline{S}_{11} & \overline{S}_{12} & \overline{S}_{13} & 0 & 0 & \overline{S}_{16} \\ \overline{S}_{12} & \overline{S}_{22} & \overline{S}_{23} & 0 & 0 & \overline{S}_{26} \\ \overline{S}_{13} & \overline{S}_{23} & \overline{S}_{33} & 0 & 0 & \overline{S}_{36} \\ 0 & 0 & 0 & \overline{S}_{44} & \overline{S}_{45} & 0 \\ 0 & 0 & 0 & \overline{S}_{45} & \overline{S}_{55} & 0 \\ \overline{S}_{16} & \overline{S}_{26} & \overline{S}_{36} & 0 & 0 & \overline{S}_{66} \end{bmatrix} \tag{2.26}$$

The transformed elastic coefficients $\overline{C}_{ij}$ and $\overline{S}_{ij}$ are calculated by means of Eq. (2.24).

2.2.4 Classical laminated plate theory

Classical laminated plate theory is an extension of classical plate theory (Timoshenko and Woinowsky-Krieger 1959) to laminated composites. Therefore, the Kirchhoff hypothesis holds and it is assumed that: (1) straight lines perpendicular to the mid-surface (transverse normals) before deformation remain straight after deformation; (2) transverse normals are inextensible; and (3) the transverse normals remain perpendicular to the mid-surface after deformation.

The first two assumptions imply that the transverse displacement does not depend on the transverse coordinate and that the transverse normal strain ε_{zz} is zero. The third assumption results in zero transverse shear strains, $\gamma_{xz} = \gamma_{yz} = 0$. From the constitutive equations in Eq. (2.5), it is clear that for an orthotropic layer the transverse shear stresses therefore are also zero, i.e. $\tau_{xz} = \tau_{yz} = 0$, although from the equilibrium equations they

are not zero. From practical considerations, a thin or moderately thick plate is in a state of plane stress because of the thickness being small compared to the in-plane dimensions. Therefore full plane stress can be assumed and so the transverse normal stress σ_{zz} also becomes zero.

The plane-stress reduced constitutive relations are now derived. From Eqs. (2.4) and (2.6), for an orthotropic lamina we have

$$\begin{Bmatrix}\sigma_{11}\\ \sigma_{22}\\ \tau_{12}\end{Bmatrix} = \begin{bmatrix}Q_{11} & Q_{12} & 0\\ Q_{12} & Q_{22} & 0\\ 0 & 0 & Q_{66}\end{bmatrix}\begin{Bmatrix}\varepsilon_{11}\\ \varepsilon_{22}\\ \gamma_{12}\end{Bmatrix} = \begin{bmatrix}\frac{1}{E_1} & -\frac{\nu_{21}}{E_2} & 0\\ -\frac{\nu_{12}}{E_1} & \frac{1}{E_2} & 0\\ 0 & 0 & \frac{1}{\mu_{12}}\end{bmatrix}^{-1}\begin{Bmatrix}\varepsilon_{11}\\ \varepsilon_{22}\\ \gamma_{12}\end{Bmatrix} \tag{2.27}$$

The Q_{ij} quantities are the *reduced* stiffness coefficients. They replace the C_{ij} quantities in Eq. (2.4). Inverting the matrix in Eq. (2.27) gives

$$Q_{11} = \frac{E_1}{1-\nu_{12}\nu_{21}};\quad Q_{12} = \frac{\nu_{12}E_2}{1-\nu_{12}\nu_{21}};\quad Q_{22} = \frac{E_2}{1-\nu_{12}\nu_{21}}\quad\text{and}\quad Q_{66} = \mu_{12} \tag{2.28}$$

Reducing Eq. (2.12) in order to get the transformation matrix that will transform Eq. (2.27) into the global coordinate system, gives

$$\Big[T\Big] = \begin{bmatrix}\cos^2\theta & \sin^2\theta & -\sin 2\theta\\ \sin^2\theta & \cos^2\theta & \sin 2\theta\\ \sin\theta\cos\theta & -\sin\theta\cos\theta & \cos^2\theta-\sin^2\theta\end{bmatrix} \tag{2.29}$$

From Eq. (2.24), the transformed reduced stiffness matrix is therefore

$$\Big[\overline{Q}\Big] = \Big[T\Big]\Big[Q\Big]\Big[T\Big]^T = \begin{bmatrix}\overline{Q}_{11} & \overline{Q}_{12} & \overline{Q}_{16}\\ \overline{Q}_{12} & \overline{Q}_{22} & \overline{Q}_{26}\\ \overline{Q}_{16} & \overline{Q}_{26} & \overline{Q}_{66}\end{bmatrix} \tag{2.30}$$

where, by carrying out the matrix multiplication, the $\overline{Q}_{ij}$ transformed reduced stiffness quantities are easily calculated to be

$$\begin{aligned}
\overline{Q}_{11} &= Q_{11}\cos^4\theta + 2\left(Q_{12}+2Q_{66}\right)\sin^2\theta\cos^2\theta + Q_{22}\sin^4\theta\\
\overline{Q}_{12} &= \left(Q_{11}+Q_{22}-4Q_{66}\right)\sin^2\theta\cos^2\theta + Q_{12}\left(\sin^4\theta+\cos^4\theta\right)\\
\overline{Q}_{22} &= Q_{11}\sin^4\theta + 2\left(Q_{12}+2Q_{66}\right)\sin^2\theta\cos^2\theta + Q_{22}\cos^4\theta\\
\overline{Q}_{16} &= \left(Q_{11}-Q_{12}-2Q_{66}\right)\sin\theta\cos^3\theta + \left(Q_{12}-Q_{22}+2Q_{66}\right)\sin^3\theta\cos\theta\\
\overline{Q}_{26} &= \left(Q_{11}-Q_{12}-2Q_{66}\right)\sin^3\theta\cos\theta + \left(Q_{12}-Q_{22}+2Q_{66}\right)\sin\theta\cos^3\theta\\
\overline{Q}_{66} &= \left(Q_{11}+Q_{22}-2Q_{12}-2Q_{66}\right)\sin^2\theta\cos^2\theta + Q_{66}\left(\sin^4\theta+\cos^4\theta\right)
\end{aligned} \tag{2.31}$$

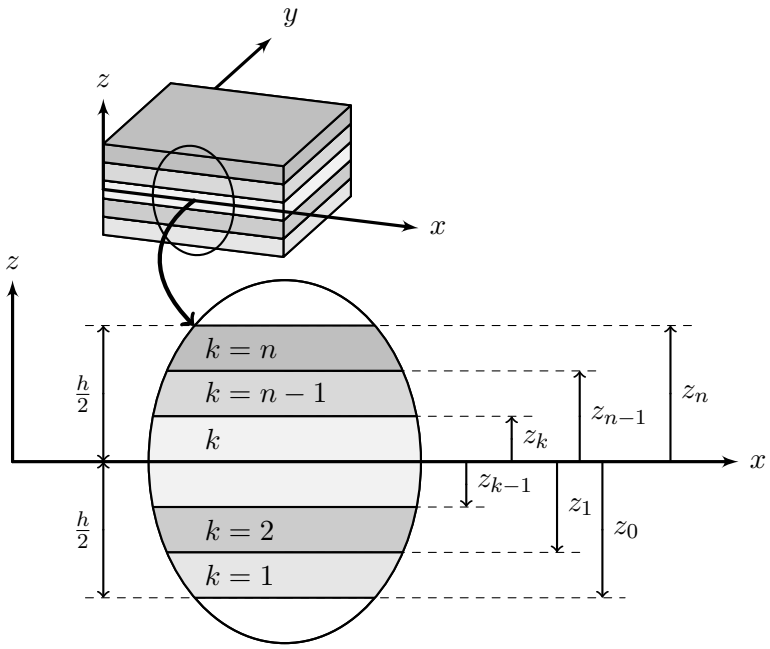

Figure 2.5: The coordinate system and layer numbering for a laminated plate.

Therefore, from Eq. (2.21), the plane-stress reduced constitutive relations for a classical orthotropic lamina are

$$\begin{Bmatrix} \sigma_{xx} \\ \sigma_{yy} \\ \tau_{xy} \end{Bmatrix} = \begin{bmatrix} \overline{Q}_{11} & \overline{Q}_{12} & \overline{Q}_{16} \\ \overline{Q}_{12} & \overline{Q}_{22} & \overline{Q}_{26} \\ \overline{Q}_{16} & \overline{Q}_{26} & \overline{Q}_{66} \end{bmatrix} \begin{Bmatrix} \varepsilon_{xx} \\ \varepsilon_{yy} \\ \gamma_{xy} \end{Bmatrix} \tag{2.32}$$

Consider a plate of total thickness h and composed of n orthotropic layers, as shown in Fig. 2.5. Although in lamination theory, the z-axis is typically taken positive downward from the mid-plane, for the purpose of maintaining a consistent coordinate system throughout this work, it is taken as positive upward. Fig. 2.6 shows the force and moment resultants on such a plate element which spans the thickness of a laminate. The quantities N_{xx}, N_{yy} and N_{xy} are the in-plane force resultants; M_{xx}, M_{yy} and M_{xy} are the moment resultants; and Q_x and Q_y are the transverse force resultants. Note that the transverse force resultants are not considered in classical plate theory, as discussed above. They are shown in the figure because they are referred to later in the first-order plate theory.

With reference to Figs. 2.5 and 2.6, integrating through the thickness gives the following for the force resultants on a laminated plate element:

$$\begin{Bmatrix} N_{xx} \\ N_{yy} \\ N_{xy} \end{Bmatrix} = \int_{-\frac{h}{2}}^{\frac{h}{2}} \begin{Bmatrix} \sigma_{xx} \\ \sigma_{yy} \\ \tau_{xy} \end{Bmatrix} dz = \sum_{k=1}^{n} \int_{z_{k-1}}^{z_k} \begin{bmatrix} \overline{Q}_{11} & \overline{Q}_{12} & \overline{Q}_{16} \\ \overline{Q}_{12} & \overline{Q}_{22} & \overline{Q}_{26} \\ \overline{Q}_{16} & \overline{Q}_{26} & \overline{Q}_{66} \end{bmatrix}^{(k)} \begin{Bmatrix} \varepsilon_{xx} \\ \varepsilon_{yy} \\ \gamma_{xy} \end{Bmatrix}^{(k)} dz \tag{2.33}$$

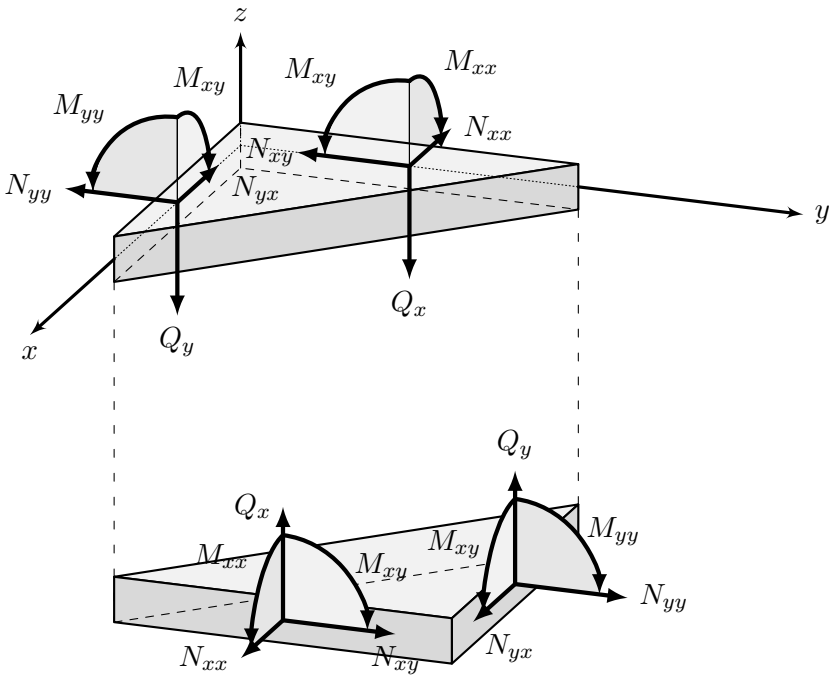

Figure 2.6: Force and moment resultants on a plate element.

Similarly, for the moments resultants on a laminated plate element, the following is obtained:

$$\begin{Bmatrix} M_{xx} \\ M_{yy} \\ M_{xy} \end{Bmatrix} = \int_{-\frac{h}{2}}^{\frac{h}{2}} \begin{Bmatrix} \sigma_{xx} \\ \sigma_{yy} \\ \tau_{xy} \end{Bmatrix} z\, dz = \sum_{k=1}^{n} \int_{z_{k-1}}^{z_k} \begin{bmatrix} \overline{Q}_{11} & \overline{Q}_{12} & \overline{Q}_{16} \\ \overline{Q}_{12} & \overline{Q}_{22} & \overline{Q}_{26} \\ \overline{Q}_{16} & \overline{Q}_{26} & \overline{Q}_{66} \end{bmatrix}^{(k)} \begin{Bmatrix} \varepsilon_{xx} \\ \varepsilon_{yy} \\ \gamma_{xy} \end{Bmatrix}^{(k)} z\, dz \tag{2.34}$$

The superscript (k) denotes quantities for the kth lamina. Now the strain fields are required. The Kirchhoff hypothesis requires the u, v and w displacements, which are directed along the x, y, and z coordinates respectively, to be (see Fig. 2.7)

$$u = u^0 - z\frac{dw^0}{dx}; \quad v = v^0 - z\frac{dw^0}{dy} \quad \text{and} \quad w = w^0 \tag{2.35}$$

where u^0, v^0 and w^0 are the corresponding displacements of a material point lying on the xy-plane, that is, the mid-plane. The strains in Eqs. (2.33) and (2.34) can now be calculated using the linear strain-displacement relations for infinitesimal strain. They are

$$\begin{aligned} \varepsilon_{xx} &= \frac{\partial u}{\partial x} = \frac{\partial u^0}{\partial x} - z\frac{\partial^2 w^0}{\partial x^2} = \varepsilon^0_{xx} + zk_x \\ \varepsilon_{yy} &= \frac{\partial v}{\partial y} = \frac{\partial v^0}{\partial y} - z\frac{\partial^2 w^0}{\partial y^2} = \varepsilon^0_{yy} + zk_y \\ \gamma_{xy} &= \frac{\partial u}{\partial y} + \frac{\partial v}{\partial x} = \frac{\partial u^0}{\partial y} + \frac{\partial v^0}{\partial x} - 2z\frac{d^2 w^0}{\partial x \partial y} = \gamma^0_{xy} + zk_{xy} \end{aligned} \tag{2.36}$$

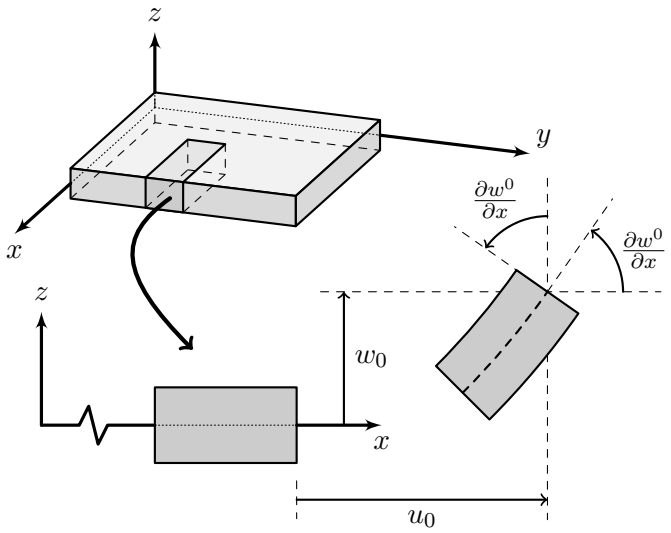

Figure 2.7: Undeformed and deformed geometries of an edge of a plate under the Kirchhoff assumptions.

where ε^0_{xx}, ε^0_{yy} and γ^0_{xy} are the membrane strains and k_x, k_y and k_{xy} are the 'curvatures'. They are defined as

$$\begin{aligned} \varepsilon^0_{xx} &= \frac{\partial u^0}{\partial x}; \quad \varepsilon^0_{yy} = \frac{\partial v^0}{\partial y}; \quad \gamma^0_{xy} = \frac{\partial u^0}{\partial y} + \frac{\partial v^0}{\partial x} \\ k_x &= -\frac{\partial^2 w^0}{\partial x^2}; \quad k_y = -\frac{\partial^2 w^0}{\partial y^2} \quad \text{and} \quad k_{xy} = -2\frac{d^2 w^0}{\partial x \partial y} \end{aligned} \tag{2.37}$$

The force resultant-strain and moment resultant-strain relationships for a laminated composite plate are obtained by substituting Eq. (2.36) into Eqs. (2.33) and (2.34).

$$\begin{Bmatrix} N_{xx} \\ N_{yy} \\ N_{xy} \end{Bmatrix} = \sum_{k=1}^{n} \begin{bmatrix} \overline{Q}_{11} & \overline{Q}_{12} & \overline{Q}_{16} \\ \overline{Q}_{12} & \overline{Q}_{22} & \overline{Q}_{26} \\ \overline{Q}_{16} & \overline{Q}_{26} & \overline{Q}_{66} \end{bmatrix}^{(k)} \left(\int_{z_{k-1}}^{z_k} \begin{Bmatrix} \varepsilon^0_{xx} \\ \varepsilon^0_{yy} \\ \gamma^0_{xy} \end{Bmatrix} dz + \int_{z_{k-1}}^{z_k} \begin{Bmatrix} k_x \\ k_y \\ k_{xy} \end{Bmatrix} z \, dz \right) \tag{2.38}$$

$$\begin{Bmatrix} M_{xx} \\ M_{yy} \\ M_{xy} \end{Bmatrix} = \sum_{k=1}^{n} \begin{bmatrix} \overline{Q}_{11} & \overline{Q}_{12} & \overline{Q}_{16} \\ \overline{Q}_{12} & \overline{Q}_{22} & \overline{Q}_{26} \\ \overline{Q}_{16} & \overline{Q}_{26} & \overline{Q}_{66} \end{bmatrix}^{(k)} \left(\int_{z_{k-1}}^{z_k} \begin{Bmatrix} \varepsilon^0_{xx} \\ \varepsilon^0_{yy} \\ \gamma^0_{xy} \end{Bmatrix} z \, dz + \int_{z_{k-1}}^{z_k} \begin{Bmatrix} k_x \\ k_y \\ k_{xy} \end{Bmatrix} z^2 \, dz \right) \tag{2.39}$$

By defining the following stiffness quantities

$$\begin{aligned} A_{ij} &= \sum_{k=1}^{n} \overline{Q}^{(k)}_{ij} \left(z_k - z_{k-1} \right) \\ B_{ij} &= \frac{1}{2} \sum_{k=1}^{n} \overline{Q}^{(k)}_{ij} \left(z_k^2 - z_{k-1}^2 \right) \end{aligned}$$

$$D_{ij} = \frac{1}{3}\sum_{k=1}^{n} \overline{Q}_{ij}^{(k)} \left(z_k^3 - z_{k-1}^3\right) \tag{2.40}$$

where A_{ij} are the extensional stiffnesses, B_{ij} are the coupling stiffnesses and D_{ij} are the bending stiffnesses, the laminate constitutive equations can be written as

$$\begin{Bmatrix} N_{xx} \\ N_{yy} \\ N_{xy} \\ M_{xx} \\ M_{yy} \\ M_{xy} \end{Bmatrix} = \begin{bmatrix} A_{11} & A_{12} & A_{16} & B_{11} & B_{12} & B_{16} \\ A_{12} & A_{22} & A_{26} & B_{12} & B_{22} & B_{26} \\ A_{16} & A_{26} & A_{66} & B_{16} & B_{26} & B_{66} \\ B_{11} & B_{12} & B_{16} & D_{11} & D_{12} & D_{16} \\ B_{12} & B_{22} & B_{26} & D_{12} & D_{22} & D_{26} \\ B_{16} & B_{26} & B_{66} & D_{16} & D_{26} & D_{66} \end{bmatrix} \begin{Bmatrix} \varepsilon_{xx}^0 \\ \varepsilon_{yy}^0 \\ \gamma_{xy}^0 \\ k_x \\ k_y \\ k_{xy} \end{Bmatrix} \tag{2.41}$$

2.2.5 First-order laminated plate theory

In the FSDT for plates, the Kirchhoff hypothesis is relaxed by removing the third assumption, that is, the transverse normals no longer remain perpendicular to the mid-surface after deformation, as shown in Fig. 2.8. This amounts to including transverse shear strains γ_{xz} and γ_{yz} in the theory. Under the remaining assumptions and restrictions, the theory is often called the Mindlin–Reissner plate theory (Mindlin 1951) and the displacement field is of the form

$$u = u^0 - z\psi_x; \quad v = v^0 - z\psi_y \quad \text{and} \quad w = w^0 \tag{2.42}$$

where ψ_x and ψ_y are the rotations of transverse normals about the y- and x-axes respectively. Using the linear strain-displacement relations for infinitesimal strain, the strains in Eqs. (2.33) and (2.34) are

$$\begin{aligned} \varepsilon_{xx} &= \frac{\partial u}{\partial x} = \frac{\partial u^0}{\partial x} - z\frac{\partial \psi_x}{\partial x} = \varepsilon_{xx}^0 - z\frac{\partial \psi_x}{\partial x} \\ \varepsilon_{yy} &= \frac{\partial v}{\partial y} = \frac{\partial v^0}{\partial y} - z\frac{\partial \psi_y}{\partial y} = \varepsilon_{yy}^0 - z\frac{\partial \psi_y}{\partial y} \\ \gamma_{xy} &= \frac{\partial u}{\partial y} + \frac{\partial v}{\partial x} = \gamma_{xy}^0 - z\frac{\partial \psi_x}{\partial y} - z\frac{\partial \psi_y}{\partial x} \end{aligned} \tag{2.43}$$

and the out-of-plane strains are

$$\begin{aligned} \gamma_{xz} &= \frac{\partial u}{\partial z} + \frac{\partial w}{\partial x} = \frac{\partial w^0}{\partial x} - \psi_x \\ \gamma_{yz} &= \frac{\partial v}{\partial z} + \frac{\partial w}{\partial y} = \frac{\partial w^0}{\partial y} - \psi_y \end{aligned} \tag{2.44}$$

Since transverse shear strains and stresses are accounted for in the FSDT, the only condition to be applied to the lamina constitutive equations is that σ_{zz} is zero. Therefore,

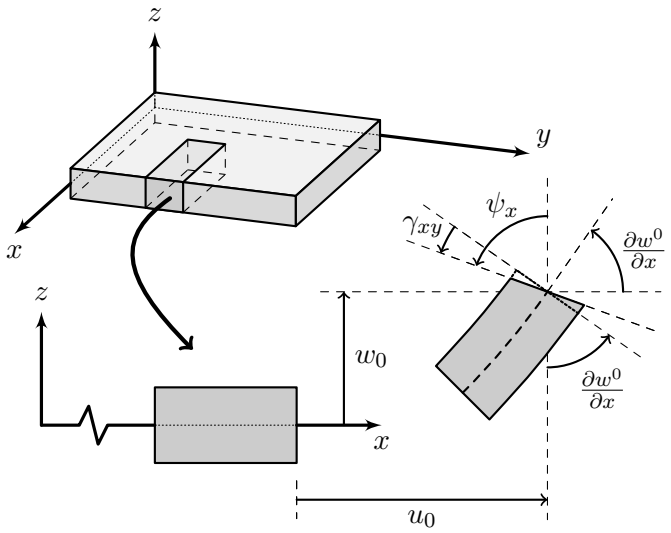

Figure 2.8: Undeformed and deformed geometries of an edge of a plate under the assumptions of first-order plate theory.

from Eqs. (2.4) and (2.6), we have

$$\begin{Bmatrix} \sigma_{11} \\ \sigma_{22} \\ \tau_{23} \\ \tau_{13} \\ \tau_{12} \end{Bmatrix} = \begin{bmatrix} Q_{11} & Q_{12} & 0 & 0 & 0 \\ Q_{12} & Q_{22} & 0 & 0 & 0 \\ 0 & 0 & Q_{44} & 0 & 0 \\ 0 & 0 & 0 & Q_{55} & 0 \\ 0 & 0 & 0 & 0 & Q_{66} \end{bmatrix} \begin{Bmatrix} \varepsilon_{11} \\ \varepsilon_{22} \\ \gamma_{23} \\ \gamma_{13} \\ \gamma_{12} \end{Bmatrix}$$
$$= \begin{bmatrix} \frac{1}{E_1} & -\frac{\nu_{21}}{E_2} & 0 & 0 & 0 \\ -\frac{\nu_{12}}{E_1} & \frac{1}{E_3} & 0 & 0 & 0 \\ 0 & 0 & \frac{1}{\mu_{23}} & 0 & 0 \\ 0 & 0 & 0 & \frac{1}{\mu_{13}} & 0 \\ 0 & 0 & 0 & 0 & \frac{1}{\mu_{12}} \end{bmatrix}^{-1} \begin{Bmatrix} \varepsilon_{11} \\ \varepsilon_{22} \\ \gamma_{23} \\ \gamma_{13} \\ \gamma_{12} \end{Bmatrix} \tag{2.45}$$

Inverting the matrix in Eq. (2.45) gives

$$Q_{44} = \mu_{23} \quad \text{and} \quad Q_{55} = \mu_{13} \tag{2.46}$$

in addition to the other Q_{ij} quantities, which are unchanged from Eq. (2.28). Carrying out the transformation into the global coordinate system in the same way as before gives

$$\begin{Bmatrix} \sigma_{xx} \\ \sigma_{yy} \\ \tau_{yz} \\ \tau_{xz} \\ \tau_{xy} \end{Bmatrix} = \begin{bmatrix} \overline{Q}_{11} & \overline{Q}_{12} & 0 & 0 & \overline{Q}_{16} \\ \overline{Q}_{12} & \overline{Q}_{22} & 0 & 0 & \overline{Q}_{26} \\ 0 & 0 & \overline{Q}_{44} & \overline{Q}_{45} & 0 \\ 0 & 0 & \overline{Q}_{45} & \overline{Q}_{55} & 0 \\ \overline{Q}_{16} & \overline{Q}_{26} & 0 & 0 & \overline{Q}_{66} \end{bmatrix} \begin{Bmatrix} \varepsilon_{xx} \\ \varepsilon_{yy} \\ \gamma_{yz} \\ \gamma_{xz} \\ \gamma_{xy} \end{Bmatrix} \tag{2.47}$$

where the remaining $\overline{Q}_{ij}$ quantities, not defined in Eq. (2.31), are

$$\begin{aligned}\overline{Q}_{44} &= Q_{44}\cos^2\theta + Q_{55}\sin^2\theta \\ \overline{Q}_{45} &= (Q_{55} - Q_{44})\cos\theta\sin\theta \\ \overline{Q}_{55} &= Q_{55}\cos^2\theta + Q_{44}\sin^2\theta\end{aligned} \tag{2.48}$$

Now the transverse shear resultants, denoted by Q_x and Q_y and shown in Fig. 2.6, must be calculated (they were neglected in the classical theory). Since the transverse shear strains are represented as constant through the laminate thickness, it follows that the transverse shear stresses will also be constant. However, it is well known that transverse shear stress varies parabolically through the thickness of homogeneous beams. In laminated composites, it must therefore vary at least quadratically. This discrepancy between the actual stress state and the constant stress predicted by the first-order theory is often corrected by multiplying the transverse shear stress integrals by a shear correction factor, denoted by κ.

With reference to Figs. 2.5 and 2.6 and Eq. (2.47), integrating through the thickness gives the following expressions for the transverse shear resultants:

$$\begin{Bmatrix} Q_y \\ Q_x \end{Bmatrix} = \kappa \int_{-\frac{h}{2}}^{\frac{h}{2}} \begin{Bmatrix} \tau_{yz} \\ \tau_{xz} \end{Bmatrix} dz = \kappa \sum_{k=1}^{n} \int_{z_{k-1}}^{z_k} \begin{bmatrix} \overline{Q}_{44} & \overline{Q}_{45} \\ \overline{Q}_{45} & \overline{Q}_{55} \end{bmatrix}^{(k)} \begin{Bmatrix} \gamma_{yz} \\ \gamma_{xz} \end{Bmatrix}^{(k)} dz \tag{2.49}$$

As before, the superscript (k) denotes quantities for the kth lamina. An approximate value for the shear correction factor κ can be calculated by equating the strain energy due to transverse shear, based on a constant shear stress distribution, with actual strain energy due to shear, as calculated from full elasticity theory. It is easily shown that for a homogeneous beam with a rectangular cross-section, κ is 5/6. The shear correction factor for a general laminate also depends on lamina properties and lamination scheme. Therefore calculating κ accurately is complex. In practice however, the value of 5/6 offers a satisfactory approximation.

The constitutive equations for a FSDT laminated composite plate are obtained by substituting Eqs. (2.43) and (2.44) into Eqs. (2.33), (2.34) and (2.49), which gives

$$\begin{Bmatrix} N_{xx} \\ N_{yy} \\ N_{xy} \end{Bmatrix} = \sum_{k=1}^{n} \begin{bmatrix} \overline{Q}_{11} & \overline{Q}_{12} & \overline{Q}_{16} \\ \overline{Q}_{12} & \overline{Q}_{22} & \overline{Q}_{26} \\ \overline{Q}_{16} & \overline{Q}_{26} & \overline{Q}_{66} \end{bmatrix}^{(k)} \left(\int_{z_{k-1}}^{z_k} \begin{Bmatrix} \varepsilon^0_{xx} \\ \varepsilon^0_{yy} \\ \gamma^0_{xy} \end{Bmatrix} dz - \int_{z_{k-1}}^{z_k} \begin{Bmatrix} \frac{\partial \psi_x}{\partial x} \\ \frac{\partial \psi_y}{\partial y} \\ \frac{\partial \psi_x}{\partial y} + \frac{\partial \psi_y}{\partial x} \end{Bmatrix} z\, dz \right) \tag{2.50}$$

$$\begin{Bmatrix} M_{xx} \\ M_{yy} \\ M_{xy} \end{Bmatrix} = \sum_{k=1}^{n} \begin{bmatrix} \overline{Q}_{11} & \overline{Q}_{12} & \overline{Q}_{16} \\ \overline{Q}_{12} & \overline{Q}_{22} & \overline{Q}_{26} \\ \overline{Q}_{16} & \overline{Q}_{26} & \overline{Q}_{66} \end{bmatrix}^{(k)} \left(\int_{z_{k-1}}^{z_k} \begin{Bmatrix} \varepsilon^0_{xx} \\ \varepsilon^0_{yy} \\ \gamma^0_{xy} \end{Bmatrix} z\, dz - \int_{z_{k-1}}^{z_k} \begin{Bmatrix} \frac{\partial \psi_x}{\partial x} \\ \frac{\partial \psi_y}{\partial y} \\ \frac{\partial \psi_x}{\partial y} + \frac{\partial \psi_y}{\partial x} \end{Bmatrix} z^2\, dz \right) \tag{2.51}$$

$$\begin{Bmatrix} Q_y \\ Q_x \end{Bmatrix} = \kappa \sum_{k=1}^{n} \begin{bmatrix} \overline{Q}_{44} & \overline{Q}_{45} \\ \overline{Q}_{45} & \overline{Q}_{55} \end{bmatrix}^{(k)} \int_{z_{k-1}}^{z_k} \begin{Bmatrix} \frac{\partial w^0}{\partial y} - \psi_y \\ \frac{\partial w^0}{\partial x} - \psi_x \end{Bmatrix}^{(k)} dz \tag{2.52}$$

In compact form and using the stiffness quantities defined in Eq. (2.40), these equations can be written as

$$\begin{Bmatrix} N_{xx} \\ N_{yy} \\ N_{xy} \\ M_{xx} \\ M_{yy} \\ M_{xy} \\ Q_y \\ Q_x \end{Bmatrix} = \begin{bmatrix} A_{11} & A_{12} & A_{16} & B_{11} & B_{12} & B_{16} & 0 & 0 \\ A_{12} & A_{22} & A_{26} & B_{12} & B_{22} & B_{26} & 0 & 0 \\ A_{16} & A_{26} & A_{66} & B_{16} & B_{26} & B_{66} & 0 & 0 \\ B_{11} & B_{12} & B_{16} & D_{11} & D_{12} & D_{16} & 0 & 0 \\ B_{12} & B_{22} & B_{26} & D_{12} & D_{22} & D_{26} & 0 & 0 \\ B_{16} & B_{26} & B_{66} & D_{16} & D_{26} & D_{66} & 0 & 0 \\ 0 & 0 & 0 & 0 & 0 & 0 & \kappa A_{44} & \kappa A_{45} \\ 0 & 0 & 0 & 0 & 0 & 0 & \kappa A_{45} & \kappa A_{55} \end{bmatrix} \begin{Bmatrix} \varepsilon^0_{xx} \\ \varepsilon^0_{yy} \\ \gamma^0_{xy} \\ -\frac{\partial \psi_x}{\partial x} \\ -\frac{\partial \psi_y}{\partial y} \\ -\frac{\partial \psi_x}{\partial y} - \frac{\partial \psi_y}{\partial x} \\ \frac{\partial w^0}{\partial y} - \psi_y \\ \frac{\partial w^0}{\partial x} - \psi_x \end{Bmatrix} \tag{2.53}$$

Note that Eq. (2.40) is valid for calculating A_{ij} with i and j as 4 or 5 as well as 1, 2 or 6.

2.2.6 One-dimensional laminated beams theories

So far, only theories for laminated plates have been presented. For the study of one-dimensional delamination, it is useful to reduce the constitutive equations further for application to laminated beams. The term 'beam' here is used to mean 'one-dimensional laminate'. If the beams bend in the xz-plane, then Eq. (2.41) for the classical theory can be written as

$$\begin{Bmatrix} N_{xx} \\ M_{xx} \end{Bmatrix} = \begin{bmatrix} A & B \\ B & D \end{bmatrix} \begin{Bmatrix} \varepsilon^0_{xx} \\ k_x \end{Bmatrix} \tag{2.54}$$

Since this classical theory for laminated beams corresponds with the Euler theory for isotropic beams, in this thesis it is simply referred to as the 'Euler laminated composite beam theory' or simply the 'Euler beam theory'. Similarly, Eq. (2.53) for the FSDT can be written as

$$\begin{Bmatrix} N_{xx} \\ M_{xx} \\ Q_x \end{Bmatrix} = \begin{bmatrix} A & B & 0 \\ B & D & 0 \\ 0 & 0 & H \end{bmatrix} \begin{Bmatrix} \varepsilon^0_{xx} \\ -\frac{\partial \psi_x}{\partial x} \\ \frac{\partial w^0}{\partial x} - \psi_x \end{Bmatrix} \tag{2.55}$$

Since this FSDT for laminated beams corresponds with the Timoshenko theory for isotropic beams, in this thesis it is simply referred to as the 'Timoshenko laminated composite beam theory' or simply the 'Timoshenko beam theory'.

The equivalent stiffness quantities in Eqs. (2.54) and (2.55), A, B, D and H must be calculated according to an assumed loading condition, such as plane stress, plane strain or some mixed condition. Li (1996) and Li and Lim (2005) gave some details on this.

In this work, either plane stress or plane strain is assumed in the xz-plane. For plane strain, the stiffnesses are immediately available by zeroing the appropriate strains in

Eq. (2.53). They are found to be

$$A = A_{11}; \quad B = B_{11}; \quad D = D_{11} \quad \text{and} \quad H = \kappa A_{55} \tag{2.56}$$

For plane stress, there are two options. The first is from Li (1996), where the equivalent stiffnesses are calculated such that the laminate resultants N_{yy}, N_{xy}, M_{yy}, M_{xy} and Q_y are all zero. By inverting Eq. (2.53), the following is obtained:

$$\begin{Bmatrix} \varepsilon^0_{xx} \\ \varepsilon^0_{yy} \\ \gamma^0_{xy} \\ -\frac{\partial \psi_x}{\partial x} \\ -\frac{\partial \psi_y}{\partial y} \\ -\frac{\partial \psi_x}{\partial y} - \frac{\partial \psi_y}{\partial x} \\ \frac{\partial w^0}{\partial y} - \psi_y \\ \frac{\partial w^0}{\partial x} - \psi_x \end{Bmatrix} = \begin{bmatrix} A'_{11} & A'_{12} & A'_{16} & B'_{11} & B'_{12} & B'_{16} & 0 & 0 \\ A'_{12} & A'_{22} & A'_{26} & B'_{12} & B'_{22} & B'_{26} & 0 & 0 \\ A'_{16} & A'_{26} & A'_{66} & B'_{16} & B'_{26} & B'_{66} & 0 & 0 \\ B'_{11} & B'_{12} & B'_{16} & D'_{11} & D'_{12} & D'_{16} & 0 & 0 \\ B'_{12} & B'_{22} & B'_{26} & D'_{12} & D'_{22} & D'_{26} & 0 & 0 \\ B'_{16} & B_{26} & B'_{66} & D'_{16} & D'_{26} & D'_{66} & 0 & 0 \\ 0 & 0 & 0 & 0 & 0 & 0 & A'_{44} & A'_{45} \\ 0 & 0 & 0 & 0 & 0 & 0 & A'_{45} & A'_{55} \end{bmatrix} \begin{Bmatrix} N_{xx} \\ N_{yy} \\ N_{xy} \\ M_{xx} \\ M_{yy} \\ M_{xy} \\ Q_y \\ Q_x \end{Bmatrix} \tag{2.57}$$

Zeroing the necessary resultants and inverting again gives

$$\begin{Bmatrix} N_{xx} \\ M_{xx} \\ Q_x \end{Bmatrix} = \begin{bmatrix} A'_{11} & B'_{11} & 0 \\ B'_{11} & D'_{11} & 0 \\ 0 & 0 & A'_{55} \end{bmatrix}^{-1} \begin{Bmatrix} \varepsilon^0_{xx} \\ -\frac{\partial \psi_x}{\partial x} \\ \frac{\partial w^0}{\partial x} - \psi_x \end{Bmatrix} \tag{2.58}$$

from which expressions for A, B, D and H are obtained by correspondence with Eq. (2.55). Note that by zeroing the *resultants*, the plane-stress condition on each individual lamina is not enforced; instead the condition is that the *integral* of the stresses over the thickness of the laminate is zero. In most circumstances, this a good definition of plane stress, however it is easy to show that if a laminate is modelled as an assembly of two or more sub-laminates, then some basic requirements, such as the sum of the extensional stiffnesses for each sub-laminate equalling the extensional stiffness for the assembled laminate, are not satisfied. This becomes particularly important when modelling fracture in laminates.

The second approach is to apply the plane-stress condition to the transformed reduced constitutive equations for each lamina and then to assemble all the laminae into the laminate. By inverting Eq. (2.47), the following is obtained for a lamina:

$$\begin{Bmatrix} \varepsilon_{xx} \\ \varepsilon_{yy} \\ \gamma_{yz} \\ \gamma_{xz} \\ \gamma_{xy} \end{Bmatrix} = \begin{bmatrix} \overline{Q}'_{11} & \overline{Q}'_{12} & 0 & 0 & \overline{Q}'_{16} \\ \overline{Q}'_{12} & \overline{Q}'_{22} & 0 & 0 & \overline{Q}'_{26} \\ 0 & 0 & \overline{Q}'_{44} & \overline{Q}'_{45} & 0 \\ 0 & 0 & \overline{Q}'_{45} & \overline{Q}'_{55} & 0 \\ \overline{Q}'_{16} & \overline{Q}'_{26} & 0 & 0 & \overline{Q}'_{66} \end{bmatrix} \begin{Bmatrix} \sigma_{xx} \\ \sigma_{yy} \\ \tau_{yz} \\ \tau_{xz} \\ \tau_{xy} \end{Bmatrix} \tag{2.59}$$

Zeroing the necessary stresses and inverting again gives

$$\begin{Bmatrix} \sigma_{xx} \\ \tau_{xz} \end{Bmatrix} = \begin{bmatrix} \overline{Q}'_{11} & 0 \\ 0 & \overline{Q}'_{55} \end{bmatrix}^{-1} \begin{Bmatrix} \varepsilon_{xx} \\ \gamma_{xz} \end{Bmatrix} \tag{2.60}$$

The A, B, D and H stiffnesses for the plane-stress condition are therefore calculated as

$$\begin{aligned} A &= \sum_{k=1}^{n} \frac{1}{\overline{Q}'^{(k)}_{11}} \left(z_k - z_{k-1}\right) \\ B &= \frac{1}{2} \sum_{k=1}^{n} \frac{1}{\overline{Q}'^{(k)}_{11}} \left(z_k^2 - z_{k-1}^2\right) \\ D &= \frac{1}{3} \sum_{k=1}^{n} \frac{1}{\overline{Q}'^{(k)}_{11}} \left(z_k^3 - z_{k-1}^3\right) \\ H &= \kappa \sum_{k=1}^{n} \frac{1}{\overline{Q}'^{(k)}_{55}} \left(z_k - z_{k-1}\right) \end{aligned} \tag{2.61}$$

Of course, both of these approaches can be similarly applied with different loading conditions. It is the second one however that is used in the theoretical development in following chapters.

2.3 Linear elastic fracture mechanics

2.3.1 The Griffith theory

Fracture mechanics is the field of mechanics concerned with the propagation of cracks in materials. Griffith (1921) pioneered the original theories because of some obvious shortcomings and flaws in the linear elastic theory of strength.

With the linear elastic theory of strength, the procedure is to determine the maximum stress in a body and the strength of the material. The body is supposed to fracture when the maximum stress in the body reaches the material strength. As an example, consider an infinite sheet, subject to an applied stress and containing a hole. Timoshenko and Goodier (1970) solved the boundary value problem analytically and showed that the maximum stress is at the surface of the hole and equal to three times the applied stress. The strength of the material must be determined experimentally, by for example loading a specimen of that material until it breaks (the theory of elasticity cannot answer this question). Such a procedure might appear simple and convenient, but in practice it is difficult. The maximum stress in a body is sensitive to the shape of the flaw and furthermore, the shape of the flaw is rarely known. Also, linear elasticity is assumed everywhere, which is never true. Finally, it is assumed that the strength of a material is independent of the specimen used in the experiment. In reality, different strengths are measured from different specimens because they all have different flaws. In short, it is very difficult in practice to calculate the maximum stress in a body and to determine the material strength.

Two experimental observations offer some clues for a resolution. The first observation is the discrepancy between the theoretical strength of a material and the experimentally measured strength. The theoretical strength is obtained by considering the stress required to break atomic bonds, which can be calculated by atomistic simulation. A rough approximation is that the theoretical strength is 10% of the modulus. Using glass as an example (its Young's modulus is $\sim 70\,\text{GPa}$), a material strength of 7 GPa would be expected. Experimentally, it is measured at $\sim 100\,\text{MPa}$, which is about two orders of magnitude lower than the theoretical value. The second observation was mentioned above: that experimental strength varies from one specimen to another.

Both of these observations can be explained if the strength of a sample depends on micro-scale flaws in the sample. Inglis (1913) derived a formula which can quantify this. The formula is for the maximum stress $\sigma_{\max}$ in an infinite sheet, subject to an applied stress σ, with an elliptic hole. His formula is

$$\frac{\sigma_{\max}}{\sigma} = 1 + \frac{2a}{b} \tag{2.62}$$

where a and b are the semi-axes of the ellipse. The radius of curvature at the tip of the ellipse is $\rho = b^2/a$. To approximate a deep, sharp flaw, Inglis set the flaw size to $a = 10^{-6}\,\text{m}$ and made the tip curvature $\rho = 10^{-10}\,\text{m}$, based on the size of an atom. From the formula, the maximum stress in the material is 200 times the applied stress. This would explain why the theoretical material strength (from atomic simulations with no flaws) and experimental material strength are very different.

The problem therefore seems to be that there are multiple scales involved in the calculation: the scales of the structure, the flaw and the atoms. The problem could be solved by calculating the material stresses very accurately, by running atomistic simulations on powerful computers. This is certainly not a viable option presently. Alternatively, the qualitative approach of simply reducing the material strength by several orders of magnitude could be used. This is both inaccurate and inefficient. Griffith (1921) came up with a solution. His work pioneered the theory of fracture.

Griffith worked with the notion that bodies generally contain small, pre-existing cracks and that the intense stress at the tip of a crack progressively breaks atomic bonds. The concept is a simple one, but it is difficult to quantify because the atomic behaviour at the tip of the crack is non-linear and differs in details for different materials; also the shape of the tip is unknown and the shape of the tip greatly affects the magnitude of stress, at least within the theory of linear elasticity. Griffith therefore derived equations from the principle of energy conservation. The reasoning is as follows:

As a crack advances, fresh surfaces are created and this disrupts the intermolecular bonds. The surface energy quantifies this disruption. Surface energy is the excess energy per unit area at the surface compared to the bulk of the material. By the principle of energy conservation, the energy that must be supplied to an advancing crack must be balanced by the amount of energy dissipated due to the formation of new surfaces. For the

moment, it is assumed that no work is done on the body during crack growth. Therefore the energy required to advance the crack surface area comes from the elastic energy stored in the body. Therefore, as a crack grows, the surface energy increases, but the elastic energy decreases. The crack advances if doing so reduces the sum of the surface energy and elastic energy.

By taking the limit as $b/a \to 0$, Griffith used Inglis's (1913) linear elasticity solution for an ellipse in an infinite sheet subject to a stress σ, given in Eq. (2.62), to derive the *decrease* in elastic energy relative to an uncracked plate, when a crack of length $2a$ begins to exist. Timoshenko and Goodier (1970) gave a full analytical solution to the problem. The result is

$$\pi \frac{a^2 \sigma^2}{E} \tag{2.63}$$

Relative to the uncracked sheet, the combined surface energy and elastic energy is

$$\Gamma = 4\gamma a - \pi \frac{a^2 \sigma^2}{E} \tag{2.64}$$

where γ is the surface energy. It is assumed that the applied stress remains constant during crack growth. As expected, when the crack advances the surface energy increases but the elastic energy decreases. Recall that a crack will advance if it causes the sum of the surface and elastic energy to decrease. The point at which this occurs is determined by $d\Gamma/da = 0$. With this condition, a critical crack length can be determined.

$$a_c = \frac{2E\gamma}{\pi \sigma^2} \tag{2.65}$$

If $a > a_c$ then the crack grows and it does this by progressively breaking atomic bonds at the crack tip. Similarly, a critical stress σ_c can also be determined.

$$\sigma_c = \sqrt{\frac{2E\gamma}{a\pi}} \tag{2.66}$$

This is the main prediction from Griffith's (1921) theory. It says that $\sigma_c \sqrt{a} =$ constant. He carried out several experiments to ascertain the different parts of this equation and to confirm his hypothesis.

2.3.2 Energy release rate

Griffith's (1921) original work dealt with very brittle materials—specifically glass. For ductile materials such as steel, although the form of Eq. (2.66) still holds, the surface energy predicted by Griffith's theory is usually unrealistically high. Irwin (1957) remedied this deficiency by suggesting that in a ductile material, most of the energy supplied to the crack tip was not absorbed by creating new surfaces but instead by energy dissipation due to plastic flow in the material near the crack tip. Irwin therefore modified Griffith's original criterion by saying that a crack will advance if doing so reduces the sum of the surface

energy, elastic energy *and* all other energy 'sinks', that is, the strain energy reduction when a crack grows must satisfy the *total* energy requirements, including surface creation and plasticity.

The reduction in total potential energy per unit area of crack growth is called the critical ERR and is denoted by G_c. Whereas Griffith's theory says that the critical ERR is equal to twice the surface energy (because two fracture surfaces are created), i.e.

$$G_c = 2\gamma \tag{2.67}$$

Irwin's modified criterion says that

$$G_c = 2\gamma + G_p \tag{2.68}$$

where G_p is the plastic dissipation per unit area of crack growth. Eq. (2.65) can therefore be rewritten as

$$\sigma_c = \sqrt{\frac{EG_c}{a\pi}} \tag{2.69}$$

Since the potential reduction in total potential energy in the body for a unit crack growth must exceed G_c in order for the crack to grow, G_c can be thought of as the 'resistance' to the extension of the crack.

Irwin was the first to observe that if the size of the plastic zone around a crack is small in comparison to the size of the crack, the energy required to grow the crack will not be critically dependent on the state of stress at the crack tip. In other words, a purely elastic solution may be used to calculate the amount of energy available for fracture if the plastic zone is small. This is typically the case in fibre-reinforced laminated composites with polymeric matrices. Now, the concept of ERR will be carried forward.

If the critical ERR is the 'resistance' to crack growth, then it is helpful to define a similar quantity which is the 'driving force' for crack growth. This quantity is simply the ERR and is defined as the energy that *would* be dissipated if the crack were to grow by a unit area. It is denoted by G. For a general case, where work can be done on a body during crack growth, this dissipated energy must be equal to the change in total potential energy Π, i.e.

$$G = -\frac{d\Pi}{dS} \tag{2.70}$$

where S is the crack area. For a purely elastic body during crack extension, the change in total potential energy of the body is equal to the change in any strain energy dU stored in the body less the work done dW by any external forces.

$$d\Pi = dU - dW \tag{2.71}$$

Therefore the ERR can be written as

$$G = \frac{dW}{dS} - \frac{dU}{dS} \tag{2.72}$$

If the displacements of the points of load application remain constant during crack growth, which is typical in testing, then no external work is done. Therefore for fixed displacements, Eq. (2.72) becomes

$$G = -\frac{\partial U}{\partial S} \tag{2.73}$$

The partial derivative signifies that the displacements of the applied loads are held fixed when the crack grows. If instead the applied loads remain fixed during crack growth, they now do work. Consider a linear elastic body, subject to a fixed force P, which undergoes a displacement u at the point of force application. (One may, in the broader sense, regard the variables P and u as a generalised load and a generalised displacement, respectively.) During crack extension, the change in strain energy dU in the body and the work done by the force dW are

$$dU = \frac{1}{2} P\, du \quad \text{and} \quad dW = P\, du \tag{2.74}$$

which, substituting into Eq. (2.72). give

$$G = P\frac{du}{dS} - \frac{1}{2}P\frac{du}{dS} = \frac{1}{2}P\frac{du}{dS} \tag{2.75}$$

By comparing Eqs. (2.74) and (2.75), the ERR for fixed loads is

$$G = \frac{\partial U}{\partial S} \tag{2.76}$$

The partial derivative signifies that the applied loads are held fixed when the crack grows. The difference between the equations for ERR for fixed loads and fixed displacements is only in the sign of $\partial U/\partial S$, although obviously the values of ERR are the same. This is a very useful result since analytically and in the FEM, it is often convenient to use fixed loads. However in experimental testing, loads tend to be applied with fixed displacements.

Two quantities have now been derived: G_c (the critical ERR) and G (the ERR), which can be thought of as the resistance to the extension of the crack and as the driving force for the extension of the crack, respectively. The relationship between G and G_c is analogous to the relationship between stress and strength, however, the fracture mechanics formulation of the problem in terms of energies has avoided many of the pitfalls of the linear elastic theory of strength.

2.3.3 Stress intensity factor

An alternative to the energy-based approach is to consider the stress field around the crack tip using linear elastic theory. It turns out that within this idealised model, the field around

the crack tip is singular. This is clearly an artefact of the idealised model, but Irwin and others made the singular field a main feature of fracture mechanics.

In three-dimensional space, the singular field around the crack tip is nearly two-dimensional. The origin of the coordinate system is placed at the crack tip; the x-axis points in the direction of propagation; the y-axis is normal to the plane of the crack; and the z-axis is tangential to the crack front. If the front is assumed to be a smooth curve, the field around the front is singular in the xy-plane, but smooth along the z-axis. Consequently the $\partial/\partial z$ derivatives are dropped and the problem becomes two-dimensional.

In two-dimensional stress problems, Airy's stress function, represented by ϕ can be used. A homogeneous material is assumed. It is convenient to switch to polar coordinates, where r is the radius from the crack tip and θ is the angle from the x-axis. In polar coordinates, the stresses are represented by

$$\sigma_{rr} = \frac{\partial^2 \phi}{r^2 \partial \theta^2} + \frac{\partial \phi}{r \partial r}; \quad \sigma_{\theta\theta} = \frac{\partial^2 \phi}{\partial r^2} \quad \text{and} \quad \tau_{r\theta} = -\frac{\partial}{\partial r}\left(\frac{\partial \phi}{r \partial \theta}\right) \tag{2.77}$$

The equation of compatibility from linear elasticity theory can be written in terms of ϕ as a bi-harmonic equation.

$$\left(\frac{\partial^2}{r^2 \partial \theta^2} + \frac{\partial}{r \partial r} + \frac{\partial^2}{\partial r^2}\right)\left(\frac{\partial^2}{r^2 \partial \theta^2} + \frac{\partial}{r \partial r} + \frac{\partial^2}{\partial r^2}\right)\phi = 0 \tag{2.78}$$

Eq. (2.78) represents a boundary-value problem. Williams (1957) solved the boundary-value problem for a crack tip. People before him had solved individual boundary value problems but Williams focused on the singular field around the tip of the crack, in a very small zone, so that the boundary of the body could be assumed to be infinitely far away. He showed that the solution to Eq. (2.78) is

$$\phi = r^{\lambda+1}\left[A\cos\left((\lambda+1)\,\theta\right) + B\cos\left((\lambda-1)\,\theta\right)\right] \tag{2.79}$$

where λ, A and B are constants to be determined. By applying the condition that at $\theta = \pi$ (on the cracked surfaced), both traction components disappear, i.e. $\sigma_{\theta\theta} = \tau_{r\theta} = 0$, and the result is a pair of linear equations for A and B in terms of λ. It is therefore an eigenvalue problem. To have a solution such that A and B are not zero, the determinant must vanish and this gives a set of possible values for λ as follows:

$$\lambda = ..., -1, -\frac{1}{2}, 0, \frac{1}{2}, 1, ... \tag{2.80}$$

Consequently the stress field becomes

$$\sigma_{ij} = \sum_{m=-\infty}^{+\infty} a_m r^{m/2} f_{ij}^{(m)}(\theta) \tag{2.81}$$

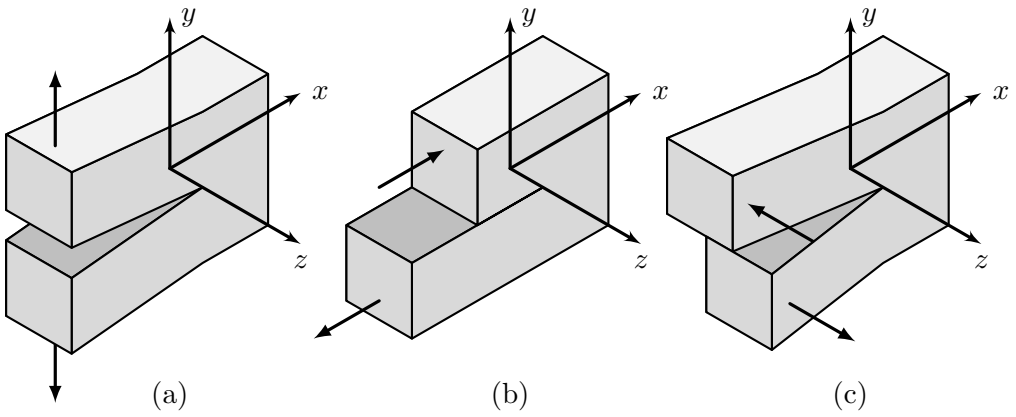

Figure 2.9: The three basic modes of fracture. (a) Mode I. (b) Mode II. (c) Mode III.

where $\sigma_{r\theta} = \tau_{r\theta}$. The functions $f_{ij}^{(m)}(\theta)$ are determined by the eigenvalue problem but the amplitudes a_m are determined by solving the full boundary-value problem. It is found that the stresses and strains are $\sim r^{\lambda-1}$ and the displacements are $\sim r^{\lambda}$. Since the field is singular and the displacements must be bounded, clearly $0 < \lambda < 1$. Hui and Ruina (1995) gave a discussion on why the value of λ must be $\frac{1}{2}$. Substituting this value of λ into the pair of linear equations for A and B gives

$$\sigma_{ij}(r,\theta) = \frac{K}{\sqrt{2\pi r}} f_{ij}(\theta) \tag{2.82}$$

where K is the stress intensity factor, introduced by Irwin (1957), which is actually equal to $-B\sqrt{2\pi r}$. Note that the $\sqrt{2\pi}$ is introduced by convention. The functions $f_{ij}(\theta)$ are known functions of θ (that are not reproduced here). K is independent of the eigenvalue problem and is found by solving a specific boundary-value problem. The form of the singular field has therefore been found for all problems in homogeneous bodies. Although Williams (1957) derived the stress field around a crack tip, Irwin (1957) used it to define a quantity K that characterises individual crack tips and which provides an alternative approach in fracture mechanics. Yarema (1996) completed an excellent survey of the many contributions made by Irwin to fracture mechanics.

A year later, Irwin (1958) classified cracks according to the directions of the displacements at the crack tip. This concept was absent from the energy-based approach. Irwin's classification distinguishes the following types of cracks (see Fig. 2.9): (1) opening displacement or tensile cracks (mode I cracks); (2) transverse (with respect to their front) shear cracks (mode II cracks); and (3) longitudinal shear cracks (mode III cracks). The first of these components is induced by the stress σ_{yy} normal to the crack surface; the second and third of these are induced by the shear stresses in the plane of the crack normal τ_{yx}, and tangential to its front τ_{yz}, respectively. Note that τ_{yz} was neglected in the above analysis, but generally exists for a three-dimensional crack. These components determine

respectively the parameters K_I, K_{II} and K_{III}.

$$K_I = \lim_{r\to 0} \sqrt{2\pi r}\,\sigma_{yy}; \quad K_{II} = \lim_{r\to 0} \sqrt{2\pi r}\,\tau_{yx} \quad \text{and} \quad K_{III} = \lim_{r\to 0} \sqrt{2\pi r}\,\tau_{yz} \tag{2.83}$$

Irwin also related the concepts of ERR and stress intensity factor for different modes. Consider a body which contains a crack. The body is so big that a small change in crack length does not change K. The ERR is defined as the difference between the strain energies stored in the two bodies before and after crack growth, divided by the change in crack area. For a mode I crack, the strain energy difference between the two bodies can be calculated in terms of K by calculating the work done by the closing stress σ_{yy} over the change in crack length. For a mode II crack, the strain energy difference is equal to the work done by the in-plane shear stress τ_{yx}. Finally, for the mode III crack, the strain energy difference is equal to the work done by the tangential shear stress τ_{yz}. The pure mode I, II and III components of ERR, denoted by G_I, G_{II} and G_{III} respectively, are found from these integrations, and are

$$G_I = \frac{K_I^2}{\overline{E}}; \quad G_{II} = \frac{K_{II}^2}{\overline{E}} \quad \text{and} \quad G_{III} = \frac{K_{III}^2}{2\mu} \tag{2.84}$$

where μ is the shear modulus and $\overline{E}$ is the equivalent Young's modulus, which depends on the loading condition. For plane stress, $\overline{E} = E$ and for plane strain, $\overline{E} = E/\left(1-\nu^2\right)$.

Irwin's approach with stress intensity factors therefore extended the original energy-based approach to resolve the modes of fracture as well. Each mode of ERR can be calculated by considering the amount of work done by the corresponding stress at the crack tip. Irwin also contended that the energy absorbed in the process of crack growth is equal to the work required to close the crack to its original length. This is the origin of the crack closure integral, discussed in §1.3.1.

2.3.4 Toughness

The simplest way to account for the fracture process under the stress-intensity approach is to stipulate that the crack extends when the stress intensity factor K reaches a critical value K_c, which is known as the 'fracture toughness'. Note that whilst the stress intensity factor is a loading parameter, the fracture toughness is an intrinsic material property. For a given material, K_c is determined by a fracture test. Irwin's equivalence between the two approaches also applies for the fracture toughness, i.e.

$$G_c = \frac{K_c^2}{\overline{E}}; \quad G_{Ic} = \frac{K_{Ic}^2}{\overline{E}}; \quad G_{IIc} = \frac{K_{IIc}^2}{\overline{E}} \quad \text{and} \quad G_{IIIc} = \frac{K_{IIIc}^2}{2\mu} \tag{2.85}$$

where the subscript c indicates that these are critical ERRs.

2.3.5 Interfacial fracture

Although the analytical work on subject of interfacial fracture has been thoroughly reviewed in §1.2, some details from the original work are given here to provide some context.

Consider a body consisting of two materials, bonded at an interface which contains a crack. If the body is subject to a load then the faces of the crack open and slide relative to each other. At a critical load, the crack either extends along the interface or kinks out of the interface. For laminated fibre-reinforced composites, it tends to be the former because of the relative weakness of their interfaces. Under these circumstances, the crack grows as a mixed mode because it cannot kink to maintain mode I conditions if it is to remain on the interface (Cotterell and Rice 1980, Gold'stein and Salganik 1974).

By solving an eigenvalue problem, Williams (1959) discovered that the singular field around the tip of a crack on an interface is not square-root singular, but takes a new form. At a distance r ahead the tip of the crack, the stresses on the interface are given by

$$\sigma_{22} + i\sigma_{12} = \frac{Kr^{i\varepsilon}}{\sqrt{2\pi r}} \tag{2.86}$$

where complex notation is used. The constant ε is dimensionless and depends on the elastic constants of both materials. When the two materials have identical elastic constants, the constant ε vanishes and the field becomes square-root singular, similar to that around the tip of a crack in a homogeneous material. The stress intensity factor K is a complex quantity. When $\varepsilon \neq 0$, Williams's field predicts that the stresses are oscillatory as r approaches the tip of the crack. The relative displacements of the two materials on the interface are

$$\delta_2 + i\delta_1 = \left(\frac{1}{\overline{E}_1} + \frac{1}{\overline{E}_2}\right) \frac{Kr^{i\varepsilon}}{2\left(1 + 2i\varepsilon\right)\cosh\left(\pi\varepsilon\right)} \sqrt{\frac{2r}{\pi}} \tag{2.87}$$

When $\varepsilon \neq 0$, this expression indicates that for some values of r, the two faces of the crack interpenetrate. This prediction has disturbed many researchers, and has been perhaps the single most significant objection against the Williams field. In posing the problem, Williams assumed that the two faces of the crack are traction-free, however his solution to the problem indicates that the two faces of the crack interpenetrate. To remove this contradiction, some researchers have allowed the faces of the crack to contact each other, and solved the resulting boundary-value problems. This comprises some of the work reviewed in §1.2. Another approach has been to simply set $\varepsilon = 0$. In doing this, the stress field becomes square-root singular

$$\sigma_{22} + i\sigma_{11} = \frac{K}{\sqrt{2\pi r}} \tag{2.88}$$

and separating the complex K into real and imaginary parts gives

$$\sigma_{22} = \frac{K_I}{\sqrt{2\pi r}} \quad \text{and} \quad \sigma_{12} = \frac{K_{II}}{\sqrt{2\pi r}} \tag{2.89}$$

Suo and Hutchinson (1989) argued for the insignificance of the parameter ε saying 'there is no compelling evidence to date which suggests an important role for ε'.

For a crack existing on an interface, the ERR is still defined as the reduction in the total potential energy associated with the crack advancing a unit area. All the methods for determining the ERR in homogeneous materials still apply. However, it is evident that the critical condition for the extension of the crack also depends on the mode of the load.

2.4 Conclusion

In this chapter the essential background theory, on which the following chapters are based, has been presented. Firstly, the constitutive equations for classical and FSDT laminated composite plates and beams have been derived. In doing so, the coordinate system and other conventions have been established. Secondly, some basic concepts from fracture mechanics have been explained.

Numerical simulation using the FEM forms an important part of the procedure in this work. It remains to implement the methods from this chapter in the FEM. This is the subject of the next chapter.

Chapter 3

Finite element method

Contents

3.1 Introduction

In this chapter, the theories of laminated composite beams and plates, and principles from fracture mechanics are implemented in the FEM. Reddy (1984), Zienkiewicz and Taylor (1989) and Rao (1982) are the main references for this. Details are also given on the FEM techniques for modelling interfaces and for contact simulation that have been used in later chapters.

For the purpose of studying one-dimensional fracture, beam and plate finite elements are derived. For comparisons with two-dimensional elasticity, some elements based on the two-dimensional theory of elasticity are also derived. Since isotropic materials can be considered as just a special case of orthotropic (or anisotropic) materials, here the orthotropic version of the formulation is preferred. In all cases, the deformation is chosen to occur in the xz-plane (or the rz-plane for axisymmetric elements). This is consistent with the formulations in §2.2.

3.2 Finite element derivations

3.2.1 Cubic Euler beams

The coordinate system and nodal forces acting on an Euler beam finite element are shown in Fig. 3.1. The constitutive equations for such beams are given in Eq. (2.54). They are

Figure 3.1: An Euler beam finite element.

repeated here for convenience.

$$\left\{\overline{\sigma}\right\} = \begin{Bmatrix} N_{xx} \\ M_{xx} \end{Bmatrix} = \begin{bmatrix} A & B \\ B & D \end{bmatrix} \begin{Bmatrix} \varepsilon^0_{xx} \\ k_x \end{Bmatrix} = \left[\overline{E}\right] \left\{\varepsilon\right\} \tag{3.1}$$

New notation is introduced in Eq. (3.1): $\left\{\overline{\sigma}\right\}$ is the effective stress, which contains the force and moment resultants; and $\left[\overline{E}\right]$ is the corresponding effective elastic modulus. Recall from §2.2.6 that the stiffness quantities A, B and D must be determined from Eq. (2.41) and a loading condition, such as plane stress or plane strain.

Displacement models are needed for the extension u and deflection w. A Linear displacement model is suitable for for the extension; a cubic displacement model is chosen for deflection, as follows:

$$u = a_1 + a_2 x \tag{3.2}$$

$$w = a_3 + a_4 x + a_5 x^2 + a_6 x^3 \tag{3.3}$$

The coefficients a_i must be found by means of boundary conditions, which are in the form of nodal displacements.

$$\begin{gathered} (u)_{x=0} = u_1; \quad (u)_{x=L} = u_2; \quad (w)_{x=0} = w_1; \quad (w)_{x=L} = w_2; \\ (dw/dx)_{x=0} = \theta_1 \quad \text{and} \quad (dw/dx)_{x=L} = \theta_2 \end{gathered} \tag{3.4}$$

where L is the length of the beam element; u_i and w_i are the u and w displacements respectively at node i; and θ_i is the rotation dw/dx at node i. Solving Eqs. (3.2) to (3.4) gives the following values for a_i:

$$\begin{gathered} a_1 = u_1; \quad a_2 = \frac{u_2 - u_1}{L}; \quad a_3 = w_1; \quad a_4 = \theta_1; \\ a_5 = -\frac{3w_1}{L^2} - \frac{2\theta_1}{L} + \frac{3w_2}{L^2} - \frac{\theta_2}{L} \quad \text{and} \quad a_6 = \frac{2w_1}{L^3} + \frac{\theta_1}{L^2} - \frac{2w_2}{L^3} + \frac{\theta_2}{L^2} \end{gathered} \tag{3.5}$$

The element displacement model in matrix form is therefore

$$\left\{\begin{matrix} u \\ w \end{matrix}\right\} = \Big[N\Big] \left\{\begin{matrix} u_1 \\ w_1 \\ \theta_1 \\ u_2 \\ w_2 \\ \theta_2 \end{matrix}\right\} = \Big[N\Big]\,\Big\{d\Big\} \tag{3.6}$$

where $\Big[N\Big]$ is the shape function matrix, which is given in Eq. (3.7).

$$\Big[N\Big] = \begin{bmatrix} 1-\frac{x}{L} & 0 & 0 & \frac{x}{L} & 0 & 0 \\ 0 & \frac{2x^3-3Lx^2+L^3}{L^3} & \frac{x^3-2Lx^2+L^2x}{L^2} & 0 & \frac{3Lx^2-2x^3}{L^3} & \frac{x^3-Lx^2}{L^2} \end{bmatrix} \tag{3.7}$$

The strain vector in Eq. (3.1) is needed to calculate the strain energy in the beam. The membrane strain and curvature are written using the linear strain-displacement relations for infinitesimal strain, as in Eq. (2.37). The superscript 0 in Eq. (2.37), which indicates a mid-surface quantity, is now omitted.

$$\Big\{\varepsilon\Big\} = \left\{\begin{matrix} du/dx \\ -d^2w/dx^2 \end{matrix}\right\} = \begin{bmatrix} \frac{d}{dx} & 0 \\ 0 & -\frac{d^2}{dx^2} \end{bmatrix} \left\{\begin{matrix} u \\ v \end{matrix}\right\} = \begin{bmatrix} \frac{d}{dx} & 0 \\ 0 & -\frac{d^2}{dx^2} \end{bmatrix} \Big[N\Big]\,\Big\{d\Big\} \tag{3.8}$$

At this point it is convenient to define a matrix, $\Big[B\Big]$

$$\Big[B\Big] = \begin{bmatrix} \frac{d}{dx} & 0 \\ 0 & -\frac{d^2}{dx^2} \end{bmatrix} \Big[N\Big] = \begin{bmatrix} -\frac{1}{L} & 0 & 0 & \frac{1}{L} & 0 & 0 \\ 0 & \frac{6L-12x}{L^3} & \frac{4L-6x}{L^2} & 0 & \frac{12x-6L}{L^3} & \frac{2L-6x}{L^2} \end{bmatrix} \tag{3.9}$$

such that

$$\Big\{\varepsilon\Big\} = \Big[B\Big]\,\Big\{d\Big\} \tag{3.10}$$

For a constant beam width b, the strain energy in the element can be calculated as follows by integrating the strain energy density over the volume:

$$\begin{aligned} U &= \frac{1}{2}\int_V \Big\{\sigma\Big\}^T \Big\{\varepsilon\Big\}\, dV \\ &= \frac{1}{2}\int_0^L \Big\{\varepsilon\Big\}^T \Big[\overline{E}\Big] \Big\{\varepsilon\Big\}\, b\, dx \\ &= \frac{1}{2}\Big\{d\Big\}^T \left(b\int_0^L \Big[B\Big]^T \Big[\overline{E}\Big] \Big[B\Big]\, dx\right) \Big\{d\Big\} \end{aligned} \tag{3.11}$$

Another expression for strain energy is

$$U = \frac{1}{2}\Big\{d\Big\}^T \Big[k\Big]\,\Big\{d\Big\} \tag{3.12}$$

Comparing Eqs. (3.11) and (3.12) gives an expression for the element stiffness matrix, $\Big[k\Big]$.

$$\Big[k\Big] = b\int_0^L \Big[B\Big]^T \Big[\overline{E}\Big] \Big[B\Big]\, dx \tag{3.13}$$

The element stiffness matrix $\Big[k\Big]$ relates the nodal loads $\Big\{r\Big\}$ to the nodal displacements $\Big\{d\Big\}$ in the following way:

$$\Big\{r\Big\} = \Big[k\Big]\Big\{d\Big\} \tag{3.14}$$

Carrying out the integration in Eq. (3.13) and substituting the resulting $\Big[k\Big]$ matrix into Eq. (3.14) gives

$$\begin{Bmatrix} N_1 \\ P_1 \\ M_1 \\ N_2 \\ P_2 \\ M_2 \end{Bmatrix} = b \begin{bmatrix} \frac{A}{L} & 0 & -\frac{B}{L} & -\frac{A}{L} & 0 & \frac{B}{L} \\ 0 & \frac{12D}{L^3} & \frac{6D}{L^2} & 0 & -\frac{12D}{L^3} & \frac{6D}{L^2} \\ -\frac{B}{L} & \frac{6D}{L^2} & \frac{4D}{L} & \frac{B}{L} & -\frac{6D}{L^2} & \frac{2D}{L} \\ -\frac{A}{L} & 0 & \frac{B}{L} & \frac{A}{L} & 0 & -\frac{B}{L} \\ 0 & -\frac{12D}{L^3} & -\frac{6D}{L^2} & 0 & \frac{12D}{L^3} & -\frac{6D}{L^2} \\ \frac{B}{L} & \frac{6D}{L^2} & \frac{2D}{L} & -\frac{B}{L} & -\frac{6D}{L^2} & \frac{4D}{L} \end{bmatrix} \begin{Bmatrix} u_1 \\ w_1 \\ \theta_1 \\ u_2 \\ w_2 \\ \theta_2 \end{Bmatrix} \tag{3.15}$$

The nodal loads are defined as positive in the direction of the corresponding nodal displacements (see Fig. 3.1).

Eq. (3.15) can now be reduced to the corresponding form for an isotropic beam element. For isotropic materials, $B = 0$ since there is no material coupling. The isotropic and laminated relations for a beam therefore become

$$N_{xx} = A\varepsilon_{xx} = (ES/b)\,\varepsilon_{xx} \quad \Longrightarrow \quad A = ES/b \tag{3.16}$$

$$-M_{xx} = Dk_x = (EI_{yy}/b)\,k_x \quad \Longrightarrow \quad D = EI_{yy}/b \tag{3.17}$$

where S is the cross-sectional area and I_{yy} is the second moment of area of the cross-section around the y-axis. Evaluating Eq. (3.15) with the isotropic values of A, B and D gives

$$\Big[k\Big] = \frac{EI_{yy}}{L^3} \begin{bmatrix} \frac{L^2S}{I_{yy}} & 0 & 0 & -\frac{L^2S}{I_{yy}} & 0 & 0 \\ 0 & 12 & 6L & 0 & -12 & 6L \\ 0 & 6L & 4L^2 & 0 & -6L & 2L^2 \\ -\frac{L^2S}{I_{yy}} & 0 & 0 & \frac{L^2S}{I_{yy}} & 0 & 0 \\ 0 & -12 & -6L & 0 & 12 & 6L \\ 0 & 6L & 2L^2 & 0 & 6L & 4L^2 \end{bmatrix} \tag{3.18}$$

3.2.2 Linear Timoshenko beams

The Euler beam element, derived in §3.2.1, does not account for shear deformation and is therefore not accurate for thick or short laminates. Timoshenko beam theory does take

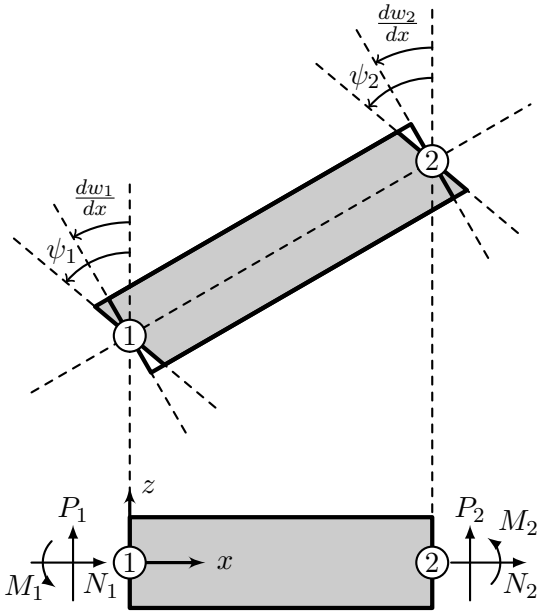

Figure 3.2: A Timoshenko beam finite element.

into account shear deformation, making it suitable for these types of structures. The effect of shear deformation is to rotate the normal to the mid-surface of the beam by a small amount.

Two formulations of the Timoshenko beam finite element are given in this section. Both use linear interpolation for all of the displacement quantities, however in the calculation of the strain energy, the first uses full integration but the second uses reduced integration. Reddy (1997) gave a detailed explanation of the reasons for doing this. Briefly, the first element suffers from a phenomenon known as 'shear locking', which causes it to behave in an over-stiff way. The second element avoids the problem by using one-point integration. Further details are given later.

Fig. 3.2 shows a Timoshenko beam finite element. The quantities ψ_1 and ψ_2 are the angles of rotation of the normals to the undeformed mid-surface of the beam at nodes 1 and 2 respectively; the quantities dw_1/dx and dw_2/dx are the rotations of the mid-surface of the beam at nodes 1 and 2 respectively.

The constitutive equations for a Timoshenko beam are given by Eq. (2.55) and are repeated here. The superscript 0 in Eq. (2.55), which indicates a mid-surface quantity, is omitted.

$$\left\{\overline{\sigma}\right\} = \begin{Bmatrix} N_{xx} \\ M_{xx} \\ Q_x \end{Bmatrix} = \begin{bmatrix} A & B & 0 \\ B & D & 0 \\ 0 & 0 & H \end{bmatrix} \begin{Bmatrix} \varepsilon_{xx} \\ -\frac{\partial \psi_x}{\partial x} \\ \frac{\partial w}{\partial x} - \psi_x \end{Bmatrix} = \left[\overline{E}\right] \left\{\varepsilon\right\} \tag{3.19}$$

Both the full- and reduced-integration elements use linear interpolation for the three independent displacement quantities. The displacement functions are therefore

$$u = u_1 N_1 + u_2 N_2 \tag{3.20}$$

$$w = w_1 N_1 + w_2 N_2 \tag{3.21}$$

$$\psi_x = \psi_1 N_1 + \psi_2 N_2 \tag{3.22}$$

where u_i, w_i and ψ_i are the u, w and ψ_x displacements respectively at node i. The shape functions N_1 and N_2 are

$$N_1 = 1 - \frac{x}{L} \quad \text{and} \quad N_2 = \frac{x}{L} \tag{3.23}$$

The strain vector $\Big\{\varepsilon\Big\}$ is related to the nodal displacement vector $\Big\{d\Big\}$ through the $\Big[B\Big]$ matrix, as in Eq. (3.10). If $\Big\{d\Big\} = \Big\{u_1 \quad w_1 \quad \psi_1 \quad u_2 \quad w_2 \quad \psi_2\Big\}^T$ then the $\Big[B\Big]$ matrix is

$$\Big[B\Big] = \begin{bmatrix} \frac{dN_1}{dx} & 0 & 0 & \frac{dN_2}{dx} & 0 & 0 \\ 0 & 0 & -\frac{dN_1}{dx} & 0 & 0 & -\frac{dN_2}{dx} \\ 0 & \frac{dN_1}{dx} & -N_1 & 0 & \frac{dN_2}{dx} & -N_2 \end{bmatrix} \tag{3.24}$$

The stiffness matrix $\Big[k\Big]$, which relates the nodal loads $\Big\{r\Big\}$ to the nodal displacements $\Big\{d\Big\}$, as in Eq. (3.14), may now be derived with full integration using Eq. (3.13). The nodal loads are defined as positive in the direction of the corresponding nodal displacements (see Fig. 3.2). Therefore $\Big\{r\Big\} = \Big\{N_1 \quad P_1 \quad M_1 \quad N_2 \quad P_2 \quad M_2\Big\}^T$. The stiffness matrix $\Big[k\Big]$ is

$$\Big[k\Big] = b \begin{bmatrix} \frac{A}{L} & 0 & -\frac{B}{L} & -\frac{A}{L} & 0 & \frac{B}{L} \\ 0 & \frac{H}{L} & \frac{H}{2} & 0 & -\frac{H}{L} & \frac{H}{2} \\ -\frac{B}{L} & \frac{H}{2} & \frac{HL}{3} + \frac{D}{L} & \frac{B}{L} & -\frac{H}{2} & \frac{HL}{6} - \frac{D}{L} \\ -\frac{A}{L} & 0 & \frac{B}{L} & \frac{A}{L} & 0 & -\frac{B}{L} \\ 0 & -\frac{H}{L} & -\frac{H}{2} & 0 & \frac{H}{L} & -\frac{H}{2} \\ \frac{B}{L} & \frac{H}{2} & \frac{HL}{6} - \frac{D}{L} & -\frac{B}{L} & -\frac{H}{2} & \frac{HL}{3} + \frac{D}{L} \end{bmatrix} \tag{3.25}$$

It is well known that when equal interpolation (especially linear) of w and ψ is used in conjunction with full integration, the element behaves in an over-stiff way. This is especially true in the thin beam limit, i.e. as the length-to-thickness ratio becomes large. This locking is due to the inconsistency of the interpolation used for w and ψ. For a thin beam, the shear strain energy terms must vanish. It is easily shown that this requirement leads to two constraints:

$$\frac{\theta_2 + \theta_1}{2} - \frac{w_2 - w_1}{L} \to 0 \qquad \text{and} \qquad \frac{\theta_2 - \theta_1}{2} \to 0 \tag{3.26}$$

The first constraint is meaningful but the second constraint is a spurious one (Prathap and Bhashyam 1982). For an isotropic material, it effectively increases the element's bending

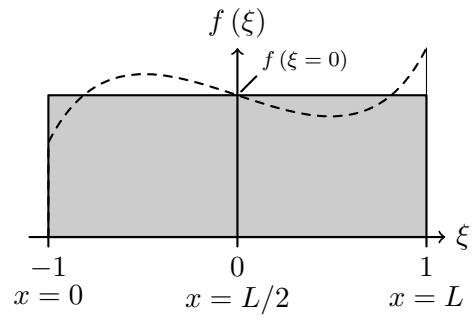

Figure 3.3: One-point Gaussian quadrature.

stiffness from EI to $EI + LS\kappa^2\mu/12$, which causes locking. Prathap and Bhashyam's (1982) method to overcome shear locking is to use reduced integration. The integral in Eq. (3.13) is instead evaluated using one-point Gaussian quadrature, which eliminates the shear locking by ignoring the spurious term.

A quadrature rule is an approximation of the definite integral of a function, usually stated as the weighted sum of function values at specified points within the domain of integration. An n-point Gaussian quadrature rule is a quadrature rule constructed to yield an exact result for polynomials of degree $2n - 1$ or less by a suitable choice of the points ξ_i and weighting factors H_i for $i = 1, \ldots, n$. The domain of integration is conventionally taken from -1 to 1, so the rule is stated as

$$I = \int_{-1}^{1} f(\xi)\, d\xi = \sum_{i=1}^{n} f(\xi_i)\, H_i \tag{3.27}$$

For one-point reduced integration (i.e. $n = 1$), a polynomial of order one is required to represent $f(\xi)$.

$$f(\xi) = C_0 + C_1\xi \tag{3.28}$$

where C_0 and C_1 are unknown coefficients. Evaluating Eq. (3.27) using Eq. (3.28) gives

$$I = 2C_0 \tag{3.29}$$

implying that $\xi_1 = 0$ and $H_1 = 2$. This approximate integral is represented in Fig. 3.3. The dashed line is the original function to be approximated as linear by $f(\xi)$. The approximate integral is represented by the shaded area. Note that since $n = 1$, Eq. (3.29) is the exact integral for linear equations, such as the one in Eq. (3.28). If the integrand of Eq. (3.27) is not a linear equation, then Eq. (3.29) is an approximation.

To evaluate Eq. (3.13) using one-point Gaussian quadrature, the integrand must be transformed into the ξ-coordinate. The integration point lies at $x = L/2$ (see Fig. 3.3).

Therefore $C_0 = f(\xi = 0) = f(x = L/2)$ and

$$x = \frac{L}{2} + \frac{L}{2}\xi \quad \text{and} \quad dx = \frac{L}{2}\,d\xi \tag{3.30}$$

Applying this transformation to Eq. (3.13) gives

$$\Big[k\Big] = \int_{-1}^{1} \Big[B\Big]^T \Big[\overline{E}\Big] \Big[B\Big] \frac{bL}{2}\,d\xi \tag{3.31}$$

Therefore clearly

$$C_0 = \left(\Big[B\Big]^T \Big[\overline{E}\Big] \Big[B\Big] \frac{bL}{2} \right)_{x=L/2} \tag{3.32}$$

and from Eq. (3.29), the resulting stiffness matrix is

$$\Big[k\Big] = \left(\Big[B\Big]^T \Big[\overline{E}\Big] \Big[B\Big] bL \right)_{x=L/2} \tag{3.33}$$

When Eq. (3.33) is evaluated, the following is obtained:

$$\Big[k\Big] = \begin{bmatrix} \frac{A}{L} & 0 & -\frac{B}{L} & -\frac{A}{L} & 0 & \frac{B}{L} \\ 0 & \frac{H}{L} & \frac{H}{2} & 0 & -\frac{H}{L} & \frac{H}{2} \\ -\frac{B}{L} & \frac{H}{2} & \frac{HL}{4} + \frac{D}{L} & \frac{B}{L} & -\frac{H}{2} & \frac{HL}{4} - \frac{D}{L} \\ -\frac{A}{L} & 0 & \frac{B}{L} & \frac{A}{L} & 0 & -\frac{B}{L} \\ 0 & -\frac{H}{L} & -\frac{H}{2} & 0 & \frac{H}{L} & -\frac{H}{2} \\ \frac{B}{L} & \frac{H}{2} & \frac{HL}{4} - \frac{D}{L} & -\frac{B}{L} & -\frac{H}{2} & \frac{HL}{4} + \frac{D}{L} \end{bmatrix} \tag{3.34}$$

The only changes are to k_{33}, k_{36}, k_{63} and k_{66}. Nevertheless, this reduced-integration stiffness matrix successfully eliminates shear locking.

3.2.3 Axisymmetric Mindlin–Reissner plates

An axisymmetric Mindlin–Reissner plate is the axisymmetric equivalent of a Timoshenko beam. Equations for axisymmetric isotropic Mindlin–Reissner plates can be found in Wang and Lee (1996) and Timoshenko and Woinowsky-Krieger (1959). A Mindlin–Reissner plate finite element is shown in Fig. 3.4.

The constitutive equations for a plate lying in the xy-plane are given in Eq. (2.53). For cylindrical coordinates, the x-axis maps onto the r-axis; the y-axis maps onto the ϕ-axis and the z-axis remains unchanged. Because of axisymmetry, $\gamma_{r\phi} = \gamma_{\phi z} = 0$. The resulting constitutive equations for a laminated axisymmetric plate are given in Eq. (3.35). Linear strain-displacement relations for infinitesimal strain in cylindrical coordinates are used to expand the strain vector. Again, the superscript 0, which indicates a mid-surface quantity,

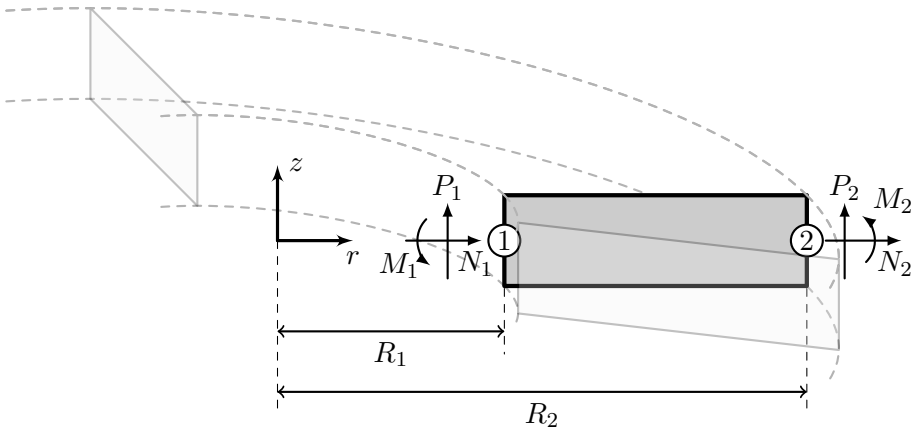

Figure 3.4: An axisymmetric Mindlin–Reissner plate finite element.

is omitted.

$$\left\{\overline{\sigma}\right\} = \begin{Bmatrix} N_{rr} \\ N_{\phi\phi} \\ M_r \\ M_\phi \\ Q_r \end{Bmatrix} = \begin{bmatrix} A_{11} & A_{12} & B_{11} & B_{12} & 0 \\ A_{12} & A_{22} & B_{12} & B_{22} & 0 \\ B_{11} & B_{12} & D_{11} & D_{12} & 0 \\ B_{12} & B_{22} & D_{12} & D_{22} & 0 \\ 0 & 0 & 0 & 0 & A_{55} \end{bmatrix} \begin{Bmatrix} du/dr \\ u/r \\ -d\psi_r/dr \\ -\psi_r/r \\ dw/dr - \psi_r \end{Bmatrix} = \left[\overline{E}\right] \left\{\varepsilon\right\} \tag{3.35}$$

As was the case for the linear Timoshenko beam, this element uses linear interpolation for the three independent displacement quantities. The displacement functions are therefore given by Eqs. (3.20) to (3.22), but in this case, ψ_x becomes ψ_r and the shape functions N_1 and N_2 are

$$N_1 = \frac{r - R_2}{R_1 - R_2} \quad \text{and} \quad N_2 = \frac{R_1 - r}{R_1 - R_2} \tag{3.36}$$

The strain vector $\left\{\varepsilon\right\}$ is related to the nodal displacement vector $\left\{d\right\}$ through the $\left[B\right]$ matrix, as in Eq. (3.10). If $\left\{d\right\} = \left\{u_1 \quad w_1 \quad \psi_1 \quad u_2 \quad w_2 \quad \psi_2\right\}^T$ then the $\left[B\right]$ matrix is

$$\left[B\right] = \begin{bmatrix} \frac{dN_1}{dr} & 0 & 0 & \frac{dN_2}{dr} & 0 & 0 \\ \frac{N_1}{r} & 0 & 0 & \frac{N_2}{r} & 0 & 0 \\ 0 & 0 & -\frac{dN_1}{dr} & 0 & 0 & -\frac{dN_2}{dr} \\ 0 & 0 & -\frac{N_1}{r} & 0 & 0 & -\frac{N_2}{r} \\ 0 & \frac{dN_1}{dr} & -N_1 & 0 & \frac{dN_2}{dr} & -N_2 \end{bmatrix} \tag{3.37}$$

The stiffness matrix $\left[k\right]$, which relates the nodal loads $\left\{r\right\}$ to the nodal displacements $\left\{d\right\}$, as in Eq. (3.14), may now be derived by considering two expressions for the strain energy in an element. One expression is given by Eq. (3.12); the second expression, which

corresponds to Eq. (3.11) but which is for an axisymmetric plate, is as follows:

$$\begin{aligned} U &= \frac{1}{2}\int_V \Big\{\sigma\Big\}^T \Big\{\varepsilon\Big\}\, dV \\ &= \frac{1}{2}\int_{R_1}^{R_2} \Big\{\varepsilon\Big\}^T \Big[\overline{E}\Big] \Big\{\varepsilon\Big\}\, 2\pi r\, dr \\ &= \frac{1}{2}\Big\{d\Big\}^T \left(2\pi \int_{R_1}^{R_2} \Big[B\Big]^T \Big[\overline{E}\Big] \Big[B\Big]\, r\, dr\right) \Big\{d\Big\} \end{aligned} \tag{3.38}$$

Comparing Eqs. (3.38) and (3.12) gives

$$\Big[k\Big] = 2\pi \int_{R_1}^{R_2} \Big[B\Big]^T \Big[\overline{E}\Big] \Big[B\Big]\, r\, dr \tag{3.39}$$

The nodal loads are defined as positive in the direction of the corresponding nodal displacements (see Fig. 3.4). Therefore $\Big\{r\Big\} = \Big\{N_1 \quad P_1 \quad M_1 \quad N_2 \quad P_2 \quad M_2\Big\}^T$. Note that the nodal loads are *totals* for the whole circumference.

The integration in Eq. (3.39) may be carried out using either full or reduced integration. The full-integration result is obtained by integrating in the usual way, however as discussed in §3.2.2, this leads to shear locking for thin elements. For one-point reduced integration, by a method equivalent to that presented in §3.2.2, $\Big[k\Big]$ becomes

$$\Big[k\Big] = (R_2 - R_1)\left(\pi r \Big[B\Big]^T \Big[\overline{E}\Big] \Big[B\Big]\right)_{r=R_1+R_2} \tag{3.40}$$

The resulting matrices from Eqs. (3.39) and (3.40) are not presented here because they are extensive, however they can easily be computed using symbolic computation software.

3.2.4 Linear quadrilaterals

Quadrilateral elements will allow fractured structures to be studied within the context of two-dimensional elasticity. In this section, a four node quadrilateral (QUAD4) element with linear displacement functions is derived. The element deforms in the xz-plane. Its thickness dimension is in the direction of the y-axis. Isoparametric transformation is not necessary in this work, so no details are given here, although this can easily be implemented. The technique for doing this is detailed by Zienkiewicz and Taylor (1989, pp. 150–205). As a result of not using any isoparametric transformations, the QUAD4 elements are rectangular. The element is shown in Fig. 3.5.

The element is formulated in terms of two independent quantities u and w, which exist at each of the four nodes, giving the element eight degrees of freedom. Interpolation of

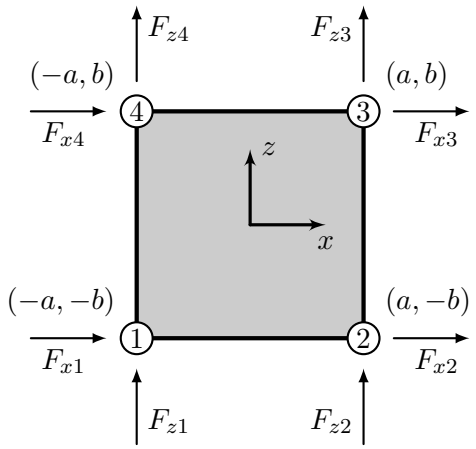

Figure 3.5: A quadrilateral finite element.

these quantities is linear. The displacement field is

$$u = a_1 + a_2x + a_3z + a_4xz \tag{3.41}$$

$$w = b_1 + b_2x + b_3z + b_4xz \tag{3.42}$$

In matrix form, Eqs. (3.41) and (3.42) can be written as

$$\begin{Bmatrix} u \\ w \end{Bmatrix} = \begin{bmatrix} N_1 & 0 & N_2 & 0 & N_3 & 0 & N_4 & 0 \\ 0 & N_1 & 0 & N_2 & 0 & N_3 & 0 & N_4 \end{bmatrix} \Big\{ d \Big\} \tag{3.43}$$

where the nodal displacements vector $\Big\{ d \Big\} = \Big\{ u_1 \quad w_1 \quad u_2 \quad w_2 \quad u_3 \quad w_3 \quad u_4 \quad w_4 \Big\}^T$, u_i and w_i are the u and w displacements respectively at node i and the shape functions N_i are given by

$$\begin{gathered} N_1 = \frac{(a-x)(b-z)}{4ab}; \quad N_2 = \frac{(a+x)(b-z)}{4ab}; \\ N_3 = \frac{(a+x)(b+z)}{4ab} \quad \text{and} \quad N_4 = \frac{(a-x)(b+z)}{4ab} \end{gathered} \tag{3.44}$$

In contrast to the beams and plates considered so far, this two-dimensional element does deform in the z-axis. The laminate constitutive equations in Chapter 2 are for thin laminates where $\sigma_z = \tau_{xz} = \tau_{yz} = 0$, i.e. a plane-stress condition in the xy-plane. The constitutive equations for this element must therefore either be derived for a whole laminate thickness by assembling the constitutive equations for individual laminae with no plane stress assumptions; or by using the lamina constitutive equations from §2.2.2 and §2.2.3 with no loading assumptions and simply spanning one lamina thickness with at least one element.

The first option is more complicated because, in addition to there being force resultants on every face of the element, due to possible material coupling there may also be couples

(systems of forces with a resultant moment but no resultant force) present on each face. These couples would then need to be decomposed into an equivalent force distribution on each face before the work-equivalent nodal loads could be calculated.

The second option is more simple as well as desirable. The behaviour of a laminate under two-dimensional elasticity will be more accurately modelled when the mechanical behaviour of multiple laminae is not 'smeared out' over one element. This must be especially true in the region around a crack tip. Also, since there does not tend to be any material coupling for individual fibre-reinforced laminae, there are no additional considerations in the formulation. Therefore, in this work, the QUAD4 element spans at most the thickness of one lamina only—it is not intended to span multiple lamina in a plate-like fashion.

The constitutive equations for this element depend on the loading conditions, i.e. plane stress, plane strain or a mixed-loading condition. The general form of the constitutive equations for a lamina is given in Eq. (2.21) where the material stiffness matrix for an orthotropic material, $\left[\overline{C}\right]$ is given by Eq. (2.25). They are repeated here for convenience.

$$\begin{Bmatrix} \sigma_{xx} \\ \sigma_{yy} \\ \sigma_{zz} \\ \tau_{yz} \\ \tau_{xz} \\ \tau_{xy} \end{Bmatrix} = \begin{bmatrix} \overline{C}_{11} & \overline{C}_{12} & \overline{C}_{13} & 0 & 0 & \overline{C}_{16} \\ \overline{C}_{12} & \overline{C}_{22} & \overline{C}_{23} & 0 & 0 & \overline{C}_{26} \\ \overline{C}_{13} & \overline{C}_{23} & \overline{C}_{33} & 0 & 0 & \overline{C}_{36} \\ 0 & 0 & 0 & \overline{C}_{44} & \overline{C}_{45} & 0 \\ 0 & 0 & 0 & \overline{C}_{45} & \overline{C}_{55} & 0 \\ \overline{C}_{16} & \overline{C}_{26} & \overline{C}_{36} & 0 & 0 & \overline{C}_{66} \end{bmatrix} \begin{Bmatrix} \varepsilon_{xx} \\ \varepsilon_{yy} \\ \varepsilon_{zz} \\ \gamma_{yz} \\ \gamma_{xz} \\ \gamma_{xy} \end{Bmatrix} \tag{3.45}$$

For some assumed loading conditions in the direction of the y-axis, Eq. (3.45) reduces to

$$\left\{\sigma\right\} = \begin{Bmatrix} \sigma_{xx} \\ \sigma_{zz} \\ \tau_{xz} \end{Bmatrix} = \begin{bmatrix} a_{11} & a_{13} & 0 \\ a_{13} & a_{33} & 0 \\ 0 & 0 & a_{55} \end{bmatrix} \begin{Bmatrix} \varepsilon_{xx} \\ \varepsilon_{zz} \\ \gamma_{xz} \end{Bmatrix} = \left[E\right] \left\{\varepsilon\right\} \tag{3.46}$$

where the a_{ij} quantities represent the equivalent stiffnesses. If the element is in plane strain in the xz-plane (i.e. $\varepsilon_{yy} = \gamma_{xy} = \gamma_{yz} = 0$), then $a_{11} = \overline{C}_{11}$, $a_{13} = \overline{C}_{13}$, $a_{33} = \overline{C}_{33}$ and $a_{55} = \overline{C}_{55}$. If the element is in plane stress in the xz-plane (i.e. $\sigma_{yy} = \tau_{xy} = \tau_{yz} = 0$), then by inverting Eq. (3.45)

$$\begin{Bmatrix} \varepsilon_{xx} \\ \varepsilon_{yy} \\ \varepsilon_{zz} \\ \gamma_{yz} \\ \gamma_{xz} \\ \gamma_{xy} \end{Bmatrix} = \begin{bmatrix} \overline{S}_{11} & \overline{S}_{12} & \overline{S}_{13} & 0 & 0 & \overline{S}_{16} \\ \overline{S}_{12} & \overline{S}_{22} & \overline{S}_{23} & 0 & 0 & \overline{S}_{26} \\ \overline{S}_{13} & \overline{S}_{23} & \overline{S}_{33} & 0 & 0 & \overline{S}_{36} \\ 0 & 0 & 0 & \overline{S}_{44} & \overline{S}_{45} & 0 \\ 0 & 0 & 0 & \overline{S}_{45} & \overline{S}_{55} & 0 \\ \overline{S}_{16} & \overline{S}_{26} & \overline{S}_{36} & 0 & 0 & \overline{S}_{66} \end{bmatrix} \begin{Bmatrix} \sigma_{xx} \\ \sigma_{yy} \\ \sigma_{zz} \\ \tau_{yz} \\ \tau_{xz} \\ \tau_{xy} \end{Bmatrix} \tag{3.47}$$

and applying the plane-stress conditions, the following is obtained:

$$\begin{Bmatrix} \sigma_{xx} \\ \sigma_{zz} \\ \tau_{xz} \end{Bmatrix} = \begin{bmatrix} \overline{S}_{11} & \overline{S}_{13} & 0 \\ \overline{S}_{13} & \overline{S}_{33} & 0 \\ 0 & 0 & \overline{S}_{55} \end{bmatrix}^{-1} \begin{Bmatrix} \varepsilon_{xx} \\ \varepsilon_{zz} \\ \gamma_{xz} \end{Bmatrix} \tag{3.48}$$

The a_{ij} stiffnesses are found by comparing Eqs. (3.46) and (3.48). A similar procedure can be carried out for a mixed-loading condition.

Regardless of the loading conditions, there are three strains to consider. Using the linear strain-displacement relations for infinitesimal strain in two dimensions gives

$$\Big\{\varepsilon\Big\} = \begin{Bmatrix} \varepsilon_{xx} \\ \varepsilon_{zz} \\ \gamma_{xz} \end{Bmatrix} = \begin{Bmatrix} du/dx \\ dw/dz \\ du/dz + dw/dx \end{Bmatrix} \tag{3.49}$$

The strain vector $\Big\{\varepsilon\Big\}$ is related to the nodal displacement vector $\Big\{d\Big\}$ through the $\Big[B\Big]$ matrix, as in Eq. (3.10). With reference to Eqs. (3.43) and (3.49), the $\Big[B\Big]$ matrix is

$$\Big[B\Big] = \begin{bmatrix} \frac{dN_1}{dx} & 0 & \frac{dN_2}{dx} & 0 & \frac{dN_3}{dx} & 0 & \frac{dN_4}{dx} & 0 \\ 0 & \frac{dN_1}{dz} & 0 & \frac{dN_2}{dz} & 0 & \frac{dN_3}{dz} & 0 & \frac{dN_4}{dz} \\ \frac{dN_1}{dz} & \frac{dN_1}{dx} & \frac{dN_2}{dz} & \frac{dN_2}{dx} & \frac{dN_3}{dz} & \frac{dN_3}{dx} & \frac{dN_4}{dz} & \frac{dN_4}{dx} \end{bmatrix} \tag{3.50}$$

If the thickness of the element (in the direction of the y-axis) is t, then the strain energy is

$$\begin{aligned} U &= \frac{1}{2}\int_V \Big\{\sigma\Big\}^T \Big\{\varepsilon\Big\}\, dV \\ &= \frac{1}{2}\int_{-b}^{b}\int_{-a}^{a} \Big\{\varepsilon\Big\}^T \Big[E\Big] \Big\{\varepsilon\Big\}\, t\, dx\, dz \\ &= \frac{1}{2}\Big\{d\Big\}^T \left(\int_{-b}^{b}\int_{-a}^{a} \Big[B\Big]^T \Big[E\Big] \Big\{B\Big\}\, t\, dx\, dz\right) \Big\{d\Big\} \end{aligned} \tag{3.51}$$

The expression for stiffness matrix $\Big[k\Big]$, which relates the nodal loads $\Big\{r\Big\}$ to the nodal displacements $\Big\{d\Big\}$, as in Eq. (3.14), is obtained by comparing Eqs. (3.12) and (3.51). The nodal loads are defined as positive in the direction of the corresponding nodal displacements (see Fig. 3.5). Therefore $\Big\{r\Big\} = \Big\{F_{x1} \quad F_{z1} \quad F_{x2} \quad F_{z2} \quad \dots \quad F_{z4}\Big\}^T$.

$$\Big[k\Big] = t\int_{-b}^{b}\int_{-a}^{a} \Big[B\Big]^T \Big[E\Big] \Big[B\Big]\, dx\, dz \tag{3.52}$$

The resulting matrix is not presented here because it is extensive, however it can easily be computed using symbolic computation software.

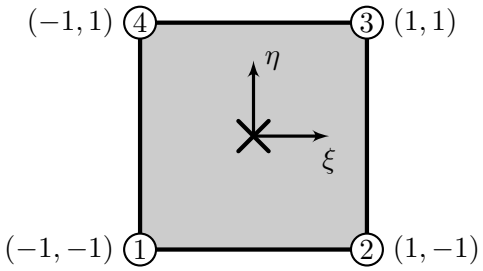

Figure 3.6: One-point Gaussian quadrature of a QUAD4 finite element.

One-point Gaussian quadrature can also be used to evaluate the integration in Eq. (3.52). For two dimensions and an $n \times n$ distribution of Gauss points, the n-point Gaussian quadrature rule in Eq. (3.27) becomes

$$I = \int_{-1}^{1} \int_{-1}^{1} f(\xi, \eta)\, d\xi\, d\eta = \sum_{i=1}^{n^2} f(\xi_i, \eta_i)\, H_i \tag{3.53}$$

where ξ and η are the conventional coordinates, running from -1 to 1. They are shown in Fig. 3.6. For one-point Gaussian quadrature, the following polynomial is required to represent $f(\xi, \eta)$:

$$f(\xi, \eta) = C_0 + C_1\xi + C_2\eta + C_3\xi\eta \tag{3.54}$$

where C_0, C_1, C_2 and C_3 are unknown coefficients. Evaluating Eq. (3.53) using Eq. (3.54) gives

$$I = 4C_0 \tag{3.55}$$

implying that $\xi_1 = 0$, $\eta_1 = 0$ and $H_1 = 4$. The single integration point therefore lies at the centre of the element, as indicated by the cross in Fig. 3.6. To evaluate Eq. (3.52) using one-point Gaussian quadrature, the integrand must be transformed into the ξ and η coordinates. With reference to Figs. 3.5 and 3.6, the relationships between x and ξ, and y and η are

$$x = a\xi; \quad dx = a\, d\xi; \quad y = b\eta \quad \text{and} \quad dy = b\, d\eta$$

Transforming Eq. (3.52) into the ξ and η coordinates gives

$$\Big[k\Big] = t \int_{-1}^{1} \int_{-1}^{1} \Big[B\Big]^T \Big[E\Big] \Big[B\Big]\, ab\, d\xi\, d\eta \tag{3.56}$$

Therefore clearly

$$C_0 = \left(\Big[B\Big]^T \Big[E\Big] \Big[B\Big]\, ab \right)_{(x=0, y=0)} \tag{3.57}$$

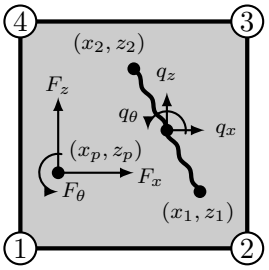

Figure 3.7: Concentrated and distributed loads acting on a quadrilateral finite element.

and from Eq. (3.55), the resulting stiffness matrix is

$$\left[k\right] = 4\left(\left[B\right]^T\left[E\right]\left[B\right]ab\right)_{(x=0,y=0)} \tag{3.58}$$

The full-integration QUAD4 element has some flaws when combined with incompressible material. The displacements in the mesh are orders of magnitude smaller than in the reality. This is called 'volumetric locking'. Using reduced-integration elements (with one central integration point) can resolve the volumetric locking problem, but doing so also introduces another problem. Consider a QUAD4 element: if the nodes on the lower edge move towards each other, and the nodes on the upper edge move away from each other by the same amount, then the element has deformed and has become a trapezium. However, in this mode, the integration point at the centre of the element does not 'detect' the deformation, as indicated by vertical and horizontal lines through the centre of the element which neither extend nor rotate. Therefore, if this element deforms in this mode, it can produce no forces to resist it, and the deformation pattern can grow unbounded. This deformation pattern is called the 'hourglass mode' or the 'zero energy mode'.

Consequently, reduced-integration QUAD4 elements must be stabilised against hourglassing by building in artificial stiffness. There are several methods to do this. Zienkiewicz and Taylor (1989, pp. 383–5) describe a simple stabilisation technique. Commercial FEM software packages, such as SIMULIA's Abaqus, implement similar methods for hourglass control.

In general, a finite element of any type may be subject to loads which are not located at the nodes. Equivalent nodal loads replace any concentrated and distributed loads acting on an element. For the beam and plate finite elements in the preceding sections, equivalent nodal loads have not been considered because in this work there is no need for them. However, for QUAD4 elements, especially in modelling of beam-like structures and in the application of distributed bending moments, equivalent nodal loads are required.

Fig. 3.7 shows point loads (F_x, F_z, F_θ) acting at a point (x_p, z_p) and distributed loads (q_x, q_z, q_θ) acting along a straight line joining (x_1, z_1) and (x_2, z_2). The potential energy of the concentrated loads is

$$\Omega = -F_x u\left(x_p, z_p\right) - F_z w\left(x_p, z_p\right) - F_\theta \theta\left(x_p, z_p\right) \tag{3.59}$$

and the potential energy of the distributed loads is

$$\Omega = -\int_{x_1}^{x_2} q_x u\,(x,z)\,dx - \int_{x_1}^{x_2} q_z w\,(x,z)\,dz - \int_{x_1}^{x_2} q_\theta \theta\,(x,z)\,d\theta \tag{3.60}$$

where θ is the rotation, which is equal to $(dw/dx - du/dz)/2$. The integrations are written with respect to x so the displacements must be written as a function of x only. Since the loads are distributed over a straight line, the z-coordinate in terms of x is

$$z = z_1 + (x - x_1)\,\frac{z_2 - z_1}{x_2 - x_1} \tag{3.61}$$

By combining these two potential energies, the work-equivalent nodal loads vector $\left\{r\right\}$ is easily obtained by means of the principle of minimum total potential energy. It is found to be

$$\left\{r\right\} = \int_{x_1}^{x_2} \begin{Bmatrix} q_x N_1 - \frac{q_\theta}{2}\frac{dN_1}{dy} \\ q_z N_1 + \frac{q_\theta}{2}\frac{dN_1}{dx} \\ q_x N_2 - \frac{q_\theta}{2}\frac{dN_2}{dy} \\ q_z N_2 + \frac{q_\theta}{2}\frac{dN_2}{dx} \\ \vdots \\ q_z N_4 + \frac{q_\theta}{2}\frac{dN_4}{dx} \end{Bmatrix} dx + \begin{Bmatrix} F_x N_1 - \frac{F_\theta}{2}\frac{dN_1}{dy} \\ F_z N_1 + \frac{F_\theta}{2}\frac{dN_1}{dx} \\ F_x N_2 - \frac{F_\theta}{2}\frac{dN_2}{dy} \\ F_z N_2 + \frac{F_\theta}{2}\frac{dN_2}{dx} \\ \vdots \\ F_z N_4 + \frac{F_\theta}{2}\frac{dN_4}{dx} \end{Bmatrix}_{(x_p,y_p)} \tag{3.62}$$

The expressions that result from the evaluation of Eq. (3.62) are extensive and are therefore not presented here. However as before, they can easily be computed using symbolic computation software.

3.2.5 Axisymmetric linear quadrilaterals

In this section, an axisymmetric QUAD4 element, as shown in Fig. 3.8, is derived. This element is the axisymmetric equivalent of the linear QUAD4 element derived in §3.2.4. It also is intended to span the thickness of at most one lamina only and is therefore based on the constitutive equations of a lamina, as given in §2.2.2 and §2.2.3. As before, no isoparametric transformation is implemented, so the element is rectangular (i.e. the annulus has a rectangular cross-section in the rz-plane).

The general form of the constitutive equations for a lamina is given in Eq. (2.21) where the material stiffness matrix for an orthotropic material, $\left[\overline{C}\right]$ is given by Eq. (2.25). For cylindrical coordinates, the x-axis maps onto the r-axis; the y-axis maps onto the ϕ-axis and the z-axis remains unchanged. Because of axisymmetry, $\gamma_{r\phi} = \gamma_{\phi z} = 0$. The resulting constitutive equations for a laminated axisymmetric plate are given in Eq. (3.63). The linear strain-displacement relations for infinitesimal strain in two dimensions in cylindrical

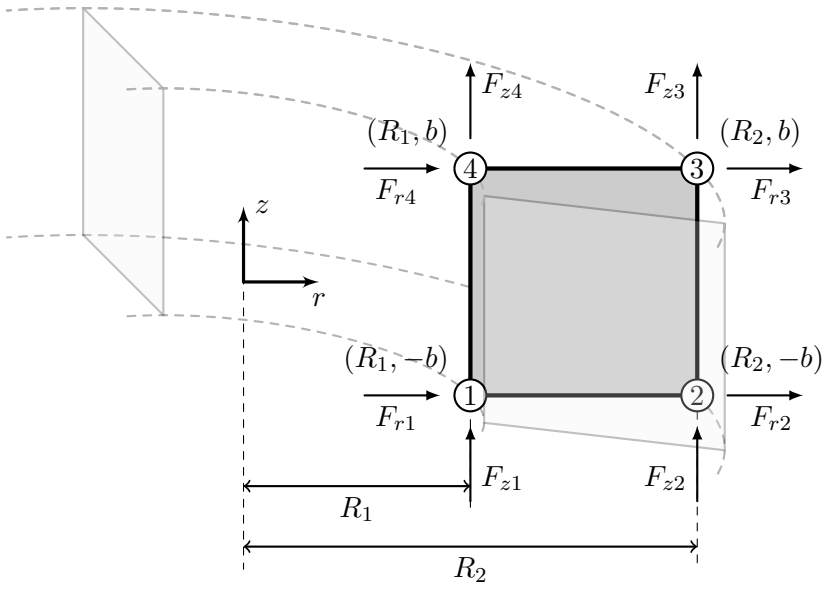

Figure 3.8: An axisymmetric quadrilateral finite element.

coordinates are used to expand the strain vector.

$$\Big\{\sigma\Big\} = \begin{Bmatrix} \sigma_{rr} \\ \sigma_{\phi\phi} \\ \sigma_{zz} \\ \tau_{rz} \end{Bmatrix} = \begin{bmatrix} \overline{C}_{11} & \overline{C}_{12} & \overline{C}_{13} & 0 \\ \overline{C}_{12} & \overline{C}_{22} & \overline{C}_{23} & 0 \\ \overline{C}_{13} & \overline{C}_{23} & \overline{C}_{33} & 0 \\ 0 & 0 & 0 & \overline{C}_{55} \end{bmatrix} \begin{Bmatrix} \varepsilon_{rr} \\ \varepsilon_{\phi\phi} \\ \varepsilon_{zz} \\ \gamma_{rz} \end{Bmatrix} = \Big[E\Big] \begin{Bmatrix} du/dr \\ u/r \\ dw/dz \\ du/dz + dw/dr \end{Bmatrix} \tag{3.63}$$

The element is formulated in terms of two independent quantities u and w, which exist at each of the four nodes, giving the element eight degrees of freedom. The displacement field is still given by Eq. (3.43) but now the shape functions N_i are

$$\begin{aligned} N_1 &= \frac{(r - R_2)(b - z)}{2b(R_1 - R_2)}; \quad N_2 = \frac{(R_1 - r)(b - z)}{2b(R_1 - R_2)}; \\ N_3 &= \frac{(R_1 - r)(b + z)}{2b(R_1 - R_2)} \quad \text{and} \quad N_4 = \frac{(r - R_2)(b + z)}{2b(R_1 - R_2)} \end{aligned} \tag{3.64}$$

The strain vector $\Big\{\varepsilon\Big\}$ is related to the nodal displacement vector $\Big\{d\Big\}$ through the $\Big[B\Big]$ matrix, as in Eq. (3.10). If $\Big\{d\Big\} = \Big\{u_1 \quad w_1 \quad u_2 \quad w_2 \quad \dots \quad w_4\Big\}^T$ then the $\Big[B\Big]$ matrix is

$$\Big[B\Big] = \begin{bmatrix} \frac{dN_1}{dr} & 0 & \frac{dN_2}{dr} & 0 & \frac{dN_3}{dr} & 0 & \frac{dN_4}{dr} & 0 \\ 0 & \frac{dN_1}{dz} & 0 & \frac{dN_2}{dz} & 0 & \frac{dN_3}{dz} & 0 & \frac{dN_4}{dz} \\ \frac{N_1}{r} & 0 & \frac{N_2}{r} & 0 & \frac{N_3}{r} & 0 & \frac{N_4}{r} & 0 \\ \frac{dN_1}{dz} & \frac{dN_1}{dr} & \frac{dN_2}{dz} & \frac{dN_2}{dr} & \frac{dN_3}{dz} & \frac{dN_3}{dr} & \frac{dN_4}{dz} & \frac{dN_4}{dr} \end{bmatrix} \tag{3.65}$$

The strain energy of the element can now be calculated as follows:

$$\begin{aligned} U &= \frac{1}{2}\int_V \Big\{\sigma\Big\}^T \Big\{\varepsilon\Big\}\, dV \\ &= \frac{1}{2}\int_{-b}^{b}\int_{R_1}^{R_2} \Big\{\varepsilon\Big\}^T \Big[E\Big] \Big\{\varepsilon\Big\}\, 2\pi r\, dr\, dz \\ &= \frac{1}{2}\Big\{d\Big\}^T \left(\int_{-b}^{b}\int_{R_1}^{R_2} \Big[B\Big]^T \Big[E\Big] \Big\{B\Big\}\, 2\pi r\, dr\, dz\right) \Big\{d\Big\} \end{aligned} \tag{3.66}$$

The expression for stiffness matrix $\Big[k\Big]$, which relates the nodal loads $\Big\{r\Big\}$ to the nodal displacements $\Big\{d\Big\}$, as in Eq. (3.14), is obtained by comparing Eqs. (3.12) and (3.66). The nodal loads are defined as positive in the direction of the corresponding nodal displacements (see Fig. 3.8). Therefore $\Big\{r\Big\} = \Big\{F_{r1} \quad F_{z1} \quad F_{r2} \quad F_{z2} \quad \dots \quad F_{z4}\Big\}^T$. Note that the nodal loads are *totals* for the whole circumference.

$$\Big[k\Big] = 2\pi \int_{-b}^{b}\int_{R_1}^{R_2} \Big[B\Big]^T \Big[E\Big] \Big[B\Big]\, r\, dr\, dz \tag{3.67}$$

The resulting matrix is not presented here because it is extensive, however it can easily be computed using symbolic computation software. The work-equivalent nodal loads are derived in the same way as in §3.2.4.

3.2.6 Mode I interface springs

In the FEM simulations carried out in this work, interface springs are used to simulate the interfaces between laminae or sub-laminates. Briefly, for two-dimensional FEM simulations, two types of interface spring are required: mode I interface springs to carry normal stress across the interface; and mode II interface springs to carry shear stress. Further details on using interface springs are given in §3.3. In this section, only the mode I interface spring finite element is presented.

Fig. 3.9 shows a mode I interface spring finite element, connecting the mid-surface nodes of two beam or plate finite elements. The spring can also be used to join QUAD4

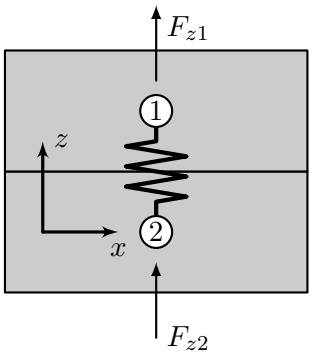

Figure 3.9: A mode I interface spring finite element.

elements, in which case the two nodes would be co-located. The stiffness matrix for a mode I interface spring is the same as for a standard spring. The nodal load-displacement relation is well known and easily derived. It is

$$\begin{Bmatrix} F_{z1} \\ F_{z2} \end{Bmatrix} = k_s \begin{bmatrix} 1 & -1 \\ -1 & 1 \end{bmatrix} \begin{Bmatrix} w_1 \\ w_2 \end{Bmatrix} \tag{3.68}$$

where k_s is the interface spring stiffness. The value of k_s is discussed in §3.3.

3.2.7 Mode II interface springs

Fig. 3.10 shows a mode II interface spring finite element. The stiffness matrix for such an element can be derived by considering the strain energy in the spring.

$$U = \frac{1}{2} k_s \left(\overline{u}_1 - \overline{u}_2\right)^2 \tag{3.69}$$

The quantities $\overline{u}_1$ and $\overline{u}_2$ are the axial displacements at the interface of the upper and lower sub-laminates respectively. For beam or plate finite elements, where the spring nodes are located on the mid-surface, the rotation $\theta = dw/dx$ at each node needs to be accounted for in the calculation of the interface displacements, as follows:

$$\overline{u}_1 = u_1 + \frac{h_1\theta_1}{2} \quad \text{and} \quad \overline{u}_2 = u_2 - \frac{h_2\theta_2}{2} \tag{3.70}$$

For QUAD4 elements, where nodes exist on the interface, terms containing h_1 or h_2 should be ignored. This can be done by simply set them to zero. The resulting stiffness matrix in this case is the same as for a standard spring. Therefore this derivation continues with the assumption of mid-surface nodes for the upper and lower sub-laminates.

The potential energy of the nodal forces Ω is

$$\Omega = -F_{x1}u_1 - M_1\theta_1 - F_{x2}u_2 - M_2\theta_2 \tag{3.71}$$

Therefore the total potential energy Π of the spring element is

$$\Pi = \frac{1}{2} k_s \left(u_1 + \frac{h_1\theta_1}{2} - u_2 + \frac{h_2\theta_2}{2}\right)^2 - F_{x1}u_1 - M_1\theta_1 - F_{x2}u_2 - M_2\theta_2 \tag{3.72}$$

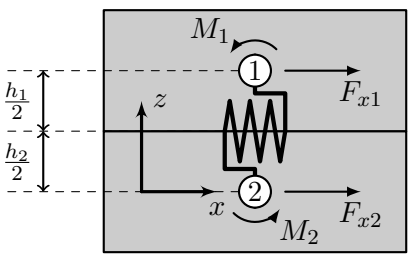

Figure 3.10: A mode II interface spring finite element.

The principle of minimum potential energy states that

$$\delta\Pi = \frac{\partial\Pi}{\partial u_1}\delta u_1 + \frac{\partial\Pi}{\partial\theta_1}\delta\theta_1 + \frac{\partial\Pi}{\partial u_2}\delta u_2 + \frac{\partial\Pi}{\partial\theta_2}\delta\theta_2 = 0 \tag{3.73}$$

which implies that each differential must be independently zero.

$$\begin{aligned}
\frac{\partial\Pi}{\partial u_1} &= k_s\left(u_1 + \frac{h_1\theta_1}{2} - u_2 + \frac{h_2\theta_2}{2}\right) - F_{x1} = 0 \\
\frac{\partial\Pi}{\partial\theta_1} &= k_s\left(\frac{h_1u_1}{2} + \frac{h_1^2\theta_1}{4} - \frac{h_1u_2}{2} + \frac{h_1h_2\theta_2}{4}\right) - M_1 = 0 \\
\frac{\partial\Pi}{\partial u_2} &= k_s\left(-u_1 - \frac{h_1\theta_1}{2} + u_2 - \frac{h_2\theta_2}{2}\right) - F_{x2} = 0 \\
\frac{\partial\Pi}{\partial\theta_2} &= k_s\left(\frac{h_2u_1}{2} + \frac{h_1h_2\theta_1}{4} - \frac{h_2u_2}{2} + \frac{h_2^2\theta_2}{4}\right) - M_2 = 0
\end{aligned} \tag{3.74}$$

Writing these equations in matrix form gives

$$\begin{Bmatrix} F_{x1} \\ M_1 \\ F_{x2} \\ M_2 \end{Bmatrix} = \Big[k\Big] \begin{Bmatrix} u_1 \\ \theta_1 \\ u_2 \\ \theta_2 \end{Bmatrix} \tag{3.75}$$

where $\Big[k\Big]$ is the stiffness matrix

$$\Big[k\Big] = k_s \begin{bmatrix} 1 & \frac{h_1}{2} & -1 & \frac{h_2}{2} \\ \frac{h_1}{2} & \frac{h_1^2}{4} & -\frac{h_1}{2} & \frac{h_1h_2}{4} \\ -1 & -\frac{h_1}{2} & 1 & -\frac{h_2}{2} \\ \frac{h_2}{2} & \frac{h_1h_2}{4} & -\frac{h_2}{2} & \frac{h_2^2}{4} \end{bmatrix} \tag{3.76}$$

3.3 Interface modelling

For fibre-reinforced laminated composites, interface modelling is based on the assumption that a resin-rich interface layer exists between laminae and that delamination occurs within this layer. Micrographs reveal that such a layer does exist and that delamination does normally occur preferentially within it.

The most simple and convenient interface model uses point springs to model a zero-thickness interface layer (Cui and Wisnom 1993, Zhang and Wang 2009, Harvey and Wang 2012*d*). The interface springs bind together laminae or sub-laminates. They are imaginary in that they have stiffness but no volume or mass and are non-physical.

For two-dimensional FEM simulations, each pair of nodes requires two independent springs to connect sub-laminates: a spring normal to the interface, which carries a force equal to the integration of the interface normal stress over the element length; and a spring

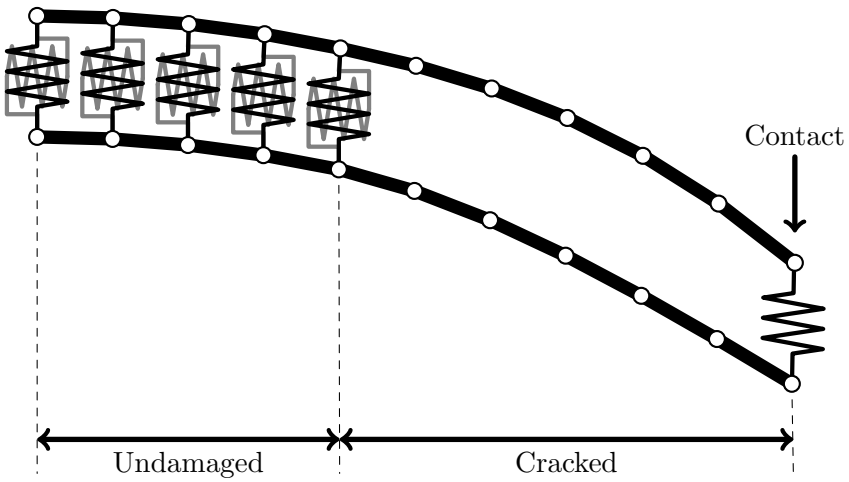

Figure 3.11: Interface modelling with point interface springs.

tangential to the interface, which carries a force equal to the integration of the through-thickness shear over the element length. The first is known as a 'mode I interface spring' since it acts to prevent opening; the second is known as a 'mode II interface spring' since it acts to prevent sliding (see Fig. 2.9 for Irwin's classification of fracture modes according to the directions of the displacements at the crack tip). In two-dimensional simulations, no mode III interface spring is required.

The behaviour of the interface springs can be linear or non-linear. In this work it is assumed that they have linear behaviour. Also, it is assumed that the interface is perfectly rigid until failure (except for the work on non-rigid elastic interfaces in Chapter 8). A constant, very large spring stiffness k_s, which precludes any significant displacements, is used to achieve this.

Fig. 3.11 shows the use of interface springs to model an interface. It shows the mid-surfaces of two layers of beam elements in a DCB configuration. Under certain loads, there are three regions: (1) an undamaged region, joined by means of the two types of interface spring; (2) a cracked region, with either no interface springs or with zero-stiffness interface springs; and (3) a contact region within the cracked part. No friction between the crack surfaces is considered. Therefore only mode I interface springs are used in contact regions to prevent interpenetration.

3.4 Contact algorithm

A delaminated laminate under a general loading may experience contact between sub-laminates. There are two effects to consider: (1) the intersection of elements; and (2) friction. In this work, friction between laminae in contact is not considered because Jansson and Larsson (2001) have shown that a cracked interface is approximately frictionless. They

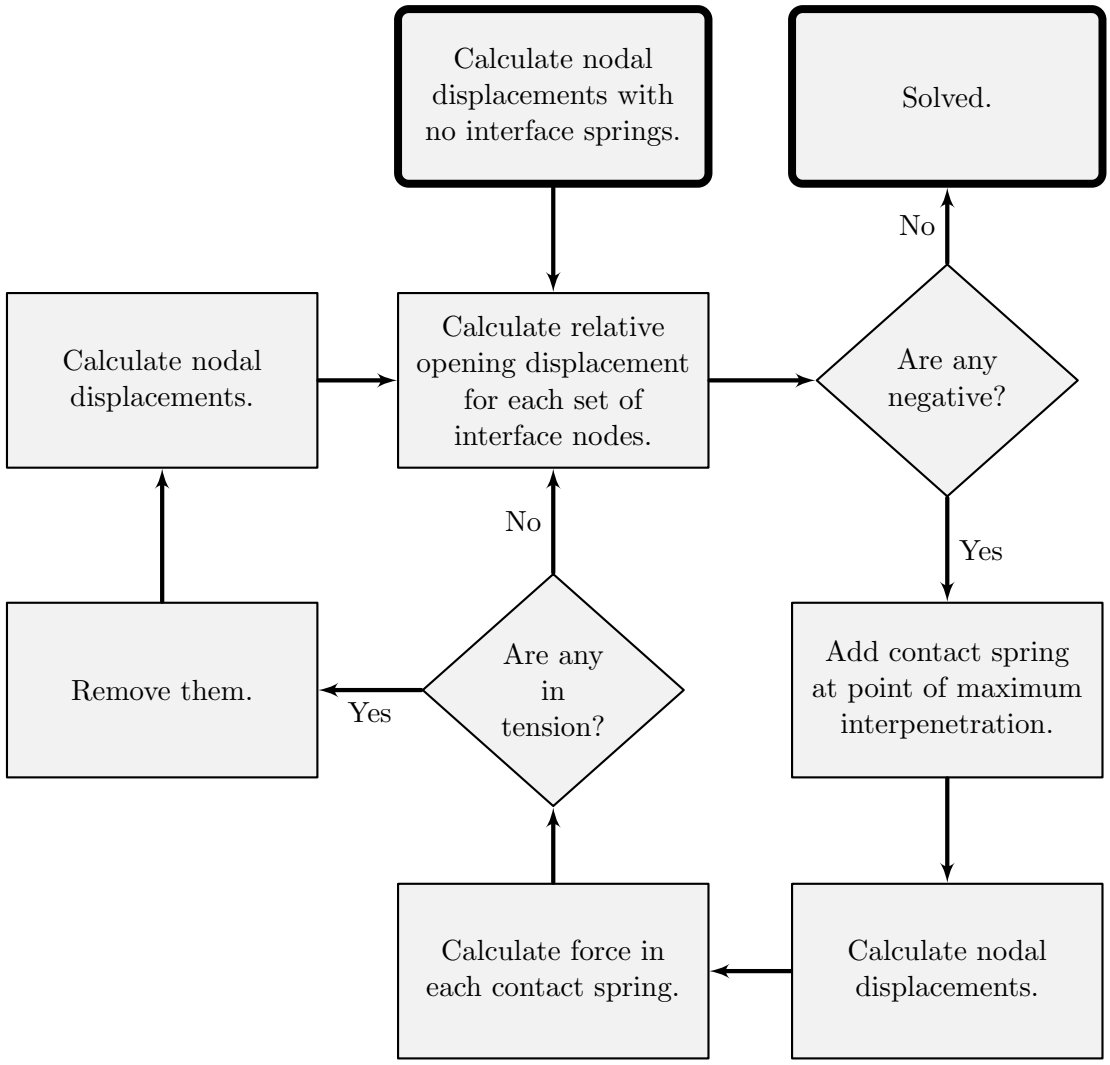

Figure 3.12: A simple contact algorithm.

compared results from simulations of frictionless contact against results from simulations with a friction coefficient of 0.2 and found the difference to be negligible.

To prevent interpenetration of surfaces in FEM simulations, a simple contact algorithm has been implemented. The philosophy is to add very high stiffness mode I interface springs where interpenetration would otherwise occur. Regions where these springs exist are considered to be in contact. Fig. 3.12 shows the contact algorithm in flowchart form.

3.5 Virtual crack closure technique

Even though the virtual crack closure technique (VCCT) is the focus of this section, it is appropriate to begin by mentioning the crack closure method, which is related to the VCCT. The crack closure method is based on Irwin's (1958) crack closure integral. The method is based on the assumption that the energy released when the crack is extended by

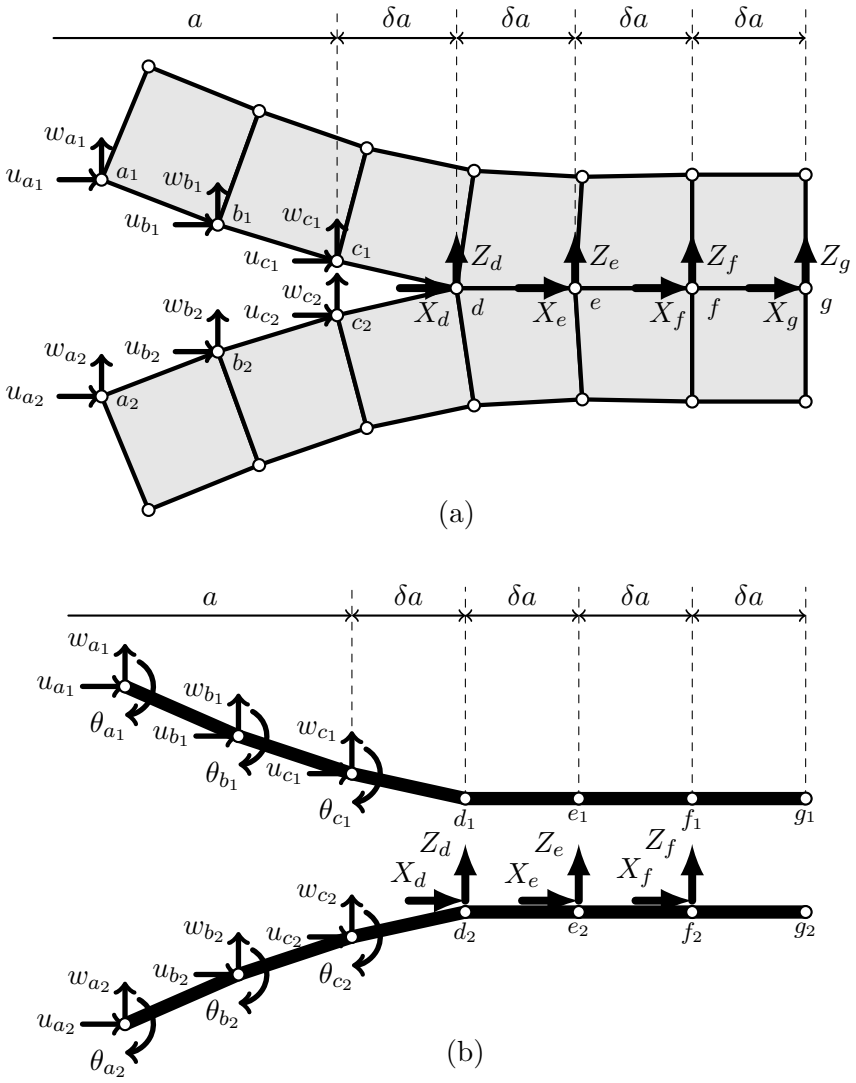

Figure 3.13: The VCCT for (a) QUAD4 elements; and (b) beam and plate elements.

δa is identical to the energy required to re-close the crack by that same distance. Using this method, two complete FEM simulations are required (before and after crack extension).

The VCCT is based on the same assumptions as the crack closure method. However, in addition, it is assumed that a crack extension of δa does not significantly alter the state at the crack tip. As a result of this assumption, the ERR partition can be calculated with one FEM simulation only using the VCCT.

Krueger (2002) gave a thorough overview of the VCCT. He presented different forms of the VCCT when applied to different types of finite element. In this section, the VCCT is applied to the finite elements derived in §3.2.

Fig. 3.13 shows two FEM meshes of a cracked laminate. The first is constructed from QUAD4 elements and the second, from beam or plate elements. In the undamaged region, the layers are joined with pairs of interface springs at the nodes. Recall that the forces

in the mode I and II springs represent the integrations of the interface normal stress and shear stress over the element length respectively. In Fig. 3.13 these integrations at node i are denoted by Z_i and X_i respectively. For clarity, they are only shown on the lower sub-laminate, although for equilibrium there are clearly also equal opposing forces at each node on the upper sub-laminate. The displacements tangential and normal to the crack surfaces at node i are denoted by u_i and w_i respectively. In the cracked region, an additional subscript 1 or 2 indicates quantities relating to the upper and lower sub-laminate respectively.

The crack tip before extension lies at $x = a$ which is at node c. The crack extends by δa to a length $a + \delta a$ to node d. Since the state at the crack tip is assumed not to change during crack extension, the relative displacements at node c behind the extended crack tip are approximately equal to the displacements at node b behind the original crack tip. Further, the energy released when the crack is extended by δa from a to $a + \delta a$ is identical to the energy required to close the crack again between locations d and c. Thus, the forces and displacements required to calculate the energy to close the crack may be obtained from one single FEM simulation.

For a crack modelled with two-dimensional QUAD4 elements, as shown in Fig. 3.13 (a), the work W required to close the crack by one element is

$$W = \frac{1}{2} Z_d \left(w_{c_1} - w_{c_2} \right) + \frac{1}{2} X_d \left(u_{c_1} - u_{c_2} \right) \tag{3.77}$$

The displacements at the points of load application remain fixed during crack extension and consequently do no work.

The ERR is the energy released per unit area of crack extension, i.e. $G = W/\Delta A$. The mode I and II components of ERR are obtained by splitting the total ERR into contributions from opening and shearing action respectively, which gives

$$G_I = \frac{Z_d \left(w_{c_1} - w_{c_2} \right)}{2t\, \delta a} \quad \text{and} \quad G_{II} = \frac{X_d \left(u_{c_1} - u_{c_2} \right)}{2t\, \delta a} \tag{3.78}$$

where t is the thickness of the QUAD4 element (in the y-direction). Eq. (3.78) represents what is referred to in this work as the 'local partition', because only quantities local to the crack tip are involved. By using more spring pairs in the calculation, a 'global partition' can be approached. Note that the terms 'local partition' and 'global partition' in this work do not mean the same as they do in work by Charalambides et al. (1992), Hashemi et al. (1991), etc. They used 'global partition' to refer the the energy-based approach as opposed to one based on two-dimensional elasticity theory, which is what they called the 'local partition'. In this work, these terms refer to the size of the region included in the crack closure integral.

The ERR partition with two spring pairs is

$$G_I = \frac{Z_d\left(w_{b_1} - w_{b_2}\right) + Z_e\left(w_{c_1} - w_{c_2}\right)}{4t\,\delta a}$$
$$G_{II} = \frac{X_d\left(u_{b_1} - u_{b_2}\right) + X_e\left(u_{c_1} - u_{c_2}\right)}{4t\,\delta a} \tag{3.79}$$

and with three spring pairs is

$$G_I = \frac{Z_d\left(w_{a_1} - w_{a_2}\right) + Z_e\left(w_{b_1} - b_{c_2}\right) + Z_f\left(w_{c_1} - b_{c_2}\right)}{6t\,\delta a}$$
$$G_{II} = \frac{X_d\left(u_{a_1} - u_{a_2}\right) + X_e\left(u_{b_1} - u_{c_2}\right) + X_f\left(u_{c_1} - u_{c_2}\right)}{6t\,\delta a} \tag{3.80}$$

For a crack modelled with beam or plate elements, as shown in Fig. 3.13 (b), the nodal displacements do not lie on the crack surfaces and some additional terms are required to account for the nodal rotation. If $\overline{u}$ and $\overline{w}$ denote the horizontal and vertical displacements at the interface respectively, then

$$G_I = \frac{Z_d\left(\overline{w}_{c_1} - \overline{w}_{c_2}\right)}{2b\,\delta a} = \frac{Z_d\left(w_{c_1} - w_{c_2}\right)}{2b\,\delta a}$$
$$G_{II} = \frac{X_d\left(\overline{u}_{c_1} - \overline{u}_{c_2}\right)}{2b\,\delta a} = \frac{X_d\left(u_{c_1} + h_1\theta_{c_1}/2 - u_{c_2} + h_2\theta_{c_2}/2\right)}{2b\,\delta a} \tag{3.81}$$

where b is the width of the beam. For two spring pairs

$$G_I = \frac{Z_d\left(\overline{w}_{b_1} - \overline{w}_{b_2}\right) + Z_e\left(\overline{w}_{c_1} - \overline{w}_{c_2}\right)}{4b\,\delta a} = \frac{Z_d\left(w_{b_1} - w_{b_2}\right) + Z_e\left(w_{c_1} - w_{c_2}\right)}{4b\,\delta a}$$
$$G_{II} = \frac{X_d\left(\overline{u}_{b_1} - \overline{u}_{b_2}\right) + X_e\left(\overline{u}_{b_1} - \overline{u}_{b_2}\right)}{4b\,\delta a} \tag{3.82}$$

where

$$\overline{u}_{i_1} - \overline{u}_{i_2} = u_{i_1} + \frac{h_1}{2}\theta_{i_1} - u_{i_2} + \frac{h_2}{2}\theta_{i_2} \tag{3.83}$$

The ERR for three or more spring pairs is calculated by simply extending the same procedure. Note that for axisymmetric structures, $b\,\delta a$ (or $t\,\delta a$ for QUAD4 elements) in Eqs. (3.78) and Eq. (3.81), which are for one spring pair, must be replaced with $\pi\left(r_d^2 - r_c^2\right)$, where r_d are r_c are the radii at nodes d and c respectively. Similarly, for Eqs. (3.79) and (3.82), which are for two spring pairs, $2b\,\delta a$ (or $2t\,\delta a$ for QUAD4 elements) must be replaced with $\pi\left(r_d^2 - r_b^2\right)$, etc.

3.6 Conclusion

Finite elements that are suitable for modelling one-dimensional fractures, have been derived. These have included cubic Euler beams, linear Timoshenko beams with full and reduced integration, linear QUAD4 elements and the axisymmetric equivalents of each of these.

Two or more layers of elements are used to represent laminates with at least one layer on each side of a fracture. Normal and shear point interface springs with very high stiffness are used to model perfectly bonded layers. Cracked regions are modelled with either no interface springs or with zero-stiffness interface springs. With this approach to interface modelling, the VCCT can be easily used to determine the ERR partition with just one complete FEM simulation.

A simple contact algorithm has also been developed. The philosophy is to add very high stiffness mode I interface springs where interpenetration would otherwise occur.

The theories of laminated composite beams and plates, and principles from fracture mechanics have been implemented in the FEM. The detailed analytical and numerical studies of one-dimensional fracture, which constitute the major part of this work, can now commence.

Chapter 4

Layered isotropic homogeneous double cantilever beams

Contents

4.1 Introduction

The crack in a DCB is the most fundamental one-dimensional fracture problem, yet there has been a considerable amount of difficulty and confusion in calculating its mixed-mode ERR partition. In this chapter, an isotropic homogeneous DCB is taken as a typical representative of one-dimensional fracture problems and completely analytical partition theories are developed by a new approach, based on orthogonal pure fracture modes.

Although fracture of engineering materials or structures is in general a three-dimensional problem, the study of one-dimensional fracture is still of great importance for several reasons. One-dimensional fracture is often used in experimental tests to obtain the critical ERR or toughness of a material in pure fracture modes, for example the DCB and ENF tests for pure mode I and mode II fracture respectively. In the case of mixed-mode fracture, for example in the MMB test, one-dimensional fracture is often used to investigate fracture propagation criteria. In addition, many practical fractures in materials can be approximated as one-dimensional fracture. Some examples include through-width fracture in straight or curved beams, circular ring-type fracture in plates and shells during drilling, separation of material layers in a bio-cell under needle puncture, separation of stiffeners and skins in stiffened plate and shell panels, etc.

Some of the earliest analytical work on the topic of ERR partition in layered isotropic beams was carried out by Williams (1988), who made significant contributions to the understanding. He successfully identified one pair of pure mode conditions (mode I and mode II), which are valid for classical DCBs with applied bending moments, however the partition of a mixed mode was in error. A semi-analytical partition theory was given by Schapery and Davidson (1990), which was also for isotropic DCBs based on classical beam theory. They claimed that beam or plate theory does not provide enough information to partition the ERR. They therefore used the FEM to solve the two-dimensional continuum problem around the crack tip in order to partition the ERR. Suo and Hutchinson (1990), Suo (1990) and Hutchinson and Suo (1992) used a similar approach to Schapery and Davidson (1990), but instead of using the FEM, they used integral equation methods to obtain a two-dimensional linear elasticity solution for the crack tip region. The resulting partition theory is analytical except for one parameter, which is determined numerically. Schapery and Davidson's (1990) and Suo and Hutchinson's (1990) partition theories generally give different partitions to Williams's (1988) partition theory (except when the thicknesses of the DCB arms are equal). Suo and Hutchinson claimed that Williams's theory contains 'conceptual errors'. Zou et al. (2002) derived a completely analytical partition theory for isotropic DCBs based on FSDT beam theory. Bruno et al. (2003) obtained the same partition for classical beams, but by a different approach. Neither were in agreement with the partition theories of Williams (1988), Suo and Hutchinson (1990) or Schapery and Davidson (1990).

Clearly, a lot of analytical work has been done on the problem and in many cases, different theories do not agree with each other. There are two main analytical approaches to partitioning ERR: (1) an approach based on an assumed square-root singular stress field at the crack tip; and (2) an approach based on ERR. In most circumstances, they give different partitions. It should be noted however that the one point of universal agreement between all partition theories seems to be for homogenous, isotropic DCBs with equal thickness upper and lower arms. In terms of relating the partition theories to each other, also of interest is Bruno et al.'s (2003) finding that by using multiple layers of FSDT plates, the ERR partition from Suo and Hutchinson's (1990) theory is approached. Despite these two points of agreement between the theories, there still remains a large 'gap' in the understanding.

The work in this chapter focuses on brittle one-dimensional fracture in isotropic homogeneous DCBs, which is a sensible starting point before the complexity of the problem is increased, which is done in later chapters. The materials in consideration are assumed to be linearly elastic. The primary goal is to develop theories to find pure fracture modes and to partition a mixed mode into pure modes.

This chapter has been published in Wang and Harvey (2012*a*). A convenient summary is given in Wang and Harvey (2012*c*).

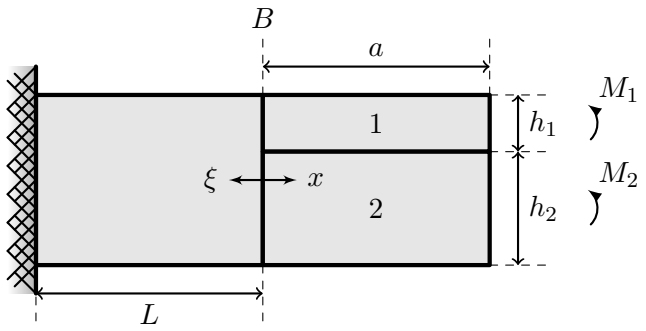

Figure 4.1: A DCB with two tip bending moments.

4.2 Theoretical development

4.2.1 Orthogonal fracture mode partition

An isotropic homogeneous DCB with its geometry and two tip bending moments is shown in Fig. 4.1. The crack tip is at point B. Throughout this formulation, it is convenient to make use of two different longitudinal axes, which are denoted by x and ξ in the figure. The origin of both axes is at the crack tip at location B. x is towards the right and ξ is towards the left. z is the vertical axis, which is positive upwards. Positive deflection, w is always upwards and a positive bending moment produces positive curvature, d^2w/dx^2 or $d^2w/d\xi^2$. No shear or axial forces are applied at the DCB tip at this stage for simplicity and in order to focus on understanding the mechanics. Assuming no interface contact within the cracked region, the strain energy U of the DCB for either an Euler beam or a Timoshenko beam made of linear elastic material is

$$U = \frac{1}{2E}\left[\int_0^a \left(\frac{M_1^2(x)}{I_1} + \frac{M_2^2(x)}{I_2}\right) dx + \int_{-L}^0 \frac{M^2(x)}{I}\, dx\right] \tag{4.1}$$

where $M(x)$ is the internal bending moment distribution, E is the Young's modulus and I is the second moment of area. The subscripts 1 and 2 refer to the upper and lower beams respectively. No subscript is used for the intact part of the DCB. Plane stress in the xz-plane is assumed. For plane strain, E can simply be replaced with $E/\left(1-\nu^2\right)$. Note that in Eq. (4.1), the strain energy contribution from the three-dimensional stress state in the neighbourhood of the crack tip is assumed to be negligible. This assumption is consistent with the work of other researchers in the area, for instance, Williams (1988) and Hutchinson and Suo (1992). This assumption will be validated by FEM simulations in §4.3 later in this chapter.

From Eq. (4.1), the total ERR is

$$G = \frac{1}{b}\frac{\partial U}{\partial a} = \frac{1}{2bE}\left(\frac{M_{1B}^2}{I_1} + \frac{M_{2B}^2}{I_2} - \frac{M_B^2}{I}\right) \tag{4.2}$$

where b is the width of the beam and a subscript B indicates a quantity at the crack tip. It is seen that G is a local quantity depending only on quantities at the crack tip cross-section, i.e. M_{1B}, M_{2B} and M_B. Also, G is of quadratic form, is positive definite and can be expressed in terms of orthogonal modes as

$$\begin{Bmatrix} M_{1B} \\ M_{2B} \end{Bmatrix} = \alpha_\theta \begin{Bmatrix} 1 \\ \theta \end{Bmatrix} + \alpha_\beta \begin{Bmatrix} 1 \\ \beta \end{Bmatrix} = \alpha_\theta \left\{\varphi_\theta\right\} + \alpha_\beta \left\{\varphi_\beta\right\} \tag{4.3}$$

where $\left\{\varphi_\theta\right\}$ and $\left\{\varphi_\beta\right\}$ are a pair of orthogonal mode vectors, and α_θ and α_β are mode partition coefficients. When either θ or β is given, the other can be found by enforcing orthogonality between the $\left\{\varphi_\theta\right\}$ and $\left\{\varphi_\beta\right\}$ mode vectors through the ERR. This can easily be done by writing Eq. (4.2) in matrix form, as follows:

$$G = \frac{1}{2bE} \begin{Bmatrix} M_{1B} \\ M_{2B} \end{Bmatrix}^T \begin{bmatrix} \left(I_1^{-1} - I^{-1}\right) & -I^{-1} \\ -I^{-1} & \left(I_2^{-1} - I^{-1}\right) \end{bmatrix} \begin{Bmatrix} M_{1B} \\ M_{2B} \end{Bmatrix} \tag{4.4}$$

If the $\left\{\varphi_\theta\right\}$ and $\left\{\varphi_\beta\right\}$ mode vectors are orthogonal to each other, then

$$0 = \frac{1}{2bE} \begin{Bmatrix} 1 \\ \theta \end{Bmatrix}^T \begin{bmatrix} \left(I_1^{-1} - I^{-1}\right) & -I^{-1} \\ -I^{-1} & \left(I_2^{-1} - I^{-1}\right) \end{bmatrix} \begin{Bmatrix} 1 \\ \beta \end{Bmatrix} \tag{4.5}$$

The mode partition coefficients α_θ and α_β in Eq. (4.3) can be determined for any given values of M_{1B} and M_{2B}. Substituting Eq. (4.3) into Eq. (4.2) gives

$$\begin{aligned} G &= \frac{1}{2bE} \left[\alpha_\theta^2 \left(\frac{1}{I_1} + \frac{\theta^2}{I_2} - \frac{(1+\theta)^2}{I} \right) + \alpha_\beta^2 \left(\frac{1}{I_1} + \frac{\beta^2}{I_2} - \frac{(1+\beta)^2}{I} \right) \right] \\ &= \alpha_\theta^2 G_\theta + \alpha_\beta^2 G_\beta \end{aligned} \tag{4.6}$$

where G_θ and G_β are the ERRs corresponding to the orthogonal modes $\left\{\varphi_\theta\right\}$ and $\left\{\varphi_\beta\right\}$ respectively. In general, they are not the respective pure opening mode I and pure shearing mode II ERRs since an infinite number of orthogonal modes exist. An obvious question, do specific values of θ and β exist which give pure modes I and II respectively? Another question is, when the values of θ and β have been found, does Eq. (4.6) represent the true ERR partition? The following sections are concerned with answering these questions, after which the theory is extended to study a more general case where axial and shear forces are included.

4.2.2 Two orthogonal sets of locally pure modes

From mechanical considerations, two sets of locally pure modes are expected. By 'locally pure' it is meant that the pureness is defined with respect to the crack tip at location B. The local partition of ERR is therefore calculated by considering the near crack-tip region

only. The first set of locally pure modes corresponds to zero crack tip relative shearing displacement, i.e. mode I, and zero crack tip opening force, i.e. mode II. The second set of locally pure modes corresponds to zero crack tip shearing force, i.e. mode I, and zero crack tip relative opening displacement, i.e. mode II. One pair from each of these two sets of locally pure modes are determined in this section.

Globally pure modes are also expected. By 'globally pure' it is meant that the pureness is defined with respect to the whole region mechanically affected by the presence of the crack tip. The global partition of ERR is calculated by considering this whole region. The corresponding globally pure mode for each locally pure mode is also determined in this section.

Note that the usage of the terms 'local' and 'global' here and in the following chapters is not the same as that of some other researchers on this topic. Charalambides et al. (1992) for instance, and others, have described Hutchinson and Suo's (1992) partition theory (and other theories similar to it) as being local theories because they are based on two-dimensional elasticity and consider the stress fields near to the crack tip. They have also described methods based on ERRs as being global theories because they do not make these detailed considerations.

To begin with, it is assumed that the mechanical influence of the crack extends to a point A, a distance Δa ahead of the crack tip B, as shown in Fig. 4.2 (a). Only the sign convention of the interface normal stress σ_n and shear stress τ_s is shown in Fig. 4.2 (b), rather than any representative distribution. By using curvature continuity conditions at point A, the resultant shear force F_s due to τ_s, and the resultant moment M_n about point A due to σ_n are

$$F_s = b\int_0^{\Delta a} \tau_s \, d\xi = \frac{6\gamma}{h_1 \left(1+\gamma\right)^3} \left(M_{1B} + M_{2B}\right) \tag{4.7}$$

$$M_n = b\int_0^{\Delta a}\int_0^{\xi} \sigma_n \, d\xi \, d\xi = b\int_0^{\Delta a} \sigma_n \left(\Delta a - \xi\right) \, d\xi = M_{nm} + F_n \Delta a \tag{4.8}$$

where M_{nm} is the resultant moment about the crack tip at point B due to σ_n, given by

$$M_{nm} = -b\int_0^{\Delta a} \xi \sigma_n \, d\xi = \frac{1+3\gamma}{\left(1+\gamma\right)^3} \left(\beta M_{1B} - M_{2B}\right) \tag{4.9}$$

and F_n is the resultant normal force due to σ_n, which is zero since there are no crack tip shear forces. Eqs. (4.7) to (4.9) remain the same in both the Euler and Timoshenko beam theories. Here, $\gamma = h_2/h_1$ is the thickness ratio, $\beta = \gamma^2 \left(3+\gamma\right) / \left(1+3\gamma\right)$.

One globally pure mode I mode is defined as $F_s = 0$ leading to $M_{1B} = -M_{2B}$, which when written in the form of a mode vector is

$$\left\{\varphi_{\theta'}\right\} = \begin{Bmatrix} 1 \\ \theta' \end{Bmatrix} = \begin{Bmatrix} 1 \\ -1 \end{Bmatrix} \tag{4.10}$$

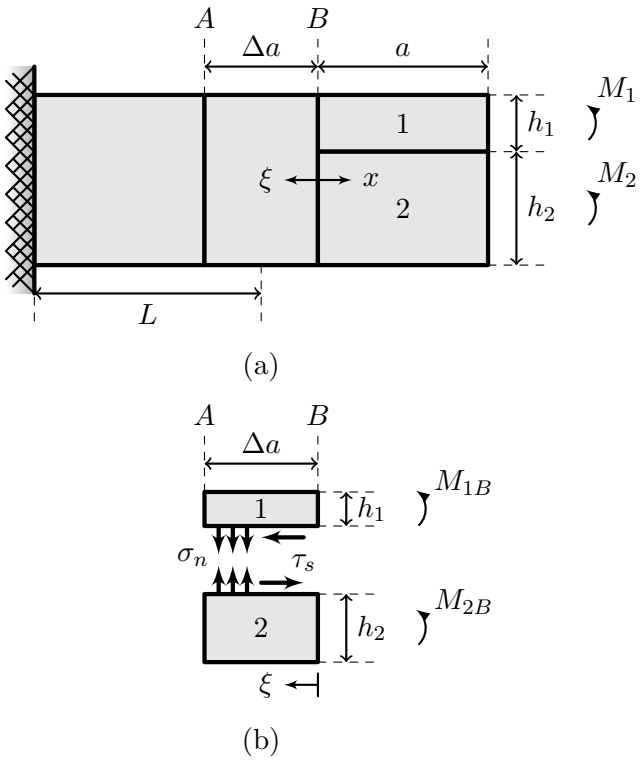

Figure 4.2: A DCB with crack influence region Δa. (a) General description. (b) Interface stresses in the Δa region.

The orthogonal globally pure mode II mode can be found using the orthogonality condition with respect to the coefficient matrix of the quadratic form of ERR, as described in §4.2.1. It is found to be

$$\left\{\varphi_{\beta'}\right\} = \begin{Bmatrix} 1 \\ \beta' \end{Bmatrix} = \begin{Bmatrix} 1 \\ \gamma^3 \end{Bmatrix} \tag{4.11}$$

This (θ', β') pair belongs to the 'second set' of globally pure modes. They happen to be the same as Williams's (1988) pair. Physically, the orthogonality condition means that any interaction between the two modes results in a zero net change in total ERR.

Similarly, a globally pure mode II mode is defined as $M_n = 0$, which gives

$$\left\{\varphi_{\beta}\right\} = \begin{Bmatrix} 1 \\ \beta \end{Bmatrix} = \begin{Bmatrix} 1 \\ \gamma^2 \left(3+\gamma\right) / \left(1+3\gamma\right) \end{Bmatrix} \tag{4.12}$$

and its orthogonal globally pure mode I mode is

$$\left\{\varphi_{\theta}\right\} = \begin{Bmatrix} 1 \\ \theta \end{Bmatrix} = \begin{Bmatrix} 1 \\ -\gamma^2 \end{Bmatrix} \tag{4.13}$$

This (θ, β) pair belongs to the 'first set' of globally pure modes. Notice that $\theta\left(\gamma^{-1}\right) = \theta^{-1}\left(\gamma\right)$ and $\beta\left(\gamma^{-1}\right) = \beta^{-1}\left(\gamma\right)$ due to mechanical symmetry.

In the remainder of this section, it will be shown that the second set is also locally pure in the Euler beam theory (but not the Timoshenko beam theory) and that the first set is also locally pure in both the Euler and Timoshenko beam theories. As explained, local pureness is defined with respect to the crack tip B whilst global pureness is defined with respect to the Δa region, which is shown in Fig. 4.2.

With reference to Fig. 4.2 and using Timoshenko beam theory, the relative opening displacement between beams 1 and 2 at an infinitely small distance δa behind the crack tip, i.e. at $x = \delta a$, is

$$D_{op} = \frac{1}{2E}\left(\frac{M_{1B}}{I_1} - \frac{M_{2B}}{I_2}\right)\delta a^2 + (\psi_{1B} - \psi_{2B})\,\delta a + (w_{1B} - w_{2B}) \tag{4.14}$$

where w is the upwards deflection and ψ represents the anticlockwise rotations of the normals to mid-surfaces of the beams. As before, a subscript B indicates a quantity at the crack tip; subscripts 1 and 2 refer to the upper and lower beams respectively (but no subscript is used for the intact part of the DCB). For a rigid interface, $w_{1B} - w_{2B} = 0$. The rotation term in Eq. (4.14) can be found by considering the through-thickness shear action in the crack influence region, i.e. the Δa region in Fig. 4.2. The equations are

$$\kappa\mu S_1\left(\frac{dw_1}{d\xi} - \psi_1\right) = b\int_0^{\xi}\sigma_n\,d\xi \tag{4.15}$$

and

$$\kappa\mu S_2\left(\frac{dw_2}{d\xi} - \psi_2\right) = -b\int_0^{\xi}\sigma_n\,d\xi \tag{4.16}$$

for beams 1 and 2 respectively, where S represents the cross-sectional area, μ is the through-thickness shear modulus and κ is the shear correction factor, usually taken to be 5/6 for isotropic materials with rectangular cross-sections. Note that since Eqs. (4.15) and (4.16) use the ξ-coordinate, the rotation ψ is now positive in a clockwise direction. Due to the opening stress singularity at the crack tip B, the two through-thickness shear strains are not continuous across the crack tip. Since both rotations ψ_1 and ψ_2 are continuous, although they are different, $dw_1/d\xi$ and $dw_2/d\xi$ are discontinuous at the crack tip and different behind the crack tip. However, it can be assumed that $(dw_1/d\xi)_{\xi=\delta a} = (dw_2/d\xi)_{\xi=\delta a}$ for a rigid interface, which are the two mid-surface rotations of beams 1 and 2 respectively at a distance δa ahead of the crack tip B. Therefore, from Eqs. (4.15) and (4.16), the quantities $(dw_1/d\xi)_{\xi=\delta a}$ and $(dw_2/d\xi)_{\xi=\delta a}$ are

$$\left(\frac{dw_1}{d\xi}\right)_{\xi=\delta a} = (\psi_1)_{\xi=\delta a} + \frac{F_{nB}}{\kappa\mu S_1} \tag{4.17}$$

and

$$\left(\frac{dw_2}{d\xi}\right)_{\xi=\delta a} = (\psi_2)_{\xi=\delta a} - \frac{F_{nB}}{\kappa\mu S_2} \tag{4.18}$$

where $F_{nB} = b\int_0^{\delta a} \sigma_n \, d\xi$, which is the crack tip opening force. Since $(dw_1/d\xi)_{\xi=\delta a} = (dw_2/d\xi)_{\xi=\delta a}$, $(\psi_1)_{\xi=\delta a} = \psi_{1B}$ and $(\psi_2)_{\xi=\delta a} = \psi_{2B}$, therefore Eqs. (4.17) and (4.18) give

$$\psi_{1B} - \psi_{2B} = -\frac{F_{nB}}{\kappa\mu}\left(\frac{1}{S_1} + \frac{1}{S_2}\right) \tag{4.19}$$

It is seen that the two crack tip rotations are generally different in Timoshenko beam theory. When the shear modulus μ tends to infinity, which gives Euler beams, they become equal. Substituting Eq. (4.19) into Eq. (4.14) gives

$$D_{op} = \frac{1}{2E}\left(\frac{M_{1B}}{I_1} - \frac{M_{2B}}{I_2}\right)\delta a^2 + \frac{F_{nB}\,\delta a}{\kappa\mu}\left(\frac{1}{S_1} + \frac{1}{S_2}\right) \tag{4.20}$$

Note that a sign was reversed in the substitution because the rotation in Eq. (4.19) is opposite to that in Eq. (4.14). When using Euler beam theory, i.e. $\mu \to \infty$, zero crack tip relative opening displacement $D_{op} = 0$ gives the pure mode II mode in Eq. (4.11), i.e. the $\left\{\varphi_{\beta'}\right\}$ mode. This proves that the $\left\{\varphi_{\beta'}\right\}$ mode is also locally pure in Euler beam theory. Therefore its orthogonal mode $\left\{\varphi_{\theta'}\right\}$, given in Eq. (4.10), is also a locally pure mode in Euler beam theory and corresponds to zero crack tip shearing force, i.e. $F_{sB} = 0$.

When using Timoshenko beam theory for a finite value of μ, the zero condition $D_{op} = 0$ yields $F_{nB} = 0$ instead of the $\left\{\varphi_{\beta'}\right\}$ mode. Therefore, it can be concluded that the second set (θ', β') is not locally pure in Timoshenko beam theory when the shear modulus has a finite value. The simultaneous zero conditions, $D_{op} = 0$ and $F_{nB} = 0$, show that the two locally pure mode II modes, which correspond to zero crack tip opening displacement and zero crack tip opening force, must coincide with each other. Therefore, effectively there is only one set of pure modes in Timoshenko beam theory. It will be shown shortly that this is the first set (θ, β).

Again, with reference to Fig. 4.2 and using Timoshenko beam theory, the relative shearing displacement between beams 1 and 2 at a distance δa behind the crack tip, i.e. at $x = \delta a$ is

$$D_{sh} = \left[(u_1)_{x=\delta a} + \frac{h_1}{2}(\psi_1)_{x=\delta a}\right] - \left[(u_2)_{x=\delta a} - \frac{h_2}{2}(\psi_1)_{x=\delta a}\right] \tag{4.21}$$

where u is the mid-surface axial displacement in the direction of the x-axis, i.e. towards the right, and the anticlockwise rotations $(\psi_{1,2})_{x=\delta a}$ are

$$(\psi_{1,2})_{x=\delta a} = \frac{M_{1,2B}\,\delta a}{EI_{1,2}} + \psi_{1,2B} \tag{4.22}$$

Note that from this point on (including in the following chapters), it is often useful to use a subscript notation to represent several equations: a comma separates each subscript; taking the first subscript from each term gives one equation; taking the second subscript from each term gives another equation, etc.

There is an axial continuity condition at the crack tip

$$u_{1B} + \frac{h_1\psi_{1B}}{2} = u_{2B} - \frac{h_2\psi_{2B}}{2} \tag{4.23}$$

Therefore Eq. (4.21) becomes

$$D_{sh} = \frac{1}{2E}\left(\frac{h_1 M_{1B}}{I_1} + \frac{h_2 M_{2B}}{I_2}\right)\delta a \tag{4.24}$$

Note that Eq. (4.24) is the same for both Euler and Timoshenko beam theories. The zero crack tip shearing displacement condition $D_{sh} = 0$ gives the pure mode I mode in Eq. (4.13), i.e. the $\left\{\varphi_\theta\right\}$ mode. This proves that the $\left\{\varphi_\theta\right\}$ mode is locally pure in both Euler and Timoshenko beam theories. Therefore, its orthogonal mode $\left\{\varphi_\beta\right\}$, given in Eq. (4.12), is also locally pure in both Euler and Timoshenko beam theories. It corresponds to zero crack tip opening force, i.e. $F_{nB} = 0$.

Since in Timoshenko beam theory, $F_{nB} = 0$ leads to $D_{op} = 0$, as seen earlier, likewise $D_{sh} = 0$ will lead to zero crack tip shear force, i.e. $F_{sB} = 0$. Therefore the two sets of locally pure modes in Timoshenko beam theory coincide with each other, i.e. the second set of pure modes is exactly the same as the first set. Some additional observations on the first set (θ, β) can be made from the equations above:

- The normal interface stress σ_n in the $\left\{\varphi_\beta\right\}$ mode is uniformly zero within the Δa region, including at the crack tip B. In this situation, the two beams above and below the interface within the Δa region, as shown in Fig. 4.2 (b), deform like a single intact beam except that a shear stress singularity exists at the very tip of the crack, at point B, which results in a pure shear mode.

- The two crack tip rotations in the $\left\{\varphi_\beta\right\}$ mode are always equal to each other in Timoshenko beam theory.

- In Timoshenko beam theory, the $\left\{\varphi_\beta\right\}$ mode, which corresponds to $F_{nB} = 0$, and the $\left\{\varphi_{\beta'_T}\right\}$ mode, which corresponds to $D_{op} = 0$, coincide. The subscript T indicates that this is the mode II mode from the second set in Timoshenko beam theory, which is not the same as the global/Euler one, given in Eq. (4.11). It is seen from Eq. (4.20) that the $\left\{\varphi_{\beta'_T}\right\}$ mode approaches the $\left\{\varphi_\beta\right\}$ mode asymptotically from above. This implies that extra care should be taken in FEM simulations to ensure that F_{nB} is very small. When μ is finite, very fine meshes are required to ensure that the $\left\{\varphi_{\beta'_T}\right\}$ mode converges to the $\left\{\varphi_\beta\right\}$ mode. This also applies generally to the second set converging to the first set.

- Since $D_{op} < 0$ beyond $M_{2B}/M_{1B} = \beta = \beta'_T$ in Timoshenko beam theory, crack tip running contact occurs, which leads to a pure mode II region up until $M_{2B}/M_{1B} = \beta'$, which is the global pure mode II mode from the second set.

In summary, in Timoshenko beam theory, there are two sets of locally pure modes and they both exactly coincide with the (θ, β) set. In Euler beam theory, there are two sets of pure modes which are both locally and globally pure: the (θ, β) set and the (θ', β') set. The Timoshenko beam theory also has two sets of globally pure modes and these are the same as the two sets from the Euler beam theory.

4.2.3 Mixed-mode partitions

Before deriving the mixed-mode partition, it is helpful to first consider the interface stresses τ_s and σ_n, which are shown in Fig. 4.2 (b). The continuity condition of axial displacement at the interfaces between the two beams within the Δa region is

$$u_1 + \frac{h_1 \psi_1}{2} = u_2 - \frac{h_2 \psi_2}{2} \tag{4.25}$$

where u is the mid-surface axial displacement in the direction of the ξ-axis and ψ is the clockwise rotation. From the differential equations of Timoshenko beam theory,

$$u_{1,2} = u_{1,2B} \mp \frac{b}{E S_{1,2}} \int_0^\xi \int_0^\xi \tau_s \, d\xi \, d\xi \tag{4.26}$$

$$\frac{d\psi_{1,2}}{d\xi} = \left(\frac{d\psi_{1,2}}{d\xi} \right)_B \mp \frac{b}{E I_{1,2}} \int_0^\xi \int_0^\xi \sigma_n \, d\xi \, d\xi - \frac{b h_{1,2}}{E I_{1,2}} \int_0^\xi \tau_s \, d\xi \tag{4.27}$$

$$\kappa \mu_{xz} S_{1,2} \left(\frac{dw_{1,2}}{d\xi} - \psi_{1,2} \right) = \pm b \int_0^\xi \sigma_n \, d\xi \tag{4.28}$$

Now, from Eqs. (4.25) to (4.28), the interface shear stress τ_s is obtained as

$$\tau_s = \delta_B + \frac{3\,(1-\gamma)}{2 h_1 \gamma} \int_0^\xi \sigma_n \, d\xi \tag{4.29}$$

where δ_B has been added to account for the shear stress singularity at the crack tip B, which is from the mode II $\left\{ \varphi_\beta \right\}$ mode. The second term in Eq. (4.29) is due to the interface normal stress σ_n, which is from the mode I $\left\{ \varphi_\theta \right\}$ mode. Eq. (4.29) remains valid in both the Euler and Timoshenko beam theories. The relationship between the crack tip shear force and the opening force in the $\left\{ \varphi_\theta \right\}$ mode can be obtained from Eq. (4.29) as

$$F_{sB\theta} = \frac{3\,(1-\gamma)\, F_{nB\theta}\, \delta a}{4 h_1 \gamma} \tag{4.30}$$

where $F_{sB\theta} = b \int_0^{\delta a} \tau_{s\theta} \, d\xi$ and $F_{nB\theta} = b \int_0^{\delta a} \sigma_{n\theta} \, d\xi$, which are respectively the crack tip shear and normal forces in the $\left\{ \varphi_\theta \right\}$ mode due to the shear and normal stresses on the interface in this mode, $\tau_{s\theta}$ and $\sigma_{n\theta}$.

Now the mixed-mode partition is considered. For any given M_{1B} and M_{2B}, the mode partition coefficients α_θ and α_β in Eq. (4.3) are

$$\begin{Bmatrix}\alpha_\theta\\ \alpha_\beta\end{Bmatrix} = \begin{bmatrix}\varphi_\theta & \varphi_\beta\end{bmatrix}^{-1}\begin{Bmatrix}M_{1B}\\ M_{2B}\end{Bmatrix} = \frac{1}{\beta-\theta}\begin{Bmatrix}\beta M_{1B}-M_{2B}\\ M_{2B}-\theta M_{1B}\end{Bmatrix} \tag{4.31}$$

The ERRs in Eq. (4.6) are therefore

$$G_\theta = \frac{6}{Eb^2h_1^3}\left[1+\frac{\theta^2}{\gamma^3}-\frac{(1+\theta)^2}{(1+\gamma)^3}\right] = \frac{24\gamma}{Eb^2h_1^3(1+\gamma)} \tag{4.32}$$

and

$$G_\beta = \frac{6}{Eb^2h_1^3}\left[1+\frac{\beta^2}{\gamma^3}-\frac{(1+\beta)^2}{(1+\gamma)^3}\right] = \frac{72\gamma(1+\gamma)}{Eb^2h_1^3(1+3\gamma)^2} \tag{4.33}$$

The total ERR is therefore

$$G = \alpha_\theta^2 G_\theta + \alpha_\beta^2 G_\beta \tag{4.34}$$

The partition of the G into G_I and G_{II} is first considered within the context of Timoshenko beam theory. In Timoshenko beam theory, the first and second sets of pure modes coincide with each other, as shown in §4.2.2. Therefore, there is no interaction between the mode I $\left\{\varphi_\theta\right\}$ mode and the mode II $\left\{\varphi_\beta\right\}$ mode. Consequently, the total ERR is simply partitioned as

$$G_I = \alpha_\theta^2 G_\theta \quad \text{and} \quad G_{II} = \alpha_\beta^2 G_\beta \tag{4.35}$$

This is now referred to as the 'present Timoshenko beam partition theory'. The mode I ERR G_I, or effectively G_θ, is due solely to the difference between the two crack tip rotations, as shown by Eqs. (4.19) and (4.20). This difference arises from the through-thickness shear strains caused by the crack tip opening force $F_{nB\theta}$. Both the crack tip opening force $F_{nB\theta}$ and opening displacement $D_{op\theta}$ vary with the variation of shear modulus μ. However, the ERR G_θ remains constant. The crack tip opening force $F_{nB\theta}$ can be determined from Eqs. (4.20) and (4.32) by means of the VCCT. It is as follows:

$$F_{nB\theta} = h_1^{-1}\left(\frac{2M_{nm\theta}}{\eta}\right)^{1/2} \tag{4.36}$$

where $\eta = E/(6\kappa\mu)$ and $M_{nm\theta} = 4\gamma^2/(1+\gamma)^2$, which is from Eq. (4.9). $M_{nm\theta}$ is the resultant moment of the normal stress σ_n about point B in the $\left\{\varphi_\theta\right\}$ mode. From Eq. (4.30), $F_{sB\theta}$ is zero since the $\left\{\varphi_\theta\right\}$ mode, which corresponds to $D_{sh}=0$, also coincides with $F_{sB}=0$ in the case of Timoshenko beam theory. Varying the shear modulus μ has no effect on $F_{sB\beta}$, $D_{sh\beta}$ and $D_{op\beta}$ since there is no interface normal stress in the $\left\{\varphi_\beta\right\}$ mode.

It was mentioned at the end of §4.2.2 that the second set of pure modes in Timoshenko beam theory (θ_T', β_T') approaches the first set (θ, β) asymptotically from above as $F_{nB\theta}\,\delta a \to 0$. This implies that extra care should be taken in FEM simulations to ensure

that this is the case. When μ is finite, very fine meshes are required to ensure that the second set does indeed converge to the first set, otherwise a non-coincident second set can be numerically generated, which lies between the (θ, β) and (θ', β') sets, which are the global/Euler pure modes.

Partition of a mixed mode based on Euler beam theory is not as straightforward as when using Timoshenko beam theory, due to there being interaction between the $\left\{\varphi_\theta\right\}$ mode I and the $\left\{\varphi_\beta\right\}$ mode II. The interactions are the work done by the crack tip forces $F_{nB\theta}$ and $F_{sB\theta}$ of the $\left\{\varphi_\theta\right\}$ mode I on the crack tip displacement $D_{op\beta}$ and $D_{sh\beta}$ of the $\left\{\varphi_\beta\right\}$ mode II. The interactions are

$$W_I = \frac{F_{nB\theta} D_{op\beta}}{2} = \frac{F_{nB\theta}}{4E}\left(\frac{1}{I_1} - \frac{\beta}{I_2}\right)\delta a^2 \tag{4.37}$$

and

$$W_{II} = \frac{F_{sB\theta} D_{sh\beta}}{2} = \frac{F_{sB\theta}}{4E}\left(\frac{h_1}{I_1} + \frac{h_2\beta}{I_2}\right)\delta a \tag{4.38}$$

Using Eq. (4.30), it can be shown that $W_I + W_{II} = 0$. This means that the interactions do not produce any net work, which is expected since the two modes are orthogonal to each other. However, these 'stealthy' interactions cause energy flow between the two modes, which results in a changed mode partition. Eqs. (4.20) and (4.32) can be used in conjunction with the VCCT to calculate $F_{nB\theta}$. It is as follows:

$$F_{nB\theta}\,\delta a = 2M_{nm\theta} \tag{4.39}$$

Therefore, from Eq. (4.30), the corresponding crack tip shear force $F_{sB\theta}$ is

$$F_{sB\theta} = \frac{6\gamma\,(1-\gamma)}{h_1\,(1+\gamma)^2} \tag{4.40}$$

It is seen that $F_{sB\theta}$ has the same value as the resultant interface shear force F_s given in Eq. (4.7). Of course, $F_{sB\theta}$ is no longer zero, as in Timoshenko beam theory. Also $F_{nB\theta}$ is now of infinite value here in Euler beam theory instead of a finite value, as in Timoshenko beam theory. Substituting Eq.(4.39) into Eq. (4.37) gives

$$\Delta G_{\theta\beta} = \frac{W_I}{b\,\delta a} = \frac{72\gamma\,(\gamma-1)}{Eb^2h_1^3\,(1+\gamma)\,(1+3\gamma)} = \frac{3\,(\gamma-1)}{1+3\gamma}G_\theta \tag{4.41}$$

Therefore, the mixed-mode ERR partition in Euler beam theory is

$$G_I = \alpha_\theta^2 G_\theta + \alpha_\theta\alpha_\beta\Delta G_{\theta\beta} \quad \text{and} \quad G_{II} = \alpha_\beta^2 G_\beta - \alpha_\theta\alpha_\beta\Delta G_{\theta\beta} \tag{4.42}$$

This is now referred to as the 'present Euler beam partition theory'. It gives the second set of pure modes (θ', β') in addition to the first set (θ, β).

It is worth noting that problems can arise when using the FEM with cubic Euler beams due to displacement incompatibility at the interface. For example, when using Euler beam elements with point interface springs, a set of 'pure' modes will be generated numerically, which lies somewhere between the first set (θ, β) and the second set (θ', β')

Finally, it is also worth noting the following: when the whole Δa region is considered in the evaluation of mixed-mode ERR partition, the through-thickness shear effect at the crack tip due to the normal stress σ_n, which arises from the $\left\{\varphi_\theta\right\}$ mode I, will disappear. Therefore, for any values of the shear modulus, the ERR partitions will remain the same as those for infinitely large shear modulus, that is, the partitions based on Euler beam theory. This is why the second set (θ', β') in the present Euler beam partition theory is also the second globally pure set in the present Timoshenko beam partition theory, as mentioned at the end of §4.2.2.

It is not surprising that there has been so much confusion on this subject. As explained, there is complex behaviour in both the analytical and numerical aspects, which includes globally and locally pure modes, stealthy interaction, crack tip running contact, etc.

4.2.4 Fracture mode partition spaces

In this section, fracture mode partition spaces in both the (M_1, M_2) and (M_{1B}, M_{2B}) spaces are studied by considering the DCB in Fig. 4.1. Without losing any generality, it is assumed that $\gamma \geq 1$. The right half of the space of (M_1, M_2) in Fig. 4.3 is studied first. The bending moment M_1 is fixed at a positive value while the bending moment M_2 varies from $-\infty$ to $+\infty$, i.e. from A to G. From A to F, $M_{1B} = M_1$ and $M_{2B} = M_2$. As shown in Fig. 4.4 (a), pure mode I modes $\left\{\varphi_\theta\right\}$ and $\left\{\varphi_{\theta'}\right\}$, which correspond to zero crack tip relative shearing displacement and zero crack tip shearing force, occur at B and C respectively. Similarly, pure mode II modes $\left\{\varphi_\beta\right\}$ and $\left\{\varphi_{\beta'}\right\}$, which correspond to zero crack tip opening force and zero crack tip relative opening displacement, occur at D and E respectively. From E to F, crack tip running contact occurs, which results in zero relative opening displacement. Thus, pure mode II occurs from E to F throughout. From F to G, DCB tip contact occurs. The contact force is

$$P_c = \frac{3\left(M_2 - \gamma^3 M_1\right)}{2a\left(1+\gamma^3\right)} \tag{4.43}$$

The crack tip bending moments are therefore given by

$$M_{1B} = \frac{3M_2 - \left(\gamma^3 - 2\right) M_1}{2\left(1+\gamma^3\right)} \tag{4.44}$$

and

$$M_{2B} = \frac{\left(2\gamma^3 - 1\right) M_2 + 3\gamma^3 M_1}{2\left(1+\gamma^3\right)} \tag{4.45}$$

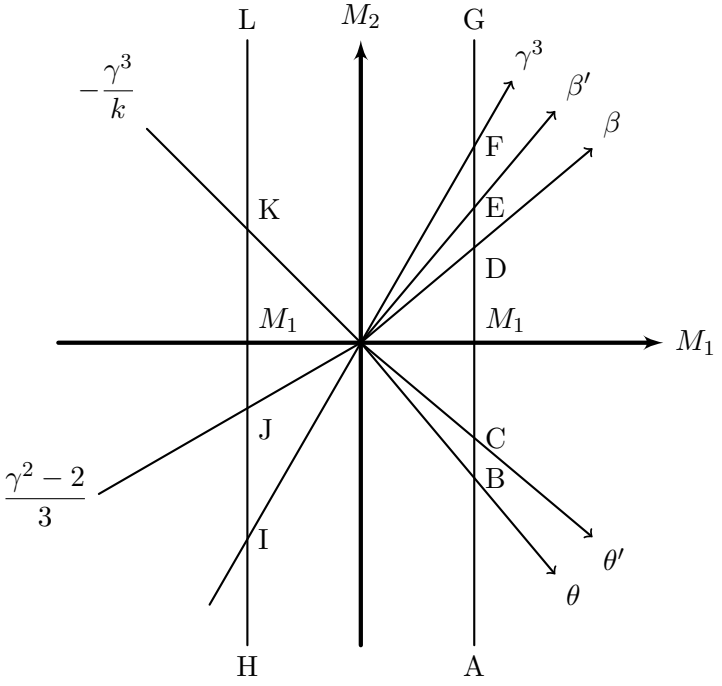

Figure 4.3: Fracture mode partitions in the (M_1, M_2) space.

Eqs. (4.44) and (4.45) give

$$M_{2B} = kM_{1B} + \left(1+\gamma^3\right) M_1/3 \tag{4.46}$$

where

$$k = \left(2\gamma^3 - 1\right)/3 \tag{4.47}$$

Since k is always smaller than γ^3, the path at F will be deflected into the (M_{1B}, M_{2B}) space, corresponding to the route from F to G in the (M_1, M_2) space. Three distinctive paths, as shown in Fig. 4.4, can occur depending on the value of k, i.e. the value of γ. When $k > \beta'$, the fracture mode will remain in the pure mode II region. When $\beta < k < \beta'$, the path will pass through the $\left\{\varphi_{\beta'}\right\}$ mode and enter the mixed mode region. When $k < \beta$, the path will pass through both the $\left\{\varphi_{\beta'}\right\}$ and $\left\{\varphi_{\beta}\right\}$ modes.

Now, the left half space of (M_1, M_2) in Fig. 4.3 is studied. The bending moment M_1 is fixed at a negative value while the bending moment M_2 varies from $-\infty$ to $+\infty$, i.e. from H to L. From H to I, $M_{1B} = M_1$ and $M_{2B} = M_2$. From I to L, DCB tip contact occurs. The contact force and crack tip bending moments are given in Eqs. (4.43) to (4.45). Again, the path at I will be deflected into the (M_{1B}, M_{2B}), corresponding to the route from I to L in the (M_1, M_2) space. Again, three distinctive paths, as shown in Fig. 4.4 (b), can occur depending on the value of k, i.e. the value of γ. All three paths enter the right half space at J, passing through the two mode I modes, and enter the upper half space at K. When $k > \beta'$, the path will pass through both the $\left\{\varphi_{\beta'}\right\}$ and $\left\{\varphi_{\beta}\right\}$ modes and enter the pure

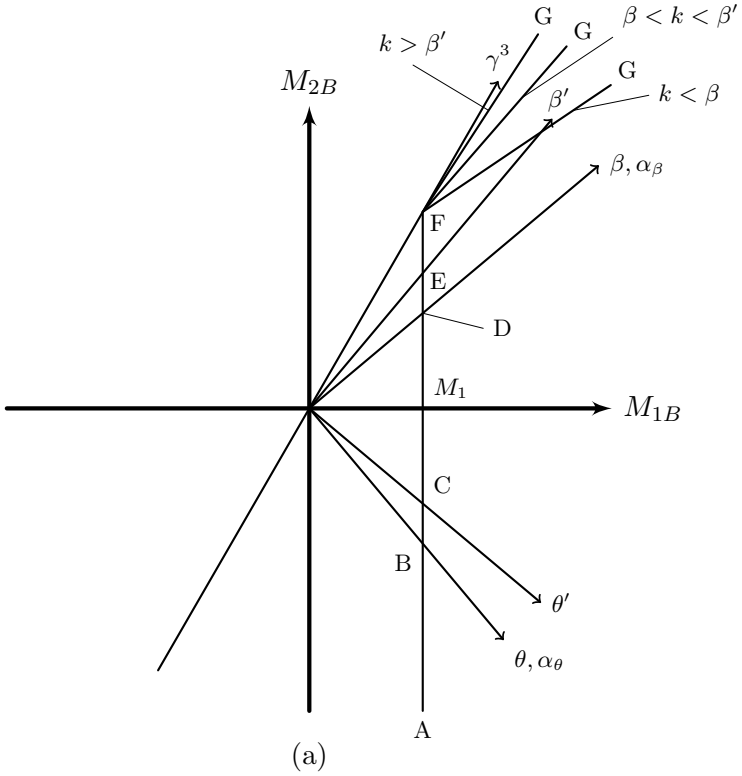

Figure 4.4: Fracture mode partitions in the (M_{1B}, M_{2B}) space. (a) Constant positive M_{1B} and varying M_{2B}. (b) Constant negative M_{1B} and varying M_{2B}.

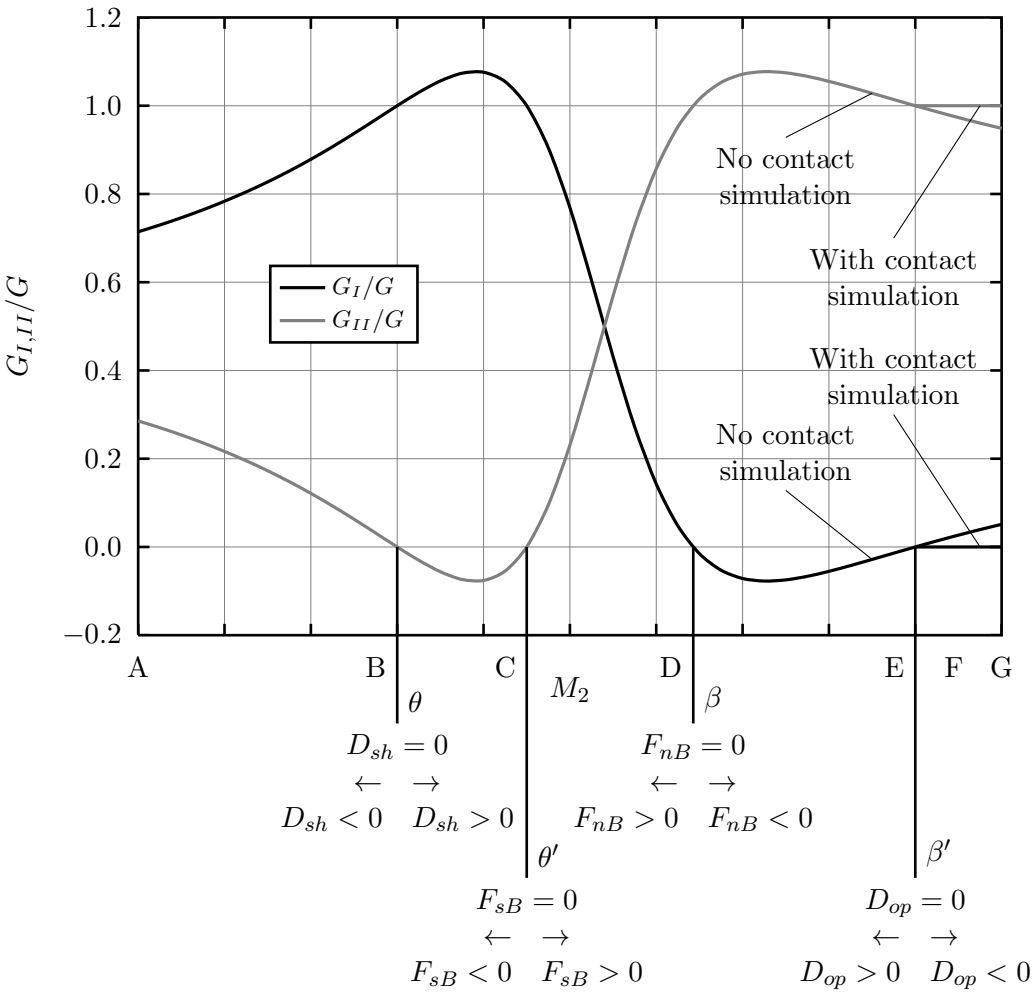

Figure 4.5: Variation of G_I/G and G_{II}/G for constant positive M_1 and varying M_2.

mode II region. When $\beta < k < \beta'$, the path will pass the $\left\{\varphi_\beta\right\}$ mode. When $k < \beta$, pure mode II does not occur. It is also noted that the upper half space above γ^3 is physically prohibited in the (M_{1B}, M_{2B}) space.

As mentioned earlier, the interaction between the mode I $\left\{\varphi_\theta\right\}$ mode and the mode II $\left\{\varphi_\beta\right\}$ mode results in energy flow $\Delta G_{\theta\beta}$ between mode I and mode II. Eq. (4.42) shows that in the first quadrant of $(\alpha_\theta, \alpha_\beta)$, the flow is from mode II to mode I, while in the second and fourth quadrants, the flow is from mode I to mode II. Fig. 4.5 shows the fracture mode partitions in terms of the variations of G_I/G and G_{II}/G. The scale on the horizontal axis corresponds to the points A to G in Figs. 4.3 and 4.4 (b). The signs of crack tip opening and shear forces, i.e. F_{nB} and F_{sB}, and crack tip relative opening and shearing displacements, i.e. D_{op} and D_{sh} are also shown to help with understanding the partitions.

Now, for the first time, the consequences of having two distinct sets of orthogonal pure modes (as in the present Euler beam partition theory) can be seen. Fig. 4.5 shows

that are regions between the two sets of modes where the partitions of ERR, G_I/G and G_{II}/G can be greater than one or less than zero. These are now simply referred to as 'negative partitions of ERR'. Note that, as has been shown, negative partitions of ERR must exist in the general case of orthogonal mixed-mode partitioning. It is only in special cases, for example, in the Timoshenko beam theory, where the two sets of orthogonal pure modes coincide, and the negative partitions of ERR disappear. The potential for negative partitions of ERR may seem unintuitive and some objections have been raised by the fracture mechanics research community. The major topics concerning negative partitions of ERR are discussed in detail in Appendix A.

4.2.5 Averaged partition rules

In §4.2.3, two mixed-mode partition theories have been established, based on the Euler and Timoshenko beam theories. In this section, two averaged mixed-mode partition rules are given, based on the arithmetic average of the present Euler beam partition theory, given in Eq. (4.42), and the present Timoshenko beam partition theory, given in Eq. (4.35).

Within the context of the present Timoshenko beam partition theory, there is no interaction between the mode I $\left\{\varphi_\theta\right\}$ mode and the mode II $\left\{\varphi_\beta\right\}$ mode. On the other hand, there is full interaction between the mode I $\left\{\varphi_\theta\right\}$ mode and the mode II $\left\{\varphi_\beta\right\}$ mode in the present Euler beam partition theory.

In the first quadrant of the partition space of $(\alpha_\theta, \alpha_\beta)$, i.e. between $M_{2B} = M_2 = \theta$ and $M_{2B} = M_2 = \beta$ (see Figs. 4.3 and 4.4), the interaction causes energy flow from mode II to mode I, as shown by Eq. (4.42). The Euler G_I is larger than the Timoshenko G_I by $\alpha_\theta\alpha_\beta\Delta G_{\theta\beta}$, while the Euler G_{II} is smaller than the Timoshenko G_{II} by the same amount.

In the second quadrant of the partition space of $(\alpha_\theta, \alpha_\beta)$, i.e. between $M_{2B} = M_2 = \beta$ and $M_{2B} = M_2 = \gamma^3$, and in the fourth quadrant, i.e. between $M_{2B} = M_2 = -\infty$ and $M_{2B} = M_2 = \theta$, the interaction causes energy flow from mode I to mode II. The Euler G_I is smaller than the Timoshenko G_I by $\alpha_\theta\alpha_\beta\Delta G_{\theta\beta}$, while the Euler G_{II} is larger than the Timoshenko G_{II} by the same amount.

It is therefore reasonable to suggest that the present Euler and Timoshenko beam partition theories act as the upper and lower bounds of the partition of ERR. Therefore, the average of the two partition theories is expected to give comparable predictions with two-dimensional FEM simulations, using QUAD4 elements for example. That is, the amount of energy flow between mode I and mode II is halved to $\alpha_\theta\alpha_\beta\Delta G_{\theta\beta}/2$. Therefore this averaged partition rule, which is now referred to as 'averaged partition rule 1' gives the following partitions:

$$G_I = \alpha_\theta^2 G_\theta + \alpha_\theta\alpha_\beta\Delta G_{\theta\beta}/2 \quad \text{and} \quad G_{II} = \alpha_\beta^2 G_\beta - \alpha_\theta\alpha_\beta\Delta G_{\theta\beta}/2 \tag{4.48}$$

A side effect of averaged partition rule 1 is that, for small ranges of loading conditions, it can produce negative partitions of ERR. When this happens, the total ERR rate G

remains non-negative, but either G_I or G_{II} becomes negative (see Appendix A). As will be confirmed later by the numerical results in §4.3: (1) the local partitions of ERR from two-dimensional elasticity theory are always positive; and (2) there exists only one set of pure modes, that is, there is no interaction. An obvious modification can therefore be made to averaged partition rule 1, which may give even better agreement with ERR partitions from two-dimensional elasticity. The modification is as follows: new pure modes can be derived which, when employed in the partition of ERR with zero interaction, give zero G_I/G and G_{II}/G where averaged partition rule 1 gives minimum values (that are negative). The negative partitions of ERR are thus removed. In this new modified partition rule, the orthogonality between the pure modes is maintained. This modified partition rule is now referred to as 'averaged partition rule 2'.

Since in averaged partition rule 1, β and θ give the ratio M_{2B}/M_{1B} for pure mode II and I respectively, to calculate the modified ratios, denoted by β_{A2} and θ_{A2}, solve

$$\frac{d\left(G_I/G\right)}{d\left(M_{2B}\right)} = 0 \tag{4.49}$$

for M_{2B} where $M_{1B} = 1$ and G_I is given by averaged partition rule 1 in Eq. (4.48). Eq. (4.49) has two solutions: one is β_{A2} and the other is θ_{A2}. Solving Eq. (4.49) gives

$$\begin{aligned}\beta_{A2} = \Big[&\gamma^5 + \left(2\sqrt{7\gamma^2+2\gamma+7}+3\right)\gamma^4 + \left(4\sqrt{7\gamma^2+2\gamma+7}-3\right)\gamma^3 \\ &+ \left(2\sqrt{7\gamma^2+2\gamma+7}-1\right)\gamma^2\Big] \Big/ \left(9\gamma^3+11\gamma^2+9\gamma+3\right)\end{aligned} \tag{4.50}$$

$$\begin{aligned}\theta_{A2} = \Big[&\gamma^2\left(\gamma^3+3\gamma^2-2\gamma^2\sqrt{7\gamma^2+2\gamma+7}-3\gamma-4\gamma\sqrt{7\gamma^2+2\gamma+7}\right. \\ &\left.-1-2\sqrt{7\gamma^2+2\gamma+7}\right)\Big] \Big/ \left(9\gamma^3+11\gamma^2+9\gamma+3\right)\end{aligned} \tag{4.51}$$

With these modified pure modes, the ERR partition for averaged partition rule 2 is simply given by

$$G_I = \alpha_{\theta_{A2}}^2 G_{\theta_{A2}} \tag{4.52}$$

where $\alpha_{\theta_{A2}}$ is given by α_θ in Eq. (4.31) but β_{A2} replaces β, and θ_{A2} replaces θ. $G_{\theta_{A2}}$ is given by G_θ in Eq. (4.32) but θ_{A2} replaces θ. The total ERR is still given by Eq. (4.2) and therefore $G_{II} = G - G_I$.

4.2.6 Addition of axial forces

In the above development, the axial forces have not been considered for the sake of simplicity and focusing on understanding the mechanics. In this section, they are considered. Two axial forces N_{1B} and N_{2B} act at the crack tips of the upper and lower beams respectively. They are positive when in the tensile sense. A DCB, subject to general tip loading is shown in Fig. 4.6 (a). The DCB tip loads give rise to loads on the cross-section at the crack tip. These are shown in Fig. 4.6 (b). The shear forces are not considered until the next section. The ERR is therefore

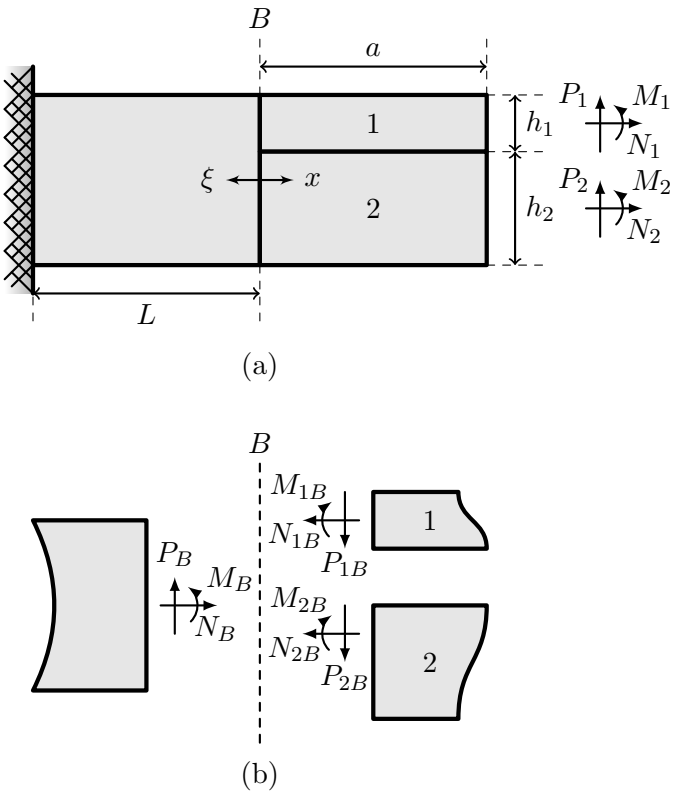

Figure 4.6: A DCB. (a) General description. (b) Crack tip forces.

$$G = \frac{1}{b}\frac{\partial U}{\partial a} = \frac{1}{2bE}\left(\frac{M_{1B}^2}{I_1} + \frac{M_{2B}^2}{I_2} - \frac{M_B^2}{I} + \frac{N_{1B}^2}{S_1} + \frac{N_{2B}^2}{S_2} - \frac{N_B^2}{S}\right) \tag{4.53}$$

in which

$$N_B = N_{1B} + N_{2B} \tag{4.54}$$

and

$$M_B = M_{1B} + M_{2B} + (h_1 N_{2B} - h_2 N_{1B})/2 \tag{4.55}$$

It appears that the ERR is now of quadratic form with four variables. In fact, only three variables are necessary. Since uniform axial stress does not produce any ERR, an effective axial force can be defined as

$$N_{1Be} = N_{1B} - N_{2B} S_1/S_2 \tag{4.56}$$

Then the ERR in Eq. (4.53) becomes

$$G = \frac{1}{2bE}\left[\frac{M_{1B}^2}{I_1} + \frac{M_{2B}^2}{I_2} - \frac{1}{I}\left(M_{1B} + M_{2B} - \frac{h_2 N_{1Be}}{2}\right)^2 + \left(\frac{1}{S_1} - \frac{1}{S}\right) N_{1Be}^2\right] \tag{4.57}$$

The resultant shear force F_s and moment M_n in Eqs. (4.7) and (4.8) change to be

$$F_s = \frac{6\gamma}{h_1\left(1+\gamma\right)^3}\left(M_{1B}+M_{2B}\right)+\frac{\gamma\left(1+\gamma^3\right)}{\left(1+\gamma\right)^4}N_{1Be} \tag{4.58}$$

and

$$M_n = M_{nm} = \frac{1+3\gamma}{\left(1+\gamma\right)^3}\left(\beta M_{1B}-M_{2B}\right)+\frac{h_1\gamma^2\left(1-\gamma\right)}{2\left(1+\gamma\right)^3}N_{1Be} \tag{4.59}$$

Since it is the first set of pure modes that is used in the mixed-mode partitioning, they are considered first. Recall that the pure mode II mode of the first set is given by zero crack tip opening force, and the pure mode I of the first set is given by zero crack tip relative shearing displacement. Equating M_n to zero gives the following pure mode II condition:

$$2\left(1+3\gamma\right)\left(\beta M_{1B}-M_{2B}\right)+h_1\gamma^2\left(1-\gamma\right)N_{1Be}=0 \tag{4.60}$$

The case when $M_{1B}=M_{2B}=0$ is considered first to examine the role of axial forces alone. When $h_1=h_2$, any N_{1B} and N_{2B} produce pure mode II. When $h_1\neq h_2$, N_{1Be} has to be zero, resulting in uniform stress on the cross-section and leading to zero ERR. Therefore, it can be concluded that in general, N_{1B} and N_{2B} alone cannot produce a pure mode II mode that is characterised by zero crack tip opening force. However, when M_{1B} and M_{2B} are present, they have important effects on the ERR by changing the shear stress singularity at the crack tip. Generally, since there are three independent variables, the condition in Eq. (4.60) provides two independent pure mode II modes. The new mode vector, which includes all three variables, is defined as $\left\{M_{1B}\quad M_{2B}\quad N_{1Be}\right\}^T$. Here, the following two modes are chosen in order to correspond with Eq. (4.12):

$$\left\{\varphi_{\beta_1}\right\}=\begin{Bmatrix}1\\ \beta_1\\ 0\end{Bmatrix}=\begin{Bmatrix}1\\ \gamma^3\left(3+\gamma\right)/\left(1+3\gamma\right)\\ 0\end{Bmatrix} \tag{4.61}$$

$$\left\{\varphi_{\beta_2}\right\}=\begin{Bmatrix}1\\ 0\\ \beta_2\end{Bmatrix}=\begin{Bmatrix}1\\ 0\\ 2\left(3+\gamma\right)/\left[h_1\left(\gamma-1\right)\right]\end{Bmatrix} \tag{4.62}$$

When $h_1=h_2$, then $\left\{\varphi_{\beta_2}\right\}$ becomes

$$\left\{\varphi_{\beta_2}\right\}=\begin{Bmatrix}0\\ 0\\ \beta_2\end{Bmatrix}=\begin{Bmatrix}0\\ 0\\ 1\end{Bmatrix} \tag{4.63}$$

Note that β_1 is used to replace the previous β.

The pure mode I condition, i.e. $D_{sh} = 0$, changes to be

$$D_{sh} = \frac{1}{2E}\left[\frac{h_1 M_{1B}}{I_1} + \frac{h_2 M_{2B}}{I_2} + \frac{2N_{1Be}}{S_1}\right]\delta a = 0 \tag{4.64}$$

where previously it was given in Eq. (4.24). This condition simplifies to

$$6\left(\gamma^2 M_{1B} + M_{2B}\right) + h_1\gamma^2 N_{1Be} = 0 \tag{4.65}$$

which provides also two independent pure mode I modes. Here, the following two are chosen in order to correspond with Eq. (4.13):

$$\left\{\varphi_{\theta_1}\right\} = \begin{Bmatrix} 1 \\ \theta_1 \\ 0 \end{Bmatrix} = \begin{Bmatrix} 1 \\ -\gamma^2 \\ 0 \end{Bmatrix} \tag{4.66}$$

$$\left\{\varphi_{\theta_2}\right\} = \begin{Bmatrix} 1 \\ 0 \\ \theta_2 \end{Bmatrix} = \begin{Bmatrix} 1 \\ 0 \\ -6/h_1 \end{Bmatrix} \tag{4.67}$$

Note that θ_1 is used here to replace the previous θ. Also note that the $\left\{\varphi_{\theta_2}\right\}$ mode is independent of γ. It can be shown that the two conditions in Eqs. (4.60) and (4.65) are orthogonal to each other with respect to the coefficient matrix of the ERR. Therefore, the first set of pure modes now consists of two pure mode II modes, $\left\{\varphi_{\beta_1}\right\}$ and $\left\{\varphi_{\beta_2}\right\}$ and two pure mode I modes, $\left\{\varphi_{\theta_1}\right\}$ and $\left\{\varphi_{\theta_2}\right\}$. Each of the pure mode I modes in Eqs. (4.61) and (4.62) is orthogonal to each of the pure mode II modes in Eqs. (4.66) and (4.67). Finally, note that N_{1B} and N_{2B} alone cannot produce a pure mode I mode that is characterised by zero crack tip relative shearing displacement.

For a given mixed mode, with crack tip forces M_{1B}, M_{2B} and N_{1Be}, the ERR partition can be made using any three of the four independent modes. Any combination of pure modes may be selected and the same mixed-mode partition will be obtained. However, since the $\left\{\varphi_{\beta_1}\right\}$ and $\left\{\varphi_{\beta_2}\right\}$ modes do not contribute to the crack tip opening force F_{nB} by definition (see §4.2.2), it is convenient to select the pure modes $\left\{\varphi_{\theta_1}\right\}$, $\left\{\varphi_{\beta_1}\right\}$ and $\left\{\varphi_{\beta_2}\right\}$. Therefore F_{nB} is simply given by the crack tip opening force from the $\left\{\varphi_{\theta_1}\right\}$ pure mode, i.e. $F_{nB} = \alpha_{\theta_1} F_{nB\theta_1}$. This simplifies the formulation. With this choice of modes vectors, the mode partition coefficients are obtained from

$$\begin{Bmatrix} M_{1B} \\ M_{2B} \\ N_{1Be} \end{Bmatrix} = \begin{bmatrix} 1 & 1 & 0 \\ \theta_1 & \beta_1 & 0 \\ 0 & 0 & 1 \end{bmatrix} \begin{Bmatrix} \alpha_{\theta_1} \\ \alpha_{\beta_1} \\ \alpha_{\beta_2} \end{Bmatrix} \tag{4.68}$$

for $h_1 = h_2$, and for $h_1 \neq h_2$ they are obtained from

$$\begin{Bmatrix} M_{1B} \\ M_{2B} \\ N_{1Be} \end{Bmatrix} = \begin{bmatrix} 1 & 1 & 1 \\ \theta_1 & \beta_1 & 0 \\ 0 & 0 & \beta_2 \end{bmatrix} \begin{Bmatrix} \alpha_{\theta_1} \\ \alpha_{\beta_1} \\ \alpha_{\beta_2} \end{Bmatrix} \tag{4.69}$$

From Eq. (4.69), the partition coefficients for the $h_1 \neq h_2$ case are

$$\alpha_{\beta_2} = \frac{N_{1Be}}{\beta_2} \quad \text{and} \quad \begin{Bmatrix} \alpha_{\theta_1} \\ \alpha_{\beta_1} \end{Bmatrix} = \frac{1}{\beta_1 - \theta_1} \begin{Bmatrix} \beta_1 \left(M_{1B} - \alpha_{\beta_2} \right) - M_{2B} \\ M_{2B} - \theta_1 \left(M_{1B} - \alpha_{\beta_2} \right) \end{Bmatrix} \tag{4.70}$$

Then the mode I ERR, G_I is

$$G_I = \alpha_{\theta_1}^2 G_{\theta_1} + \alpha_{\theta_1} \alpha_{\beta_1} \Delta G_{\theta_1 \beta_1} + \alpha_{\theta_1} \alpha_{\beta_2} \Delta G_{\theta_1 \beta_2} \tag{4.71}$$

As has been shown in §4.2.2, the second set exactly coincides with the first set in the present Timoshenko beam partition theory. The same reasoning as used in that section confirms that this is also true when axial forces are included. Therefore, within the context of the present Timoshenko beam partition theory, the second and third terms simply disappear. Within the context of the present Euler beam partition theory, the interaction term $\Delta G_{\theta_1 \beta_1}$ is given by Eq. (4.41) and the interaction term $\Delta G_{\theta_1 \beta_2}$ is

$$\Delta G_{\theta_1 \beta_2} = \frac{24 \gamma^2}{E b^2 h_1^3 \left(1 + \gamma\right)^2} = \frac{\gamma}{1 + \gamma} G_{\theta_1} \tag{4.72}$$

for $h_1 \neq h_2$. For $h_1 = h_2$, then $\Delta G_{\theta_1 \beta_2} = 0$. The mode II ERR is simply $G_{II} = G - G_I$. For averaged partition rule 1, both of these interaction terms are halved.

For averaged partition rule 2, the partition is still given by Eq. (4.52) but now the notation θ_{A2} is replaced everywhere with the more general notation θ_{1A2}. Therefore the mode I partition of ERR G_I from averaged partition rule 2 is

$$G_I = \alpha_{\theta_{1A2}}^2 G_{\theta_{1A2}} \tag{4.73}$$

where $G_{\theta_{1A2}}$ is given by G_θ in Eq. (4.32) but θ_{1A2} replaces θ; the mode partition coefficient $\alpha_{\theta_{1A2}}$ is given by α_{θ_1} in Eq. (4.68) or Eq. (4.69) but θ_{1A2} replaces θ_1, β_{1A2} replaces β_1, and β_{2A2} replaces β_2. In line with the discussion in §4.2.5, β_{2A2} is derived by solving

$$\frac{d\left(G_I / G\right)}{d\left(N_{1Be}\right)} = 0 \tag{4.74}$$

for N_{1Be} where $M_{1B} = 1$, $M_{2B} = 0$ and G_I is given by averaged partition rule 1. Eq. (4.74) has two solutions: one is β_{2A2} and the other is θ_{2A2}. Only β_{2A2} is required here. Solving

Eq. (4.74) for β_{2A2} gives

$$\begin{aligned}\beta_{2A2} = \Big[2\Big(&\gamma^3 + 5\gamma^2 + 2\gamma^2\sqrt{7\gamma^2 + 2\gamma + 7} + \gamma \\ &+2\gamma\sqrt{7\gamma^2 + 2\gamma + 7} + 9\Big)\Big] / \left[3h_1\left(\gamma - 1\right)\left(\gamma^2 + 1\right)\right]\end{aligned} \tag{4.75}$$

The total ERR is still given by Eq. (4.2) and therefore $G_{II} = G - G_I$.

Finally, in this section, attention is turned to the second set of pure modes. Since the second set exactly coincides with the first set in the present Timoshenko beam partition theory, only the second set only needs to be considered for the present Euler beam partition theory. Note that the second set from the present Euler beam partition theory is also the globally pure second set in the present Timoshenko beam partition theory.

The pure mode I modes of the second set are given by the zero resultant shear force condition, i.e. $F_s = 0$, which is as follows:

$$6\left(1 + \gamma\right)\left(M_{1B} + M_{2B}\right) + h_1\left(1 + \gamma^3\right)N_{1Be} = 0 \tag{4.76}$$

This yields two independent pure mode I modes, which are

$$\left\{\varphi_{\theta_1'}\right\} = \begin{Bmatrix} 1 \\ \theta_1' \\ 0 \end{Bmatrix} = \begin{Bmatrix} 1 \\ -1 \\ 0 \end{Bmatrix} \tag{4.77}$$

$$\left\{\varphi_{\theta_2'}\right\} = \begin{Bmatrix} 1 \\ 0 \\ \theta_2' \end{Bmatrix} = \begin{Bmatrix} 1 \\ 0 \\ -6\left(1 + \gamma\right) / \left[h_1\left(1 + \gamma^3\right)\right] \end{Bmatrix} \tag{4.78}$$

Note that here, θ_1' is used to replace the previous θ'. Just as for the $\left\{\varphi_{\theta_1'}\right\}$ mode, the $\left\{\varphi_{\theta_2'}\right\}$ mode is both globally and locally pure, that is, both the resultant shear force $F_{s\theta_2'}$ in the Δa region and the crack tip shear force $F_{sB\theta_2'}$ are zero within the context of the present Euler beam theory. Within the context of the present Timoshenko beam partition theory, it is only globally pure, i.e. only the resultant shear force $F_{s\theta_2'}$ is zero.

Although the $\left\{\varphi_{\theta_1'}\right\}$ mode has its orthogonal partner, the $\left\{\varphi_{\beta_1'}\right\}$ mode, which corresponds to $D_{op\beta_1'} = 0$, the $\left\{\varphi_{\theta_2'}\right\}$ mode has no orthogonal partner corresponding to $D_{op\beta_2'} = 0$. This is because the expression for crack tip opening displacement does not contain axial forces, as shown in Eq. (4.14). Recall that N_{1B} and N_{2B} alone cannot produce a pure mode I mode that is characterised by zero crack tip relative shearing displacement. However N_{1B} and N_{2B} alone can produce a pure mode II mode that is characterised by zero crack tip opening displacement.

4.2.7 Addition of shear forces

The two crack tip shear forces shown in Fig. 4.6 (b), i.e. P_{1B} and P_{2B}, are now added. The resultant shear force F_s and moment M_n in Eqs. (4.7) and (4.8) change to

$$F_s = \frac{6\gamma}{h_1\left(1+\gamma\right)^3}\left[M_{1B}+M_{2B}+\left(P_{1B}+P_{2B}\right)\Delta a\right]+\frac{\gamma\left(1+\gamma^3\right)}{\left(1+\gamma\right)^4}N_{1Be} \tag{4.79}$$

and

$$M_n = M_{nm}+F_n\Delta a = \frac{1+3\gamma}{\left(1+\gamma\right)^3}\left(\beta_1 M_{1B}-M_{2B}\right)+\frac{h_1\gamma^2\left(1-\gamma\right)}{2\left(1+\gamma\right)^3}N_{1Be}+F_n\Delta a \tag{4.80}$$

where

$$F_n = b\int_0^{\Delta a}\sigma_n\, d\xi = \frac{1+3\gamma}{\left(1+\gamma\right)^3}\left(\beta_1 P_{1B}-P_{2B}\right) \tag{4.81}$$

in Euler beam theory and

$$F_n = b\int_0^{\Delta a}\sigma_n\, d\xi = \frac{\gamma P_{1B}-P_{2B}}{1+\gamma} \tag{4.82}$$

in Timoshenko beam theory. The crack tip shearing displacement becomes

$$D_{sh} = \frac{1}{2E}\left[\left(\frac{h_1 M_{1B}}{I_1}+\frac{h_2 M_{2B}}{I_2}\right)\delta a-\left(\frac{h_1 P_{1B}}{I_1}+\frac{h_2 P_{2B}}{I_2}\right)\frac{\delta a^2}{2}+\left(\frac{2N_{1Be}}{S_1}\right)\delta a\right] \tag{4.83}$$

By neglecting the higher order P_{1B} and P_{2B} term, the condition $D_{sh}=0$ stays the same as in Eq. (4.64). Therefore, the same $\left\{\varphi_{\theta_1}\right\}$ and $\left\{\varphi_{\theta_2}\right\}$ modes as those in Eqs. (4.66) and (4.67) are obtained. Since Δa can take any value provided that it includes the region affected by the presence of the crack tip, $M_n=0$ requires that both $M_{nm}=0$ and $F_n=0$. Therefore, Eq. (4.60) is still valid and we have the same $\left\{\varphi_{\beta_1}\right\}$ and $\left\{\varphi_{\beta_2}\right\}$ modes as those in Eqs. (4.61) to (4.63). The condition $F_n=0$ requires that P_{1B} and P_{2B} satisfy $P_{2B}=\beta_1 P_{1B}$ in Euler beam theory and $P_{2B}=\gamma P_{1B}$ in Timoshenko beam theory. Since P_{1B} and P_{2B} do not contribute to the strain energy in Euler beam theory, we only consider their contributions to the mixed-mode partition using Timoshenko beam theory.

Since the through-thickness shear effect does not generate any axial displacement in Timoshenko beam theory, the two crack tip forces P_{1B} and P_{2B} produce pure mode I fracture only. This mode is now referred to as the 'P mode'. Quantities in this mode are denoted by a subscript P. The crack tip opening displacement D_{opP} is given by

$$D_{opP} = \frac{\left(\gamma P_{1B}-P_{2B}\right)\delta a}{\gamma b h_1 \kappa\mu} \tag{4.84}$$

Within the Δa region, as shown in Fig. 4.2 (b), the through-thickness shearing equations in Eqs. (4.15) and (4.16) change to

$$\kappa\mu S_1 \left(\frac{dw_1}{d\xi} - \psi_1 \right) = b \int_0^\xi \sigma_n \, d\xi - P_{1B} \tag{4.85}$$

and

$$\kappa\mu S_2 \left(\frac{dw_2}{d\xi} - \psi_2 \right) = -b \int_0^\xi \sigma_n \, d\xi - P_{2B} \tag{4.86}$$

for beams 1 and 2 respectively. Eq. (4.87) can now be obtained in the same way as Eq. (4.19).

$$\psi_{1B} - \psi_{2B} = \frac{1}{\kappa\mu} \left[\left(\frac{P_{1B}}{S_1} - \frac{P_{2B}}{S_2} \right) - F_{nB} \left(\frac{1}{S_1} + \frac{1}{S_2} \right) \right] \tag{4.87}$$

In the presence of P_{1B} and P_{2B} alone, $\psi_{1B} - \psi_{2B} = 0$. Therefore, the crack tip opening force F_{nBP} in the P mode is

$$F_{nBP} = \frac{\gamma P_{1B} - P_{2B}}{1 + \gamma} \tag{4.88}$$

which has the same value as the resultant normal force F_n in Eq. (4.82). Therefore, the ERR due to the mode I P mode G_P is obtained from Eqs. (4.84) and (4.88) using the VCCT, and is as follows:

$$G_P = \frac{(\gamma P_{1B} - P_{2B})^2}{2b^2 h_1 \gamma \kappa\mu \, (1 + \gamma)} \tag{4.89}$$

It is easy to show that G_P above is also equal to

$$G_P = \frac{1}{2b\kappa\mu} \left[\frac{P_{1B}^2}{S_1} + \frac{P_{2B}^2}{S_2} - \frac{(P_{1B} + P_{2B})^2}{S} \right] \tag{4.90}$$

Using Eqs. (4.36) and (4.84), the interaction between the mode I $\left\{ \varphi_{\theta_1} \right\}$ and P modes is

$$\Delta G_{\theta_1 P} = \frac{4\sqrt{3} \, (\gamma P_{1B} - P_{2B})}{b^2 h_1^2 \, (1 + \gamma) \, (\kappa\mu E)^{1/2}} \tag{4.91}$$

It can be shown that the same relationship as that in Eq. (4.30) can be obtained between the crack tip opening force F_{nBP} and the crack tip shearing force F_{sBP} in the P mode. Since F_{nBP}, given in Eq. (4.88), is finite, then F_{sBP} is zero. Moreover, the first and second sets coincide with each other in the present Timoshenko beam partition theory and therefore the mode I P mode has no interaction with the $\left\{ \varphi_{\beta_1} \right\}$ and $\left\{ \varphi_{\beta_2} \right\}$ modes. Consequently, within the context of the present Timoshenko beam partition theory, the mode I partition of ERR is

$$G_I = \alpha_{\theta_1}^2 G_{\theta_1} + G_P + \alpha_{\theta_1} \Delta G_{\theta_1 P} \tag{4.92}$$

The mode II ERR is the same as before. In the averaged partition rule 1, half of the interaction terms, i.e. $\left(\alpha_{\theta_1}\alpha_{\beta_1}\Delta G_{\theta_1\beta_1} + \alpha_{\theta_1}\alpha_{\beta_2}\Delta G_{\theta_1\beta_2}\right)/2$ is added to G_I in Eq. (4.92) and is deducted from G_{II}.

In averaged partition rule 2, the mode I partition of ERR G_I can still be calculated using Eq. (4.92) but with some small modifications. The first term in Eq. (4.92) is replaced with $\alpha^2_{\theta_{1A2}} G_{\theta_{1A2}}$ in Eq. (4.73); G_P is still given by Eq. (4.89) or (4.90); and in the third term, α_{θ_1} and $\Delta G_{\theta_1 P}$ are replaced with $\alpha_{\theta_{1A2}}$ and $\Delta G_{\theta_{1A2}P}$ respectively. $\Delta G_{\theta_{1A2}P}$ is the interaction term and it is found in the same way as $\Delta G_{\theta_1 P}$ in Eq. (4.91) but this time by considering the interaction between the P mode and the $\left\{\varphi_{\theta_{1A2}}\right\}$ mode. It is found to be

$$\Delta G_{\theta_{1A2}P} = \frac{P_{1B}\gamma - P_{2B}}{b^2\gamma h_1}\sqrt{\frac{24}{Eh_1^2\kappa\mu\left(2+h_1\right)}\left(1+\frac{\theta_{1A2}^2}{\gamma^3}-\frac{\left(1+\theta_{1A2}\right)^2}{\left(1+\gamma\right)^3}\right)} \tag{4.93}$$

Finally, it is seen from Eq. (4.79) that when $P_{1B}+P_{2B}=0$, the same $\left\{\varphi_{\theta_1'}\right\}$ and $\left\{\varphi_{\theta_2'}\right\}$ modes as those in Eqs. (4.77) and (4.78) are obtained. However, when $P_{1B}+P_{2B}\neq 0$, it is not generally possible to get $F_s = 0$ and there is then no second set of pure modes in the present Euler beam partition theory.

4.3 Numerical investigations

To validate the partition theories, an FEM simulation capability has been developed based on the Euler and Timoshenko beam theories and two-dimensional elasticity. Imaginary normal and shear point interface springs with the very high stiffness of $k_s = 10^6\,\mathrm{kN/mm}$ were used to model perfectly bonded plies. Appendix B gives details on how this value was determined and also presents the mesh convergence studies for this section and how suitable meshes were chosen to obtain mesh-independent results. The ERR partitions were calculated using the VCCT in conjunction with the interface springs. A contact algorithm was also implemented to deal with any possible contact in loading. Full details are given in §3.3, §3.4 and §3.5.

4.3.1 Tests with crack tip bending moments

The first test aimed to examine the present Euler beam partition theory (or the present Timoshenko beam partition theory with an infinitely large shear modulus). A DCB, as shown in Fig. 4.1, was considered. In line with the theoretical development, a plane-stress condition was assumed. For plane strain, E can simply be replaced with $E/\left(1-\nu^2\right)$, and ν with $\nu/\left(1-\nu\right)$. The units of these FEM simulations are kN and mm. The Young's modulus is a unit parameter and was therefore set to $E = 1\,\mathrm{GPa}$, and the Poisson's ratio is $\nu = 0.3$. The intact length is $L = 100\,\mathrm{mm}$ and the crack length is $a = 10\,\mathrm{mm}$ unless stated otherwise. The width is a unit parameter and was therefore set to $b = 1\,\mathrm{mm}$. The thickness is $h = h_1 + h_2 = 3\,\mathrm{mm}$ with $h_1 = 1\,\mathrm{mm}$. Therefore, the thickness ratio is $\gamma = 2$.

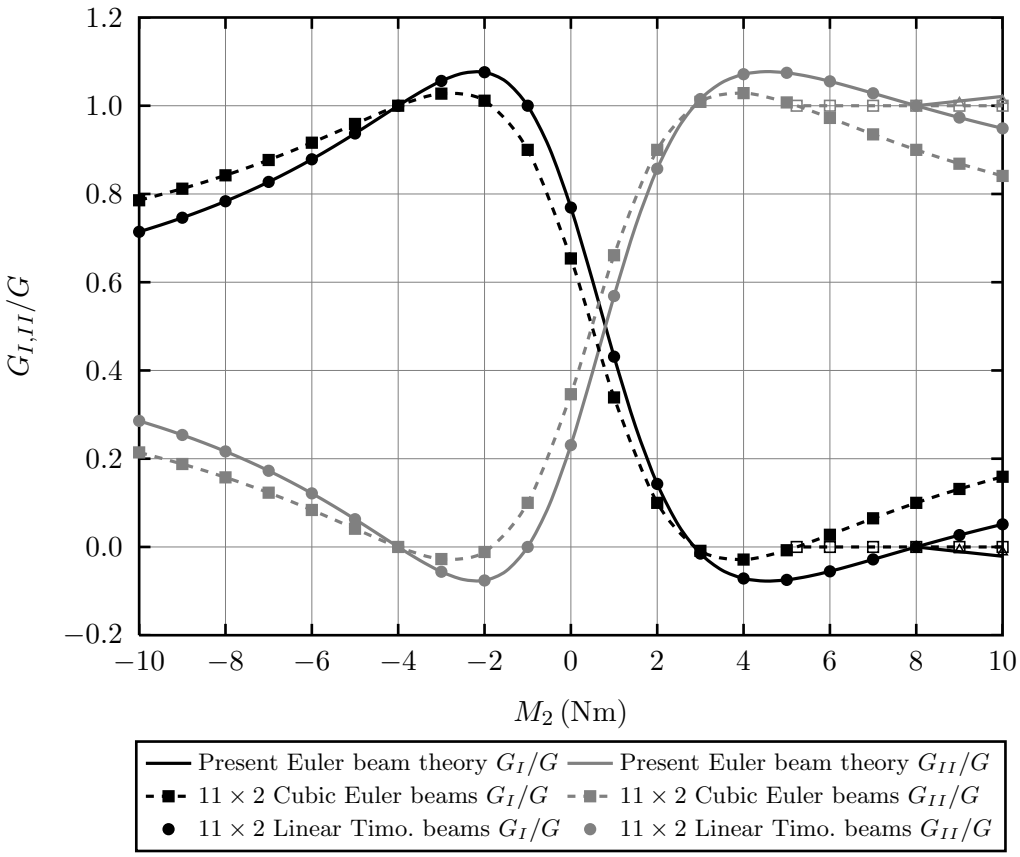

Figure 4.7: Comparisons between the present Euler beam partition theory and FEM Euler beam results with varying M_2 and $M_1 = 1\,\text{Nm}$, $N_1 = 0$, $N_2 = 0$, $P_1 = 0$, $P_2 = 0$, $\mu = 10^4\,\text{GPa}$, $\gamma = 2$.

Tip bending moments were applied to the DCB tip. M_1 was held constant at 1 Nm and M_2 was varied. All other DCB tip loads were 0. Both analytical and numerical results are presented in Fig. 4.7 and Tables 4.1 and 4.2.

One set of numerical results, which is given in Fig. 4.7 and Tables 4.1 and 4.2, is from FEM simulations with 11×2 uniformly distributed linear Timoshenko beam elements. A large shear modulus of $\mu = 10^4\,\text{GPa}$ was used to simulate Euler beams. This value is 10^4 times larger than the Young's modulus E. This large value prevents the Timoshenko beam elements from shearing and therefore causes them to behave like Euler beams. To avoid shear locking, reduced-integration elements were used. Several features in Fig. 4.7 are consistent with Fig. 4.5. They are discussed in detail in §4.2.4. It is seen that this set of numerical results is virtually identical to the analytical results from the present Euler beam partition theory. Both pairs of pure modes, $(\theta_1, \beta_1) = (-4, 2.86)$ from the first set and $(\theta_1', \beta_1') = (-1, 8)$ from the second set, are predicted. As expected, since there are two distinct pairs of pure modes, in the regions between $(\theta_1, \beta_1) = (-4, 2.86)$ and $(\theta_1', \beta_1') = (-1, 8)$, negative partitions of ERR exist. This is discussed in detail in Appendix A. When M_2/M_1 is increased above $\beta_1' = 8$, DCB tip contact starts. In the

Table 4.1: Comparisons between the present Euler beam partition theory and FEM Euler beam results with varying M_2 and $M_1 = 1\,\text{Nm}$, $N_1 = 0$, $N_2 = 0$, $P_1 = 0$, $P_2 = 0$, $\mu = 10^4\,\text{GPa}$, $\gamma = 2$ and ignoring contact.

M_2 (Nm)	G_I/G (%)		
	Present Euler beam theory	11×2 cubic Euler beams	11×2 linear Timo. beams
-10	71.43	78.57	71.43
-8	78.35	84.23	78.35
-6	87.85	91.62	87.85
-4	100.00	100.00	100.00
-2	107.59	101.14	107.59
0	76.92	65.38	76.92
2	14.29	10.00	14.29
4	-7.14	-2.86	-7.14
6	-5.53	2.76	-5.53
8	0.00	10.00	0.00
10	5.13	15.91	5.13

Table 4.2: Comparisons between the present Euler beam partition theory and FEM Euler beam results for contact with varying M_2 and $M_1 = 1\,\text{Nm}$, $N_1 = 0$, $N_2 = 0$, $P_1 = 0$, $P_2 = 0$, $\mu = 10^4\,\text{GPa}$, $\gamma = 2$.

	Crack tip contact		DCB tip contact		After DCB tip contact	
	M_2 (Nm)	G_I/G (%)	M_2 (Nm)	G_I/G (%)	M_2 (Nm)	G_I/G (%)
Present Euler beam theory	8	0	8	0	10	-2.11
11×2 cubic Euler beams	5.23	0	8	0	10	0
11×2 linear Timo. beams	8	0	8	0	10	-1.16

present Euler beam partition theory, the fracture mode is deflected immediately into a mixed-mode region between the $\beta_1 = 2.86$ line and the $\beta_1' = \gamma^3 = 8$ line, as shown in Fig. 4.4. As given in Eq. (4.47), $k = 5 > \beta_1$ so the fracture mode stays in the mixed mode region with increasing M_2. This set of numerical predictions agrees very well with the present Euler beam partition theory.

Another set of numerical results, which is also given in Fig. 4.7 and Tables 4.1 and 4.2, is from simulations with 11×2 uniformly distributed cubic Euler beam elements. It is seen that the first pair $(\theta_1, \beta_1) = (-4, 2.86)$ is accurately predicted but the second pair (θ_1', β_1') is predicted as $(-1.81, 5.23)$ instead of $(-1, 8)$. When M_2/M_1 is in the range from $\beta_1' = 5.23$ to $\gamma^3 = 8$, crack tip running contact occurs, resulting in a pure mode II region. When M_2/M_1 is increased further above $\gamma^3 = 8$, both crack tip running contact and DCB tip contact occur and the fracture mode remains in the pure mode II region. Since $k = 5$, therefore $\beta_1 = 2.86 < k < \beta_1' = 5.23$ and the fracture mode should enter the mixed-mode region beyond $M_2/M_1 = \gamma^3$. It is seen that this set of results does not agree with the analytical predictions. As mentioned earlier in §4.2.3, the difference is due to the

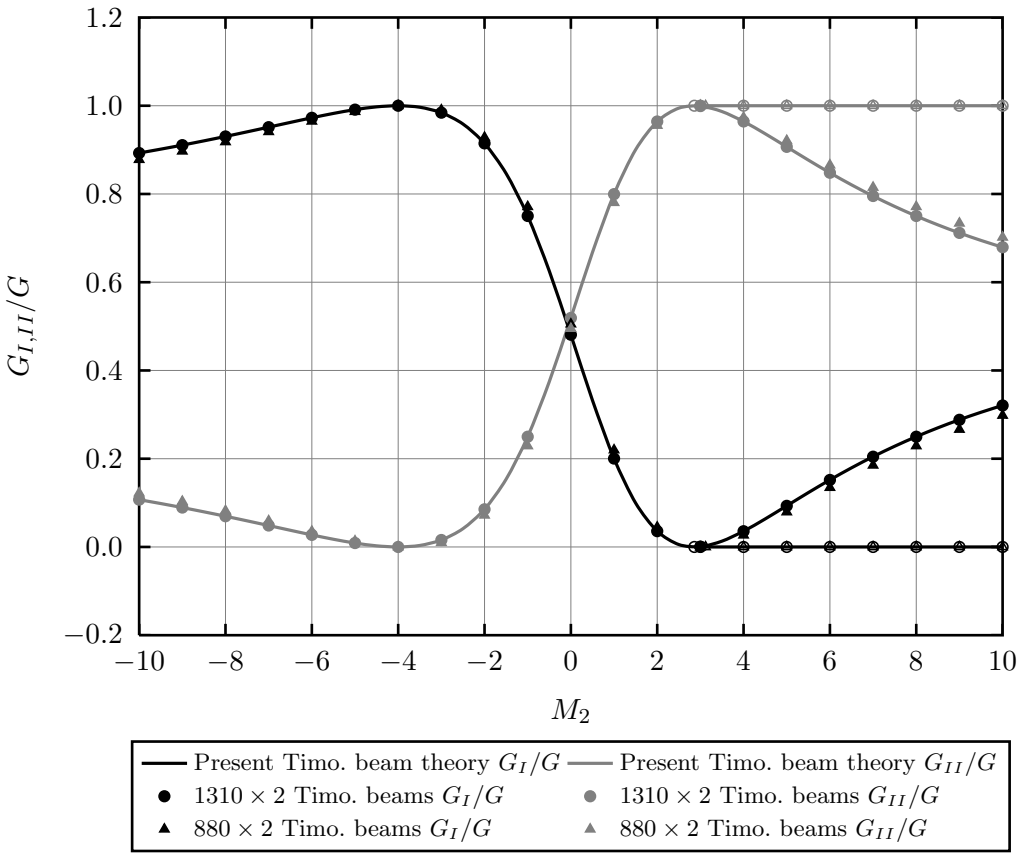

Figure 4.8: Comparisons between the present Timoshenko beam partition theory and FEM Timoshenko beam results with varying M_2 and $M_1 = 1\,\text{Nm}$, $N_1 = 0$, $N_2 = 0$, $P_1 = 0$, $P_2 = 0$, $\mu = 1/2.6\,\text{GPa}$, $\gamma = 2$.

displacement incompatibility at the interface in this set FEM simulations with cubic Euler beam elements.

In both sets of numerical results, 11 identical elements were used along the whole length of each beam, with ten elements in the intact section and one in the cracked section. However, since both types of contact can occur beyond $M_2/M_1 = \gamma^3 = 8$, in contact tests the cracked length was increased to 30 mm and three element were used over this length in order to differentiate between crack tip running contact and DCB tip contact.

The second test aimed to examine the present Timoshenko beam partition theory (with a finite shear modulus). An identical DCB to that in the first test was considered, but this time a shear modulus of $\mu = E/\left[2\left(1+\nu\right)\right] = 1/2.6\,\text{GPa}$ was used. The results are presented in Fig. 4.8 and Tables 4.3 and 4.4. Two sets of numerical results were calculated using reduced-integration Timoshenko beam elements: one set used came from a fine nonuniform mesh with 1310×2 elements and the other set came from a relatively coarse uniform mesh with 880×2 elements (see Appendix B). In order to obtain accurate, mesh-independent partitions of ERR, simulations with linear Timoshenko beams and normal values for the shear modulus require a very fine mesh in the vicinity of the crack tip. For the fine

Table 4.3: Comparisons between the present Timoshenko beam partition theory and FEM Timoshenko beam results with varying M_2 and $M_1 = 1\,\text{Nm}$, $N_1 = 0$, $N_2 = 0$, $P_1 = 0$, $P_2 = 0$, $\mu = 1/2.6\,\text{GPa}$, $\gamma = 2$.

M_2 (Nm)	$G_I/G\,(\%)$		
	Present Timo. beam theory	1310×2 Timo. beams	880×2 Timo. beams
-10	89.29	89.27	87.78
-8	93.04	93.03	91.80
-6	97.27	97.26	96.47
-4	100.00	100.00	100.00
-2	91.46	91.47	92.81
0	48.08	48.10	50.51
2	3.57	3.58	4.47
4	3.57	3.56	2.67
6	15.20	15.19	13.46
8	25.00	24.98	22.90
10	32.08	32.06	29.82

Table 4.4: Comparisons between the present Timoshenko beam partition theory and FEM Timoshenko beam results for contact with varying M_2 and $M_1 = 1\,\text{Nm}$, $N_1 = 0$, $N_2 = 0$, $P_1 = 0$, $P_2 = 0$, $\mu = 1/2.6\,\text{GPa}$, $\gamma = 2$.

	Crack tip contact		DCB tip contact		After DCB tip contact	
	$M_2\,(\text{Nm})$	$G_I/G\,(\%)$	$M_2\,(\text{Nm})$	$G_I/G\,(\%)$	$M_2\,(\text{Nm})$	$G_I/G\,(\%)$
Present Timo. beam theory	2.86	0	8	0	10	0
1310×2 Timo. beams	2.86	0	8	0	10	0
880×2 Timo. beams	3.12	0	8	0	10	0

nonuniform mesh, in the region of length 1.2 mm centred on the crack tip, 1200 elements with a length of 0.001 mm were uniformly distributed. In the remaining intact section of the DCB, 100 elements were uniformly distributed. In the remaining cracked section of the DCB, 10 elements were uniformly distributed. The coarse uniform mesh used 880 identical elements along the whole length of the DCB with 800 in the intact section and 80 in the cracked section. It is seen that the FEM results converge excellently to the present Timoshenko beam partition theory. The fine mesh is in virtually exact agreement with the Timoshenko beam partition theory; the coarse mesh is in less good agreement but is still very close. The two pairs of pure modes, i.e. (θ_1, β_1) and $(\theta'_{1T}, \beta'_{1T})$, coincide on the first pair (θ_1, β_1). Crack tip running contact starts at $M_2/M_1 = \beta_1 = 2.86$ and the fracture mode is in a pure mode II region between $\beta_1 = 2.86$ and $\beta'_1 = 8$, as shown in Fig. 4.4. DCB tip contact starts beyond $M_2/M_1 = \beta'_1 = 8$. As given in Eq. (4.47), $k = 5 > \beta_1$ so the fracture mode stays in the pure mode II region with increasing M_2/M_1. The present Timoshenko beam partition theory agrees very well with the FEM predictions. It is worth

Table 4.5: Local and global pureness using 15×2 cubic Euler beam elements with varying M_2 and $M_1 = 1\,\text{Nm}$, $N_1 = 0$, $N_2 = 0$, $P_1 = 0$, $P_2 = 0$, $\gamma = 2$.

M_2 (Nm)	G_I/G (%) for n spring pairs				
	1	2	3	4	5
$\theta_1' = -1$	90.00	96.00	97.20	97.92	98.33
$\beta_1' = 8$	10.00	4.00	2.80	2.08	1.67
$\theta_1 = -4$	100.00	100.00	100.00	100.00	100.00
$\beta_1 = 20/7$	0.00	0.00	0.00	0.00	0.00

Table 4.6: Local and global pureness using 15×2 linear Timoshenko beam elements with varying M_2 and $M_1 = 1\,\text{Nm}$, $N_1 = 0$, $N_2 = 0$, $P_1 = 0$, $P_2 = 0$, $\mu = 10^4\,\text{GPa}$, $\gamma = 2$.

M_2 (Nm)	G_I/G (%) for n spring pairs				
	1	2	3	4	5
$\theta_1' = -1$	100.00	100.00	100.00	100.00	100.00
$\beta_1' = 8$	0.00	0.00	0.00	0.00	0.00
$\theta_1 = -4$	100.00	100.00	100.00	100.00	100.00
$\beta_1 = 20/7$	0.00	0.00	0.00	0.00	0.00

noting that the region between $\beta_1 = 2.86$ and $\beta_1' = 8$, as shown in Fig. 4.4, is a mixed-mode region in the present Euler beam partition theory.

It should be noted that a very fine mesh in the vicinity of the crack tip is required to ensure that $F_{nB\theta_1}\delta a$ is negligible in order to zero the interactions between the $\left\{\varphi_{\theta_1}\right\}$ and $\left\{\varphi_{\beta_1}\right\}$ modes and to avoid a numerically generated second pair of pure modes, which is different to the first pair (θ_1, β_1) with $\theta_1 < \theta_1' < -1$ and $\beta_1 < \beta_1' < \gamma^3$.

The third test aimed to show the local and global pureness of the two pairs of pure modes, i.e. the first (θ_1, β_1) pair and the second (θ_1', β_1') pair, using the FEM. Multiple pairs of interface springs were used in the calculation of the ERR partitions, as shown in §3.5. The DCB is the same as that in the first and second test.

Table 4.5 shows the results from simulations with 15×2 uniformly distributed cubic Euler beam elements. The crack length was increased to $a = 50\,\text{mm}$ with five elements in this region to allow the VCCT with multiple spring pairs to be used. The local and global pureness of the $(\theta_1, \beta_1) = (-4, 20/7)$ pair from the first set is demonstrated well. However, the local pureness of the $(\theta_1', \beta_1') = (-1, 8)$ pair from the second set cannot be predicted due to the incompatibility of displacement at the interface. Despite this, global pureness is predicted when using more springs.

Table 4.6 shows the results from simulations with 15×2 uniformly distributed linear Timoshenko beam elements with the large shear modulus $\mu = 10^4\,\text{MPa}$ to represent Euler beams (the crack length a is still 50 mm with five elements in this region). It is seen that the two pairs are both locally and globally pure within the context of Euler beam theory.

Table 4.7: Local and global pureness using 880×2 linear Timoshenko beam elements with varying M_2 and $M_1 = 1\,\text{Nm}$, $N_1 = 0$, $N_2 = 0$, $P_1 = 0$, $P_2 = 0$, $\mu = 1/2.6\,\text{GPa}$, $\gamma = 2$.

M_2 (Nm)	G_I/G (%) for n spring pairs						
	1	2	3	4	5	10	20
$\theta_1' = -1$	77.10	79.03	80.74	82.27	83.62	88.55	93.37
$\beta_1' = 8$	22.90	20.97	19.26	17.73	16.38	11.45	6.63
$\theta_1 = -4$	100.00	100.00	100.00	100.00	100.00	100.00	100.00
$\beta_1 = 20/7$	0.00	0.00	0.00	0.00	0.00	0.00	0.00

Table 4.8: Local and global pureness using 330×6 QUAD4 elements with varying M_2 and $M_1 = 1\,\text{Nm}$, $N_1 = 0$, $N_2 = 0$, $P_1 = 0$, $P_2 = 0$, $\gamma = 2$..

M_2 (Nm)	G_I/G (%) for n spring pairs						
	1	2	3	4	5	10	20
$\theta_1' = -1$	85.27	86.16	87.41	88.82	90.20	94.70	97.67
$\beta_1' = 8$	16.10	15.19	13.91	12.47	11.06	6.47	4.25
$\theta_1 = -4$	98.43	98.39	98.34	98.31	98.31	98.49	98.20
$\beta_1 = 20/7$	1.04	1.03	1.01	0.97	0.90	0.49	0.10

Table 4.7 shows the results from simulations with 880×2 uniformly distributed linear Timoshenko beam elements with the normal shear modulus of $\mu = 1/2.6$. It is seen that the $(\theta_1, \beta_1) = (-4, 20/7)$ pair from the first set is always both locally and globally pure. However, the $(\theta_1', \beta_1') = (-1, 8)$ pair from the second set is not locally pure and is only globally pure.

Table 4.8 shows the results from simulations with 330×6 uniformly distributed plane-stress QUAD4 elements with a normal shear modulus of $\mu = 1/2.6\,\text{GPa}$. 300 identical QUAD4 elements were used along the intact length and 30 identical QUAD4 elements were used along the cracked length. Two elements were used through the thickness of the upper beam and four elements through the thickness of the lower beam. Details on the mesh convergence studies, which determined the design of this mesh, are available in Appendix B. The local and global pureness of the $(\theta_1, \beta_1) = (-4, 20/7)$ pair from the first set is demonstrated again. However, as before in Table 4.7, the $(\theta_1', \beta_1') = (-1, 8)$ pair from the second set is not locally pure and is only globally pure.

The fourth test compares the predictions from various mixed-mode partition theories, including the present Euler and Timoshenko beam partition theories and the averaged partition rules. Comparisons are also made with Suo and Hutchinson's (1990) partition theory, based on two-dimensional elasticity, and also results from FEM simulations with QUAD4 elements. The same DCB as in the previous tests was considered. Results are presented in Fig. 4.9 and Tables 4.9 and 4.10.

The FEM simulations with QUAD4 elements used the same mesh as that used in the third test, i.e. 300 identical QUAD4 elements were used along the intact length and 30 identical QUAD4 elements were used along the cracked length. Two elements were used

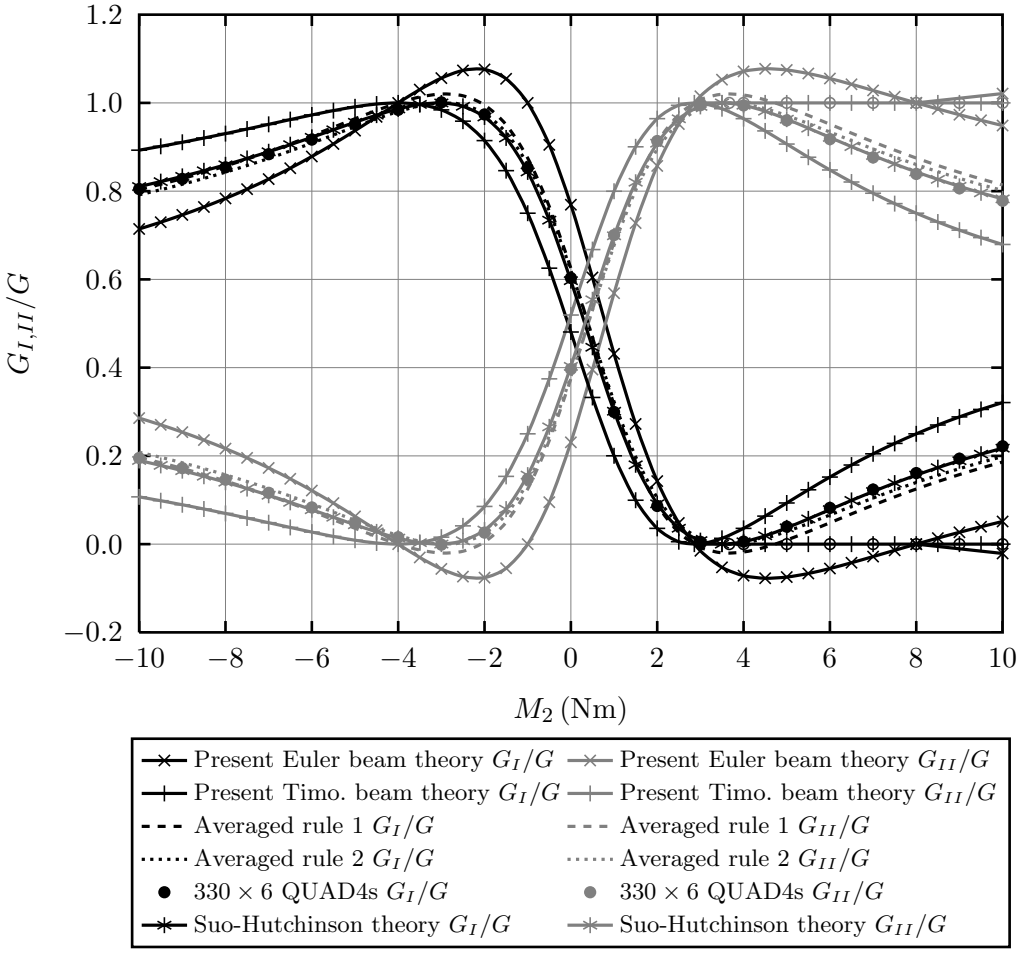

Figure 4.9: Comparisons between various theories and FEM results with varying M_2 and $M_1 = 1\,\text{Nm}$, $N_1 = 0$, $N_2 = 0$, $P_1 = 0$, $P_2 = 0$, $\gamma = 2$.

Table 4.9: Comparisons between various theories and FEM results with varying M_2 and $M_1 = 1\,\text{Nm}$, $N_1 = 0$, $N_2 = 0$, $P_1 = 0$, $P_2 = 0$, $\gamma = 2$ and ignoring contact.

M_2 (Nm)	G_I/G (%)					
	Present Euler beam theory	Present Timo. beam theory	Averaged rule 1	Averaged rule 2	330 × 6 QUAD4s	Suo-Hutchinson theory
−10	71.43	89.29	80.36	79.17	80.48	81.05
−8	78.35	93.04	85.70	84.30	85.39	85.97
−6	87.85	97.27	92.56	90.89	91.69	92.20
−4	100.00	100.00	100.00	98.04	98.43	98.64
−2	107.59	91.46	99.53	97.58	97.39	96.81
0	76.92	48.08	62.50	62.01	60.32	59.71
2	14.29	3.57	8.93	10.54	8.64	9.14
4	−7.14	3.57	−1.79	0.25	0.57	0.53
6	−5.53	15.20	4.84	6.61	8.21	7.83
8	0.00	25.00	12.50	13.97	16.10	15.64
10	5.13	32.08	18.61	19.84	22.19	21.75

Table 4.10: Comparisons between various theories and FEM results for contact with varying M_2 and $M_1 = 1\,\text{Nm}$, $N_1 = 0$, $N_2 = 0$, $P_1 = 0$, $P_2 = 0$, $\gamma = 2$.

	Crack tip contact		DCB tip contact		After DCB tip contact	
	M_2 (Nm)	G_I/G (%)	M_2 (Nm)	G_I/G (%)	M_2 (Nm)	G_I/G (%)
Present Euler beam theory	8	0	8	0	10	−2.11
Present Timo. beam theory	2.86	0	8	0	10	0
Averaged rule 1	3.38	0	8	0	10	0
Averaged rule 2	3.66	0	8	0	10	0
330×6 QUAD4s	3.67	0	8	0	10	0
Suo-Hutchinson theory	-	-	-	-	-	-

through the thickness of the upper beam and four elements through the thickness of the lower beam.

Fig. 4.9 and Tables 4.9 and 4.10 show that the present Euler and Timoshenko beam partition theories represent either the upper or lower bounds for the ERR partition. In the first quadrant of the partition space of $(\alpha_{\theta_1}, \alpha_{\beta_1})$ (see Fig. 4.4), i.e. between $M_{2B}/M_{1B} = \theta_1 = -4$ and $M_{2B}/M_{1B} = \beta_1 = 2.86$, the interaction causes energy flow from mode II to mode I, as shown by Eq. (4.42). Therefore, the values of G_I from the present Euler beam partition theory are larger than the values of G_I from the present Timoshenko beam partition theory by $\alpha_{\theta_1}\alpha_{\beta_1}\Delta G_{\theta_1\beta_1}$. In the second quadrant of the partition space of $(\alpha_{\theta_1}, \alpha_{\beta_1})$, i.e. between $M_{2B} = \beta_1 = 2.86$ and $M_{2B} = \beta_1' = 8$, and also in the fourth quadrant, i.e. between $M_{2B} = -\infty$ and $M_{2B} = \theta_1' = -4$, the values of G_I from the present Euler beam partition theory are smaller than the values of G_I from the present Timoshenko beam partition theory by $\alpha_{\theta_1}\alpha_{\beta_1}\Delta G_{\theta_1\beta_1}$. The reverse is true in all cases for the values of G_{II}, so that the value of the total ERR is unchanged by the interaction.

Averaged partition rule 1 shows very good agreement with the QUAD4 results. Averaged partition rule 2 shows excellent agreement with the QUAD4 results. Both of these rules are derived directly from the present Euler and Timoshenko beam partition theories, which themselves are completely analytical and exactly agree with the corresponding FEM results. Suo and Hutchinson's (1990) partition theory, which is a combined numerical and analytical theory, agrees well with the averaged partition rule 1, averaged partition rule 2, and the QUAD4 results. It does not agree well with the FEM results using beam elements, which is as expected.

The present Euler beam partition theory does not predict any crack tip running contact. The present Timoshenko beam partition theory does predict it to occur at $M_2/M_1 = \beta_1 = \beta_{1T}' = 2.86$, which agrees very well with the value from the corresponding FEM simulations.

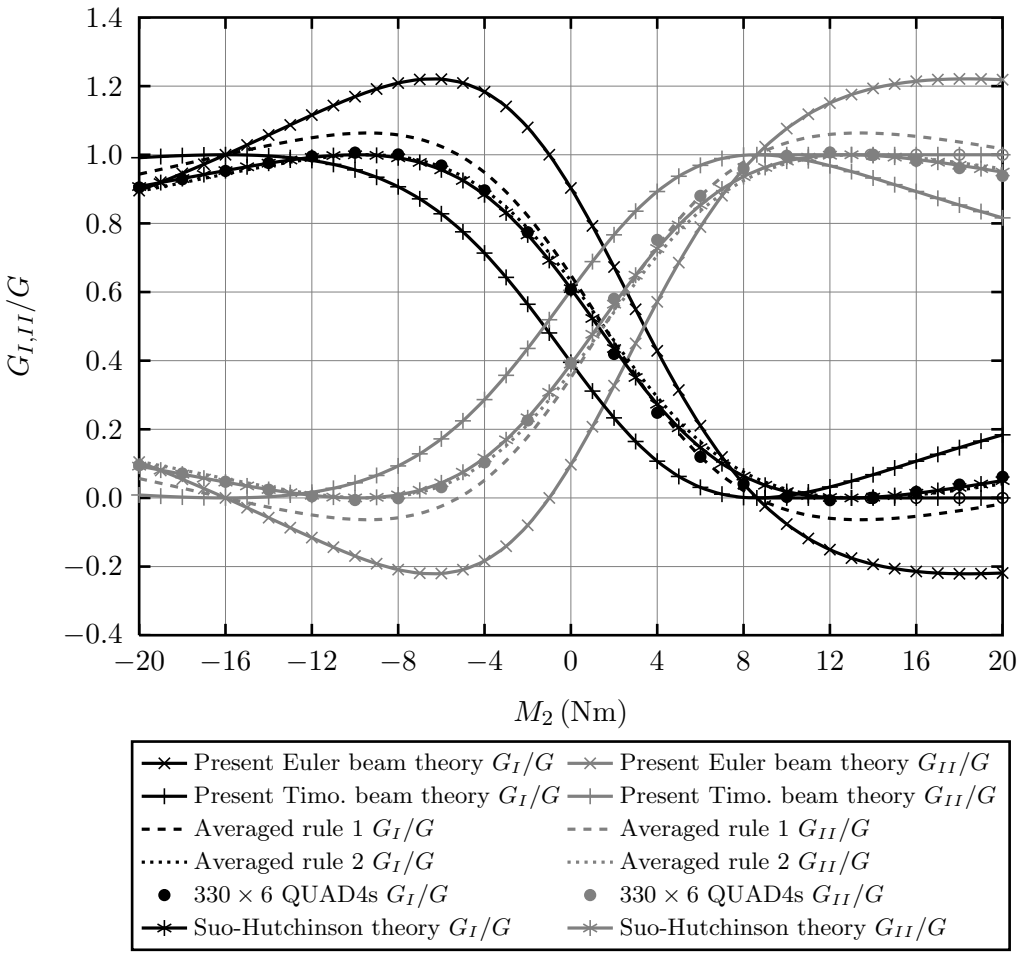

Figure 4.10: Comparisons between various theories and FEM results with varying M_2 and $M_1 = 1\,\text{Nm}$, $N_1 = 0$, $N_2 = 0$, $P_1 = 0$, $P_2 = 0$, $\gamma = 4$.

Due to crack tip running contact, a pure mode II region exists between $M_2/M_1 = \beta_1 = 2.86$ and $M_2/M_1 = \beta_1' = 8$. Averaged partition rule 1 predicts crack tip running contact to occur at $M_2/M_1 = 3.38$. This is close to the value from the FEM simulations with QUAD4 elements, which predicts it to occur at $M_2/M_1 = 3.67$. Averaged partition rule 2, is even closer with $M_2/M_1 = 3.66$. Suo and Hutchinson's (1990) partition theory does not provide this information.

The fifth test is the same as the fourth test except that the thickness ratio is $\gamma = 4$. Results are presented in Fig. 4.10 and Tables 4.11 and 4.12.

Again, the present Euler and Timoshenko beam partition theories form either the upper or lower bounds of the ERR partition. Averaged partition rule 1 is in good agreement with the FEM results using QUAD4 elements. Averaged partition rule 2 is in excellent agreement with the same FEM results and also with Suo and Hutchinson's (1990) partition theory. The present Euler beam partition theory does not predict any crack tip running contact. The present Timoshenko beam partition theory predicts it, occurring at $M_2/M_1 = \beta_1 = \beta_{1T}' = 8.62$. Averaged partition rule 1 predicts crack tip running contact to occur

Table 4.11: Comparisons between various theories and FEM results with varying M_2 and $M_1 = 1\,\text{Nm}$, $N_1 = 0$, $N_2 = 0$, $P_1 = 0$, $P_2 = 0$, $\gamma = 4$ and ignoring contact.

M_2 (Nm)	$G_I/G\,(\%)$					
	Present Euler beam theory	Present Timo. beam theory	Averaged rule 1	Averaged rule 2	330×6 QUAD4s	Suo-Hutchinson theory
-20	89.55	99.14	94.34	89.35	90.48	90.73
-16	100.00	100.00	100.00	94.37	95.29	95.39
-12	111.57	98.36	104.96	98.77	99.53	99.23
-8	120.90	90.67	105.78	99.50	100.09	99.12
-4	118.34	71.35	94.84	89.79	89.63	88.35
0	90.32	39.52	64.92	63.24	60.70	60.99
4	42.86	10.71	26.79	29.40	24.81	27.31
8	4.14	0.15	2.14	7.54	4.09	6.36
12	-15.07	3.19	-5.94	0.36	-0.67	0.14
16	-21.43	10.71	-5.36	0.88	1.76	1.36
20	-21.87	18.39	-1.74	4.09	6.17	5.05

Table 4.12: Comparisons between various theories and FEM results for contact with varying M_2 and $M_1 = 1\,\text{Nm}$, $N_1 = 0$, $N_2 = 0$, $P_1 = 0$, $P_2 = 0$, $\gamma = 4$.

	Crack tip contact		DCB tip contact		After DCB tip contact	
	$M_2\,(\text{Nm})$	$G_I/G\,(\%)$	$M_2\,(\text{Nm})$	$G_I/G\,(\%)$	$M_2\,(\text{Nm})$	$G_I/G\,(\%)$
Present Euler beam theory	64	0	64	0	100	-11.35
Present Timo. beam theory	8.62	0	64	0	100	0
Averaged rule 1	21.65	0	64	0	100	0
Averaged rule 2	13.40	0	64	0	100	0
330×6 QUAD4s	13.88	0	64	0	100	0
Suo-Hutchinson theory	-	-	-	-	-	-

at $M_2/M_1 = 21.65$. Averaged partition rule 2 predicts it to occur at $M_2/M_1 = 13.40$. The corresponding value from the FEM simulations with QUAD4 elements is 13.88. The various different theories are very different when γ is large. However, it is also observed that the FEM simulations with QUAD4 elements give values for G_I which are very close to zero between $M_2/M_1 = 8.62$ and $M_2/M_1 = 13.82$. Therefore, the present Timoshenko beam partition theory predicts the mode II region very well in comparison with the QUAD4 results.

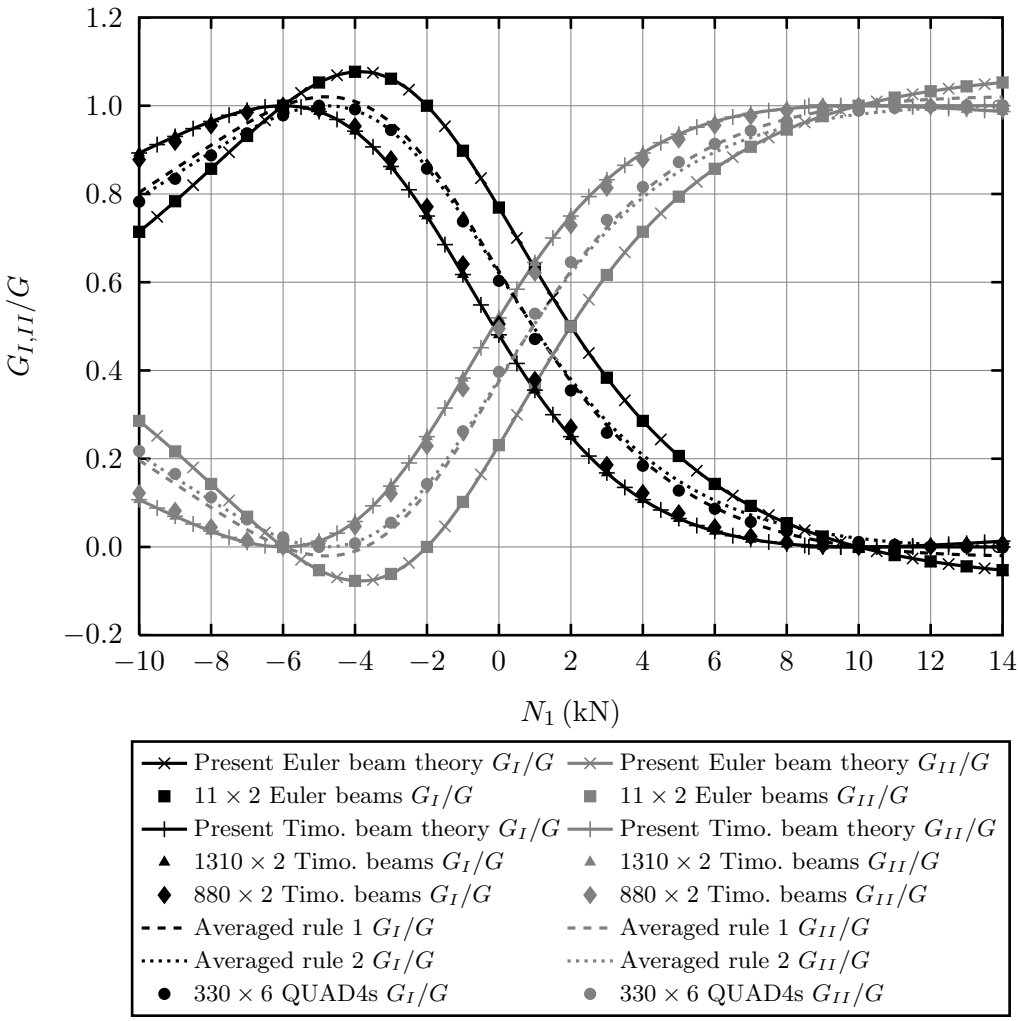

Figure 4.11: Comparisons between various theories and FEM results with varying N_1 and $M_1 = 1\,\text{Nm}$, $M_2 = 0$, $N_2 = 0$, $P_1 = 0$, $P_2 = 0$, $\gamma = 2$.

4.3.2 Tests with a crack tip bending moment and axial force

The DCB considered in this section is the same as that in §4.3.1. The thickness ratio is $\gamma = 2$. The DCB was subjected to a tip bending moment $M_1 = 1\,\text{Nm}$ and an axial force N_1, which varied from $-10\,\text{kN}$ to $14\,\text{kN}$. All other DCB tip loads were 0. The predictions from the present Euler beam, Timoshenko beam and averaged partition rules are presented in Fig. 4.11 and Table 4.13 alongside results from FEM simulations. It is seen that averaged partition rules 1 and 2 are both in excellent agreement with the QUAD4 results. The Euler and Timoshenko beam partition theories agree almost exactly with the Euler and Timoshenko FEM results. The pure $(\theta_2, \beta_2) = (-6, 10)$ pair from the first set is correctly predicted by Eqs. (4.67) and (4.62). The second pure $\left\{\varphi_{\theta_2'}\right\}$ mode, as given by Eq. (4.78) for the Timoshenko beam partition theory, is also correctly predicted at $N_1/M_1 = -2$. Finally, as the Euler beam partition theory predicts, the orthogonal partner, $\left\{\varphi_{\beta_2'}\right\}$ does not exist.

Table 4.13: Comparisons between various theories and FEM results with varying N_1 and $M_1 = 1$, $M_2 = 0$, $N_2 = 0$, $P_1 = 0$, $P_2 = 0$, $\gamma = 2$.

N_1 (kN)	G_I/G (%)							
	Present Euler beam theory	11×2 Euler beams	Present Timo. beam theory	1310×2 Timo. beams	880×2 Timo. beams	Averaged rule 1	Averaged rule 2	330×6 QUAD4s
−10	71.43	71.43	89.29	89.27	87.78	80.36	79.17	78.26
−8	85.71	85.71	96.43	96.42	95.53	91.07	89.46	88.74
−6	100.00	100.00	100.00	100.00	100.00	100.00	98.04	97.82
−4	107.69	107.69	94.23	94.24	95.36	100.96	98.96	99.19
−2	100.00	100.00	75.00	75.02	77.10	87.50	86.03	85.74
0	76.92	76.92	48.08	48.10	50.51	62.50	62.01	60.32
2	50.00	50.00	25.00	25.02	27.10	37.50	37.99	35.46
4	28.57	28.57	10.71	10.73	12.22	19.64	20.83	18.41
6	14.29	14.28	3.57	3.58	4.47	8.93	10.54	8.65
8	5.41	5.41	0.68	0.68	1.07	3.04	4.88	3.57
10	0.00	0.00	0.00	0.00	0.00	0.00	1.96	1.13
12	−3.28	−3.28	0.41	0.41	0.10	−1.43	0.58	0.12
14	−5.26	−5.26	1.32	1.32	0.76	−1.97	0.07	−0.12

4.3.3 Tests with crack tip axial forces

The DCB considered in this section is the same as that in §4.3.1. The thickness ratio is $\gamma = 2$. The DCB was subjected to tip axial forces $N_1 = 1\,\text{kN}$ and N_2, which varied from $-10\,\text{kN}$ to $10\,\text{kN}$. All other DCB tip loads were 0. The predictions from the present Euler beam, Timoshenko beam and averaged partition rules are presented in Fig. 4.12 and Table 4.14 alongside results from FEM simulations. The present Euler beam partition theory gives pure mode II, while the present Timoshenko beam partition theory gives mixed modes with a constant partition G_I/G. This is as expected since there is effectively only one load parameter, i.e. N_{1Be}. This result is significant for structural components that are loaded axially, for example struts. Regardless of the what the effective axial load N_{1Be} is, any fractures in these components will have a constant ERR partition that is either pure mode II, or dominant in mode II. Both of the averaged partition rules agree very well with the FEM results using QUAD4 elements. The Euler and Timoshenko beam partition theories agree almost exactly with the Euler and Timoshenko FEM results. Note that the ERR is zero when $N_2 = \gamma N_1 = 2$, which accounts for the missing data points at $N_2 = 2$ in Fig. 4.12 and Table 4.14.

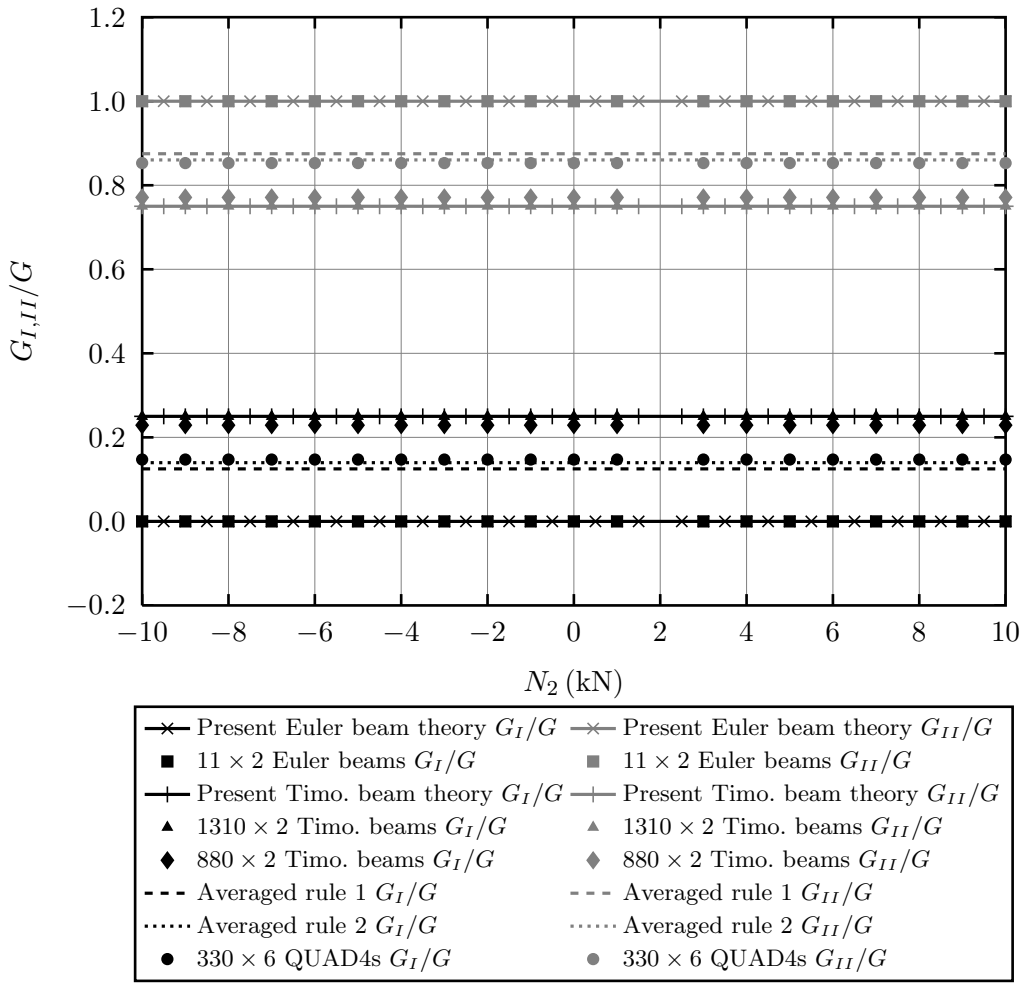

Figure 4.12: Comparisons between various theories and FEM results with varying N_2 and $M_1 = 0$, $M_2 = 0$, $N_1 = 1\,\text{kN}$, $P_1 = 0$, $P_2 = 0$, $\gamma = 2$.

Table 4.14: Comparisons between various theories and FEM results with varying N_2 and $M_1 = 0$, $M_2 = 0$, $N_1 = 1\,\text{kN}$, $P_1 = 0$, $P_2 = 0$, $\gamma = 2$.

N_2	$G_I/G\,(\%)$							
	Present Euler beam theory	11 × 2 Euler beams	Present Timo. beam theory	1310 × 2 Timo. beams	880 × 2 Timo. beams	Averaged rule 1	Averaged rule 2	330 × 6 QUAD4s
−10	0	0	25	24.98	22.90	12.5	13.97	14.72
−8	0	0	25	24.98	22.90	12.5	13.97	14.72
−6	0	0	25	24.98	22.90	12.5	13.97	14.72
−4	0	0	25	24.98	22.90	12.5	13.97	14.72
−2	0	0	25	24.98	22.90	12.5	13.97	14.72
0	0	0	25	24.98	22.90	12.5	13.97	14.72
2	-	-	-	-	-	-	-	-
4	0	0	25	24.98	22.90	12.5	13.97	14.72
6	0	0	25	24.98	22.90	12.5	13.97	14.72
8	0	0	25	24.98	22.90	12.5	13.97	14.72
10	0	0	25	24.98	22.90	12.5	13.97	14.72

4.3.4 Tests with crack tip bending moments and shear forces

The first test in this section aimed to demonstrate the mode I P mode and its interaction with the mode I $\left\{\varphi_{\theta_1}\right\}$ mode. The DCB in §4.3.1 is considered again. Here, the cracked length a is 10. Two values of through-thickness shear modulus are used, namely $\mu = 1/2.6\,\text{GPa}$ and $\mu = 1/26\,\text{GPa}$. Two DCB tip shear forces were applied, namely $P_1 = 1\,\text{kN}$ and $P_2 = \theta_1 P_1 = -4\,\text{kN}$. All other DCB tip loads were 0. FEM simulations were carried out using the fine nonuniform mesh with 1310×2 Timoshenko beam elements, and the uniform mesh with 330×6 QUAD4 elements. The analytical and numerical results are recorded in Table 4.15. Good agreement is observed in both cases, both in the mode I pureness of the $\left\{\varphi_{\theta_1}\right\}$ mode, and in the total value of G.

The next test in this section aimed to compare the various partition theories and results from FEM simulations. The DCB tip force P_1 was held fixed at $P_1 = 1\,\text{kN}$ and P_2 varied from $-10\,\text{kN}$ to $10\,\text{kN}$. All other DCB tip loads were 0. The results are presented in Fig. 4.13 and Tables 4.16 and 4.17. The FEM results using Timoshenko beams agree very well with the present Timoshenko beam partition theory. The FEM results using QUAD4 elements agree very well with both averaged partition rule 1 and averaged partition rule 2. Suo and Hutchinson's (1990) partition theory is not able to consider this case.

Table 4.15: Through-thickness shear effects on ERR with $P_2 = \theta_1 P_1$ and $M_1 = 0$, $M_2 = 0$, $N_1 = 0$, $N_2 = 0$, $P_1 = 1\,\text{kN}$, $\gamma = 2$.

	$\mu = 1/2.6\,\text{GPa}$			$\mu = 1/26\,\text{GPa}$		
	Present Timo. beam theory	1310×2 Timo. beams	330×6 QUAD4s	Present Timo. beam theory	1310×2 Timo. beams	330×6 QUAD4s
G_I (N/m)	1854.1	1825.0	1788.1	2467.6	2364.1	2280.4
G_{II} (N/m)	0	0	29.1	0	0	37.3
G (N/m)	1854.1	1825.0	1817.2	2467.6	2364.1	2317.7

Table 4.16: Comparisons between various theories and FEM results with varying P_2 and $M_1 = 0$, $M_2 = 0$, $N_1 = 0$, $N_2 = 0$, $P_1 = 1\,\text{kN}$, $\gamma = 2$ and ignoring contact.

P_2 (kN)	$G_I/G\,(\%)$					
	Present Timo. beam theory	1310×2 Timo. beams	880×2 Timo. beams	Averaged rule 1	Averaged rule 2	330×6 QUAD4s
-10	90.70	90.47	89.05	82.94	81.77	82.04
-8	93.98	93.84	92.68	87.62	86.33	86.51
-6	97.64	97.59	96.85	93.58	92.11	92.23
-4	100.00	100.00	100.00	100.00	98.31	98.40
-2	92.48	92.44	93.71	99.58	97.88	97.99
0	51.05	51.38	53.79	64.64	64.45	63.61
2	3.57	4.06	5.01	8.93	10.54	9.17
4	4.69	4.05	3.10	-0.60	0.61	0.90
6	18.12	16.96	15.15	8.12	8.81	9.87
8	28.81	27.53	25.38	16.95	17.34	18.60
10	36.28	35.00	32.70	23.64	23.84	25.13

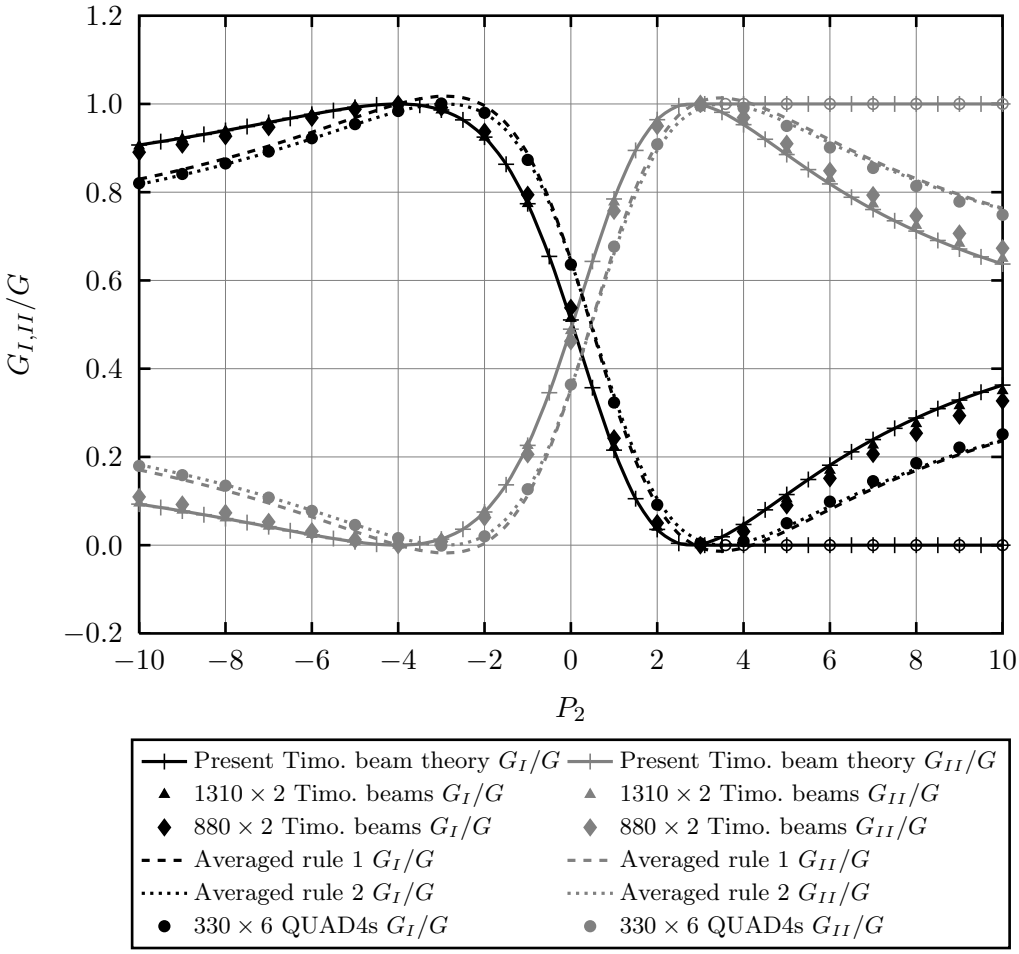

Figure 4.13: Comparisons between various theories and FEM results with varying P_2 and $M_1 = 0$, $M_2 = 0$, $N_1 = 0$, $N_2 = 0$, $P_1 = 1\,\text{kN}$, $\gamma = 2$.

Table 4.17: Comparisons between various theories and FEM results for contact with varying P_2 and $M_1 = 0$, $M_2 = 0$, $N_1 = 0$, $N_2 = 0$, $P_1 = 1\,\text{kN}$, $\gamma = 2$.

	Crack tip contact		DCB tip contact		After DCB tip contact	
	P_2 (kN)	G_I/G (%)	P_2 (kN)	G_I/G (%)	P_2 (kN)	G_I/G (%)
Present Timo. beam theory	2.86	0	8	0	10	0
1310 × 2 Timo. beams	2.86	0	8	0	10	0
880 × 2 Timo. beams	3.10	0	8	0	10	0
Averaged rule 1	2.86	0	8	0	10	0
Averaged rule 2	3.51	0	8	0	10	0
330 × 6 QUAD4s	3.58	0	8	0	10	0

4.4 Conclusion

Due to the many complexities, the DCB fracture problem has caused considerable confusion over many years. Analytical theories for layered isotropic homogeneous DCBs have been developed in this chapter based on the Euler and Timoshenko beam theories using a completely new approach, which reveal the hidden mechanics: the present Euler beam partition theory and the present Timoshenko beam partition theory, respectively. Two approximate 'averaged partition rules' have also been suggested for two-dimensional elasticity. Averaged partition rule 1 is the average of the present Euler and Timoshenko beam partition theories. Averaged partition rule 2 removes the small regions in averaged partition rule 1 where the partitions of ERR, G_I/G and G_{II}/G can be greater than one or less than zero.

Two sets of pure modes have been found. The first set consists of pure mode I modes that are characterised by zero crack tip relative shearing displacement and pure mode II modes that are characterised by zero crack tip normal force. The second set consists of pure mode I modes that are characterised by zero crack tip shearing force and pure mode II modes that are characterised by zero crack tip opening displacement.

Both the present Euler and Timoshenko beam partition theories have the same first set of pure modes. The second set coincides with the first set in the Timoshenko beam partition theory, but is only locally pure. The second set is different to the first set in the present Euler beam partition theory. The first set is both locally and globally pure in the present Euler and Timoshenko beam partition theories. The second set is both locally and globally pure in the present Euler beam partition theory but is only globally pure in the present Timoshenko beam partition theory. Therefore, the first set forms a complete basis for mixed-mode partitioning.

In the context of the present Euler beam partition theory, when there are mixed modes, 'stealthy' interaction exists between the pure mode I and II modes of the first set. This interaction disappears in the present Timoshenko beam partition theory. The fracture mode partition space has also been thoroughly investigated and a region of crack tip running contact has been found, which results in pure mode II ERR.

Axial forces alone produce pure mode II ERR in the present Euler beam partition theory and a mixed mode in the present Timoshenko beam partition theory. Through-thickness shear forces at the crack tip produce pure mode I ERR. The present Euler and Timoshenko beam partition theories both agree very well with results from the corresponding FEM simulations. Both of the averaged partition rules agree very well with results from FEM simulations using QUAD4 elements.

All of the present theories and rules are completely analytical. Suo and Hutchinson's (1990) partition theory is a analytical, except for one parameter which is determined numerically. It agrees well with the present averaged rules and FEM simulations with QUAD4 elements. It does not however provide any information on the pure mode II region and is not able to deal with applied shear forces. The present theories and rules

have been derived using a completely new approach and will provide an excellent tool for studying delamination in laminated fibre-reinforced composite beams, plates and shells. This is the subject of the following chapters, where the findings from this chapter are extended to more complex structures and further validated.

This chapter has been published in Wang and Harvey (2012*a*). A convenient summary is given in Wang and Harvey (2012*c*).

Chapter 5

Laminated composite double cantilever beams

Contents

5.1 Introduction

In the previous chapter, the principles of mixed-mode partitioning using orthogonal pure modes have been developed for layered isotropic homogeneous DCBs. This chapter builds on that foundation by extending the theories to delamination in laminated composite DCBs. Recall that a DCB is considered a typical representative of one-dimensional fracture problems.

Extension of the theories to laminated composites is particularly important. This work is concerned with interfacial fracture in layered materials. Fibre-reinforced laminated composites are an example of such a material. Not only are they increasingly being used in many complex and demanding applications, but they are also especially susceptible to delamination, due to their general lack of reinforcement in the thickness direction. When delamination occurs, there is a significant reduction in stiffness and load-carrying capacity. A further consideration is the propagation of delamination, which can cause the whole structure to fail. A thorough understanding of delamination and its propagation is therefore required. It is well known that the fracture toughness is different in different modes. Fracture mode partitions therefore play a key role in the propagation of delamination and

in the development of fracture propagation criteria. This of course is the subject of this work—the partitioning of mixed modes.

There is significantly less published theoretical work on partitioning mixed modes in laminated composite materials than in isotropic homogeneous materials. However, as before for the isotropic homogeneous materials, there have been two main approaches: (1) an approach based on an assumed square-root singular stress field at the crack tip; and (2) an approach based on ERR. Suo and Hutchinson's (1990) partition theory for isotropic homogeneous beams is the original work in the first category and Williams's (1988) partition theory is the original work for isotropic homogeneous beams in the second category. Sheinman and Kardomateas (1997) extended Suo and Hutchinson's (1990) partition theory to general non-homogeneous laminated composites. In order to recover the square-root singular stress field at the crack tip, they modelled the delamination as a crack in an equivalent anisotropic body and 'smeared out' the material interface. Wang and Qiao (2004) further extended the work of Suo and Hutchinson (1990) and Sheinman and Kardomateas (1997) to model a delamination between two shear deformable elastic layers with different material properties. Zou et al. (2001) developed the VCCT to calculate the ERR partition in laminated composites. They modelled a laminate as an assembly of FSDT plates and allowed for stress resultant discontinuities across the crack tip. With knowledge of these stress resultants and the displacements at the crack tip, they were able to calculate the ERR partition. Bruno and Greco (2001) used classical laminated composite plate theory to derive an analytical partition theory. Their results agreed with results from Zou et al. (2002) for FSDT plates.

On the numerical side, Raju et al. (1988) discovered that when modelling laminated composites with two- or three-dimensional elasticity, the partitions of ERR do not always show good convergence behaviour as the size of the delamination tip element is made smaller and smaller. Zou et al. (2001) and Bruno et al. (2003) showed that this can be overcome using laminates and a layer of interface elements instead of a 'bare interface'.

The one-dimensional partition theories derived in this chapter are of great value. They are simple, concise, easy to understand and also useful in many different applications. Mode-partitioning theories are often used in experimental tests, such as the DCB, ELS and ENF tests, to obtain the critical ERRs or material toughness in either pure mode I or mode II fracture. Fracture propagation criteria are often investigated in mixed-mode tests, such as the MMB test. With these theories, advances can be made in developing fracture propagation criteria. With a more robust understanding of delamination in laminated composite materials, expensive and time-consuming experimental testing of structures could also be reduced.

This chapter has been published in Harvey and Wang (2012*c*). A convenient summary is given in Wang and Harvey (2012*c*).

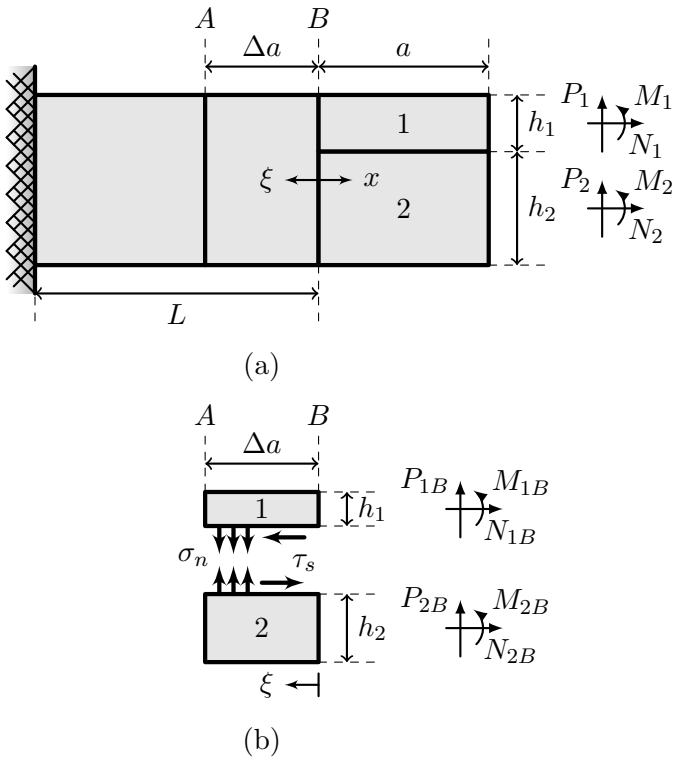

Figure 5.1: A laminated composite DCB and its loading conditions. (a) General description. (b) Details of the crack influence region Δa.

5.2 Theoretical development

5.2.1 Energy release rate

A laminated composite DCB with a delamination of length a is shown in Fig. 5.1 (a). Throughout the formulation in §5.2, it is convenient to make use of two different longitudinal axes, which are denoted by x and ξ in the figure. The origin of both axes is at the crack tip at location B. x is towards the right and ξ is towards the left; positive deflection, w is always upwards and a positive bending moment produces positive curvature, d^2w/dx^2 or $d^2w/d\xi^2$. Contact between the upper and lower sub-laminates is not treated initially. This is dealt with in §5.2.8. The interface stresses in the crack influence length Δa are shown in Fig. 5.1 (b). They only show the sign convention rather than any representative distribution.

The constitutive equations for laminated composite plates were derived in §2.2. The reduced equations for one-dimensional laminated beam theories are in §2.2.6. Since the classical theory for laminated beams corresponds with the Euler theory for isotropic beams, in this thesis it is simply referred to as the 'Euler laminated composite beam theory' or simply the 'Euler beam theory'. Similarly, since the FSDT for laminated beams corresponds with the Timoshenko theory for isotropic beams, in this thesis it is simply referred

to as the 'Timoshenko laminated composite beam theory' or simply the 'Timoshenko beam theory'.

Using the constitutive relation from Euler laminated composite beam theory, the strain energy per unit length, U_0 is

$$\begin{aligned} U_0 &= \frac{1}{2b}\begin{Bmatrix} N(x) \\ -M(x) \end{Bmatrix}^T \begin{bmatrix} A & B \\ B & D \end{bmatrix}^{-1} \begin{Bmatrix} N(x) \\ -M(x) \end{Bmatrix} \\ &= \frac{AM^2(x) + 2BM(x)N(x) + DN^2(x)}{2b(AD - B^2)} \end{aligned} \tag{5.1}$$

where $N(x)$ and $M(x)$ are the internal axial force and bending moment respectively and b is the width of the beam. A, B and D are the equivalent extensional, coupling and bending stiffness respectively which take different values under the plane-strain assumption to those under the plane-stress assumption. Further details on this are given in §2.2.6. However, there is no difference between the two assumptions in the following development. Subscripts 1 and 2 are used to indicate the upper and lower sub-laminates respectively. No subscript is used for the intact part of the laminate. A_1 is therefore the extensional stiffness of the upper sub-laminate and A is the extensional stiffness of the intact laminate, etc. Integrating Eq. (5.1) with respect to x along the length of the DCB gives the strain energy.

$$\begin{aligned} U = \frac{1}{2b}\Bigg[&\int_0^a \frac{A_1 M_1^2(x)}{A_1 D_1 - B_1^2}\,dx + \int_0^a \frac{A_2 M_2^2(x)}{A_2 D_2 - B_2^2}\,dx + \int_{-L}^0 \frac{AM^2(x)}{AD - B^2}\,dx \\ &+ \int_0^a \frac{2B_1 M_1(x) N_1(x)}{A_1 D_1 - B_1^2}\,dx + \int_0^a \frac{2B_2 M_2(x) N_2(x)}{A_2 D_2 - B_2^2}\,dx + \int_{-L}^0 \frac{2BM(x)N(x)}{AD - B^2}\,dx \\ &+ \int_0^a \frac{D_1 N_1^2(x)}{A_1 D_1 - B_1^2}\,dx + \int_0^a \frac{D_2 N_2^2(x)}{A_2 D_2 - B_2^2}\,dx + \int_{-L}^0 \frac{DN^2(x)}{AD - B^2}\,dx \Bigg] \end{aligned} \tag{5.2}$$

The total ERR, G is defined as

$$G = \frac{\partial U}{\partial S} = \frac{1}{b}\frac{\partial U}{\partial a} \tag{5.3}$$

Therefore from Eq. (5.2) we have

$$\begin{aligned} G = \frac{1}{2b^2}\Bigg(&\frac{M_{1B}^2}{D_1^*} + \frac{M_{2B}^2}{D_2^*} - \frac{M_B^2}{D^*} + \frac{N_{1B}^2}{A_1^*} + \frac{N_{2B}^2}{A_2^*} - \frac{N_B^2}{A^*} \\ &- \frac{2B_1 M_{1B} N_{1B}}{B_1^*} - \frac{2B_2 M_{2B} N_{2B}}{B_2^*} + \frac{2BM_B N_B}{B^*} \Bigg) \end{aligned} \tag{5.4}$$

where

$$A_i^* = A_i - B_i^2/D_i \tag{5.5}$$

$$B_i^* = B_i^2 - A_i D_i \tag{5.6}$$

$$D_i^* = D_i - B_i^2/A_i \tag{5.7}$$

The range of the subscript i is 1 and 2, which again refers to the upper and lower sublaminates respectively. For the intact laminate, the subscript i is dropped. Other terms in Eq. (5.4) are

$$N_B = N_{1B} + N_{2B} \tag{5.8}$$

$$M_B = M_{1B} + M_{2B} + \frac{1}{2}\left(h_1 N_{2B} - h_2 N_{1B}\right) \tag{5.9}$$

Note that B_i^* is not defined in the same way as A_i^* and D_i^*, which would have been $B_i^* = B_i - A_i D_i / B_i$ with the final three terms in Eq. (5.4) adjusted accordingly, in order to avoid division by zero when there is no material coupling, that is, when $B_i = 0$.

From Eq. (5.4) it is seen that the total ERR is of quadratic form in terms of crack tip axial forces and bending moments. It can be expressed in matrix form as follows:

$$G = \frac{1}{2b^2} \begin{Bmatrix} M_{1B} \\ M_{2B} \\ N_{1B} \\ N_{2B} \end{Bmatrix}^T \Big[C\Big] \begin{Bmatrix} M_{1B} \\ M_{2B} \\ N_{1B} \\ N_{2B} \end{Bmatrix} \tag{5.10}$$

where

$$\Big[C\Big] = \begin{bmatrix} \frac{1}{D_1^*} - \frac{1}{D^*} & -\frac{1}{D^*} & \frac{h_2}{2D^*} - \frac{B_1}{B_1^*} + \frac{B}{B^*} & \frac{B}{B^*} - \frac{h_1}{2D^*} \\ \cdots & \frac{1}{D_2^*} - \frac{1}{D^*} & \frac{h_2}{2D^*} + \frac{B}{B^*} & \frac{B}{B^*} - \frac{B_2}{B_2^*} - \frac{h_1}{2D^*} \\ \cdots & \cdots & \frac{1}{A_1^*} - \frac{Bh_2}{B^*} - \frac{1}{A^*} - \frac{h_2^2}{4D^*} & \frac{B(h_1-h_2)}{2B^*} - \frac{1}{A^*} + \frac{h_1 h_2}{4D^*} \\ \cdots & \cdots & \cdots & \frac{Bh_1}{B^*} + \frac{1}{A_2^*} - \frac{1}{A^*} - \frac{h_1^2}{4D^*} \end{bmatrix} \tag{5.11}$$

which is the symmetric coefficient matrix of the quadratic form given in Eq. (5.10), with symmetry terms denoted by '...'. In the following development, the pure modes are determined first and are then used to partition the ERR G in Eq. (5.10) for a mixed mode.

5.2.2 The first set of orthogonal pure modes

As shown in Chapter 4, there are two sets of orthogonal pure modes. The first set corresponds to zero relative shearing displacement just behind the crack tip (mode I) and zero crack tip opening force ahead of the crack tip (mode II). The second set corresponds to zero relative opening displacement just behind the crack tip (mode II) and zero crack tip shearing force (mode I).

It is simple to derive the zero relative displacement modes first and then to find the zero force modes by applying orthogonality through Eq. 5.10. This is the approach used here although an alternative and more complex derivation, in which the interface stresses are considered, is given in §5.2.6. Now the mode I modes of the first set, which correspond to zero relative shearing displacement, are derived. With reference to Fig. 5.1 (a) and using

the constitutive relationship from Euler laminated composite beam theory,

$$\begin{Bmatrix} N_{1,2}(x)/b \\ -M_{1,2}(x)/b \end{Bmatrix} = \begin{Bmatrix} N_{1,2B}/b \\ (P_{1,2B}x - M_{1,2B})/b \end{Bmatrix} = \begin{bmatrix} A_{1,2} & B_{1,2} \\ B_{1,2} & D_{1,2} \end{bmatrix} \begin{Bmatrix} du_{1,2}/dx \\ -d^2w_{1,2}/dx^2 \end{Bmatrix} \tag{5.12}$$

The following are easily derived from Eq. (5.12):

$$\frac{du_{1,2}}{dx} = \frac{D_{1,2}N_{1,2B} + B_{1,2}(M_{1,2B} - P_{1,2B}x)}{b\left(A_{1,2}D_{1,2} - B_{1,2}^2\right)} \tag{5.13}$$

$$u_{1,2} = \frac{D_{1,2}N_{1,2B}x + B_{1,2}\left(M_{1,2B}x - P_{1,2B}x^2/2\right)}{b\left(A_{1,2}D_{1,2} - B_{1,2}^2\right)} + u_{1,2B} \tag{5.14}$$

$$\frac{dw_{1,2}}{dx} = \frac{A_{1,2}\left(M_{1,2B}x - P_{1,2B}x^2/2\right) + B_{1,2}N_{1,2B}x}{b\left(A_{1,2}D_{1,2} - B_{1,2}^2\right)} + \left(\frac{dw_{1,2}}{dx}\right)_B \tag{5.15}$$

$$w_{1,2} = \frac{A_{1,2}\left(M_{1,2B}x^2/2 - P_{1,2B}x^3/6\right) + B_{1,2}N_{1,2B}x^2/2}{b\left(A_{1,2}D_{1,2} - B_{1,2}^2\right)} + \left(\frac{dw_{1,2}}{dx}\right)_B x + w_{1,2B} \tag{5.16}$$

Mathematically, the relative shearing displacement at an infinitely small distance δa behind the crack tip, D_{sh} is expressed as

$$D_{sh} = (\overline{u}_1)_{x=\delta a} - (\overline{u}_2)_{x=\delta a} = (u_1)_{x=\delta a} + \frac{h_1}{2}\left(\frac{dw_1}{dx}\right)_{x=\delta a} - (u_2)_{x=\delta a} + \frac{h_2}{2}\left(\frac{dw_2}{dx}\right)_{x=\delta a} \tag{5.17}$$

where $\overline{u}$ represents the axial displacement at the interface. Making the necessary substitutions gives

$$\begin{aligned} D_{sh} = &\left[\frac{M_{1B}(B_1 + h_1A_1/2)}{b\left(A_1D_1 - B_1^2\right)} - \frac{M_{2B}(B_2 - h_2A_2/2)}{b\left(A_2D_2 - B_2^2\right)}\right]\delta a \\ &+ \left[\frac{P_{1B}(-B_1 - h_1A_1/2)}{b\left(A_1D_1 - B_1^2\right)} - \frac{P_{2B}(-B_2 + h_2A_2/2)}{b\left(A_2D_2 - B_2^2\right)}\right]\frac{\delta a^2}{2} \\ &+ \left[\frac{N_{1B}(D_1 + h_1B_1/2)}{b\left(A_1D_1 - B_1^2\right)} - \frac{N_{2B}(D_2 - h_2B_2/2)}{b\left(A_2D_2 - B_2^2\right)}\right]\delta a \end{aligned} \tag{5.18}$$

in which the continuity of interface axial displacement at the crack tip has been accounted for, resulting in the disappearance of $u_{1,2B}$ and $(dw_{1,2}/dx)_B$. For a mode I mode of the first set, $D_{sh} = 0$, which since $\delta a \to 0$, gives the following relationship:

$$\begin{aligned} 0 = &\frac{M_{1B}(B_1 + h_1A_1/2)}{A_1D_1 - B_1^2} - \frac{M_{2B}(B_2 - h_2A_2/2)}{A_2D_2 - B_2^2} \\ &+ \frac{N_{1B}(D_1 + h_1B_1/2)}{A_1D_1 - B_1^2} - \frac{N_{2B}(D_2 - h_2B_2/2)}{A_2D_2 - B_2^2} \end{aligned} \tag{5.19}$$

Three independent mode I modes, $\left\{\varphi_{\theta_1}\right\}$, $\left\{\varphi_{\theta_2}\right\}$ and $\left\{\varphi_{\theta_3}\right\}$ are obtained from Eq. (5.19). The order of the four independent variables is $\left\{M_{1B} \quad M_{2B} \quad N_{1B} \quad N_{2B}\right\}^T$.

$$\left\{\varphi_{\theta_1}\right\} = \begin{Bmatrix} 1 \\ \theta_1 \\ 0 \\ 0 \end{Bmatrix}; \quad \left\{\varphi_{\theta_2}\right\} = \begin{Bmatrix} 1 \\ 0 \\ \theta_2 \\ 0 \end{Bmatrix} \quad \text{and} \quad \left\{\varphi_{\theta_3}\right\} = \begin{Bmatrix} 1 \\ 0 \\ 0 \\ \theta_3 \end{Bmatrix} \tag{5.20}$$

where

$$\theta_1 = \frac{M_{2B}}{M_{1B}} = \frac{\left(B_2^2 - A_2 D_2\right)\left(B_1 + h_1 A_1/2\right)}{\left(B_1^2 - A_1 D_1\right)\left(B_2 - h_2 A_2/2\right)} \tag{5.21}$$

$$\theta_2 = \frac{N_{1B}}{M_{1B}} = -\frac{B_1 + h_1 A_1/2}{D_1 + h_1 B_1/2} \tag{5.22}$$

$$\theta_3 = \frac{N_{2B}}{M_{1B}} = \frac{\left(B_2^2 - A_2 D_2\right)\left(B_1 + h_1 A_1/2\right)}{\left(B_1^2 - A_1 D_1\right)\left(D_2 - h_2 B_2/2\right)} \tag{5.23}$$

The orthogonal counterparts to the modes in Eq. (5.20) correspond to zero crack tip opening force. It is quite possible to derive these modes using this condition (see §5.2.6), however it is far simpler to apply orthogonality through Eq. (5.10). Let the mode II modes of the first set be

$$\left\{\varphi_{\beta_1}\right\} = \begin{Bmatrix} 1 \\ \beta_1 \\ 0 \\ 0 \end{Bmatrix}; \quad \left\{\varphi_{\beta_2}\right\} = \begin{Bmatrix} 1 \\ 0 \\ \beta_2 \\ 0 \end{Bmatrix} \quad \text{and} \quad \left\{\varphi_{\beta_3}\right\} = \begin{Bmatrix} 1 \\ 0 \\ 0 \\ \beta_3 \end{Bmatrix} \tag{5.24}$$

The values β_1, β_2 and β_3 are obtained from the following orthogonality condition:

$$0 = \left\{\varphi_{\beta_i}\right\}^T \left[C\right] \left\{\varphi_{\theta_j}\right\} \tag{5.25}$$

The matrix $\left[C\right]$ is given by Eq. (5.11). Solving Eq. (5.25) for $\left\{\varphi_{\beta_1}\right\}$, $\left\{\varphi_{\beta_2}\right\}$ and $\left\{\varphi_{\beta_3}\right\}$ gives

$$\beta_1 = \frac{M_{2B}}{M_{1B}} = -\frac{D_2^* \left(D_1^* + D_1^* \theta_1 - D^*\right)}{D_1^* \left(D_2^* + D_2^* \theta_1 - D^* \theta_1\right)} \tag{5.26}$$

$$\beta_2 = \frac{N_{1B}}{M_{1B}} = \frac{\theta_2 \left(\dfrac{h_2}{2D^*} - \dfrac{B_1}{B_1^*} + \dfrac{B}{B^*}\right) + \dfrac{1}{D_1^*} - \dfrac{1}{D^*}}{\theta_2 \left(\dfrac{B h_2}{B^*} - \dfrac{1}{A_1^*} + \dfrac{1}{A^*} + \dfrac{h_2^2}{4D^*}\right) - \dfrac{h_2}{2D^*} + \dfrac{B_1}{B_1^*} - \dfrac{B}{B^*}} \tag{5.27}$$

$$\beta_3 = \frac{N_{2B}}{M_{1B}} = \frac{\theta_3\left(\dfrac{h_1}{2D^*} - \dfrac{B}{B^*}\right) - \dfrac{1}{D_1^*} + \dfrac{1}{D^*}}{\theta_3\left(\dfrac{Bh_1}{B^*} + \dfrac{1}{A_2^*} - \dfrac{1}{A^*} - \dfrac{h_1^2}{4D^*}\right) - \dfrac{h_1}{2D^*} + \dfrac{B}{B^*}} \tag{5.28}$$

5.2.3 Mixed-mode partitioning using orthogonal pure modes

Since there are four independent variables, four modes are required to partition a mixed mode. Any combination of pure modes may be selected and the same mixed-mode partition will be obtained. However, since the $\left\{\varphi_{\beta_1}\right\}$, $\left\{\varphi_{\beta_2}\right\}$ and $\left\{\varphi_{\beta_3}\right\}$ modes do not contribute to the crack tip opening force F_{nB} by definition (see §5.2.2 or §5.2.6), it is convenient to select the pure modes $\left\{\varphi_{\theta_1}\right\}$, $\left\{\varphi_{\beta_1}\right\}$, $\left\{\varphi_{\beta_2}\right\}$ and $\left\{\varphi_{\beta_3}\right\}$. Therefore F_{nB} is simply given by the crack tip opening force from the $\left\{\varphi_{\theta_1}\right\}$ pure mode. As will be seen in §5.2.4, where F_{nB} is used in the VCCT, this greatly simplifies the formulation.

Using these modes, the crack tip bending moments M_{1B} and M_{2B} and crack tip axial forces N_{1B} and N_{2B} can be expressed as

$$\begin{Bmatrix} M_{1B} \\ M_{2B} \\ N_{1B} \\ N_{2B} \end{Bmatrix} = \begin{bmatrix} \varphi_{\theta_1} & \varphi_{\beta_1} & \varphi_{\beta_2} & \varphi_{\beta_3} \end{bmatrix} \begin{Bmatrix} \alpha_{\theta_1} \\ \alpha_{\beta_1} \\ \alpha_{\beta_2} \\ \alpha_{\beta_3} \end{Bmatrix} \tag{5.29}$$

from which the mode partition coefficients are obtained as

$$\begin{Bmatrix} \alpha_{\theta_1} \\ \alpha_{\beta_1} \\ \alpha_{\beta_2} \\ \alpha_{\beta_3} \end{Bmatrix} = \begin{Bmatrix} \dfrac{M_{2B}\beta_2 + N_{1B}\beta_1 - M_{1B}\beta_1\beta_2}{\beta_2\left(\theta_1 - \beta_1\right)} + \dfrac{N_{2B}\beta_1}{\beta_3\left(\theta_1 - \beta_1\right)} \\ \dfrac{M_{1B}\theta_1\beta_2 - M_{2B}\beta_2 - N_{1B}\theta_1}{\beta_2\left(\theta_1 - \beta_1\right)} - \dfrac{N_{2B}\theta_1}{\beta_3\left(\theta_1 - \beta_1\right)} \\ N_{1B}/\beta_2 \\ N_{2B}/\beta_3 \end{Bmatrix} \tag{5.30}$$

Substituting Eq. (5.29) into Eq. (5.4) and collecting mode partition coefficients gives

$$\begin{aligned} G = {} & \alpha_{\theta_1}^2 G_{\theta_1} + \alpha_{\beta_1}^2 G_{\beta_1} + \alpha_{\beta_2}^2 G_{\beta_2} + \alpha_{\beta_3}^2 G_{\beta_3} \\ & + \alpha_{\beta_1}\alpha_{\beta_2} G_{\beta_1\beta_2} + \alpha_{\beta_1}\alpha_{\beta_3} G_{\beta_1\beta_3} + \alpha_{\beta_2}\alpha_{\beta_3} G_{\beta_2\beta_3} \end{aligned} \tag{5.31}$$

As discussed, the mode I condition of zero shearing displacement is orthogonal to the mode II condition of zero crack tip opening force. Therefore by definition and as shown by Eq. (5.25), all mode I modes must be orthogonal to all mode II modes. The result of this is that $G_{\theta_1\beta_1} = G_{\theta_1\beta_2} = G_{\theta_1\beta_3} = 0$, which is why these terms do not appear in Eq. (5.31). The remaining terms in Eq. (5.31) are

$$G_{\theta_1} = \frac{1}{2b^2}\left[\frac{1}{D_1^*} + \frac{\theta_1^2}{D_2^*} - \frac{\left(1+\theta_1\right)^2}{D^*}\right] \tag{5.32}$$

$$G_{\beta_1} = \frac{1}{2b^2}\left[\frac{1}{D_1^*} + \frac{\beta_1^2}{D_2^*} - \frac{(1+\beta_1)^2}{D^*}\right] \tag{5.33}$$

$$G_{\beta_2} = \frac{1}{2b^2}\left[\frac{\beta_2^2}{A_1^*} - \frac{\beta_2^2}{A^*} - \frac{2B_1\beta_2}{B_1^*} - \frac{B\beta_2\left(h_2\beta_2-2\right)}{B^*} + \frac{1}{D_1^*} - \frac{\left(h_2\beta_2-2\right)^2}{4D^*}\right] \tag{5.34}$$

$$G_{\beta_3} = \frac{1}{2b^2}\left[\frac{\beta_3^2}{A_2^*} - \frac{\beta_3^2}{A^*} + \frac{B\beta_3\left(h_1\beta_3+2\right)}{B^*} + \frac{1}{D_1^*} - \frac{\left(h_1\beta_3+2\right)^2}{4D^*}\right] \tag{5.35}$$

$$G_{\beta_1\beta_2} = \frac{1}{b^2}\left[-\frac{B_1\beta_2}{B_1^*} + \frac{B\beta_2\left(1+\beta_1\right)}{B^*} + \frac{1}{D_1^*} - \frac{2\left(1+\beta_1\right) - h_2\beta_2\left(1+\beta_1\right)}{2D^*}\right] \tag{5.36}$$

$$G_{\beta_1\beta_3} = \frac{1}{b^2}\left[-\frac{B_2\beta_1\beta_3}{B_2^*} + \frac{B\beta_3\left(1+\beta_1\right)}{B^*} + \frac{1}{D_1^*} - \frac{\left(2+h_1\beta_3\right)\left(1+\beta_1\right)}{2D^*}\right] \tag{5.37}$$

$$\begin{aligned} G_{\beta_2\beta_3} = \frac{1}{b^2}\Bigg[&-\frac{\beta_2\beta_3}{A^*} - \frac{B_1\beta_2}{B_1^*} + \frac{2B\left(\beta_2+\beta_3\right) + B\beta_2\beta_3\left(h_1-h_2\right)}{2B^*} \\ &+ \frac{1}{D_1^*} - \frac{2\left(2+h_1\beta_3\right) - h_2\beta_2\left(2+h_1\beta_3\right)}{4D^*}\Bigg] \end{aligned} \tag{5.38}$$

5.2.4 Interaction between two orthogonal pure modes

Within the context of Euler beam theory, where the out-of-plane shear moduli are infinite, 'stealthy' interaction exists between each orthogonal pair of pure modes (see §4.2.3). By stealthy interaction, it is meant that there is a flow of energy from one mode to another with the total energy being conserved. To partition mixed modes, the interaction must be determined. The mode I component of ERR is expressed, using the VCCT, as

$$G_I = \frac{F_{nB}D_{op}}{2b\,\delta a} \tag{5.39}$$

where D_{op} is the relative opening displacement at an infinitesimal distance δa behind the crack tip and F_{nB} is the crack tip opening force. This force is defined as

$$F_{nB} = b\int_0^{\delta a}\sigma_n\,d\xi \tag{5.40}$$

From Eq. (5.16), the opening displacement is

$$\begin{aligned} D_{op} = \left(w_1\right)_{x=\delta a} - \left(w_2\right)_{x=\delta a} = \Bigg[&\frac{A_1M_{1B}}{A_1D_1-B_1^2} - \frac{A_2M_{2B}}{A_2D_2-B_2^2} + \frac{B_1N_{1B}}{A_1D_1-B_1^2} \\ &- \frac{B_2N_{2B}}{A_2D_2-B_2^2} - \left(\frac{A_1P_{1B}}{A_1D_1-B_1^2} - \frac{A_2P_{2B}}{A_2D_2-B_2^2}\right)\frac{\delta a}{3}\Bigg]\frac{\delta a^2}{2b} \\ &+ \left[\left(\frac{dw_1}{dx}\right)_B - \left(\frac{dw_2}{dx}\right)_B\right]\delta a + \left(w_{1B} - w_{2B}\right) \end{aligned} \tag{5.41}$$

The δa^3 terms are an order of magnitude smaller than the other terms and can be ignored. In addition, the crack tip deflections and rotations are equal due to the interface continuity requirement of Euler beam theory. Substituting Eq. (5.29) into Eq. (5.41) and collecting

mode partition coefficients gives

$$D_{op} = \left[\alpha_{\theta_1}\left(\frac{1}{D_1^*} - \frac{\theta_1}{D_2^*}\right) + \alpha_{\beta_1}\left(\frac{1}{D_1^*} - \frac{\beta_1}{D_2^*}\right) + \alpha_{\beta_2}\left(\frac{1}{D_1^*} - \frac{B_1\beta_2}{B_1^*}\right) + \alpha_{\beta_3}\left(\frac{1}{D_1^*} + \frac{B_2\beta_3}{B_2^*}\right)\right]\frac{\delta a^2}{2b} \tag{5.42}$$

Of the four pure modes selected to make the partition, only mode I $\left\{\varphi_{\theta_1}\right\}$ mode contributes to the crack tip opening force. The mode II condition itself dictates that the contribution to the normal force from modes $\left\{\varphi_{\beta_1}\right\}$, $\left\{\varphi_{\beta_2}\right\}$, and $\left\{\varphi_{\beta_3}\right\}$ is zero.

$$F_{nB} = \alpha_{\theta_1} F_{nB\theta_1} \tag{5.43}$$

Making these substitutions into Eq. (5.39) gives

$$G_I = \alpha_{\theta_1}^2 G_{\theta_1} + \alpha_{\theta_1}\alpha_{\beta_1}\Delta G_{\theta_1\beta_1} + \alpha_{\theta_1}\alpha_{\beta_2}\Delta G_{\theta_1\beta_2} + \alpha_{\theta_1}\alpha_{\beta_3}\Delta G_{\theta_1\beta_3} \tag{5.44}$$

where $\Delta G_{\theta_1\beta_i}$ are the additional ERR contributions to G_I due to the interaction between mode $\left\{\varphi_{\theta_1}\right\}$ and mode $\left\{\varphi_{\beta_i}\right\}$ $(i = 1, 2, 3)$, which are

$$\Delta G_{\theta_1\beta_1} = \frac{F_{nB\theta_1}\,\delta a}{4b^2}\left(\frac{1}{D_1^*} - \frac{\beta_1}{D_2^*}\right) \tag{5.45}$$

$$\Delta G_{\theta_1\beta_2} = \frac{F_{nB\theta_1}\,\delta a}{4b^2}\left(\frac{1}{D_1^*} - \frac{B_1\beta_2}{B_1^*}\right) \tag{5.46}$$

$$\Delta G_{\theta_1\beta_3} = \frac{F_{nB\theta_1}\,\delta a}{4b^2}\left(\frac{1}{D_1^*} + \frac{B_2\beta_3}{B_2^*}\right) \tag{5.47}$$

An alternative expression for G_{θ_1} is also obtained, which is

$$G_{\theta_1} = \frac{F_{nB\theta_1}\,\delta a}{4b^2}\left(\frac{1}{D_1^*} - \frac{\theta_1}{D_2^*}\right) \tag{5.48}$$

From Eqs. (5.31) and (5.44), the mode II ERR G_{II} is

$$G_{II} = \alpha_{\beta_1}^2 G_{\beta_1} + \alpha_{\beta_2}^2 G_{\beta_2} + \alpha_{\beta_3}^2 G_{\beta_3} + \alpha_{\beta_1}\alpha_{\beta_2} G_{\beta_1\beta_2} + \alpha_{\beta_1}\alpha_{\beta_3} G_{\beta_1\beta_3} + \alpha_{\beta_2}\alpha_{\beta_3} G_{\beta_2\beta_3} - \alpha_{\theta_1}\alpha_{\beta_1}\Delta G_{\theta_1\beta_1} - \alpha_{\theta_1}\alpha_{\beta_2}\Delta G_{\theta_1\beta_2} - \alpha_{\theta_1}\alpha_{\beta_3}\Delta G_{\theta_1\beta_3} \tag{5.49}$$

The ERR interactions $\Delta G_{\theta_1\beta_i}$ are subtracted from G_{II} since the sum of Eqs. (5.44) and (5.49) must give Eq. (5.31). The orthogonality of modes $\left\{\varphi_{\theta_1}\right\}$ and $\left\{\varphi_{\beta_i}\right\}$ requires that the net contribution to the total ERR from the interaction is zero. Eqs. (5.44) and (5.49) are the present Euler beam partition theory for laminated composite beams.

It remains to find the crack tip opening force $F_{nB\theta_1}$. Equating Eqs. (5.32) and (5.48) gives

$$F_{nB\theta_1}\,\delta a = \frac{2\left(D_1^* D^* \theta_1^2 + D_2^* D^* - D_1^* D_2^* - 2D_1^* D_2^* \theta_1 - D_1^* D_2^* \theta_1^2\right)}{D^*\left(D_2^* - D_1^* \theta_1\right)} \tag{5.50}$$

Interaction only occurs within the context of the present Euler beam partition theory, where the out-of-plane shear moduli are infinite. When the out-of-plane shear moduli have finite values, $F_{nB\theta_1}\,\delta a$ becomes zero and the interaction disappears (see §4.2.2). This is proved again in §5.2.7. Therefore within the context of the present Timoshenko beam partition theory, where there is no interaction, the ERRs are

$$G_I = \alpha_{\theta_1}^2 G_{\theta_1} \tag{5.51}$$

$$G_{II} = \alpha_{\beta_1}^2 G_{\beta_1} + \alpha_{\beta_2}^2 G_{\beta_2} + \alpha_{\beta_3}^2 G_{\beta_3} + \alpha_{\beta_1}\alpha_{\beta_2} G_{\beta_1\beta_2} + \alpha_{\beta_1}\alpha_{\beta_3} G_{\beta_1\beta_3} + \alpha_{\beta_2}\alpha_{\beta_3} G_{\beta_2\beta_3} \tag{5.52}$$

The interaction in the present Euler beam partition theory gives rise to a second set of different pure modes (derived in the following section). When the out-of-plane shear moduli are finite and the interaction disappears, the second set of pure modes becomes the same as the first set. The first set of pure modes, which have just been derived, therefore form a complete basis for mixed-mode partitioning.

It will be seen that for finite element simulations where the out-of-plane shear moduli are finite, the element size δa needs to be small enough to ensure that $F_{nB\theta_1}\,\delta a$ is negligible and to avoid a numerically generated second set of pure modes.

5.2.5 The second set of orthogonal pure modes

Expressions for the second set of pure-mode load relationships in the present Euler beam partition theory, denoted by β_i' and θ_i' $(i = 1, 2, 3)$, are now most easily and concisely found by using the mixed-mode partition theory in the preceding section. Alternative derivations include considering zero relative opening displacement or zero crack tip shearing force (see §5.2.6 for the latter) and these two conditions are of course orthogonal to each other as well.

For $\beta_1' = M_{2B}/M_{1B}$, it can be written that

$$\begin{Bmatrix} 1 \\ \beta_1' \\ 0 \\ 0 \end{Bmatrix} = \alpha_{\theta_1} \begin{Bmatrix} 1 \\ \theta_1 \\ 0 \\ 0 \end{Bmatrix} + \alpha_{\beta_1} \begin{Bmatrix} 1 \\ \beta_1 \\ 0 \\ 0 \end{Bmatrix} + \alpha_{\beta_2} \begin{Bmatrix} 1 \\ 0 \\ \beta_2 \\ 0 \end{Bmatrix} + \alpha_{\beta_3} \begin{Bmatrix} 1 \\ 0 \\ 0 \\ \beta_3 \end{Bmatrix} \tag{5.53}$$

All the β_i' modes give $G_I = 0$. Solving Eqs. (5.44) and (5.53) simultaneously for $G_I = 0$ gives

$$\beta_1' = \frac{M_{2B}}{M_{1B}} = \frac{G_{\theta_1}\beta_1 - \Delta G_{\theta_1\beta_1}\theta_1}{G_{\theta_1} - \Delta G_{\theta_1\beta_1}} = \frac{D_2^*}{D_1^*} \tag{5.54}$$

Its orthogonal counterpart θ_1' is obtained by correspondence with Eq. (5.26).

$$\theta_1' = \frac{M_{2B}}{M_{1B}} = -\frac{D_2^*\,(D_1^* + D_1^*\beta_1' - D^*)}{D_1^*\,(D_2^* + D_2^*\beta_1' - D^*\beta_1')} = -1 \tag{5.55}$$

The remaining β_i' and θ_i' values are found in a similar way. They are

$$\beta_2' = \frac{N_{1B}}{M_{1B}} = \frac{\beta_2 \left(G_{\theta_1}\beta_1 - \Delta G_{\theta_1\beta_1}\theta_1\right)}{G_{\theta_1}\beta_1 - \Delta G_{\theta_1\beta_1}\theta_1 + \Delta G_{\theta_1\beta_2}\theta_1 - \Delta G_{\theta_1\beta_2}\beta_1} = -\frac{A_1}{B_1} \tag{5.56}$$

$$\theta_2' = \frac{N_{1B}}{M_{1B}} = \frac{\beta_2'\left(\dfrac{h_2}{2D^*} - \dfrac{B_1}{B_1^*} + \dfrac{B}{B^*}\right) + \dfrac{1}{D_1^*} - \dfrac{1}{D^*}}{\beta_2'\left(\dfrac{Bh_2}{B^*} - \dfrac{1}{A_1^*} + \dfrac{1}{A^*} + \dfrac{h_2^2}{4D^*}\right) - \dfrac{h_2}{2D^*} + \dfrac{B_1}{B_1^*} - \dfrac{B}{B^*}} \tag{5.57}$$

$$\beta_3' = \frac{N_{2B}}{M_{1B}} = \frac{\beta_3 \left(G_{\theta_1}\beta_1 - \Delta G_{\theta_1\beta_1}\theta_1\right)}{G_{\theta_1}\beta_1 - \Delta G_{\theta_1\beta_1}\theta_1 + \Delta G_{\theta_1\beta_3}\theta_1 - \Delta G_{\theta_1\beta_3}\beta_1} = -\frac{B_2^*}{D_1^* B_2} \tag{5.58}$$

$$\theta_3' = \frac{N_{2B}}{M_{1B}} = \frac{\beta_3'\left(\dfrac{h_1}{2D^*} - \dfrac{B}{B^*}\right) - \dfrac{1}{D_1^*} + \dfrac{1}{D^*}}{\beta_3'\left(\dfrac{Bh_1}{B^*} + \dfrac{1}{A_2^*} - \dfrac{1}{A^*} - \dfrac{h_1^2}{4D^*}\right) - \dfrac{h_1}{2D^*} + \dfrac{B}{B^*}} \tag{5.59}$$

Within the context of the present Euler beam partition theory, all of the pure modes are both locally and globally pure. Note that local pureness is defined with respect to the crack tip B whilst global pureness is defined with respect to the whole crack influence region Δa. This can be seen from Eqs. (5.18) and (5.42), which provide the pure-mode load relationships θ_i and β_i' respectively. In these equations the δa quantity can take any value without the load relationships for zero relative shearing or opening displacement being affected. The pure-mode load relationships θ_i' and β_i are therefore also both locally and globally pure because of orthogonality.

The relative shearing displacement from Timoshenko beam theory is identical to that from Euler beam theory in Eq. (5.18). As before, the θ_i and β_i pure-mode load relationships are therefore both locally and globally pure within the context of the present Timoshenko beam partition theory. As explained in §5.2.4, the second set of pure modes coincides with the first set in the present Timoshenko beam partition theory.

Finally, it is worth noting that when the whole crack influence region Δa is considered in the evaluation of ERR partitions for Timoshenko beams, the through-thickness shear effect due to the normal stress σ_n, arising from the $\left\{\varphi_{\theta_1}\right\}$ mode, will disappear. Therefore, for any values of the out-of-plane shear moduli, the ERR partitions will remain the same as those with infinitely large out-of-plane shear moduli. The pure-mode load relationships θ_i' and β_i' from the present Euler beam partition theory therefore form a second globally pure mode pair in the present Timoshenko beam partition theory (see §4.2.2).

5.2.6 Interface stress analysis

Consider the crack influence region ahead of the crack tip $0 < \xi < \Delta a$, shown in Fig. 5.1 (b). The origin of ξ is at the crack tip B and to the left. The interface stresses show the sign convention rather than any representative distribution. From Euler laminated composite

beam theory

$$\begin{aligned}\frac{d^2w_{1,2}}{d\xi^2} = &\frac{B_{1,2}\left(N_{1,2B} \mp b\int_0^\xi \tau_s\, d\xi\right)}{b\left(A_{1,2}D_{1,2} - B_{1,2}^2\right)} \\ &+ \frac{A_{1,2}\left(M_{1,2B} + P_{1,2B}\xi \mp b\int_0^\xi\int_0^\xi \sigma_n\, d\xi\, d\xi - bh_{1,2}\int_0^\xi \tau_s\, d\xi/2\right)}{b\left(A_{1,2}D_{1,2} - B_{1,2}^2\right)}\end{aligned} \tag{5.60}$$

$$\frac{d^3w_{1,2}}{d\xi^3} = \frac{\mp bB_{1,2}\tau_s + A_{1,2}\left(P_{1,2B} \mp b\int_0^\xi \sigma_n\, d\xi - bh_{1,2}\tau_s/2\right)}{b\left(A_{1,2}D_{1,2} - B_{1,2}^2\right)} \tag{5.61}$$

Now consider the region ahead of the crack influence region $\xi > \Delta a$, where beams above and below the interface behave as a single intact beam. From Euler laminated composite beam theory

$$\frac{d^2w}{d\xi^2} = \frac{AM_A + B\left(N_{1B} + N_{2B}\right)}{b\left(AD - B^2\right)} \quad \text{and} \quad \frac{d^3w}{d\xi^3} = \frac{A\left(P_{1B} + P_{2B}\right)}{b\left(AD - B^2\right)} \tag{5.62}$$

where

$$M_A = M_{1B} + M_{2B} + \frac{1}{2}\left(h_1N_{2B} + h_2N_{1B}\right) + \left(P_{1B} + P_{2B}\right)\xi \tag{5.63}$$

Using Eqs. (5.61) (5.62), the continuity of $d^3w/d\xi^3$ at $\xi = \Delta a$ gives two equations in F_n and τ_{sA}. These quantities are defined as

$$F_n = b\int_0^{\Delta a} \sigma_n\, d\xi \quad \text{and} \quad \tau_{sA} = \left(\tau_s\right)_{\xi=\Delta a} \tag{5.64}$$

which are the resultant normal force on the crack influence region and the shear stress at A respectively. Solving the two equations simultaneously gives

$$\begin{aligned}F_n = &\left[\frac{A_1P_{1B}}{b\left(B_1 + h_1A_1/2\right)} + \frac{A_2P_{2B}}{b\left(B_2 - h_2A_2/2\right)} - \frac{A\left(B_1^2 - A_1D_1\right)\left(P_{1B} + P_{2B}\right)}{b\left(B_1 + A_1h_1/2\right)\left(B^2 - AD\right)}\right. \\ &\left. - \frac{A\left(B_2^2 - A_2D_2\right)\left(P_{1B} + P_{2B}\right)}{b\left(B_2 + A_2h_2/2\right)\left(B^2 - AD\right)}\right] \Bigg/ \left[\frac{A_1}{b\left(B_1 + h_1A_1/2\right)} - \frac{A_2}{b\left(B_2 - h_2A_2/2\right)}\right]\end{aligned} \tag{5.65}$$

As expected, the resultant normal force F_n depends only on the two shear forces at the crack tip B. Using Eqs. (5.60) and (5.62), the continuity of $d^2w/d\xi^2$ at $\xi = \Delta a$ gives two equations in F_s and M_n. These quantities are defined as

$$F_s = b\int_0^{\Delta a} \tau_s\, d\xi \tag{5.66}$$

and

$$M_n = b\int_0^{\Delta a}\int_0^{\xi}\sigma_n\,d\xi\,d\xi = b\int_0^{\Delta a}\sigma_n\left(\Delta a-\xi\right)\,d\xi \tag{5.67}$$

which are the resultant shear force on the crack influence region and resultant moment around A due to the normal stress distribution respectively. Solving the two equations simultaneously gives

$$\begin{aligned} F_s = \Bigg[&M_{1B}+M_{2B}+\left(P_{1B}+P_{2B}\right)\Delta a+\frac{B_1N_{1B}}{A_1}+\frac{B_2N_{2B}}{A_2}\\ &-\frac{B\left(N_{1B}+N_{2B}\right)+AM_A}{B^2-AD}\left(\frac{B_1^2-A_1D_1}{A_1}+\frac{B_2^2-A_2D_2}{A_2}\right)\Bigg]\\ &\Bigg/\left(\frac{h_1}{2}+\frac{h_2}{2}+\frac{B_1}{A_1}-\frac{B_2}{A_2}\right) \end{aligned} \tag{5.68}$$

$$\begin{aligned} M_n = M_{1B}+P_{1B}\Delta a-\frac{h_1F_s}{2}+\frac{B_1\left(N_{1B}-F_s\right)}{A_1}\\ -\frac{\left(B_1^2-A_1D_1\right)\left[B\left(N_{1B}+N_{2B}\right)+AM_A\right]}{A_1\left(B^2-AD\right)} \end{aligned} \tag{5.69}$$

From Eqs. (5.64) and (5.67), the resultant moment around the crack tip B due to the normal stress distribution is

$$M_{nm} = -b\int_0^{\Delta a}\sigma_n\xi\,d\xi = M_n - F_n\Delta a \tag{5.70}$$

In §5.2.2, it was stated that the pure mode II modes of the first set, denoted by $\left\{\varphi_{\beta_i}\right\}$ $(i=1,2,3)$, are characterised by zero normal stress ahead of the crack tip, i.e. both $F_n=0$ and $M_{nm}=0$ are zero. This can now be proved. The $\left\{\varphi_{\beta_i}\right\}$ modes, given by Eqs. (5.26) to (5.28), are easily derived using Eq. (5.70) and the $M_{nm}=0$ condition. The pure mode I modes of the second set, denoted by $\left\{\varphi_{\theta_i'}\right\}$ $(i=1,2,3)$, are characterised by $F_s=0$. The $\left\{\varphi_{\theta_i'}\right\}$ modes, given by Eqs. (5.55), (5.57) and (5.59) can be derived using Eq. (5.68) and the $F_s=0$ condition.

5.2.7 Addition of shear forces

When the out-of-plane shear moduli are finite, shear forces cause shear deformation, which requires additional consideration. Two shear forces, shown in Fig. 5.1 (b), act at the crack tip of the two sub-laminates. The laminate shearing stiffness, represented by H in the present notation, is required. Again, this is not necessarily equal to A_{55} from lamination theory. Assumptions of plane stress, plane strain or mixed conditions need to be considered

(see §2.2.6). With reference to Fig. 5.1 (a), the constitutive relationships are

$$\begin{Bmatrix} N_{1,2}(x)/b \\ -M_{1,2}(x)/b \\ P_{1,2}(x)/b \end{Bmatrix} = \begin{Bmatrix} N_{1,2B}/b \\ (P_{1,2B}x - M_{1,2B})/b \\ P_{1,2B}/b \end{Bmatrix} = \begin{bmatrix} A_{1,2} & B_{1,2} & 0 \\ B_{1,2} & D_{1,2} & 0 \\ 0 & 0 & H_{1,2} \end{bmatrix} \begin{Bmatrix} du_{1,2}/dx \\ -d\psi_{1,2}/dx \\ dw_{1,2}/dx - \psi_{1,2} \end{Bmatrix} \tag{5.71}$$

Solving Eq. (5.71) gives

$$w_{1,2} = \frac{P_{1,2B}x}{bH_{1,2}} + \frac{A_{1,2}\left(M_{1,2B}x^2/2 - P_{1,2B}x^3/6\right) + B_{1,2}N_{1,2B}x^2/2}{b\left(A_{1,2}D_{1,2} - B_{1,2}^2\right)} + \psi_{1,2B}x + w_{1,2B} \tag{5.72}$$

which now replaces Eq. (5.16). In the presence of P_{1B} and P_{2B} alone, $\psi_{1B} - \psi_{2B} = 0$. Therefore the relative opening displacement due to shearing, D_{opP} is

$$D_{opP} = \left(\frac{P_{1B}}{H_1} - \frac{P_{2B}}{H_2}\right)\frac{\delta a}{b} \tag{5.73}$$

The crack tip normal force due to shearing, F_{nBP} is found by considering the normal stress ahead of the crack tip. From the shear strain part of Eq. (5.71), we have

$$\frac{dw_{1,2}}{d\xi} - \psi_{1,2} = \frac{P_{1,2B} \mp b\int_0^{\xi} \sigma_n \, d\xi}{bH_{1,2}} \tag{5.74}$$

Evaluating Eq. (5.74) at an infinitely small distance δa ahead of the crack tip, i.e. at $\xi = \delta a$, and noting that the mid-surface rotations are equal here due to interface continuity gives

$$\psi_{1B} - \psi_{2B} = \frac{P_{2B} + F_{nB}}{bH_2} - \frac{P_{1B} - F_{nB}}{bH_1} \tag{5.75}$$

Note that $\psi_{1,2B} = (\psi_{1,2})_{\xi=\delta a}$ is used to obtain Eq. (5.75). As noted above, in the presence of P_{1B} and P_{2B} alone, $\psi_{1B} - \psi_{2B} = 0$ and $F_{nB} = F_{nBP}$. The crack tip normal force due to shearing is therefore

$$F_{nBP} = \frac{H_2P_{1B} - H_1P_{2B}}{H_1 + H_2} \tag{5.76}$$

Using Eqs. (5.73) and (5.76) in conjunction with the VCCT gives the contribution to the mode I ERR from shearing, G_P.

$$G_P = \frac{(H_1P_{2B} - H_2P_{1B})^2}{2b^2H_1H_2(H_1 + H_2)} \tag{5.77}$$

If the higher order P_{1B} and P_{2B} terms are neglected then Eq. (5.71) gives identical expressions to those in Eqs. (5.18) and (5.19). Therefore the previously derived $\left\{\varphi_{\theta_i}\right\}$ modes remain the same and the mode II ERR G_{II} is not affected by shearing. There are however additional contributions to the mode I ERR G_I from G_P, and also from two interactions:

(1) the interaction between the $\left\{\varphi_{\theta_1}\right\}$ mode crack tip normal force and the relative opening displacement due to shearing; and (2) the interaction between the $\left\{\varphi_{\theta_1}\right\}$ mode relative opening displacement and crack tip normal force due to shearing. Due to reciprocity, these latter two contributions are equal to each other. This is easily shown mathematically. Their combined contribution is denoted by $\Delta G_{\theta_1 P}$. To quantify these interactions, the VCCT is used again. From Eqs. (5.72) and (5.75), the relative opening displacement due to the $\left\{\varphi_{\theta_1}\right\}$ mode is

$$D_{op\theta_1} = (\psi_{1B} - \psi_{2B})\,\delta a = \frac{F_{nB\theta_1}\,\delta a\,(H_1 + H_2)}{bH_1H_2} \tag{5.78}$$

where high powers of δa have been ignored. Since G_{θ_1} is already known from Eq. (5.32), then using the VCCT, the crack tip normal force in mode $\left\{\varphi_{\theta_1}\right\}$ is

$$F_{nB\theta_1} = \frac{2bG_{\theta_1}\,\delta a}{D_{op\theta_1}} = \left[\frac{H_1H_2}{H_1+H_2}\left(\frac{1}{D_1^*} + \frac{\theta_1^2}{D_2^*} - \frac{(1+\theta_1)^2}{D^*}\right)\right]^{1/2} \tag{5.79}$$

It is seen that if the out-of-plane shear moduli are finite then $F_{nB\theta_1}$ is also finite and that therefore $F_{nB\theta_1}\,\delta a$ is zero, which is why there is no interaction between the $\left\{\varphi_{\theta_i}\right\}$ modes and the $\left\{\varphi_{\beta_i}\right\}$ modes when using Timoshenko beam theory (discussed in §5.2.4). The $\Delta G_{\theta_1 P}$ interaction term is therefore

$$\begin{aligned}\Delta G_{\theta_1 P} &= \frac{F_{nB\theta_1} D_{opP}}{b\,\delta a} \\ &= \frac{1}{b^2}\left(\frac{P_{1B}}{H_1} - \frac{P_{2B}}{H_2}\right)\left[\frac{H_1H_2}{H_1+H_2}\left(\frac{1}{D_1^*} + \frac{\theta_1^2}{D_2^*} - \frac{(1+\theta_1)^2}{D^*}\right)\right]^{1/2}\end{aligned} \tag{5.80}$$

and the ERR partitions are

$$G_I = \alpha_{\theta_1}^2 G_{\theta_1} + G_P + \alpha_{\theta_1}\Delta G_{\theta_1 P} \tag{5.81}$$

$$G_{II} = \alpha_{\beta_1}^2 G_{\beta_1} + \alpha_{\beta_2}^2 G_{\beta_2} + \alpha_{\beta_3}^2 G_{\beta_3} + \alpha_{\beta_1}\alpha_{\beta_2} G_{\beta_1\beta_2} + \alpha_{\beta_1}\alpha_{\beta_3} G_{\beta_1\beta_3} + \alpha_{\beta_2}\alpha_{\beta_3} G_{\beta_2\beta_3} \tag{5.82}$$

5.2.8 Contacting crack surfaces

The contact behaviour is briefly summarised here for DCBs with M_1 and M_2 applied at the DCB tip. The analysis is easily repeated for other load combinations, including axial and shear forces.

Using the present Euler beam partition theory, crack tip contact and DCB tip contact occur simultaneously at $M_{2B}/M_{1B} = \beta_1'$. This is easily shown using Eq. (5.41). If one load is held fixed and the other is varied, after DCB tip contact the crack can either open leaving just point contact at the DCB tip, or remain closed. Assuming that the crack tip opens after DCB tip contact allows the circumstances under which the crack tip remains

closed to be determined. With point contact at the DCB tip only, the contact force P_c is

$$P_c = \frac{3D_1^* M_2 - 3D_2^* M_1}{2a\left(D_1^* + D_2^*\right)} \tag{5.83}$$

The following relationship is now easily derived:

$$M_{2B} = kM_{1B} + \left(\frac{D_2^*}{3D_1^*} + \frac{1}{3}\right) M_1 \tag{5.84}$$

where

$$k = \frac{2D_2^*}{3D_1^*} - \frac{1}{3} \tag{5.85}$$

If $k > \beta_1'$ then the fracture will remain a pure mode II fracture, i.e. the crack tip remains closed. If $\beta_1 < k < \beta_1'$ then the fracture will pass through the $\left\{\varphi_{\beta_1}\right\}$ mode and become a mixed-mode fracture. Finally, if $k < \beta_1$ then the fracture will pass through both the $\left\{\varphi_{\beta_1}\right\}$ and $\left\{\varphi_{\beta_1'}\right\}$ modes. Examining Eqs. (5.85) and (5.54) reveals that k is always less than β_1'. Therefore in the present Euler beam partition theory, the mode always becomes mixed after contact.

Using the present Timoshenko beam partition theory, crack tip running contact occurs at $M_{2B}/M_{1B} = \beta_1 = \beta_1'$. DCB tip contact occurs at

$$\frac{M_{2B}}{M_{1B}} = \beta_1 + \frac{\dfrac{a}{2}\left(\dfrac{1}{D_1^*} - \dfrac{\beta_1}{D_2^*}\right)}{\dfrac{a}{2D_2^*} + \dfrac{F_{nB\theta_1}}{\beta_1 - \theta_1}\left(\dfrac{1}{H_1} + \dfrac{1}{H_2}\right)} \tag{5.86}$$

If crack tip running contact occurs before DCB tip contact then Eq. (5.86) is no longer valid, since it assumes point contact at the DCB tip only and no running contact. In this case, a far more complex analysis of the running contact is required to determine when DCB tip contact occurs and this is not done here. The absolute values of β_1 and Eq. (5.86) must be compared to determine which type of contact occurs first.

If one load is held fixed and the other is varied, after DCB tip contact it is assumed that the crack tip opens leaving just point contact at the DCB tip. Then the circumstances under which the crack tip closes can be determined. The DCB tip contact force P_c is

$$P_c = \frac{M_2\left[\dfrac{a}{2D_2^*} + \dfrac{F_{nB\theta_1}}{\beta_1 - \theta_1}\left(\dfrac{1}{H_1} + \dfrac{1}{H_2}\right)\right] - M_1\left[\dfrac{a}{2D_1^*} + \dfrac{F_{nB\theta_1}\beta_1}{\beta_1 - \theta_1}\left(\dfrac{1}{H_1} + \dfrac{1}{H_2}\right)\right]}{\dfrac{a^3}{3}\left(\dfrac{1}{D_1^*} + \dfrac{1}{D_2^*}\right) + \left(\dfrac{1}{H_1} + \dfrac{1}{H_2}\right)\left(1 + \dfrac{aF_{nB\theta_1}\left(1+\beta_1\right)}{\beta_1 - \theta_1}\right)} \tag{5.87}$$

The following relationship is now easily derived:

$$M_{2B} = k_1 M_{1B} + k_2 M_1 \tag{5.88}$$

where

$$\begin{aligned} k_1 = \big\{ & \beta_1 \left[6D_1^* D_2^* \left(H_1 + H_2 \right) - a^2 H_1 H_2 \left(D_1^* - 2D_2^* \right) + 6aD_1^* D_2^* F_{nB\theta_1} \left(H_1 + H_2 \right) \right] \\ & - \theta_1 \left[6D_1^* D_2^* \left(H_1 + H_2 \right) - a^2 H_1 H_2 \left(D_1^* - 2D_2^* \right) \right] \big\} \big/ \left[3a^2 D_1^* H_1 H_2 \left(\beta_1 - \theta_1 \right) \right. \\ & \left. + 6aD_1^* D_2^* F_{nB\theta_1} \left(H_1 + H_2 \right) \right] \end{aligned} \tag{5.89}$$

and

$$k_2 = \frac{\left(\theta_1 - \beta_1 \right) \left[6D_1^* D_2^* \left(H_1 + H_2 \right) - a^2 H_1 H_2 \left(D_1^* + D_2^* \right) \right]}{3aD_1^* \left[2D_2^* F_{nB\theta_1} \left(H_1 + H_2 \right) + aH_1 H_2 \left(\beta_1 - \theta_1 \right) \right]} \tag{5.90}$$

If $k_1 > \beta_1$ then the fracture will remain a pure mode II fracture and there is crack tip running contact. Otherwise, it is a mixed mode and there is only DCB tip contact.

5.2.9 Averaged partition rules

Mixed-mode partition theories have been established in §5.2.4 based on the Euler and Timoshenko beam theories: the present Euler beam partition theory and the present Timoshenko beam partition theory. Within the context of the present Timoshenko beam partition theory there is no interaction between the $\left\{ \varphi_{\theta_i} \right\}$ modes and the $\left\{ \varphi_{\beta_i} \right\}$ modes ($i = 1, 2, 3$). On the other hand, there is full interaction between these modes in the present Euler beam partition theory. It was suggested in §4.2.5 (for layered isotropic homogeneous DCBs) that the present Euler and Timoshenko beam partition theories act as either upper or lower bounds of the ERR partition. All the numerical simulations carried out so far (for layered isotropic homogeneous DCBs in §4.3) have supported this suggestion. It is therefore very reasonable to expect the average of the two theories, i.e. corresponding to half the interaction of the present Euler beam partition theory, to give comparable predictions with the partition from two-dimensional FEM simulations, for example using QUAD4 elements. This averaged partition rule, which is now referred to as 'averaged partition rule 1', gives the following ERR partitions:

$$\begin{aligned} G_I = & \alpha_{\theta_1}^2 G_{\theta_1} + \alpha_{\theta_1} \alpha_{\beta_1} \Delta G_{\theta_1 \beta_1} / 2 + \alpha_{\theta_1} \alpha_{\beta_2} \Delta G_{\theta_1 \beta_2} / 2 \\ & + \alpha_{\theta_1} \alpha_{\beta_3} \Delta G_{\theta_1 \beta_3} / 2 + G_P + \alpha_{\theta_1} \Delta G_{\theta_1 P} \end{aligned} \tag{5.91}$$

$$\begin{aligned} G_{II} = & \alpha_{\beta_1}^2 G_{\beta_1} + \alpha_{\beta_2}^2 G_{\beta_2} + \alpha_{\beta_3}^2 G_{\beta_3} + \alpha_{\beta_1} \alpha_{\beta_2} G_{\beta_1 \beta_2} + \alpha_{\beta_1} \alpha_{\beta_3} G_{\beta_1 \beta_3} \\ & + \alpha_{\beta_2} \alpha_{\beta_3} G_{\beta_2 \beta_3} - \alpha_{\theta_1} \alpha_{\beta_1} \Delta G_{\theta_1 \beta_1} / 2 - \alpha_{\theta_1} \alpha_{\beta_2} \Delta G_{\theta_1 \beta_2} / 2 \\ & - \alpha_{\theta_1} \alpha_{\beta_3} \Delta G_{\theta_1 \beta_3} / 2 \end{aligned} \tag{5.92}$$

Note that the $\Delta G_{\theta_1 \beta_i}$ terms are calculated using $F_{nB\theta_1}\, \delta a$ from Eq. (5.50), which is from the present Euler beam partition theory. The $\Delta G_{\theta_1 P}$ interaction term is calculated using $F_{nB\theta_1}$ from Eq. (5.79), which is from the present Timoshenko beam partition theory with finite out-of-plane shear moduli.

A side effect of averaged partition rule 1 is that, for small ranges of loading conditions, it can produce negative partitions of ERR. When this happens, the total ERR G remains non-negative, but either G_I or G_{II} becomes negative. As will be confirmed later by the numerical results in §5.3: (1) the local partitions of ERR from two-dimensional elasticity are always positive; and (2) there exists only one set of pure modes, i.e. there is no interaction. An obvious modification can therefore be made to averaged partition rule 1, which may give even better agreement with ERR partitions from two-dimensional elasticity. The modification is as follows: new pure modes can be derived which, when employed in the partition of ERR with zero interaction, give zero G_I/G and G_{II}/G where averaged partition rule 1 gives minimum values (that are negative). The negative partitions of ERR are thus removed. In this new modified partition rule, the orthogonality between the pure modes is maintained. This modified partition rule is now referred to as 'averaged partition rule 2'.

The new pure modes, are simple to derive, however for a general laminated composite, the expressions are long and unwieldy. It is more useful to derive them using the following method and obtain numerical rather than completely algebraic quantities.

Since in averaged partition rule 1, β_1 and θ_1 give the ratio M_{2B}/M_{1B} for pure mode II and I respectively, to calculate the modified ratios, denoted by β_{1A2} and θ_{1A2}, solve

$$\frac{d\,(G_I/G)}{d\,(M_{2B})} = 0 \tag{5.93}$$

for M_{2B} where $M_{1B} = 1$, $N_{1B} = 0$, $N_{2B} = 0$ and G_I is given by averaged partition rule 1 in Eq. (5.91). Eq. (5.93) has two solutions: one is β_{1A2} and the other is θ_{1A2}. Similarly, since in averaged partition rule 1, β_2 and θ_2 give the ratio N_{1B}/M_{1B} for pure mode II and I respectively, the modified ratios β_{2A2} and θ_{2A2} are found by solving

$$\frac{d\,(G_I/G)}{d\,(N_{1B})} = 0 \tag{5.94}$$

for N_{1B} where $M_{1B} = 1$, $M_{2B} = 0$ and $N_{2B} = 0$. Eq. (5.94) has two solutions: one is β_{2A2} and the other is θ_{2A2}. Finally, the modified ratios β_{3A2} and θ_{3A2} are found by solving

$$\frac{d\,(G_I/G)}{d\,(N_{2B})} = 0 \tag{5.95}$$

for N_{2B} where $M_{1B} = 1$, $M_{2B} = 0$ and $N_{1B} = 0$. Eq. (5.95) has two solutions: one is β_{3A2} and the other is θ_{3A2}.

With the modified pure modes, the ERR partition for averaged partition rule 2 is simply given by

$$G_I = \alpha^2_{\theta_{1A2}} G_{\theta_{1A2}} + G_P + \alpha_{\theta_{1A2}} \Delta G_{\theta_{1A2}P} \tag{5.96}$$

where $\alpha_{\theta_{1A2}}$ is given by α_{θ_1} in Eq. (5.30) but β_{iA2} replaces β_i $(i = 1, 2, 3)$, and θ_{1A2} replaces θ_1. $G_{\theta_{1A2}}$ is given by G_{θ_1} in Eq. (5.32) but θ_{1A2} replaces θ_1. Similarly, $\Delta G_{\theta_{1A2}P}$ is given

by $\Delta G_{\theta_1 P}$ in Eq. (5.80) but θ_{1A2} replaces θ_1. The total ERR is still given by Eq. (5.4) and therefore $G_{II} = G - G_I$.

5.2.10 Surface layer spalling

Consider a sub-surface delamination ($h_2/h_1 \to \infty$). Thouless et al. (1987) considered this problem for homogeneous semi-infinite plates using stress intensity factors. They noted the many practical cases in which spalling phenomena arise, including edge machining, edge mounting and residually stressed thin films and coatings, such as those used in electronic devices and in barrier coatings. They also pointed out that their method can be extended to heterogeneous systems, which is important for addressing phenomena such as decohesion of thin films from substrates and delamination in composites.

The partitions from the theories presented in this paper, which are simple, intuitive and versatile, are now given for a bi-layer case, which is clearly of practical importance. The through-thickness shear effect is ignored since the spall is thin. The ERR partitions from the present Euler and Timoshenko beam partition theories, averaged partition rule 1 and averaged partition rule 2, are respectively

$$G_I = \frac{3M_{1B}\left(2M_{1B} - h_1 N_{1B}\right)}{b^2 h_1^3 E_1} \quad \text{and} \quad G_{II} = \frac{N_{1B}\left(6M_{1B} + h_1 N_{1B}\right)}{2b^2 h_1^2 E_1} \tag{5.97}$$

$$G_I = \frac{3\left(2M_{1B} - h_1 N_{1B}\right)^2}{8b^2 h_1^3 E_1} \quad \text{and} \quad G_{II} = \frac{\left(6M_{1B} + h_1 N_{1B}\right)^2}{8b^2 h_1^3 E_1} \tag{5.98}$$

$$G_I = \frac{3\left(2M_{1B} - h_1 N_{1B}\right)\left(10M_{1B} - h_1 N_{1B}\right)}{16b^2 h_1^3 E_1}$$

$$\text{and} \quad G_{II} = \frac{\left(6M_{1B} + h_1 N_{1B}\right)\left(6M_{1B} + 5h_1 N_{1B}\right)}{16b^2 h_1^3 E_1} \tag{5.99}$$

$$G_I = \frac{3.56695\left(M_{1B} - 0.23841 h_1 N_{1B}\right)^2}{b^2 h_1^3 E_1}$$

$$\text{and} \quad G_{II} = \frac{2.43305\left(M_{1B} + 0.34953 h_1 N_{1B}\right)^2}{b^2 h_1^3 E_1} \tag{5.100}$$

where E_1 is the Young's modulus of the spall. Note that the total ERR G is the same for all three theories. It is given by

$$G = \frac{12M_{1B}^2 + h_1^2 N_{1B}^2}{2b^2 h_1^3 E_1} \tag{5.101}$$

The total ERR and partition are dependent only on the thickness and material properties of the spall. The properties of the substrate have no effect. Therefore the isotropic results can also be obtained by simply replacing E_1 with E. Now a direct comparison can be made with the partition reported by Hutchinson and Suo (1992) using two-dimensional elasticity for an isotropic case. The corresponding theories are averaged partition rules in Eqs. (5.99) and (5.100). The results from averaged partition rule 1, averaged partition rule 2 and two-dimensional elasticity (Hutchinson and Suo 1992) for the case when $N_1 = 0$ are

respectively

$$G_I = \frac{3.75M_1^2}{b^2h_1^3E}; \quad G_I = \frac{3.567M_1^2}{b^2h_1^3E} \quad \text{and} \quad G_I = \frac{3.744M_1^2}{b^2h_1^3E} \tag{5.102}$$

The agreement between averaged partition rule 1 and Suo and Hutchinson's (1990) two-dimensional elasticity partition is excellent. Some further comparisons are made between the partition theories in this chapter and the spalling experiments (with more complex loading configurations) of Thouless et al. (1987) in Chapter 7.

5.3 Numerical investigations

The FEM was used to validate the theories. Finite elements, based on the Euler and Timoshenko beam theories and two-dimensional elasticity, were employed to model laminated composite DCBs. Normal and shear point interface springs with the very high stiffness of 10^{14} N/m were used to model perfectly bonded plies. It was shown in §B.1 in Appendix B that for the layered isotropic homogeneous DCBs in Chapter 4, an interface spring stiffness value which is just 10^2 times larger than the Young's modulus of the material in the units of the FEM simulations is indeed sufficient to model perfectly bonded layers. As discussed in §B.1, a larger value for k_s is desirable, but without introducing numerical errors. In the simulations in this section, which are in SI units, $E_1 = 139.3\,\text{GPa}$, $E_2 = E_3 = 9.72\,\text{GPa}$ and $k_s = 10^{14}\,\text{N/m}$. Therefore k_s is between $\sim 10^3$ and $\sim 10^4$ times larger than the Young's moduli of the material in the units of the FEM simulations. It has been verified through simulations equivalent to those in §B.1 that this value for k_s is sufficient to model perfectly bonded plies. The ERR partition was calculated using the VCCT in conjunction with these interface springs. A contact algorithm was also implemented to deal with any possible contact in loading. Full details are given in §3.3, §3.4 and §3.5 respectively.

Two laminated composite DCB cases were investigated. The material properties are for T300/976 graphite/epoxy laminae (Wang and Zhang 2009). The first case is a type of 'orthogonal bi-layer' one, the data for which is given in Table 5.1. There is a central delamination, which gives a thickness ratio of $h_2/h_1 = 1$.

The second case has a cross-ply lay-up with 12 plies. There is a delamination between the eighth and ninth plies, which gives a thickness ratio of $h_2/h_1 = 2$. The data for case 2 is given in Table 5.2. The ply material properties are not repeated since they are unchanged. The sub-laminate lay-ups are asymmetric both individually and in combination in order to test cases with the greatest degree of material coupling.

Three numerical tests were carried out. Results from the first test, which used linear Timoshenko beam elements, are compared against the present Euler beam partition theory. The plane-strain assumption is used. Under this assumption, $A = A_{11}$, $B = B_{11}$, $D = D_{11}$ and $H = A_{55}$. Very large out-of-plane shear moduli $\mu_{13} = \mu_{23} = 10^{14}\,\text{Pa}$ were used to simulate Euler beams. Two layers of elements were used to represent the laminate with one on either side of the delamination. The elements were distributed uniformly. To avoid

Table 5.1: Case 1 data for FEM simulations of an orthotropic bi-layer DCB.

Ply longitudinal modulus, E_1	139.3 GPa
Ply transverse modulus, E_2	9.72 GPa
Out-of-plane modulus, E_3	9.72 GPa
In-plane shear modulus, μ_{12}	5.58 GPa
Out-of-plane shear modulus, μ_{13}	5.58 GPa
Out-of-plane shear modulus, μ_{23}	3.45 GPa
In-plane Poisson's ratio, ν_{12}	0.29
Out-of-plane Poisson's ratio, ν_{13}	0.29
Out-of-plane Poisson's ratio, ν_{23}	0.4
Thickness of lamina, t_p	0.125 mm
Sub-laminate lay-up 1 and 2 (bottom and top)	0_8 and 90_8
Laminate thicknesses, h_1 and h_2	1 mm and 1 mm
Intact length of beam, L	100 mm
Length of delamination, a	10 mm
Width of beam, b	10 mm
Modes θ_1, θ_2 and θ_3 (zero shearing displacement)	-14.33, -6000 and 85987.65
Modes β_1, β_2 and β_3 (zero opening force)	3.02, 3200.19 and -45862.74
Modes θ_1', θ_2' and θ_3' (zero shearing force)	-1, -782.71 and 11217.29
Modes β_1', β_2' and β_3' (zero opening displacement)	14.33, $-\infty$ and ∞
Modes θ_{1A2}, θ_{2A2} and θ_{3A2}	-6.78, -3853.40, 55224.20
Modes β_{1A2}, β_{2A2} and β_{3A2}	4.77, 5984.47, -85765.08

Table 5.2: Case 2 data for FEM simulations of a laminated composite DCB.

Sub-laminate lay-up 1 and 2 (bottom and top)	$(0/90)_4$ and $(90/0)_2$
Laminate thicknesses, h_1 and h_2	0.5 mm and 1 mm
Intact length of beam, L	100 mm
Length of delamination, a	10 mm
Width of beam, b	10 mm
Modes θ_1, θ_2 and θ_3 (zero shearing displacement)	-4.94, -8842.14 and 24762.53
Modes β_1, β_2 and β_3 (zero opening force)	2.49, 17877494.84 and -20392.16
Modes θ_1', θ_2' and θ_3' (zero shearing force)	-1, -3811.22 and -6314.53
Modes β_1', β_2' and β_3' (zero opening displacement)	8.99, -18400.37 and -165440.36
Modes θ_{1A2}, θ_{2A2} and θ_{3A2}	-3.34, -7623.04, 18289.16
Modes β_{1A2}, β_{2A2} and β_{3A2}	3.44, -48360.94, -30625.32

shear locking, reduced integration was applied. Use of linear Timoshenko beam elements correctly enforces continuity along the interface ahead of the crack tip.

The second test was the same as the first but instead used the normal out-of-plane shear moduli (those given in Table 5.1) and a shear correction factor of $\kappa = 5/6$. Results from this test are compared against the present Timoshenko beam partition theory.

The third and final test used plane-strain QUAD4 elements with the normal out-of-plane shear moduli. Layers of QUAD4 elements model the sub-laminates and they are also joined with very high-stiffness normal and shear interface springs. Using this approach, the problem of oscillatory singularities (Raju et al. 1988) when modelling fractures in composite materials with two- and three-dimensional elasticity is not encountered (Kutlu and Chang 1995, Zhang and Wang 2009, Wang and Zhang 2009). In the composite case 2, a layer of QUAD4 elements was used for each individual ply, as is required by the

element derivation in §3.2.4. In the orthotropic bi-layer case 1, three layers of QUAD4 elements were used in each sub-laminate and this gave an excellent degree of convergence. The elements were distributed uniformly along the length and thickness. The results from these simulations are compared against the averaged partition rules.

All the finite element meshes, except for the ones marked as having 1310×2 elements (in the following figures and tables), had uniform element density along the length and through the thickness. In order to obtain accurate, mesh-independent partitions of ERR, the simulations with linear Timoshenko beams and the normal value of shear modulus required a very fine mesh in the vicinity of the crack tip. For these cases, meshes with a total of 1310×2 elements were used. In the region of length 1.2 mm centred on the crack tip, 1200 elements with a length of 0.001 mm were uniformly distributed. In the remaining intact section of the DCB, 100 elements were uniformly distributed. In the remaining cracked section of the DCB, 10 elements were uniformly distributed. All other simulations converged adequately without the need for such high numbers of elements around the crack tip. Therefore uniformly distributed elements did not result in prohibitively high computational requirements. Some additional comments on the convergence studies for the cases in this section are provided in the following and also in §B.5 in Appendix B.

5.3.1 Tests with DCB tip bending moments

In this set of simulations, M_1 was held constant at 1 Nm and M_2 was varied. Results from the various analytical theories and numerical simulations are presented in Tables 5.3 and 5.4 and Fig. 5.2 for case 1. In Fig. 5.2 and for every figure in this section, unfilled data markers indicate results from simulations with contact modelling and filled markers indicate results from simulations without. The results from the simulations using Euler beam elements (i.e. Timoshenko beam elements with very large out-of-plane shear moduli) are compared against the present Euler beam partition theory. Full interaction is expected. Excellent agreement is seen between the two sets of data. The $\left\{\varphi_{\beta_1}\right\}$ and $\left\{\varphi_{\theta_1'}\right\}$ modes are plainly visible where $G_I/G = 0$ and $G_I/G = 1$ respectively. The two methods are in agreement that DCB tip contact and crack tip contact occur simultaneously at $M_2 = 14.33\,\text{Nm}$. Because k, given by Eq. (5.85), is less than β_1', i.e. $9.22 < 14.33$, after DCB tip contact the mode is mixed. The numerical value of the mode partition after DCB tip contact can be converged closer to the analytical value by using more elements. Also, as was the case for layered isotropic homogeneous DCBs, it is seen that the present Euler beam partition theory predicts regions where the partitions of ERR are negative. This may seem an unintuitive result at first. It is discussed in §4.2.4 and §4.3.1. Further detailed discussion is also given in Appendix A.

The present Timoshenko beam partition theory is compared with results from numerical simulations using Timoshenko beam elements with the normal out-of-plane shear moduli. As expected, the $\left\{\varphi_{\theta_1'}\right\}$ and $\left\{\varphi_{\beta_1'}\right\}$ modes coincide with the $\left\{\varphi_{\theta_1}\right\}$ and $\left\{\varphi_{\beta_1}\right\}$ modes respectively since there is no interaction. Both the $\left\{\varphi_{\theta_1}\right\}$ and $\left\{\varphi_{\beta_1}\right\}$ modes are visible in

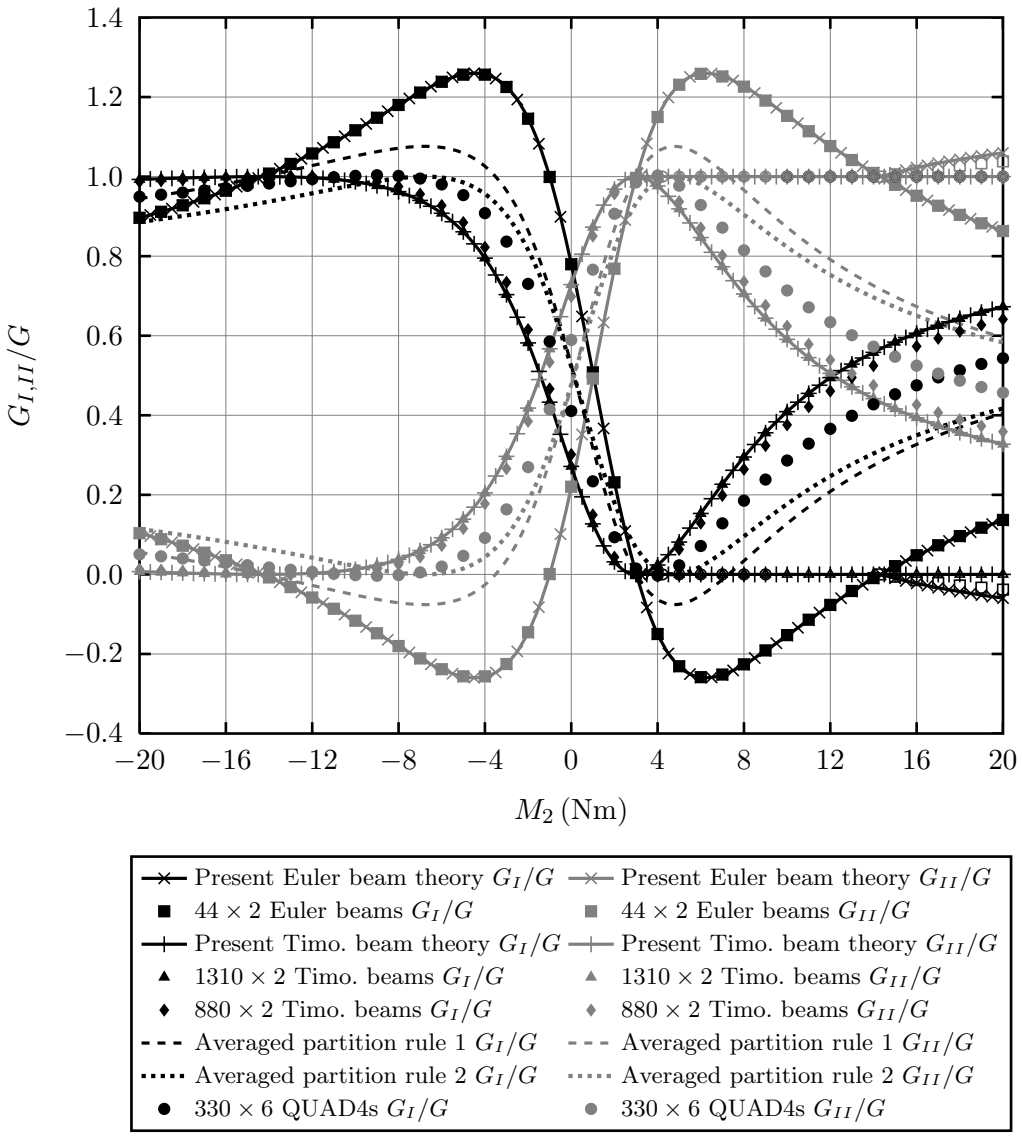

Figure 5.2: Comparisons between various theories and FEM results for case 1 with varying M_2 and $M_1 = 1\,\text{Nm}$, $N_1 = 0$, $N_2 = 0$, $P_1 = 0$, $P_2 = 0$.

the figure. The numerical results with 880×2 elements very closely follow the analytical values. By using the non-uniform mesh with 1310×2 elements (with elements of length 0.001 mm around the crack tip), the agreement can be made virtually exact. Many more elements are required in comparison to when the out-of-plane shear moduli are very large. This demonstrates what Eq. (5.50) shows, that the element size δa needs to be very small otherwise $F_{nB\theta_1}\,\delta a$ is not negligible and a second set of pure modes is generated numerically.

Also as expected, crack tip running contact begins at the $\left\{\varphi_{\beta_1}\right\}$ mode. Crack tip running contact necessarily gives $G_I/G = 0$. The value of M_2 for DCB tip contact could not be computed numerically with 1310×2 or 880×2 elements because of constraints on computational resources. However, using 220×2 elements and then halving the numbers of elements to 110×2 causes little change, which suggests that the value from 220×2 elements

Table 5.3: Comparisons between various theories and FEM results for case 1 with varying M_2 and $M_1 = 1\,\text{Nm}$, $N_1 = 0$, $N_2 = 0$, $P_1 = 0$, $P_2 = 0$ and ignoring contact.

M_2 (Nm)	G_I/G (%)							
	Present Euler beam theory	44×2 Euler beams	Present Timo. beam theory	1310×2 Timo. beams	880×2 Timo. beams	Averaged rule 1	Averaged rule 2	220×4 QUAD4s
−20	89.63	89.65	99.28	99.28	98.71	94.46	88.59	94.95
−18	92.77	92.79	99.64	99.64	99.23	96.21	90.10	95.99
−16	96.45	96.45	99.91	99.91	99.70	98.18	91.82	97.10
−14	100.76	100.76	100.00	100.00	100.04	100.38	93.73	98.26
−12	105.82	105.81	99.71	99.72	100.08	102.77	95.80	99.37
−10	111.66	111.64	98.70	98.71	99.47	105.18	97.89	100.19
−8	118.05	118.01	96.22	96.23	97.51	107.13	99.59	100.18
−6	123.89	123.83	90.78	90.80	92.74	107.34	99.76	98.03
−4	125.70	125.63	79.50	79.53	82.23	102.60	95.66	90.81
−2	114.64	114.55	58.19	58.22	61.53	86.42	81.61	73.03
0	78.05	77.96	27.15	27.17	30.15	52.60	52.25	41.07
2	23.18	23.14	3.16	3.17	4.34	13.17	18.03	9.35
4	−15.01	−14.98	2.36	2.35	1.33	−6.33	1.11	−0.28
6	−25.90	−25.83	15.32	15.30	12.89	−5.29	2.01	7.14
8	−22.69	−22.60	29.51	29.48	26.43	3.41	9.56	18.53
10	−15.36	−15.26	40.91	40.89	37.59	12.78	17.69	28.63
12	−7.77	−7.67	49.45	49.43	46.08	20.84	24.69	36.60
14	−1.02	−0.92	55.82	55.79	52.47	27.40	30.38	42.75
16	4.72	4.81	60.63	60.61	57.33	32.68	34.96	47.53
18	9.54	9.63	64.35	64.33	61.12	36.95	38.67	51.30
20	13.59	13.69	67.29	67.26	64.12	40.44	41.70	54.34

is sufficiently converged. As k_1, given by Eq. (5.89), is greater than β_1, i.e. $7.78 > 3.02$, the crack tip remains closed after DCB tip contact giving $G_I/G = 0$ for all values of M_2. The numerical simulations model this contact behaviour very closely.

Averaged partition rule 1 has half the interaction of the present Euler beam partition theory and therefore is halfway between the curves from the present Euler and Timoshenko beam partition theories (because there are no shear forces P_1 and P_2 in this case). It was suggested in §5.2.9 that averaged partition rule 1 might be a good approximation for the ERR partition from two-dimensional elasticity. It is seen that the results from FEM simulations with QUAD4 elements are all contained within 'limits' of the present Timoshenko and Euler beam partitions, as predicted. Averaged partition rule 2 uses the points of minimum G_I/G and G_{II}/G as pure modes, and partitions the ERR around these pure modes with no interaction. It is seen that averaged partition rule 2 gives no negative partitions of ERR, as expected. As a result, it is indeed closer to the two-dimensional elasticity partition than averaged partition rule 1 for most of the plotted range of M_2.

It is also clear from tables and the figure that neither beam partition theory agrees with the two-dimensional elasticity partition. This is exactly as expected and does not devalue at all either beam partition theory. The present Euler beam partition theory has full interaction; the present Timoshenko beam partition theory has zero interaction. The

Table 5.4: Comparisons between various theories and FEM results for case 1 contact with varying M_2 and $M_1 = 1\,\mathrm{Nm}$, $N_1 = 0$, $N_2 = 0$, $P_1 = 0$, $P_2 = 0$.

	Crack tip contact		DCB tip contact		After DCB tip contact	
	M_2 (Nm)	G_I/G (%)	M_2 (Nm)	G_I/G (%)	M_2 (Nm)	G_I/G (%)
Present Euler beam theory	14.33	0	14.33	0	20	−5.96
44 × 2 Euler beams	14.30	0	14.32	0	20	−3.81
Present Timo. beam theory	3.02	0	-	-	20	0
1310 × 2 Timo. beams	3.02	0	-	-	20	0
880 × 2 Timo. beams	3.43	0	-	-	20	0
220 × 2 Timo. beams	4.51	0	12.70	0	20	0
110 × 2 Timo. beams	5.66	0	12.66	0	20	0
Averaged rule 1	7.28	0	-	-	20	0
Averaged rule 2	4.77	0	-	-	20	0
330 × 6 QUAD4s	4.23	0	-	-	20	0

numerical results show that by averaging the present Euler and Timoshenko beam partition theories, which are simple, concise and easy to understand, the average of them, i.e. the half-interaction partition, is a very good approximation to the two-dimensional elasticity partition.

The orthotropic bi-layer case 1 gives a much larger difference between θ_1 and θ_1' than is normally expected for a composite lay-up with a larger number of plies and a lesser degree of anisotropy (compare Tables 5.1 and 5.2). Having a partition curve from the present Euler beam partition theory with substantially different θ_1 and θ_1' makes it substantially different to the corresponding partition curve from the present Timoshenko beam partition theory. This large difference might therefore have strained the accuracy of the approximate averaged partition rules. Despite this possibility, the agreement observed between the averaged partition rules and the results from FEM simulations with QUAD4 is good and for large parts of the range of M_2 is close.

The case 2 data is now presented. Since many of the observations are the same as for the case 1 data, they are not repeated. New observations are simply added. Tables 5.5 and 5.6 and Fig. 5.3 compare the results from the various analytical theories and numerical simulations.

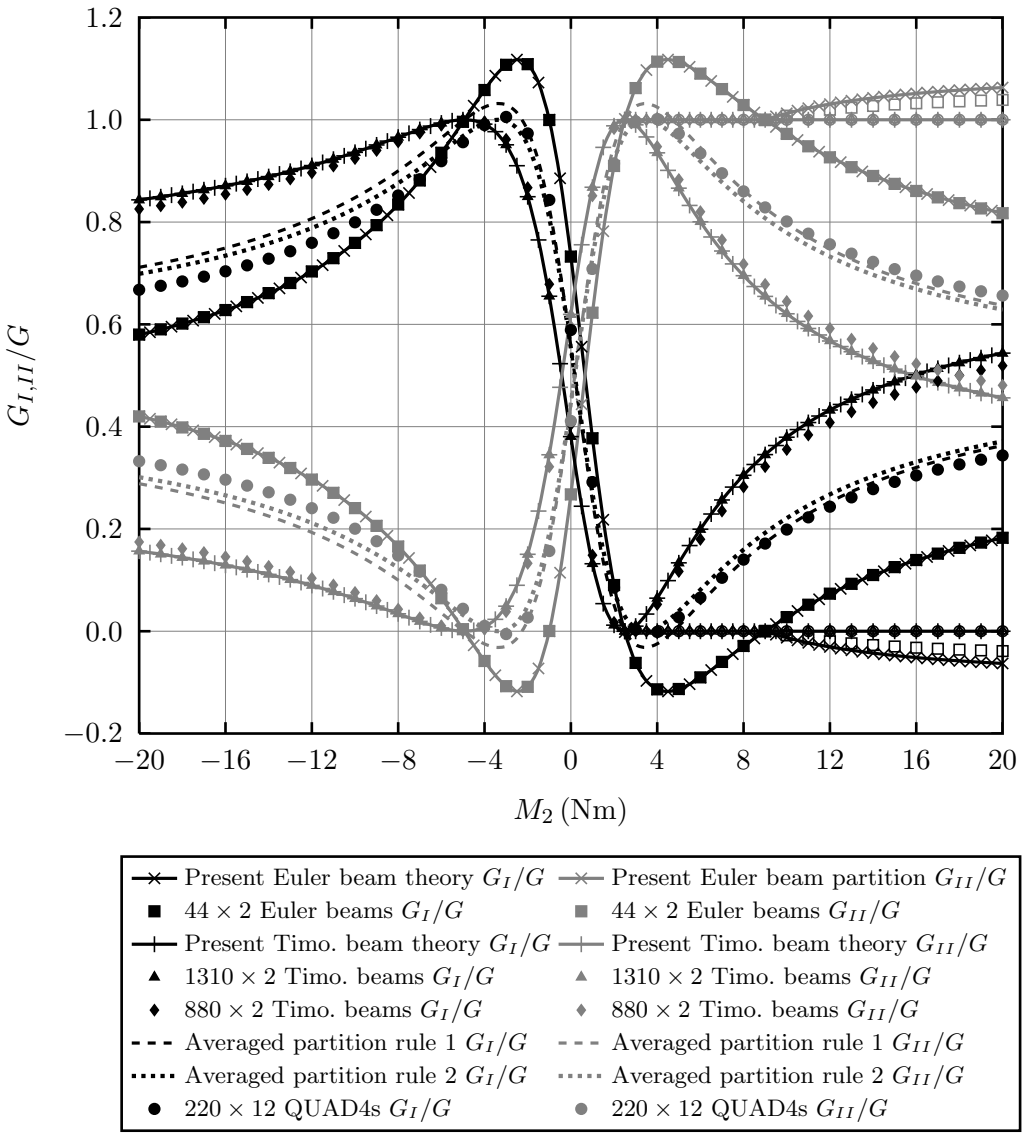

Figure 5.3: Comparisons between various theories and FEM results for case 2 with varying M_2 and $M_1 = 1\,\text{Nm}$, $N_1 = 0$, $N_2 = 0$, $P_1 = 0$, $P_2 = 0$.

The present Euler and Timoshenko beam partition theories are both very close to the corresponding numerical results. The pure modes are now much closer to the corresponding isotropic pure modes (see §4.2.2), which in comparison to the orthotropic bi-layer case, are also much closer together. The result of this is that the partition curves from the present Euler and Timoshenko beam partition theories are not so significantly different to each other. It might therefore be expected that the averaged partition rules would be very good approximations for the partition from two-dimensional elasticity. This is exactly what is observed. Also, as before, averaged partition rule 2 is closer to the results from the FEM simulations with QUAD4 elements than averaged partition rule 1 for most of the plotted range of M_2.

Table 5.5: Comparisons between various theories and FEM results for case 2 with varying M_2 and $M_1 = 1\,\text{Nm}$, $N_1 = 0$, $N_2 = 0$, $P_1 = 0$, $P_2 = 0$ and ignoring contact.

M_2 (Nm)	G_I/G (%)							
	Present Euler beam theory	44×2 Euler beams	Present Timo. beam theory	1310×2 Timo. beams	880×2 Timo. beams	Averaged rule 1	Averaged rule 2	220×12 QUAD4s
−20	57.97	58.00	84.34	84.32	82.55	71.15	69.88	66.76
−18	60.12	60.15	85.60	85.58	83.87	72.86	71.49	68.39
−16	62.76	62.80	87.09	87.08	85.44	74.93	73.43	70.37
−14	66.07	66.11	88.89	88.87	87.34	77.48	75.83	72.83
−12	70.32	70.35	91.05	91.03	89.64	80.68	78.84	75.94
−10	75.91	75.93	93.63	93.62	92.43	84.77	82.68	79.95
−8	83.42	83.44	96.59	96.58	95.70	90.00	87.60	85.20
−6	93.54	93.55	99.35	99.35	98.96	96.45	93.66	91.90
−4	105.83	105.82	99.15	99.15	99.60	102.49	99.34	98.96
−2	110.90	110.87	84.96	84.97	86.72	97.93	95.06	97.33
0	73.29	73.24	38.05	38.08	40.45	55.67	55.33	58.89
2	9.04	9.03	1.19	1.19	1.72	5.11	7.81	8.54
4	−11.38	−11.36	6.46	6.44	5.25	−2.46	0.69	−0.14
6	−9.06	−9.02	19.94	19.91	17.97	5.44	8.12	6.58
8	−2.92	−2.88	30.49	30.45	28.22	13.78	15.96	14.00
10	2.72	2.76	37.93	37.89	35.54	20.32	22.10	19.88
12	7.29	7.34	43.25	43.21	40.81	25.27	26.76	24.35
14	10.94	10.99	47.18	47.14	44.71	29.06	30.32	27.78
16	13.87	13.92	50.16	50.12	47.70	32.02	33.10	30.47
18	16.26	16.31	52.50	52.46	50.04	34.38	35.31	32.62
20	18.22	18.27	54.37	54.34	51.92	36.30	37.12	34.37

Table 5.6: Comparisons between various theories and FEM results for case 2 contact with varying M_2 and $M_1 = 1\,\text{Nm}$, $N_1 = 0$, $N_2 = 0$, $P_1 = 0$, $P_2 = 0$.

	Crack tip contact		DCB tip contact		After DCB tip contact	
	M_2 (Nm)	G_I/G (%)	M_2 (Nm)	G_I/G (%)	M_2 (Nm)	G_I/G (%)
Present Euler beam theory	8.99	0	8.99	0	20	−6.30
44×2 Euler beams	8.97	0	8.99	0	20	−3.88
Present Timo. beam theory	2.49	0	-	-	20	0
1310×2 Timo. beams	2.49	0	-	-	20	0
880×2 Timo. beams	2.73	0	-	-	20	0
220×2 Timo. beams	3.36	0	8.07	0	20	0
110×2 Timo. beams	4.03	0	8.05	0	20	0
Averaged rule 1	4.75	0	-	-	20	0
Averaged rule 2	3.44	0	-	-	20	0
220×12 QUAD4s	4.07	0	-	-	20	0

5.3.2 Tests with DCB tip axial forces

In this set of simulations, M_1 was held constant at 1 Nm and N_1 was varied. Results from the various analytical theories and numerical simulations are presented in Tables 5.7 and 5.8 and Fig. 5.4 for case 1. The results from the Euler beam partition theory are in excellent agreement with the results from the simulations using Timoshenko beam elements and very large out-of-plane shear moduli. The $\left\{\varphi_{\theta_2}\right\}$, $\left\{\varphi_{\theta_2'}\right\}$ and $\left\{\varphi_{\beta_2}\right\}$ modes can be seen in the figure. From Table 5.1, the β_2' value is $-\infty$. There is therefore no DCB tip contact.

Results from the numerical simulations using Timoshenko beam elements with the normal out-of-plane shear moduli closely approach the Timoshenko partition theory when

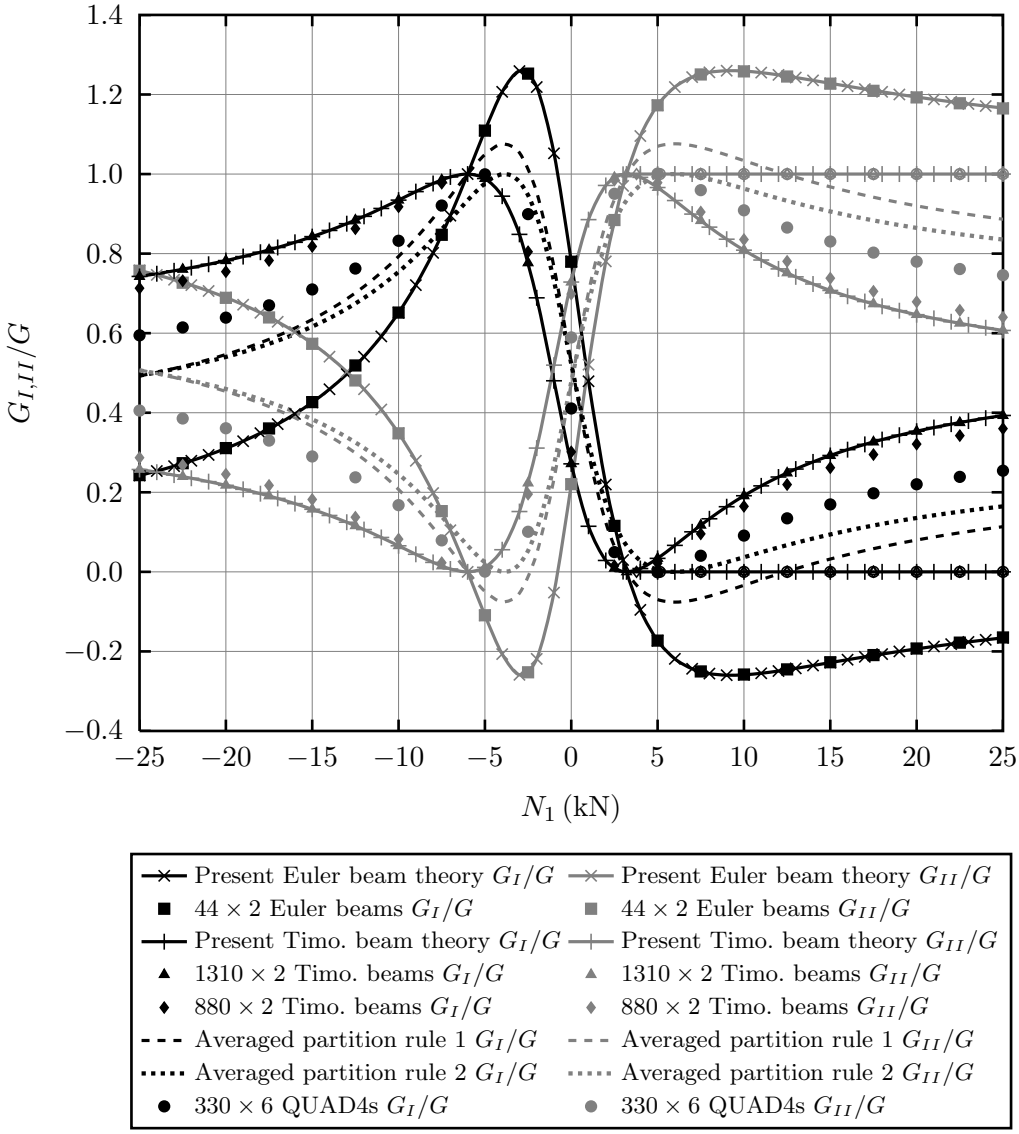

Figure 5.4: Comparisons between various theories and FEM results for case 1 with varying N_1 and $M_1 = 1\,\text{Nm}$, $M_2 = 0$, $N_2 = 0$, $P_1 = 0$, $P_2 = 0$.

Table 5.7: Comparisons between various theories and FEM results for case 1 with varying N_1 and $M_1 = 1\,\mathrm{Nm}$, $M_2 = 0$, $N_2 = 0$, $P_1 = 0$, $P_2 = 0$ and ignoring contact.

N_1 (kN)	G_I/G (%)							
	Present Euler beam theory	44×2 Euler beams	Present Timo. beam theory	1310×2 Timo. beams	880×2 Timo. beams	Averaged rule 1	Averaged rule 2	330×6 QUAD4s
−25	24.23	24.31	74.26	74.24	71.31	49.25	49.35	59.46
−20	31.03	31.11	78.25	78.22	75.46	54.64	54.03	63.90
−15	42.60	42.67	84.27	84.25	81.81	63.43	61.66	70.99
−10	65.13	65.18	93.45	93.43	91.78	79.29	75.42	83.23
−5	110.94	110.91	98.88	98.88	99.59	104.91	97.66	99.94
0	78.05	77.96	27.15	27.17	30.15	52.60	52.25	41.07
5	−17.32	−17.28	3.39	3.38	2.16	−6.97	0.56	−0.11
10	−25.89	−25.81	19.13	19.11	16.47	−3.38	3.67	9.11
15	−22.81	−22.72	29.26	29.23	26.18	3.22	9.40	16.95
20	−19.36	−19.27	35.35	35.33	32.12	8.00	13.54	22.02
25	−16.59	−16.49	39.31	39.28	36.00	11.36	16.46	25.42

Table 5.8: Comparisons between various theories and FEM results for case 1 contact with varying N_1 and $M_1 = 1\,\mathrm{Nm}$, $M_2 = 0$, $N_2 = 0$, $P_1 = 0$, $P_2 = 0$.

	Crack tip contact		DCB tip contact		After DCB tip contact	
	N_1 (kN)	G_I/G (%)	N_1 (kN)	G_I/G (%)	N_1 (kN)	G_I/G (%)
Present Timo. beam theory	3.20	0	-	-	100	0
1310×2 Timo. beams	3.20	0	-	-	100	0
880×2 Timo. beams	3.78	0	-	-	100	0
220×2 Timo. beams	5.51	0	93.34	0	100	0
110×2 Timo. beams	7.82	0	91.03	0	100	0
Averaged rule 1	12.40	0	-	-	100	0
Averaged rule 2	5.98	0	-	-	100	0
330×6 QUAD4s	5.13	0	-	-	100	0

880×2 elements are used. With the non-uniform mesh with 1310×2 elements, there is no discernible difference. In the Timoshenko partition theory, the $\left\{\varphi_{\beta_2'}\right\}$ and $\left\{\varphi_{\theta_2'}\right\}$ modes coincide with the $\left\{\varphi_{\beta_2}\right\}$ and $\left\{\varphi_{\theta_2}\right\}$ modes respectively. With 1310×2 Timoshenko beam elements, this is exactly what is observed. With 880×2 elements, there is a numerically generated second pure pair very close to the $\left\{\varphi_{\beta_2}\right\}$ and $\left\{\varphi_{\theta_2}\right\}$ pairs. With even fewer elements (and therefore a larger element length δa), the numerically generated second pure pair is further away still. The $\left\{\varphi_{\beta_2}\right\}$ mode is the point where crack tip running contact starts. If N_1/M_1 is increased beyond β_2 then eventually DCB tip contact occurs. After this, for this case the crack tip remains closed and $G_I/G = 0$. This can easily be shown by deriving the corresponding equations in §5.2.8 for M_1 and N_1.

Once more the results from FEM simulations with QUAD4 elements are approximated well by the averaged partition rules. Even when these numerical results begin to deviate from closely following averaged partition rule 1, they are still very much bound by the Euler and Timoshenko beam partition theories. As expected, averaged partition rule 2 does not have any regions of negative ERR. It is closer to the results from FEM simulations with QUAD4 elements over most of the plotted range of N_1.

Tables 5.9 and 5.10 and Fig. 5.5 present the results from the various analytical theories and numerical simulations for case 2. The Timoshenko partitions show some different characteristics to those seen previously. DCB tip contact and crack tip running contact occur at opposite ends of the range of N_1 and therefore DCB tip contact does not follow crack tip running contact (which occurs at $N_1/M_1 = \beta_2$) if N_1 is progressively increased. It is easily shown mathematically using the procedure in §5.2.8 that after DCB tip contact, the mode partition is mixed. There is excellent agreement between the analytical and corresponding numerical values over the whole range of N_1 looked at, including in the contact region. In the present Timoshenko beam partition theory, crack tip running contact occurs at $N_1/M_1 = \beta_2$, which here is a very large positive value (shown in Table 5.10). Numerically it was not possible to find N_1 for crack tip contact, with Timoshenko beam elements. This is attributed to numerical error. It is seen from Fig. 5.5 that G_I/G approaches the x-axis very slowly and that the numerical data points are on the high side. This suggests that with 1310×2 elements or less, the $\left\{\varphi_{\beta_2}\right\}$ mode is not resolved and that therefore crack tip contact never occurs. Finally, the very close agreement between both averaged partition rules and the two-dimensional FEM results is noted.

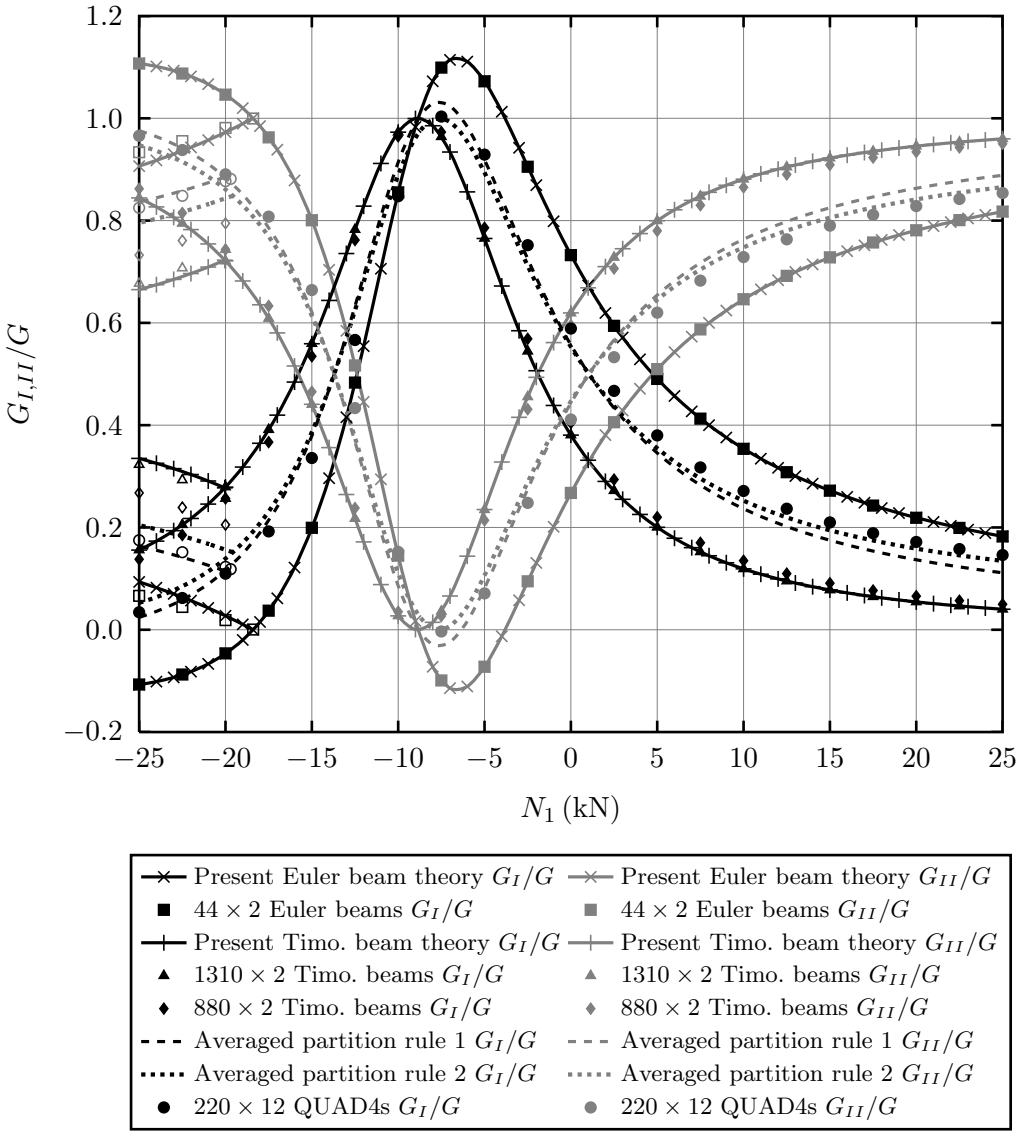

Figure 5.5: Comparisons between various theories and FEM results for case 2 with varying N_1 and $M_1 = 1\,\mathrm{Nm}$, $M_2 = 0$, $N_2 = 0$, $P_1 = 0$, $P_2 = 0$.

Table 5.9: Comparisons between various theories and FEM results for case 2 with varying N_1 and $M_1 = 1\,\text{Nm}$, $M_2 = 0$, $N_2 = 0$, $P_1 = 0$, $P_2 = 0$ and ignoring contact.

N_1 (kN)	G_I/G (%)							
	Present Euler beam theory	44×2 Euler beams	Present Timo. beam theory	1310×2 Timo. beams	880×2 Timo. beams	Averaged rule 1	Averaged rule 2	220×12 QUAD4s
−25	−10.74	−10.71	15.57	15.60	13.78	2.42	5.27	3.42
−20	−4.66	−4.62	27.88	27.91	25.67	11.61	13.91	10.96
−15	19.89	19.94	55.92	55.95	53.47	37.90	38.63	33.58
−10	85.50	85.51	97.29	97.28	96.48	91.39	88.91	84.77
−5	107.27	107.23	76.50	76.53	78.59	91.89	89.37	92.89
0	73.29	73.24	38.05	38.08	40.45	55.67	55.33	58.89
5	49.08	49.04	20.03	20.04	22.01	34.56	35.48	38.00
10	35.41	35.38	11.90	11.91	13.50	23.66	25.24	27.13
15	27.22	27.19	7.78	7.78	9.10	17.50	19.45	20.98
20	21.92	21.90	5.45	5.45	6.57	13.68	15.86	17.17
25	18.26	18.24	4.01	4.01	4.98	11.14	13.47	14.61

Table 5.10: Comparisons between various theories and FEM results for case 2 contact with varying N_1 and $M_1 = 1\,\text{Nm}$, $M_2 = 0$, $N_2 = 0$, $P_1 = 0$, $P_2 = 0$.

	Crack tip contact		DCB tip contact		After DCB tip contact	
	N_1 (kN)	G_I/G (%)	N_1 (kN)	G_I/G (%)	N_1 (kN)	G_I/G (%)
Present Euler beam theory	−18.40	0	−18.40	0	−25	9.35
44×2 Euler beams	−18.40	0	−18.40	0	−25	6.63
Present Timo. beam theory	17877.49	0	−20.04	27.74	−25	33.50
1310×2 Timo. beams	-	-	−20.04	27.77	−25	34.70
880×2 Timo. beams	-	-	−20.04	25.67	−25	32.29
220×2 Timo. beams	-	-	−20.04	20.53	−25	26.75
Averaged rule 1	-	-	−20.04	11.49	−25	16.37
Averaged rule 2	-	-	−19.58	15.15	−25	20.44
220×12 QUAD4s	-	-	−19.65	11.84	−25	17.51

5.3.3 Tests with DCB tip shear forces

In this set of simulations, P_1 was held constant at 1 N and P_2 was varied. There are therefore bending moments as well as shear forces at the crack tip. Under the present Euler beam partition theory, only the bending causes deflection. The Euler case therefore gives identical mode partitions to those in Table 5.3 and Fig. 5.2 for case 1 and Table 5.5 and Fig. 5.3 for case 2. In both cases however, after DCB tip contact, instead of being a mixed mode as has been the case previously in the present Euler beam partition theory, the crack tip remains just closed and $G_I/G = 0$. Obviously under the present Timoshenko beam partition theory, the shear forces have an additional effect and the theory in §5.2.7 must be used.

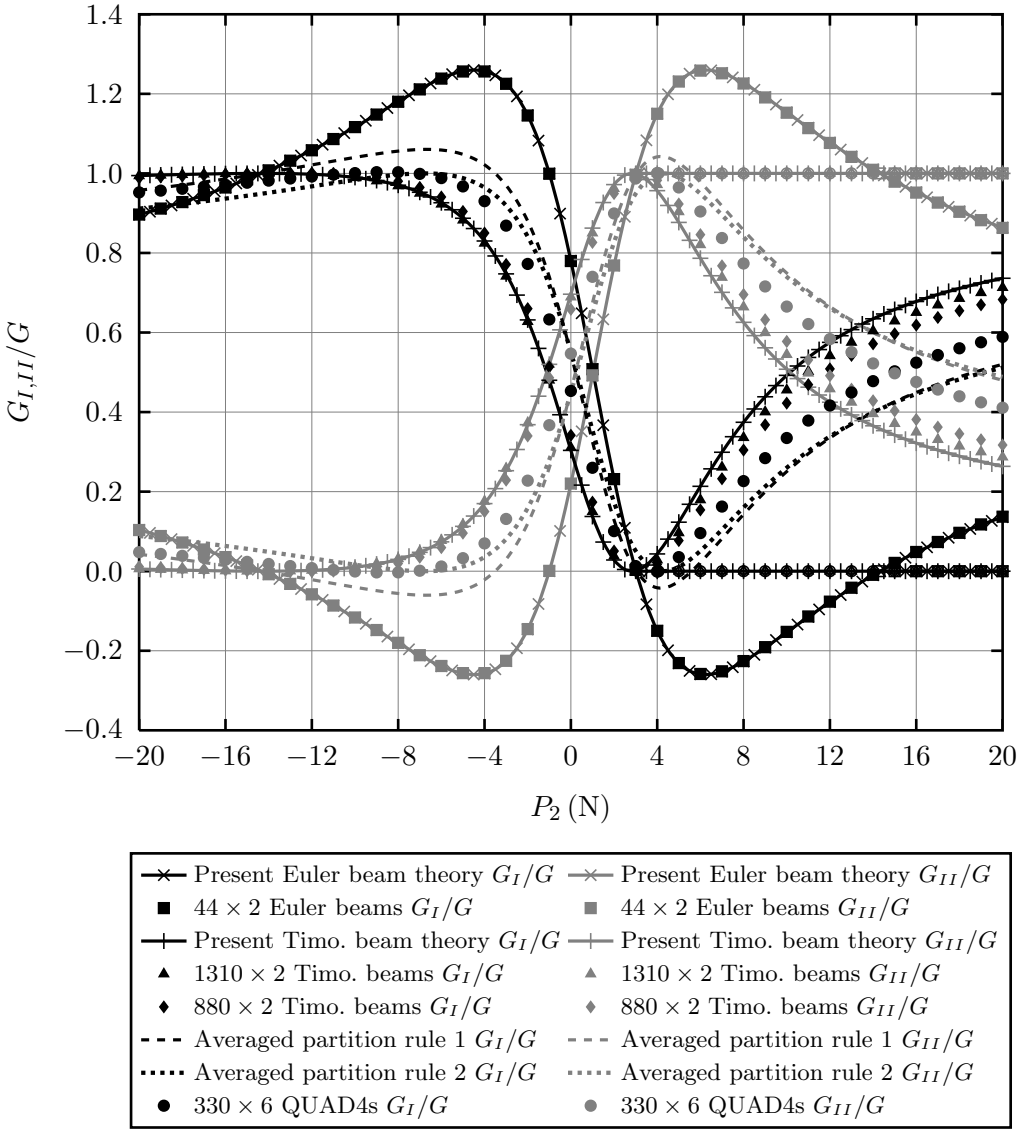

Figure 5.6: Comparisons between various theories and FEM results for case 1 with varying P_2 and $M_1 = 0$, $M_2 = 0$, $N_1 = 0$, $N_2 = 0$, $P_1 = 1$ N.

Table 5.11: Comparisons between various theories and FEM results for case 1 with varying P_2 and $M_1 = 0$, $M_2 = 0$, $N_1 = 0$, $N_2 = 0$, $P_1 = 1\,\mathrm{N}$ and ignoring contact.

P_2 (N)	G_I/G (%)							
	Present Euler beam theory	44×2 Euler beams	Present Timo. beam theory	1310×2 Timo. beams	880×2 Timo. beams	Averaged rule 1	Averaged rule 2	330×6 QUAD4s
−20	89.63	89.65	99.45	99.40	98.89	95.75	91.15	95.22
−18	92.77	92.79	99.72	99.70	99.33	97.09	92.33	96.14
−16	96.45	96.45	99.93	99.92	99.74	98.60	93.66	97.13
−14	100.76	100.76	100.00	100.00	100.04	100.29	95.14	98.18
−12	105.82	105.81	99.78	99.77	100.09	102.14	96.74	99.22
−10	111.66	111.64	98.99	98.93	99.62	104.03	98.36	100.07
−8	118.05	118.01	97.03	96.86	98.04	105.60	99.68	100.30
−6	123.89	123.83	92.62	92.27	94.07	105.87	99.81	98.82
−4	125.70	125.62	83.01	82.44	85.01	102.16	96.45	93.02
−2	114.64	114.55	63.17	62.75	66.00	88.03	84.13	77.24
0	78.05	77.97	30.37	31.08	34.17	54.69	55.11	45.31
2	23.18	23.15	2.82	3.80	5.06	12.86	17.32	10.07
4	−15.01	−14.98	4.34	2.83	1.73	−4.17	0.24	−0.10
6	−25.90	−25.83	21.34	17.93	15.40	2.19	5.11	9.58
8	−22.69	−22.60	37.44	33.58	30.46	14.27	16.03	22.65
10	−15.36	−15.25	49.23	45.55	42.24	25.05	26.01	33.48
12	−7.77	−7.66	57.53	54.17	50.86	33.48	33.87	41.65
14	−1.02	−0.91	63.45	60.41	57.16	39.94	39.90	47.77
16	4.72	4.83	67.80	65.04	61.87	44.93	44.56	52.42
18	9.54	9.65	71.09	68.56	65.47	48.86	48.23	56.04
20	13.59	13.70	73.64	71.30	68.29	52.00	51.16	58.90

Tables 5.11 and 5.12 and Fig. 5.6 present the results from the various analytical theories and numerical simulations for case 1. It is clear that the numerical results with Timoshenko beams converge towards the present Timoshenko beam partition theory. For averaged partition rule 1, whereas previously it lay halfway between the present Euler and Timoshenko beam partition curves, from Eq. (5.81) it is seen that G_I has additional components G_P and $\alpha_{\theta_1}\Delta G_{\theta_1 P}$ due to the shearing effect. The curve from averaged partition rule 1 is therefore not the average of the Euler and Timoshenko beam partition theories in this case. It is seen that the results from the two-dimensional FEM simulations closely follow averaged partition rule 1. Averaged partition rule 2 removes the small regions of negative ERR partitions, which are predicted by averaged partition rule 1, and as a result is even closer to the two-dimensional FEM simulations over most of the plotted range of P_2.

Tables 5.13 and 5.14 and Fig. 5.7 present the results from the various analytical theories and numerical simulations for case 2. In all cases, the agreement between the analytical theories and the corresponding numerical results is excellent.

Table 5.12: Comparisons between various theories and FEM results for case 1 contact with varying P_2 and $M_1 = 0$, $M_2 = 0$, $N_1 = 0$, $N_2 = 0$, $P_1 = 1\,\mathrm{N}$.

	Crack tip contact		DCB tip contact		After DCB tip contact	
	P_2 (N)	G_I/G (%)	P_2 (N)	G_I/G (%)	P_2 (N)	G_I/G (%)
Present Euler beam theory	14.33	0	14.33	0	20	0
44×2 Euler beams	14.29	0	14.32	0	20	0
Present Timo. beam theory	3.02	0	-	-	20	0
1310×2 Timo. beams	3.02	0	-	-	20	0
880×2 Timo. beams	3.39	0	-	-	20	0
220×2 Timo. beams	4.36	0	11.32	0	20	0
Averaged rule 1	3.02	0	-	-	20	0
Averaged rule 2	3.39	0	-	-	20	0
330×6 QUAD4s	4.06	0	-	-	20	0

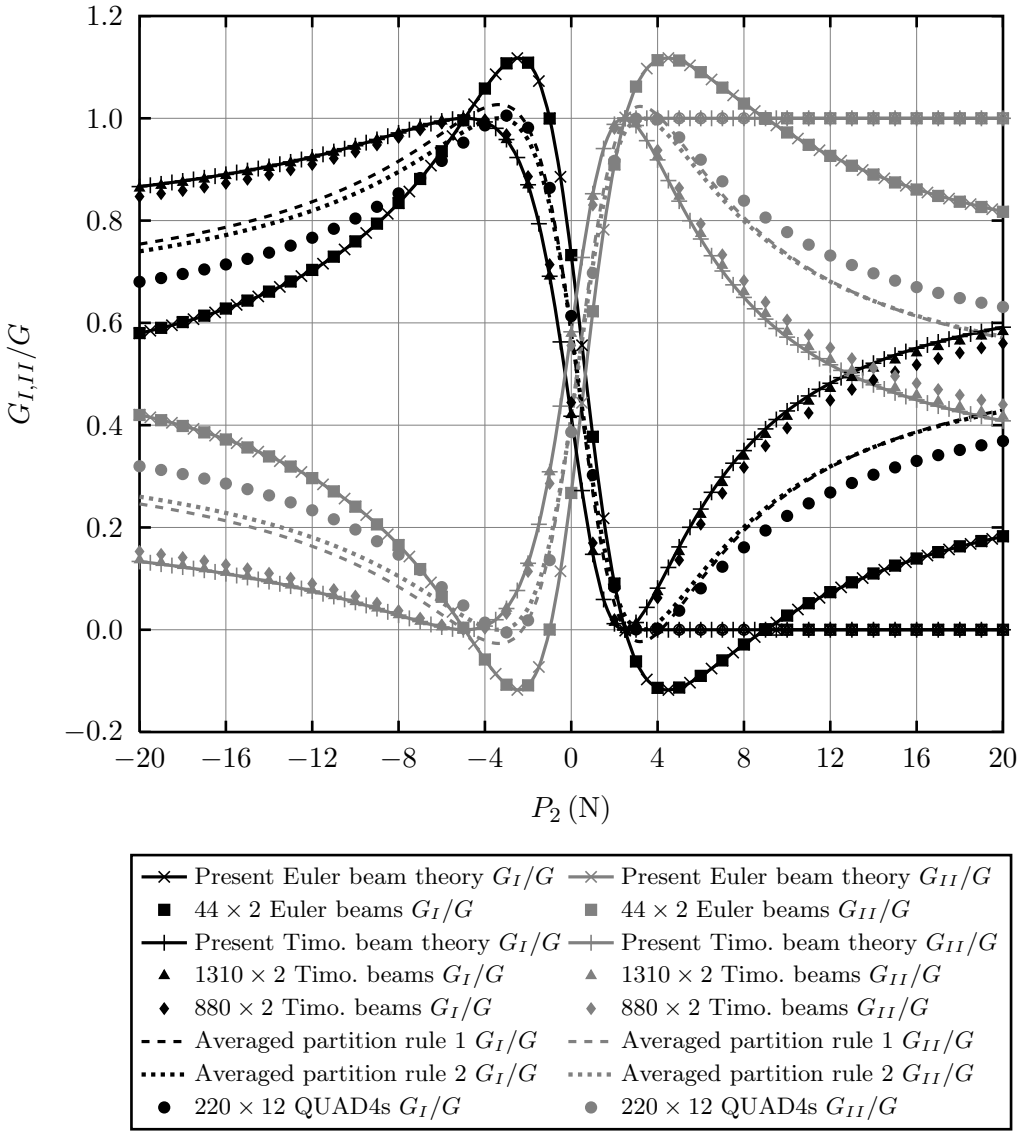

Figure 5.7: Comparisons between various theories and FEM results for case 2 with varying P_2 and $M_1 = 0$, $M_2 = 0$, $N_1 = 0$, $N_2 = 0$, $P_1 = 1\,\mathrm{N}$.

Table 5.13: Comparisons between various theories and FEM results for case 2 with varying P_2 and $M_1 = 0$, $M_2 = 0$, $N_1 = 0$, $N_2 = 0$, $P_1 = 1\,\mathrm{N}$ and ignoring contact.

P_2 (N)	$G_I/G\,(\%)$							
	Present Euler beam theory	44×2 Euler beams	Present Timo. beam theory	1310×2 Timo. beams	880×2 Timo. beams	Averaged rule 1	Averaged rule 2	220×12 QUAD4s
−20	57.97	58.01	86.64	86.34	84.70	75.40	73.99	68.03
−18	60.12	60.16	87.74	87.46	85.88	76.89	75.43	69.56
−16	62.76	62.80	89.04	88.79	87.28	78.70	77.16	71.42
−14	66.07	66.11	90.58	90.37	88.96	80.92	79.29	73.73
−12	70.32	70.36	92.44	92.27	90.98	83.68	81.94	76.64
−10	75.91	75.94	94.64	94.52	93.42	87.18	85.29	80.40
−8	83.42	83.44	97.14	97.08	96.26	91.62	89.53	85.32
−6	93.54	93.55	99.46	99.45	99.09	97.03	94.67	91.67
−4	105.83	105.82	99.28	99.28	99.69	102.09	99.44	98.61
−2	110.90	110.87	87.00	86.94	88.60	98.21	95.76	98.16
0	73.29	73.25	41.75	42.06	44.43	58.31	58.48	61.34
2	9.04	9.03	1.19	1.43	1.97	5.11	7.81	8.33
4	−11.38	−11.36	8.13	7.43	6.24	−0.63	1.35	0.21
6	−9.06	−9.02	23.60	22.54	20.64	9.76	10.92	8.09
8	−2.92	−2.87	35.02	33.92	31.75	19.40	20.07	16.11
10	2.72	2.77	42.78	41.71	39.45	26.55	26.91	22.25
12	7.29	7.35	48.19	47.17	44.87	31.78	31.93	26.84
14	10.94	11.00	52.11	51.13	48.82	35.69	35.69	30.31
16	13.87	13.93	55.06	54.12	51.81	38.69	38.59	33.01
18	16.26	16.31	57.34	56.43	54.13	41.06	40.88	35.15
20	18.22	18.28	59.16	58.28	55.99	42.98	42.72	36.89

Table 5.14: Comparisons between various theories and FEM results for case 2 contact with varying P_2 and $M_1 = 0$, $M_2 = 0$, $N_1 = 0$, $N_2 = 0$, $P_1 = 1\,\mathrm{N}$.

	Crack tip contact		DCB tip contact		After DCB tip contact	
	P_2 (N)	G_I/G (%)	P_2 (N)	G_I/G (%)	P_2 (N)	G_I/G (%)
Present Euler beam theory	8.99	0	8.99	0	10	0
44×2 Euler beams	8.97	0	8.98	0	10	0
Present Timo. beam theory	2.49	0	-	-	10	0
1310×2 Timo. beams	2.50	0	-	-	10	0
880×2 Timo. beams	2.71	0	-	-	10	0
220×2 Timo. beams	3.29	0	7.31	0	10	0
Averaged rule 1	4.15	0	-	-	10	0
Averaged rule 2	3.29	0	-	-	10	0
220×12 QUAD4s	3.91	0	-	-	10	0

5.4 Conclusion

The work in Chapter 4 on the mode partition of fractures in layered isotropic homogeneous DCBs has been successfully extended to laminated composite DCBs. In this chapter, completely analytical theories for mode partitioning have been developed based on the Euler and Timoshenko laminated composite beam theories.

Both the present Euler and Timoshenko beam partition theories have the same first set of pure modes $\left\{\varphi_{\theta_i}\right\}$ and $\left\{\varphi_{\beta_i}\right\}$ $(i = 1, 2, 3)$. In the present Euler beam partition theory, there is a second set of pure modes $\left\{\varphi_{\theta'_i}\right\}$ and $\left\{\varphi_{\beta'_i}\right\}$, which is different to the first set. In the present Timoshenko beam partition theory, the second set of pure modes coincides with the first set. Therefore it is the first set of pure modes which forms a complete basis for mixed-mode partitioning.

Unobvious stealthy interactions exist between the mode I $\left\{\varphi_{\theta_i}\right\}$ modes and the mode II $\left\{\varphi_{\beta_i}\right\}$ modes in the present Euler beam partition theory. These interactions do not exist in the present Timoshenko beam partition theory. This is what leads to the second set of pure modes coinciding with the first set in the present Timoshenko beam partition theory.

The present Euler and Timoshenko beam partition theories agree very well with the corresponding beam FEM predictions. Approximate 'averaged partition rules' have also been established. Averaged partition rule 1 halves the interactions between the mode I $\left\{\varphi_{\theta_i}\right\}$ modes and the mode II $\left\{\varphi_{\beta_i}\right\}$ modes in the Euler beam partition theory. Averaged partition rule 2 removes the small regions of negative ERR partitions (where the total ERR is still non-negative) by using the points of minimum G_I/G and G_{II}/G from averaged partition rule 1 as pure modes. Both approximations agree very well with results from FEM simulations with QUAD4 elements, even when the difference between the curves from the Euler and Timoshenko beam partition theories is substantial and the accuracy of the approximation might have become strained. Generally, averaged partition rule 2 is closer than averaged partition rule 1.

The contact behaviour was also investigated and two types of contact can exist: crack tip running contact, which results in a region of pure mode II ERR; and point contact at the DCB tip, which can result in either in mixed modes or pure mode II ERR. The analytical framework for determining the contact behaviour of a specimen was laid-down for a single loading scenario, which can easily be repeated for other cases.

So far, all the work has focused on DCBs. Now that the fundamental theory for layered isotropic homogeneous and laminated composite DCBs has been established, a natural question is, how does the theory apply to more complex structures? This is the subject of the next chapter, where straight beam structures and axisymmetric plates are considered.

Chapter 6

Fractured beam and plate structures

Contents

6.1 Introduction

The analytical and numerical models developed in the preceding chapters for the mode partitioning of layered isotropic homogeneous and laminated composite DCBs are readily applicable to a wide range of engineering structures. The fundamental theory has been developed for DCBs since these are considered to be the simplest example of one-dimensional fracture. However real engineering structures are considerably more complex. This chapter continues with the study of one-dimensional fracture, but in more complex structures. The theory is extended to fractures in layered isotropic homogeneous and laminated composite straight beams. Some consideration is also briefly given to fractures in layered isotropic annuli and circular plates.

Although fracture of engineering materials or structures is in general a three-dimensional mechanical problem, study of one-dimensional fracture is still greatly important for several reasons. One-dimensional fracture is often used in experimental tests, such as DCB, ELS, ENF and MMB, to obtain critical ERR or toughness of a material in either pure

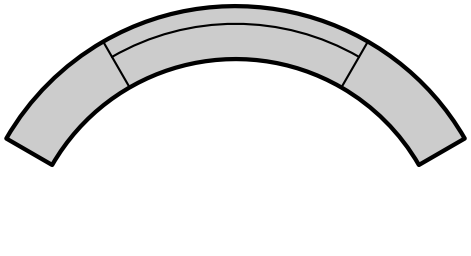

(a) Fractured curved beam.

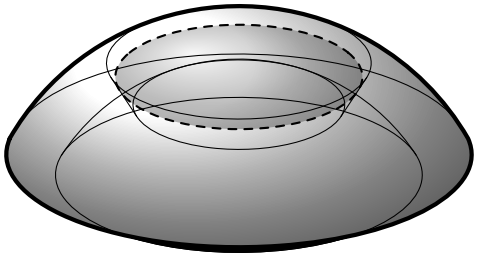

(b) Fractured shell.

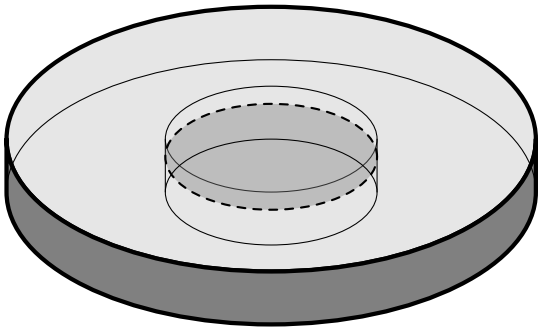

(c) Fractured plate.

Figure 6.1: Some engineering structures with one-dimensional fracture.

mode I or mode II fracture. In the case of a mixed mode, it is often used to investigate fracture propagation criteria. Moreover, many practical fractures in materials can be approximated as one-dimensional fracture. The most common ones are through-width fracture in straight or curved beams, circular ring-type fracture in plates and shells in a drilling process, separation of two material layers in a bio-cell under a needle puncture, separation of stiffeners and skins in stiffened plate or shell panels, etc. Fig. 6.1 shows some examples of one-dimensional cracks or delaminations in engineering structures composed of isotropic homogeneous or laminated composite materials.

Parts of this chapter have been published in Wang and Harvey (2012*c*). Further publications from this work are in preparation in Harvey et al. (2012) and Harvey and Wang (2012*b*).

6.2 Clamped-clamped isotropic homogeneous beams

As shown in the preceding chapters, ERR is a local quantity, affected only by the forces at the crack tip. If all these forces are known, then the ERRs for any one-dimensional fracture can be found in the same way as for isotropic homogeneous DCBs (see Chapter 4) and laminated composite DCBs (see Chapter 5). This is now demonstrated for a variety of beam structures.

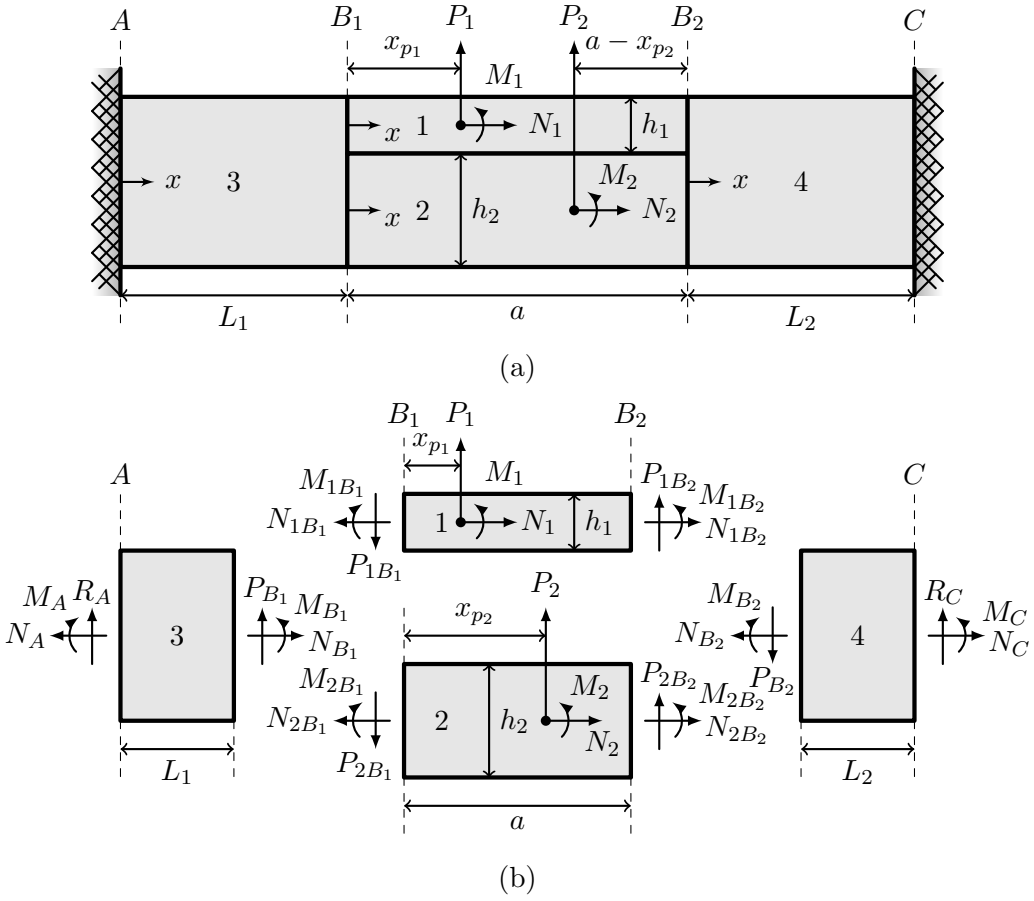

Figure 6.2: A clamped-clamped beam with a fracture and its loading conditions. (a) General description. (b) Force diagram of each beam.

6.2.1 Governing equations

A general clamped-clamped beam with a fracture is shown in Fig. 6.2. Contact between the upper and lower beams is not treated initially. With reference to Fig. 6.2 and using the constitutive relation from Timoshenko beam theory for isotropic materials, the following are easily derived:

$$\psi_{1,2} = \frac{1}{EI_{1,2}}\left(M_{1,2B_1}x - \frac{P_{1,2B_1}x^2}{2} - M_{1,2}\left\langle x - x_{p_{1,2}}\right\rangle + \frac{P_{1,2}}{2}\left\langle x - x_{p_{1,2}}\right\rangle^2\right) + \psi_{1,2B_1} \tag{6.1}$$

$$\begin{aligned} w_{1,2} = \frac{1}{EI_{1,2}}&\left(\frac{M_{1,2B_1}x^2}{2} - \frac{P_{1,2B_1}x^3}{6} - \frac{M_{1,2}}{2}\left\langle x - x_{p_{1,2}}\right\rangle^2 + \frac{P_{1,2}}{6}\left\langle x - x_{p_{1,2}}\right\rangle^3\right) \\ &+ \psi_{1,2B_1}x + w_{1,2B_1} + \frac{1}{bh_{1,2}\kappa\mu}\left(P_{1,2B_1}x - P_{1,2}\left\langle x - x_{p_{1,2}}\right\rangle\right) \end{aligned} \tag{6.2}$$

$$\psi_3 = \frac{1}{EI}\left(\frac{R_A x^2}{2} - M_A x\right) \quad \text{and} \quad w_3 = \frac{1}{EI}\left(\frac{R_A x^3}{6} - \frac{M_A x^2}{2}\right) + \frac{P_{B_1}x}{bh\kappa\mu} \tag{6.3}$$

$$\psi_4 = \frac{1}{EI}\left(M_{B_2}x - M_{B_2}L_2 - \frac{P_{B_2}x^2}{2} + \frac{P_{B_2}L_2^2}{2}\right) \tag{6.4}$$

$$w_4 = \frac{1}{EI}\left(\frac{M_{B_2}x^2}{2} - M_{B_2}L_2x + \frac{M_{B_2}L_2^2}{2} - \frac{P_{B_2}x^3}{6} + \frac{P_{B_2}L_2^2x}{2} - \frac{P_{B_2}L_2^3}{3}\right) + \frac{P_{B_2}x}{bh\kappa\mu} \quad (6.5)$$

Subscripts 1 and 2 refer to the upper and lower beams respectively. Subscripts 3 and 4 refer to the left- and right-hand intact laminates respectively. As shown in Fig. 6.2 (a), the origin of x in these equations depends on the beam in question: it is at the left crack tip and to the right for beams 1 and 2; for beams 3 and 4 it is at the respective left-hand sides and to the right. Positive deflection, w is always upwards and the rotations dw/dx and ψ are positive in the anticlockwise direction. The angle brackets are Macaulay brackets, denoting the ramp function. The axial displacements of the beams are

$$u_{1,2} = \frac{1}{bEh_{1,2}}\left(N_{1,2B_1}x - N_{1,2}\left\langle x - x_{p_{1,2}}\right\rangle\right) + u_{1,2B_1} \quad (6.6)$$

$$u_3 = \frac{N_{B_1}x}{bEh} \quad \text{and} \quad u_4 = \frac{1}{bEh}\left(N_{B_2}x - N_{B_2}L_2\right) \quad (6.7)$$

Equilibrium can be used to describe all the forces in Fig. 6.2 (b) in terms of the six left crack tip forces $M_{1,2B_1}$, $N_{1,2B_1}$, $P_{1,2B_1}$ and the applied loads $M_{1,2}$, $N_{1,2}$, $P_{1,2}$.

$$R_A = -P_{B_1}; \quad M_A = -M_{B_1} - P_{B_1}L_1 \quad \text{and} \quad N_A = N_{B_1} \quad (6.8)$$

$$R_C = P_{B_2}; \quad M_C = P_{B_2}L_2 - M_{B_2} \quad \text{and} \quad N_C = N_{B_2} \quad (6.9)$$

$$M_{B_{1,2}} = M_{1B_{1,2}} + M_{2B_{1,2}} + \left(h_1N_{2B_{1,2}} - h_2N_{1B_{1,2}}\right)/2 \quad (6.10)$$

$$N_{B_{1,2}} = N_{1B_{1,2}} + N_{2B_{1,2}} \quad \text{and} \quad P_{B_{1,2}} = P_{1B_{1,2}} + P_{2B_{1,2}} \quad (6.11)$$

$$M_{1,2B_2} = M_{1,2B_1} - M_{1,2} - aP_{1,2B_1} + P_{1,2}\left(a - x_{p_{1,2}}\right) \quad (6.12)$$

$$N_{1,2B_2} = N_{1,2B_1} - N_{1,2} \quad \text{and} \quad P_{1,2B_2} = P_{1,2B_1} - P_{1,2} \quad (6.13)$$

Eqs. (6.1) to (6.7) therefore contain 12 unknown quantities: the six left crack tip forces $M_{1,2B_1}$, $N_{1,2B_1}$, $P_{1,2B_1}$ and the deflections, rotations and axial displacements at the left crack tip $w_{1,2B_1}$, $\psi_{1,2B_1}$, $u_{1,2B_1}$. 12 boundary conditions are therefore required to enforce continuity at the crack tip. There is continuity of deflection at the two crack tips.

$$w_{1B_1} = w_{2B_1} = (w_3)_{x=L_1} \quad \text{and} \quad (w_1)_{x=a} = (w_2)_{x=a} = (w_4)_{x=0} \quad (6.14)$$

There is also continuity of rotation at the two crack tips but this boundary condition requires special consideration. In recent work (Wang and Harvey 2012*c*), the mode partitioning of statically indeterminate beam structures was briefly considered in cases where the shear modulus is finite, but the through-thickness shear effect is still small relative to bending. It was therefore sufficient to use the following approximation:

$$\psi_{1B_1} = \psi_{2B_1} = (\psi_3)_{x=L_1} \quad \text{and} \quad (\psi_1)_{x=a} = (\psi_2)_{x=a} = (\psi_4)_{x=0} \quad (6.15)$$

When considering statically determinate structures, such as DCBs, this boundary condition (approximate or otherwise) is not required, and the partition is exact. This is because the

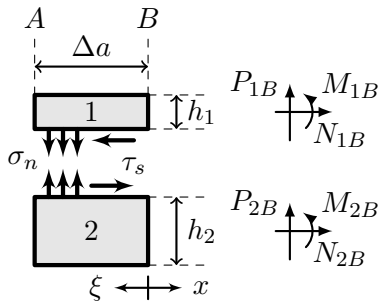

Figure 6.3: Details of the Δa-length crack influence region.

crack tip forces, which determine the ERR partition, can be calculated exactly from equilibrium considerations alone. For statically indeterminate structures, such as those in this chapter, the crack tip forces are calculated by considering equilibrium and compatibility together and continuity boundary conditions at the crack tip become necessary.

In this chapter, the correct boundary condition is derived and used instead of the approximation in Eq. (6.15). In reality, due to the normal and shear stress distribution on the interface ahead of the crack tip, the shear strain is not generally constant through the thickness. The rotations ψ_1 and ψ_2 are indeed continuous across the crack tips (although the mid-surface rotations dw_1/dx and dw_2/dx are not) but they are not equal. One way to represent the mechanics is to model the intact side of each crack tip using two Timoshenko beams with normal and shear stress distributions on the interface and continuous rotations across the crack tip. This would be both complex and incompatible with Eqs. (6.3) to (6.5). Instead, the method used in this work, which turns out to be very accurate, is to use a single Timoshenko beam to model the intact side of each crack tip, and account for the presence of the normal and shear stress distributions on the interface with discontinuous rotations $\psi_{1,2}$ across the crack tip. This is justified because the region affected by the crack tip is small.

Consider the region around a crack tip, as shown in Fig. 6.3. The origin of the ξ coordinate is at the crack tip B and towards the left; As before, the deflection w is upwards and the rotations dw/dx and ψ are positive in the anticlockwise direction. The interface stresses in the figure show only the sign convention rather than any representative distribution. Within the region affected by the crack tip, the through-thickness shearing equations from Timoshenko beam theory are

$$bh_{1,2}\kappa\mu\left(\frac{dw_{1,2}}{dx}-\psi_{1,2}\right)=P_{1,2B}\mp b\int_0^{\xi}\sigma_n\,d\xi \tag{6.16}$$

The mid-surface rotations dw_1/dx and dw_2/dx are discontinuous at the crack tip but for a rigid interface, it can be assumed that $(dw_1/dx)_{\xi=\delta a}=(dw_2/dx)_{\xi=\delta a}$, which are the rotations of beams 1 and 2 at a very small distance δa ahead of the crack tip B. Since the rotations and ψ_1 and ψ_2 are continuous and δa is very small, $(\psi_{1,2})_{\xi=\delta a}=\psi_{1,2B}$.

Also, if the intact side of the crack tip is modelled with a single Timoshenko beam across the thickness, then $(dw_{1,2}/dx)_{\xi=\delta a} = (dw/dx)_B$. The rotation boundary conditions are therefore

$$\psi_{1,2B_1} = \left(\frac{dw_3}{dx}\right)_{x=L_1} - \frac{P_{1,2B_1} \mp F_{nB_1}}{bh_{1,2}\kappa\mu} \tag{6.17}$$

$$\psi_{1,2B_2} = \left(\frac{dw_4}{dx}\right)_{x=0} - \frac{P_{1,2B_2} \mp F_{nB_2}}{bh_{1,2}\kappa\mu} \tag{6.18}$$

where $F_{nB} = b\int_0^{\delta a} \sigma_n \, d\xi$, which is the crack tip opening force. Note that Eqs. (6.17) and (6.18) reduce to Eq. (6.15) for Euler beams, for which $bh\kappa\mu \to \infty$. The crack tip opening force F_{nB} is known from the previously established mode partition theory for one-dimensional fracture in isotropic homogeneous DCBs. It is given by the sum of Eqs. (4.36) and (4.88), i.e.

$$F_{nB} = \alpha_{\theta_1} F_{nB\theta_1} + F_{nBP} \tag{6.19}$$

where $F_{nB\theta_1}$ is the crack tip opening force in the $\left\{\varphi_{\theta_1}\right\}$ mode, F_{nBP} is the crack tip opening force due to shearing, and α_{θ_1} is the partition coefficient for the $\left\{\varphi_{\theta_1}\right\}$ mode, which can be written in terms of the crack tip loads and the beam geometry. Full details are given in Chapter 4.

There is also continuity of axial displacement at the two crack tips.

$$u_{1,2B_1} = (u_3)_{x=L_1} \mp \frac{h_{2,1}}{2}(\psi_3)_{x=L_1} \tag{6.20}$$

$$(u_{1,2})_{x=a} = (u_4)_{x=0} \mp \frac{h_{2,1}}{2}(\psi_4)_{x=0} \tag{6.21}$$

The system of 12 equations, given by Eqs. (6.14), (6.17) (6.18), (6.20) and (6.21), can now be solved, giving all the unknown quantities in terms of the six independent variables $M_{1,2}$, $N_{1,2}$ and $P_{1,2}$. The resulting expressions for the unknowns in these equations are extensive. It is therefore more practical to present the Matlab script file that derives these expressions than to present the expressions themselves. This listing can be found in §C.1 in Appendix C.

6.2.2 Two sets of orthogonal pure modes

Unlike for DCBs, crack tip loads cannot be set independently of the loads applied at x_{p_1} and x_{p_2} and it is clearly not possible to obtain the pure mode vectors $\left\{\varphi_{\theta_1}\right\}$, $\left\{\varphi_{\beta_1}\right\}$ or $\left\{\varphi_{\beta_2}\right\}$ in isolation at a given crack tip. In this chapter, these modes are referred to as 'crack tip modes' because they relate crack tip quantities only. Some combinations of these modes can give pure mode I or II fractures. These modes are now derived for the *left* crack tip for the special case when $bh\kappa\mu \to \infty$ (Euler beam theory) and $\gamma \neq 1$; P_1 and P_2 are applied at the same location, i.e. $x_{p_1} = x_{p_2} = x_p$ and $M_1 = M_2 = N_1 = N_2 = 0$. These

fracture modes are now referred to as 'F modes' and denoted by a subscript F, because they relate the forces P_1 and P_2.

According to the present Euler beam partition theory, there are expected to be two sets of pure F modes, where the first set corresponds to zero relative shearing displacement just behind the crack tip (pure mode I) and zero normal force ahead of the crack tip (pure mode II). The second set corresponds to zero relative opening displacement just behind the crack tip (pure mode II) and zero crack tip shearing force (pure mode I).

Mathematically, the relative shearing displacement at an infinitely small distance δa behind the crack tip, $(D_{sh})_{x=\delta a}$ is expressed as

$$(D_{sh})_{x=\delta a} = (\overline{u}_1)_{x=\delta a} - (\overline{u}_2)_{x=\delta a} = (u_1)_{x=\delta a} + \frac{h_1}{2}(\psi_1)_{x=\delta a} - (u_2)_{x=\delta a} + \frac{h_2}{2}(\psi_2)_{x=\delta a} \quad (6.22)$$

where $\overline{u}$ represents the axial displacement at the interface. For the pure mode I mode from the first set, the relative shearing displacement at $x = \delta a$ is zero $(D_{sh})_{x=\delta a} = 0$. Making the necessary substitutions and taking the limit as $\delta a \to 0$ gives

$$\frac{P_2}{P_1} = \theta_F = -\frac{\gamma^2\left(C_1\gamma^2 - C_2\gamma + C_3\right)}{C_3\gamma^2 - C_2\gamma + C_1} \quad \text{and} \quad \left\{\varphi_{\theta_F}\right\} = \begin{Bmatrix} 1 \\ \theta_F \end{Bmatrix} \quad (6.23)$$

where

$$C_1 = 2x_p\left(a - x_p\right)^2\left(a + L_1 + L_2\right)^3 \quad (6.24)$$

$$C_2 = 2x_p\left(a - x_p\right)^2\left(C_7 + 3a^2\left(L_1 + L_2\right) - 2a^3\right) \quad (6.25)$$

$$\begin{aligned} C_3 = {} & 2a^3x_p^3 - ax_p^2\left(C_7 + 6a^2L_2 + 4a^3\right) \\ & + 2a^2x_p\left(C_7 - 3aL_1L_2 + 3a^2L_2 + a^3\right) - aC_8 \end{aligned} \quad (6.26)$$

$$C_7 = \left(L_1 + L_2\right)^3 + 3a\left(L_1 + L_2\right)^2 \quad (6.27)$$

$$C_8 = a^2L_1^2\left(L_1 + 3L_2 + 3a\right) \quad (6.28)$$

and $\left\{\varphi_F\right\}$ represents mode vector format $\begin{Bmatrix} P_1 & P_2 \end{Bmatrix}^T$. The orthogonal condition to the zero relative shearing displacement condition is zero normal force ahead of the crack tip. The mode corresponding to this condition could be derived by applying orthogonality through the ERR, however it is more convenient in this instance to simply enforce $F_{nB} = 0$. Noting that $F_{nB\theta_1}$ is infinite in present Euler beam partition theory and that therefore the finite F_{nBP} in Eq. (6.19) is negligible, the requirement for $F_{nB} = 0$ is simply $\alpha_{\theta_1} = 0$, which from Eq. (4.70) gives

$$\frac{P_2}{P_1} = \beta_F = \frac{\gamma^2\left(C_1\gamma^3 + C_4\gamma^2 + C_5\gamma + C_6\right)}{C_6\gamma^3 + C_5\gamma^2 + C_4\gamma + C_1} \quad \text{and} \quad \left\{\varphi_{\beta_F}\right\} = \begin{Bmatrix} 1 \\ \beta_F \end{Bmatrix} \quad (6.29)$$

where

$$C_4 = 2x_p\left(a - x_p\right)^2\left(2C_7 + 6a^2\left(L_1 + L_2\right) + 5a^3\right) \tag{6.30}$$

$$\begin{aligned} C_5 = {} & x_p^3\left(2C_7 + 6a^2\left(L_1 + L_2\right) + 14a^3\right) - ax_p^2\left(C_7 + 12a^2L_1 - 6a^2L_2 + 28a^3\right) \\ & - 2a^2x_p\left(2C_7 - 3a^2L_1 + 6a^2L_2 - 7a^3 - 9aL_1L_2\right) + 3aC_8 \end{aligned} \tag{6.31}$$

$$\begin{aligned} C_6 = {} & 6a^3x_p^3 - 3ax_p^2\left(C_7 + 6a^2L_2 + 4a^3\right) \\ & + 6a^2x_p\left(C_7 - 3aL_1L_2 + 3a^2L_2 + a^3\right) - 3aC_8 \end{aligned} \tag{6.32}$$

Now considering the second set of pure modes, the pure mode I mode is given by zero shear force at the crack tip. The shear force at the crack tip is

$$F_{sB} = \alpha_{\theta_1}F_{sB\theta_1} + \alpha_{\beta_1}F_{sB\beta_1} + \alpha_{\beta_2}F_{sB\beta_2} \tag{6.33}$$

The mode partition coefficients are known from Eq. (4.70) and the modal crack tip shear forces are known from simple calculations that run parallel with Eq. (4.40).

$$F_{sB\theta_1} = \frac{6\gamma\left(1-\gamma\right)}{h_1\left(1+\gamma\right)^2}; \quad F_{sB\beta_1} = \frac{6\gamma}{h_1\left(1+3\gamma\right)} \quad \text{and} \quad F_{sB\beta_2} = \frac{2\gamma^2}{h_1\left(\gamma^2-1\right)} \tag{6.34}$$

Making these substitutions and setting $F_{sB} = 0$ gives

$$\frac{P_2}{P_1} = \theta'_F = -1 \quad \text{and} \quad \left\{\varphi_{\theta'_F}\right\} = \begin{Bmatrix} 1 \\ \theta'_F \end{Bmatrix} \tag{6.35}$$

Finally, for the pure mode II mode from the second set, the relative opening displacement at $x = \delta a$ is zero $\left(D_{op}\right)_{x=\delta a} = 0$ where

$$\left(D_{op}\right)_{x=\delta a} = \left(w_1\right)_{x=\delta a} - \left(w_2\right)_{x=\delta a} \tag{6.36}$$

Making the necessary substitutions and taking the limit as $\delta a \to 0$ gives

$$\frac{P_2}{P_1} = \beta'_F = \gamma^3 \quad \text{and} \quad \left\{\varphi_{\beta'_F}\right\} = \begin{Bmatrix} 1 \\ \beta'_F \end{Bmatrix} \tag{6.37}$$

That θ'_F and β'_F, relating P_2 to P_1, are the same as θ'_1 and β'_1 respectively, which relate M_2 to M_1 (see §4.2.2), should be no surprise since the axial forces N_{1B} and N_{2B} induced at the crack tip by P_1 and P_2 obviously have no effect on the opening displacement. Also, if P_1 and P_2 are equal and opposite $P_2/P_1 = -1$, then regardless of how beams 1 and 2 deflect, beams 3 and 4 remain undeflected and the crack tip rotations are zero. Therefore N_{1B} and N_{2B} are both zero and the two crack tip bending moments are in the ratio of θ'_1. If P_1 and P_2 are applied in different locations then this would not be observed because each load would have a different moment arm around the crack tip.

If the above procedure is repeated for Timoshenko beams, it is found that the $\left\{\varphi_{\theta'_F}\right\}$ mode changes to coincide with the $\left\{\varphi_{\theta_F}\right\}$ mode, which is different to that obtained from the present Euler beam partition theory due to the static indeterminacy of clamped-clamped beams (the relative shearing displacement is otherwise not affected by through-thickness shear). Similarly the $\left\{\varphi_{\beta'_F}\right\}$ mode coincides with the $\left\{\varphi_{\beta_F}\right\}$ mode, which is also different to that obtained from present Euler beam partition theory. However for cases when the through-thickness shear effect is not excessively large, Eqs. (6.23) and (6.29) are good approximations. The expressions for the F modes from the present Timoshenko beam partition theory are not as simple as those for the F modes from the present Euler beam partition theory, so are not presented here. They are however easily derived for specific cases.

6.2.3 Contacting crack surfaces

For some values of P_1 and P_2, the beams either side of the fracture will come into contact. This raises two questions: (1) where is the point of first contact? And (2) what happens after contact?

To find the point of first contact x_c using Euler beam theory, the conditions are that the relative opening displacement must be both zero and a minimum at this point. The latter condition implies that it is the point of *first* contact.

$$(D_{op})_{x=x_c} = 0 \quad \text{and} \quad (\partial D_{op}/\partial x)_{x=x_c} = 0 \tag{6.38}$$

Solving these equations simultaneously for P_2/P_1 and x_c, and ignoring the obvious and unavailing solutions for the crack tips, gives

$$\frac{P_2}{P_1} = \gamma^3 = \beta'_F \tag{6.39}$$

for all values of x. This implies simultaneous contact everywhere along the fracture for this value of P_2/P_1.

If P_2/P_1 is increased beyond β'_F, the contact can either be at a point or distributed. Obviously, the solution must not allow interpenetration between the upper and lower beams anywhere. Furthermore, since linear elastic mechanics is being used, there can only be one valid solution. Therefore point contact at $x = x_p$, which is a reasonable assumption, will be considered and shown to satisfy the requirements, thus demonstrating that it is the correct solution.

Say that two loads P_{1c} and P_{2c} are applied to the beam at $x = x_p$ and that they cause point contact at this same location. Call the point contact force P_c. It acts to prevent non-physical interpenetration. The net shear loads P_1 and P_2 acting on the beams are therefore

$$P_1 = P_{1c} + P_c \quad \text{and} \quad P_2 = P_{2c} - P_c \tag{6.40}$$

Note that P_1 and P_2 in this equation are the same quantities that appear in all the equations thus far. The final condition that must be satisfied is

$$(D_{op})_{x=x_p} = 0 \tag{6.41}$$

Solving Eqs. (6.40) and (6.41) for P_1, P_2 and P_c gives

$$P_1 = \frac{P_{1c} + P_{2c}}{1+\gamma^3}; \quad P_2 = \frac{\gamma^3 (P_{1c} + P_{2c})}{1+\gamma^3} \quad \text{and} \quad P_c = \frac{P_{2c} - \gamma P_{1c}}{1+\gamma^3} \tag{6.42}$$

Substituting these equations into $D_{op} = w_1 - w_2$ reveals that $D_{op} = 0$ for all values of x. Therefore the requirements for physical contact behaviour are satisfied by this solution and the ERR partition is then found in the usual way.

According to the present Timoshenko beam partition theory, at $P_2/P_1 = \beta_F = \beta'_F$ there is both zero normal force ahead of the crack tip and zero relative opening displacement just behind. Therefore crack tip running contact occurs at $P_2/P_1 = \beta_F$ and pure mode II ERR is obtained. Since there is running contact, if the loading ratio P_2/P_1 is increased further then the crack tip remains closed as the contacting region grows.

6.3 Simply supported isotropic homogeneous beams

The theory presented in §6.2 is easily modified for isotropic homogeneous beams with simple supports at both ends. In this section, the modified theory is briefly summarised. For this new case, Eqs. (6.43) to (6.46) replace Eqs. (6.3) to (6.5) and (6.7).

$$\psi_3 = \frac{1}{EI}\left(\frac{R_A x^2}{2} - M_A x\right) + \psi_A \tag{6.43}$$

$$w_3 = \frac{1}{EI}\left(\frac{R_A x^3}{6} - \frac{M_A x^2}{2}\right) + \psi_A x + \frac{P_{B_1} x}{bh\kappa\mu} \tag{6.44}$$

$$\psi_4 = \frac{1}{EI}\left(M_{B_2} x - \frac{P_{B_2} x^2}{6}\right) + \psi_{B_2} \tag{6.45}$$

$$w_4 = \frac{1}{EI}\left(\frac{M_{B_2} x^2}{2} - \frac{M_{B_2} L_2^2}{2} - \frac{P_{B_2} x^3}{6} + \frac{P_{B_2} L_2^3}{6}\right) + \psi_{B_2}(x - L_2) + \frac{P_{B_2}(x - L_2)}{bh\kappa\mu} \tag{6.46}$$

Since zero rotation is no longer enforced at the supports, two additional boundary conditions are required at these locations. For simple supports these are

$$M_A = 0 = -P_{B_1} L_1 - M_{B_1} \quad \text{and} \quad M_C = 0 = P_{B_2} L_2 - M_{B_2} \tag{6.47}$$

When this new system of 14 equations is solved, all the unknown quantities are then known in terms of the independent variables P_1 and P_2. The resulting expressions for the unknowns are extensive. It is therefore more practical to present the Matlab script file that derives these expressions than to present the expressions themselves. This listing can be found in §C.2 in Appendix C. The system of equations is now solved for the left crack

tip for the special case when $bh\kappa\mu \to \infty$ (Euler beam theory). If the analysis is carried out for when $\gamma \neq 1$, for when P_1 and P_2 are applied at the same location, i.e. $x_{p_1} = x_{p_2} = x_p$, and for when $M_1 = M_2 = N_1 = N_2 = 0$, then the four pure mode relationships for both the left and right crack tips are

$$\frac{P_2}{P_1} = \theta_F = \frac{\gamma^2\left(C_1\gamma^2 - C_1\gamma - C_2\right)}{C_2\gamma^2 + C_1\gamma - C_1} \tag{6.48}$$

$$\frac{P_2}{P_1} = \beta_F = \frac{\gamma^2\left(C_1\gamma^3 + 2C_1\gamma^2 + C_3\gamma + C_4\right)}{C_4\gamma^3 + C_3\gamma^2 + 2C_1\gamma + C_1} \tag{6.49}$$

$$\frac{P_2}{P_1} = \theta'_F = -1 \quad \text{and} \quad \frac{P_2}{P_1} = \beta'_F = \gamma^3 \tag{6.50}$$

where

$$C_1 = 2x_p\left(a - x_p\right)^2\left(a + L_1 + L_2\right) \tag{6.51}$$

$$C_2 = C_5x_p^2 + ax_p\left(a^2 - 2C_5\right) + a^3L_1 \tag{6.52}$$

$$C_3 = 2x_p^3\left(a + L_1 + L_2\right) - C_5x_p^2 + ax_p\left(3a^2 - 4C_5\right) + 3a^3L_1 \tag{6.53}$$

$$C_4 = -3C_5x_p^2 + ax_p\left(6C_5 - 3a^2\right) - 3a^3L_1 \tag{6.54}$$

$$C_5 = a\left(a + L_1 + L_2\right) \tag{6.55}$$

The contact behaviour is found to be identical to the clamped-clamped case, i.e. contact between beams 1 and 2 at $P_2/P_1 = \gamma^3$ for all values of x and point contact at $x = x_p$ afterwards.

If the above procedure is repeated for Timoshenko beams then as before, it is found that the $\left\{\varphi_{\theta'_F}\right\}$ mode coincides with the $\left\{\varphi_{\theta_F}\right\}$ mode; the $\left\{\varphi_{\beta'_F}\right\}$ mode coincides with the $\left\{\varphi_{\beta_F}\right\}$ mode; and the $\left\{\varphi_{\theta_F}\right\}$ and $\left\{\varphi_{\beta_F}\right\}$ modes are different to those obtained from present Euler beam partition theory. However for cases when the through-thickness shear effect is not excessively large, Eqs. (6.48) and (6.49) are good approximations. The expressions for the F modes from the present Timoshenko beam partition theory are not so simple, so are not presented here. They are however easily derived for specific cases.

6.4 Clamped-clamped laminated composite beams

6.4.1 Governing equations

A general clamped-clamped laminated composite beam with a delamination now receives the same analysis. Contact between the upper and lower sub-laminates is not treated initially. The extensional, coupling, bending and shearing stiffness are denoted by A, B, D and H respectively. Subscripts 1 and 2 are used to indicate the upper and lower sub-laminates respectively. No subscript is used for the intact part of the laminate. A_1 is therefore the extensional stiffness of the upper sub-laminate and A is the extensional stiffness of the intact laminate, etc. With reference to Fig. 6.2 and using the constitutive

relation from §2.2.6 gives

$$\begin{Bmatrix} N_{1,2}(x)/b \\ -M_{1,2}(x)/b \\ P_{1,2}(x)/b \end{Bmatrix} = \begin{bmatrix} A_{1,2} & B_{1,2} & 0 \\ B_{1,2} & D_{1,2} & 0 \\ 0 & 0 & H_{1,2} \end{bmatrix} \begin{Bmatrix} du_{1,2}/dx \\ -d\psi_{1,2}/dx \\ dw_{1,2}/dx - \psi_{1,2} \end{Bmatrix} \tag{6.56}$$

$$\begin{Bmatrix} N_{3,4}(x)/b \\ -M_{3,4}(x)/b \\ P_{3,4}(x)/b \end{Bmatrix} = \begin{bmatrix} A & B & 0 \\ B & D & 0 \\ 0 & 0 & H \end{bmatrix} \begin{Bmatrix} du_{3,4}/dx \\ -d\psi_{3,4}/dx \\ dw_{3,4}/dx - \psi_{3,4} \end{Bmatrix} \tag{6.57}$$

where

$$N_{1,2}(x) = N_{1,2B_1} - N_{1,2}\left\langle x - x_{p_{1,2}}\right\rangle^0 \quad \text{and} \quad P_{1,2}(x) = P_{1,2B_1} - P_{1,2}\left\langle x - x_{p_{1,2}}\right\rangle^0 \tag{6.58}$$

$$M_{1,2}(x) = M_{1,2B_1} - P_{1,2B_1}x - M_{1,2}\left\langle x - x_{p_{1,2}}\right\rangle^0 + P_{1,2}\left\langle x - x_{p_{1,2}}\right\rangle \tag{6.59}$$

$$N_{3,4}(x) = N_{B_{1,2}} \quad \text{and} \quad P_{3,4}(x) = P_{B_{1,2}} \tag{6.60}$$

$$M_3(x) = M_{B_1} - P_{B_1}(x - L_1) \quad \text{and} \quad M_4(x) = M_{B_2} - P_{B_2}x \tag{6.61}$$

As shown in Fig. 6.2 (a), the origin of x in these equations depends on the beam in question: it is at the left crack tip and to the right for beams 1 and 2; for beams 3 and 4 it is at the respective left-hand sides and to the right. Positive deflection, w is always upwards and the rotations dw/dx and ψ are positive in the anticlockwise direction. From Eqs. (6.56) to (6.61), the following are easily derived:

$$\begin{aligned} \psi_{1,2} = {} & \frac{B_{1,2}\left(N_{1,2B_1}x - N_{1,2}\left\langle x - x_{p_{1,2}}\right\rangle\right)}{b\left(A_{1,2}D_{1,2} - B_{1,2}^2\right)} + \psi_{1,2B_1} \\ & + \frac{A_{1,2}\left(2M_{1,2B_1}x - 2M_{1,2}\left\langle x - x_{p_{1,2}}\right\rangle + P_{1,2}\left\langle x - x_{p_{1,2}}\right\rangle^2 - P_{1,2B_1}x^2\right)}{2b\left(A_{1,2}D_{1,2} - B_{1,2}^2\right)} \end{aligned} \tag{6.62}$$

$$\begin{aligned} w_{1,2} = {} & \frac{B_{1,2}\left(N_{1,2B_1}x^2 - N_{1,2}\left\langle x - x_{p_{1,2}}\right\rangle^2\right)}{2b\left(A_{1,2}D_{1,2} - B_{1,2}^2\right)} + \psi_{1,2B_1}x + w_{1,2B_1} \\ & + \frac{A_{1,2}\left(3M_{1,2B_1}x^2 - 3M_{1,2}\left\langle x - x_{p_{1,2}}\right\rangle^2 + P_{1,2}\left\langle x - x_{p_{1,2}}\right\rangle^3 - P_{1,2B_1}x^3\right)}{6b\left(A_{1,2}D_{1,2} - B_{1,2}^2\right)} \\ & + \frac{P_{1,2B_1}x - P_{1,2}\left\langle x - x_{p_{1,2}}\right\rangle}{bH_{1,2}} \end{aligned} \tag{6.63}$$

$$\psi_3 = \frac{2BN_{B_1}x + 2AM_{B_1}x + 2AL_1P_{B_1}x - AP_{B_1}x^2}{2b(AD - B^2)} \tag{6.64}$$

$$w_3 = \frac{3BN_{B_1}x^2 + 3AM_{B_1}x^2 + 3AL_1P_{B_1}x^2 - AP_{B_1}x^3}{6b(AD - B^2)} + \frac{P_{B_1}x}{bH} \tag{6.65}$$

$$\psi_4 = \frac{(2BN_{B_2} + 2AM_{B_2})(x - L_2) - AP_{B_2}\left(x^2 - L_2^2\right)}{2b(AD - B^2)} \tag{6.66}$$

$$w_4 = \frac{\left(3BN_{B_2} + 3AM_{B_2}\right)\left(x^2 - 2L_2x + L_2^2\right) - AP_{B_2}\left(x^3 - 3L_2^2x + 2L_2^2\right)}{6b\left(AD - B^2\right)} + \frac{P_{B_2}\left(x - L_2\right)}{bH} \tag{6.67}$$

$$u_{1,2} = \frac{D_{1,2}\left(N_{1,2B_1}x - N_{1,2}\left\langle x - x_{p_{1,2}}\right\rangle\right)}{b\left(A_{1,2}D_{1,2} - B_{1,2}^2\right)} + u_{1,2B_1} + \frac{B_{1,2}\left(2M_{1,2B_1}x - 2M_{1,2}\left\langle x - x_{p_{1,2}}\right\rangle + P_{1,2}\left\langle x - x_{p_{1,2}}\right\rangle^2 - P_{1,2B_1}x^2\right)}{2b\left(A_{1,2}D_{1,2} - B_{1,2}^2\right)} \tag{6.68}$$

$$u_3 = \frac{2DN_{B_1}x + 2BM_{B_1}x + 2BL_1P_{B_1}x - BP_{B_1}x^2}{2b\left(AD - B^2\right)} \tag{6.69}$$

$$u_4 = \frac{2DN_{B_2}\left(x - L_2\right) + 2BM_{B_2}\left(x - L_2\right) - BP_{B_2}\left(x^2 - L_2^2\right)}{2b\left(AD - B^2\right)} \tag{6.70}$$

As before, there are 12 unknown quantities: the six left crack tip forces $M_{1,2B_1}$, $N_{1,2B_1}$, $P_{1,2B_1}$ and the deflections, rotations and axial displacements at the left crack tip $w_{1,2B_1}$, $\psi_{1,2B_1}$, $u_{1,2B_1}$. Eqs. (6.14), (6.20) (6.21) are still applicable. The continuity of rotation at the two crack tips is treated in the same way as in §6.2.1 and the following boundary conditions are obtained:

$$\psi_{1,2B_1} = \left(\frac{dw_3}{dx}\right)_{x=L_1} - \frac{P_{1,2B_1} \mp F_{nB_1}}{bH_{1,2}} \tag{6.71}$$

$$\psi_{1,2B_2} = \left(\frac{dw_4}{dx}\right)_{x=0} - \frac{P_{1,2B_2} \mp F_{nB_2}}{bH_{1,2}} \tag{6.72}$$

Note that Eqs. (6.71) and (6.72) reduce to Eq. (6.15) for Euler beams, for which $bH \to \infty$. The crack tip opening force F_{nB} is known from the previously established mode partition theory for one-dimensional fracture in laminated composite DCBs. It is given by the sum of Eqs. (5.76) and (5.79), i.e.

$$F_{nB} = \alpha_{\theta_1}F_{nB\theta_1} + F_{nBP} \tag{6.73}$$

where $F_{nB\theta_1}$ is the crack tip opening force in the $\left\{\varphi_{\theta_1}\right\}$ mode, F_{nBP} is the crack tip opening force due to shearing, and α_{θ_1} is the partition coefficient for the $\left\{\varphi_{\theta_1}\right\}$ mode, which can be written in terms of the crack tip loads and the beam geometry. Full details are given in Chapter 5.

The algebraic solution for the general case is extensive. The solution for the much simpler symmetric case with Euler beams is instead given for reasons of practicality. From symmetry we have

$$L_1 = L_2 = L; \quad x_{p_1} = x_{p_2} = a/2 \quad \text{and} \quad M_1 = M_2 = N_1 = N_2 = 0 \tag{6.74}$$

Symmetry provides two additional boundary conditions, which simplify the calculations. These are zero axial displacement and zero rotation at the mid-span.

$$(u_1)_{x=a/2} = (u_2)_{x=a/2} = 0 \quad \text{and} \quad (\psi_1)_{x=a/2} = (\psi_2)_{x=a/2} = 0 \tag{6.75}$$

The resulting crack tip forces are

$$\begin{aligned} M_{1,2B_1} = C_1 P_{1,2} \Big[& 2aA_1A_2L^2(h_1+h_2)^2 - 8A_{1,2}L^2(2D_{1,2}L - aD_{2,1} \pm ah_1B_{2,1} \pm ah_2B_{2,1}) \\ & + 4A_{2,1}L^2(-4D_{1,2}L + 2aD_{2,1} \pm ah_1B_{1,2} \pm ah_2B_{1,2} - 2h_1B_{1,2}L - 2h_2B_{1,2}L) \\ & + aAL\left(ah_1^2A_2 + ah_2^2A_1 \mp 4ah_{1,2}B_{2,1} \pm 2ah_{2,1}B_{1,2} \mp 4h_{2,1}B_{1,2}L - 8D_{1,2}L + 4aD_{2,1}\right) \\ & + 4aBL(-aB_{1,2} + 2B_{1,2}L - 2aB_{2,1} + ah_1A_2 - ah_2A_1) + 4a^2DL(A_1+A_2) \\ & + 8L^2\left(2B_{1,2}^2L + 2B_1B_2L - aB_{2,1}^2 - aB_1B_2\right) - 2a^3B^2 + 2a^3AD\Big] \\ & - 2C_1LP_{2,1}(a+2L)\left[-4B_{1,2}L(B_1+B_2) + 4D_{1,2}L(A_1+A_2)\right. \\ & \left. + aA(2D_{1,2} \pm h_{2,1}B_{1,2}) - 2aBB_{1,2} \pm 2A_{2,1}B_{1,2}L(h_1+h_2)\right] \end{aligned} \tag{6.76}$$

$$\begin{aligned} N_{1,2B_1} = \pm 2C_1L(a+2L)(P_1+P_2)\big[& 2A_1A_2L(h_1+h_2) + ah_{2,1}AA_{1,2} \\ & + 4L(A_2B_1 - A_1B_2) \pm 2a(AB_{1,2} - A_{1,2}B)\big] \end{aligned} \tag{6.77}$$

where

$$\begin{aligned} C_1 = \big[& 64A_1L^2(D_1 + D_2 - h_1B_2 - h_2B_2) + 64A_2L^2(D_1 + D_2 + h_1B_1 + h_2B_1) \\ & + 32aL(A_1D + AD_1 + A_2D + AD_2 - h_2A_1B + h_1A_2B + h_2AB_1 - h_1AB_2) \\ & + 16A_1A_2L^2(h_1+h_2)^2 + 8aAL\left(h_2^2A_1 + h_1^2A_2\right) - 64L^2(B_1+B_2)^2 \\ & - 64aBL(B_1+B_2) + 16a^2\left(AD - B^2\right)\big]^{-1} \end{aligned} \tag{6.78}$$

6.4.2 Two sets of orthogonal pure modes

For the symmetric case and using the present Euler beam partition theory for laminated composite beams, the F modes arising from the displacement conditions, i.e. zero relative shearing when $P_2/P_1 = \theta_F$, and zero relative opening displacement when $P_2/P_1 = \beta'_F$, are compact enough to be presented here. By substituting the displacements and crack tip forces for this symmetric case into Eqs. (6.22) and (6.36) and equating them to zero, the following F modes are obtained:

$$\frac{P_2}{P_1} = \theta_F = -\frac{B_2^*(2B_1 + h_1A_1)}{B_1^*(2B_2 - h_2A_2)} \quad \text{and} \quad \left\{\varphi_{\theta_F}\right\} = \begin{Bmatrix} 1 \\ \theta_F \end{Bmatrix} \tag{6.79}$$

$$\frac{P_2}{P_1} = \beta'_F = \frac{D_2^*}{D_1^*} \quad \text{and} \quad \left\{\varphi_{\beta'_F}\right\} = \begin{Bmatrix} 1 \\ \beta'_F \end{Bmatrix} \tag{6.80}$$

The $B_{1,2}^*$ and $D_{1,2}^*$ quantities are defined in Eqs. (5.6) and (5.7).

The F mode arising from the zero crack tip opening force condition, which occurs when $P_2/P_1 = \beta_F$, is too extensive to be presented here algebraically. However, for specific cases, a numerical value for β_F can be calculated by enforcing orthogonality between the $\left\{\varphi_{\beta_F}\right\}$ mode and the $\left\{\varphi_{\theta_F}\right\}$ mode through the ERR. The ERR can be written as

$$G = \begin{Bmatrix} P_1 & P_2 \end{Bmatrix} \Big[C\Big] \begin{Bmatrix} P_1 \\ P_2 \end{Bmatrix} \tag{6.81}$$

where $\Big[C\Big]$ is found by examining the coefficients of P_1 and P_2 in Eq. (5.4) when Eqs. (6.76) and (6.77) have been substituted in. Therefore β_F can be found by solving

$$0 = \begin{Bmatrix} 1 & \beta_F \end{Bmatrix} \Big[C\Big] \begin{Bmatrix} 1 \\ \theta_F \end{Bmatrix} \tag{6.82}$$

Similarly θ'_F can be found by solving

$$0 = \begin{Bmatrix} 1 & \theta'_F \end{Bmatrix} \Big[C\Big] \begin{Bmatrix} 1 \\ \beta'_F \end{Bmatrix} \tag{6.83}$$

which gives

$$\theta'_F = -1 \tag{6.84}$$

6.4.3 Contacting crack surfaces

To find the point of first contact x_c using Euler beam theory, again the two conditions in Eq. (6.38) must be satisfied. Solving these equations simultaneously for P_2/P_1 and x_c and ignoring the obvious and unavailing solutions for the crack tips, gives

$$\frac{P_2}{P_1} = \frac{D_2^*}{D_1^*} = \beta'_F \tag{6.85}$$

for all values of x. This implies simultaneous contact everywhere along the fracture for this value of P_2/P_1.

If P_2/P_1 is increased beyond β'_F, the contact can either be at a point or distributed. In the same way as before for the isotropic homogeneous case, point contact at $x = x_p$ is assumed, which is a reasonable assumption, and shown to satisfy the requirement that it prevents interpenetration between the upper and lower sub-laminates for all values of x.

Two loads P_{1c} and P_{2c} are applied to the beam at $x = x_p$ and they cause point contact at this same location. The point contact force P_c acts to prevent non-physical interpenetration. The net shear loads P_1 and P_2 acting on the beams are given by Eq. (6.40). Eq. (6.41) is the equation that must be satisfied to prevent intersection at $x = x_p$. Solving

Eqs. (6.40) and (6.41) for P_1, P_2 and P_c gives

$$P_1 = \frac{A_2 B_1^* \left(P_{1c} + P_{2c}\right)}{A_2 B_1^2 + A_1 B_2^2 - A_1 A_2 D_1 - A_1 A_2 D_2} \tag{6.86}$$

$$P_2 = \frac{A_1 B_2^* \left(P_{1c} + P_{2c}\right)}{A_2 B_1^2 + A_1 B_2^2 - A_1 A_2 D_1 - A_1 A_2 D_2} \tag{6.87}$$

$$P_c = \frac{\left(A_1 A_2 D_2 - A_1 B_2^2\right) P_{1c} - \left(A_1 A_2 D_1 - A_2 B_1^2\right) P_{2c}}{A_2 B_1^2 + A_1 B_2^2 - A_1 A_2 D_1 - A_1 A_2 D_2} \tag{6.88}$$

Substituting Eqs. (6.86) to (6.88) into $D_{op} = w_1 - w_2$ reveals that $D_{op} = 0$ for all values of x. Therefore the requirements for physical contact behaviour are satisfied by this solution, demonstrating that it is the correct one.

According to the present Timoshenko beam partition theory, at $P_2/P_1 = \beta_F = \beta'_F$ there is both zero normal force beyond the crack tip and zero relative opening displacement just behind. Therefore crack tip running contact occurs at $P_2/P_1 = \beta_F$ and pure mode II ERR is obtained. Since there is running contact, if the loading ratio P_2/P_1 is increased further then the crack tip remains closed as the contacting region grows.

6.5 Isotropic homogeneous double annuli

6.5.1 Governing equations

When considering plates, the present Kirchhoff–Love plate partition theory is the equivalent of the present Euler beam partition theory. Similarly, the present Mindlin–Reissner plate partition theory is the equivalent of the present Timoshenko beam partition theory. In order to demonstrate the generalness and ease of application of the present theories, isotropic homogeneous axisymmetric plates are briefly considered in this section.

An isotropic homogeneous 'double annulus' is shown in Fig. 6.4. It is the axisymmetric equivalent of a DCB, which is the most fundamental one-dimensional fracture problem. The double annulus is therefore the logical choice for studying one-dimensional fracture in plates. The plate radius has an outer radius R, a fracture of radius a and a central hole of radius b. The fracture radius is always greater than the radius of the hole $a > b$.

Axisymmetric Kirchhoff–Love plates are considered first. According to Timoshenko and Woinowsky-Krieger (1959), the general solution for these plates is

$$\frac{d}{dr}\left[\frac{1}{r}\frac{d}{dr}\left(r\frac{dw}{dr}\right)\right] = -\frac{Q_r}{D} \tag{6.89}$$

where D is the bending stiffness, given by

$$D = \frac{Eh^3}{12\left(1-\nu^2\right)} \tag{6.90}$$

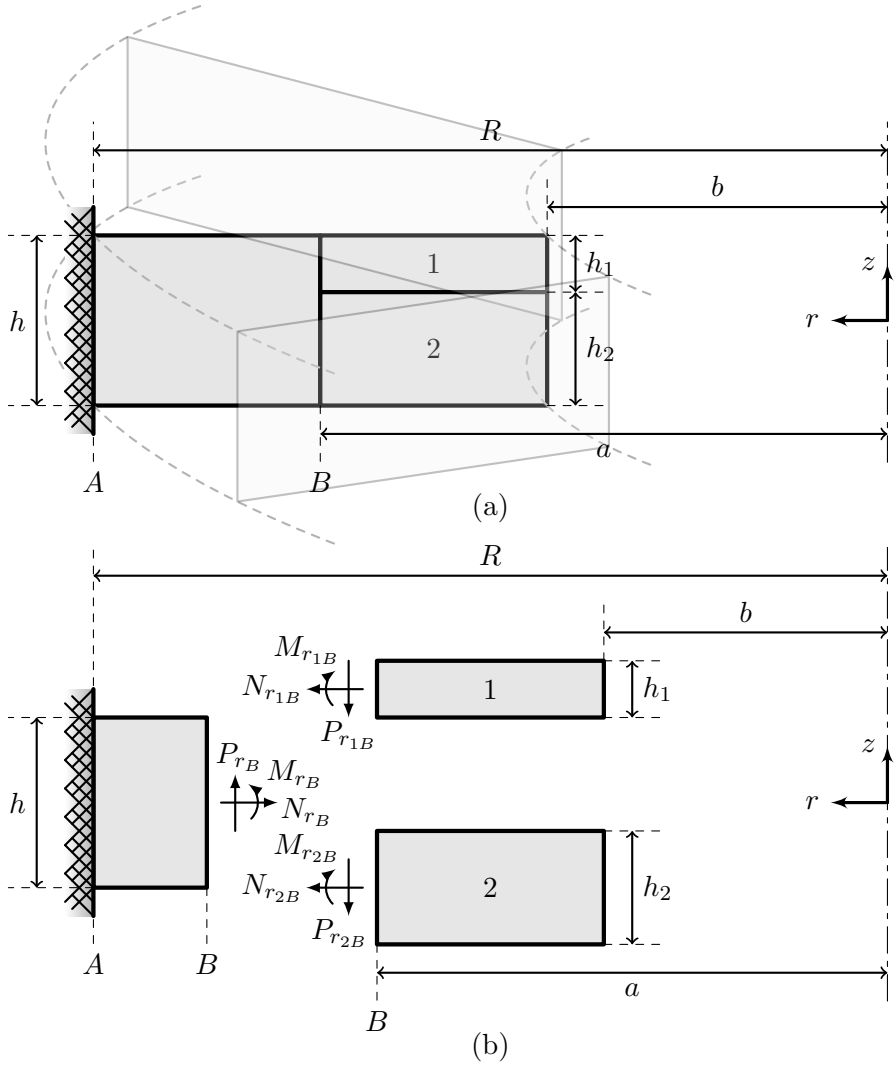

Figure 6.4: A clamped double annulus with a fracture and its loading conditions. (a) General description. (b) Force diagram of each plate.

and Q_r is the shearing force per unit length, which according to the convention, is positive downwards on the inner circumference of the hole. Since ERR is a quantity that is local to the crack tip, it is helpful to derive the governing equations in terms of the crack tip loads. Therefore, with reference to Fig. 6.4, the distributed shear forces for the upper and lower plates is

$$Q_{r_{1,2}} = -\frac{P_{r_{1,2B}} a}{r} \tag{6.91}$$

where $P_{r_{1B}}$ and $P_{r_{2B}}$ are the distributed shear forces over the circumference at the crack tip on the upper and lower plates respectively. Integrating Eq. (6.89) three times with respect to r gives the following for the deflection of the upper and lower plates:

$$w_{1,2} = \frac{P_{r_{1,2B}} a r^2}{4D_{1,2}} \left(\ln \frac{r}{a} - 1 \right) + \frac{C_{1,2} r^2}{4} + C_{3,4} \ln \frac{r}{a} + C_{5,6} \tag{6.92}$$

Timoshenko and Goodier (1970) gave the general solution for the in-plane displacements of the plates.

$$u_{1,2} = \frac{C_{7,8} r}{2} + \frac{C_{9,10}}{r} \tag{6.93}$$

The C_i quantities are unknown coefficients, which need to be determined according to the boundary conditions. Similar equations are obtained for the intact plate as well.

$$w = \frac{P_{r_B} a r^2}{4D}\left(\ln\frac{r}{R} - 1\right) + \frac{C_{11} r^2}{4} + C_{12}\ln\frac{r}{R} + C_{13} \tag{6.94}$$

$$u = \frac{C_{14} r}{2} + \frac{C_{15}}{r} \tag{6.95}$$

where

$$P_{r_B} = P_{r_{1B}} + P_{r_{2B}} \tag{6.96}$$

There are 15 unknown coefficients, C_1 to C_{15}. Therefore 15 boundary conditions are required. First, there are three displacement boundary conditions for the clamped edge.

$$(w)_{r=R} = 0; \quad (dw/dr)_{r=R} = 0 \quad \text{and} \quad (u)_{r=R} = 0 \tag{6.97}$$

There are also six displacement boundary conditions at the crack tip at $r = a$, which enforce continuity between the intact plate and the upper and lower plates (straddling the fracture).

$$\begin{gathered}(w)_{r=a} = (w_{1,2})_{r=a}\,; \quad (dw/dr)_{r=a} = (dw_{1,2}/dr)_{r=a} \\ \text{and} \quad (u)_{r=a} = (u_{1,2})_{r=a} \pm \frac{h_{2,1}}{2}\left(\frac{dw_{1,2}}{dr}\right)_{r=a}\end{gathered} \tag{6.98}$$

The remaining boundary conditions are the radial forces and bending moments at the crack tip. According to Timoshenko and Woinowsky-Krieger (1959), the distributed radial and circumferential bending moments at r are

$$M_r = D\left(\frac{d^2 w}{dr^2} + \frac{\nu}{r}\frac{dw}{dr}\right) \quad \text{and} \quad M_\phi = D\left(\frac{1}{r}\frac{dw}{dr} + \nu\frac{d^2 w}{dr^2}\right) \tag{6.99}$$

Timoshenko and Goodier (1970) gave the radial and circumferential stresses as

$$\sigma_r = \frac{E}{1-\nu^2}\left(\frac{du}{dr} + \nu\frac{u}{r}\right) \quad \text{and} \quad \sigma_\phi = \frac{E}{1-\nu^2}\left(\frac{u}{r} + \nu\frac{du}{dr}\right) \tag{6.100}$$

Therefore, the remaining boundary conditions are

$$\begin{gathered}M_{r_B} = D\left(\frac{d^2 w}{dr^2} + \frac{\nu}{r}\frac{dw}{dr}\right)_{r=a}\,; \quad M_{r_{1,2B}} = D\left(\frac{d^2 w_{1,2}}{dr^2} + \frac{\nu}{r}\frac{dw_{1,2}}{dr}\right)_{r=a}\,; \\ \frac{N_{r_B}}{h} = \frac{E}{1-\nu^2}\left(\frac{du}{dr} + \nu\frac{u}{r}\right)_{x=a} \quad \text{and} \quad \frac{N_{r_{1,2B}}}{h_{1,2}} = \frac{E}{1-\nu^2}\left(\frac{du_{1,2}}{dr} + \nu\frac{u_{1,2}}{r}\right)_{x=a}\end{gathered} \tag{6.101}$$

where

$$M_{r_B} = M_{r_{1B}} + M_{r_{2B}} + \left(N_{r_{2B}} h_1 - N_{r_{1B}} h_2\right)/2 \quad \text{and} \quad N_{r_B} = N_{r_{1B}} + N_{r_{2B}} \tag{6.102}$$

The 15 boundary conditions in Eqs. (6.97), (6.98) and (6.101) can now be solved for the 15 unknown coefficients, C_1 to C_{15}. The deflection of the fractured plate is then completely known in terms of $M_{r_{1B}}$, $M_{r_{2B}}$, $N_{r_{1B}}$, $N_{r_{2B}}$, $P_{r_{1B}}$ and $P_{r_{2B}}$.

6.5.2 Energy release rate

The total ERR for a fracture in an axisymmetric plate is

$$G = \frac{1}{2\pi a}\frac{\partial U}{\partial a} \tag{6.103}$$

where U is the strain energy, which is the sum of the strain energies due to radial and circumferential bending and the strain energies due to radial and circumferential normal stress. Since these are Kirchhoff–Love plates, there is no strain energy due to shearing. First consider the bending action. From Timoshenko and Woinowsky-Krieger (1959), the stresses due to bending are

$$\sigma_r = \frac{12 M_r z}{h^3} \quad \text{and} \quad \sigma_\phi = \frac{12 M_\phi z}{h^3} \tag{6.104}$$

Hooke's law in polar coordinates is

$$\varepsilon_r = \frac{\sigma_r}{E} - \nu\frac{\sigma_\phi}{E} \quad \text{and} \quad \varepsilon_\phi = \frac{\sigma_\phi}{E} - \nu\frac{\sigma_r}{E} \tag{6.105}$$

Therefore, the strain energy density due to radial bending is

$$\frac{1}{2}\sigma_r \varepsilon_r = \frac{72 M_r \left(M_r - \nu M_\phi\right) z^2}{h^6 E} \tag{6.106}$$

Integrating Eq. (6.106) over the volume of a plate gives the strain energy due to radial bending, which is

$$\int_0^R \int_0^{2\pi} \int_{-h/2}^{h/2} \frac{72 M_r \left(M_r - \nu M_\phi\right) z^2}{h^6 E}\, dz\, r d\phi\, dr = \int_0^R \frac{12\pi r \left(M_r^2 - \nu M_r M_\phi\right)}{h^3 E}\, dr \tag{6.107}$$

Similarly, the strain energy due to circumferential bending is

$$\int_0^R \frac{12\pi r \left(M_\phi^2 - \nu M_r M_\phi\right)}{h^3 E}\, dr \tag{6.108}$$

Now the strain energy due to in-plane forces is considered. N_r is the distributed radial force. Let N_ϕ be the distributed circumferential force. The radial stress due to N_r is $\sigma_r = N_r/h$ and the circumferential stress due N_ϕ is $\sigma_\phi = N_\phi/h$. Therefore, the strain

energy density due to N_r is

$$\frac{1}{2}\sigma_r\varepsilon_r = \frac{N_r\left(N_r - \nu N_\phi\right)}{2h^2E} \tag{6.109}$$

Integrating Eq. (6.109) of the volume of a plate gives the strain energy due to N_r which is

$$\int_0^R \int_0^{2\pi} \int_{-h/2}^{h/2} \frac{N_r\left(N_r - \nu N_\phi\right)}{2h^2E}\, dz\, r d\phi\, dr = \int_0^R \frac{\pi r\left(N_r^2 - \nu N_r N_\phi\right)}{hE}\, dr \tag{6.110}$$

Similarly, the strain energy due to N_ϕ is

$$\int_0^R \frac{\pi r\left(N_\phi^2 - \nu N_r N_\phi\right)}{hE}\, dr \tag{6.111}$$

Therefore, the total strain energy in the double annulus shown in Fig. 6.4 is

$$\begin{aligned}
U = &\int_b^a \frac{12\pi r\left(M_{r_1}^2 - \nu M_{r_1}M_{\phi_1}\right)}{h_1^3E}\, dr + \int_b^a \frac{12\pi r\left(M_{r_2}^2 - \nu M_{r_2}M_{\phi_2}\right)}{h_2^3E}\, dr \\
&+ \int_a^R \frac{12\pi r\left(M_r^2 - \nu M_r M_\phi\right)}{h^3E}\, dr + \int_b^a \frac{12\pi r\left(M_{\phi_1}^2 - \nu M_{r_1}M_{\phi_1}\right)}{h_1^3E}\, dr \\
&+ \int_b^a \frac{12\pi r\left(M_{\phi_2}^2 - \nu M_{r_2}M_{\phi_2}\right)}{h_2^3E}\, dr + \int_a^R \frac{12\pi r\left(M_\phi^2 - \nu M_r M_\phi\right)}{h^3E}\, dr \\
&+ \int_b^a \frac{\pi r\left(N_{r_1}^2 - \nu N_{r_1}N_{\phi_1}\right)}{h_1E}\, dr + \int_b^a \frac{\pi r\left(N_{r_2}^2 - \nu N_{r_2}N_{\phi_2}\right)}{h_2E}\, dr \\
&+ \int_a^R \frac{\pi r\left(N_r^2 - \nu N_r N_\phi\right)}{hE}\, dr + \int_b^a \frac{\pi r\left(N_{\phi_1}^2 - \nu N_{r_1}N_{\phi_1}\right)}{h_1E}\, dr \\
&+ \int_b^a \frac{\pi r\left(N_{\phi_2}^2 - \nu N_{r_2}N_{\phi_2}\right)}{h_2E}\, dr + \int_a^R \frac{\pi r\left(N_\phi^2 - \nu N_r N_\phi\right)}{hE}\, dr
\end{aligned} \tag{6.112}$$

Substituting Eq. (6.112) into Eq. (6.103) gives

$$\begin{aligned}
G = \frac{6}{E}\Bigg(&\frac{M_{r_{1B}}^2}{h_1^3} + \frac{M_{r_{2B}}^2}{h_2^3} - \frac{M_{r_B}^2}{h^3} + \frac{M_{\phi_{1B}}^2}{h_1^3} + \frac{M_{\phi_{2B}}^2}{h_2^3} - \frac{M_{\phi_B}^2}{h^3} \\
&- \frac{2\nu M_{r_{1B}}M_{\phi_{1B}}}{h_1^3} - \frac{2\nu M_{r_{2B}}M_{\phi_{2B}}}{h_2^3} + \frac{2\nu M_{r_B}M_{\phi_B}}{h^3} \\
&+ \frac{N_{r_{1Be}}^2}{12}\left(\frac{1}{h_1} - \frac{1}{h}\right) + \frac{N_{\phi_{1B}}^2}{12h_1} + \frac{N_{\phi_{2B}}^2}{12h_2} - \frac{N_{\phi_B}^2}{12h} \\
&- \frac{\nu N_{r_{1Be}}N_{\phi_{1B}}}{6h_1} + \frac{\nu N_{r_{1Be}}N_{\phi_B}}{6h}\Bigg)
\end{aligned} \tag{6.113}$$

where $N_{r_{1Be}}$ is the equivalent radial force, acting on the upper plate, which is defined as

$$N_{r_{1Be}} = N_{r_{1B}} - h_1 N_{r_{2B}}/h_2 \tag{6.114}$$

Eq. (6.113) only contains three independent variables, $M_{r_{1B}}$, $M_{r_{2B}}$ and $N_{r_{1Be}}$. The other crack tip forces are dependent on these. The deflection of the plates is known in terms of the three independent variables from §6.5.1. Therefore, by substituting

$$M_{\phi_B} = D\left(\frac{1}{r}\frac{dw}{dr} + \nu\frac{d^2w}{dr^2}\right)_{r=a}; \quad M_{\phi_{1,2B}} = D_{1,2}\left(\frac{1}{r}\frac{dw_{1,2}}{dr} + \nu\frac{d^2w_{1,2}}{dr^2}\right)_{r=a};$$
$$N_{\phi_B} = \frac{Eh}{1-\nu^2}\left(\frac{u}{r} + \nu\frac{du}{dr}\right)_{r=a} \quad \text{and} \quad N_{\phi_{1,2B}} = \frac{Eh_{1,2}}{1-\nu^2}\left(\frac{u_{1,2}}{r} + \nu\frac{du_{1,2}}{dr}\right)_{r=a} \tag{6.115}$$

into Eq. (6.113) and simplifying, the following expression is obtained for G:

$$\begin{aligned} G = \frac{1-\nu^2}{2h_1^3 E\gamma^3(1+\gamma)^3}\Big[&12\gamma^4\left(\gamma^2+3\gamma+3\right)M_{r_{1B}}^2 + 12\left(3\gamma^2+3\gamma+1\right)M_{r_{2B}}^2 \\ &+ h_1^2\gamma^4\left(\gamma^2-\gamma+1\right)N_{r_{1Be}}^2 - 24\gamma^3 M_{r_{1B}}M_{r_{2B}} \\ &+ 12h_1\gamma^4 M_{r_{1B}}N_{r_{1Be}} + 12h_1\gamma^4 M_{r_{2B}}N_{r_{1Be}}\Big] \end{aligned} \tag{6.116}$$

Recall that $\gamma = h_2/h_1$. The crack tip shear forces do not appear because only Kirchhoff–Love plates are considered. Eq. (6.116) can be written in matrix form as

$$G = \frac{1-\nu^2}{h_1^3 E(1+\gamma)^3}\begin{Bmatrix} M_{r_{1B}} \\ M_{r_{2B}} \\ N_{r_{1Be}} \end{Bmatrix}^T \Big[C\Big] \begin{Bmatrix} M_{r_{1B}} \\ M_{r_{2B}} \\ N_{r_{1Be}} \end{Bmatrix} \tag{6.117}$$

where

$$\Big[C\Big] = \begin{bmatrix} 6\gamma\left(\gamma^2+3\gamma+3\right) & -6 & 3h_1\gamma \\ \dots & 6\left(3\gamma^2+3\gamma+1\right)/\gamma^3 & 3h_1\gamma \\ \dots & \dots & h_1^2\gamma\left(\gamma^2-\gamma+1\right)/2 \end{bmatrix} \tag{6.118}$$

6.5.3 Two sets of orthogonal pure modes

According to the established theory, there are expected to be two sets of pure modes for Kirchhoff–Love plates. The first set corresponds to zero relative shearing displacement just behind the crack tip (pure mode I) and zero normal force ahead of the crack tip (pure mode II). The second set corresponds to zero relative opening displacement just behind the crack tip (pure mode II) and zero crack tip shearing force (pure mode I).

Using the equations from §6.5.1, zeroing the relative opening displacement at an infinitely small distance δa behind the crack tip gives

$$(D_{op})_{r=a-\delta a} = 0 = \frac{3\left(M_{r_{2B}} - M_{r_{1B}}\gamma^3\right)\left(1-\nu^2\right)\left(2a\,\delta a + 2a^2\ln\frac{a-\delta a}{a} - \delta a^2\right)}{h_1^3 E\gamma^3} \tag{6.119}$$

Now, zeroing the relative shearing displacement at an infinitely small distance δa behind the crack tip gives

$$(D_{sh})_{r=a-\delta a} = 0 = \frac{\left(6M_{r_{2B}} + 6\gamma^2 M_{r_{1B}} + h_1\gamma^2 N_{r_{1Be}}\right)\left(\nu^2-1\right)(2a-\delta a)\,\delta a}{2h_1^2 E\gamma^2\,(a-\delta a)} \tag{6.120}$$

From Eqs. (6.119) and (6.120), if the mode form is $\left\{\varphi\right\} = \left\{M_{r_{1B}} \quad M_{r_{2B}} \quad N_{r_{1Be}}\right\}^T$, then the pure modes are

$$\left\{\varphi_{\beta_1'}\right\} = \begin{Bmatrix} 1 \\ \beta_1' \\ 0 \end{Bmatrix}; \quad \left\{\varphi_{\theta_1}\right\} = \begin{Bmatrix} 1 \\ \theta_1 \\ 0 \end{Bmatrix} \quad \text{and} \quad \left\{\varphi_{\theta_2}\right\} = \begin{Bmatrix} 1 \\ 0 \\ \theta_2 \end{Bmatrix} \tag{6.121}$$

where $\beta_1' = \gamma^3$, $\theta_1 = -\gamma^2$ and $\theta_2 = -6/h_1$. The $\left\{\varphi_{\beta_1'}\right\}$ mode is the pure mode II mode from the second set. It corresponds to zero relative opening displacement at the crack tip. The $\left\{\varphi_{\theta_i}\right\}$ modes are the pure mode I modes from the first set. They correspond to zero relative shearing displacement at the crack tip.

The corresponding orthogonal pure modes are characterised by zero crack tip opening and shear force. It is more simple to find them using the orthogonality condition. From Eq. (6.117), two modes are orthogonal if

$$0 = \left\{\varphi_1\right\}^T \left[C\right] \left\{\varphi_2\right\} \tag{6.122}$$

Therefore, the following can be written:

$$0 = \begin{Bmatrix} 1 \\ \theta_1' \\ 0 \end{Bmatrix} \left[C\right] \left\{\varphi_{\beta_1'}\right\}; \quad 0 = \begin{Bmatrix} 1 \\ \beta_1 \\ 0 \end{Bmatrix} \left[C\right] \left\{\varphi_{\theta_i}\right\} \quad \text{and} \quad 0 = \begin{Bmatrix} 1 \\ 0 \\ \beta_2 \end{Bmatrix} \left[C\right] \left\{\varphi_{\theta_i}\right\} \tag{6.123}$$

Solving these equations gives

$$\left\{\varphi_{\theta_1'}\right\} = \begin{Bmatrix} 1 \\ \theta_1' \\ 0 \end{Bmatrix}; \quad \left\{\varphi_{\beta_1}\right\} = \begin{Bmatrix} 1 \\ \beta_1 \\ 0 \end{Bmatrix} \quad \text{and} \quad \left\{\varphi_{\beta_2}\right\} = \begin{Bmatrix} 1 \\ 0 \\ \beta_2 \end{Bmatrix} \tag{6.124}$$

where $\beta_1 = \gamma^2\,(3+\gamma)\,/\,(1+3\gamma)$, $\beta_2 = 2\,(3+\gamma)\,/\,[h_1\,(\gamma-1)]$ and $\theta_1' = -1$. For $\gamma = 1$, $\beta_2 = \infty$. The mode is therefore written as

$$\left\{\varphi_{\beta_2}\right\} = \begin{Bmatrix} 0 \\ 0 \\ 1 \end{Bmatrix} \tag{6.125}$$

for $\gamma = 1$. It is seen that the pure modes for isotropic homogeneous double annuli are equivalent to the pure modes for isotropic homogeneous DCBs.

6.5.4 Mixed-mode partitions

There are three independent variables for the ERR in Eq. (6.116). Therefore, three modes are required to mode partition G into G_I and G_{II}. For consistency with the previous chapters, the $\left\{\varphi_{\theta_1}\right\}$, $\left\{\varphi_{\beta_1}\right\}$ and $\left\{\varphi_{\beta_2}\right\}$ modes are chosen. The mode partition coefficients are therefore

$$\begin{Bmatrix} \alpha_{\theta_1} \\ \alpha_{\beta_1} \\ \alpha_{\beta_2} \end{Bmatrix} = \begin{bmatrix} 1 & 1 & 1 \\ \theta_1 & \beta_1 & 0 \\ 0 & 0 & \beta_2 \end{bmatrix}^{-1} \begin{Bmatrix} M_{r_{1B}} \\ M_{r_{2B}} \\ N_{r_{1Be}} \end{Bmatrix} \tag{6.126}$$

for $\gamma \neq 1$. If $\gamma = 1$, then

$$\begin{Bmatrix} \alpha_{\theta_1} \\ \alpha_{\beta_1} \\ \alpha_{\beta_2} \end{Bmatrix} = \begin{bmatrix} 1 & 1 & 0 \\ \theta_1 & \beta_1 & 0 \\ 0 & 0 & 1 \end{bmatrix}^{-1} \begin{Bmatrix} M_{r_{1B}} \\ M_{r_{2B}} \\ N_{r_{1Be}} \end{Bmatrix} \tag{6.127}$$

Substituting $M_{r_{1B}}$, $M_{r_{2B}}$ and $N_{r_{1Be}}$ from Eq. (6.126) or Eq. (6.127) into Eq. (6.116) gives

$$G = \alpha_{\theta_1}^2 G_{\theta_1} + \alpha_{\beta_1}^2 G_{\beta_1} + \alpha_{\beta_2}^2 G_{\beta_2} + \alpha_{\beta_1}\alpha_{\beta_2} G_{\beta_1\beta_2} \tag{6.128}$$

where

$$G_{\theta_1} = \frac{24\gamma\left(1-\nu^2\right)}{h_1^3 E\left(1+\gamma\right)} \tag{6.129}$$

$$G_{\beta_1} = \frac{72\gamma\left(1-\nu^2\right)\left(1+\gamma\right)}{h_1^3 E\left(1+3\gamma\right)^2} \tag{6.130}$$

$$G_{\beta_2} = \frac{8\gamma^3\left(1-\nu^2\right)}{h_1^3 E\left(1-\gamma\right)^2\left(1+\gamma\right)} \quad \text{for } \gamma \neq 1 \quad \text{and} \quad G_{\beta_2} = \frac{1-\nu^2}{16 h_1 E} \quad \text{for } \gamma = 1 \tag{6.131}$$

$$G_{\beta_1\beta_2} = \frac{48\gamma^2\left(1-\nu^2\right)}{h_1^3 E\left(3\gamma^2-2\gamma-1\right)} \quad \text{for } \gamma \neq 1 \quad \text{and} \quad G_{\beta_1\beta_2} = \frac{3\left(1-\nu^2\right)}{2h_1^2 E} \quad \text{for } \gamma = 1 \tag{6.132}$$

Note that there are no $G_{\theta_1\beta_1}$ or $G_{\theta_1\beta_2}$ terms in Eq. (6.128) because the $\left\{\varphi_{\theta_i}\right\}$ modes are orthogonal to the $\left\{\varphi_{\beta_i}\right\}$ modes.

Since interaction exists between the $\left\{\varphi_{\theta_i}\right\}$ and $\left\{\varphi_{\beta_i}\right\}$ modes in the present Euler beam partition, it is also expected to exist in the present Kirchhoff–Love plate partition theory. Using the VCCT, the mode I ERR for the whole circumference of the crack front is

$$G_I = \frac{F_{nB}\left(D_{op}\right)_{r=a-\delta a}}{2\,\delta a} \tag{6.133}$$

where F_{nB} is the distributed opening force at the crack tip, i.e. $F_{nB} = \int_a^{a+\delta a} \sigma_r \, dr$ and $\delta a \to 0$. By definition, the $\left\{\varphi_{\beta_i}\right\}$ modes produce zero crack tip opening force. Therefore

$$F_{nB} = \alpha_{\theta_1} F_{nB\theta_1} \tag{6.134}$$

where $F_{nB\theta_1}$ is the crack tip opening force in the $\left\{\varphi_{\theta_1}\right\}$ mode. Substituting Eq. (6.134) and the relative opening displacement in terms of the mode partition coefficients into Eq. (6.133) gives

$$G_I = \alpha_{\theta_1}^2 G_{\theta_1} + \alpha_{\theta_1}\alpha_{\beta_1}\Delta G_{\theta_1\beta_1} + \alpha_{\theta_1}\alpha_{\beta_2}\Delta G_{\theta_1\beta_2} \tag{6.135}$$

where

$$G_{\theta_1} = \frac{3F_{nB\theta_1}\left(\nu^2-1\right)(1+\gamma)\left(2a\,\delta a + 2a^2 \ln\frac{a-\delta a}{a} - \delta a^2\right)}{2h_1^3 E\gamma\,\delta a} \tag{6.136}$$

$$\Delta G_{\theta_1\beta_1} = \frac{3(\gamma-1)}{1+3\gamma} G_{\theta_1} \tag{6.137}$$

$$\Delta G_{\theta_1\beta_2} = \frac{\gamma}{1+\gamma} G_{\theta_1} \tag{6.138}$$

A more useful expression for G_{θ_1} is given in Eq. (6.129). The mode I ERR, G_I can now be calculated from Eq. (6.135). The mode II ERR is simply $G_{II} = G - G_I$.

Finally in this section, attention is turned to Mindlin–Reissner plates. The above analysis can easily be repeated for these plates. Wang and Lee (1996) relate the governing equations for these plates to the forms for Kirchhoff–Love plates, which makes the analysis easier. However, for the case where there are no shear forces, it is known from the previous work that if the shear modulus is finite, the interaction disappears and the second set of modes changes to coincide with the first set of modes. Therefore, the present Mindlin–Reissner plate partition theory is

$$G_I = \alpha_{\theta_1}^2 G_{\theta_1} + G_P + \alpha_{\theta_1}\Delta G_{\theta_1 P} \quad \text{and} \quad G_{II} = \alpha_{\beta_1}^2 G_{\beta_1} + \alpha_{\beta_2}^2 G_{\beta_2} + \alpha_{\beta_1}\alpha_{\beta_2} G_{\beta_1\beta_2} \tag{6.139}$$

where G_P and $\Delta G_{\theta_1 P}$ are found by calculations, which are equivalent to those in §4.2.7. They are found to be

$$G_P = \frac{\left(P_{r_{2B}} - P_{r_{1B}}\gamma\right)^2}{2h_1\gamma\kappa\mu\,(1+\gamma)} \tag{6.140}$$

and

$$\Delta G_{\theta_1 P} = -\frac{4\sqrt{3E\mu}\sqrt{1-\nu^2}\left(P_{r_{2B}} - P_{r_{1B}}\gamma\right)}{h_1^2 E\kappa\mu\,(1+\gamma)} \tag{6.141}$$

6.6 Circular isotropic homogeneous plates

A more typical example of an axisymmetric fracture would be in a circular isotropic homogeneous plate. Consider a clamped circular plate of radius R, with a fracture of radius a, a distance h_1 from the top surface of the plate and a distance h_2 from the bottom surface

of the plate. If P_1 is applied vertically upwards at the centre of the top plate and P_2 is applied vertically upwards at the centre of the bottom plate, then a simple analysis yields the crack tip forces, which are required to calculate and partition the ERR. The crack tip forces are

$$M_{r_{1B}} = \frac{P_1}{4\pi} + \frac{(1+\nu)\left(\ln\frac{a}{R}\right)(P_1+P_2)}{4\pi(1+\gamma)^3} \tag{6.142}$$

$$M_{r_{2B}} = \frac{P_2\left(1+3\gamma+3\gamma^2+\gamma^3+\gamma^3\ln\frac{a}{R}+\gamma^3\nu\ln\frac{a}{R}\right)+P_1\left(\gamma^3\ln\frac{a}{R}+\gamma^3\nu\ln\frac{a}{R}\right)}{4\pi(1+\gamma)^3} \tag{6.143}$$

and

$$N_{r_{1Be}} = -\frac{3(1+\nu)\left(\ln\frac{a}{R}\right)(P_1+P_2)}{2\pi h_1(1+\gamma)^2} \tag{6.144}$$

The partition of ERR is now easily found using the equations in §6.5. Comparisons will be made between these analytical partitions and results from FEM simulations in §6.7.3.

6.7 Numerical investigations

The FEM was used to validate the theories. Finite elements, based on the Euler and Timoshenko beam theories and two-dimensional elasticity, were employed to model isotropic homogeneous and laminated composite straight beam structures. Finite elements, based on the Kirchhoff–Love and Mindlin–Reissner plate theories and axisymmetric elasticity, were employed to model circular isotropic homogeneous plates. Normal and shear point interface springs with very high stiffness were used to model perfectly bonded plies: 10^{14} N/m for the beam simulations and 10^{16} N/m for the plate simulations. It was shown in §B.1 in Appendix B that for the layered isotropic homogeneous DCBs in Chapter 4, an interface spring stiffness value which is just 10^2 times larger than the Young's modulus of the material in the units of the FEM simulations is indeed sufficient to model perfectly bonded layers. As discussed in §B.1, a larger value for k_s is desirable, but without introducing numerical errors. For the isotropic homogeneous and laminated composite beam simulations in this section, which are in SI units, k_s is between $\sim 10^3$ and $\sim 10^4$ times larger than the Young's moduli of the material in the units of the FEM simulations. For the plate simulations in this section, which are also in SI units, k_s is $\sim 10^5$ times larger than the Young's moduli of the material. It has been verified through simulations equivalent to those in §B.1 that these values of k_s are sufficient to model perfectly bonded plies. The ERR partition was calculated using the VCCT in conjunction with these interface springs. A contact algorithm was also implemented to deal with any possible contact in loading. Full details of the numerical methods are given in §3.3, §3.4 and §3.5 respectively.

Two clamped-clamped beam cases, as shown in Fig. 6.2 (a), were investigated. The first case is an isotropic homogeneous one, which is asymmetric about the mid-span. The data for this beam is given in Table 6.1. The second case is a symmetric laminated composite one. It has a quasi-isotropic lay-up with 16 plies. There is a delamination between the

Table 6.1: Data for FEM simulations of a clamped-clamped isotropic homogeneous beam.

Elastic modulus, E	70 GPa
Shear modulus, μ	26 GPa
Poisson's ratio, ν	0.35
Beam thicknesses, h_1 and h_2	1 mm and 2 mm
Intact lengths of beam, L_1 and L_2	10 mm and 25 mm
Length of fracture, a	65 mm
Width of beam, b	10 mm
Loading location, x_p	20 mm
Euler pure modes, θ_F, β_F, θ'_F and β'_F	-3.92, 2.81, -1 and 8
Timoshenko pure modes, θ_F and β_F	-3.84 and 2.75

Table 6.2: Data for FEM simulations of a clamped-clamped laminated composite beam.

Ply longitudinal modulus, E_1	139.3 GPa
Ply transverse modulus, E_2	9.72 GPa
Out-of-plane modulus, E_3	9.72 GPa
In-plane shear modulus, μ_{12}	5.58 GPa
Out-of-plane shear modulus, μ_{13}	5.58 GPa
Out-of-plane shear modulus, μ_{23}	3.45 GPa
In-plane Poisson's ratio, ν_{12}	0.29
Out-of-plane Poisson's ratio, ν_{13}	0.29
Out-of-plane Poisson's ratio, ν_{23}	0.4
Thickness of lamina, t_p	0.125 mm
Sub-laminate lay-up 1 (top)	$90/-45/0/45$
Sub-laminate lay-up 2 (bottom)	$(45/0/-45/90)_2/90/-45/0/45$
Laminate thicknesses, h_1 and h_2	0.5 mm and 1.5 mm
Intact lengths of beam, $L_1 = L_2$	25 mm
Length of delamination, a	50 mm
Width of beam, b	10 mm
Loading location, x_p	25 mm
Euler pure modes, θ_F, β_F, θ'_F and β'_F	-26.45, 4.98, -1 and 66.90
Timoshenko pure modes, θ_F and β_F	-23.20 and 4.74

Table 6.3: Data for FEM simulations of a clamped circular isotropic homogeneous plate.

Elastic modulus, E	70 GPa
Shear modulus, μ	26 GPa
Poisson's ratio, ν	0.35
Beam thicknesses, h_1 and h_2	1 mm and 2 mm
Radius of plate, R	100 mm
Length of fracture, a	20 mm

fourth and fifth plies, which gives a thickness ratio of $\gamma = 3$. The data for this case is given in Table 6.2. The material properties are for T300/976 graphite/epoxy laminae (Wang and Zhang 2009). Finally, a clamped circular plate case was investigated. Located on its centre is a circular fracture. Forces P_1 and P_2 are applied at the centre ($r = 0$). The data for the plate is given in Table 6.3.

One set of simulations, which used linear Timoshenko beam elements, is compared against the present Euler beam partition theory. Very large out-of-plane shear moduli

$\mu = \mu_{13} = \mu_{23} = 10^{16}\,\text{Pa}$ were used to simulate Euler beams. Similarly, for the circular plate case, Mindlin–Reissner plates with $\mu = 10^{16}\,\text{Pa}$ were used to simulate Kirchhoff–Love plates. Comparisons are made with the present Kirchhoff–Love plate partition theory. In all cases, two layers of elements were used to represent the material either side of the fracture. The elements were distributed uniformly. To avoid shear locking, reduced integration was applied. Use of linear Timoshenko beams and Mindlin–Reissner plates correctly enforces continuity along the interface ahead of the crack tip.

Another set of simulations, which was the same as the first set but which instead used the normal out-of-plane shear moduli (those given in Tables 6.1 to 6.3) and a shear correction factor of $\kappa = 5/6$, is compared against the present Timoshenko beam partition theory or the present Mindlin–Reissner plate partition theory.

The final set of simulations used QUAD4 elements with the normal out-of-plane shear moduli. Layers of QUAD4 elements model the sub-laminates and they are also joined with very high stiffness normal and shear interface springs. Using this approach, the problem of oscillatory singularities (Raju et al. 1988) when modelling fractures in composite materials with two- and three-dimensional elasticity is not encountered (Kutlu and Chang 1995, Zhang and Wang 2009, Wang and Zhang 2009). In the composite case, a layer of QUAD4 elements was used for each individual ply, as is required by the element derivation in §3.2.4. In the isotropic homogeneous beam and plate cases, two and four layers of QUAD4 elements were needed in the top and bottom beams/plates respectively for sufficient convergence. The elements were distributed uniformly along the length/radius and thickness. The results from these simulations are compared against averaged partition rule 1, which is described in §4.2.5 and §5.2.9.

Some additional comments on the convergence studies for the cases in this section are provided in the following and also in §B.5 in Appendix B.

In all the tests, a vertical upwards force P_1 was applied to the upper beam/plate and held constant at 1 N. A vertical upwards force P_2 was applied to the lower beam/plate and varied between $-10\,\text{N}$ and 10 N.

6.7.1 Tests with a clamped-clamped isotropic homogeneous beam

Results from the various analytical theories and numerical simulations of the clamped-clamped isotropic homogeneous beam are presented in Tables 6.4 and 6.5 and Fig. 6.5. Plane stress is assumed in all analytical and numerical calculations. The ERR partition for the *left* crack tip is given. In Fig. 6.5 and for every figure in this section, unfilled data markers indicate results from simulations with contact modelling and filled markers indicate results from simulations without. The results from the simulations using Timoshenko beam elements and the very large shear modulus are compared against the present Euler beam partition theory. Full interaction is expected. Excellent agreement is seen between the two sets of data. The two sets of pure modes are plainly visible where $G_I/G = 0$ and $G_I/G = 1$ and these agree with the F modes from the present Euler beam partition theory, which are

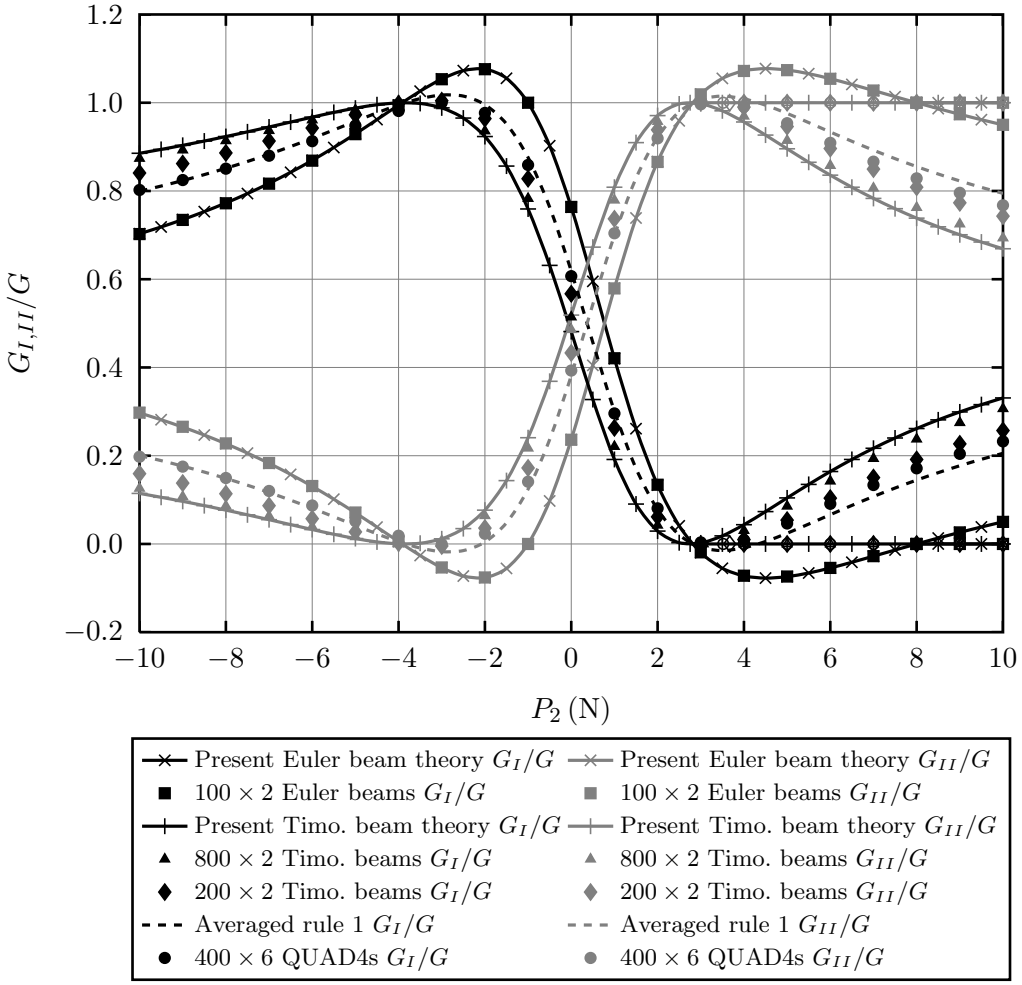

Figure 6.5: Comparisons between various theories and FEM results for the clamped-clamped isotropic homogeneous beam with varying P_2 and $P_1 = 1\,\mathrm{N}$.

given in Table 6.1. Also, as was the case for layered isotropic homogeneous and laminated composite DCBs, it is seen that the present Euler beam partition theory predicts regions where the partitions of ERR are negative. This is discussed in §4.2.4 and §4.3.1. Further detailed discussion is also given in Appendix A. Now considering the contact behaviour, the analytical and numerical results methods are in agreement that point contact at the loading location and at the crack tips contact occur simultaneously at $P_2 = 8\,\mathrm{N}$; and that after first contact, both crack tips remain closed and the fracture is pure mode II.

The present Timoshenko beam partition theory is compared with results from numerical simulations with the normal shear modulus. As expected, the $\left\{\varphi_{\theta'_F}\right\}$ and $\left\{\varphi_{\beta'_F}\right\}$ modes coincide with the $\left\{\varphi_{\theta_F}\right\}$ and $\left\{\varphi_{\beta_F}\right\}$ modes respectively since there is no interaction, and these agree with the F modes from the present Timoshenko beam partition theory, which are given in Table 6.1. The numerical results with 800×2 elements very closely follow the analytical values. The results with 200×2 elements are in less good agreement. This demonstrates that the element size needs to be very small otherwise $F_{nB\theta_1}\,\delta a$ is not

Table 6.4: Comparisons between various theories and FEM results for the clamped-clamped isotropic homogeneous beam with varying P_2 and $P_1 = 1\,\mathrm{N}$.

P_2 (N)	G_I/G (%)						
	Present Euler beam theory	100×2 Euler beams	Present Timo. beam theory	800×2 Timo. beams	200×2 Timo. beams	Averaged rule 1	400×6 QUAD4s
-10	70.30	70.30	88.54	87.39	84.07	79.94	80.23
-8	77.28	77.27	92.34	91.38	88.62	85.15	85.05
-6	86.94	86.93	96.73	96.09	94.27	91.92	91.28
-4	99.46	99.45	99.97	99.92	99.77	99.49	98.13
-2	107.63	107.62	92.34	93.60	96.40	99.58	97.69
0	76.34	76.34	48.13	51.43	56.70	61.84	60.69
2	13.35	13.36	2.92	4.24	6.15	7.78	8.07
4	-7.25	-7.23	4.36	3.05	0.99	-0.87	0.91
6	-5.45	-5.44	16.42	14.24	10.38	6.64	9.10
8	0.00	0.01	26.16	23.76	19.15	14.47	17.14
10	5.01	5.02	33.09	30.65	25.70	20.54	23.25

Table 6.5: Comparisons between various theories and FEM results for the clamped-clamped isotropic homogeneous beam contact with varying P_2 and $P_1 = 1\,\mathrm{N}$.

	First contact		After first contact	
	P_2 (N)	G_I/G (%)	P_2 (N)	G_I/G (%)
Present Euler beam theory	8	0	10	0
100×2 Euler beams	7.99	0	10	0
Present Timo. beam theory	2.75	0	10	0
800×2 Timo. beams	3.06	0	10	0
200×2 Timo. beams	3.67	0	10	0
Averaged rule 1	4.33	0	10	0
400×6 QUAD4s	3.52	0	10	0

negligible and a second set of pure modes is generated numerically. This is consistent with the discussion and observations in Chapters 4 and 5. As expected, crack tip running contact begins at the $\left\{\varphi_{\beta_F}\right\}$ mode. Crack tip running contact necessarily gives $G_I/G = 0$. Beyond the $\left\{\varphi_{\beta_F}\right\}$ mode, the crack tips remain closed. The numerical simulations model this contact behaviour very closely.

Averaged partition rule 1 has been suggested in the previous two chapters as a potentially good approximation for the ERR partition from two-dimensional elasticity. The effect of shearing is small in this case because the beam is relatively thin. Therefore the curve from averaged partition rule 1 lies approximately midway between the curves from the present Euler and Timoshenko beam theories. There is excellent agreement between this curve and the results from FEM simulations with QUAD4 elements. In addition to the above, it is once again seen that the $\left\{\varphi_{\theta_F}\right\}$ and $\left\{\varphi_{\beta_F}\right\}$ modes are still the pure modes.

6.7.2 Tests with a clamped-clamped laminated composite beam

The data is now presented for the clamped-clamped laminated composite beam. The plane-strain assumption was used in all these analytical and numerical calculations. Under this assumption, $A = A_{11}$, $B = B_{11}$, $D = D_{11}$ and $H = A_{55}$. Since many of the observations are the same as for the isotropic homogenous case, they are not repeated. New observations are simply added. Tables 6.6 and 6.7 and Fig. 6.6 present results from the various analytical theories and from numerical simulations of the laminated composite clamped-clamped beam. There is excellent agreement between the present Euler beam partition theory and the numerical Euler beam results. There is also excellent agreement between the present Timoshenko beam partition theory and the numerical Timoshenko beam results.

In this composite case, there is a much larger difference between the $\left\{\varphi_{\theta_F}\right\}$ and $\left\{\varphi_{\theta'_F}\right\}$ modes than that seen for the isotropic homogeneous case (compare Tables 6.1 and 6.2).

Table 6.6: Comparisons between various theories and FEM results for the clamped-clamped laminated composite beam with varying P_2 and $P_1 = 1\,\text{N}$.

P_2 (N)	G_I/G (%)						
	Present Euler beam theory	100×2 Euler beams	Present Timo. beam theory	800×2 Timo. beams	200×2 Timo. beams	Averaged rule 1	200×16 QUAD4s
−10	145.33	145.33	87.57	89.20	98.46	113.51	101.99
−8	147.63	147.62	79.89	82.13	93.05	111.45	100.40
−6	145.01	145.00	68.83	71.93	84.24	105.37	95.65
−4	134.61	134.60	54.04	58.15	71.19	93.47	86.17
−2	114.10	114.09	36.51	41.43	53.97	74.79	70.87
0	83.82	83.81	19.27	24.13	34.51	50.90	50.73
2	48.24	48.24	6.41	9.90	16.58	26.46	29.71
4	14.30	14.30	0.47	1.65	3.83	6.72	12.78
6	−12.60	−12.61	0.98	−0.24	−2.39	−5.75	2.50
8	−30.77	−30.77	5.66	2.59	−3.12	−11.51	−1.66
10	−41.30	−41.29	12.21	7.99	−0.36	−12.56	−1.69

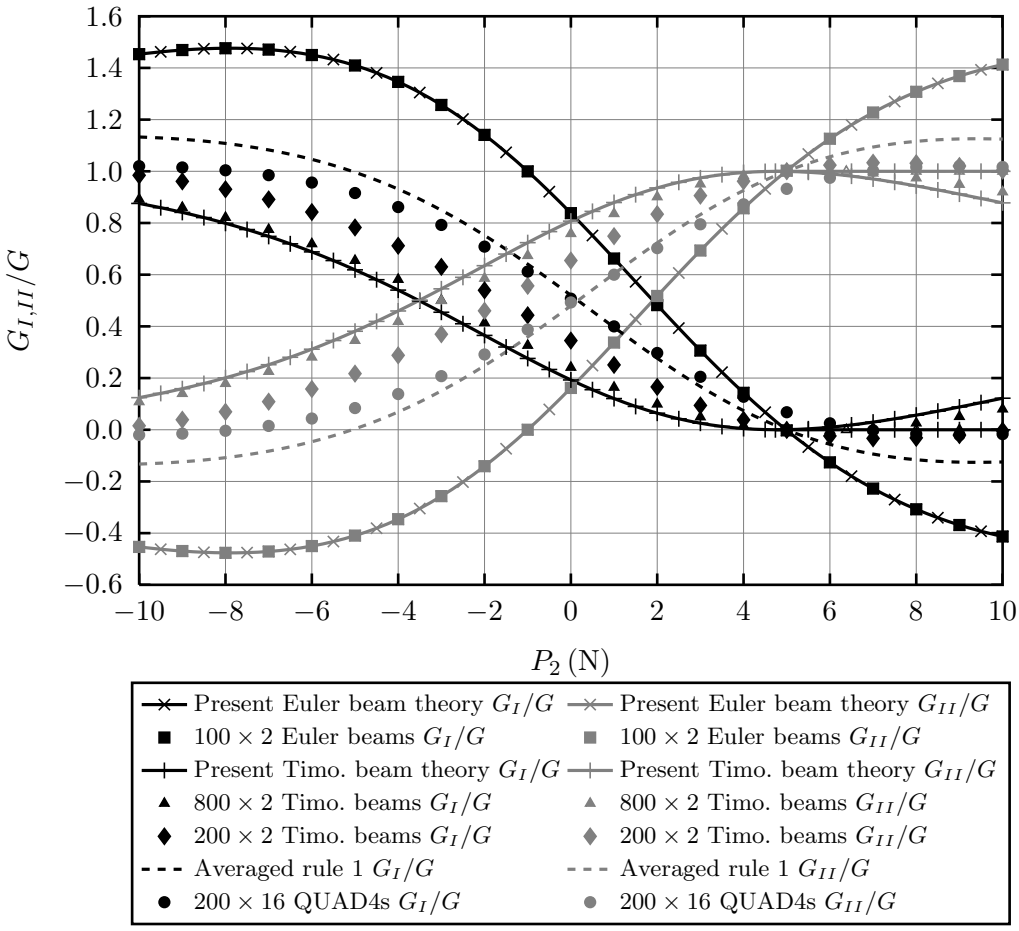

Figure 6.6: Comparisons between various theories and FEM results for the clamped-clamped laminated composite beam with varying P_2 and $P_1 = 1\,\mathrm{N}$.

Table 6.7: Comparisons between various theories and FEM results for the clamped-clamped laminated composite beam contact with varying P_2 and $P_1 = 1\,\mathrm{N}$.

	First contact		After first contact	
	P_2 (N)	G_I/G (%)	P_2 (N)	G_I/G (%)
Present Euler beam theory	66.90	0	100	0
100 × 2 Euler beams	66.77	0	100	0
Present Timo. beam theory	4.74	0	100	0
800 × 2 Timo. beams	6.38	0	100	0
200 × 2 Timo. beams	10.18	0	100	0
Averaged rule 1	18.23	0	100	0
200 × 16 QUAD4s	11.60	0	100	0

Having a curve from the present Euler beam partition theory with substantially different $\left\{\varphi_{\theta_F}\right\}$ and $\left\{\varphi_{\theta'_F}\right\}$ modes makes it substantially different to the curve from the present Timoshenko beam partition theory. This large difference might therefore have strained the accuracy of the present averaged partition theory. Despite this possibility, the agreement observed between averaged partition rule 1 and results from FEM simulations using QUAD4 elements is excellent for the whole the range of P_2, which is looked at.

6.7.3 Tests with a clamped circular isotropic homogeneous plate

Finally in this chapter, comparisons are made between the various analytical theories and the FEM results for the circular isotropic homogeneous plate. The results are given in Tables 6.8 and 6.9 and Fig. 6.7. The abbreviations 'KL' and 'MR' are used to indicate Kirchhoff–Love and Mindlin–Reissner plates respectively. Excellent agreement is seen in all cases between the analytical partition theories and their corresponding numerical results.

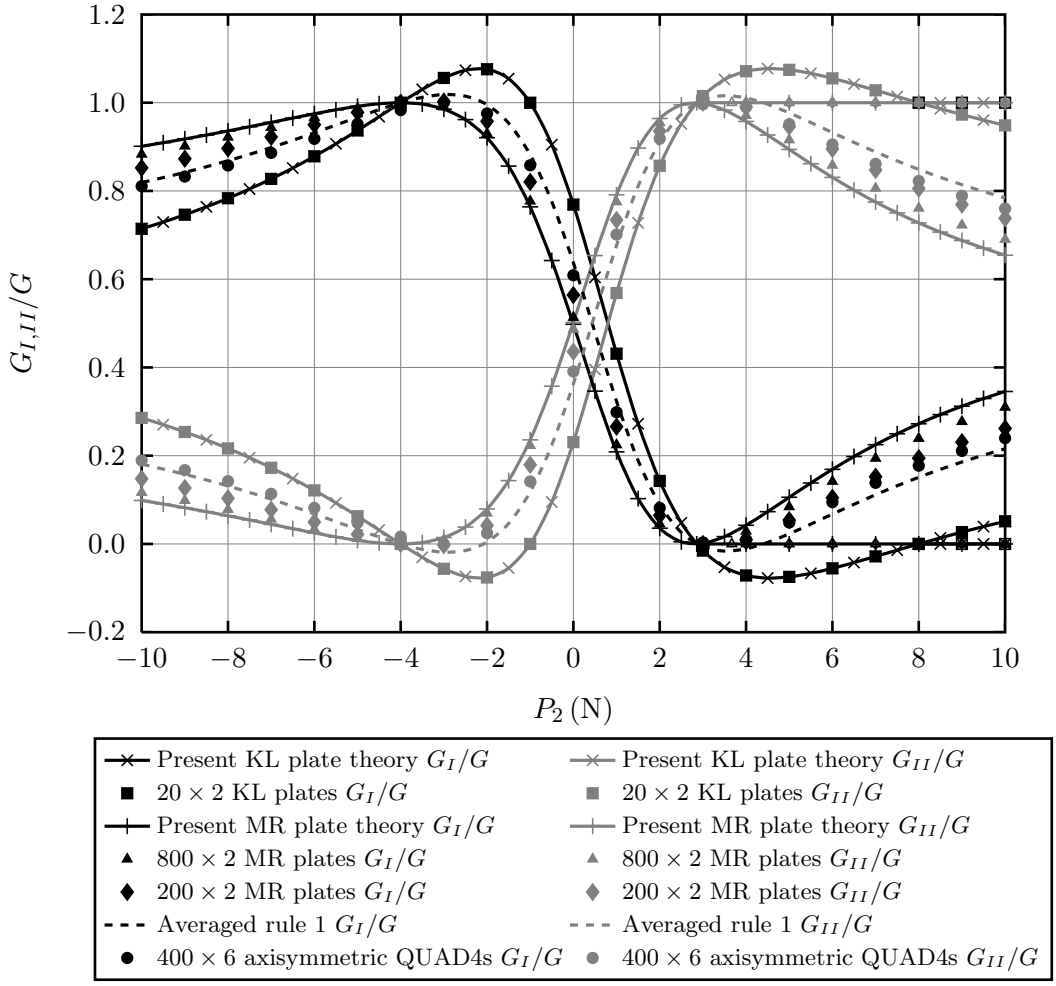

Figure 6.7: Comparisons between various theories and FEM results for the clamped circular isotropic homogeneous plate with varying P_2 and $P_1 = 1\,\mathrm{N}$.

Table 6.8: Comparisons between various theories and FEM results for the clamped circular isotropic homogeneous plate with varying P_2 and $P_1 = 1\,\mathrm{N}$.

P_2 (N)	G_I/G (%)						
	Present KL plate theory	20×2 KL plates	Present MR plate theory	800×2 MR plates	200×2 MR plates	Averaged rule 1	400×6 axisymmetric QUAD4s
−10	71.43	71.43	90.14	88.32	85.23	81.92	81.08
−8	78.35	78.35	93.61	92.19	89.65	86.86	85.78
−6	87.85	87.86	97.49	96.66	95.03	93.18	91.82
−4	100.00	100.00	100.00	100.00	100.00	100.00	98.34
−2	107.59	107.59	92.07	93.02	95.81	99.56	97.56
0	76.92	76.92	49.79	51.34	56.42	63.74	60.90
2	14.29	14.28	3.57	4.53	6.44	8.93	8.16
4	−7.14	−7.14	4.23	2.90	0.97	−1.09	0.98
6	−5.53	−5.52	16.91	14.18	10.47	6.76	9.47
8	0.00	0.01	27.24	23.91	19.45	15.11	17.74
10	5.13	5.14	34.55	30.97	26.18	21.57	23.99

Table 6.9: Comparisons between various theories and FEM results for the clamped circular isotropic homogeneous plate contact with varying P_2 and $P_1 = 1\,\mathrm{N}$.

	First contact		After first contact	
	P_2 (N)	G_I/G (%)	P_2 (N)	G_I/G (%)
Present KL plate theory	8	0	10	0
20×2 KL plates	8.00	0	10	0
Present MR plate theory	2.86	0	10	0
800×2 MR plates	3.08	0	10	0
200×2 MR plates	3.67	0	10	0
Averaged rule 1	4.39	0	10	0
400×6 axisymmetric QUAD4s	3.49	0	10	0

6.8 Conclusion

The completely analytical theories, which have been developed in the preceding chapters for mixed-mode ERR partitions in layered isotropic homogeneous and laminated composite DCBs, have been shown to give the correct ERR partition for one-dimensional fractures in general straight beam structures. In these types of structures, the internal forces at the crack tips are generally complex functions of remotely applied loads. It is not generally possible to obtain pure 'crack tip modes', i.e. modes, which relate crack tip quantities, because these quantities cannot be set independently of each other. Instead some combinations of these modes can give pure mode I or II fractures.

This chapter mainly focused on the specific cases of layered isotropic homogeneous and laminated composite straight beam structures with shear forces applied at an arbitrary location in the delaminated region. For these beams, 'F modes' have been derived. The F modes give the ratios required between the applied shear forces P_1 and P_2, required to give pure fracture modes.

The theories have been developed based on the present Euler and Timoshenko isotropic and laminated composite beam theories. Both theories have their own orthogonal $\left\{\varphi_{\theta_F}\right\}$ and $\left\{\varphi_{\beta_F}\right\}$ pure modes which are called the first set. They correspond to zero relative shearing displacement just behind the crack tip and zero crack tip opening force respectively. For the statically indeterminate beam structures examined in this paper, the first set of pure modes from present Euler beam partition theory is generally different in value to the first set from the present Timoshenko beam partition theory. However when the through-thickness shear effect is small, the pure modes from the present Euler beam partition theory may be a close approximation to the pure modes from the present Timoshenko beam partition theory.

In present Euler beam partition theory, there is a second set of orthogonal pure modes $\left\{\varphi_{\theta'_F}\right\}$ and $\left\{\varphi_{\beta'_F}\right\}$, which is different to the first set. These modes correspond to zero crack tip shearing force and zero relative opening displacement just behind the crack tip respectively. Within the context of the present Timoshenko beam partition theory, the $\left\{\varphi_{\theta'_F}\right\}$ and $\left\{\varphi_{\beta'_F}\right\}$ modes coincide with the $\left\{\varphi_{\theta_F}\right\}$ and $\left\{\varphi_{\beta_F}\right\}$ modes. Consequently the second set of pure modes effectively does not exist.

In addition to the above, the present Euler and Timoshenko beam partition theories have been re-derived for axisymmetric plates, giving the present Kirchhoff–Love and Mindlin–Reissner plate partition theories respectively.

The present Euler and Timoshenko beam theories agree very well with the corresponding beam FEM predictions. Similarly, the present Kirchhoff–Love and Mindlin–Reissner plate partition theories agree very well with the corresponding plate FEM predictions. Averaged partition rule 1, which has been suggested in the preceding chapters, has been further tested. The approximation generally agrees very well with two-dimensional FEM

results, even when the difference between the present Euler and Timoshenko beam partition theories is substantial and the accuracy of the approximation might have become strained.

The theories for the mode partition of DCBs have been extended to and shown to work excellently for general straight beam structures and axisymmetric plates. This gives further support for the theories being the general ones for the mode partitioning of one-dimensional fractures. They are readily applicable to a wide-range of engineering structures and will be a valuable analytical tool in many applications, for example for researchers to develop fracture propagation criteria; for design engineers to design high integrity structures and for numerical analysts to benchmark their simulations, etc.

Parts of this chapter have been published in Wang and Harvey (2012*c*). Further publications from this work are in preparation in Harvey et al. (2012) and Harvey and Wang (2012*b*).

Chapter 7

Experimental validation

Contents

7.1 Introduction

In the preceding chapters, completely analytical partition theories have been developed for one-dimensional fractures in straight beams and axisymmetric plates made of either isotropic homogeneous or laminated composite materials. These theories are based on classical and FSDT beams and plates. The theories have been validated through extensive FEM simulations. Experimental validation is also very important. In this chapter, the propagation of mixed-mode interlaminar fractures is investigated using existing experimental results from the literature and various partition theories. These are (1) a partition theory by Williams (1988) based on Euler beam theory; (2) a partition theory by Suo and Hutchinson (1990), Suo (1990) and Hutchinson and Suo (1992), based on two-dimensional elasticity; and (3) the present partition theories and rules from the preceding chapters, which are based on the Euler and Timoshenko beam theories.

Hashemi et al. (1991) carried out extensive experimental investigations to establish which out of Williams's (1988) partition theory (referred to as the 'global approach' in Hashemi et al.'s work) and Suo and Hutchinson's (1990) partition theory (referred to as the 'local approach' in Hashemi et al.'s work) is the most appropriate for partitioning mixed modes in laminated composites. Their approach to compare the two theories was to experimentally measure the critical ERR by measuring the load and displacement at the identified moment of initiation and/or propagation and to partition this ERR into mode I and mode II components using the two theories. Results were then plotted on a graph of mode I versus mode II ERR, which gave a failure locus for each partition theory. Since the failure locus is considered to be an intrinsic material property, it was expected that

the results from all tests should lie on the same failure locus. They used a variety of test methods, including variations on some of the test methods described in §1.4.1, in order to obtain mixed modes. The two partition theories often produced quite different results.

Charalambides et al. (1992) presented the results from a very similar investigation to the one carried out by Hashemi et al. (1991). Under the assumption that Williams's (1988) partition is the correct one, they suggested a general criterion for fracture under mixed-mode loading, which fitted their observed failure locus. Charalambides et al. (1992) also made some comparisons with spalling data from the work of Thouless et al. (1987). Spalling is where cracks occur very close to the surface. Thouless et al. (1987) carried out experiments on glass and PMMA, by loading the spall axially at a specified distance from the free surface. They discovered some trends in crack location, crack propagation load and in the onset of spalling. In particular, they observed that as the cracks propagated, they stabilised at a constant distance from the free surface. Under the assumption that in an isotropic homogeneous material, the crack propagates in such a way as to maintain pure mode I conditions at the crack tip (Cotterell and Rice 1980, Gold'stein and Salganik 1974), they used Suo and Hutchinson's (1990) partition theory to predict the stabilised crack depth and the crack propagation load. They made comparisons between the predicted and experimentally measured values. They noted 'appreciable discrepancies'. Charalambides et al. (1992) were unable to get better agreement using Williams's (1988) partition theory without postulating an additional sliding component to the mode II ERR due to 'fracture surface roughness'. Some other work by Thouless (1990) looked at interfacial failure of bonded glass slides under mixed-mode loading.

Kinloch et al. (1993) continued the work of Hashemi et al. (1991) by comparing the failure loci obtained from multiple different mixed-mode fracture tests and Williams's (1988) partition theory. They also included data from the modified MMB test (Reeder and J. H. Crews 1991). In the work, they made further comparisons with Suo and Hutchinson's (1990) partition theory and concluded that Williams's (1988) partition theory gave better results. Finally, they also fitted the mixed-mode failure criterion, suggested by Charalambides et al. (1992), to each set of data and found that all the failure loci could be described by this criterion.

Finally, it is work noting that many experimental investigations make use of Williams's (1988) partition theory to set up test apparatus and to partition the experimentally measured ERR (Hashemi et al. 1990, Kinloch et al. 1993, Charalambides et al. 1992, Hashemi et al. 1991, Reeder 1992, etc.). Williams's (1988) partition theory is very prevalent in the field of experimental fracture mechanics. The results from this chapter, which assesses the performance of each partition theory, are therefore very important.

This chapter has been published in Harvey and Wang (2012*a*).

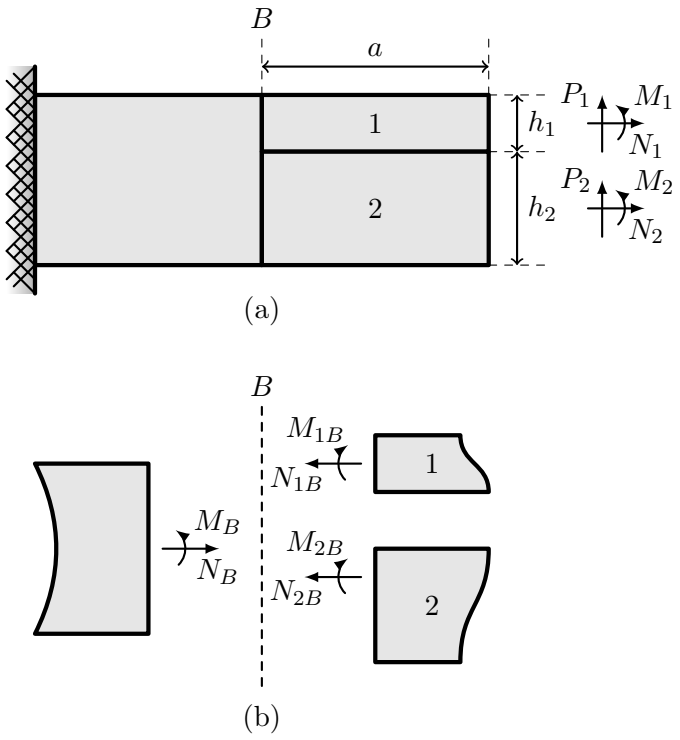

Figure 7.1: A DCB. (a) General description. (b) Crack tip forces.

7.2 Mixed-mode partition theories

7.2.1 The present partition theories

The present partition theories and rules are for one-dimensional fractures in straight beams and axisymmetric plates made of either isotropic homogeneous or laminated composite materials. Full details of the theories are given in the preceding chapters. In this chapter, the final expressions for ERR partition are presented in a *new* format, which is considered the most convenient for use by academic researchers and industrial engineers. In the preceding chapters, they have been presented in a format, which is most revealing of the underlying mechanics. No extra discussion is given—just the final expressions.

Fig. 7.1 (a) shows a DCB with its associated geometry, two tip bending moments, two tip axial forces and two tip shear forces. The partition is based on the bending moments and axial forces acting at the crack tip B, which are shown in Fig. 7.1 (b). Note that for the tests considered in this chapter, the through-thickness shear effect due to applied shear forces is small and is safely ignored. According to the present Euler beam partition theory for laminated composites (see Chapter 5), the mode I and II components of the total ERR, denoted by G_{IE} and G_{IIE} respectively, are

$$G_{IE} = c_{IE}\left(M_{1B} - \frac{M_{2B}}{\beta_1} - \frac{N_{1B}}{\beta_2} - \frac{N_{2B}}{\beta_3}\right)\left(M_{1B} - \frac{M_{2B}}{\beta_1'} - \frac{N_{1B}}{\beta_2'} - \frac{N_{2B}}{\beta_3'}\right) \tag{7.1}$$

$$G_{IIE} = c_{IIE}\left(M_{1B} - \frac{M_{2B}}{\theta_1} - \frac{N_{1B}}{\theta_2} - \frac{N_{2B}}{\theta_3}\right)\left(M_{1B} - \frac{M_{2B}}{\theta'_1} - \frac{N_{1B}}{\theta'_2} - \frac{N_{2B}}{\theta'_3}\right) \tag{7.2}$$

where

$$c_{IE} = G_{\theta_1}\left[\left(1 - \frac{\theta_1}{\beta_1}\right)\left(1 - \frac{\theta_1}{\beta'_1}\right)\right]^{-1} \tag{7.3}$$

$$c_{IIE} = G_{\beta_1}\left[\left(1 - \frac{\beta_1}{\theta_1}\right)\left(1 - \frac{\beta_1}{\theta'_1}\right)\right]^{-1} \tag{7.4}$$

and the values of θ_i are given by Eqs. (5.21) to (5.23), the values of β_i are given by Eq. (5.26) to (5.28) and the values of θ'_i and β'_i are given by Eqs. (5.54) to (5.59). The ERRs, G_{θ_1} and G_{β_1} are given by Eqs. (5.32) and (5.33) respectively.

According to the present Timoshenko beam partition theory for laminated composites (see Chapter 5), the mode I and II components of the total ERR, denoted by G_{IT} and G_{IIT} respectively, are

$$G_{IT} = c_{IT}\left(M_{1B} - \frac{M_{2B}}{\beta_1} - \frac{N_{1B}}{\beta_2} - \frac{N_{2B}}{\beta_3}\right)^2 \tag{7.5}$$

$$G_{IIT} = c_{IIT}\left(M_{1B} - \frac{M_{2B}}{\theta_1} - \frac{N_{1B}}{\theta_2} - \frac{N_{2B}}{\theta_3}\right)^2 \tag{7.6}$$

where

$$c_{IT} = G_{\theta_1}\left(1 - \frac{\theta_1}{\beta_1}\right)^{-2} \tag{7.7}$$

$$c_{IIT} = G_{\beta_1}\left(1 - \frac{\beta_1}{\theta_1}\right)^{-2} \tag{7.8}$$

Finally, averaged partition rule 1 is the average of the present Euler and Timoshenko beam partition theories. The mode I and II components of the ERR from averaged partition rule 1, denoted by G_{IA} and G_{IIA} respectively, are

$$G_{IA} = \left(G_{IE} + G_{IT}\right)/2 \tag{7.9}$$

$$G_{IIA} = \left(G_{IIE} + G_{IIT}\right)/2 \tag{7.10}$$

These three partitions are easily reduced for isotropic homogeneous materials (see Chapter 4). A thickness ratio $\gamma = h_2/h_1$ is now used. The present Euler beam partition theory for isotropic homogeneous beams reduces to

$$G_{IE} = c_{IE}\left(M_{1B} - \frac{M_{2B}}{\beta_1} - \frac{N_{1Be}}{\beta_2}\right)\left(M_{1B} - \frac{M_{2B}}{\beta'_1}\right) \tag{7.11}$$

$$G_{IIE} = c_{IIE}\left(M_{1B} - \frac{M_{2B}}{\theta_1} - \frac{N_{1Be}}{\theta_2}\right)\left(M_{1B} - \frac{M_{2B}}{\theta'_1} - \frac{N_{1Be}}{\theta'_2}\right) \tag{7.12}$$

where c_{IE} and c_{IIE} are still given by Eqs. (7.3) and (7.4) but now the values of θ_i are given by Eqs. (4.66) to (4.67), the values of β_i are given by Eq. (4.61) to (4.62), the values of θ_i' are given by Eqs. (4.77) to (4.78) and $\beta_1' = \gamma^3$, as given by Eq. (4.11). Note that for $\gamma = 1$, $\beta_2 = \infty$. The modal ERRs, G_{θ_1} and G_{β_1} are given by Eqs. (4.32) and (4.33) respectively. The equivalent axial force N_{1Be} is defined in Eq. (4.56).

The present Timoshenko beam partition theory for isotropic homogeneous beams reduces to

$$G_{IT} = c_{IT}\left(M_{1B} - \frac{M_{2B}}{\beta_1} - \frac{N_{1Be}}{\beta_2}\right)^2 \tag{7.13}$$

$$G_{IIT} = c_{IIT}\left(M_{1B} - \frac{M_{2B}}{\theta_1} - \frac{N_{1Be}}{\theta_2}\right)^2 \tag{7.14}$$

where c_{IT} and c_{IIT} are still given by Eqs. (7.7) and (7.8)

Finally, the present partition theories are presented for the special case of spalling (subsurface cracks), where $\gamma \to \infty$. The present Euler and Timoshenko beam partition theories and the averaged partition rule 1 are respectively

$$G_{IE} = \frac{3M_{1B}\left(2M_{1B} - h_1 N_{1B}\right)}{b^2 h_1^3 E} \quad \text{and} \quad G_{IIE} = \frac{N_{1B}\left(6M_{1B} + h_1 N_{1B}\right)}{2b^2 h_1^2 E} \tag{7.15}$$

$$G_{IT} = \frac{3\left(2M_{1B} - h_1 N_{1B}\right)^2}{8b^2 h_1^3 E} \quad \text{and} \quad G_{IIT} = \frac{\left(6M_{1B} + h_1 N_{1B}\right)^2}{8b^2 h_1^3 E} \tag{7.16}$$

$$G_{IA} = \frac{3\left(2M_{1B} - h_1 N_{1B}\right)\left(10M_{1B} - h_1 N_{1B}\right)}{16b^2 h_1^3 E}$$

$$\text{and} \quad G_{IIA} = \frac{\left(6M_{1B} + h_1 N_{1B}\right)\left(6M_{1B} + 5h_1 N_{1B}\right)}{16b^2 h_1^3 E} \tag{7.17}$$

The total ERR G is the same for all three theories

$$G = \frac{12M_{1B}^2 + h_1^2 N_{1B}^2}{2b^2 h_1^3 E} \tag{7.18}$$

7.2.2 The Suo–Hutchinson partition theory

Suo and Hutchinson (1990), Suo (1990) and Hutchinson and Suo (1992) considered a crack in a semi-infinite strip of orthotropic material and derived expressions for the mixed-mode intensity factors, which are analytical except for one parameter, which is determined numerically. These expressions are now referred to as the 'Suo–Hutchinson' partition theory. Good agreement between the Suo–Hutchinson partition theory and averaged partition rule 1 has been observed in §4.3.1. The partition theory is now reproduced here. For consistency, the notation has been changed where appropriate to match the conventions used elsewhere in this thesis. This partition theory assumes that a square-root singular field exists, so the partition is expressed in terms of stress intensity factors. With reference to

Fig. 7.1, the mode I and II stress intensity factors, K_{ISH} and K_{IISH} are

$$K_{ISH} = \frac{N}{\sqrt{2h_1 U}} \cos(\omega) + \frac{M}{\sqrt{2h_1^3 V}} \sin(\omega + \varepsilon) \tag{7.19}$$

$$K_{IISH} = \frac{N}{\sqrt{2h_1 U}} \sin(\omega) - \frac{M}{\sqrt{2h_1^3 V}} \cos(\omega + \varepsilon) \tag{7.20}$$

where M and N are linear combinations of the applied loads:

$$bN = -N_1 + C_1 (N_1 + N_2) - \frac{C_2}{h_1} \left[M_1 + M_2 + \frac{h_1}{2} (N_2 - \gamma N_1) \right] \tag{7.21}$$

$$bM = M_1 - C_3 \left[M_1 + M_2 + \frac{h_1}{2} (N_2 - \gamma N_1) \right] \tag{7.22}$$

$$C_1 = \frac{1}{1+\gamma}; \quad C_2 = \frac{6\gamma}{(1+\gamma)^3} \quad \text{and} \quad C_3 = \frac{1}{(1+\gamma)^3} \tag{7.23}$$

The geometric factors U, V and ε are functions of γ.

$$U = \frac{\gamma^3}{3 + 6\gamma + 4\gamma^2 + \gamma^3}; \quad V = \frac{\gamma^3}{12(1+\gamma^3)} \quad \text{and} \quad \frac{\sin\varepsilon}{\sqrt{UV}} = \frac{6(1+\gamma)}{\gamma^3} \tag{7.24}$$

The quantity ω is determined from the following approximate formula:

$$\omega = 52.1^\circ - 3^\circ/\gamma \tag{7.25}$$

For the spalling case, taking the limit where $\gamma \to \infty$ gives

$$K_{ISH} = \frac{M_1}{b} \sqrt{\frac{6}{h_1^3}} \sin(52.1^\circ) - \frac{N_1}{b} \sqrt{\frac{2}{h_1}} \cos(52.1^\circ) \tag{7.26}$$

$$K_{IISH} = -\frac{M_1}{b} \sqrt{\frac{6}{h_1^3}} \cos(52.1^\circ) - \frac{N_1}{b} \sqrt{\frac{1}{2h_1}} \sin(52.1^\circ) \tag{7.27}$$

For comparison with the present partition theories, Irwin's equivalence between the ERRs and the stress intensity factors can be used. They are given in §2.3.3 and are repeated here for convenience.

$$G_I = \frac{K_I^2}{\overline{E}} \quad \text{and} \quad G_{II} = \frac{K_{II}^2}{\overline{E}} \tag{7.28}$$

$\overline{E}$ is the equivalent Young's modulus, which depends on the loading condition. For plane stress, $\overline{E} = E$ and for plane strain, $\overline{E} = E/\left(1 - \nu^2\right)$.

7.2.3 The Williams partition theory

Williams (1988) was one of the first researchers to attempt to partition a mixed mode. His theory has been applied to the various test methods for laminates (Williams 1988, Hashemi

et al. 1990, Kinloch et al. 1993). Some work has been also been done to experimentally assess the performance of the theory (Kinloch et al. 1993, Charalambides et al. 1992, Hashemi et al. 1991). His pioneering work was partially successful in that, when it is compared against the present Euler beam partition theory, it correctly predicts a pair of pure modes. It can also give the correct partition for a symmetric DCB, i.e. $\gamma = 1$. However, it cannot identify the other pure modes from the present Euler beam partition theory and also missed the stealthy interaction between pure modes. The limitations have been reported many times and by several different researchers (Hutchinson and Suo 1992, etc.).

The Williams partition, denoted by G_{IW} and G_{IIW}, is now reproduced here. Again, for consistency, the notation has been changed where appropriate to match the conventions used in this thesis.

$$G_{IW} = \frac{6\left(M_{2B} - M_{1B}\gamma^3\right)^2}{b^2 h_1^3 E\gamma^3\left(1+\gamma^3\right)} \tag{7.29}$$

$$G_{IIW} = \frac{18\gamma\left(M_{1B}+M_{2B}\right)^2}{b^2 E h_1^3\left(1+\gamma\right)^3\left(1-\gamma+\gamma^2\right)} + \frac{\left(1-\gamma\right)^2\left(N_{2B}-\gamma N_{1B}\right)^2}{2b^2 h_1 E\gamma^3\left(1+\gamma\right)} \tag{7.30}$$

For the spalling case, taking the limit where $\gamma \to \infty$ gives

$$G_{IW} = \frac{6M_{1B}^2}{b^2 h_1^3 E} \quad \text{and} \quad G_{IIW} = \frac{N_{1B}^2}{2b^2 h_1 E} \tag{7.31}$$

7.3 Nature of local and global partitions

There is an important difference between a local ERR partition and a global ERR partition. This difference is important because it is not known which is more appropriate for determining fracture propagation between interfaces and under what circumstances. In the next section, published experimental data will be used to try to make an assessment of this. Simply put, local pureness is defined with respect to the crack tip whilst the global pureness is defined with respect to the entire region that is mechanically affected by the presence of the crack (i.e. the Δa region, shown in Fig. 4.2). Mathematically, the difference is in the integration limits of the crack closure integral: the global ERR partition is calculated by including the whole crack influence region in the integration limits; the local partition only considers the near-crack tip region. Note that the total ERR is not affected by the limits of the crack closure integral (Rice 1968), however the partition of ERR *is* affected. This was analytically shown in §4.2.2 and numerically shown in §4.3.1. Since the difference between local and global pureness turns out to be particularly relevant to the discussion in the remainder of this chapter, the differences between and meaning of the two types of partition are now further demonstrated and explained.

In summary, the findings in §4.2.2 are that the present Euler beam partition theory has two sets of pure modes—the first (θ, β) set and the second (θ', β') set—that are both locally

and globally pure. The local and global partitions are therefore the same when using the present Euler beam partition theory. For the present Timoshenko beam partition theory, there are two sets of locally pure modes, which exactly coincide on the first (θ, β) set from the present Euler beam partition theory. There are also two sets of globally pure modes and they are the same as the pure modes from the present Euler beam partition theory. Therefore, when using the present Timoshenko beam partition theory, the local partition exhibits no interaction (because the two sets of local pure modes coincide) and is different to the present Euler beam partition theory. However, the global partition is the same as the present Euler beam partition theory. Since averaged partition rule 1 is the average of the present Euler and Timoshenko beam partition theories, it behaves in the same way. The global partition is the same as the present Euler beam partition theory but the local partition is generally different. Note that in all cases, the first (θ, β) set of pure modes is always both locally and globally pure. This is why it provides the complete basis for mode partitioning.

It was numerically shown in §4.3.1 that the globally pure modes from the present Timoshenko beam partition theory and two-dimensional elasticity are the same as the pure modes from the present Euler beam partition theory. Now, it is shown numerically that the global ERR partitions from present Timoshenko beam partition theory and two-dimensional elasticity are the same as the ERR partitions the present Euler beam partition theory. The FEM simulation capability, which was developed in Chapter 3 and which is based on the Euler and Timoshenko beam theories and two-dimensional elasticity, is used. Normal and shear point interface springs with very high stiffness are used to model perfectly bonded plies. The ERR partition is calculated using the VCCT in conjunction with these interface springs. The number of spring pairs used in the calculation of ERR can easily be adjusted, from one spring pair for the local partition to many spring pairs to approach the global partition. Full details are given in §3.3 and §3.5.

Numerical tests were carried out on the DCB shown in Fig. 7.1 (a). The same configuration as that in §4.3 was used. A plane-stress condition was assumed. The units of these FEM simulations are kN and mm. The Young's modulus is $E = 1\,\text{GPa}$, the Poisson's ratio is $\nu = 0.3$ and the shear modulus is $\mu = E/\left[2\left(1+\nu\right)\right] = 1/2.6\,\text{GPa}$. The intact length is $L = 100\,\text{mm}$, the crack length is $a = 10\,\text{mm}$ and the width is $b = 1\,\text{mm}$. The thickness is $h = h_1 + h_2 = 3\,\text{mm}$ with $h_1 = 1\,\text{mm}$. Therefore, the thickness ratio is $\gamma = 2$. Tip bending moments were applied to the DCB tip. M_1 was held constant at $1\,\text{Nm}$ and M_2 was varied from $-10\,\text{Nm}$ to $10\,\text{Nm}$. There are no axial forces or shear forces in this example. Imaginary normal and shear point interface springs with the very high stiffness of $k_s = 10^6\,\text{kN/mm}$ were used to model perfectly bonded plies. Appendix B gives details on how this value was determined and also presents the mesh convergence studies for this section and how suitable meshes were chosen to obtain mesh-independent results. Contact between crack surfaces was not considered.

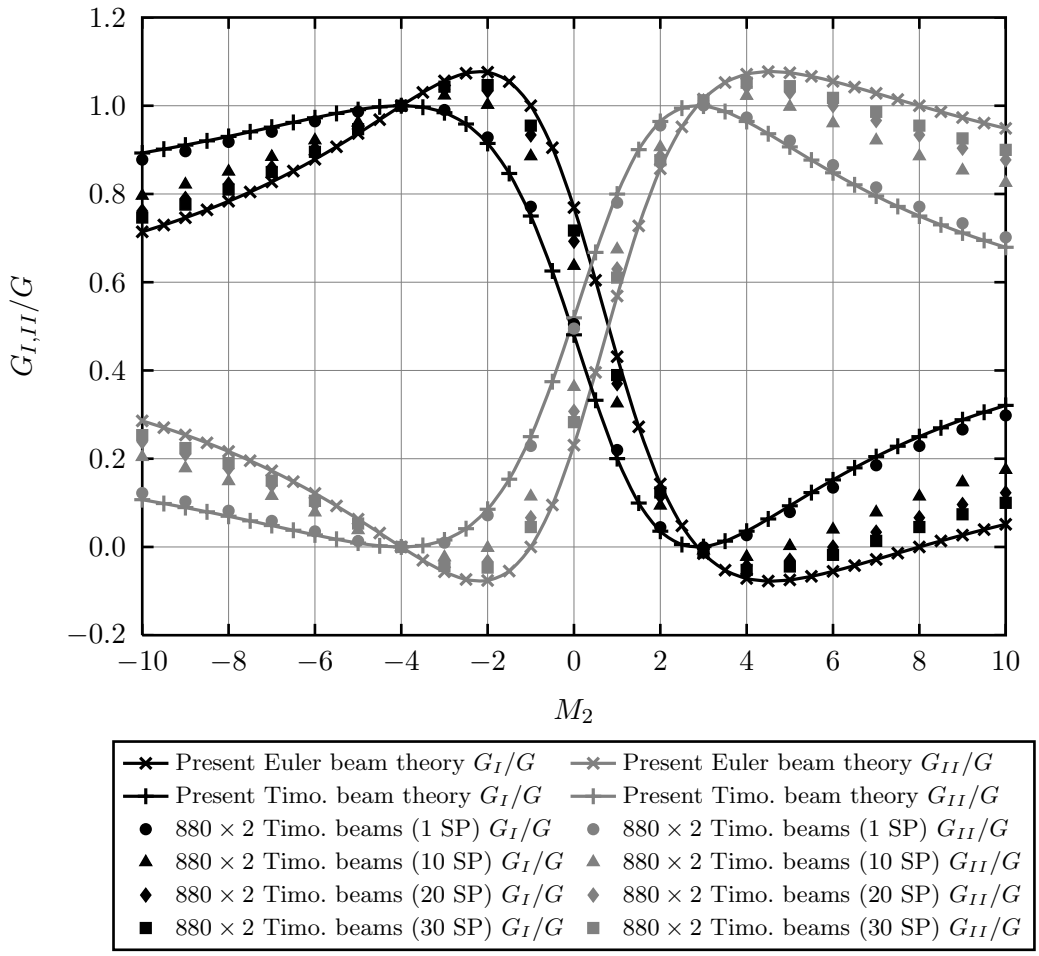

Figure 7.2: Analytical and FEM Timoshenko beam partitions of local and global ERR G_I/G of a DCB with varying M_2 and $M_1 = 1$.

Firstly, two layers of uniformly distributed linear Timoshenko beam elements were used to model the specimen. 1, 10, 20 and 30 spring pairs were used in the VCCT to calculate the ERR partition. The numerical ERR partitions for different values of M_2 are shown in Fig. 7.2 along with the present Timoshenko and Euler beam partition theories. In the legend, the abbreviations '1 SP', '10 SP', etc. are used to indicate one and ten spring pairs being used in the calculation of G_I and G_{II}. It is seen that as the number of spring pairs is increased, the numerical partition closely approaches the present Euler beam partition theory, which as has just been described, is also the global form of the present Timoshenko beam partition theory.

Secondly, six layers of uniformly distributed plane-stress QUAD4 elements were used to model the specimen. Again, the ERR partition G_I and G_{II} was calculated using the VCCT with 1, 10, 20 and 30 spring pairs. The numerical ERR partitions for different values of M_2 are shown in Fig. 7.3 along with the present Euler beam partition theory and averaged partition rule 1. As expected, as the numerical partition becomes a global one, it closely approaches the present Euler beam partition theory.

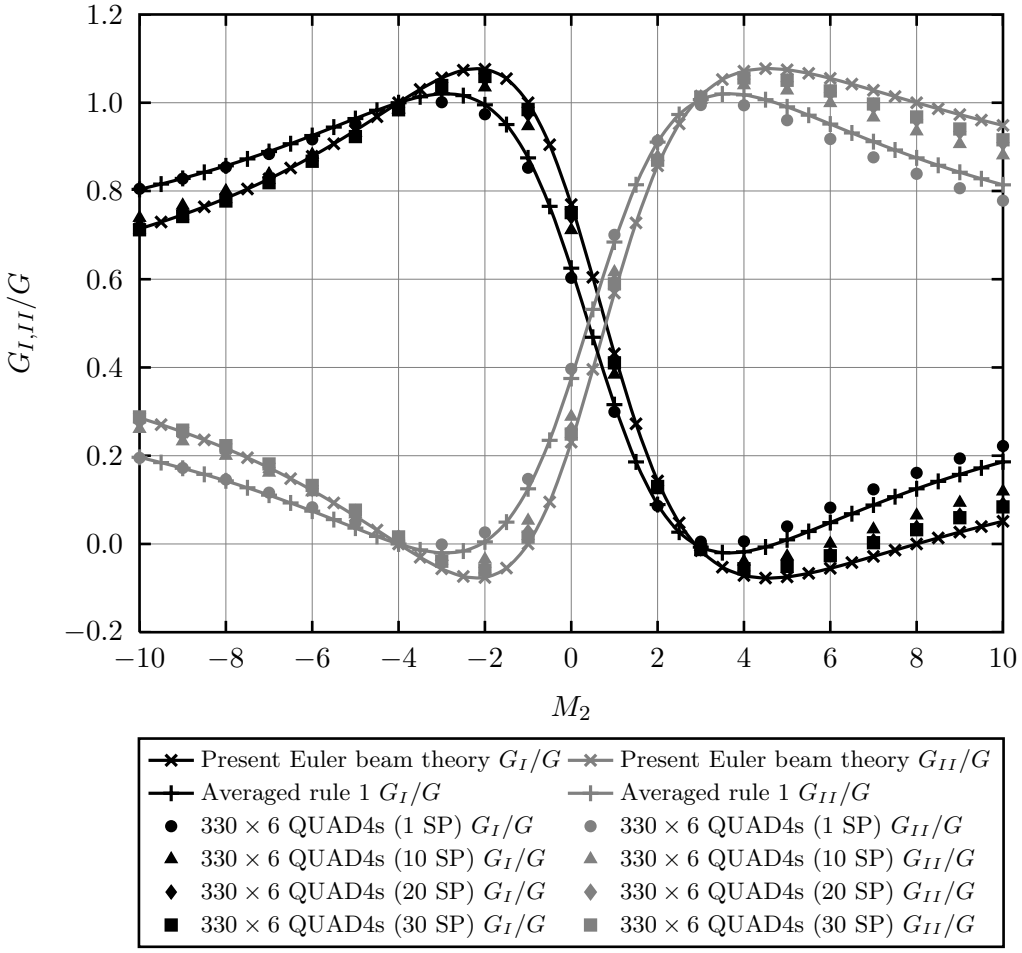

Figure 7.3: Analytical and FEM two-dimensional elasticity partitions of local and global ERR G_I/G of a DCB with varying M_2 and $M_1 = 1$.

Note that although in both cases 30 spring pairs represents a fairly large proportion of the length of the specimen, this is due to the discrete nature of the FEM. Using more elements along the length shows that a similarly converged global partition can be obtained over a shorter length.

7.4 Experimental validation

7.4.1 A note on mixed-mode failure criteria

Before reviewing experimental data from the literature and making comparative analyses, it is worth making some comments on mixed-mode failure criteria. In §7.4.2 and §7.4.3, some calculations and comparisons are made using the linear failure criterion, given by Eq. (7.32). Many different mixed-mode failure criteria have been suggested for predicting delamination growth. Reeder (1992) gave a comprehensive review of them.

The linear failure criterion is the one most often used in the literature (Reeder 1992). In addition there is a wealth of data that either strongly supports the criterion (Kutlu and

Chang 1995, Wang and Zhang 2009, Jurf and Pipes 1982, Sanford and Stonesifer 1970, Donaldson 1985, etc.), or suggests criteria that are close to it (Donaldson 1985, Wu 1967, McKinney 1972, Yoon and Hong 1990, etc.).

Therefore, in this work, the linear failure criterion is expected to be reasonably accurate and to give a good approximation to the failure locus, against which different analytical partition theories can be compared. This is also the approach used by Charalambides et al. (1992).

7.4.2 Asymmetric double cantilever beam test

The asymmetric DCB test is shown in Fig. 7.4 (a). Equal and opposite bending moments are applied to the upper and lower arms of an asymmetric beam specimen. The crack tip forces are therefore $M_{1B} = -M_{2B} = M$ and $N_{1Be} = 0$. Experimental measurements of the total critical ERR from unidirectional carbon/epoxy specimens with various values for h_1 and h_2 are given in Table 7.1 (Charalambides et al. 1992).

If the failure locus and critical ERRs G_{Ic} and G_{IIc} for the material are known, then for a given partition theory the total critical ERR for a specimen can be inferred. The linear failure locus is

$$\frac{G_I}{G_{Ic}} + \frac{G_{II}}{G_{IIc}} = 1 \tag{7.32}$$

As noted in §7.4.1, the actual failure locus is generally not far from this empirically suggested form (Charalambides et al. 1992). Hashemi et al. (1990) obtained critical ERR values. From the DCB test $G_{Ic} = 0.27 \pm 0.015\,\mathrm{kN/m}$; from the ELS test $G_{IIc} = 0.60 \pm 0.03\,\mathrm{kN/m}$ and from the ENF test $G_{IIc} = 0.65 \pm 0.02\,\mathrm{kN/m}$. In this work the values used are: $G_{Ic} = 0.27\,\mathrm{kN/m}$ and $G_{IIc} = 0.63\,\mathrm{kN/m}$, which is an average of the two pure

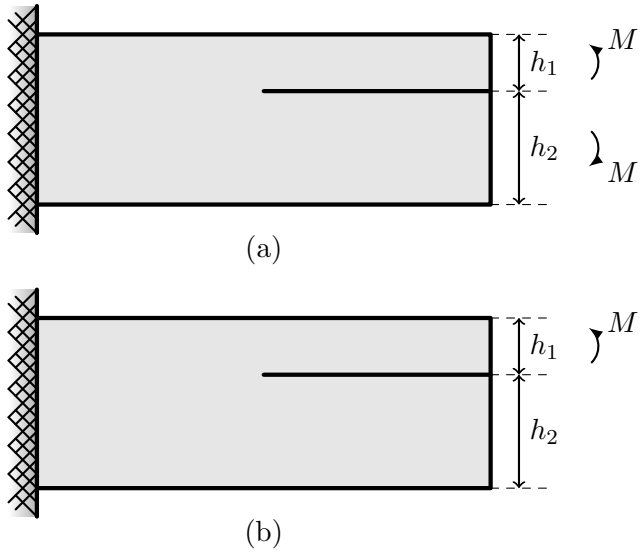

Figure 7.4: Tests with asymmetric beam specimens. (a) Asymmetric DCB test. (b) FRMM test.

Table 7.1: Values of measured critical ERR G_c for a unidirectional carbon/epoxy asymmetric DCB with the values expected from various partition theories.

							Present partition theories					
	Measured		Suo–Hutchinson		Williams		Euler		Timoshenko		Averaged	
γ	h (mm)	G_c (kN/m)	G_I/G (%)	G_c (kN/m)	G_I/G (%)	G_c (kN/m)	G_I/G (%)	G_c (kN/m)	G_I/G (%)	G_c (kN/m)	G_I/G (%)	G_c (kN/m)
1.33	3.85	0.26	96.4	0.28	100.0	0.27	100.0	0.27	94.2	0.28	97.1	0.27
1.55	3.70	0.27	92.4	0.28	100.0	0.27	100.0	0.27	87.7	0.29	93.9	0.28
1.97	3.33	0.28	85.5	0.29	100.0	0.27	100.0	0.27	75.7	0.31	87.8	0.29
3.72	10.00	0.29	75.3	0.31	100.0	0.27	100.0	0.27	50.1	0.38	75.1	0.31
4.11	2.86	0.29	75.2	0.31	100.0	0.27	100.0	0.27	47.4	0.39	73.7	0.32

mode II tests and permitted by the error margins of both tests as well. From Eq. (7.32), the mode I ERR partition G_I/G from a given partition theory predicts the following total critical ERR G_c:

$$G_c = \left[\frac{(G_I/G)}{G_{Ic}} + \frac{1 - (G_I/G)}{G_{IIc}} \right]^{-1} \tag{7.33}$$

In Table 7.1, the values predicted by the various partition theories in §7.2 for each specimen are compared against the experimentally measured G_c values. Both the present Euler beam partition theory and the Williams partition theory predict that the fracture is pure mode I for all values of h_1 and h_2. This is the $M_{2B}/M_{1B} = \theta_1'$ pure mode I mode. Therefore $G_c = G_{Ic}$ for all the specimens. The experimental G_c values show very small variation. As the specimen thickness ratio γ changes from 1.33 to 4.11, the change in measured G_c is only 0.03 kN/m. Given that the error margin for G_{Ic} is 0.015 kN/m and that the experimental G_c values are distributed evenly around 0.27 kN/m, the present Euler beam and Williams partition theories are certainly both compatible with the experimental results.

The present Timoshenko beam partition theory shows significantly more variation and in the majority of cases is not close to the experimental values. In particular, for the thickest specimen for which $h = 10$ mm (the length is 120 mm, giving an aspect ratio of 12, which is very low), the measured G_c is not any closer to the value predicted by the present Timoshenko beam partition theory. Since the present Timoshenko beam partition theory might be expected to give a better prediction for low aspect ratios, this implies that perhaps the partition that determines failure is global and therefore given by the present Euler beam partition theory. Observations from individual specimens must be treated with caution however and this possibility is far from conclusive.

The Suo–Hutchinson partition theory and averaged partition rule 1 are very similar, as expected. These two theories show a gradual increase in G_c with increasing γ, which is in agreement with the experimental results. Each result is also within the experimental error margin. It is therefore concluded that all theories, except the present Timoshenko beam partition theory, are compatible with these experimental results. From this test, it is not possible to make further conclusions.

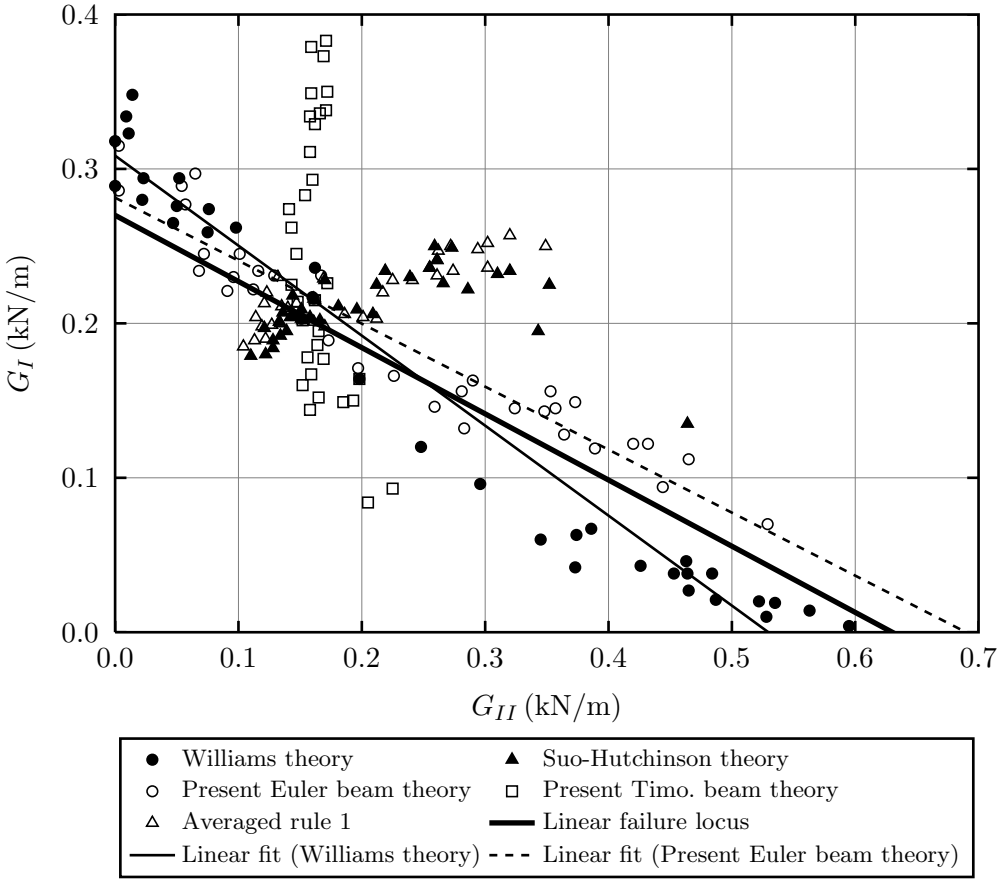

Figure 7.5: FRMM test partitions from various partition theories and the linear failure locus for unidirectional carbon/epoxy specimens.

7.4.3 Fixed ratio mixed-mode test

Fig. 7.4 (b) shows the FRMM test (see §1.4.2), in which a bending moment M is applied to the upper arm only of an asymmetric beam specimen. The crack tip forces are therefore $M_{1B} = M$ and $M_{2B} = N_{1Be} = 0$, which produce a mixed-mode fracture. The total critical ERR can be measured experimentally.

Charalambides et al. (1992) took experimental measurements of G_c for multiple unidirectional carbon/epoxy specimens, loaded in the FRMM test, and partitioned them into G_I and G_{II}. The partition was made using the Williams partition theory. These values of G_I and G_{II} are the black, filled circle markers in Fig. 7.5. As noted by Hashemi et al. (1991), there is no evidence for an R-curve for carbon/epoxy specimens and hence $G_c\,(\text{initiation}) = G_c\,(\text{propagation})$. Since both the partition of G_c and the method by which it was partitioned are known, there is sufficient information to re-partition the data according to the different partition theories in §7.2.

First, the thickness ratio γ must be determined for each specimen. Because the total G is known from G_I+G_{II}, the critical load M_{1B} can be determined for each data point. Under this critical load and using the Williams partition theory, only one value of thickness ratio

γ can give the G_I and G_{II} values. The thickness ratio γ of each specimen can therefore be calculated using Eq. (7.29) or Eq. (7.30). Now the experimentally measured G_c can be partitioned into G_I and G_{II} for each specimen, characterised by its thickness ratio γ, using the different partition theories in §7.2. The partitions from the Suo–Hutchinson partition theory, the two present beam partition theories and averaged rule 1 are also presented in Fig. 7.5. The linear failure locus is also shown.

From Eq. (7.32), the importance of having a significant difference between G_{Ic} and G_{IIc} can be seen. If $G_{Ic} = G_{IIc}$, then the failure locus is not affected by the partition and all data points will lie on the linear failure locus regardless of the partition. However if $G_{Ic} \neq G_{IIc}$, then the partition *does* affect the failure locus. This has also been pointed out by Hashemi et al. (1991). To assess the quality of the competing theories, it is therefore better to use a more brittle thermoset-matrix material, where there is usually a larger difference (Charalambides et al. 1992). The carbon/epoxy composite specimens fulfil this requirement.

From Fig. 7.5, it is seen that the present Euler beam partition theory performs much better than the other partition theories when compared with the linear failure locus. This could be because the specimens tested have a high aspect ratio ($\sim$ 27) and therefore essentially behave as Euler beams. As has been shown in §7.3, global measurements of G_c correspond to the present Euler beam partition theory. Alternatively, it is therefore also possible that failure, at least in the experimental cases considered, is based on the present global partition. It is not possible to distinguish which is the correct reason from these results. This latter possibility was also the conclusion of Charalambides et al. (1992). A trend line, which is represented by the black dashed line in Fig. 7.5, has been plotted through the present Euler beam partition. For comparison, a solid black trend line has also been plotted through the Williams partition. For clarity, Fig. 7.6 shows the linear failure locus and these two data sets with their corresponding trend lines in isolation. It is seen that the present Euler beam partition gives much closer agreement with the expected linear failure locus and expected G_{Ic} and G_{IIc} than the Williams partition. Quantitative statistical measures can also be given for better comparison. Comparing the present Euler beam partition against the linear failure locus, the root mean square of the residuals is 0.025 kN/m. This is the 'standard error' or 'standard deviation'. For a normally distributed deviation, 68.3% of the data points would lie within one standard deviation of the linear failure locus and 95.5% within two standard deviations. For the Williams partition, the standard error (also against the linear failure locus) is 0.040 kN/m, which is 1.6 times greater than that from the present Euler beam partition.

Now consider the other partition theories shown in Fig. 7.5. The present Timoshenko beam partition of the experimental measurements forms a separate vertical curve. The partitions from the Suo–Hutchinson partition theory and averaged partition rule 1 are very similar as expected and form another curve half way between the curves from the present Euler and the Timoshenko beam partitions. Since the linear failure locus is generally

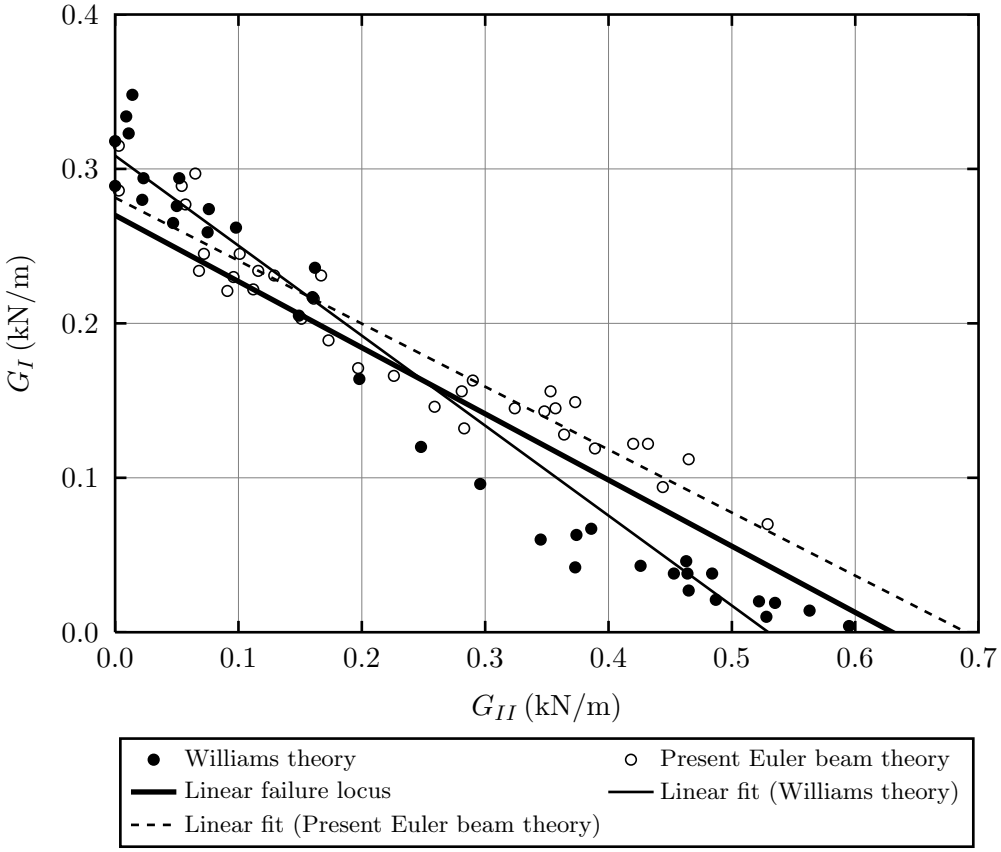

Figure 7.6: FRMM test partitions from the Williams and present Euler beam partition theories and the linear failure locus for unidirectional carbon/epoxy specimens.

regarded to be a good approximation to the actual failure locus, it must be concluded that, at least for these specimens, the present local Timoshenko beam partition theory, averaged partition rule 1 and the Suo–Hutchinson partition theory cannot give the partition that controls the fracture propagation. As stated above, there are two possible reasons for this. It might be because of the local nature of all these partition theories. If failure is dependent on the global partition then only the present Euler beam partition theory can give the right partition. Alternatively, it could be because these specimens approach Euler beams in their behaviour because of their high aspect ratio.

Further evidence for the correctness of the present Euler beam partition theory is given in Fig. 7.7. The figure responds to the inevitable question: if the present Euler beam partition theory is the correct one and the linear failure locus is a good approximation, can it successfully predict the curve of the Williams partition? To answer the question, the present Euler beam partition theory was used to calculate the thickness ratio γ for multiple points on the linear failure locus (the solid black line in the figure). Then the total critical ERRs G_c for these 'imaginary specimens' were repartitioned using the Williams partition theory. These partitions are represented by the black dashed line. The experimental values, partitioned using the two theories, are also shown. It is seen that the dashed line very

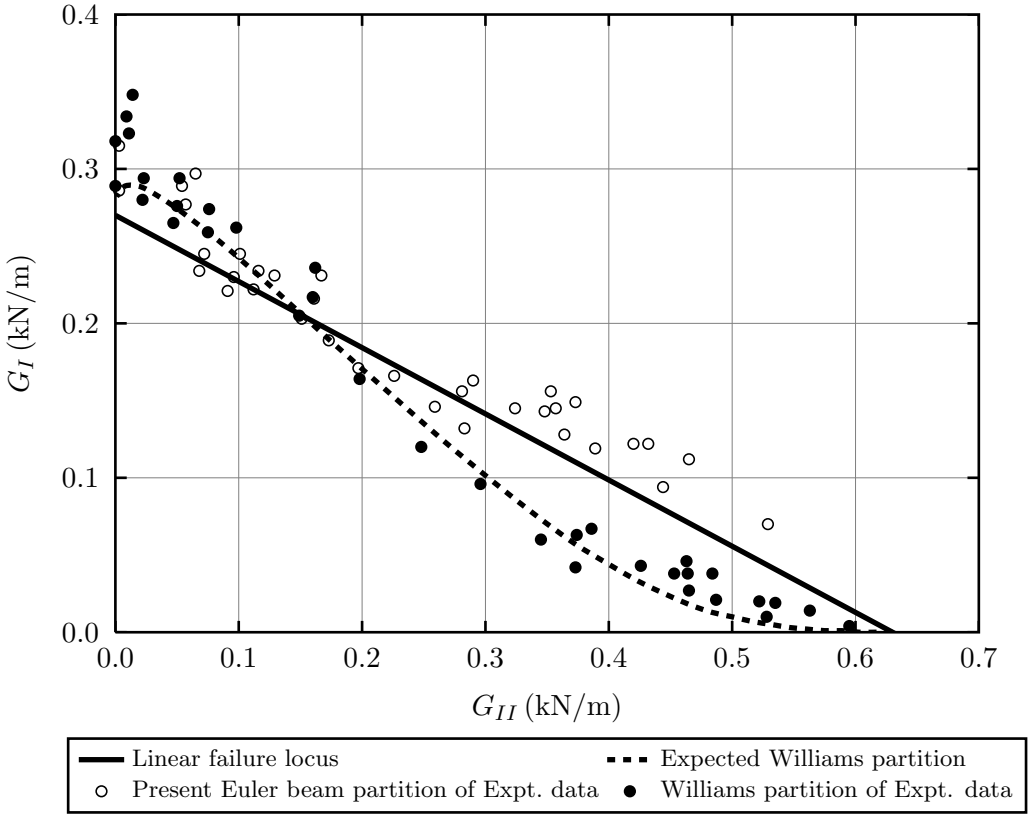

Figure 7.7: The linear failure locus for unidirectional carbon/epoxy specimens, repartitioned using the present Euler beam partition theory into the expected Williams partition curve, and FRMM test partitions from the corresponding partition theories.

closely predicts the curve of the Williams partition of the experimental measurements. Furthermore, the dashed line strongly resembles the 'general criterion for mixed-mode failure' suggested by Charalambides et al. (1992) on the basis of the Williams partition of the experimental results. This criterion is also plotted in figures in the paper by Hashemi et al. (1991).

In summary, under the assumption that the linear failure locus is accurate, the Williams partition and his suggested failure criterion can be completely explained using the present Euler beam partition theory without resorting to correction factors for surface roughness and friction, as is done by Charalambides et al. (1992). In fact, if the present Euler beam partition theory is correct, then the Williams partitions are exactly where they would be expected to be. It is therefore proposed that the present Euler beam partition theory offers the best and most simple explanation for all the observations, without having to suppose extra significant mechanical effects.

Two additional sets of experimental data from the FRMM test are available from work by Hashemi et al. (1991). The first set of data is also for unidirectional carbon/epoxy specimens. The present Euler beam and Williams partitions of this experimental data with their trend lines and the linear failure locus are shown in Fig. 7.8. It is seen that the

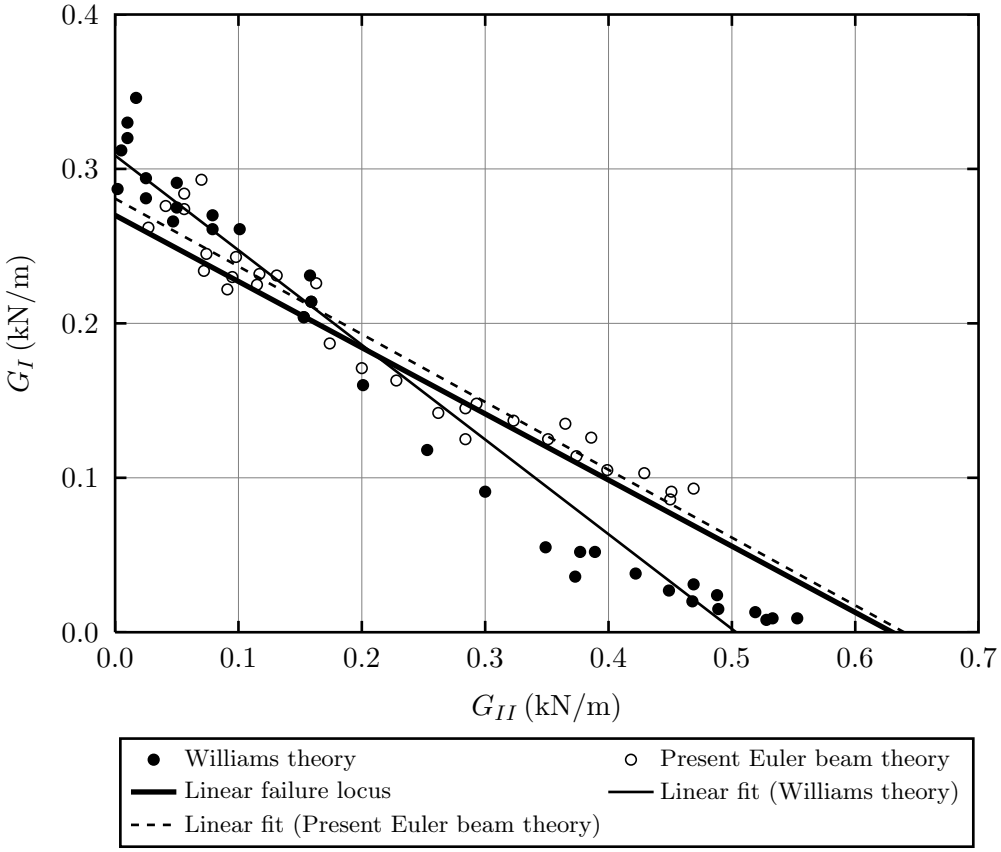

Figure 7.8: FRMM test partitions from the Williams and present Euler beam partition theories and the linear failure locus for unidirectional carbon/epoxy specimens.

present Euler beam partition is in excellent agreement with the linear failure locus. The standard error when compared with the linear failure locus is 0.018 kN/m. Once more, the Williams partition is not close to the linear failure locus. The standard error is 0.043 kN/m. The Suo–Hutchinson partitions are not shown for clarity, but as before, they form a curve approximately normal to the linear failure locus.

The second set of experimental data from Hashemi et al. (1991) is for unidirectional carbon/polyether ether ketone (PEEK) specimens. There seems to be some significant variation in the literature for the critical ERRs (Hashemi et al. 1990, Hashemi et al. 1991, Reeder 1992). In this work, the values from Hashemi et al. (1990) are used. These values also appear to be the most reliable since they are directly from pure mode testing. Considering here only crack propagation (not initiation), from the DCB test $G_{Ic} = 2.42 \pm 0.016$ kN/m and from the ELS test $G_{IIc} = 3.16 \pm 0.014$ kN/m. The present Euler beam and Williams partitions of the experimental measurements are plotted in Fig. 7.9. Both partitions are approximately linear, very close to each other and far from the linear failure locus. The distance from the failure locus is likely to be due to values of critical ERR used, which are material constants and not determined by the partition theory. The uncertainty surrounding these values has already been pointed out. The fact that both partitions are

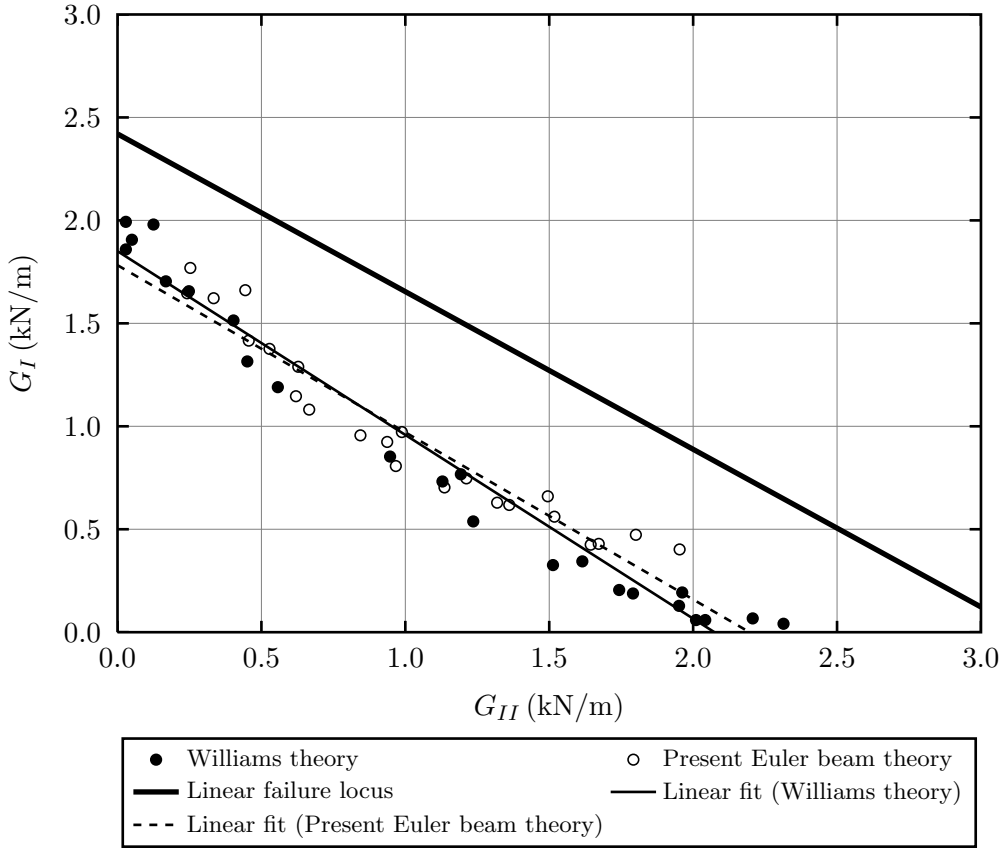

Figure 7.9: FRMM test partitions from the Williams and present Euler beam partition theories and the linear failure locus for unidirectional carbon/PEEK specimens.

close to each other and approximately linear is due to the critical ERRs being very close to each other $G_{Ic}/G_{IIc} \approx 0.8$, which is in contrast to the carbon/epoxy specimens for which $G_{Ic}/G_{IIc} \approx 0.4$. As pointed out above, when this is the case, although the individual partitions may be different, they will all lie on the same linear failure locus because the failure locus becomes

$$\frac{G}{G_{Ic}} = \frac{G}{G_{IIc}} = 1 \tag{7.34}$$

Therefore carbon/PEEK specimens are not suitable for assessing the quality of the competing theories. Donaldson (1985) came to this same conclusion after experimental testing and comparisons with several mixed-mode fracture criteria.

7.4.4 Spalling test

Thouless et al. (1987) investigated spalling in brittle plates. Spalling is where cracks occur very close to the surface, i.e. $\gamma \to \infty$. Fig. 7.10 shows the specimen and loading configuration. The spall, which has a thickness h_1 at the crack tip, is loaded axially by a force F, which is offset a distance d from the free surface. It therefore generally causes a

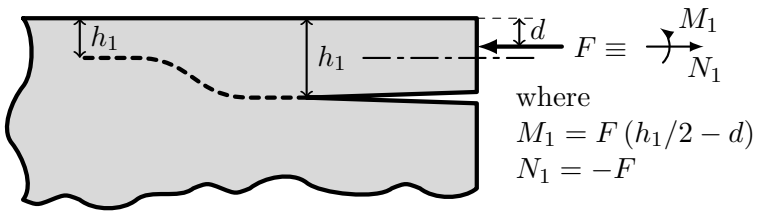

Figure 7.10: Spalling in a brittle plate with an offset load.

tip bending moment as well. Eq. (7.35) describes the crack tip forces.

$$N_{1B} = -F; \quad M_{1B} = F\left(\frac{h_1}{2} - d\right) \quad \text{and} \quad N_{2B} = M_{2B} = 0 \tag{7.35}$$

When the fracture propagates, it will propagate in pure mode I only in some direction (Cotterell and Rice 1980, Gold'stein and Salganik 1974, Thouless et al. 1987). As it propagates, it stabilises at a constant distance from the free surface. Thouless et al. (1987) described a series of experiments on PMMA and glass in which d is varied and the critical load and value of h_1 are determined. For convenience they introduced two quantities: the non-dimensional crack depth coefficient ξ

$$\xi = \frac{h_1}{d} \tag{7.36}$$

and the crack-loading coefficient Φ

$$\Phi = \frac{F}{b\sqrt{h_1}} \tag{7.37}$$

During stable propagation, the partition theories in §7.2 can be used to predict these values, which have been measured experimentally. Thouless et al. (1987) used the Suo–Hutchinson partition (assuming a square-root singular field). The resulting equations for the partition, rewritten as ERRs for easier comparison with the other theories, are

$$G_{ISH} = \frac{F^2}{2b^2 dE\xi}\left[\sqrt{3}\sin(52.1^\circ) + \cos(52.1^\circ) - \frac{2\sqrt{3}}{\xi}\sin(52.1^\circ)\right]^2 \tag{7.38}$$

$$G_{IISH} = \frac{F^2}{2b^2 dE\xi}\left[\sin(52.1^\circ) - \sqrt{3}\cos(52.1^\circ) + \frac{2\sqrt{3}}{\xi}\cos(52.1^\circ)\right]^2 \tag{7.39}$$

Setting $G_{IISH} = 0$ allows ξ to be found. Substituting this value into Eq. (7.38) and using the relation given in Eq. (7.28) gives

$$\xi = 7.741 \quad \text{and} \quad \Phi = 0.869 K_{Ic} \tag{7.40}$$

It is seen that ξ is independent of material properties whilst Φ is not. Thouless et al. (1987) gave approximate values of K_{Ic} for PMMA and for glass.

The Williams partition is as follows:

$$G_{IW} = \frac{3F^2\,(2-\xi)^2}{2b^2dE\xi} \quad \text{and} \quad G_{IIW} = \frac{F^2}{2b^2dE\xi} \tag{7.41}$$

For stable crack propagation with $G_{IIW} = 0$, the Williams partition theory requires that $\xi \to \infty$, i.e. an infinite thickness spall, which is obviously not valid for spalling when $\gamma \to \infty$ is assumed. To overcome this, Charalambides et al. (1992) postulated an additional sliding component to G_{II} and derived a mixed-mode failure criterion based on the 'fracture surface roughness'.

The partitions from the two present beam partition theories and averaged partition rule 1 are respectively

$$G_{IE} = \frac{3F^2\left(2-3\xi+\xi^2\right)}{b^2dE\xi^3} \quad \text{and} \quad G_{IIE} = \frac{F^2\,(3-\xi)}{b^2dE\xi^2} \tag{7.42}$$

$$G_{IT} = \frac{3F^2\,(1-\xi)^2}{2b^2dE\xi^3} \quad \text{and} \quad G_{IIT} = \frac{F^2\,(3-\xi)^2}{2b^2dE\xi^3} \tag{7.43}$$

$$G_{IA} = \frac{3F^2\left(5-8\xi+3\xi^2\right)}{4b^2dE\xi^3} \quad \text{and} \quad G_{IIA} = \frac{F^2\left(9-\xi^2\right)}{4b^2dE\xi^3} \tag{7.44}$$

The values of ξ and Φ for both materials from the Suo–Hutchinson partition theory, the two present beam partition theories and averaged rule 1 are given in Table 7.2. The present beam partition theories and averaged partition rule 1 all give the same results in this case, so are grouped together under the heading, 'Present theories'.

First, consider the crack-loading coefficient Φ. This is dependent on the critical mode I stress intensity factor K_{Ic}. From Thouless et al. (1987), this is $\sim 1.0\,\mathrm{MPa}\sqrt{\mathrm{m}}$ for PMMA, which is in agreement with the literature. Neither the Suo–Hutchinson nor the present partition theories are in particularly good agreement with the measurement, although the value from the present theories is the closest. However, the sensitivity of Φ to the value of ξ is noted. Using the present Euler beam partition theory, if $\xi = 2.3$ instead of 3.0 then $\Phi = 2.1\,\mathrm{MPa}\sqrt{\mathrm{m}}$, which is much closer to the measured value. For glass, Thouless et al. (1987) gave $K_{Ic} \approx 0.6\,\mathrm{MPa}\sqrt{\mathrm{m}}$. Using this value, the value of Φ from the present partition theories agrees quite well with the measured value. The present partition theories again have better agreement than the Suo–Hutchinson theory. However, other literature (Anstis, Chantikul, Lawn and Marshall 1981, Dowling 1993) gives higher values, between 0.7 and $0.8\,\mathrm{MPa}\sqrt{\mathrm{m}}$. If the value of $0.75\,\mathrm{MPa}\sqrt{\mathrm{m}}$ from Anstis et al. (1981) is used then, as shown in Table 7.2, the present partition theories are exactly in agreement with the measured value of Φ.

Now consider the crack depth coefficient ξ. For all theories, this is independent of material properties. Experimentally, there is some variation between materials. Neither the Suo–Hutchinson values nor the values from the present theories are very close to the measured values. For the PMMA specimens, the present partitions are the closest with 37.5% discrepancy, and for glass, the Suo–Hutchinson partition is the closest with 29%

Table 7.2: Crack-loading coefficient Φ and crack depth coefficient ξ propagation constants from the various partition theories for the spalling of brittle plates.

Material	K_{Ic} (MPa$\sqrt{\text{m}}$)	Measured		Suo–Hutchinson		Present theories (all the same here)	
		Φ (MPa$\sqrt{\text{m}}$)	ξ	Φ (MPa$\sqrt{\text{m}}$)	ξ	Φ (MPa$\sqrt{\text{m}}$)	ξ
PMMA	~ 1.0	2.4	4.8	~ 0.87	7.74	~ 1.22	3.0
Glass	~ 0.6	0.9	6.0	~ 0.52	7.74	~ 0.73	3.0
"	~ 0.75	0.9	"	~ 0.64	"	~ 0.91	"

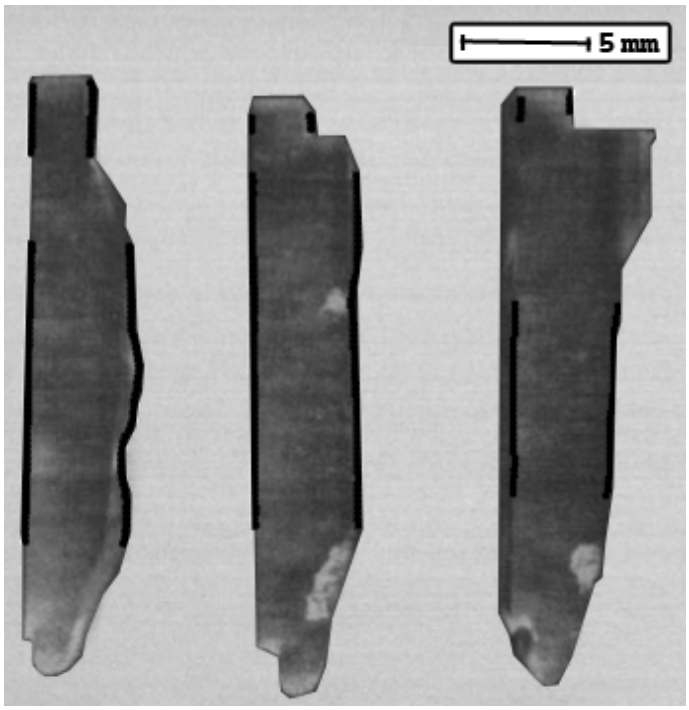

Figure 7.11: Photographs of spalled segments of PMMA (Thouless et al. 1987).

discrepancy. Thouless et al. (1987) published a photograph of three spalled specimens of PMMA. These are reproduced with permission in Fig. 7.11. They are potentially revealing because a scale is given and values of d and h_1 can be measured from the photograph. Note that the load was evenly applied to an elevated region on the specimen, so d is half the thickness of this elevated region. Black lines have been added over the specimens in Fig. 7.11 to indicate the regions over which d and h_1 were averaged. From left to right, the measured values of ξ are 3.5, 3.4 and 3.9, which are significantly less than the value of 4.8 given by Thouless et al. and much closer to the value predicted by the present partition theories. This photograph was presented by Thouless et al. to indicate the consistency of the measured ξ values. Therefore these measurements should be representative of the whole sample of experimental measurements. No photographs are available for the glass.

Overall, it can be concluded that the present partition theories perform better than the Suo–Hutchinson and Williams partition theories in modelling this test. Observed discrepancies can be explained, but further experimental data is needed to confirm these explanations.

7.5 Conclusion

The performance of five different partition theories has been investigated using experimental results from the literature for a range of tests. The partition theories used are the Williams theory (Williams 1988), the Suo–Hutchinson theory (Suo and Hutchinson 1990, Suo 1990, Hutchinson and Suo 1992) and the present partition theories from the preceding chapters, which are based on the Euler and Timoshenko beam theories.

The present Euler beam partition theory offers the best and most simple explanation for all the experimental observations. There are two possible reasons for this:

1. The aspect ratios of the specimens, which have been tested, are high enough for their behaviour to be essentially that of Euler beams. The most suitable partition theory would therefore be the present Euler beam partition theory. If this is correct, then for some specimens the present Timoshenko beam partition theory or averaged partition rule 1 might provide the best result. This seems less likely though because for the thicker specimens tested, where the through-thickness shear effect is greater, there is no tendency towards the present Timoshenko beam partition.

2. The global partition from the present partition theories, which has been shown to be equal to the present Euler beam partition, is the one that determines failure.

All the partition theories, except the present Timoshenko beam partition theory, are compatible with the results of the asymmetric DCB test, due to the error margin of the measurements. No further conclusions were possible from this test. For the FRMM test, the present Euler beam partition theory partitions the measurements of the total G_c so that the resulting G_I and G_{II} closely follow the expected linear failure locus. Under the assumption that the linear failure locus is accurate, the Williams partition and his suggested failure criterion can be completely explained using the present Euler beam partition theory. No recourse to extra significant mechanical effects, such as fracture roughness and friction is required. In fact, if the present Euler beam partition theory is correct, then the Williams partitions are exactly where they would be expected to be. For this test, the other partition theories give very different partitions and form curves approximately normal to the linear failure locus.

Finally, results from spalling tests have been looked at. In these tests, the spall stabilises at a constant distance from the free surface, allowing interfacial partition theories to be used, and propagates in pure mode I. The present theories all predict the same crack depth and ERR. Generally, these theories give better agreement with the measured values than

the Suo–Hutchinson partition theory. In some cases, values from the present theories are in very close agreement with the measured values. When this is not the case, plausible explanations are offered. First, the crack-loading coefficient Φ is particularly sensitive to the crack depth, represented by ξ. A small change in ξ can reconcile the value of Φ predicted by the present partition theories with the measured value. In addition, by examining scaled photos of the spalled specimens, there appears to be a discrepancy between the measured and quoted values of ξ in the work by Thouless et al. (1987). Measurements from the photos give much better agreement with the values from the present partition theories.

This chapter has been published in Harvey and Wang (2012*a*).

Chapter 8

Non-rigid elastic interfaces

Contents

8.1 Introduction

The partition theories in the preceding chapters are based on the assumption of a rigid interface. Such an assumption is a good approximation for brittle bonding between laminae in laminated composite materials. Adhesive bonding however is a common and important joining technique in manufacturing structures. For this reason, it is important to extend the theories to non-rigid elastic interfaces. This chapter considers the effects of non-rigid elastic interfaces on mixed-mode ERR partitions for layered isotropic homogeneous DCBs.

Ouyang and Li (2009) developed an analytical method to study non-rigid elastic interface shear fracture in ENF specimens of bi-layer materials. No opening mode or mixed-mode partitions were studied. Nguyen and Levy (2009) reported an exact theory of interfacial debonding in layered elastic composites using Fourier series solutions. Non-linear, non-uniform, decohesive interfaces were assumed. Their theory resulted in a system of non-linear algebraic equations. A numerical solution procedure was required.

On the numerical front, the interface spring model (Cui and Wisnom 1993, Zhang and Wang 2009, Wang and Harvey 2009) has been shown to be an accurate approach for partitioning mixed modes for rigid interfaces. On the other hand, the cohesive model (Chen, Crisfield, Kinloch, Busso, Matthews and Qiu 1999, Chen 2002, etc.) has been shown to be an accurate approach for cohesive interfaces. There are a large number of experimental studies on the topic. Some representative work is given by Brunner (2000), Blackman, Kinloch and Paraschi (2005) and Brunner, Blackman and Williams (2006).

This chapter has been published in Wang et al. (2012).

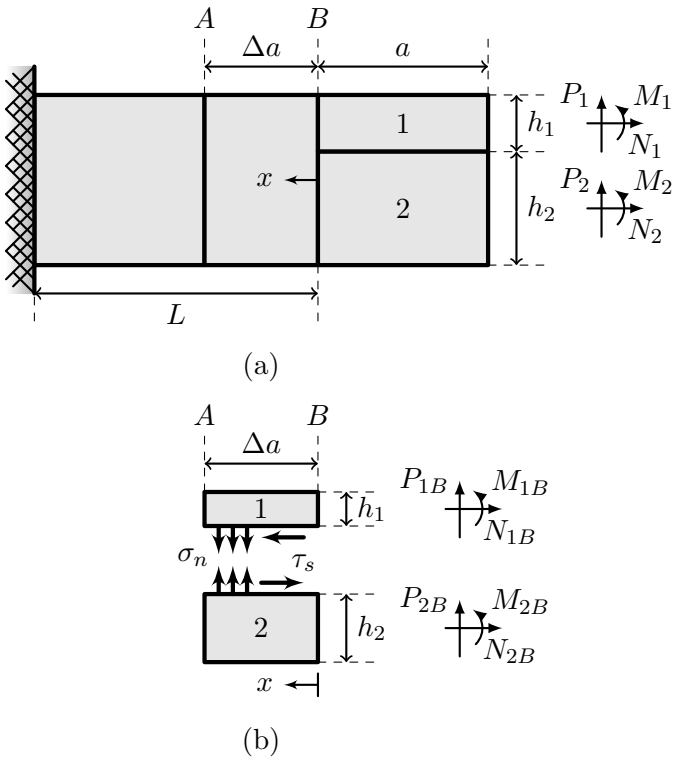

Figure 8.1: A DCB with a Δa-length cohesive zone. (a) General description. (b) Interface stresses.

8.2 Theoretical development

8.2.1 Non-rigid elastic interfaces in Euler beam theory

Fig. 8.1 (a) shows a DCB with its geometry and tip loads. The cohesive zone extends to a point A, a distance Δa ahead of the crack tip B. Fig. 8.1 (b) only shows the sign convention of the interface normal stress σ_n and shear stress τ_s instead of any representative distribution. From Fig. 8.1, the differential equations of beams 1 and 2 in the Δa region can be written as

$$ES_{1,2}u^{(1)}_{1,2} = N_{1,2B} \mp b\int_0^x \tau_s\, dx \tag{8.1}$$

$$EI_{1,2}w^{(2)}_{1,2} = \mp b\int_0^x\int_0^x \sigma_n\, dx\, dx - \frac{bh_{1,2}}{2}\int_0^x \tau_s\, dx + P_{1,2B}x + M_{1,2B} \tag{8.2}$$

where $u^{(1)} = du/dx$ and $w^{(2)} = d^2w/dx^2$. The remaining notation is the same as that used in Chapter 4. As shown in Fig. 8.1, the origin of x is at point B and towards the left. The relative shearing displacement at the interface $\overline{u}$ is therefore

$$\overline{u} = \overline{u}_2 - \overline{u}_1 = u_2 - h_2w_2^{(1)}/2 - u_1 - h_1w_1^{(1)}/2 \tag{8.3}$$

Positive $\overline{u}$ corresponds to positive interface shear stress τ_s, which can be found by substituting Eqs. (8.1) and (8.2) into Eq. (8.3), as follows:

$$\begin{aligned}\overline{u} = &\int_0^x \frac{N_{2B} + b\int_0^x \tau_s\,dx}{ES_2}\,dx - \int_0^x \frac{N_{1B} - b\int_0^x \tau_s\,dx}{ES_1}\,dx \\ &- \frac{h_2}{2}\int_0^x \frac{M_{2B} + P_{2B}x + b\int_0^x\int_0^x \sigma_n\,dx\,dx - bh_2\int_0^x \tau_s\,dx/2}{EI_2}\,dx - \\ &- \frac{h_1}{2}\int_0^x \frac{M_{1B} + P_{1B}x - b\int_0^x\int_0^x \sigma_n\,dx\,dx - bh_1\int_0^x \tau_s\,dx/2}{EI_1}\,dx\end{aligned} \tag{8.4}$$

$$\begin{aligned}\overline{u}^{(2)} = &-\frac{h_1\left(P_{1B} - b\int_0^x \sigma_n\,dx\right)}{2EI_1} - \frac{h_2\left(P_{2B} + b\int_0^x \sigma_n\,dx\right)}{2EI_2} \\ &+ \tau_s\left(\frac{b}{ES_1} + \frac{b}{ES_2} + \frac{bh_1^2}{4EI_1} + \frac{bh_2^2}{4EI_2}\right)\end{aligned} \tag{8.5}$$

Rearranging for τ_s gives

$$\tau_s = \tau_{sP} + \tau_{s\sigma} + \tau_{s\overline{u}} \tag{8.6}$$

where

$$\tau_{sP} = \frac{3\left(\gamma^2 P_{1B} + P_{2B}\right)}{2bh_1\gamma\left(1+\gamma\right)} \tag{8.7}$$

$$\tau_{s\sigma} = \frac{3\left(1-\gamma\right)}{2h_1\gamma}\int_0^x \sigma_n\,dx \tag{8.8}$$

$$\tau_{s\overline{u}} = \frac{h_1 E\gamma\,\overline{u}^{(2)}}{4\left(1+\gamma\right)} \tag{8.9}$$

Recall that $\gamma = h_2/h_1$. Therefore, the mode II ERR G_{II} is found by using the J-integral.

$$\begin{aligned}G_{IIE} &= \lim_{\delta a\to 0}\left\{\frac{1}{\delta a}\int_0^{\delta a}\int_0^{\overline{u}} \tau_s\,d\overline{u}\,dx\right\} \\ &= \int_0^{\overline{u}_B} \tau_{sB}\,d\overline{u}_B \\ &= \int_0^{\overline{u}_B} \tau_{sP}\,d\overline{u}_B + \int_0^{\overline{u}_B} \tau_{s\sigma_B}\,d\overline{u}_B + \int_0^{\overline{u}_B} \tau_{s\overline{u}B}\,d\overline{u}_B \\ &= \int_0^{\overline{u}_B} \tau_{sP}\,d\overline{u}_B + \frac{h_1 E\gamma}{4\left(1+\gamma\right)}\int_0^{\overline{u}_B} \overline{u}_B^{(1)}\,d\overline{u}_B^{(1)} \\ &= \int_0^{\overline{u}_B} \tau_{sP}\,d\overline{u}_B + \frac{h_1 E\gamma}{8\left(1+\gamma\right)}\left\{\left[\overline{u}_B^{(1)}\left(\overline{u}_B\right)\right]^2 - \left[\overline{u}_B^{(1)}\left(0\right)\right]^2\right\} \\ &= \int_0^{\overline{u}_B} \tau_{sP}\,d\overline{u}_B + \frac{h_1 E\gamma}{8\left(1+\gamma\right)}\left(\overline{u}_B^{(1)}\right)^2 \\ &= \int_0^{\overline{u}_B} \tau_{sP}\,d\overline{u}_B + G_{IIE}^L\end{aligned} \tag{8.10}$$

The subscript B indicates quantities at the crack tip. Note the following points were used in the derivation of Eq. (8.10): (1) since there is no stress singularity at the crack tip for

a non-rigid elastic interface, crack tip shear stress $\tau_{s\sigma B} = 0$; and (2) when the crack tip relative shearing displacement is zero $\overline{u}_B = 0$, the crack tip relative shearing strain is also zero, i.e. $\overline{u}_B^{(1)}(0) = 0$. The crack tip shearing displacement $\overline{u}_B^{(1)}(\overline{u}_B)$ in the second term of Eq. (8.10) is found from Eq. (8.3) to be

$$\begin{aligned}\overline{u}_B^{(1)} &= \frac{N_{2B}}{ES_2} - \frac{N_{1B}}{ES_1} - \frac{h_2 M_{2B}}{2EI_2} - \frac{h_1 M_{1B}}{2EI_1} \\ &= -\frac{6\gamma^2 M_{1B} + 6M_{2B} + h_1^2\gamma^2 N_{1Be}}{bh_1^2 E\gamma^2}\end{aligned} \tag{8.11}$$

where $N_{1Be} = N_{1B} - N_{2B}/\gamma$. It is easy to show that the second term G_{IIE}^L in Eq. (8.10) is equal to the ERR from the $\left\{\varphi_{\beta_1}\right\}$ and $\left\{\varphi_{\beta_2}\right\}$ modes for a rigid interface without the stealthy interaction, that is, it equals the mode II ERR based on the present Timoshenko beam theory. Substituting Eq. (8.11) into the second term of Eq. (8.10) gives

$$G_{IIE}^L = \frac{\left(6M_{1B}\gamma^2 + 6M_{2B} + N_{1B}h_1^2\gamma^2 - N_{2B}h_1\gamma\right)^2}{8b^2h_1^3E\gamma^3\left(1+\gamma\right)} \tag{8.12}$$

which is the same as the value of G_{II} obtained by expanding Eq. (7.6). The first term in Eq. (8.10) is from the $\left\{\varphi_{\beta_1}\right\}$ mode of shear force and is determined below. Since the final ERR is independent of the order of application of τ_{sP} and $\tau_{s\overline{u}}$ in the case of elastic interfaces and plastic interfaces with no unloading, it can be assumed that τ_{sP} is applied first and then $\tau_{s\overline{u}}$ is applied afterwards, that is, the two crack tip shear forces P_{1B} and P_{2B} are applied first, then the two crack tip bending moments M_{1B} and M_{2B}, and axial force N_{1Be} are applied afterwards. Moreover, since τ_{sP} is always on the ascending part of an ascending-descending type cohesive law, the first term in Eq. (8.10) can be calculated as

$$\begin{aligned}\int_0^{\overline{u}_B} \tau_{sP}\, d\overline{u}_B &= \int_0^{\overline{u}_{B\tau_{sP}}} \tau_{sB}\, d\overline{u}_B + \int_{\overline{u}_{B\tau_{sP}}}^{\overline{u}_{B\tau_{sP}}+\overline{u}_{B\tau_{s\overline{u}}}} \tau_{sP}\, d\overline{u}_B \\ &= \int_0^{\overline{u}_{B\tau_{sP}}} \tau_{sB}\, d\overline{u}_B + \tau_{sP}\overline{u}_{B\tau_{s\overline{u}}}\end{aligned} \tag{8.13}$$

By using a given interface cohesive law, and τ_{sP} from Eq. (8.7), the interface relative shearing displacement $\overline{u}_{B\tau_{sP}}$ due to τ_{sP} is easily calculated and the first term in Eq. (8.13) is then determined. $\overline{u}_{B\tau_{s\overline{u}}}$ due to $\tau_{s\overline{u}}$ can be determined from

$$G_{IIE}^L = \int_{\overline{u}_{B\tau_{sP}}}^{\overline{u}_{B\tau_{sP}}+\overline{u}_{B\tau_{s\overline{u}}}} \tau_{s\overline{u}B}\, d\overline{u}_B = \int_{\overline{u}_{B\tau_{sP}}}^{\overline{u}_{B\tau_{sP}}+\overline{u}_{B\tau_{s\overline{u}}}} \left(\tau_{sB} - \tau_{sP}\right) d\overline{u}_B \tag{8.14}$$

for a given interface cohesive law where G_{IIE}^L is given in Eq. (8.10). Finally, the mode II ERR is found to be

$$G_{IIE} = G_{IIE}^L + \int_0^{\overline{u}_{B\tau_{sP}}} \tau_{sB}\, d\overline{u}_B + \tau_{sP}\overline{u}_{B\tau_{s\overline{u}}} = G_{IIE}^L + G_{IIE}^{NR} \tag{8.15}$$

which is a complete analytical solution and explicitly independent of the size of the cohesive zone Δa.

The pure mode I condition can be obtained by letting $G_{IIE} = 0$. This results in both $\overline{u}_B^{(1)} = 0$ and $\tau_{sP} = 0$ which are the same conditions as for the $\left\{\varphi_{\theta_i}\right\}$ modes given in Chapters 4 and 5 for rigid interfaces. The condition $\overline{u}_B^{(1)} = 0$, for non-rigid elastic interfaces, nullifies the contribution of the shear stress $\tau_{s\overline{u}B}$ to the ERR. That is, $\tau_{s\overline{u}B}$ is effectively zeroed. However, note that $\tau_{s\overline{u}B} = 0$ leads to $\overline{u}_B^{(2)} = 0$ instead of $\overline{u}_B^{(1)} = 0$. In addition, the shear stress at the crack tip $\tau_{s\sigma B}$ is always zero for non-rigid elastic interfaces. Therefore, for non-rigid elastic interfaces both shear stress and strain at the crack tip are zero for pure mode I. The two sets of mode I $\left\{\varphi_{\theta_i}\right\}$ modes and $\left\{\varphi_{\theta_i'}\right\}$ modes therefore coincide on the $\left\{\varphi_{\theta_i}\right\}$ modes. Consequently, the two sets of mode II $\left\{\varphi_{\beta_i}\right\}$ modes and $\left\{\varphi_{\beta_i'}\right\}$ modes should also coincide on the $\left\{\varphi_{\beta_i}\right\}$ modes. There will be no stealthy interactions between the mode I $\left\{\varphi_{\theta_i}\right\}$ modes and the mode II $\left\{\varphi_{\beta_i}\right\}$ modes, which shows that it is the singular shear stress $\tau_{s\sigma}$ at the crack tip for a rigid interface that causes the stealthy interactions.

Next, the mode I partition of ERR G_{IE} is considered. The relative opening displacement at the interface is defined as

$$\overline{w} = \overline{w}_1 - \overline{w}_2 = w_1 - w_2 \tag{8.16}$$

Positive $\overline{w}$ corresponds to positive interface normal stress σ_n, which is found from Eqs. (8.1), (8.2), (8.6) and (8.16), and is given by

$$\sigma_n = -\frac{h_1^3 E\gamma^3}{3\left(1+\gamma\right)^3}\left(\overline{w}^{(4)} + \frac{3\overline{u}^{(3)}\left(1-\gamma\right)}{2h_1\gamma}\right) \tag{8.17}$$

The mode I ERR G_{IE} is found by using the J-integral.

$$G_{IE} = \lim_{\delta a\to 0}\left\{\frac{1}{\delta a}\int_0^{\delta a}\int_0^{\overline{w}} \sigma_n\, d\overline{w}\, dx\right\} = \int_0^{\overline{w}_B} \sigma_{nB}\, d\overline{w}_B \tag{8.18}$$

The following integrals are required to evaluate G_{IE}:

$$\begin{aligned}
\int_0^{\overline{w}_B} \overline{w}_B^{(4)}\, d\overline{w}_B &= \int_0^{\overline{w}_B} \overline{w}_B^{(1)}\, d\overline{w}_B^{(3)} \\
&= \overline{w}_B^{(1)}\left(\overline{w}_B\right)\overline{w}_B^{(3)}\left(\overline{w}_B\right) - \overline{w}_B^{(1)}\left(0\right)\overline{w}_B^{(3)}\left(0\right) - \int_0^{\overline{w}_B} \overline{w}_B^{(2)}\, d\overline{w}_B^{(2)} \\
&= \overline{w}_B^{(1)}\left(\overline{w}_B\right)\overline{w}_B^{(3)}\left(\overline{w}_B\right) - \left(\overline{w}_B^{(2)}\right)^2/2 \\
&= \frac{12\overline{w}_B^{(1)}\left(\gamma^3 P_{1B} - P_{2B}\right)}{bh_1^3 E\gamma^3} - \frac{72\left(\gamma^3 M_{1B} - M_{2B}\right)^2}{\left(bh_1^3 E\gamma^3\right)^2}
\end{aligned} \tag{8.19}$$

$$\begin{aligned}\int_0^{\overline{w}_B} \overline{u}_B^{(3)}\, d\overline{w}_B &= \int_0^{\overline{w}_B} \overline{w}_B^{(1)}\, d\overline{u}_B^{(2)} \\ &= \overline{w}_B^{(1)}\left(\overline{w}_B\right)\overline{u}_B^{(2)}\left(\overline{w}_B\right) - \overline{w}_B^{(1)}\left(0\right)\overline{u}_B^{(2)}\left(0\right) - \int_0^{\overline{w}_B} \overline{u}_B^{(2)}\, d\overline{w}_B^{(1)} \\ &= \overline{w}_B^{(1)}\left(\overline{w}_B\right)\overline{u}_B^{(2)}\left(\overline{w}_B\right) - \int_0^{\overline{w}_B} \overline{u}_B^{(2)}\, d\overline{w}_B^{(1)} \end{aligned} \tag{8.20}$$

As seen earlier, the shear stress at the crack tip $\tau_{s\overline{u}B}$ is effectively zero in mode I leading to $\overline{u}_B^{(2)} = 0$ from Eq. (8.9). Therefore, Eq. (8.20) becomes zero. Moreover, it is the $\left\{\varphi_{\theta_i}\right\}$ set of mode I modes that produces the mode I ERR. Any given P_{1B} and P_{2B} in question can be decomposed by

$$\begin{Bmatrix} P_{1B} \\ P_{2B} \end{Bmatrix} = \begin{bmatrix} 1 & 1 \\ \theta_1 & \beta_1 \end{bmatrix} \begin{Bmatrix} \alpha_{\theta_1} \\ \alpha_{\beta_1} \end{Bmatrix} \tag{8.21}$$

where $\theta_1 = -\gamma^2$, $\beta_1 = \gamma^2\left(3+\gamma\right)/\left(1+3\gamma\right)$, and α_{θ_1} and α_{β_1} are mode partition coefficients, which are given by

$$\begin{Bmatrix} \alpha_{\theta_1} \\ \alpha_{\beta_1} \end{Bmatrix} = \frac{1}{\beta_1 - \theta_1} \begin{Bmatrix} \beta_1 P_{1B} - P_{2B} \\ P_{2B} - \theta_1 P_{1B} \end{Bmatrix} \tag{8.22}$$

Any given M_{1B}, M_{2B} and N_{1Be} can be decomposed by

$$\begin{Bmatrix} M_{1B} \\ M_{2B} \\ N_{1Be} \end{Bmatrix} = \begin{bmatrix} 1 & 1 & 0 \\ \theta_1 & \beta_1 & 0 \\ 0 & 0 & 1 \end{bmatrix} \begin{Bmatrix} \alpha_{\theta_1} \\ \alpha_{\beta_1} \\ \alpha_{\beta_2} \end{Bmatrix} \tag{8.23}$$

for $h_1 = h_2$ and

$$\begin{Bmatrix} M_{1B} \\ M_{2B} \\ N_{1Be} \end{Bmatrix} = \begin{bmatrix} 1 & 1 & 1 \\ \theta_1 & \beta_1 & 0 \\ 0 & 0 & \beta_2 \end{bmatrix} \begin{Bmatrix} \alpha_{\theta_1} \\ \alpha_{\beta_1} \\ \alpha_{\beta_2} \end{Bmatrix} \tag{8.24}$$

for $h_1 \neq h_2$, where $\beta_2 = 2\left(3+\gamma\right)/\left[h_1\left(\gamma-1\right)\right]$. From Eq. (8.23), the mode partition coefficients are

$$\alpha_{\beta_2} = N_{1Be} \quad \text{and} \quad \begin{Bmatrix} \alpha_{\theta_1} \\ \alpha_{\beta_1} \end{Bmatrix} = \frac{1}{\beta_1 - \theta_1} \begin{Bmatrix} \beta_1 M_{1B} - M_{2B} \\ M_{2B} - \theta_1 M_{1B} \end{Bmatrix} \tag{8.25}$$

for $h_1 = h_2$, and from Eq. (8.24) the mode partition coefficients are

$$\alpha_{\beta_2} = \frac{N_{1Be}}{\beta_2} \quad \text{and} \quad \begin{Bmatrix} \alpha_{\theta_1} \\ \alpha_{\beta_1} \end{Bmatrix} = \frac{1}{\beta_1 - \theta_1} \begin{Bmatrix} \beta_1\left(M_{1B} - \alpha_{\beta_2}\right) - M_{2B} \\ M_{2B} - \theta_1\left(M_{1B} - \alpha_{\beta_2}\right) \end{Bmatrix} \tag{8.26}$$

for $h_1 \neq h_2$. Substituting the $\left\{\varphi_{\theta_1}\right\}$ mode I component from Eq. (8.21) for shear forces and the $\left\{\varphi_{\theta_1}\right\}$ mode I component from Eq. (8.23) or Eq. (8.24) for bending moments and

axial forces into Eq. (8.19) gives

$$\int_0^{\overline{w}_B} \overline{w}_B^{(4)}\, d\overline{w}_B = \frac{3\overline{w}_B^{(1)}\left(1+3\gamma\right)\left(\beta_1 P_{1B} - P_{2B}\right)}{bh_1^3 E\gamma^3} - \frac{72\alpha_{\theta_1}^2\gamma^4\left(1+\gamma\right)^2}{\left(bh_1^3 E\gamma^3\right)^2} \tag{8.27}$$

Substituting Eq. (8.27) into Eq. (8.18) gives

$$\begin{aligned} G_{IE} &= G_{IE}^L + \frac{\overline{w}_B^{(1)}\left(1+3\gamma\right)\left(P_{2B} - \beta_1 P_{1B}\right)}{b\left(1+\gamma\right)^3} \\ &= G_{IE}^L - F_n\overline{w}_B^{(1)}/b \\ &= G_{IE}^L + G_{IE}^{NR} \end{aligned} \tag{8.28}$$

The first term $G_{IE}^L = \alpha_{\theta_1}^2 G_{\theta_1} = 24\alpha_{\theta_1}^2\gamma/\left[b^2h_1^3E\left(1+\gamma\right)\right]$ in Eq. (8.28) is equal to the ERR from the mode I $\left\{\varphi_{\theta_1}\right\}$ mode for rigid interfaces, where α_{θ_1} is given by Eq. (8.25) or Eq. (8.26). The $\overline{w}_B^{(1)}$ in the second term is the relative crack tip rotation and F_n is the resultant normal force in the cohesive zone Δa which is defined as

$$F_n = b\int_0^{\Delta a}\sigma_n\, dx \tag{8.29}$$

It is seen that Eq. (8.28) is not completely analytical due to the second term, i.e. G_{IE}^{NR}, which arises due to crack tip shear forces. However, it can be neglected for most practical engineering applications which have non-rigid but hard interfaces.

8.2.2 Non-rigid elastic interfaces in Timoshenko beam theory

Using the Timoshenko beam theory, the governing equations become

$$ES_{1,2}u_{1,2}^{(1)} = N_{1,2B} \mp b\int_0^x \tau_s\, dx \tag{8.30}$$

$$EI_{1,2}\psi_{1,2}^{(1)} = \mp b\int_0^x\int_0^x \sigma_n\, dx\, dx - \frac{bh_{1,2}}{2}\int_0^x \tau_s\, dx + P_{1,2B}x + M_{1,2B} \tag{8.31}$$

$$S_{1,2}\kappa\mu\left(w_{1,2}^{(1)} - \psi_{1,2}\right) = -P_{1,2B} \pm b\int_0^x \sigma_n\, dx \tag{8.32}$$

where μ is the through-thickness shear modulus, κ is the shear correction factor, and ψ is the cross-sectional rotation, which is positive in the clockwise direction. It is simple to verify that the mode II ERR G_{IIT} remains the same as the mode II ERR G_{IIE} in Eq. (8.15). However, the mode I ERR G_{IT} needs reconsideration. From the above three equations, the governing equation for the interface normal stress σ_n is

$$\sigma_n^{(2)} - \lambda^2\sigma_n = \alpha\left(\overline{w}^{(4)} + \frac{3\overline{u}^{(3)}\left(1-\gamma\right)}{2h_1\gamma}\right) \tag{8.33}$$

where $\lambda = (1+\gamma)\left(3\kappa\mu/E\right)^{1/2}/\left(\gamma h_1\right)$ and $\alpha = h_1\gamma\kappa\mu/\left(1+\gamma\right)$. By using the method of parameter variation, the solution to Eq. (8.33) is found.

$$\begin{aligned}\sigma_n = {} & c_1 e^{\lambda x} + c_2 e^{-\lambda x} + \alpha\left(\lambda^2\overline{w} + \overline{w}^{(2)} + \frac{3\overline{u}^{(1)}\left(1-\gamma\right)}{2h_1\gamma}\right) \\ & + \frac{\alpha\lambda^3}{2}\left(e^{\lambda x}\int_0^x \overline{w}e^{-\lambda x}\,dx - e^{-\lambda x}\int_0^x \overline{w}e^{\lambda x}\,dx\right) \\ & + \frac{3\alpha\lambda^2\left(1-\gamma\right)}{4h_1\gamma}\left(e^{\lambda x}\int_0^x \overline{u}e^{-\lambda x}\,dx + e^{-\lambda x}\int_0^x \overline{u}e^{\lambda x}\,dx\right)\end{aligned} \tag{8.34}$$

The two integration constants c_1 and c_2 are determined using the conditions $\sigma_n\left(\Delta a\right) = \sigma_n^{(1)}\left(\Delta a\right) = 0$, which give

$$c_1 = -\frac{\alpha\lambda^3}{2}\int_0^{\Delta a}\overline{w}e^{-\lambda x}\,dx - \frac{3\alpha\lambda^2\left(1-\gamma\right)}{4h_1\gamma}\int_0^{\Delta a}\overline{u}e^{-\lambda x}\,dx \tag{8.35}$$

$$c_2 = \frac{\alpha\lambda^3}{2}\int_0^{\Delta a}\overline{w}e^{\lambda x}\,dx - \frac{3\alpha\lambda^2\left(1-\gamma\right)}{4h_1\gamma}\int_0^{\Delta a}\overline{u}e^{\lambda x}\,dx \tag{8.36}$$

Then, the mode I ERR G_I is found using the J-integral.

$$G_I = \lim_{\delta a\to 0}\left\{\frac{1}{\delta a}\int_0^{\delta a}\int_0^{\overline{w}}\sigma_n\,d\overline{w}\,dx\right\} \tag{8.37}$$

$$= \int_0^{\overline{w}_B}\sigma_{nB}\,d\overline{w}_B \tag{8.38}$$

$$= \int_0^{\overline{w}_B}\left(c_1+c_2\right)\,d\overline{w}_B + \frac{\alpha\lambda^2\overline{w}_B^2}{2} + \frac{\alpha}{2}\left(\overline{w}_B^{(1)}\right)^2 + \frac{3\alpha\left(1-\gamma\right)}{2h_1\gamma}\int_0^{\overline{w}_B}\overline{u}_B^{(1)}\,d\overline{w}_B \tag{8.39}$$

The two integration constants c_1 and c_2 are determined in the following. The resultant normal force F_n is defined in Eq. (8.29). The resultant moment M_n about point A due to σ_n in the cohesive zone Δa is defined as

$$M_n = b\int_0^{\Delta a}\int_0^x \sigma_n\,dx\,dx = b\int_0^{\Delta a}\sigma_n\left(\Delta a - x\right)\,dx = M_{nm} + F_n\Delta a \tag{8.40}$$

where

$$F_n = \frac{1+3\gamma}{\left(1+\gamma\right)^3}\left(\beta_1 P_{1B} - P_{2B}\right) \tag{8.41}$$

when transverse stress is calculated by considering the equilibrium of bending stress, or

$$F_n = \frac{1}{1+\gamma}\left(\gamma P_{1B} - P_{2B}\right) \tag{8.42}$$

when transverse shear stress is calculated from the constitutive law, and

$$M_{nm} = \frac{1+3\gamma}{\left(1+\gamma\right)^3}\left(\beta_1 M_{1B} - M_{2B}\right) + \frac{h_1\gamma^2\left(1-\gamma\right)N_{1Be}}{2\left(1+\gamma\right)^3} \tag{8.43}$$

Substituting σ_n, given by Eq. (8.34), into Eqs. (8.29) and (8.40) gives

$$c_1 - c_2 = -\lambda \left\{ \alpha \left[\overline{w}_B^{(1)} + \frac{3\overline{u}_B (1-\gamma)}{2h_1\gamma} \right] + \frac{F_n}{b} \right\} \tag{8.44}$$

and

$$c_1 + c_2 = -\lambda^2 \left(\alpha \overline{w}_B + \frac{M_{nm}}{b} \right) \tag{8.45}$$

Substituting Eq. (8.45) into Eq. (8.39) gives

$$\begin{aligned} G_{IT} &= -\int_0^{\overline{w}_B} \frac{\lambda^2 M_{nm}}{b}\, d\overline{w}_B + \frac{\alpha}{2}\left(\overline{w}_B^{(1)}\right)^2 + \frac{3\alpha(1-\gamma)}{2h_1\gamma} \int_0^{\overline{w}_B} \overline{u}_B^{(1)}\, d\overline{w}_B \\ &= \int_0^{\overline{w}_{B\sigma_I}} \sigma_I\, d\overline{w}_B + \sigma_I \left(\overline{w}_B - \overline{w}_{B\sigma_I}\right) + \frac{\alpha}{2}\left(\overline{w}_B^{(1)}\right)^2 \end{aligned} \tag{8.46}$$

Note that the first term in Eq. (8.46) is calculated from a given interface cohesive law with $\sigma_I = -\lambda^2 M_{nm}/b + 3\alpha(1-\gamma)/(2h_1\gamma)\,\overline{u}_B^{(1)}$ in which M_{nm} and $\overline{u}_B^{(1)}$ are given in Eqs. (8.44) and (8.11) respectively. $\overline{w}_B$ and $\overline{w}_B^{(1)}$ need to be determined numerically. It is easy to show that for a rigid interface, G_{IT} reduces to

$$G_{IT} = G_{IT}^L = \alpha_{\theta_1}^2 G_{\theta_1} + G_P + \alpha_{\theta_1} \Delta G_{\theta_1 P} \tag{8.47}$$

which is the same as that given in Eq. (4.92) for isotropic homogeneous DCBs with rigid interfaces modelled with Timoshenko beam theory. For most engineering problems with hard interfaces, the third term in Eq. (8.46) can be replaced with G_{IT}^L in Eq. (8.47). Therefore $\overline{w}_B$ in Eq. (8.46) can be calculated using a given interface cohesive law and the following:

$$G_{IT}^L = \int_{\overline{w}_{B\sigma_I}}^{\overline{w}_B} (\sigma_{nB} - \sigma_I)\, d\overline{w}_B \tag{8.48}$$

The mode I ERR G_{IT} for a hard interface is obtained analytically. Again, the ERR G_{IT} in Eq. (8.46) is explicitly independent of the size of the cohesive zone Δa.

8.2.3 Non-rigid elastic interfaces in two-dimensional elasticity theory

In general, the total ERR can be written in the form

$$G = G_I^L + G_{II}^L + G_I^{NR} + G_{II}^{NR} = G^L + G^{NR} \tag{8.49}$$

Moreover, it is expected that

$$G^L = G_{IE}^L + G_{IIE}^L \tag{8.50}$$

is a good approximation for non-rigid hard interfaces. The aim in the following is to partition G in Eq. (8.49). In §4.2.5, averaged partition rules have been developed for rigid interfaces in two-dimensional elasticity. It has been found that the pure mode I (or II) modes $\left\{\varphi_{\theta_{iA}}\right\}$ (or $\left\{\varphi_{\beta_{iA}}\right\}$) in the averaged rules ($i = 1, 2$) are between the two sets of

pure mode I (or II) modes $\left\{\varphi_{\theta_i}\right\}$ and $\left\{\varphi_{\theta'_i}\right\}$ (or $\left\{\varphi_{\beta_i}\right\}$ and $\left\{\varphi_{\beta'_i}\right\}$). It is expected that for a non-rigid interface, the pure mode I (or II) modes $\left\{\varphi_{\theta_i^{NR}}\right\}$ (or $\left\{\varphi_{\beta_i^{NR}}\right\}$) based on two-dimensional elasticity are between the two sets of pure mode I (or II) modes $\left\{\varphi_{\theta_{iA}}\right\}$ and $\left\{\varphi_{\theta'_{iA}}\right\}$ (or $\left\{\varphi_{\beta_{iA}}\right\}$ and $\left\{\varphi_{\beta'_{iA}}\right\}$). Therefore, a first approximate partition theory for the partition of G^L can be developed using the second set of pure modes from the present Euler beam partition theory with rigid interfaces, i.e. the $\left\{\varphi_{\theta'_i}\right\}$ and $\left\{\varphi_{\beta'_i}\right\}$ modes. It is worth noting that the $\left\{\varphi_{\theta'_1}\right\}$ and $\left\{\varphi_{\beta'_1}\right\}$ modes from the second set are the same as those given in Williams's (1988) work. The partition of G^L is therefore given by

$$G_I^L = c_I \left(M_{1B} - \frac{M_{2B}}{\beta'_1} \right)^2 \tag{8.51}$$

$$G_{II}^L = c_{II} \left(M_{1B} - \frac{M_{2B}}{\theta'_1} - \frac{N_{1Be}}{\theta'_2} \right)^2 \tag{8.52}$$

where c_I and c_{II} are

$$c_I = G_{\theta'_1} \left(1 - \frac{\theta'_1}{\beta'_1} \right)^{-2} \tag{8.53}$$

$$c_{II} = G_{\beta'_1} \left(1 - \frac{\beta'_1}{\theta'_1} \right)^{-2} \tag{8.54}$$

and

$$\theta'_1 = -1 \tag{8.55}$$

$$\theta'_2 = -\frac{6\left(1+\gamma\right)}{h_1\left(1+\gamma^3\right)} \tag{8.56}$$

$$\beta'_1 = \gamma^3 \tag{8.57}$$

$$G_{\theta'_1} = \frac{6\left(1+\gamma^3\right)}{b^2 h_1^3 E \gamma^3} \tag{8.58}$$

$$G_{\beta'_1} = \frac{18\gamma\left(1+\gamma^3\right)}{b^2 h_1^3 E \left(1+\gamma\right)^2} \tag{8.59}$$

This is now referred to as 'present two-dimensional elasticity partition theory 1'. The partition from this theory however can be made much more accurate in a second approximate partition theory by using improved β'_1 and θ'_1 values. A double bi-section approximation based on the two sets of pure modes from Chapter 4 can achieve this. The new value of β'_1 is calculated by using a double bi-section approximation as follows:

$$\beta'_{1A} = \frac{1}{2}\left(\frac{\beta_1 + \beta'_1}{2} + \beta'_1 \right) = \frac{\beta_1}{4} + \frac{3\beta'_1}{4} \tag{8.60}$$

By finding its orthogonal mode, the new value of θ_1' is

$$\theta_{1A}' = -\frac{\gamma^4 + 11\gamma^3 + 4\gamma^2}{9\gamma^3 + 4\gamma^2 + 2\gamma + 1} \tag{8.61}$$

The second approximate partition theory is obtained by using these two values in Eqs. (8.51) to (8.59). It is now referred to as 'present two-dimensional elasticity partition theory 2'.

Next, the partition of G^{NR} in Eq. (8.49) is considered. Its mode I component G_I^{NR} is determined first. Based on the expression for G_{IE}^{NR} in Eq. (8.28), G_I^{NR} in the case of P_{1B} and P_{2B} acting alone is written in the following form:

$$G_{IP}^{NR}(\gamma) = \frac{\xi(\gamma)\left[P_{2B} - \beta_P(\gamma) P_{1B}\right]^2}{h_1^3 E} \tag{8.62}$$

where $\xi(\gamma)$ and $\beta_P(\gamma)$ are two γ-dependent parameters which can be determined numerically by consideration of two loading cases. The two cases chosen here are $P_{1B} = 1$, $P_{2B} = 0$ and $P_{1B} = 1$, $P_{2B} = -1$, giving

$$G_{IP,0}^{NR}(\gamma) = \frac{\xi(\gamma)\beta_P^2(\gamma)}{h_1^3 E} \tag{8.63}$$

and

$$G_{IP,-1}^{NR}(\gamma) = \frac{\xi(\gamma)\left[1 + \beta_P(\gamma)\right]^2}{h_1^3 E} \tag{8.64}$$

where $G_{IP,0}^{NR}(\gamma)$ and $G_{IP,-1}^{NR}(\gamma)$ are determined numerically. The two parameters $\xi(\gamma)$ and $\beta_P(\gamma)$ are therefore determined as

$$\xi(\gamma) = \left[\frac{G_{IP,0}^{NR}(\gamma)}{\beta_P^2(\gamma)}\right] E h_1^3 \tag{8.65}$$

and

$$\beta_P(\gamma) = \left[g^{1/2}(\gamma) - 1\right]^{-1} \tag{8.66}$$

where $g(\gamma) = G_{IP,-1}^{NR}(\gamma) / G_{IP,0}^{NR}(\gamma)$. Thus, $G_{IP}^{NR}(\gamma)$ for any given crack tip shear forces P_{1B} and P_{2B} can be determined using Eq. (8.62).

Now, consider G_I^{NR} in a general loading condition. For a given interface cohesive law, the G_{IP}^{NR} in Eq. (8.62) and G_I^L in Eq. (8.51) can also be written as

$$G_{IP}^{NR} = \int_0^{\overline{w}_{BP}} \sigma_{nBP}\, d\overline{w}_B \tag{8.67}$$

and

$$G_I^L = \int_{\overline{w}_{BP}}^{\overline{w}_B} \left(\sigma_{nB} - \sigma_{nBP}\right) d\overline{w}_B \tag{8.68}$$

Since both G_{IP}^{NR} and G_I^L are known, both σ_{nBP} and $\overline{w}_{BP}$ can be found from Eq. (8.67) and $\overline{w}_B$ from Eq. (8.68). Therefore, the G_I^{NR} in a general loading condition is now determined

as

$$G_I^{NR} = G_{IP}^{NR} + \sigma_{nBP}\left(\overline{w}_B - \overline{w}_{BP}\right) \tag{8.69}$$

The mode II component G_{II}^{NR} in Eq. (8.49) is now considered. Based on Eq. (8.7), the crack tip shear stress τ_{sP} due to the shear forces P_{1B} and P_{2B} is written in the following form:

$$\tau_{sP}\left(\gamma\right) = \frac{\zeta\left(\gamma\right)\left[P_{2B} - \theta_P\left(\gamma\right)P_{1B}\right]}{bh_1} \tag{8.70}$$

where $\zeta\left(\gamma\right)$ and $\theta_P\left(\gamma\right)$ are two γ-dependent parameters and are determined numerically by consideration of two loading cases. The two cases chosen here are $P_{1B} = 1$, $P_{2B} = 0$ and $P_{1B} = 1$, $P_{2B} = -1$, giving

$$\zeta\left(\gamma\right) = \left[\tau_{sP,0}\left(\gamma\right) - \tau_{sP,-1}\left(\gamma\right)\right]bh_1 \tag{8.71}$$

and

$$\theta_P\left(\gamma\right) = \left[\tau\left(\gamma\right) - 1\right]^{-1} \tag{8.72}$$

with $\tau\left(\gamma\right) = \tau_{sP,-1}\left(\gamma\right)/\tau_{sP,0}\left(\gamma\right)$ determined numerically. Therefore, in a similar way to Eq. (8.13), the ERR G_{II}^{NR} is given by

$$G_{II}^{NR} = \int_0^{\overline{u}_B} \tau_{sP}\, d\overline{u}_B = \int_0^{\overline{u}_{B\tau_{sP}}} \tau_{sB}\, d\overline{u}_B + \int_{\overline{u}_{B\tau_{sP}}}^{\overline{u}_B} \tau_{sP}\, d\overline{u}_B \tag{8.73}$$

$$= \int_0^{\overline{u}_{B\tau_{sP}}} \tau_{sB}\, d\overline{u}_B + \tau_{sP}\left(\overline{u}_B - \overline{u}_{B\tau_{sP}}\right) \tag{8.74}$$

For a given interface cohesive law, the first term in Eq. (8.74) is readily obtained and $\overline{u}_{B\tau_{sP}}$ is also known. The $\overline{u}_B$ in the second term in Eq. (8.74) can be obtained using

$$G_{II}^{L} = \int_{\overline{u}_{B\tau_{sP}}}^{\overline{u}_B} \left(\tau_{sB} - \tau_{sP}\right)\, d\overline{u}_B \tag{8.75}$$

8.3 Numerical investigations with beams

The FEM was used to validate the theories. Finite elements, based on the Euler and Timoshenko beam theories and two-dimensional elasticity, were employed to model isotropic DCBs. Normal and shear point interface springs were used to bond the plies. The ERR partition was calculated using the VCCT in conjunction with these interface springs. Full details are given in §3.3 and §3.5 respectively. Contact was not considered, although it has been dealt with in detail in Chapter 4 for isotropic homogeneous DCBs.

Two numerical tests were carried out on the DCB shown in Fig. 8.1 (a). In line with the theoretical development, a plane-stress condition was assumed. For plane strain, E can simply be replaced with $E/\left(1-\nu^2\right)$, and ν with $\nu/\left(1-\nu\right)$. The units of these FEM simulations are kN and mm. The Young's modulus is a unit parameter and was therefore set to $E = 1\,\text{GPa}$, and the Poisson's ratio is $\nu = 0.3$. The intact length is $L = 100\,\text{mm}$ and

the crack length is $a = 10\,\text{mm}$. The width is a unit parameter and was therefore set to $b = 1\,\text{mm}$. The thickness is $h = h_1 + h_2 = 3\,\text{mm}$ with $h_1 = 1\,\text{mm}$. Therefore, the thickness ratio is $\gamma = 2$. In each test, the DCB was either under tip bending moments $M_1 = 1\,\text{Nm}$ and M_2, which was varied from $-10\,\text{Nm}$ to $10\,\text{Nm}$, or under tip shear forces $P_1 = 1\,\text{N}$ and P_2, which was varied from $-10\,\text{N}$ to $10\,\text{N}$. In the first of the two numerical tests, linear Timoshenko beam elements with the very large shear modulus of $\mu = 10^4\,\text{GPa}$ were used to simulate Euler beam theory. The second test used linear Timoshenko beam elements, but with the normal shear modulus of $\mu = E/\left[2\left(1+\nu\right)\right] = 1/2.6\,\text{GPa}$.

All the finite element meshes, except for the ones marked as having 1310×2 elements (in the following figures and tables), had uniform element density along the length and through the thickness. In order to obtain accurate, mesh-independent partitions of ERR, the simulations with linear Timoshenko beam elements and any value of shear modulus required a very fine mesh in the vicinity of the crack tip. For these cases, meshes with a total of 1310×2 elements were used. In the region of length 1.2 mm centred on the crack tip, 1200 elements with a length of 0.001 mm were uniformly distributed. In the remaining intact section of the DCB, 100 elements were uniformly distributed. In the remaining cracked section of the DCB, 10 elements were uniformly distributed. All other simulations converged adequately without the need for such high numbers of elements around the crack tip. Therefore uniformly distributed elements did not result in prohibitively high computational requirements. Further details on the mesh convergence studies, which determined the design of the meshes in this section, are available in Appendix B.

8.3.1 Linear elastic interfaces with tip bending moments

The present theories are applicable to general non-rigid elastic interfaces including both linear and non-linear ones. In this section, beams with two different linear elastic interfaces are considered. Cohesive interface laws relate the interface stresses to the relative displacements across the interface, i.e. $\sigma_n = k_\sigma \overline{w}$ and $\tau_s = k_\sigma \overline{u}$ where k_σ is the stiffness of the interface, which here is assumed to be the same for both opening and shearing action. Since the beam simulations use interface point springs, which relate the interface spring forces to the relative displacements, i.e. $F_{ns} = k_s \overline{w}$ and $F_{ss} = k_s \overline{u}$ where k_s is the spring stiffness, the stiffness of an individual interface spring force is therefore set to $k_s = b k_\sigma \delta a$ where δa is the spring pitch, i.e. the beam element length. It is usual to describe an interface as being hard or soft by comparing the interface stiffness k_σ with the Young's modulus E and shear modulus μ of the beam material. A hard interface has stiffness values k_σ which are around the order of E or μ. However, the Young's modulus E in the thickness direction is effectively infinite in both Euler and Timoshenko beam theories. It is seen in §4.3 and §B.1 in Appendix B that a rigid interface for the DCB configuration in question is well represented with interface springs of stiffness $k_s = 10^6\,\text{kN/mm}$ which corresponds to an interface stiffness k_σ varying from around $k_\sigma = 10^8\,\text{GPa/m}$ for $\delta a = 10\,\text{mm}$ to around $k_\sigma = 10^{12}\,\text{GPa/m}$ for $\delta a = 10^{-3}\,\text{mm}$. Therefore, it is reasonable to assume that a non-rigid

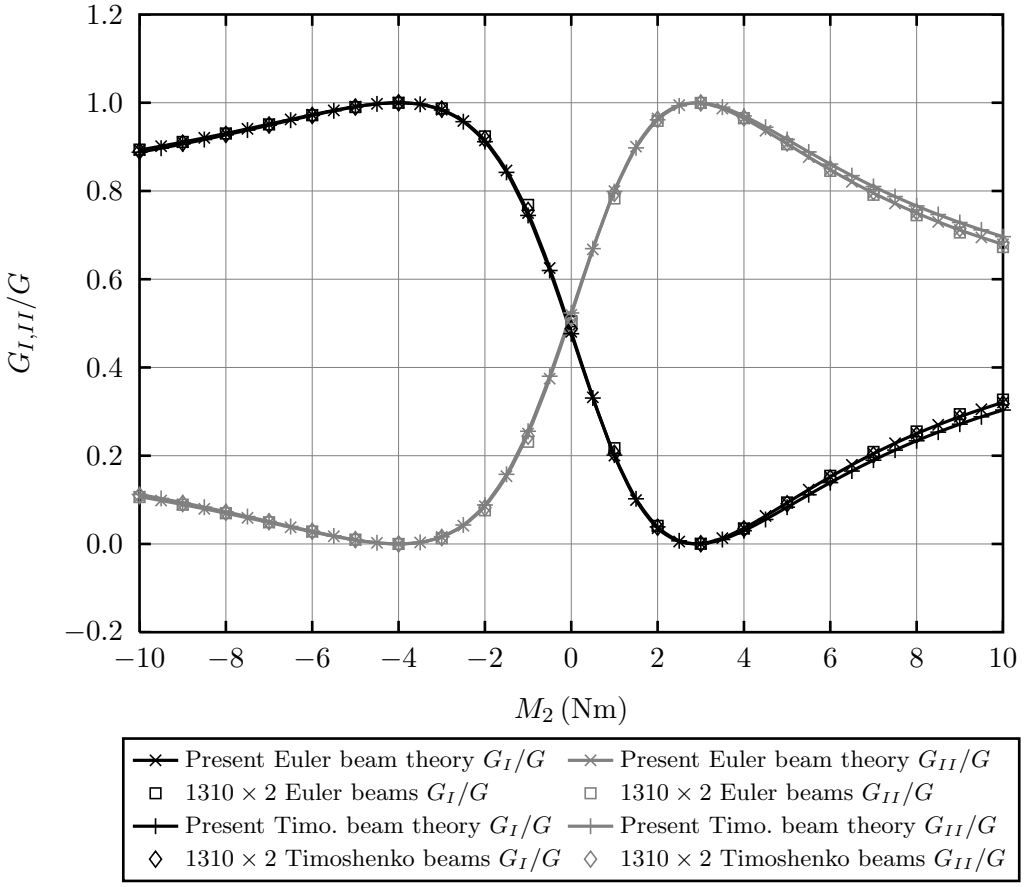

Figure 8.2: Comparisons between various theories and FEM results with an elastic interface stiffness $k_\sigma = 10^6\,\text{GPa/m}$, varying M_2 and $M_1 = 1\,\text{Nm}$, $N_1 = 0$, $N_2 = 0$, $P_1 = 0$, $P_2 = 0$, $\gamma = 2$.

hard interface can be represented by $k_\sigma = 10^6\,\text{GPa/m}$ and $k_\sigma = 10^5\,\text{GPa/m}$. These two interfaces are considered in the following applications.

The results for the DCB with the $k_\sigma = 10^6\,\text{GPa/m}$ linear elastic interface and tip bending moments $M_1 = 1\,\text{Nm}$ and M_2, which was varied from $-10\,\text{Nm}$ to $10\,\text{Nm}$, are presented in Fig. 8.2 and Tables 8.1 and 8.2. As shown by Eqs. (8.15) and (8.28), in this loading case and with the linear elastic interface, the present Euler beam partition theory results are the same as the present Timoshenko beam partition theory results with a rigid interface (see Chapter 4). There is no stealthy interaction and there is only one set of pure modes, which is the first set, i.e. $\left\{\varphi_{\theta_1}\right\}$, $\left\{\varphi_{\beta_1}\right\}$.

The mode II ERR G_{II} from the present Timoshenko beam partition theory is the same as the mode II ERR G_{II} from the present Euler beam partition theory. However, as shown by Eq. (8.46), the mode I ERR G_I from the present Timoshenko beam partition depends on $\overline{w}_B$ and $\overline{w}_B^{(1)}$, which are in turn dependent on the cohesive law for the interface. These two quantities could be determined from FEM simulations and used as arguments to Eq. (8.48). However, in the case of hard non-rigid elastic interfaces, the third term in Eq. (8.46) can be replaced with Eq. (8.47), and Eq. (8.48) can be used to calculate $\overline{w}_B$.

Table 8.1: Comparisons between various theories and FEM results for ERR partitions G_I/G with an elastic interface stiffness $k_\sigma = 10^6\,\mathrm{GPa/m}$, varying M_2 and $M_1 = 1\,\mathrm{Nm}$, $N_1 = 0$, $N_2 = 0$, $P_1 = 0$, $P_2 = 0$, $\gamma = 2$.

M_2 (Nm)	$G_I/G\,(\%)$			
	Present Euler beam theory	1310×2 Euler beams	Present Timo. beam theory	1310×2 Timo. beams
-10	89.29	89.38	88.78	89.04
-8	93.04	93.03	92.71	92.82
-6	97.27	97.17	97.14	97.12
-4	100.00	99.99	100.00	100.00
-2	91.46	92.37	91.17	91.80
0	48.08	50.46	47.65	48.77
2	3.57	4.11	3.87	3.78
4	3.57	3.50	3.00	3.42
6	15.20	15.45	13.90	14.95
8	25.00	25.50	23.39	24.71
10	32.08	32.72	30.35	31.78

Table 8.2: Comparisons between various theories and FEM results for mode I ERR G_I with an elastic interface stiffness $k_\sigma = 10^6\,\mathrm{GPa/m}$, varying M_2 and $M_1 = 1\,\mathrm{Nm}$, $N_1 = 0$, $N_2 = 0$, $P_1 = 0$, $P_2 = 0$, $\gamma = 2$.

M_2 (Nm)	G_I (kN/mm)			
	Present Euler beam theory	1310×2 Euler beams	Present Timo. beam theory	1310×2 Timo. beams
-10	56.25	55.14	53.38	52.27
-8	40.11	39.37	38.14	37.30
-6	26.69	26.24	25.45	24.85
-4	16.00	15.77	15.32	14.92
-2	8.03	7.95	7.75	7.51
0	2.78	2.78	2.73	2.62
2	0.25	0.27	0.27	0.25
4	0.44	0.40	0.37	0.39
6	3.36	3.19	3.03	3.06
8	9.00	8.63	8.24	8.25
10	17.36	16.73	16.01	15.96

This gives a completely analytical expression. In this case, since there are no applied shear forces, the partitions from the present Timoshenko beam partition theory are very close to the ones from the present Euler beam partition theory.

The Timoshenko beam element simulations with the very large shear modulus $\mu = 10^4\,\mathrm{GPa}$ converge slowly towards the present Euler beam partition theory. A large number of elements in the vicinity of the crack tip is required to obtain this good agreement. This is expected since point interface springs are more suited to capture the stress singularity at the crack tip that is observed for a rigid interface. The numerical results confirm that there is no stealthy interaction in Euler beam theory with a non-rigid elastic interface, and therefore there is a single set of pure modes which are $\left\{\varphi_{\theta_1}\right\}$ and $\left\{\varphi_{\beta_1}\right\}$. When Timoshenko beam

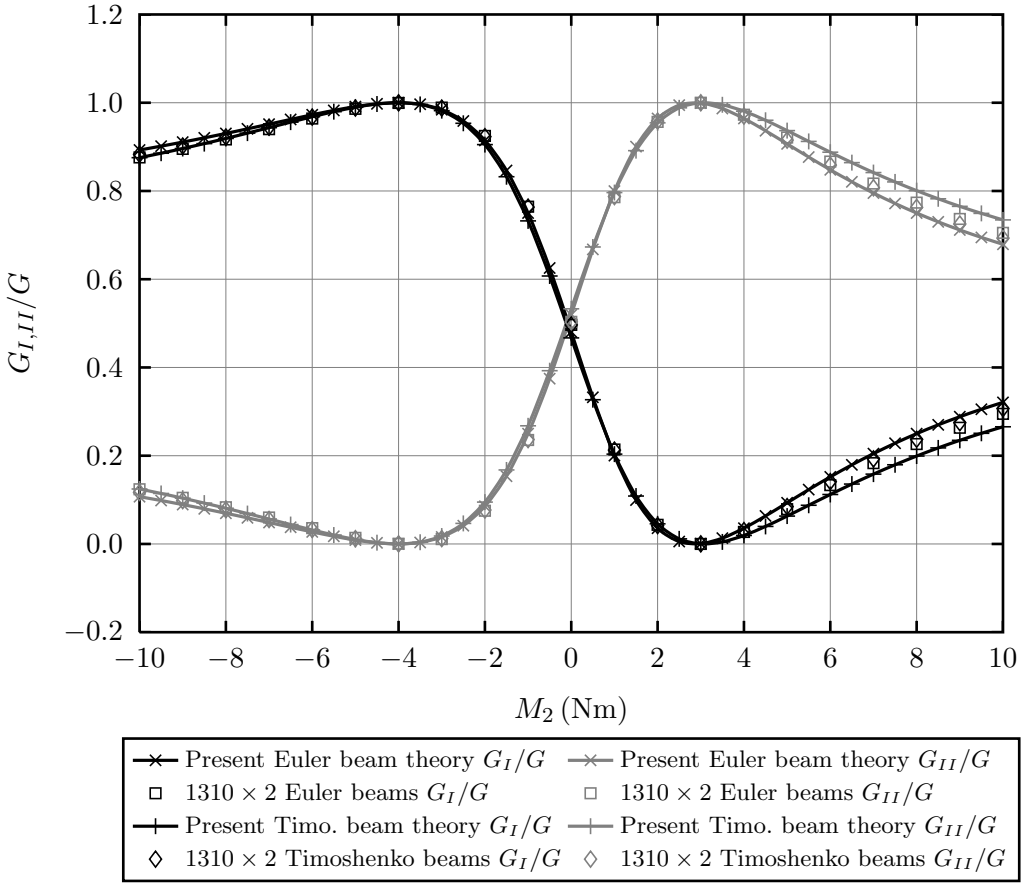

Figure 8.3: Comparisons between various theories and FEM results with an elastic interface stiffness $k_\sigma = 10^5\,\text{GPa/m}$, varying M_2 and $M_1 = 1\,\text{Nm}$, $N_1 = 0$, $N_2 = 0$, $P_1 = 0$, $P_2 = 0$, $\gamma = 2$.

elements with a normal shear modulus $\mu = 1/2.6\,\text{GPa}$ are used, the results are very close to the results from Euler beam elements, which as expected, are also close to the present Timoshenko beam partition theory with the hard-interface approximation.

The results for the $k_\sigma = 10^5\,\text{GPa/m}$ linear elastic interface are presented in Fig. 8.3 and Tables 8.3 and 8.4. The effect of reducing the interface spring stiffness can now be observed. The Timoshenko beam element simulations with the very large shear modulus $\mu = 10^4\,\text{GPa}$ converge towards the present Euler beam partition theory very slowly. The convergence is much slower now that the interface stiffness is an order of magnitude smaller. For rigid interfaces, only 11 elements along the DCB were able to give excellent agreement with the analytical results (see §4.3 and §B.2 in Appendix B). However, here the very fine non-uniform mesh with 1310×2 elements is not able to achieve the same degree of agreement. There is of course no comparison in computing time between the two meshes. When Timoshenko beam elements with the normal shear modulus of $\mu = 1/2.6\,\text{GPa}$ are used, the results are close to present Timoshenko beam partition theory, which as expected, are once again close to the Euler beam numerical results.

Table 8.3: Comparisons between various theories and FEM results for ERR partitions G_I/G with an elastic interface stiffness $k_\sigma = 10^5\,\mathrm{GPa/m}$, varying M_2 and $M_1 = 1\,\mathrm{Nm}$, $N_1 = 0$, $N_2 = 0$, $P_1 = 0$, $P_2 = 0$, $\gamma = 2$.

M_2 (Nm)	$G_I/G\,(\%)$			
	Present Euler beam theory	1310×2 Euler beams	Present Timo. beam theory	1310×2 Timo. beams
-10	89.29	87.60	87.55	88.32
-8	93.04	91.68	91.90	92.24
-6	97.27	96.41	96.82	96.74
-4	100.00	99.95	100.00	99.98
-2	91.46	92.48	90.51	92.31
0	48.08	49.66	46.70	49.63
2	3.57	4.34	4.56	4.16
4	3.57	2.72	1.93	3.03
6	15.20	13.34	11.21	14.13
8	25.00	22.64	19.93	23.71
10	32.08	29.49	26.56	30.68

Table 8.4: Comparisons between various theories and FEM results for mode I ERR G_I with an elastic interface stiffness $k_\sigma = 10^5\,\mathrm{GPa/m}$, varying M_2 and $M_1 = 1\,\mathrm{Nm}$, $N_1 = 0$, $N_2 = 0$, $P_1 = 0$, $P_2 = 0$, $\gamma = 2$.

M_2 (Nm)	G_I (kN/mm)			
	Present Euler beam theory	1310×2 Euler beams	Present Timo. beam theory	1310×2 Timo. beams
-10	56.25	52.65	47.45	54.35
-8	40.11	37.67	34.04	38.84
-6	26.69	25.19	22.86	25.93
-4	16.00	15.21	13.90	15.62
-2	8.03	7.74	7.15	7.91
0	2.78	2.77	2.63	2.80
2	0.25	0.30	0.32	0.28
4	0.44	0.33	0.24	0.37
6	3.36	2.87	2.37	3.05
8	9.00	7.91	6.72	8.33
10	17.36	15.45	13.29	16.21

8.3.2 Linear elastic interfaces with tip shear forces

In the present theories, shear forces cause additional contributions to both the mode I and mode II ERRs, which have been considered in detail in §8.2. In this section, the same two linear elastic interfaces as before are considered, corresponding to the interface stiffness values $k_\sigma = 10^6\,\text{GPa/m}$ and $k_\sigma = 10^5\,\text{GPa/m}$.

The results for the DCB with the $k_\sigma = 10^6\,\text{GPa/m}$ linear elastic interface and tip shear forces $P_1 = 1\,\text{kN}$ and P_2, which was varied from $-10\,\text{kN}$ to $10\,\text{kN}$, are presented in Fig. 8.4 and Tables 8.5 and 8.6. As shown by Eq. (8.15), the mode II ERR G_{II} from the present Euler beam partition theory depends on the cohesive law when shear forces are present. It can be calculated in a completely analytical way by means of Eq. (8.14). As shown by Eq. (8.28), the mode I ERR G_I from the present Euler beam partition theory depends on $\overline{w}_B^{(1)}$, which depends on the cohesive law. This parameter could be determined from FEM simulations and used as an argument to Eq. (8.28), however in the case of hard non-rigid elastic interfaces, the second term in Eq. (8.28) is very small and is found to be negligible. The mode I ERR G_I from the present Euler beam partition theory is therefore approximately given by just the first term in Eq. (8.28), which is completely analytical.

The values of mode II ERR G_{II} from the present Timoshenko beam partition theory are the same as the those from the present Euler beam partition theory. The mode I ERR G_I, which is given by Eq. (8.46) and which depends on $\overline{w}_B$ and $\overline{w}_B^{(1)}$, is calculated in the same way as in the previous section for DCBs with tip bending moments by assuming a hard non-rigid elastic interface.

The Timoshenko beam element simulations with the very large shear modulus $\mu = 10^4\,\text{GPa}$ converge slowly towards the present Euler beam partition theory. The Timoshenko beam elements with a normal shear modulus $1/2.6\,\text{GPa}$ converge slowly towards the present Timoshenko beam partition theory. In both cases, a large number of elements in the

Table 8.5: Comparisons between various theories and FEM results for ERR partitions G_I/G with an elastic interface stiffness $k_\sigma = 10^6\,\text{GPa/m}$, varying P_2 and $P_1 = 1\,\text{kN}$, $M_1 = 0$, $M_2 = 0$, $N_1 = 0$, $N_2 = 0$, $\gamma = 2$.

P_2 (kN)	$G_I/G\,(\%)$			
	Present Euler beam theory	1310×2 Euler beams	Present Timo. beam theory	1310×2 Timo. beams
-10	89.31	89.61	90.30	90.24
-8	93.06	93.19	93.73	93.64
-6	97.27	97.23	97.55	97.45
-4	100.00	99.99	100.00	100.00
-2	91.44	92.56	92.23	92.75
0	48.01	51.09	50.57	52.06
2	3.56	4.20	3.86	4.28
4	3.56	3.59	4.04	3.89
6	15.17	15.80	16.74	16.72
8	24.95	26.00	27.16	27.26
10	32.03	33.30	34.55	34.71

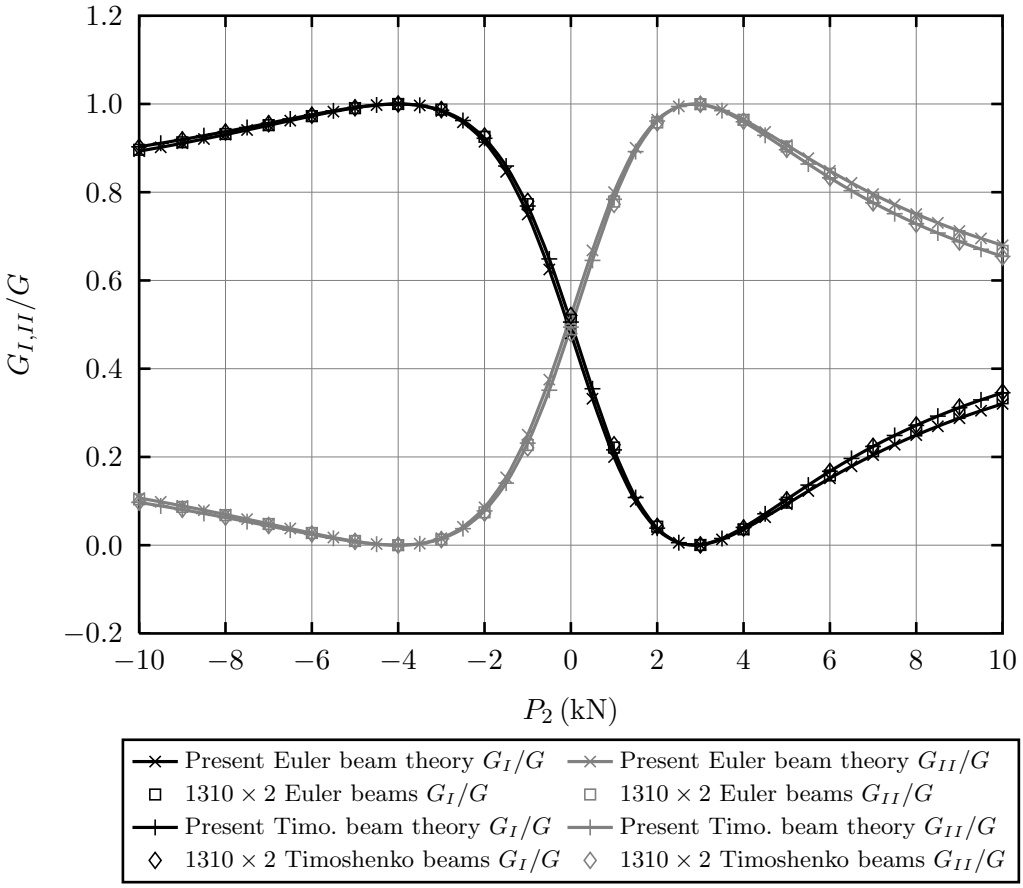

Figure 8.4: Comparisons between various theories and FEM results with an elastic interface stiffness $k_\sigma = 10^6\,\text{GPa/m}$, varying P_2 and $P_1 = 1\,\text{kN}$, $M_1 = 0$, $M_2 = 0$, $N_1 = 0$, $N_2 = 0$, $\gamma = 2$.

Table 8.6: Comparisons between various theories and FEM results for mode I ERR G_I with an elastic interface stiffness $k_\sigma = 10^6\,\text{GPa/m}$, varying P_2 and $P_1 = 1\,\text{kN}$, $M_1 = 0$, $M_2 = 0$, $N_1 = 0$, $N_2 = 0$, $\gamma = 2$.

P_2 (kN)	G_I (kN/mm)			
	Present Euler beam theory	1310 × 2 Euler beams	Present Timo. beam theory	1310 × 2 Timo. beams
−10	5625.00	5673.35	6270.07	5979.94
−8	4011.11	4049.91	4469.68	4267.03
−6	2669.44	2699.56	2973.25	2842.52
−4	1600.00	1622.10	1780.79	1706.33
−2	802.78	817.57	892.29	858.51
0	277.78	285.99	307.76	299.04
2	25.00	27.35	27.20	27.93
4	44.44	41.64	50.60	45.19
6	336.11	328.87	377.96	350.84
8	900.00	889.01	1009.29	944.77
10	1736.11	1722.17	1944.59	1827.11

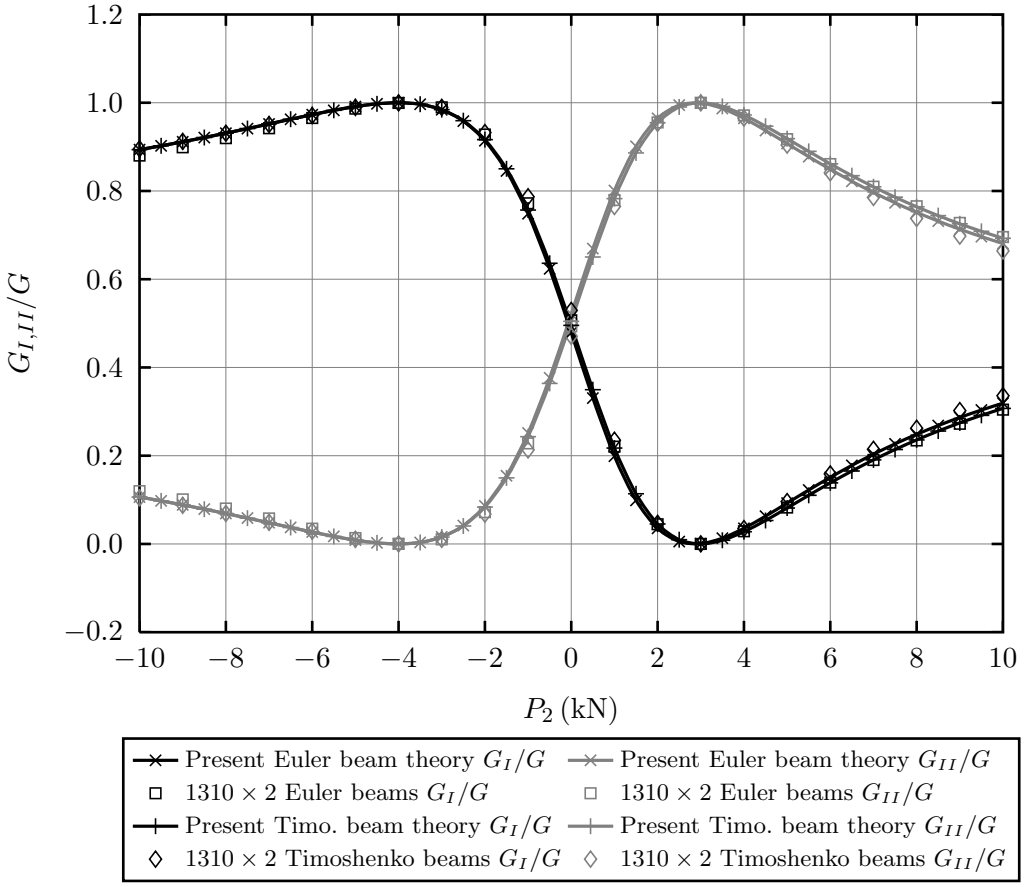

Figure 8.5: Comparisons between various theories and FEM results with an elastic interface stiffness $k_\sigma = 10^5\,\text{GPa/m}$, varying P_2 and $P_1 = 1\,\text{kN}$, $M_1 = 0$, $M_2 = 0$, $N_1 = 0$, $N_2 = 0$, $\gamma = 2$.

vicinity of the crack tip is required to obtain this good agreement. In this case where $k_\sigma = 10^6\,\text{GPa/m}$, the difference between the Euler and Timoshenko partitions is small.

The results for the $k_\sigma = 10^5\,\text{GPa/m}$ linear elastic interface are presented in Fig. 8.5 and Tables 8.7 and 8.8. The Timoshenko beam element simulations with the very large shear modulus $\mu = 10^4\,\text{GPa}$ converge towards the present Euler beam partition theory very slowly. The Timoshenko beam elements with a normal shear modulus $1/2.6\,\text{GPa}$ converge very slowly towards the present Timoshenko beam partition theory.

Table 8.7: Comparisons between various theories and FEM results for ERR partitions G_I/G with an elastic interface stiffness $k_\sigma = 10^5\,\mathrm{GPa/m}$, varying P_2 and $P_1 = 1\,\mathrm{kN}$, $M_1 = 0$, $M_2 = 0$, $N_1 = 0$, $N_2 = 0$, $\gamma = 2$.

P_2 (kN)	$G_I/G\,(\%)$			
	Present Euler beam theory	1310×2 Euler beams	Present Timo. beam theory	1310×2 Timo. beams
-10	89.36	88.03	89.36	89.56
-8	93.09	91.97	93.12	93.08
-6	97.29	96.53	97.31	97.10
-4	100.00	99.95	100.00	99.98
-2	91.39	92.79	91.64	93.24
0	47.87	50.69	49.54	52.93
2	3.54	4.47	4.53	4.68
4	3.54	2.88	2.77	3.48
6	15.10	13.90	13.84	15.87
8	24.85	23.46	23.58	26.22
10	31.91	30.44	30.72	33.59

Table 8.8: Comparisons between various theories and FEM results for mode I ERR G_I with an elastic interface stiffness $k_\sigma = 10^5\,\mathrm{GPa/m}$, varying P_2 and $P_1 = 1\,\mathrm{kN}$, $M_1 = 0$, $M_2 = 0$, $N_1 = 0$, $N_2 = 0$, $\gamma = 2$.

P_2 (kN)	G_I (kN/mm)			
	Present Euler beam theory	1310×2 Euler beams	Present Timo. beam theory	1310×2 Timo. beams
-10	5625.00	5546.02	5624.94	6255.91
-8	4011.11	3967.02	4025.44	4470.30
-6	2669.44	2651.98	2692.89	2983.98
-4	1600.00	1600.83	1627.30	1797.05
-2	802.78	813.58	828.66	909.46
0	277.78	290.24	296.98	321.23
2	25.00	30.79	32.26	32.36
4	44.44	35.26	34.50	42.84
6	336.11	303.63	303.69	352.67
8	900.00	835.88	839.84	961.89
10	1736.11	1632.07	1642.94	1870.44

8.4 Numerical tests with two-dimensional elasticity

To validate the present two-dimensional elasticity partition theories, FEM simulations were carried out using SIMULIA's Abaqus with reduced-integration QUAD4 elements and linear cohesive interfaces. The ERR and its partitions were calculated by means of the crack closure technique.

Three numerical tests were carried out on the DCB shown in Fig. 8.1 (a). The Young's modulus is $E = 1\,\text{GPa}$, the Poisson's ratio is $\nu = 0.3$ and the shear modulus $G = E/\left[2\left(1+\nu\right)\right] = 1/2.6\,\text{GPa}$. The intact length is $L = 100\,\text{mm}$, the crack length is $a = 10\,\text{mm}$ and the width is $b = 1\,\text{mm}$. The thickness is $h = h_1 + h_2 = 2\,\text{mm}$ and the thickness ratio $\gamma = h_2/h_1$ is varied according to which test is being carried out.

In the first test, the thickness ratio was set to $\gamma = 2$ and the DCB was subjected to several sets of different loading conditions with DCB tip bending moments, axial forces and shear forces. In the second test, bending moments were applied at the DCB tip, $M_1 = 1\,\text{Nm}$ and $M_2 = 0$, with all other DCB tip forces zero, and γ was varied from 1 to 9. In the third test, shear forces were applied at the DCB tip, $P_1 = 1\,\text{N}$ and $P_2 = 0$, with all other DCB tip forces zero, and γ was varied from 1 to 9.

All the finite element meshes had 1100 uniformly distributed QUAD4 elements along the length. For the first test (with constant γ), there were 7 elements through the thickness of the top beam and 13 elements through the thickness of the bottom beam. For the second and third tests (with varying γ), there were always ten uniformly distributed QUAD4 elements through the thickness of the top beam. Through the thickness of the bottom beam, there were 10, 13, 15, 16, 17, 17, 18, 18 and 18 uniformly distributed QUAD4 elements for $\gamma = 1, 2, \ldots, 9$ respectively. The interface was modelled with cohesive four node quadrilateral (COH2D4) elements in Abaqus, which were $10^{-5}\,\text{m}$ thick. The interface had the same distribution of COH2D4 elements along the length as the QUAD4 elements and one element through the thickness. The stiffness of the cohesive interface was $k_\sigma = 10^8\,\text{Pa/m}$, which is around the same order as the Young's modulus $E = 10^9\,\text{Pa}$ and shear modulus $\mu = 3.846 \times 10^8\,\text{Pa}$. It is therefore a hard non-rigid interface.

8.4.1 Results from the first test

In the first test, the thickness ratio was set to $\gamma = 2$ and several different loading configurations were applied to the DCB. In the first loading configuration, only bending moments were applied to the DCB tip with $M_1 = 1\,\text{Nm}$ and M_2 varied between $-10\,\text{Nm}$ and $10\,\text{Nm}$. The results from the two-dimensional FEM simulations and the present two-dimensional elasticity partition theories are given in Fig. 8.6 and Table 8.9. Since there are no applied shear forces, G_I^{NR} and G_{II}^{NR} in Eq. (8.49) are both zero. The remaining terms in Eq. (8.49) are G_I^L and G_{II}^L. They can be calculated either by: (1) using present two-dimensional elasticity partition theory 1, given by Eqs. (8.51) to (8.59) (referred to as 'Present 2D elasticity

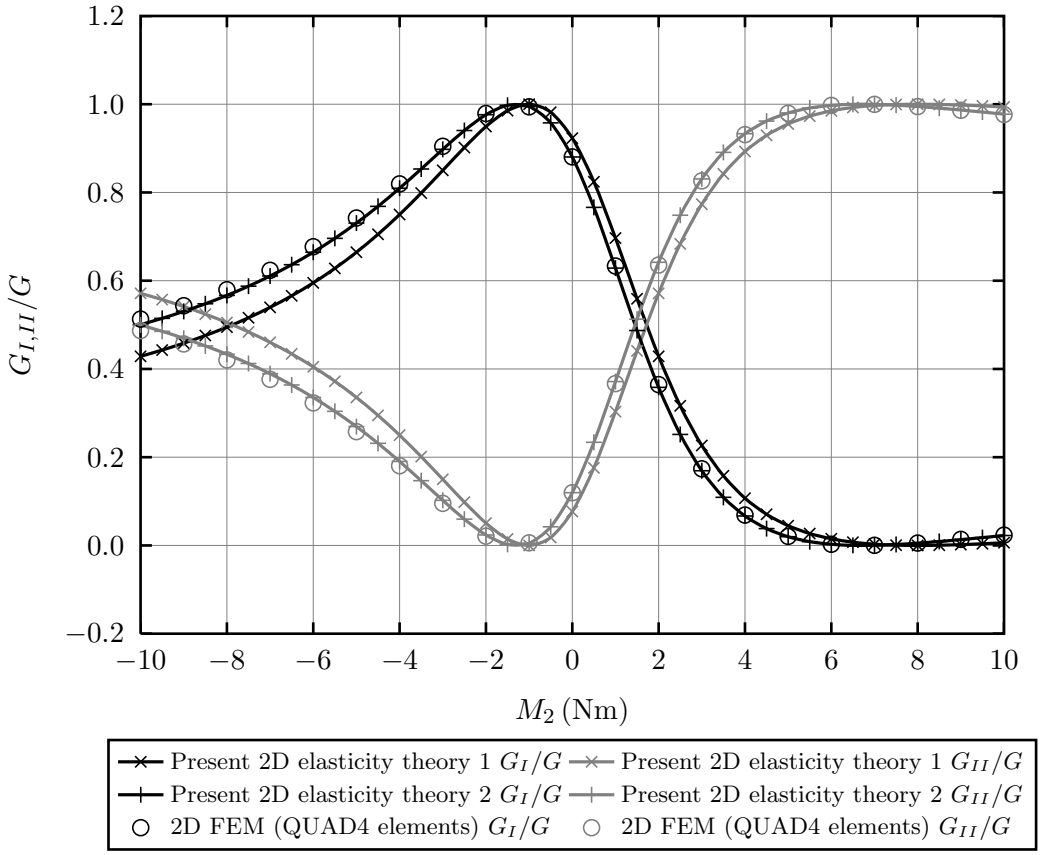

Figure 8.6: Comparisons between the present two-dimensional elasticity partition theories and FEM results with an elastic interface stiffness $k_\sigma = 10^8\,\mathrm{Pa/m}$, varying M_2 and $M_1 = 1\,\mathrm{Nm}$, $N_1 = 0$, $N_2 = 0$, $P_1 = 0$, $P_2 = 0$, $\gamma = 2$.

Table 8.9: Comparisons between the present two-dimensional elasticity partition theories and FEM results with an elastic interface stiffness $k_\sigma = 10^8\,\mathrm{Pa/m}$, varying M_2 and $M_1 = 1\,\mathrm{Nm}$, $N_1 = 0$, $N_2 = 0$, $P_1 = 0$, $P_2 = 0$, $\gamma = 2$.

M_2 (Nm)	G_I (N/m)			G_I/G (%)		
	Present 2D elasticity theory 1	Present 2D elasticity theory 2	2D FEM (QUAD4 elements)	Present 2D elasticity theory 1	Present 2D elasticity theory 2	2D FEM (QUAD4 elements)
−10	9.113×10^7	1.064×10^8	1.083×10^8	42.86	50.04	51.31
−8	7.200×10^7	8.245×10^7	8.390×10^7	49.48	56.67	57.96
−6	5.513×10^7	6.156×10^7	6.264×10^7	59.51	66.46	67.70
−4	4.050×10^7	4.372×10^7	4.448×10^7	75.00	80.96	81.94
−2	2.813×10^7	2.892×10^7	2.942×10^7	94.94	97.62	97.89
0	1.800×10^7	1.717×10^7	1.747×10^7	92.31	88.04	88.06
2	1.013×10^7	8.464×10^6	8.609×10^6	42.86	35.83	36.45
4	4.500×10^6	2.806×10^6	2.853×10^6	10.71	6.68	6.89
6	1.125×10^6	1.943×10^5	1.971×10^5	1.51	0.26	0.27
8	0.000	6.295×10^5	6.419×10^5	0.00	0.52	0.54
10	1.125×10^6	4.111×10^6	4.187×10^6	0.62	2.25	2.34

theory 1' in all the tables and figures in §8.4); or by (2) using present two-dimensional elasticity partition theory 2, by replacing β_1' and θ_1' in Eqs. (8.51) to (8.59) with β_{1A}' and θ_{1A}', which are given by Eqs. (8.60) and (8.61) respectively (referred to as 'Present 2D elasticity theory 2' in all the tables and figures in §8.4). From Fig. 8.6 and Table 8.9, it is seen that the second method gives very close agreement with the two-dimensional FEM results for all values of M_2. The first method is not as close but is still good.

In the second loading configuration, $M_1 = 1\,\text{Nm}$ and N_1 was varied between $-500\,\text{N}$ and $500\,\text{N}$. The results are given in Fig. 8.7 and Table 8.10. Both present two-dimensional elasticity partition theories predict constant G_I for the full range of N_1. This is in agreement with the two-dimensional FEM simulations. Again, the values of G_I and G_I/G from present two-dimensional elasticity partition theory 2 agree with the two-dimensional FEM results more closely than those from present two-dimensional elasticity partition theory 1.

Only shear forces were applied to the DCB tip in the third loading configuration: $P_1 = 1\,\text{N}$ and P_2 was varied between $-10\,\text{N}$ and $10\,\text{N}$. This resulted in both bending moments and shear forces at the crack tip. Therefore in this loading configuration, G_I^L and G_{II}^L in Eq. (8.49) exist due to the crack tip bending moments, and G_I^{NR} and G_{II}^{NR} also exist due to the crack tip shear forces. G_I^L and G_{II}^L are easily calculated using either present two-dimensional elasticity partition theory 1 or present two-dimensional elasticity partition theory 2. As described in §8.2.3, to calculate G_I^{NR} and G_{II}^{NR} for any given crack tip shear forces P_{1B} and P_{2B}, two loading cases need to be considered for a given value of γ. The two cases chosen here were: (1) $P_{1B} = 1\,\text{N}$, $P_{2B} = 0$ to obtain $G_{IP,0}^{NR}$ and $\tau_{IP,0}$; and (2) $P_{1B} = 1\,\text{N}$, $P_{2B} = -1\,\text{N}$ to obtain $G_{IP,-1}^{NR}$ and $\tau_{IP,-1}$. G_I^{NR} and G_{II}^{NR} are then given by Eqs. (8.69) and (8.74) respectively for any values of P_{1B} and P_{2B}. The results from the two-dimensional FEM simulations and the present two-dimensional elasticity partition theories are given in Fig. 8.8 and Table 8.11. Present two-dimensional elasticity partition theory 1 is in good agreement with the two-dimensional FEM results. Present two-dimensional elasticity partition theory 2 is in excellent agreement with the two-dimensional FEM.

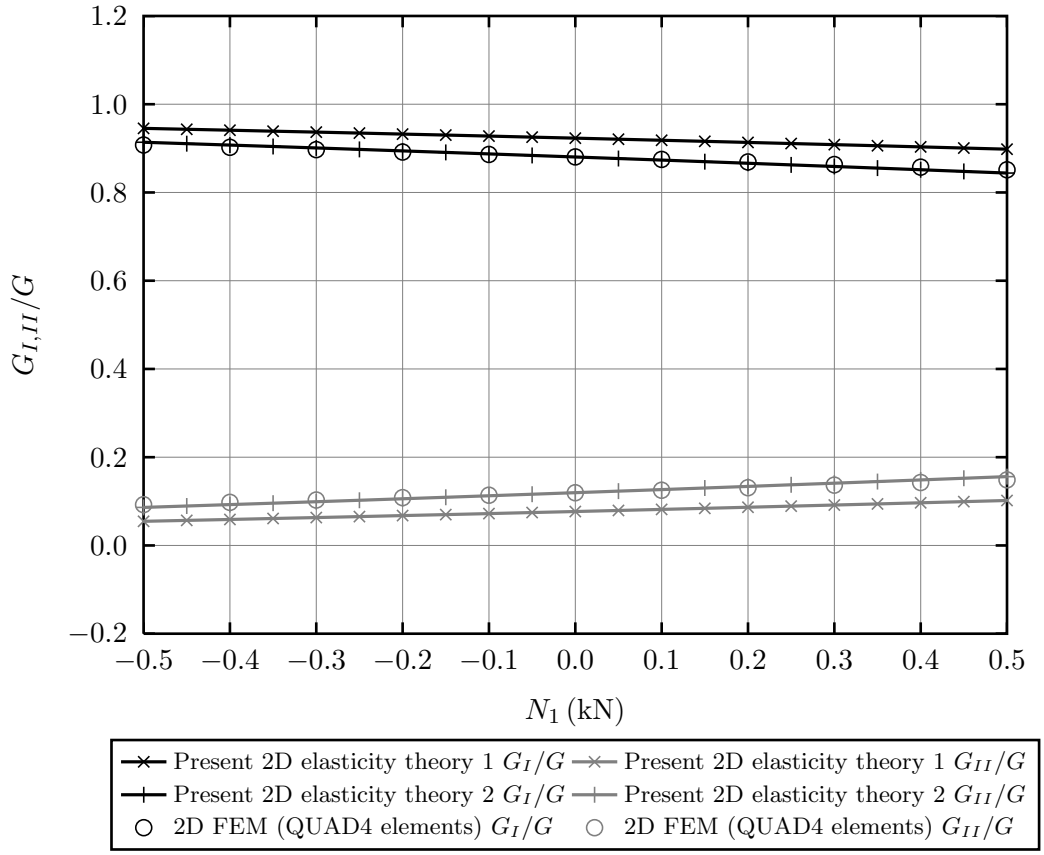

Figure 8.7: Comparisons between the present two-dimensional elasticity partition theories and FEM results with an elastic interface stiffness $k_\sigma = 10^8\,\mathrm{Pa/m}$, varying N_1 and $M_1 = 1\,\mathrm{Nm}$, $M_2 = 0$, $N_2 = 0$, $P_1 = 0$, $P_2 = 0$, $\gamma = 2$.

Table 8.10: Comparisons between the present two-dimensional elasticity partition theories and FEM results with an elastic interface stiffness $k_\sigma = 10^8\,\mathrm{Pa/m}$, varying N_1 and $M_1 = 1\,\mathrm{Nm}$, $M_2 = 0$, $N_2 = 0$, $P_1 = 0$, $P_2 = 0$, $\gamma = 2$.

N_1 (N)	G_I (N/m)			G_I/G (%)		
	Present 2D elasticity theory 1	Present 2D elasticity theory 2	2D FEM (QUAD4 elements)	Present 2D elasticity theory 1	Present 2D elasticity theory 2	2D FEM (QUAD4 elements)
−500	1.800×10^7	1.717×10^7	1.760×10^7	94.53	91.38	90.76
−400	1.800×10^7	1.717×10^7	1.757×10^7	94.11	90.74	90.24
−300	1.800×10^7	1.717×10^7	1.754×10^7	93.68	90.09	89.71
−200	1.800×10^7	1.717×10^7	1.752×10^7	93.23	89.42	89.17
−100	1.800×10^7	1.717×10^7	1.749×10^7	92.78	88.74	88.62
0	1.800×10^7	1.717×10^7	1.747×10^7	92.31	88.04	88.06
100	1.800×10^7	1.717×10^7	1.744×10^7	91.83	87.34	87.49
200	1.800×10^7	1.717×10^7	1.741×10^7	91.34	86.62	86.91
300	1.800×10^7	1.717×10^7	1.739×10^7	90.84	85.89	86.33
400	1.800×10^7	1.717×10^7	1.736×10^7	90.33	85.15	85.74
500	1.800×10^7	1.717×10^7	1.734×10^7	89.81	84.40	85.14

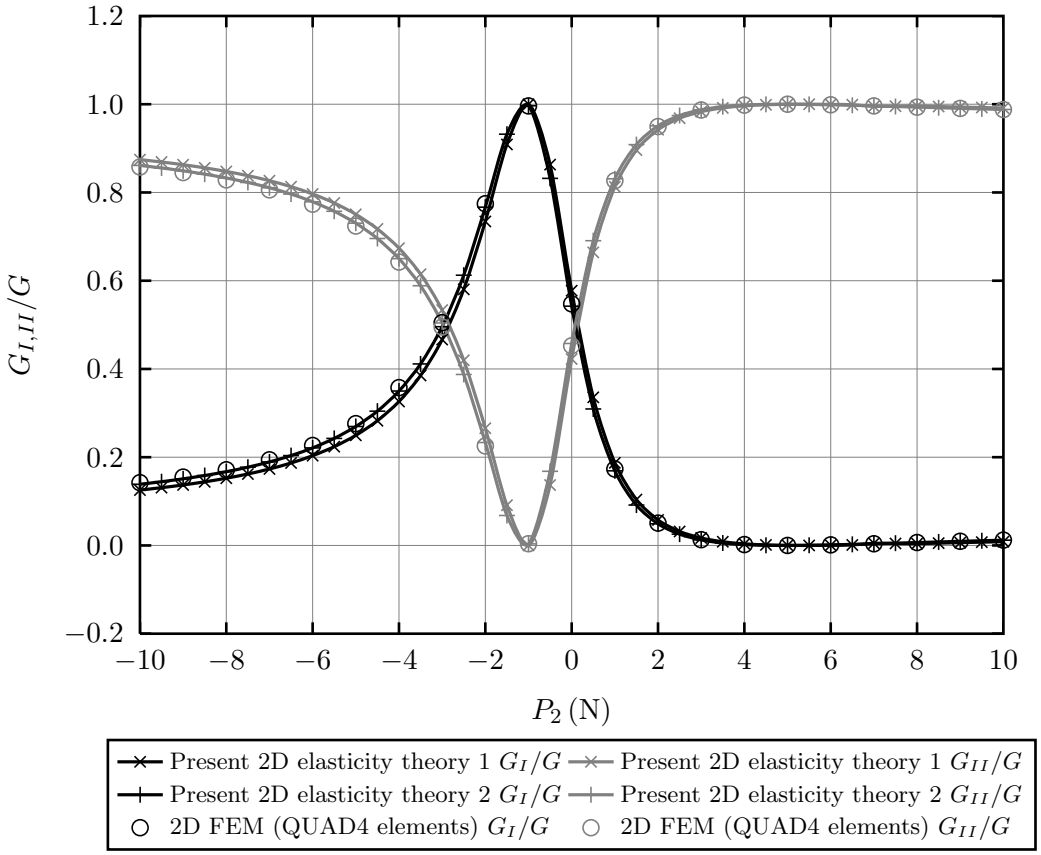

Figure 8.8: Comparisons between the present two-dimensional elasticity partition theories and FEM results with an elastic interface stiffness $k_\sigma = 10^8\,\mathrm{Pa/m}$, varying P_2 and $P_1 = 1\,\mathrm{N}$, $M_1 = 0$, $M_2 = 0$, $N_1 = 0$, $N_2 = 0$, $\gamma = 2$.

Table 8.11: Comparisons between the present two-dimensional elasticity partition theories and FEM results with an elastic interface stiffness $k_\sigma = 10^8\,\mathrm{Pa/m}$, varying P_2 and $P_1 = 1\,\mathrm{N}$, $M_1 = 0$, $M_2 = 0$, $N_1 = 0$, $N_2 = 0$, $\gamma = 2$.

P_2 (N)	G_I (N/m)			G_I/G (%)		
	Present 2D elasticity theory 1	Present 2D elasticity theory 2	2D FEM (QUAD4 elements)	Present 2D elasticity theory 1	Present 2D elasticity theory 2	2D FEM (QUAD4 elements)
−10	3.168×10^4	3.448×10^4	3.473×10^4	12.55	13.87	14.23
−8	2.398×10^4	2.585×10^4	2.606×10^4	15.24	16.72	17.14
−6	1.734×10^4	1.847×10^4	1.862×10^4	20.34	22.11	22.66
−4	1.178×10^4	1.232×10^4	1.244×10^4	32.62	35.00	35.77
−2	7.291×10^3	7.418×10^3	7.493×10^3	73.43	76.67	77.45
0	3.873×10^3	3.751×10^3	3.796×10^3	57.74	54.23	54.76
2	1.528×10^3	1.322×10^3	1.344×10^3	5.78	4.91	5.06
4	2.539×10^2	1.316×10^2	1.370×10^2	0.37	0.19	0.20
6	5.211×10^1	1.800×10^2	1.755×10^2	0.04	0.13	0.13
8	9.223×10^2	1.467×10^3	1.459×10^3	0.41	0.66	0.67
10	2.864×10^3	3.993×10^3	3.988×10^3	0.86	1.19	1.21

8.4.2 Results from the second test

In the second test, bending moments were applied at the DCB tip, $M_1 = 1\,\text{Nm}$ and $M_2 = 0$, with all other DCB tip forces zero, and γ was varied from 1 to 9. Since there are no applied shear forces, G_I^{NR} and G_{II}^{NR} in Eq. (8.49) are both zero. The remaining terms in Eq. (8.49) are G_I^L and G_{II}^L, which can be determined either by using present two-dimensional elasticity partition theory 1, or present two-dimensional elasticity partition theory 2 (as described in §8.2.3). The results from the two-dimensional FEM simulations and these two partition theories are given in Fig. 8.9 and Table 8.12. It is seen that present two-dimensional elasticity partition theory 2 gives very close agreement with the two-dimensional FEM results for all values of M_2. Present two-dimensional elasticity partition theory 1 is not as close but is still good.

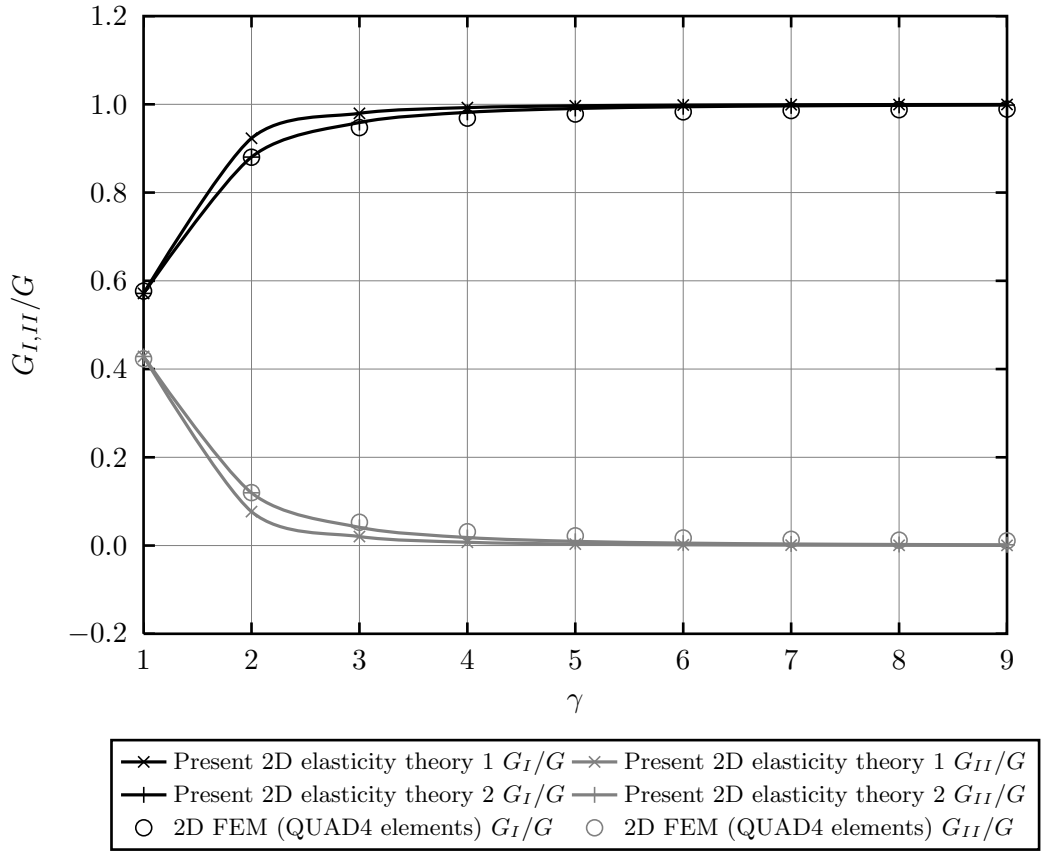

Figure 8.9: Comparisons between the present two-dimensional elasticity partition theories and FEM results with an elastic interface stiffness $k_\sigma = 10^8\,\text{Pa/m}$, varying γ and $M_1 = 1\,\text{Nm}$, $M_2 = 0$, $N_1 = 0$, $N_2 = 0$, $P_1 = 0$, $P_2 = 0$.

Table 8.12: Comparisons between the present two-dimensional elasticity partition theories and FEM results with an elastic interface stiffness $k_\sigma = 10^8\,\text{Pa/m}$, varying γ and $M_1 = 1\,\text{Nm}$, $M_2 = 0$, $N_1 = 0$, $N_2 = 0$, $P_1 = 0$, $P_2 = 0$.

γ	G_I (N/m)			G_I/G (%)		
	Present 2D elasticity theory 1	Present 2D elasticity theory 2	2D FEM (QUAD4 elements)	Present 2D elasticity theory 1	Present 2D elasticity theory 2	2D FEM (QUAD4 elements)
1	3.000×10^6	3.000×10^6	3.029×10^6	57.14	57.14	57.67
2	1.800×10^7	1.717×10^7	1.727×10^7	92.31	88.04	88.01
3	4.629×10^7	4.530×10^7	4.512×10^7	97.96	95.87	94.72
4	9.231×10^7	9.131×10^7	9.083×10^7	99.26	98.18	96.87
5	1.607×10^8	1.597×10^8	1.590×10^8	99.67	99.05	97.80
6	2.561×10^8	2.551×10^8	2.541×10^8	99.83	99.44	98.29
7	3.829×10^8	3.819×10^8	3.807×10^8	99.90	99.65	98.58
8	5.457×10^8	5.447×10^8	5.434×10^8	99.94	99.76	98.78
9	7.490×10^8	7.480×10^8	7.463×10^8	99.96	99.83	98.92

8.4.3 Results from the third test

In the third test, shear forces were applied at the DCB tip, $P_1 = 1\,\text{N}$ and $P_2 = 0$, and γ was varied from 1 to 9. In this loading configuration, there are both bending moments and shear forces at the crack tip. Therefore both G^L and G^{NR} in Eq. (8.49) are non-zero and both need to be considered. The G^L component is directly calculated using either present two-dimensional elasticity partition theory 1 or present two-dimensional elasticity theory 2 (see the discussion in §8.4.1). As described in §8.2.3, to calculate the partition of G^{NR} for any given crack tip shear forces P_{1B} and P_{2B}, two loading cases need to be considered for each value of γ. The two cases chosen here were: (1) $P_{1B} = 1\,\text{N}$, $P_{2B} = 0$ to obtain $G^{NR}_{IP,0}(\gamma)$ and $\tau_{IP,0}(\gamma)$; and (2) $P_{1B} = 1\,\text{N}$, $P_{2B} = -1\,\text{N}$ to obtain $G^{NR}_{IP,-1}(\gamma)$ and $\tau_{IP,-1}(\gamma)$. G^{NR}_I and G^{NR}_{II} are then given by Eqs. (8.69) and (8.74) respectively for any values of P_{1B} and P_{2B}. Of course, here only one loading case is being considered (i.e. $P_1 = 1\,\text{N}$ and $P_2 = 0$), but the purpose of this test is simply to demonstrate that Eqs. (8.62) to (8.75) work for any value of γ. That these equations work for any values of P_{1B} and P_{2B} at a given γ has already been shown by the third loading configuration of the first test (see §8.4.1, Fig. 8.8 and Table 8.11).

The results from the two-dimensional FEM and the two present two-dimensional elasticity partition theories are given in Fig. 8.10 and Table 8.13. Present two-dimensional elasticity partition theory 1 is in good agreement with the two-dimensional FEM results. Present two-dimensional elasticity partition theory 2 is in excellent agreement with the two-dimensional FEM results.

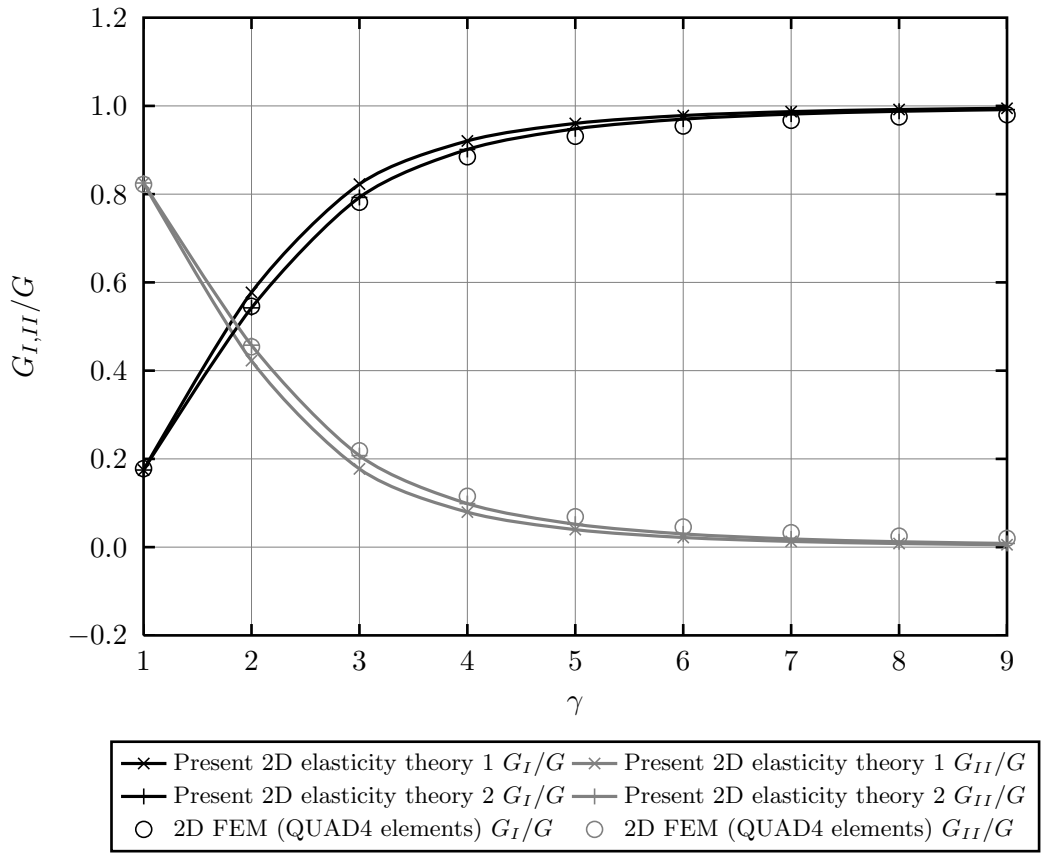

Figure 8.10: Comparisons between the present two-dimensional elasticity partition theories and FEM results with an elastic interface stiffness $k_\sigma = 10^8\,\mathrm{Pa/m}$, varying γ and $P_1 = 1\,\mathrm{N}$, $M_1 = 0$, $M_2 = 0$, $N_1 = 0$, $N_2 = 0$, $P_2 = 0$.

Table 8.13: Comparisons between the present two-dimensional elasticity partition theories and FEM results with an elastic interface stiffness $k_\sigma = 10^8\,\mathrm{Pa/m}$, varying γ and $P_1 = 1\,\mathrm{N}$, $M_1 = 0$, $M_2 = 0$, $N_1 = 0$, $N_2 = 0$, $P_2 = 0$.

γ	G_I (N/m)			G_I/G (%)		
	Present 2D elasticity theory 1	Present 2D elasticity theory 2	2D FEM (QUAD4 elements)	Present 2D elasticity theory 1	Present 2D elasticity theory 2	2D FEM (QUAD4 elements)
1	8.105×10^2	8.105×10^2	8.137×10^2	17.47	17.47	17.78
2	3.873×10^3	3.751×10^3	3.759×10^3	57.74	54.23	54.59
3	9.081×10^3	8.942×10^3	8.912×10^3	82.27	79.25	78.16
4	1.687×10^4	1.673×10^4	1.666×10^4	92.06	90.13	88.47
5	2.774×10^4	2.761×10^4	2.751×10^4	96.03	94.80	93.11
6	4.218×10^4	4.205×10^4	4.192×10^4	97.82	97.01	95.44
7	6.068×10^4	6.055×10^4	6.040×10^4	98.70	98.14	96.73
8	8.372×10^4	8.359×10^4	8.343×10^4	99.18	98.78	97.50
9	1.118×10^5	1.116×10^5	1.114×10^5	99.46	99.16	98.00

8.5 Conclusion

Within the context of Euler beam theory, when the interface of an isotropic homogeneous DCB is considered to be non-rigid and elastic, the two sets of mode I $\left\{\varphi_{\theta_i}\right\}$ and $\left\{\varphi_{\theta_i'}\right\}$ modes coincide on the first set of mode I $\left\{\varphi_{\theta_i}\right\}$ modes. Also, the two sets of mode II $\left\{\varphi_{\beta_i}\right\}$ and $\left\{\varphi_{\beta_i'}\right\}$ modes coincide on the first set of mode II $\left\{\varphi_{\beta_i}\right\}$ modes. There is therefore no stealthy interaction between the mode I $\left\{\varphi_{\theta_i}\right\}$ modes the mode II $\left\{\varphi_{\beta_i}\right\}$ modes. The total ERR G_E consists of two parts G_E^L and G_E^{NR}, i.e. $G_E = G_E^L + G_E^{NR}$. G_E^L comes from the crack tip bending moments and axial forces, i.e. M_{1B}, M_{2B}, N_{1B} and N_{2B}, and is readily partitioned into G_{IE}^L and G_{IIE}^L, i.e. $G_E^L = G_{IE}^L + G_{IIE}^L$, which correspond to the respective mode I and mode II ERRs in the present Timoshenko beam theory for rigid interfaces. Thus, the partition of G_E^L does not depend on interface cohesive laws. G_E^{NR} relates to the crack tip shear forces P_{1B} and P_{2B}, and is partitioned into G_{IE}^{NR} and G_{IIE}^{NR}, i.e. $G_E^{NR} = G_{IE}^{NR} + G_{IIE}^{NR}$. A completely analytical formula for G_{IIE}^{NR} has been derived. It is noted that the partition of G_E^{NR} depends on the interface cohesive law.

Within the context of Timoshenko beam theory the mode II ERR G_{IIT} is the same as that from the present Euler beam partition theory with non-rigid elastic interfaces, i.e. $G_{IIT} = G_{IIE}$. The mode I ERR G_{IT} however is different due to the through-thickness effect. A numerical formula for G_{IT} has been derived, which becomes completely analytical for hard interfaces.

Within the context two-dimensional elasticity, two approximate partition theories have been developed. The total ERR G again consists of two parts G^L and G^{NR}, i.e. $G = G^L + G^{NR}$. G^L comes from the crack tip bending moments and axial forces, M_{1B}, M_{2B}, N_{1B} and N_{2B}, and in present two-dimensional elasticity partition theory 1, it can be readily partitioned into G_I^L and G_{II}^L, i.e. $G^L = G_I^L + G_{II}^L$, using the second set of pure modes, $\left\{\varphi_{\theta_i'}\right\}$ and $\left\{\varphi_{\beta_i'}\right\}$, from the present Euler beam partition theory with rigid interfaces. In present two-dimensional elasticity partition theory 2, the partition is made much more accurate by using improved θ_1' and β_1' values based on a double bi-section approximation, which are called θ_{1A}' and β_{1A}' respectively. It is worth noting that $G^L = G_E^L$ and that the partition of G^L does not depend on interface cohesive laws. G^{NR} relates to the crack tip shear forces P_{1B} and P_{2B}, and is partitioned into G_I^{NR} and G_{II}^{NR}, i.e. $G^{NR} = G_I^{NR} + G_{II}^{NR}$. An analytical formula for G_{II}^{NR} has been derived based on two numerical parameters. Also, an analytical formula for G_I^{NR} has been derived based on two numerical parameters. It is noted that partition of G^{NR} depends on the interface cohesive law.

The theories in this chapter provide a valuable method for the study of fracture behaviour on adhesive interfaces in isotropic homogeneous DCBs. There is now scope for extension to laminated composite beams with non-rigid elastic interfaces. This work in this chapter has been published in Wang et al. (2012).

Chapter 9

Conclusion

Contents

9.1 Conclusion

Due to the numerous complexities, the double cantilever beam (DCB) fracture problem has caused considerable confusion over many years. In this thesis, a new approach, based on orthogonal mixed modes, has been developed and validated by extensive numerical simulations and partially validated using published experimental results. The approach reveals the hidden mechanics of the problem. It is not surprising that there has been so much confusion on this subject. There is complex behaviour in both the analytical and numerical aspects, which includes globally and locally pure modes, stealthy interaction and crack tip running contact.

Two analytical beam partition theories have been derived. These are: (1) the present Euler beam partition theory, which is based on Euler beam theory; and (2) the present Timoshenko beam partition theory, which is based on Timoshenko beam theory. Two approximate partition rules have also been suggested for the partitions from two-dimensional elasticity. These are based on the average of the present Euler and Timoshenko beam partition theories. The theories and rules have been developed for both isotropic homogeneous beams and laminated composite beams.

Two sets of pure modes have been found for each theory. The first set consists of pure mode I $\left\{\varphi_{\theta_i}\right\}$ modes that are characterised by zero crack tip relative shearing displacement and pure mode II $\left\{\varphi_{\beta_i}\right\}$ modes that are characterised by zero crack tip normal force. All the pure mode I modes of the first set are orthogonal through the energy release rate (ERR) to all the pure mode II modes of the first set. The second set consists of pure mode I $\left\{\varphi_{\theta'_i}\right\}$ modes that are characterised by zero crack tip shearing force and pure mode II $\left\{\varphi_{\beta'_i}\right\}$ modes that are characterised by zero crack tip opening displacement. All the pure mode I modes of the second set are orthogonal through the ERR to all the pure mode II modes of the second set.

Both the present Euler and Timoshenko beam partition theories have the same first set of pure modes $\left\{\varphi_{\theta_i}\right\}$ and $\left\{\varphi_{\beta_i}\right\}$. In the present Euler beam partition theory, there is a second set of pure modes $\left\{\varphi_{\theta'_i}\right\}$ and $\left\{\varphi_{\beta'_i}\right\}$, which is different to the first set. In the

present Timoshenko beam partition theory, the second set of pure modes coincides with the first set. Therefore it is the first set of pure modes which forms a complete basis for mixed-mode partitioning.

For mixed modes, unobvious stealthy interactions exist between the mode I $\left\{\varphi_{\theta_i}\right\}$ modes and the mode II $\left\{\varphi_{\beta_i}\right\}$ modes in the present Euler beam partition theory. These interactions disappear in the present Timoshenko beam partition theory, which is what leads to the disappearance of the second set of pure modes.

The fracture mode partition space has also been thoroughly investigated. This reveals how a fracture behaves as the crack tip loading varies. In doing this, the contact behaviour has also been found. For DCBs, two types of contact can exist: crack tip running contact, which results in a region of pure mode II ERR; and point contact at the DCB tip, which can result in either in mixed modes or pure mode II ERR. The analytical framework for determining the contact behaviour of a specimen has been laid-down.

Each partition theory can give two ERR partitions: a local one and a global one. The difference between the two is important because it is not clear which is more appropriate for determining fracture propagation between interfaces and under what circumstances. Simply put, local pureness is defined with respect to the crack tip whilst global pureness is defined with respect to the entire region that is mechanically affected by the presence of the crack.

It has been shown that the global form of all the partition theories is the same as the present Euler beam partition theory. The present Euler beam partition theory therefore generally represents the global partition. Of course, it also represents the local partition for Euler beams.

All the analytical theories and rules have been validated against results from finite element method (FEM) simulations. The present Euler and Timoshenko beam partition theories agree very well with the corresponding beam FEM results. Averaged partition rule 1 halves the interactions between the mode I $\left\{\varphi_{\theta_i}\right\}$ modes and the mode II $\left\{\varphi_{\beta_i}\right\}$ modes in the present Euler beam partition theory. Averaged partition rule 2 removes the small regions where partitions of ERR can become less than zero or greater than one (but where the total ERR is still non-negative) by using the points of minimum G_I/G and G_{II}/G from averaged partition rule 1 as pure modes. Both approximations agree very well with results from FEM simulations with four node quadrilateral (QUAD4) elements, even when the difference between the curves from the Euler and Timoshenko beam partition theories is substantial and the accuracy of the approximation might have become strained. Generally, averaged partition rule 2 is closer than averaged partition rule 1. There is also close agreement between Suo and Hutchinson's (1990) partition theory and the averaged partition rules.

The fundamental theories were derived for isotropic and laminated composite DCBs. The partitions were found to be entirely dependent on crack tip quantities only. Therefore, it is simple to apply them to more complex engineering structures. The theories were able

to give the correct partitions for clamped-clamped and simply supported isotropic and laminated composite straight beam structures. Pure mode conditions for these structures were also derived. In these types of structures, the internal forces at the crack tips are generally complex functions of remotely applied loads. It is not generally possible to obtain pure 'crack tip modes', i.e. modes which relate crack tip quantities, because these quantities cannot be set independently of each other. Instead some combinations of these modes can give pure mode I or II fractures. 'F modes' have been derived. The F modes give the ratios required between remotely applied forces, for example P_1 and P_2, in order to give pure fracture modes.

The present Euler and Timoshenko beam partition theories have also been re-derived for axisymmetric plates, giving the present Kirchhoff–Love and Mindlin–Reissner plate partition theories respectively. The fracture behaviour is identical to that for beams, although the mathematical expressions are obviously different. The present Kirchhoff–Love and Mindlin–Reissner plate partition theories agree very well with the corresponding plate FEM results. The averaged partition rule 1 also generally agrees very well with two-dimensional axisymmetric FEM results.

In addition to numerical validation, the performance of the present theories has been assessed using experimental results from the literature for a range of tests and compared against some existing partition theories: the Williams theory (Williams 1988) and the Suo–Hutchinson theory (Suo and Hutchinson 1990, Suo 1990, Hutchinson and Suo 1992). The present Euler beam partition theory offers the best and most simple explanation for all the experimental observations. No recourse to fracture surface roughness or new failure criteria is required. It is in excellent agreement with the linear failure locus and is significantly closer than other partition theories. There are two possible reasons for this:

1. The aspect ratios of the specimens, which have been tested, are high enough for their behaviour to be essentially that of Euler beams. The most suitable partition theory would therefore be the present Euler beam partition theory. If this is correct, then for some specimens the present Timoshenko beam partition theory or averaged partition rule 1 might provide the best result. This seems less likely though because for the thicker specimens tested, where the through-thickness shear effect is greater, there is no tendency towards the present Timoshenko beam partition.

2. The global partition from the present partition theories, which has been shown to be equal to the present Euler beam partition, is the one that determines failure.

The possibility that the present Euler beam partition theory, despite its simplicity, is the correct one to be used for predicting fracture propagation is remarkable. Further experimental investigations are definitely required.

Finally, a study into fractures in layered isotropic homogeneous materials with non-rigid elastic interfaces has also been carried out. Within the context of Euler beam theory, when the interface of an isotropic homogeneous DCB is considered to be non-rigid and elastic,

the two sets of mode I $\left\{\varphi_{\theta_i}\right\}$ and $\left\{\varphi_{\theta'_i}\right\}$ modes coincide on the first set of mode I $\left\{\varphi_{\theta_i}\right\}$ modes. Also, the two sets of mode II $\left\{\varphi_{\beta_i}\right\}$ and $\left\{\varphi_{\beta'_i}\right\}$ modes coincide on the first set of mode II $\left\{\varphi_{\beta_i}\right\}$ modes. There is therefore no stealthy interaction between the mode I $\left\{\varphi_{\theta_i}\right\}$ modes the mode II $\left\{\varphi_{\beta_i}\right\}$ modes. The ERR is readily partitioned into mode I and mode II. Within the context of Timoshenko beam theory the mode II ERR is the same as that from the present Euler beam partition theory with non-rigid elastic interfaces. The mode I ERR however is different due to the through-thickness effect. A numerical formula for the mode I ERR has been derived, which becomes completely analytical for hard interfaces. Results from FEM simulations using beam elements validate the non-rigid elastic interface beam partition theories. The numerical results however converge very slowly. The convergence becomes slower as the interface spring stiffness is made smaller. This is expected since point interface springs are more suited to capture the stress singularity at the crack tip that is observed for a rigid interface. Within the context two-dimensional elasticity, two approximate partition theories have been developed. The total ERR G consists of two parts G^L and G^{NR}, i.e. $G = G^L + G^{NR}$. G^L comes from the crack tip bending moments and axial forces, and in present two-dimensional elasticity partition theory 1, it can be readily partitioned into G^L_I and G^L_{II}, i.e. $G^L = G^L_I + G^L_{II}$, using the second set of pure modes, $\left\{\varphi_{\theta'_i}\right\}$ and $\left\{\varphi_{\beta'_i}\right\}$, from the present Euler beam partition theory with rigid interfaces. In present two-dimensional elasticity partition theory 2, the partition is made much more accurate by using improved θ'_1 and β'_1 values based on a double bi-section approximation, which are called θ'_{1A} and β'_{1A} respectively. G^{NR} relates to the crack tip shear forces, and is partitioned into G^{NR}_I and G^{NR}_{II}, i.e. $G^{NR} = G^{NR}_I + G^{NR}_{II}$. An analytical formula for G^{NR}_{II} has been derived based on two numerical parameters. Also, an analytical formula for G^{NR}_I has been derived based on two numerical parameters.

All of the present partition theories for rigid interfaces are completely analytical. All of the theories, both for rigid and non-rigid interfaces, have been derived using a completely new approach and provide an excellent tool for studying delamination in layered isotropic homogeneous and fibre-reinforced laminated composite beams and layered isotropic homogeneous plates. The ease with which the present theories can be extended to more complex structures illustrates the general applicability and usefulness of the present theories. They are the general ones for the mode partitioning of one-dimensional fractures. They are readily applicable to a wide-range of engineering structures and will be a valuable analytical tool for many applications, for example for analytical researchers to develop fracture propagation criteria, for design engineers to design high integrity structures and for numerical analysts to benchmark their simulations, etc.

Various parts of this thesis have been reported on several occasions. The full journal papers are Wang and Harvey (2012*c*), Wang and Harvey (2012*a*), Harvey and Wang (2012*c*), Wang et al. (2012) and Harvey and Wang (2012*a*). Further publications from this work are in preparation in Harvey et al. (2012) and Harvey and Wang (2012*b*). Some early journal papers are given by Harvey and Wang (2012*d*) and Wang and Harvey (2011*a*).

Finally, the conference papers are Wang and Harvey (2012*b*), Wang and Harvey (2011*b*), Wang and Harvey (2010), Harvey and Wang (in press), Wang and Harvey (2009).

9.2 Future work

As a result of this research work, important progress has been made in understanding the mechanics of this important problem. However, there still remain gaps in the knowledge. There is now great scope for completely 'bridging the gap' in the understanding by means of comprehensive experimental investigations and theoretical modelling. Areas for future research are now suggested:

- Experimental investigations.

  This should begin with validation of the seven fundamental pure modes (the four pure mode I modes and three pure mode II modes), which comprise any mixed mode. It should then proceed to validate the present partition theories. The work in Chapter 7 is a useful preliminary study and also indicates the kind of standard experimental methods that could be used in the validation. A particularly interesting experimental study would be to test specimens with varying degrees of through-thickness shear effect in order to test whether the present Euler beam partition theory is always the most suitable for mixed-mode partitioning.

  In addition to standard test procedures, there are ideas for a hybrid approach, which uses a digital image correlation (DIC) system in conjunction with a thermo-elastic stress analysis (TSA) system to take measurements in the region of the crack tip. TSA uses an infra-red camera to measure the small temperature change produced when a component is cyclically loaded. This temperature change is linearly related to the first stress invariant. The stress intensity factors are obtained by substituting the Williams equation into the thermo-elastic equation to relate the stress intensity factors to the thermo-elastic signal. Using this technique or other similar techniques, it is possible to obtain accurate measurements of the stress intensity factors. DIC could be used to obtain detailed non-linear deformation information. The combination of TSA and DIC would produce a rich data set that might allow for further breakthroughs regarding local versus global mechanical effects in the region of the crack tip.

  Theoretical studies should be conducted alongside any experimental investigations for maximum benefit. As discussed in the following items, future theoretical work should include extension to circularly curved beams and shells. Tests procedures for these types of specimen would be similar to those for straight beams. Other theoretical work would include extension of the theories to account for geometrical non-linearity and also non-rigid interfaces.

- Analytical modelling of delamination in circularly curved beams and shells.

Fibre-reinforced laminated composite shells are important structural components. The present linear theories should be extended for one-dimensional fracture in curved beams, cylindrical and spherical shells made of laminated composite materials. This would present great analytical challenges because the extremely complex Legendre equations for spherical shells would have to be solved analytically. Application to laminated composite materials would make finding simple/elegant solutions even harder. In addition to the analytical work, numerical simulations would be carried out simultaneously.

- Analytical modelling of rigid interfaces and geometrical non-linearity.

  The rigid interface model is a good approximation for brittle bonding between laminae in laminated composite materials. The present linear partition theories are based on this assumption and geometrical linearity. However, since delamination often occurs in a post-buckling process, geometrical non-linearity has to be considered.

- Analytical modelling of non-rigid interfaces.

  Adhesive bonding is a common and important joining technique in manufacturing structures. The present theories for non-rigid interfaces in isotropic homogeneous beams should be extended to non-rigid interfaces in laminated composite beams. To begin with, the assumption of geometrical linearity could be kept. Later theoretical work could combine non-rigid interfaces with geometrical non-linearity.

Appendices

Appendix A

Negative partitions of energy release rate

A.1 Introduction

One of the present partition theories is the present Euler beam partition theory. It gives rise to some interesting phenomena. One such phenomenon is the potential for the partitions of ERR, G_I/G and G_{II}/G to be greater than one or less than zero. This phenomenon is now simply referred to as 'negative partitions of ERR'. Negative partitions of ERR occur due to 'stealthy interaction', which is the flow of energy between pure modes in a mixed-mode fracture with the total energy being conserved. Another interesting phenomenon is that the Euler beam partition theory corresponds to the 'global partition' from the Euler and Timoshenko beam theories and two-dimensional elasticity theory. By 'global partition' it is meant that crack closure integral is calculated by including the whole region, which is mechanically affected by the presence of the crack.

The potential for negative partitions of ERR may seem unintuitive and some objections have been raised. In this appendix, the major topics concerning negative partitions of ERR are discussed. In §A.2, the theoretical origin of negative partitions of ERR is explained; in §A.3, the physical interpretation is considered; in §A.4, the local/global properties of the present Euler beam partition theory are described; in §A.5, some results which show the predictive power of the present Euler beam partition theory are presented.

A.2 Cause of negative energy release rate partitions

In this work, it has been shown that there are two sets of orthogonal pure modes. The first set corresponds to zero relative shearing displacement just behind the crack tip (mode I) and zero crack tip opening force ahead of the crack tip (mode II). The second set corresponds to zero relative opening displacement just behind the crack tip (mode II) and zero crack tip shearing force (mode I).

As long as these two sets of modes are distinct and do not coincide then negative ERR partitions G_I and G_{II} must exist due to 'stealthy interaction'. Consider the partition of a mixed fracture mode in terms of the first set of orthogonal pure modes. According to the pure-mode conditions above, the mode I component contributes no relative shearing displacement to the overall shearing displacement, but does contribute relative opening displacement, crack tip opening force and crack tip shearing force. The mode II component

	Crack tip force	Relative displacement
Mode I (first set)	Both **opening** and **shearing**	Just **opening** (zero shearing)
Mode II (first set)	Just **shearing** (zero opening)	Both **opening** and **shearing**

Figure A.1: Interaction in a mixed fracture mode.

contributes zero crack tip opening force, but does contribute crack tip shearing force, relative shearing displacement and relative opening displacement. Therefore in a mixed fracture mode, the relative displacements from the mode II component interact with the crack tip opening forces from the mode I component. The interaction is shown in Fig. A.1. This is what is called 'stealthy interaction'. It is so-called because it is 'hidden', resulting in a flow of energy between the modal components of ERR whilst not changing the total.

As long as the two sets of orthogonal pure modes are distinct then there is a range of loading conditions between the two sets of pure modes in which the partitions of ERR, G_I/G and G_{II}/G become greater than one or less than zero. Consider a DCB with a unit bending moment M_1 applied to the tip of the upper arm and with a varying bending moment M_2 applied to the tip of the lower arm. As the ratio M_2/M_1 changes, the crack passes through each of the four pure mode conditions, as shown in Fig. A.2. The ratios $M_2/M_1 = \theta$ and $M_2/M_1 = \theta'$ are the pure mode I modes of the first and second set respectively. The ratios $M_2/M_1 = \beta$ and $M_2/M_1 = \beta'$ are the pure mode II modes of the first and second set respectively. Between the first and second set, there is a region of negative partitions of ERR. It is seen that whenever the first and second sets are distinct and do not coincide, regions with negative partitions of ERR must exist. The notations D_{sh}, D_{op}, F_{sB} and F_{nB} denote the relative shearing and opening displacement and the crack tip shearing and opening forces respectively.

If the orthogonal pure mode conditions are applied within the context of Timoshenko beam theory or two-dimensional elasticity with a rigid interface, then it is found that the two sets of pure modes exactly coincide, there is therefore no stealthy interaction, and negative partitions of ERR do not occur. However, within the context of Euler beam theory, the two sets of pure modes are distinct and do not coincide. Therefore, as described, negative partitions of ERR do occur.

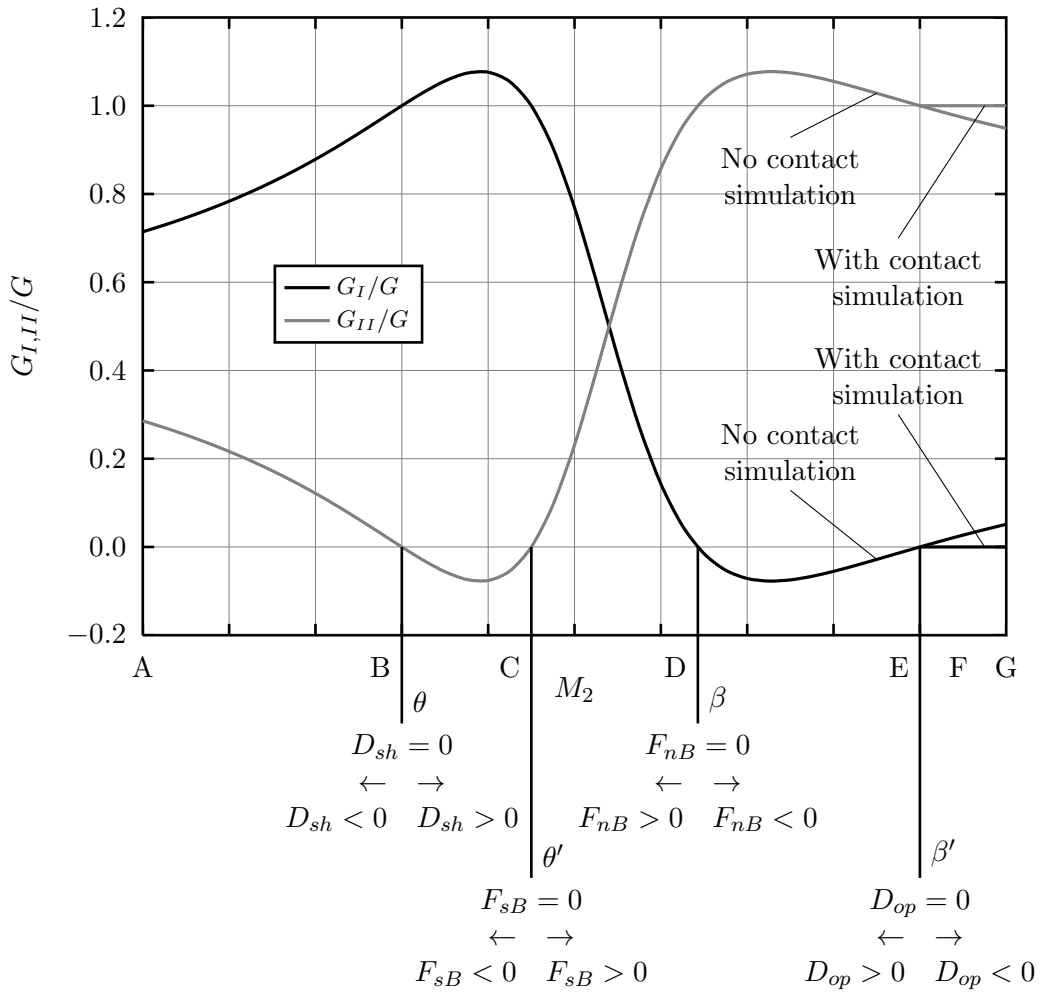

Figure A.2: Two sets of orthogonal pure modes and negative partitions of ERR.

A.3 Physical interpretation of negative energy release rate partitions

The existence of negative partitions of ERR may seem unintuitive. Common objections include the following:

1. Energy is required to propagate a crack by creating new surfaces. If ERR is negative, then this implies that the creation of new surfaces *produces* energy, which is non-physical.

2. For cracks in isotropic homogenous plates, two-dimensional elasticity theory gives the relationships $G_I = K_I^2/\overline{E}$ and $G_{II} = K_{II}^2/\overline{E}$, where K_I, K_{II} and $\overline{E}$ are the mode I and II stress intensity factors and the effective Young's modulus respectively. Clearly therefore G_I and G_{II} are always positive.

3. Two-dimensional elasticity theory must be considered more accurate than any beam theory. Since it predicts only positive partitions of ERR, any theory that predicts

negative partitions of ERR must simply be incapable of modelling the crack with sufficient accuracy.

Clearly, negative partitions of ERR do not imply that energy is produced as a crack propagates—the total ERR has been proven to be non-negative definite; it can be zero but never negative. One negative ERR partition is therefore compensated for by higher contributions of ERR from the other mode. Whether or not negative partitions of ERR actually are physical (which will be discussed shortly), there is certainly a physical meaning that can be ascribed to them. Here are some interpretations that are consistent with each other but which offer slightly different perspectives:

1. Negative ERR partitions simply indicate that the corresponding crack tip forces do negative work when closing the crack. For instance, consider the case of a mixed fracture mode. As long as the two sets of orthogonal pure modes do not coincide, then situations can be envisaged whereby one of the net crack tip forces is in the opposite sense to the corresponding net relative displacement. Therefore that crack tip force will do work over a distance in the opposite direction to that which it is acting in, that is, it does negative work.

2. As an example, consider a pure mode I fracture with zero relative shearing displacement but with a positive crack tip shearing force (this is a pure mode I mode in the first set). Also consider a pure mode II fracture subject to a small negative crack tip shearing force, which produces negative relative shearing displacement (this is a pure mode II mode in the first set). When the two pure fracture modes are superimposed, the net crack tip shear force is positive (since the negative crack tip shear force contribution from the mode II fracture is relatively small, the positive contribution of crack tip shear force from the mode I fracture prevails) and the total relative shearing displacement is negative (since only the mode II fracture contributes to it). Therefore, in this scenario, the total positive crack tip shearing force does negative work closing the crack, producing a negative mode II partition of ERR.

3. Another more qualitative perspective is like this: mode I fractures propagate by opening action; mode II fractures propagate by shearing action. For a crack propagating in a mixed fracture mode with negative partitions of ERR, one mode might act to heal the crack, but with the other mode acting to propagate the crack and more than compensating for the healing effect of the other mode. Therefore, the healing effect of one of the modes is hidden. This is why the interaction (which is what causes the negative partitions of ERR) described in §A.2, is described as ‘stealthy’.

Now the question of whether negative partitions of ERR are actually physical is briefly addressed. Certainly, for cracks in isotropic homogeneous plates, a partition theory based on two-dimensional elasticity theory, square-root singular fields and stress intensity factors (Suo and Hutchinson 1990) must be correct, in which case negative partitions of ERR do

not exist. However, for all other scenarios, the situation is far from clear. Examples include cracks on an interface where the crack is constrained to propagate along the plane of weakness; delaminations in laminated composites; long and thin DCBs; and cases where the square-root singular field is not dominant. In particular, application of two-dimensional elasticity theory to cracks on a bi-material interface have led to considerable difficulties, including oscillatory stress and displacement fields (i.e. not square-root singular) and interpenetration of crack surfaces. These problems have never been satisfactorily overcome. Therefore, a partition theory that allows negative partitions of ERR should not be ruled out on the basis of two-dimensional elasticity solutions, which themselves are in question, especially since a physical interpretation of negative partitions of ERR does not preclude them. The question is, does the structure behave like an Euler beam. If it does, then the present Euler beam partition theory must be correct and then there will therefore sometimes be negative partitions of ERR.

Finally, to further address the third objection above, an additional interesting phenomenon, which adds further credence to the existence of negative partitions of ERR, is described in the following section.

A.4 Global energy release rate partition

It is important to distinguish between local partitions and global partitions. It is not known which is more appropriate for determining fracture propagation between interfaces and under what circumstances.

Simply put, local pureness is defined with respect to the crack tip whilst global pureness is defined with respect to the region mechanically affected by the presence of a crack. Mathematically, the difference is in the integration limits of the crack closure integral: the global partition is calculated by including the whole crack influence region in the integration limits; the local partitions only considers the near-crack tip region. Note that the total ERR is not affected by the limits of the crack closure integral (Rice 1968), however the partition of ERR is affected.

In this work, it has been shown both analytically and numerically that the present Euler beam partition theory has two distinct sets of pure modes, which are both locally and globally pure. The local and global partitions are therefore always the same when using this partition theory. For the present Timoshenko beam partition theory, there are two sets of locally pure modes, which exactly coincide on the first set from the present Euler beam partition theory. There are also two sets of globally pure modes and they are the same as the pure modes from the present Euler beam partition theory. Therefore, when using the present Timoshenko beam partition theory, the local partition exhibits no stealthy interaction and is different to the present Euler beam partition theory. However, the global partition is the same as the present Euler beam partition theory.

The same behaviour is observed for partitions based on two-dimensional elasticity, that is, the local partition has two sets of pure modes, which exactly coincide, there is no stealthy interaction and the partition is different to the present Euler beam partition theory. However, the globally pure modes and the global partition are identical to the present Euler beam partition theory.

Qualitatively, when the whole crack influence region is considered in the evaluation of ERR partitions, the through-thickness shear effect at the crack tip due to the normal stress ahead of the crack tip (arising from the mode I mode of the first set) disappears. Therefore, when the shear modulus is finite with any value, the global ERR partitions remain the same as the local ones with an infinitely large shear modulus, that is, they agree with those from the present Euler beam partition theory.

This reveals an important phenomenon: the global partition is always given by the same partition theory, which is the present Euler beam partition theory. As described in §A.2, in this partition theory, there are two distinct sets of pure modes. This leads to stealthy interaction and negative partitions of ERR, even within the context of two-dimensional elasticity. This puts the present Euler beam partition theory on a firmer theoretical foundation. The third objection in §A.3 claims that two-dimensional elasticity theory must be considered more accurate than Euler beam theory. In response, this may be true, but if fracture propagation is dependent on global partitions, then the two theories are the same anyway.

A.5 Predictive power of the present Euler beam partition theory

In Chapter 7, five different partition theories were assessed using experimental results from the literature. These theories were the present Euler beam partition theory, the present Timoshenko beam partition theory, averaged partition rule 1 (which is an approximation for the two-dimensional elasticity partition), Williams's (1988) partition theory (based on Euler beams) and Suo and Hutchinson's (1990) partition theory (based on two-dimensional elasticity).

The results of the FRMM test (Charalambides et al. 1992), which are reproduced in Chapter 7, are particularly revealing. In this test, a bending moment is applied to the upper arm of a DCB. The critical ERR is measured and partitioned into G_I and G_{II} using a partition theory. This provides a failure locus. The DCBs were made from carbon/epoxy composite specimens. The linear failure locus ($G_I/G_{Ic} + G_{II}/G_{IIc} = 1$) is at least a very good approximation for this material (as discussed by Charalambides et al. (1992) and in §7.4.1). To assess the performance of each partition theory, the failure locus predicted by each is compared against the linear failure locus.

The present Euler beam partition theory performed much better than all the other partition theories when compared with the linear failure locus. After the present Euler

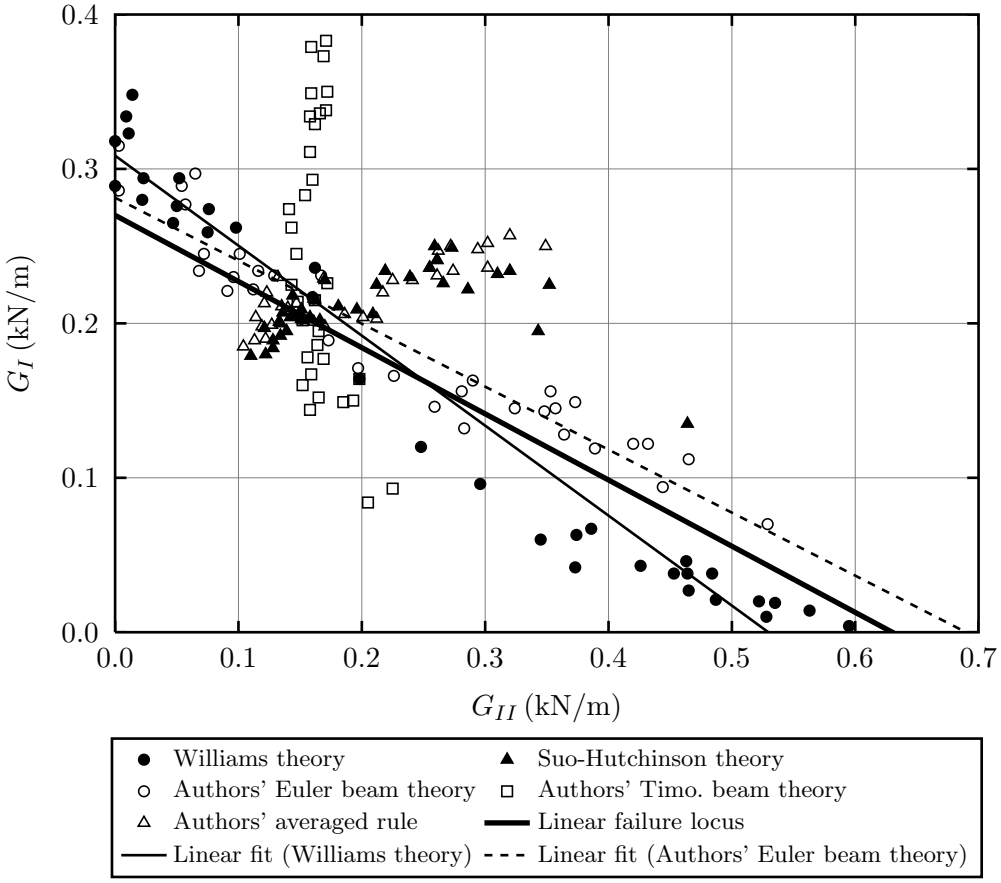

Figure A.3: FRMM test partitions from various partition theories and the linear failure locus for carbon/epoxy specimens.

beam partition theory, Williams's (1988) partition theory is the closest, but it predicts a curved failure locus. This curve can be completely explained using the present Euler beam partition theory. Suo and Hutchinson's (1990) two-dimensional elasticity partition theory forms a curve approximately normal to the linear failure locus, as does averaged partition rule 1, which is an approximation for two-dimensional elasticity partitions. These partition theories are not close to any kind failure locus that the author is aware of. Finally, the present Timoshenko beam partition theory forms an approximately vertical line, which is also not close to any kind of failure locus known to the author. An example plot from Chapter 7 is shown in Fig. A.3, although interested readers should refer to the full chapter.

As concluded in Chapter 7, there are two possible explanations for why the present Euler beam partition theory performs so well:

1. The aspect ratios of the specimens that were tested were high enough for their behaviour to be essentially that of Euler beams. The most suitable partition would therefore be the present Euler beam partition theory. If this is correct, then for some specimens, the present Timoshenko beam theory or averaged partition rule might

provide the best results. However, this seems less likely because in Chapter 7, there was no tendency at all towards the present Timoshenko beam partition theory for lower aspect ratios when the through-thickness shear effect would be greater.

2. The global partition, which is equal to the present Euler beam partition theory, is the one that determines failure.

Regardless of the real reason, the fact that the present Euler beam partition theory performs so well in these assessments indicates that the existence of negative partitions of ERR is at least a realistic possibility.

A.6 Conclusion

Negative partitions of ERR are produced by any partition theory that gives two sets of pure modes which do not coincide and which are distinct, for instance, the present Euler beam partition theory. Stealthy interaction is the cause—when the zero relative displacement conditions do not occur simultaneously with the zero crack tip force conditions then, in terms of the first set of orthogonal pure modes, the crack tip shearing and opening forces from the mode I component interact with the relative shearing and opening displacements from the mode II component, resulting in a flow of energy from one mode to the other (but not affecting the total ERR). If the structure behaves like an Euler beam, then the present Euler beam partition theory must be correct and then there will sometimes be negative partitions of ERR. Physically, negative ERR partitions simply indicate that the corresponding crack tip forces do negative work when closing the crack.

When ERR partition is calculated using the whole region mechanically affected by the presence of a crack, then the global partition is obtained. The global partition is always given by the Euler beam partition theory, regardless of whether Euler or Timoshenko beam theory or two-dimensional elasticity theory is used. Therefore, if fracture propagation is dependent on global partitions, then the Euler beam partition theory must be correct and then there will sometimes be negative partitions of ERR.

Finally, the present Euler beam partition theory, which predicts negative partitions of ERR over small ranges of loading configurations, offers the best and most simple explanation for all the experimental observations in Chapter 7. It gives the closest agreement of all the partition theories tested to the linear failure locus, which is the expected failure locus for the material in question. In line with the above conclusions, this is expected to either be due to the specimens behaving like Euler beams, or due to fracture propagation being dependent on global partitions. The excellent performance of the present Euler beam partition theory in these assessments indicates that the existence of negative partitions of ERR is at least a realistic possibility.

Appendix B

Convergence studies

B.1 Interface spring stiffness for a rigid interface

The isotropic homogeneous DCB, which is described in §4.3, is modelled with a rigid interface using the FEM. The units of these FEM simulations are kN and mm. The properties of the DCB in §4.3 are as follows: The Young's modulus is $E = 1\,\text{GPa}$, and the Poisson's ratio is $\nu = 0.3$. The intact length is $L = 100\,\text{mm}$ and the crack length is $a = 10\,\text{mm}$. The width is $b = 1\,\text{mm}$. The thickness is $h = h_1 + h_2 = 3\,\text{mm}$ with $h_1 = 1\,\text{mm}$. Therefore, the thickness ratio is $\gamma = 2$.

Imaginary normal and shear point interface springs with very high stiffness k_s are used to model perfectly bonded layers. Full details on the interface modelling are given in §3.3. This section shows how the value of $k_s = 10^6\,\text{kN/mm}$ was selected for the FEM simulations in Chapter 4

Since the theory in Chapter 4 assumes that plies are perfectly bonded, the interface spring stiffness should be infinite but there are obvious difficulties with doing this on a computer (Press, Teukolsky, Vetterling and Flannery 2007):

- Memory allocation: On most platforms, the 'double' data type corresponds to a maximum floating point value of 1.79769×10^{308}. Whilst being far from infinite, this number is many times larger than any other number likely to be encountered in these kinds of simulations. A stiffness of this magnitude is more than large enough. However there are other problems concerning large numbers.

- Rounding error: This is the numerical error introduced after a number of calculations in which the computer is constantly rounding the number to some significant figure. When all numbers are of a similar magnitude, the total round-off error is small. When very large numbers are introduced and manipulated alongside much smaller numbers, round-off errors become large in comparison to these smaller numbers and then no useful information can be extracted.

A value for k_s needs to be found that is large enough to approach a rigid interface, but which is not so large as to introduce significant numerical errors.

Tables B.1 and B.2 present the results from studies on the effect of the interface spring stiffness k_s on FEM simulations using the same DCB as in §4.3. These simulations used Timoshenko beam elements with the large shear modulus of $\mu = 10^4\,\text{GPa}$ in order to simulate Euler beams. This choice of finite element is convenient for this study because,

Table B.1: Effect of k_s on G_I results from FEM simulations of an isotropic homogeneous DCB modelled with 11×2 Euler beam elements with varying M_2 and $M_1 = 1\,\text{Nm}$, $N_1 = 0$, $N_2 = 0$, $P_1 = 0$, $P_2 = 0$, $\mu = 10^4\,\text{GPa}$, $\gamma = 2$.

M_2 (Nm)	G_I (N/m)			
	$k_s = 1 \times 10^0\,\text{kN/mm}$	$k_s = 1 \times 10^2\,\text{kN/mm}$	$k_s = 1 \times 10^4\,\text{kN/mm}$	$k_s = 1 \times 10^6\,\text{kN/mm}$
−10	44.93	45.00	45.00	45.00
−8	33.70	33.78	33.78	33.78
−6	24.03	24.11	24.11	24.11
−4	15.93	16.00	16.00	16.00
−2	9.40	9.44	9.44	9.44
0	4.43	4.44	4.44	4.44
2	1.02	1.00	1.00	1.00
4	−0.81	−0.89	−0.89	−0.89
6	−1.09	−1.22	−1.22	−1.22
8	0.21	0.00	0.00	0.00
10	3.07	2.78	2.78	2.78

Table B.2: Effect of k_s on G_{II} results from FEM simulations of an isotropic homogeneous DCB modelled with 11×2 Euler beam elements with varying M_2 and $M_1 = 1\,\text{Nm}$, $N_1 = 0$, $N_2 = 0$, $P_1 = 0$, $P_2 = 0$, $\mu = 10^4\,\text{GPa}$, $\gamma = 2$.

M_2 (Nm)	G_{II} (N/m)			
	$k_s = 1 \times 10^0\,\text{kN/mm}$	$k_s = 1 \times 10^2\,\text{kN/mm}$	$k_s = 1 \times 10^4\,\text{kN/mm}$	$k_s = 1 \times 10^6\,\text{kN/mm}$
−10	18.12	18.00	18.00	18.00
−8	9.45	9.33	9.33	9.33
−6	3.43	3.33	3.33	3.33
−4	0.08	0.00	0.00	0.00
−2	−0.61	−0.67	−0.67	−0.67
0	1.35	1.33	1.33	1.33
2	5.98	6.00	6.00	6.00
4	13.26	13.33	13.33	13.33
6	23.20	23.33	23.33	23.33
8	35.80	36.00	36.00	36.00
10	51.06	51.33	51.33	51.33

as will be shown in §B.2, few elements are needed for converged results when using Euler beam elements. This value of μ is 10^4 times larger than the Young's modulus E. This large value prevents the Timoshenko beam elements from shearing and therefore causes them to behave like Euler beams. 11×2 uniformly distributed beam elements were used in these simulations. This means that 11 identical elements were used along the whole length of each layer of beams, with one layer above the crack and one layer below. There were ten elements in the intact section and one in the cracked section. At the DCB tip, M_1 was set to $M_1 = 1\,\text{Nm}$ and M_2 was varied. All other DCB tip quantities were 0. The effect of k_s is the same regardless of whether Timoshenko beam elements with a normal value of shear modulus, QUAD4 elements or different DCB tip loading conditions are used. It is therefore sufficient just to present these results.

Table B.1 presents the effect of k_s on G_I and Table B.2 presents the effect of k_s on G_{II}. It is seen that when is k_s increased to only $1 \times 10^2\,\mathrm{kN/mm}$, both G_I and G_{II} have already reached constant values. These are the values for a rigid interface. It is also seen that the value of k_s can be increased further up to $k_s = 1 \times 10^6\,\mathrm{kN/mm}$ without adversely affecting the results by introducing numerical errors. It is obviously better to use as large a value for k_s as possible. In the units of the FEM simulations, $k_s = 1 \times 10^6\,\mathrm{kN/mm}$ is 10^6 times bigger than the Young's modulus of the material ($E = 1\,\mathrm{GPa}$). Therefore, $k_s = 1 \times 10^6\,\mathrm{kN/mm}$ is selected as an appropriate value for the interface spring stiffness in simulations with this DCB configuration.

B.2 Numerical simulations with Euler beams

The same DCB as that described in §4.3 and §B.1 is used in this section to carry out a convergence study using Timoshenko beam elements with the large shear modulus of $\mu = 10^4\,\mathrm{GPa}$, i.e. Euler beam elements. The elements are uniformly distributed along the length of each layer, with one layer above the crack and one layer below. The results are shown in Table B.3.

It is seen that converged results are obtained using 11×2 Euler beam elements. Doubling and tripling the number of elements has no effect on the values of G_I/G. A mesh with 11×2 elements is therefore suitable for these simulations.

B.3 Numerical simulations with Timoshenko beams

The same DCB as that described in §4.3 and §B.1 is used in this section to carry out a convergence study using Timoshenko beam elements with a normal value for the shear modulus, which is $\mu = E/\left[2\left(1+\nu\right)\right] = 1/2.6\,\mathrm{GPa}$. The meshes with 220×2, 880×2 and 1320×2 elements are uniformly distributed along the length of each layer, with one layer above the crack and one layer below. The mesh with 1310×2 elements has two layers of nonuniformly distributed elements. In each layer, in the region of length 1.2 mm centred on the crack tip, 1200 elements with a length of 0.001 mm were uniformly distributed. In the remaining intact section of the DCB, 100 elements were uniformly distributed. In the remaining cracked section of the DCB, 10 elements were uniformly distributed. This nonuniform mesh has almost the same total number of elements as the uniform mesh with 1320×2 elements, but the element density in the vicinity of the crack tip is much higher. The results are shown in Table B.4.

It is seen that when using Timoshenko beam elements with $\mu = 1/2.6\mathrm{GPa}$, G_I/G is much more sensitive to the number of elements. Increasing the number of elements results in very slow convergence towards constant values of G_I/G. Table B.4 shows that excellent convergence is achieved when using the nonuniform mesh with 1310×2 elements. However, it is also noted that the difference between using 880×2 uniformly distributed elements and 1310×2 nonuniformly distributed elements is relatively small.

Table B.3: Convergence study for G_I/G for an isotropic homogeneous DCB modelled with Euler beam elements with varying M_2 and $M_1 = 1\,\text{Nm}$, $N_1 = 0$, $N_2 = 0$, $P_1 = 0$, $P_2 = 0$, $\mu = 10^4\,\text{GPa}$, $\gamma = 2$.

M_2 (Nm)	G_I/G (%)		
	11×2 Euler beams	22×2 Euler beams	33×3 Euler beams
-10	76.92	76.92	76.91
-8	53.77	53.77	53.78
-6	44.88	44.88	44.89
-4	41.87	41.87	41.88
-2	40.36	40.36	40.37
0	39.45	39.46	39.46
2	38.85	38.85	38.86
4	38.42	38.42	38.43
6	38.10	38.10	38.11
8	37.85	37.85	37.85
10	37.65	37.65	37.65

Table B.4: Convergence study for G_I/G for an isotropic homogeneous DCB modelled with Timoshenko beam elements with varying M_2 and $M_1 = 1\,\text{Nm}$, $N_1 = 0$, $N_2 = 0$, $P_1 = 0$, $P_2 = 0$, $\mu = 1/2.6\,\text{GPa}$, $\gamma = 2$.

M_2 (Nm)	G_I/G (%)			
	220×2 Timo. beams	880×2 Timo. beams	1320×2 Timo. beams	1310×2 Timo. beams
-10	84.48	87.78	88.25	89.27
-8	89.09	91.80	92.19	93.03
-6	94.74	96.47	96.72	97.26
-4	100.00	100.00	100.00	100.00
-2	95.79	92.81	92.39	91.47
0	55.83	50.51	49.74	48.10
2	6.45	4.47	4.19	3.58
4	0.69	2.67	2.95	3.56
6	9.63	13.46	14.00	15.19
8	18.28	22.90	23.56	24.98
10	24.84	29.82	30.53	32.06

B.4 Numerical simulations with QUAD4 elements

The same DCB as that described in §4.3 and §B.1 is used in this section to carry out a convergence study using plane-stress QUAD4 elements. The elements are uniformly distributed along the length and through the thickness. Therefore, as an example, in the case of the mesh with 330×6 QUAD4 elements, 300 identical QUAD4 elements were used along the intact length and 30 identical QUAD4 elements were used along the cracked length. Two elements were used through the thickness of the upper beam and four elements through the thickness of the lower beam.

The results are shown in Table B.5. It is seen that excellent convergence is already obtained with 220×3 elements. Increasing the number of elements further to 330×6 and 440×9 elements results in only small changes.

Table B.5: Convergence study for G_I/G for an isotropic homogeneous DCB modelled with QUAD4 elements with varying M_2 and $M_1 = 1\,\text{Nm}$, $N_1 = 0$, $N_2 = 0$, $P_1 = 0$, $P_2 = 0$, $\mu = 10^4\,\text{GPa}$, $\gamma = 2$.

M_2 (Nm)	G_I/G (%)		
	220×3 QUAD4s	330×6 Euler beams	440×9 Euler beams
−10	81.39	80.45	80.65
−8	86.07	85.37	85.58
−6	92.09	91.67	91.87
−4	98.60	98.42	98.51
−2	97.50	97.39	97.18
0	59.03	60.31	60.22
2	6.62	8.64	8.98
4	1.29	0.57	0.51
6	10.37	8.21	7.93
8	18.76	16.09	15.76
10	25.00	22.17	21.85

In order to give a qualitative idea of these QUAD4 meshes, Fig. B.1 shows the three different QUAD4 meshes in the vicinity of the crack tip. Recall that the total thickness of the DCB in question is $h = 3\,\text{mm}$, with $h_1 = 1\,\text{mm}$ and $h_2 = 2\,\text{mm}$. The length of the crack is $a = 10\,\text{mm}$ and the length of the intact section is $L = 100\,\text{mm}$.

B.5 Other configurations

In §B.1 to §B.4, only isotropic homogeneous DCBs have been considered. For the laminated composite DCB cases and the circular isotropic homogeneous plate cases, which are also considered in this work, the same studies as described in this appendix confirm that using the same meshes (but with different material properties and geometries) will give similarly converged results.

The same is found for cases with non-rigid interfaces, with one notable exception, namely, when using Euler beam elements. A large number of elements with a very fine mesh in the vicinity of the crack tip is required to obtain converged results in this case. The nonuniform beam mesh with 1310×2 beam elements performs very well in this case. This is in comparison to §B.2 where it is shown that with a rigid interface, 11×2 Euler beam elements is sufficient. This is expected since point interface springs are more suited to capture the stress singularity at the crack tip that is observed for a rigid interface. This stress singularity does not exist for a non-rigid interface, as is shown in Chapter 8.

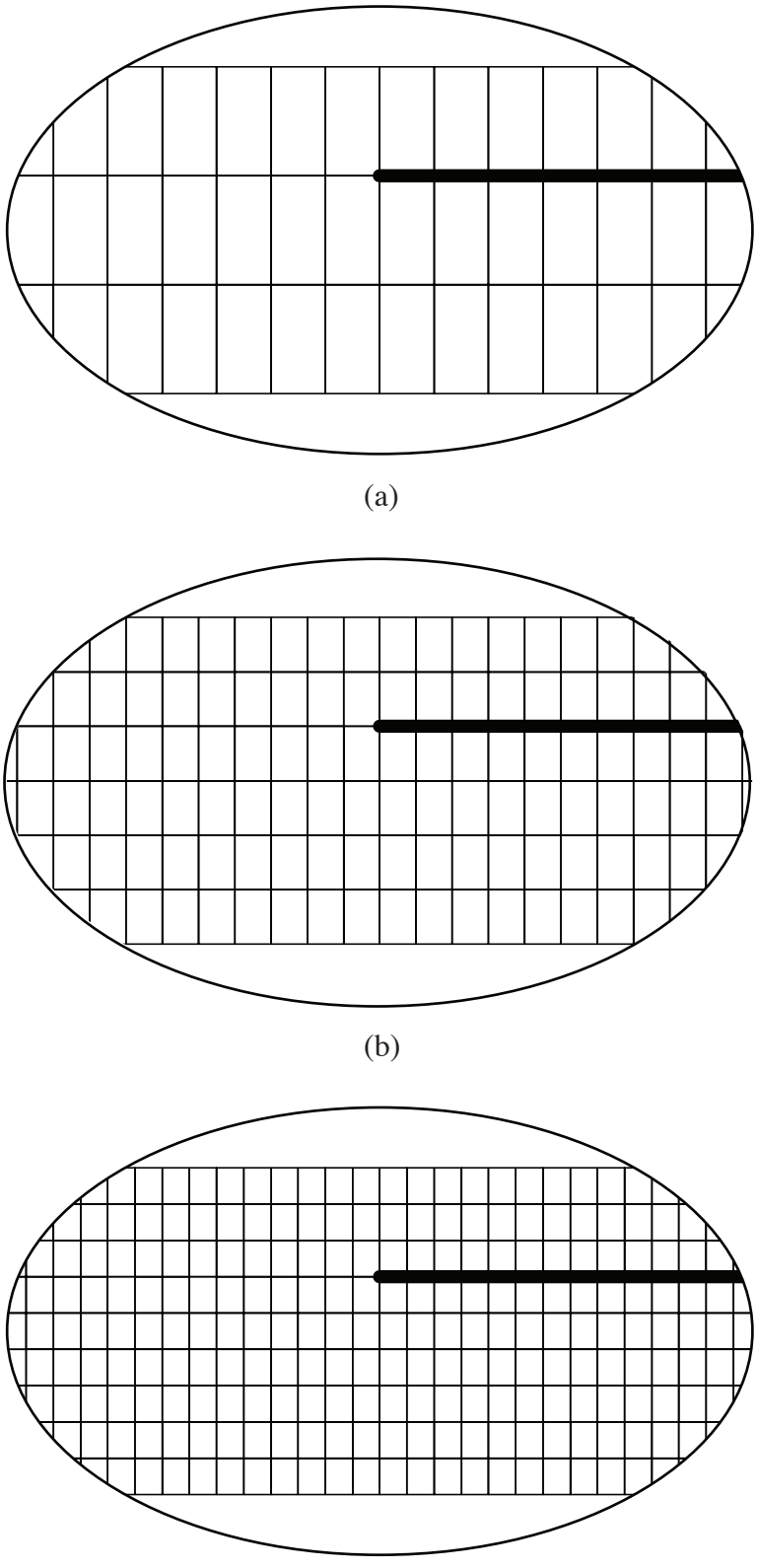

Figure B.1: QUAD4 meshes of a DCB in the vicinity of the crack tip. (a) 220×3 elements. (b) 330×6 elements. (c) 440×9 elements.

Appendix C

Matlab scripts for fractured beam structures

C.1 Clamped-clamped isotropic homogeneous beams

The governing equations for a general clamped-clamped isotropic homogeneous beam with a fracture were derived in §6.2.1. Boundary conditions were prescribed that would allow the system of 12 equations to be solved. The resulting expressions for the unknowns in these equations are extensive. It is therefore more practical to present the Matlab script file that derives these expressions than to present the expressions themselves. The following listing presents that Matlab script. The variable names correspond to those in Chapter 6. The two regions of any expression containing Macaulay brackets, which denote the ramp function, are handled in separate variables which are identified by `_p1` or `_p2` at the end of the variable name for part 1 and part 2 respectively. Only 11 equations are solved in this listing since the $w_{1B_1} = w_{2B_1}$ boundary condition of Eq. (6.14) is applied directly. Note that Matlab's *Symbolic Toolkit* is required to run this script.

```
% Symbolic variables (requires symbolic toolkit)
syms a b E h1 k L1 L2 x xp1 xp2 gam mu positive
syms M1 M1B2 M2 M2B2 N1 N1B2 N2 N2B2 P1 P1B2 P2B2 P2

% 12 Unknowns
syms M1B1 M2B1 N1B1 N2B1 P1B1 P2B1 u1B1 u2B1 w1B1 psi1B1 psi2B1

% Geometry
I1 = b*h1^3/12;
I2 = b*gam^3*h1^3/12;
I3 = b*(1+gam)^3*h1^3/12;
I4 = b*(1+gam)^3*h1^3/12;
S1 = b*h1;
S2 = b*gam*h1;
S3 = b*(1+gam)*h1;
S4 = b*(1+gam)*h1;
h2 = gam*h1;
beta1 = gam^2*(3 + gam)/(1 + 3*gam);
theta1 = -gam^2;
beta2 = 2*(3 + gam)/h1/(gam - 1);

% Crack tip forces in terms of M1B, M2B, N1B, N2B, P1B and P2B
M1B2 = M1B1 - M1 - P1B1*a + P1*(a - xp1);
M2B2 = M2B1 - M2 - P2B1*a + P2*(a - xp2);
N1B2 = N1B1 - N1;
N2B2 = N2B1 - N2;
```

```
P1B2 = P1B1 - P1;
P2B2 = P2B1 - P2;
MB1 = M1B1 + M2B1 + (h1*N2B1 - h2*N1B1)/2;
MB2 = M1B2 + M2B2 + (h1*N2B2 - h2*N1B2)/2;
NB1 = N1B1 + N2B1;
NB2 = N1B2 + N2B2;
PB1 = P1B1 + P2B1;
PB2 = P1B2 + P2B2;

% Rotations of the normals to the mid-planes
psi1_p1 = 1/E/I1*(M1B1*x - P1B1*x^2/2) + psi1B1;
psi1_p2 = 1/E/I1*(M1B1*x - P1B1*x^2/2 - M1*(x - xp1) + P1*(x - xp1)^2/2) + psi1B1;
psi2_p1 = 1/E/I2*(M2B1*x - P2B1*x^2/2) + psi2B1;
psi2_p2 = 1/E/I2*(M2B1*x - P2B1*x^2/2 - M2*(x - xp2) + P2*(x - xp2)^2/2) + psi2B1;
psi3 = 1/E/I3*(MB1*x + PB1*L1*x - PB1*x^2/2);
psi4 = 1/E/I4*(MB2*x - MB2*L2 - PB2*x^2/2 + PB2*L2^2/2);

% Deflections
w1_p1 = 1/E/I1*(M1B1*x^2/2 - P1B1*x^3/6) + psi1B1*x + w1B1 + 1/k^2/S1/mu*P1B1*x;
w1_p2 = 1/E/I1*(M1B1*x^2/2 - P1B1*x^3/6 - M1*(x - xp1)^2/2 + P1*(x - xp1)^3/6) +
    psi1B1*x + w1B1 + 1/k^2/S1/mu*(P1B1*x - P1*(x - xp1));
w2_p1 = 1/E/I2*(M2B1*x^2/2 - P2B1*x^3/6) + psi2B1*x + w1B1 + 1/k^2/S2/mu*P2B1*x;
w2_p2 = 1/E/I2*(M2B1*x^2/2 - P2B1*x^3/6 - M2*(x - xp2)^2/2 + P2*(x - xp2)^3/6) +
    psi2B1*x + w1B1 + 1/k^2/S2/mu*(P2B1*x - P2*(x - xp2));
w3 = 1/E/I3*(MB1*x^2/2 + PB1*L1*x^2/2 - PB1*x^3/6) + 1/k^2/S3/mu*PB1*x;
w4 = 1/E/I4*(MB2*x^2/2 - MB2*L2*x + MB2*L2^2/2 - PB2*x^3/6 + PB2*L2^2*x/2 - PB2*L2
    ^3/3) + 1/k^2/S4/mu*(PB2*x - PB2*L2);

% Mid-plane gradients
w1d_p1 = diff(w1_p1,x); w1d_p2 = diff(w1_p2,x);
w2d_p1 = diff(w2_p1,x); w2d_p2 = diff(w2_p2,x);
w3d = diff(w3,x);
w4d = diff(w4,x);

% Extensions
u1_p1 = 1/E/S1*(N1B1*x) + u1B1;
u1_p2 = 1/E/S1*(N1B1*x - N1*(x - xp1)) + u1B1;
u2_p1 = 1/E/S2*(N2B1*x) + u2B1;
u2_p2 = 1/E/S2*(N2B1*x - N2*(x - xp2)) + u2B1;
u3 = 1/E/S3*NB1*x;
u4 = 1/E/S4*(NB2*x - NB2*L2);

% Left crack tip force FnB1
N1Be_1 = N1B1 - N2B1*S1/S2;
alpha_beta2_1 = N1Be_1/beta2;
alpha_theta1_1 = 1/(beta1 - theta1)*(beta1*(M1B1 - alpha_beta2_1) - M2B1);
alpha_beta1_1 = 1/(beta1 - theta1)*(-theta1*(M1B1 - alpha_beta2_1) + M2B1);
FnBtheta1 = 1/h1*sqrt(48*gam^2*k^2*mu/E/(1 + gam)^2);
FnBP1 = (gam*P1B1 - P2B1)/(1 + gam);
FnB1 = alpha_theta1_1*FnBtheta1 + FnBP1;

% Right crack tip force FnB2
N1Be_2 = N1B2 - N2B2*S1/S2;
alpha_beta2_2 = N1Be_2/beta2;
alpha_theta1_2 = 1/(beta1 - theta1)*(beta1*(M1B2 - alpha_beta2_2) - M2B2);
alpha_beta1_2 = 1/(beta1 - theta1)*(-theta1*(M1B2 - alpha_beta2_2) + M2B2);
FnBP2 = (gam*P1B2 - P2B2)/(1 + gam);
FnB2 = alpha_theta1_2*FnBtheta1 + FnBP2;
```

```
82
83 % Quantities at the right crack tip
84 x = 0;
85 w40 = eval(w4);
86 w4d0 = eval(w4d);
87 psiB2 = eval(psi4);
88 u40 = eval(u4);
89
90 % 11 Boundary conditions (w2B1 = w1B1 already applied)
91 x = L1;
92 eq1 = eval(w3) - w1B1;
93 eq2 = eval(w3d) - psi1B1 - 1/k^2/S1/mu*(P1B1 - FnB1);
94 eq3 = eval(w3d) - psi2B1 - 1/k^2/S2/mu*(P2B1 + FnB1);
95 eq4 = eval(u3) - h2/2*eval(psi3) - u1B1;
96 eq5 = eval(u3) + h1/2*eval(psi3) - u2B1;
97 x = a;
98 eq6 = w40 - eval(w1_p2);
99 eq7 = w40 - eval(w2_p2);
100 eq8 = w4d0 - eval(psi1_p2) - 1/k^2/S1/mu*(P1B2 - FnB2);
101 eq9 = w4d0 - eval(psi2_p2) - 1/k^2/S2/mu*(P2B2 + FnB2);
102 eq10 = u40 - h2/2*psiB2 - eval(u1_p2);
103 eq11 = u40 + h1/2*psiB2 - eval(u2_p2);
104 syms x
105
106 % Matlab cannot solve this system of equations using the 'solve' function
107 % Instead, solve for {F} where eq1 to eq11 are written in the form,
108 %  [A] * {F} + {f} = 0
109
110 % Extract {f} coefficients
111 M1B1 = 0; M2B1 = 0; P1B1 = 0; P2B1 = 0; N1B1 = 0; N2B1 = 0; w1B1 = 0; psi1B1 = 0;
      psi2B1 = 0; u1B1 = 0; u2B1 = 0;
112 f1 = eval(eval(eq1)); f2 = eval(eval(eq2)); f3 = eval(eval(eq3)); f4 = eval(eval(
      eq4)); f5 = eval(eval(eq5)); f6 = eval(eval(eq6)); f7 = eval(eval(eq7)); f8 =
      eval(eval(eq8)); f9 = eval(eval(eq9)); f10 = eval(eval(eq10)); f11 = eval(eval(
      eq11));
113
114 % Extract [A] coefficients, column 1
115 M1B1 = 1; M2B1 = 0; P1B1 = 0; P2B1 = 0; N1B1 = 0; N2B1 = 0; w1B1 = 0; psi1B1 = 0;
      psi2B1 = 0; u1B1 = 0; u2B1 = 0;
116 A1_1 = eval(eval(eq1) - f1); A2_1 = eval(eval(eq2) - f2); A3_1 = eval(eval(eq3) -
      f3); A4_1 = eval(eval(eq4) - f4); A5_1 = eval(eval(eq5) - f5); A6_1 = eval(eval
      (eq6) - f6); A7_1 = eval(eval(eq7) - f7); A8_1 = eval(eval(eq8) - f8); A9_1 =
      eval(eval(eq9) - f9); A10_1 = eval(eval(eq10) - f10); A11_1 = eval(eval(eq11) -
       f11);
117
118 % Extract [A] coefficients, column 2
119 M1B1 = 0; M2B1 = 1; P1B1 = 0; P2B1 = 0; N1B1 = 0; N2B1 = 0; w1B1 = 0; psi1B1 = 0;
      psi2B1 = 0; u1B1 = 0; u2B1 = 0;
120 A1_2 = eval(eval(eq1) - f1); A2_2 = eval(eval(eq2) - f2); A3_2 = eval(eval(eq3) -
      f3); A4_2 = eval(eval(eq4) - f4); A5_2 = eval(eval(eq5) - f5); A6_2 = eval(eval
      (eq6) - f6); A7_2 = eval(eval(eq7) - f7); A8_2 = eval(eval(eq8) - f8); A9_2 =
      eval(eval(eq9) - f9); A10_2 = eval(eval(eq10) - f10); A11_2 = eval(eval(eq11) -
       f11);
121
122 % Extract [A] coefficients, column 3
123 M1B1 = 0; M2B1 = 0; P1B1 = 1; P2B1 = 0; N1B1 = 0; N2B1 = 0; w1B1 = 0; psi1B1 = 0;
      psi2B1 = 0; u1B1 = 0; u2B1 = 0;
```

```
124 A1_3 = eval(eval(eq1) - f1); A2_3 = eval(eval(eq2) - f2); A3_3 = eval(eval(eq3) -
        f3); A4_3 = eval(eval(eq4) - f4); A5_3 = eval(eval(eq5) - f5); A6_3 = eval(eval
        (eq6) - f6); A7_3 = eval(eval(eq7) - f7); A8_3 = eval(eval(eq8) - f8); A9_3 =
        eval(eval(eq9) - f9); A10_3 = eval(eval(eq10) - f10); A11_3 = eval(eval(eq11) -
         f11);
125
126 % Extract [A] coefficients, column 4
127 M1B1 = 0; M2B1 = 0; P1B1 = 0; P2B1 = 1; N1B1 = 0; N2B1 = 0; w1B1 = 0; psi1B1 = 0;
        psi2B1 = 0; u1B1 = 0; u2B1 = 0;
128 A1_4 = eval(eval(eq1) - f1); A2_4 = eval(eval(eq2) - f2); A3_4 = eval(eval(eq3) -
        f3); A4_4 = eval(eval(eq4) - f4); A5_4 = eval(eval(eq5) - f5); A6_4 = eval(eval
        (eq6) - f6); A7_4 = eval(eval(eq7) - f7); A8_4 = eval(eval(eq8) - f8); A9_4 =
        eval(eval(eq9) - f9); A10_4 = eval(eval(eq10) - f10); A11_4 = eval(eval(eq11) -
         f11);
129
130 % Extract [A] coefficients, column 5
131 M1B1 = 0; M2B1 = 0; P1B1 = 0; P2B1 = 0; N1B1 = 1; N2B1 = 0; w1B1 = 0; psi1B1 = 0;
        psi2B1 = 0; u1B1 = 0; u2B1 = 0;
132 A1_5 = eval(eval(eq1) - f1); A2_5 = eval(eval(eq2) - f2); A3_5 = eval(eval(eq3) -
        f3); A4_5 = eval(eval(eq4) - f4); A5_5 = eval(eval(eq5) - f5); A6_5 = eval(eval
        (eq6) - f6); A7_5 = eval(eval(eq7) - f7); A8_5 = eval(eval(eq8) - f8); A9_5 =
        eval(eval(eq9) - f9); A10_5 = eval(eval(eq10) - f10); A11_5 = eval(eval(eq11) -
         f11);
133
134 % Extract [A] coefficients, column 6
135 M1B1 = 0; M2B1 = 0; P1B1 = 0; P2B1 = 0; N1B1 = 0; N2B1 = 1; w1B1 = 0; psi1B1 = 0;
        psi2B1 = 0; u1B1 = 0; u2B1 = 0;
136 A1_6 = eval(eval(eq1) - f1); A2_6 = eval(eval(eq2) - f2); A3_6 = eval(eval(eq3) -
        f3); A4_6 = eval(eval(eq4) - f4); A5_6 = eval(eval(eq5) - f5); A6_6 = eval(eval
        (eq6) - f6); A7_6 = eval(eval(eq7) - f7); A8_6 = eval(eval(eq8) - f8); A9_6 =
        eval(eval(eq9) - f9); A10_6 = eval(eval(eq10) - f10); A11_6 = eval(eval(eq11) -
         f11);
137
138 % Extract [A] coefficients, column 7
139 M1B1 = 0; M2B1 = 0; P1B1 = 0; P2B1 = 0; N1B1 = 0; N2B1 = 0; w1B1 = 1; psi1B1 = 0;
        psi2B1 = 0; u1B1 = 0; u2B1 = 0;
140 A1_7 = eval(eval(eq1) - f1); A2_7 = eval(eval(eq2) - f2); A3_7 = eval(eval(eq3) -
        f3); A4_7 = eval(eval(eq4) - f4); A5_7 = eval(eval(eq5) - f5); A6_7 = eval(eval
        (eq6) - f6); A7_7 = eval(eval(eq7) - f7); A8_7 = eval(eval(eq8) - f8); A9_7 =
        eval(eval(eq9) - f9); A10_7 = eval(eval(eq10) - f10); A11_7 = eval(eval(eq11) -
         f11);
141
142 % Extract [A] coefficients, column 8
143 M1B1 = 0; M2B1 = 0; P1B1 = 0; P2B1 = 0; N1B1 = 0; N2B1 = 0; w1B1 = 0; psi1B1 = 1;
        psi2B1 = 0; u1B1 = 0; u2B1 = 0;
144 A1_8 = eval(eval(eq1) - f1); A2_8 = eval(eval(eq2) - f2); A3_8 = eval(eval(eq3) -
        f3); A4_8 = eval(eval(eq4) - f4); A5_8 = eval(eval(eq5) - f5); A6_8 = eval(eval
        (eq6) - f6); A7_8 = eval(eval(eq7) - f7); A8_8 = eval(eval(eq8) - f8); A9_8 =
        eval(eval(eq9) - f9); A10_8 = eval(eval(eq10) - f10); A11_8 = eval(eval(eq11) -
         f11);
145
146 % Extract [A] coefficients, column 9
147 M1B1 = 0; M2B1 = 0; P1B1 = 0; P2B1 = 0; N1B1 = 0; N2B1 = 0; w1B1 = 0; psi1B1 = 0;
        psi2B1 = 1; u1B1 = 0; u2B1 = 0;
```

```
148 A1_9 = eval(eval(eq1) - f1); A2_9 = eval(eval(eq2) - f2); A3_9 = eval(eval(eq3) -
        f3); A4_9 = eval(eval(eq4) - f4); A5_9 = eval(eval(eq5) - f5); A6_9 = eval(eval
        (eq6) - f6); A7_9 = eval(eval(eq7) - f7); A8_9 = eval(eval(eq8) - f8); A9_9 =
        eval(eval(eq9) - f9); A10_9 = eval(eval(eq10) - f10); A11_9 = eval(eval(eq11) -
         f11);
149
150 % Extract [A] coefficients, column 10
151 M1B1 = 0; M2B1 = 0; P1B1 = 0; P2B1 = 0; N1B1 = 0; N2B1 = 0; w1B1 = 0; psi1B1 = 0;
        psi2B1 = 0; u1B1 = 1; u2B1 = 0;
152 A1_10 = eval(eval(eq1) - f1); A2_10 = eval(eval(eq2) - f2); A3_10 = eval(eval(eq3)
        - f3); A4_10 = eval(eval(eq4) - f4); A5_10 = eval(eval(eq5) - f5); A6_10 = eval
        (eval(eq6) - f6); A7_10 = eval(eval(eq7) - f7); A8_10 = eval(eval(eq8) - f8);
        A9_10 = eval(eval(eq9) - f9); A10_10 = eval(eval(eq10) - f10); A11_10 = eval(
        eval(eq11) - f11);
153
154 % Extract [A] coefficients, column 11
155 M1B1 = 0; M2B1 = 0; P1B1 = 0; P2B1 = 0; N1B1 = 0; N2B1 = 0; w1B1 = 0; psi1B1 = 0;
        psi2B1 = 0; u1B1 = 0; u2B1 = 1;
156 A1_11 = eval(eval(eq1) - f1); A2_11 = eval(eval(eq2) - f2); A3_11 = eval(eval(eq3)
        - f3); A4_11 = eval(eval(eq4) - f4); A5_11 = eval(eval(eq5) - f5); A6_11 = eval
        (eval(eq6) - f6); A7_11 = eval(eval(eq7) - f7); A8_11 = eval(eval(eq8) - f8);
        A9_11 = eval(eval(eq9) - f9); A10_11 = eval(eval(eq10) - f10); A11_11 = eval(
        eval(eq11) - f11);
157
158 % Construct [A] matrix
159 A = [
160 A1_1  A1_2  A1_3  A1_4  A1_5  A1_6  A1_7  A1_8  A1_9  A1_10  A1_11;
161 A2_1  A2_2  A2_3  A2_4  A2_5  A2_6  A2_7  A2_8  A2_9  A2_10  A2_11;
162 A3_1  A3_2  A3_3  A3_4  A3_5  A3_6  A3_7  A3_8  A3_9  A3_10  A3_11;
163 A4_1  A4_2  A4_3  A4_4  A4_5  A4_6  A4_7  A4_8  A4_9  A4_10  A4_11;
164 A5_1  A5_2  A5_3  A5_4  A5_5  A5_6  A5_7  A5_8  A5_9  A5_10  A5_11;
165 A6_1  A6_2  A6_3  A6_4  A6_5  A6_6  A6_7  A6_8  A6_9  A6_10  A6_11;
166 A7_1  A7_2  A7_3  A7_4  A7_5  A7_6  A7_7  A7_8  A7_9  A7_10  A7_11;
167 A8_1  A8_2  A8_3  A8_4  A8_5  A8_6  A8_7  A8_8  A8_9  A8_10  A8_11;
168 A9_1  A9_2  A9_3  A9_4  A9_5  A9_6  A9_7  A9_8  A9_9  A9_10  A9_11;
169 A10_1 A10_2 A10_3 A10_4 A10_5 A10_6 A10_7 A10_8 A10_9 A10_10 A10_11;
170 A11_1 A11_2 A11_3 A11_4 A11_5 A11_6 A11_7 A11_8 A11_9 A11_10 A11_11
171 ];
172 A = simple(A)
173
174 % Construct {f} vector
175 f = [f1; f2; f3; f4; f5; f6; f7; f8; f9; f10; f11];
176
177 % Solve system of equations for {F} vector
178 F = -A\f;
179
180 % Solutions for unknowns
181 F = simple(F);
182 M1B1 = F(1)
183 M2B1 = F(2)
184 P1B1 = F(3)
185 P2B1 = F(4)
186 N1B1 = F(5)
187 N2B1 = F(6)
188 w1B1 = F(7)
189 psi1B1 = F(8)
190 psi2B1 = F(9)
191 u1B1 = F(10)
```

```
192 u2B1 = F(11)
```

C.2 Simply supported isotropic homogeneous beams

The governing equations for a general simply supported isotropic homogeneous beam with a fracture were derived in §6.3. Boundary conditions were prescribed that would allow the system of 14 equations to be solved. The resulting expressions for the unknowns in these equations are extensive. It is therefore more practical to present the Matlab script file that derives these expressions than to present the expressions themselves. The following listing presents that Matlab script. The variable names correspond to those in Chapter 6. The two regions of any expression containing Macaulay brackets, which denote the ramp function, are handled in separate variables which are identified by `_p1` or `_p2` at the end of the variable name for part 1 and part 2 respectively. Only 13 equations are solved in this listing since the $w_{1B_1} = w_{2B_1}$ boundary condition of Eq. (6.14) is applied directly. Note that Matlab's *Symbolic Toolkit* is required to run this script.

```
1  % Symbolic variables (requires symbolic toolkit)
2  syms a b E h1 k L1 L2 x xp1 xp2 gam mu positive
3  syms M1 M1B2 M2 M2B2 N1 N1B2 N2 N2B2 P1 P1B2 P2B2 P2
4
5  % 12 Unknowns
6  syms M1B1 M2B1 N1B1 N2B1 P1B1 P2B1 w1B1 psi1B1 psi2B1 psiA psiB2 u1B1 u2B1
7
8  % Geometry
9  I1 = b*h1^3/12;
10 I2 = b*gam^3*h1^3/12;
11 I3 = b*(1+gam)^3*h1^3/12;
12 I4 = b*(1+gam)^3*h1^3/12;
13 S1 = b*h1;
14 S2 = b*gam*h1;
15 S3 = b*(1+gam)*h1;
16 S4 = b*(1+gam)*h1;
17 h2 = gam*h1;
18 beta1 = gam^2*(3 + gam)/(1 + 3*gam);
19 theta1 = -gam^2;
20 beta2 = 2*(3 + gam)/h1/(gam - 1);
21
22 % Crack tip forces in terms of M1B, M2B, N1B, N2B, P1B and P2B
23 M1B2 = M1B1 - M1 - P1B1*a + P1*(a - xp1);
24 M2B2 = M2B1 - M2 - P2B1*a + P2*(a - xp2);
25 N1B2 = N1B1 - N1;
26 N2B2 = N2B1 - N2;
27 P1B2 = P1B1 - P1;
28 P2B2 = P2B1 - P2;
29 MB1 = M1B1 + M2B1 + (h1*N2B1 - h2*N1B1)/2;
30 MB2 = M1B2 + M2B2 + (h1*N2B2 - h2*N1B2)/2;
31 NB1 = N1B1 + N2B1;
32 NB2 = N1B2 + N2B2;
33 PB1 = P1B1 + P2B1;
34 PB2 = P1B2 + P2B2;
35
```

```
% Rotations of normals to mid-planes
psi1_p1 = 1/E/I1*(M1B1*x - P1B1*x^2/2) + psi1B1;
psi1_p2 = 1/E/I1*(M1B1*x - P1B1*x^2/2 - M1*(x - xp1) + P1*(x - xp1)^2/2) + psi1B1;
psi2_p1 = 1/E/I2*(M2B1*x - P2B1*x^2/2) + psi2B1;
psi2_p2 = 1/E/I2*(M2B1*x - P2B1*x^2/2 - M2*(x - xp2) + P2*(x - xp2)^2/2) + psi2B1;
psi3 = 1/E/I3*(MB1*x + PB1*L1*x - PB1*x^2/2) + psiA;
psi4 = 1/E/I4*(MB2*x - PB2*x^2/2) + psiB2;

% Deflections
w1_p1 = 1/E/I1*(M1B1*x^2/2 - P1B1*x^3/6) + psi1B1*x + w1B1 + 1/k^2/A1/G*P1B1*x;
w1_p2 = 1/E/I1*(M1B1*x^2/2 - P1B1*x^3/6 - M1*(x - xp1)^2/2 + P1*(x - xp1)^3/6) +
    psi1B1*x + w1B1 + 1/k^2/A1/G*(P1B1*x - P1*(x - xp1));
w2_p1 = 1/E/I2*(M2B1*x^2/2 - P2B1*x^3/6) + psi2B1*x + w1B1 + 1/k^2/A2/G*P2B1*x;
w2_p2 = 1/E/I2*(M2B1*x^2/2 - P2B1*x^3/6 - M2*(x - xp2)^2/2 + P2*(x - xp2)^3/6) +
    psi2B1*x + w1B1 + 1/k^2/A2/G*(P2B1*x - P2*(x - xp2));
w3 = 1/E/I3*(MB1*x^2/2 + PB1*L1*x^2/2 - PB1*x^3/6) + psiA*x + 1/k^2/A3/G*PB1*x;
w4 = 1/E/I4*(MB2*x^2/2 - MB2*L2^2/2 - PB2*x^3/6 + PB2*L2^3/3) + psiB2*(x - L2) + 1/
    k^2/A4/G*(PB2*x - PB2*L2);

% Mid-plane gradients
w1d_p1 = diff(w1_p1,x); w1d_p2 = diff(w1_p2,x);
w2d_p1 = diff(w2_p1,x); w2d_p2 = diff(w2_p2,x);
w3d = diff(w3,x);
w4d = diff(w4,x);

% Extensions
u1_p1 = 1/E/S1*(N1B1*x) + u1B1;
u1_p2 = 1/E/S1*(N1B1*x - N1*(x - xp1)) + u1B1;
u2_p1 = 1/E/S2*(N2B1*x) + u2B1;
u2_p2 = 1/E/S2*(N2B1*x - N2*(x - xp2)) + u2B1;
u3 = 1/E/S3*NB1*x;
u4 = 1/E/S4*(NB2*x - NB2*L2);

% Left crack tip force FnB1
N1Be_1 = N1B1 - N2B1*S1/S2;
alpha_beta2_1 = N1Be_1/beta2;
alpha_theta1_1 = 1/(beta1 - theta1)*(beta1*(M1B1 - alpha_beta2_1) - M2B1);
alpha_beta1_1 = 1/(beta1 - theta1)*(-theta1*(M1B1 - alpha_beta2_1) + M2B1);
FnBtheta1 = 1/h1*sqrt(48*gam^2*k^2*G/E/(1 + gam)^2);
FnBP1 = (gam*P1B1 - P2B1)/(1 + gam);
FnB1 = alpha_theta1_1*FnBtheta1 + FnBP1;

% Right crack tip force FnB2
N1Be_2 = N1B2 - N2B2*S1/S2;
alpha_beta2_2 = N1Be_2/beta2;
alpha_theta1_2 = 1/(beta1 - theta1)*(beta1*(M1B2 - alpha_beta2_2) - M2B2);
alpha_beta1_2 = 1/(beta1 - theta1)*(-theta1*(M1B2 - alpha_beta2_2) + M2B2);
FnBP2 = (gam*P1B2 - P2B2)/(1 + gam);
FnB2 = alpha_theta1_2*FnBtheta1 + FnBP2;

% Quantities at the right crack tip
x = 0;
w40 = eval(w4);
w4d0 = eval(w4d);
u40 = eval(u4);

% 13 Boundary conditions (w2B1 = w1B1 already applied)
x = L1;
```

```
eq1 = eval(w3) - w1B1;
eq2 = MB1 + PB1*L1;
eq3 = eval(w3d) - psi1B1 - 1/k^2/A1/G*(P1B1 - FnB1);
eq4 = eval(w3d) - psi2B1 - 1/k^2/A2/G*(P2B1 + FnB1);
eq5 = eval(u3) - h2/2*eval(psi3) - u1B1;
eq6 = eval(u3) + h1/2*eval(psi3) - u2B1;
x = a;
eq7 = w40 - eval(w1_p2);
eq8 = w40 - eval(w2_p2);
eq9 = MB2 - PB2*L2;
eq10 = w4d0 - eval(psi1_p2) - 1/k^2/A1/G*(P1B2 - FnB2);
eq11 = w4d0 - eval(psi2_p2) - 1/k^2/A2/G*(P2B2 + FnB2);
eq12 = u40 - h2/2*psiB2 - eval(u1_p2);
eq13 = u40 + h1/2*psiB2 - eval(u2_p2);
syms x

% Matlab cannot solve this system of equations using the 'solve' function
% Instead, solve for {F} where eq1 to eq11 are written in the form,
%  [A] * {F} + {f} = 0

% Extract {f} coefficients
M1B1 = 0; M2B1 = 0; P1B1 = 0; P2B1 = 0; N1B1 = 0; N2B1 = 0; w1B1 = 0; psi1B1 = 0;
    psi2B1 = 0; psiA = 0; psiB2 = 0; u1B1 = 0; u2B1 = 0;
f1 = eval(eval(eq1)); f2 = eval(eval(eq2)); f3 = eval(eval(eq3)); f4 = eval(eval(
    eq4)); f5 = eval(eval(eq5)); f6 = eval(eval(eq6)); f7 = eval(eval(eq7)); f8 =
    eval(eval(eq8)); f9 = eval(eval(eq9)); f10 = eval(eval(eq10)); f11 = eval(eval(
    eq11)); f12 = eval(eval(eq12)); f13 = eval(eval(eq13));
```

The solution procedure continues in the same way as in §C.1, extracting the coefficients of each unknown quantity in order to write the equations in matrix form. The script finishes as follows:

```
% Extract [A] coefficients, column 13
M1B1 = 0; M2B1 = 0; P1B1 = 0; P2B1 = 0; N1B1 = 0; N2B1 = 0; w1B1 = 0; psi1B1 = 0;
    psi2B1 = 0; psiA = 0; psiB2 = 0; u1B1 = 0; u2B1 = 1;
A1_13 = eval(eval(eq1) - f1); A2_13 = eval(eval(eq2) - f2); A3_13 = eval(eval(eq3)
    - f3); A4_13 = eval(eval(eq4) - f4); A5_13 = eval(eval(eq5) - f5); A6_13 = eval
    (eval(eq6) - f6); A7_13 = eval(eval(eq7) - f7); A8_13 = eval(eval(eq8) - f8);
    A9_13 = eval(eval(eq9) - f9); A10_13 = eval(eval(eq10) - f10); A11_13 = eval(
    eval(eq11) - f11); A12_13 = eval(eval(eq12) - f12); A13_13 = eval(eval(eq13) -
    f13);

% Construct [A] matrix
A = [
A1_1 A1_2 A1_3 A1_4 A1_5 A1_6 A1_7 A1_8 A1_9 A1_10 A1_11 A1_12 A1_13;
A2_1 A2_2 A2_3 A2_4 A2_5 A2_6 A2_7 A2_8 A2_9 A2_10 A2_11 A2_12 A2_13;
A3_1 A3_2 A3_3 A3_4 A3_5 A3_6 A3_7 A3_8 A3_9 A3_10 A3_11 A3_12 A3_13;
A4_1 A4_2 A4_3 A4_4 A4_5 A4_6 A4_7 A4_8 A4_9 A4_10 A4_11 A4_12 A4_13;
A5_1 A5_2 A5_3 A5_4 A5_5 A5_6 A5_7 A5_8 A5_9 A5_10 A5_11 A5_12 A5_13;
A6_1 A6_2 A6_3 A6_4 A6_5 A6_6 A6_7 A6_8 A6_9 A6_10 A6_11 A6_12 A6_13;
A7_1 A7_2 A7_3 A7_4 A7_5 A7_6 A7_7 A7_8 A7_9 A7_10 A7_11 A7_12 A7_13;
A8_1 A8_2 A8_3 A8_4 A8_5 A8_6 A8_7 A8_8 A8_9 A8_10 A8_11 A8_12 A8_13;
A9_1 A9_2 A9_3 A9_4 A9_5 A9_6 A9_7 A9_8 A9_9 A9_10 A9_11 A9_12 A9_13;
A10_1 A10_2 A10_3 A10_4 A10_5 A10_6 A10_7 A10_8 A10_9 A10_10 A10_11 A10_12 A10_13;
A11_1 A11_2 A11_3 A11_4 A11_5 A11_6 A11_7 A11_8 A11_9 A11_10 A11_11 A11_12 A11_13;
A12_1 A12_2 A12_3 A12_4 A12_5 A12_6 A12_7 A12_8 A12_9 A12_10 A12_11 A12_12 A12_13;
```

```
A13_1 A13_2 A13_3 A13_4 A13_5 A13_6 A13_7 A13_8 A13_9 A13_10 A13_11 A13_12 A13_13
];
A = simple(A)

% Construct {f} vector
f = [f1; f2; f3; f4; f5; f6; f7; f8; f9; f10; f11; f12; f13];

% Solve system of equations for {F} vector
F = -A\f;

% Solutions for unknowns
F = simple(F);
M1B1 = F(1)
M2B1 = F(2)
P1B1 = F(3)
P2B1 = F(4)
N1B1 = F(5)
N2B1 = F(6)
w1B1 = F(7)
psi1B1 = F(8)
psi2B1 = F(9)
psiA = F(10)
psiB2 = F(11)
u1B1 = F(12)
u2B1 = F(13)
```

References

Alfano, G. and Crisfield, M. A. (2001), 'Finite element interface models for the delamination analysis of laminated composites: Mechanical and computational issues', *International Journal for Numerical Methods in Engineering* **50**(7), 1701–36.

Anstis, G. R., Chantikul, P., Lawn, B. R. and Marshall, D. B. (1981), 'A critical evaluation of indentation techniques for measuring fracture toughness: I, direct drack measurements', *Journal of the American Ceramic Society* **64**(9), 533–8.

Ashari, S. E. and Mohammadi, S. (2011), 'Delamination analysis of composites by new orthotropic bimaterial extended finite element method', *International Journal for Numerical Methods in Engineering* **86**(13), 1507–43.

ASTM (2007e3), Standard test method for mode I interlaminar fracture toughness of unidirectional fiber-reinforced polymer matrix composites, ASTM Standard D5528-01, American Society for Testing and Materials, ASTM Committee D30 on Composite Materials.

Belytschko, T. and Black, T. (1999), 'Elastic crack growth in finite elements with minimal remeshing', *International Journal for Numerical Methods in Engineering* **45**(5), 601–20.

Benzeggagh, M. L. and Kenane, M. (1996), 'Measurement of mixed-mode delamination fracture toughness of unidirectional glass/epoxy composites with mixed-mode bending apparatus', *Composites Science and Technology* **56**(4), 439–49.

Blackman, B. R. K., Kinloch, A. J. and Paraschi, M. (2005), 'The determination of the mode II adhesive fracture resistance, G_{IIC}, of structural adhesive joints: An effective crack length approach', *Engineering Fracture Mechanics* **72**(6), 877–97.

Brunner, A. J. (2000), 'Experimental aspects of mode I and mode II fracture toughness testing of fibre-reinforced polymer-matrix composites', *Computer Methods in Applied Mechanics and Engineering* **185**(2–4), 161–72.

Brunner, A. J., Blackman, B. R. K. and Williams, J. G. (2006), 'Calculating a damage parameter and bridging stress from G_{IC} delamination tests on fibre composites', *Composites Science and Technology* **66**(6), 785–95.

Bruno, D. and Greco, F. (2001), 'Mixed mode delamination in plates: A refined approach', *International Journal of Solids and Structures* **38**(50–1), 9149–77.

Bruno, D., Greco, F. and Lonetti, P. (2003), 'A coupled interface-multilayer approach for mixed mode delamination and contact analysis in laminated composites', *International Journal of Solids and Structures* **40**(26), 7245–68.

Camanho, P. P., Davila, C. G. and de Moura, M. F. (2003), 'Numerical simulation of mixed-mode progressive delamination in composite materials', *Journal of Composite Materials* **37**(16), 1415–38.

Carlsson, L. A., Gillespie, J. W. and Pipes, R. B. (1986), 'On the analysis and design of the end notched flexure (ENF) specimen for mode II testing', *Journal of Composite Materials* **20**(6), 594–604.

Carlsson, L. A., Gillespie, J. W. and Trethewey, B. R. (1986), 'Mode II interlaminar fracture toughness of graphite/epoxy and graphite/PEEK', *Journal of Reinforced Plastics and Composites* **5**(3), 170–87.

Charalambides, M., Kinloch, A. J., Wang, Y. and Williams, J. G. (1992), 'On the analysis of mixed-mode failure', *International Journal of Fracture* **54**(3), 269–91.

Chen, J. (2002), 'Predicting progressive delamination of stiffened fibre-composite panel and repaired sandwich panel by decohesion models', *Journal of Thermoplastic Composite Materials* **15**(5), 429–42.

Chen, J., Crisfield, M. A., Kinloch, A. J., Busso, E. P., Matthews, F. L. and Qiu, Y. (1999), 'Predicting progressive delamination of composite material specimens via interface elements', *Journal of Mechanics of Composite Materials and Structures* **6**(4), 301–17.

Corletto, C. R. (1986), Mode II delamination fracture toughness of unidirectional graphite/epoxy composites, Master's thesis, Texas A&M University, College Station, TX.

Cotterell, B. and Rice, J. R. (1980), 'Slightly curved or kinked cracks', *International Journal of Fracture* **16**(2), 155–69.

Cui, W. and Wisnom, M. R. (1993), 'A combined stress-based and fracture-mechanics-based model for predicting delamination in composites', *Composites* **24**(6), 467–74.

Davidson, B. D., Hu, H. and Schapery, R. A. (1995), 'An analytical crack-tip element for layered elastic structures', *Journal of Applied Mechanics* **62**(2), 294–305.

Davidson, B. D., Hu, H. and Yan, H. (1996), 'An efficient procedure for determining mixed-mode energy release rates in practical problems of delamination', *Finite Elements in Analysis and Design* **23**(2–4), 193–210.

Davidson, B. D., Yu, L. and Hu, H. (2000), 'Determination of energy release rate and mode mix in three-dimensional layered structures using plate theory', *International Journal of Fracture* **105**, 81–105.

Davies, P., Blackman, B. R. K. and Brunner, A. J. (1998), 'Standard test methods for delamination resistance of composite materials: Current status', *Applied Composite Materials* **5**, 345–64.

Diaz, A. D., Caron, J.-F. and Ehrlacher, A. (2007), 'Analytical determination of the modes I, II and III energy release rates in a delaminated laminate and validation of a delamination criterion', *Composite Structures* **78**(3), 424–32.

Donaldson, S. L. (1985), 'Fracture toughness testing of graphite/epoxy and graphite/PEEK composites', *Composites* **16**(2), 103–12.

Dowling, N. E. (1993), *Mechanical behavior of materials: Engineering methods for deformation, fracture, and fatigue*, Prentice Hall, Englewood Cliffs, NJ.

England, A. H. (1965), 'A crack between dissimilar media', *Journal of Applied Mechanics* **32**, 400–2.

Ewalds, H. and Wanhill, R. (1984), *Fracture mechanics*, Edward Arnold, London.

Fedderson, C. (1967), *Plane strain crack toughness testing of high strength metallic materials, ASTM STP 937*, American Society for Testing and Materials, Philadelphia, PA, chapter Discussion on plane strain crack toughness testing, pp. 77–79.

Gold'stein, R. V. and Salganik, R. L. (1974), 'Brittle fracture of solids with arbitrary cracks', *International Journal of Fracture* **10**(4), 507–23.

Griffith, A. A. (1921), 'The phenomena of rupture and flow in solids', *Philosophical Transactions of the Royal Society of London, A* **221**, 163–98.

Harvey, C. M. (2009), Modelling of delamination propagation in composite laminated beam structures, Master's thesis, Department of Aeronautical and Automotive Engineering, Loughborough University, Loughborough, UK.

Harvey, C. M. and Wang, S. (2012*a*), 'Experimental assessment of mixed-mode partition theories', *Composite Structures* **94**(6), 2057–67. Also a lecture at the International Conference on Mechanics of Nano, Micro and Macro Composite Structures (ICNMMCS), Turin, Italy, 18–20 June 2011.

Harvey, C. M. and Wang, S. (2012*b*), 'Fracture mode partitions in layered isotropic axisymmetric plates'. In preparation.

Harvey, C. M. and Wang, S. (2012*c*), 'Mixed-mode partition theories for one-dimensional delamination in laminated composite beams', *Engineering Fracture Mechanics* . In review.

Harvey, C. M. and Wang, S. (2012*d*), 'Numerical and analytical study of delamination in composite laminates', *International Journal of Engineering Systems Modelling and Simulation* **4**(3), 120–37.

Harvey, C. M. and Wang, S. (in press), Modeling of delamination propagation in composite laminated beam structures, *in* T. E. Simos, ed., '7th International Conference

of Computational Methods in Science and Engineering (ICCMSE 2009)', American Institute of Physics, Rhodes, Greece, 29 September–4 October 2009.

Harvey, C. M., Wang, S. and Cunningham, P. (2012), 'Fracture mode partitions in layered isotropic and laminated composite straight beam structures'. In preparation.

Hashemi, S., Kinloch, A. J. and Williams, G. (1991), Mixed-mode fracture in fiber-polymer composite laminates, *in* T. K. O'Brien, ed., 'Composite materials: Fatigue and fracture, ASTM STP 110', Vol. 3, American Society for Testing and Materials, Philadelphia, PA, pp. 143–68.

Hashemi, S., Kinloch, A. J. and Williams, J. G. (1990), 'The analysis of interlaminar fracture in uniaxial fibre-polymer composites', *Proceedings of the Royal Society A* **427**(1872), 173–99.

Hellen, T. K. (1975), 'On the method of virtual crack extensions', *International Journal for Numerical Methods in Engineering* **9**(1), 187–207.

Hui, C. Y. and Ruina, A. (1995), 'Why K? high order singularities and small scale yielding', *International Journal of Fracture* **72**, 97–120.

Hutchinson, J. W., Mear, M. E. and Rice, J. R. (1987), 'Crack paralleling an interface between dissimilar materials', *Journal of Applied Mechanics* **109**, 828–32.

Hutchinson, J. W. and Suo, Z. (1992), 'Mixed mode cracking in layered materials', *Advances in Applied Mechanics* **29**, 63–191.

Inglis, C. E. (1913), 'Stresses in a plate due to the presence of cracks and sharp corners', *The Institute of Naval Architects* **55**, 219–41.

Irwin, G. R. (1957), 'Analysis of stresses and strain near the end of a crack traversing a plate', *Journal of Applied Mechanics* **24**(3), 361–4.

Irwin, G. R. (1958), 'Fracture', *Handbuch der Physik* **6**, 551–90.

Jansson, N. E. and Larsson, R. (2001), 'A damage model for simulation of mixed-mode delamination growth', *Composite Structures* **53**(4), 409–17.

JIS (2008), Testing methods for interlaminar fracture toughness of carbon fibre reinforced plastics, JIS K 7086:1993, Japanese Industrial Standards, Japan Chemical Innovation and Inspection Institute.

Jones, R. M. (1999), *Mechanics of composite materials*, 2nd edn, CRC Press, Philadelphia, PA.

Jurf, R. A. and Pipes, R. B. (1982), 'Interlaminar fracture of composite materials', *Journal of Composite Materials* **16**(5), 386–94.

Kanninen, M. F. (1973), 'An augmented double cantilever beam model for studying crack propagation and arrest', *International Journal of Fracture* **9**, 83–92.

Kinloch, A. J., Wang, Y., Williams, J. G. and Yayla, P. (1993), 'The mixed-mode delamination of fibre composite materials', *Composite Science and Technology* **47**(3), 225–37.

Krueger, R. (2002), The virtual crack closure technique: History, approach and applications, NASA Contractor Report CR 2002-21168, NASA Langley Research Center, Hampton, VA.

Kundu, T. (2008), *Fundamentals of fracture mechanics*, CRC Press, Boca Raton, FL.

Kutlu, Z. and Chang, F.-K. (1995), 'Composite panels containing multiple through-the-width delaminations and subjected to compression: Part II: Experiments and verification', *Composite Structures* **31**(4), 297–314.

Li, S. (1996), 'Rigidities of one-dimensional laminates of composite materials', *Journal of Engineering Mechanics* **122**(4), 371–4.

Li, S. and Lim, S.-H. (2005), 'Variational principles for generalized plane strain problems and their applications', *Composites Part A: Applied Science and Manufacturing* **36**(3), 353–65.

Luo, Q. and Tong, L. (2009), 'Calculation of energy release rates for cohesive and interlaminar delamination based on the classical beam-adhesive model', *Journal of Composite Materials* **43**(4), 331–48.

Martin, R. H. (1991), Interlaminar fracture characterization: A current review, NASA Contractor Report CR 187573, NASA Langley Research Center, Hampton, VA.

McKinney, J. (1972), 'Mixed-mode fracture of unidirectional graphite/epoxy composites', *Journal of Composite Materials* **6**(1), 164–6.

Meo, M. and Thieulot, E. (2005), 'Delamination modelling in a double cantilever beam', *Composite Structures* **71**(3–4), 429–34.

Mi, Y., Crisfield, M. A., Davies, G. A. O. and Hellweg, H. B. (1998), 'Progressive delamination using interface elements', *Journal of Composite Materials* **32**(14), 1246–72.

Mindlin, R. D. (1951), 'Influence of rotatory inertia and shear on flexural motions of isotropic, elastic plates', *Journal of Applied Mechanics* **18**, 31–8.

Nguyen, C. and Levy, A. J. (2009), 'An exact theory of interfacial debonding in layered elastic composites', *International Journal of Solids and Structures* **46**(13), 2712–23.

O'Brien, T. K., Johnston, N. J., Raju, I. S., Morris, D. H. and Simmonds, R. A. (1987), Comparisons of various configurations of the edge-delamination test for interlaminar

fracture toughness, *in* N. J. Johnston, ed., 'Toughened composites, ASTM STP 937', American Society for Testing and Materials, Philadelphia, PA, pp. 199–221.

O'Brien, T. K. and Martin, R. H. (1993), 'Round robin testing for mode I interlaminar fracture toughness of composite materials', *Journal of Composites Technology and Research* **15**(4), 269–81. Also in NASA Technical Memorandum TM 104222.

Ouyang, Z. and Li, G. (2009), 'Nonlinear interface shear fracture of end notched flexure specimens', *International Journal of Solids and Structures* **46**(13), 2659–68.

Parks, D. M. (1974), 'A stiffness derivative finite element technique for determination of crack tip stress intensity factors', *International Journal of Fracture* **10**, 487–502.

Petrossian, Z. and Wisnom, M. R. (1998), 'Prediction of delamination initiation and growth from discontinuous plies using interface elements', *Composites Part A: Applied Science and Manufacturing* **29**(5), 503–15.

Pinho, S. T., Iannucci, L. and Robinson, P. (2006), 'Formulation and implementation of decohesion elements in an explicit finite element code', *Composites Part A: Applied Science and Manufacturing* **37**(5), 778–89.

Prathap, G. and Bhashyam, G. R. (1982), 'Reduced integration and the shear-flexible beam element', *International Journal for Numerical Methods in Engineering* **18**(2), 195–210.

Press, W. H., Teukolsky, S. A., Vetterling, W. T. and Flannery, B. (2007), *Numerical recipes: The art of scientific computing*, 3rd edn, Cambridge University Press, Cambridge, UK.

Qiu, Y., Crisfield, M. A. and Alfano, G. (2001), 'An interface element formulation for the simulation of delamination with buckling', *Engineering Fracture Mechanics* **68**(16), 1755–76.

Raju, I. S. (1987), 'Calculation of strain-energy release rates with higher order and singular finite elements', *Engineering Fracture Mechanics* **28**(3), 251–74.

Raju, I. S., Crews Jr., J. H. and Aminpour, M. A. (1988), 'Convergence of strain energy release rate components for edge-delaminated composite laminates', *Engineering Fracture Mechanics* **30**(3), 383–96.

Rao, S. S. (1982), *The finite element method in engineering*, Pergamon Press, Oxford, UK.

Reddy, J. N. (1984), *An introduction to the finite element method*, McGraw-Hill, New York, NY.

Reddy, J. N. (1997), 'On locking-free shear deformable beam finite elements', *Computer Methods in Applied Mechanics and Engineering* **149**(1–4), 113–32.

Reddy, J. N. (2004), *Mechanics of laminated plates and shells: Theory and analysis*, 2nd edn, CRC Press, Boca Raton, FL.

Reeder, J. R. (1992), An evaluation of mixed-mode delamination failure criteria, NASA Technical Memorandum TM 104210, NASA Langley Research Center, Hampton, VA.

Reeder, J. R. and Crews Jr., J. R. (1990), 'Mixed-mode bending method for delamination testing', *AIAA Journal* **28**(7), 1270–6.

Reeder, J. R. and J. H. Crews, J. (1991), Nonlinear analysis and redesign of the mixed-mode bending delamination test, NASA Technical Memorandum TM 102777, NASA Langley Research Center, Hampton, VA.

Rice, J. R. (1968), 'A path independent integral and the approximate analysis of strain concentration by notches and cracks', *Journal of Applied Mechanics* **35**, 379–86.

Rice, J. R. (1988), 'Elastic fracture mechanics concepts for interfacial cracks', *Journal of Applied Mechanics* **55**(1), 98–103.

Rybicki, E. F. and Kanninen, M. F. (1977), 'A finite element calculation of stress intensity factors by a modified crack closure integral', *Engineering Fracture Mechanics* **9**(4), 931–8.

Sanford, R. J. and Stonesifer, F. R. (1970), Fracture toughness of filament-wound composites. Part I: Effect of material variables, NRL Report 7112, Naval Research Laboratory, Washington, DC.

Schapery, R. A. and Davidson, B. D. (1990), 'Prediction of energy release rate for mixed-mode delamination using classical plate theory', *Applied Mechanics Reviews* **43**(5S), S281–7.

Sheinman, I. and Kardomateas, G. A. (1997), 'Energy release rate and stress intensity factors for delaminated composite laminates', *International Journal of Solids and Structures* **34**(4), 451–9.

Shim, J. Y. and Hong, C. S. (1993), 'Strain energy release rates of modified ENF specimen for mixed-mode fracture', *Journal of Reinforced Plastics and Composites* **12**(12), 1295–310.

Sih, G. C., Paris, P. C. and Irwin, G. R. (1965), 'On cracks in rectilinearly anisotropic bodies', *International Journal of Fracture* **1**, 189–203.

Strawley, J. E., Jones, M. H. and Gross, B. (1964), Experimental determination of the dependence of crack extension force on crack length for a single-edge-notch tension specimens, NASA Technical Note TN D-2396, NASA Lewis Research Center, Cleveland, OH.

Suo, Z. (1990), 'Delamination specimens for orthotropic materials', *Journal of Applied Mechanics* **56**, 627–34.

Suo, Z. (2010), *Fracture mechanics*, Engineering Sciences 247: Fracture Mechanics, iMechanica.

Suo, Z. and Hutchinson, J. W. (1989), 'Sandwich specimens for measuring interface crack toughness', *Materials Science and Engineering* **A107**, 135–43.

Suo, Z. and Hutchinson, J. W. (1990), 'Interface crack between two elastic layers', *International Journal of Fracture* **43**, 1–18.

Thouless, M. D. (1990), 'Fracture of a model interface under mixed-mode loading', *Acta Metallurgica Materialia* **38**(6), 1135–40.

Thouless, M. D., Evans, A. G., Ashby, M. F. and Hutchinson, J. W. (1987), 'The edge cracking and spalling of brittle plates', *Acta Metallurgica* **35**(6), 1333–41.

Timoshenko, S. P. and Goodier, J. N. (1970), *Theory of elasticity*, 3rd edn, McGraw-Hill, New York, NY.

Timoshenko, S. P. and Woinowsky-Krieger, S. (1959), *Theory of plates and shells*, 2nd edn, McGraw-Hill, New York, NY.

Wagner, W. and Balzani, C. (2008), 'Simulation of delamination in stringer stiffened fiber-reinforced composite shells', *Computers and Structures* **86**(9), 930–9.

Wang, C. M. and Lee, K. H. (1996), 'Deflection and stress-resultants of axisymmetric Mindlin plates in terms of corresponding Kirchhoff solutions', *International Journal of Mechanical Sciences* **38**(11), 1179–85.

Wang, J. and Qiao, P. (2004), 'Interface crack between two shear deformable elastic layers', *Journal of the Mechanics and Physics of Solids* **52**(4), 891–905.

Wang, S. and Harvey, C. M. (2009), Fracture mode partition rules for DCBs, *in* '17th International Conference on Composites/Nano Engineering (ICCE-17)', Honolulu, HI, 26–31 July 2009.

Wang, S. and Harvey, C. M. (2010), Fracture mode partition theory for one dimensional fracture, *in* '18th European Conference on Fracture (ECF-18)', Dresden, Germany, 30 August–3 September 2010.

Wang, S. and Harvey, C. M. (2011*a*), 'Mixed mode partition in one dimensional fractures', *Key Engineering Materials* **462–3**, 616–21. Also a plenary lecture at the 8th International Conference on Fracture and Strength of Solids (FEOFS 2010), Kuala Lumpur, Malaysia, 7–9 June 2010.

Wang, S. and Harvey, C. M. (2011*b*), Partition and propagation of delamination in fibre reinforced composite laminates, *in* '4th IASME/WSEAS International Conference on Engineering Mechanics, Structures, Engineering Geology (EMESEG 2011)', Corfu, Greece, 14–16 July 2011. A plenary lecture.

Wang, S. and Harvey, C. M. (2012*a*), 'Mixed mode partition theories for one dimensional fracture', *Engineering Fracture Mechanics* **79**(1), 329–52.

Wang, S. and Harvey, C. M. (2012*b*), Propagation of delamination in composite laminates: Local or global?, *in* '7th IASME/WSEAS International Conference on Continuum Mechanics (CM 2012)', Kos Island, Greece, 14–17 July 2012. A plenary lecture.

Wang, S. and Harvey, C. M. (2012*c*), 'A theory of one-dimensional fracture', *Composite Structures* **94**(2), 758–67. Also a plenary lecture at the 16th International Conference on Composite Structures (ICCS-16), Porto, Portugal, 28–30 June 2011.

Wang, S., Harvey, C. M. and Guan, L. (2012), 'Partition of mixed modes in double cantilever beams with non-rigid elastic interfaces', *Engineering Fracture Mechanics* . Also a lecture at the 6th International Conference Fracture of Polymers, Composites and Adhesives (TC4PCA 2011), Les Diablerets, Switzerland, 11–15 September 2011. Accepted subject to minor revision.

Wang, S. and Zhang, Y. (2009), 'Buckling, post-buckling and delamination propagation in debonded composite laminates: Part 2: Numerical applications', *Composite Structures* **88**(1), 131–46.

Williams, J. G. (1988), 'On the calculation of energy release rates for cracked laminates', *International Journal of Fracture* **36**(2), 101–19.

Williams, M. L. (1957), 'On the stress distribution at the base of a stationary crack', *Journal of Applied Mechanics* **24**, 109–15.

Williams, M. L. (1959), 'The stress around a fault or crack in dissimilar media', *Bulletin of the Seismological Society of America* **49**, 199–204.

Wu, E. M. (1967), 'Application of fracture mechanics to anisotropic plates', *Journal of Applied Mechanics* **34**(4), 967–74.

Wu, E. M. and Reuter Jr., R. C. (1965), Crack extension in fibreglass reinforced plastics, T & A. M. Report 275, University of Illinois.

Yarema, S. Y. (1996), 'On the contribution of G. R. Irwin to fracture mechanics', *Materials Science* **31**, 617–23.

Yoon, S. and Hong, C. (1990), 'Interlaminar fracture toughness of graphite/epoxy composite under mixed-mode deformations', *Experimental Mechanics* **30**, 234–9.

Zehnder, A. T. (2007), *Fracture mechanics*, iMechanica, Sibley School of Mechanical and Aerospace Engineering Cornell University, Ithaca, NY.

Zhang, Y. and Wang, S. (2009), 'Buckling, post-buckling and delamination propagation in debonded composite laminates: Part 1: Theoretical development', *Composite Structures* **88**(1), 121–30.

Zhou, J. and He, T. (1994), 'On the analysis of the end-notched flexure specimen for measuring mode II fracture toughness of composite materials', *Composites Science and Technology* **50**(2), 209–13.

Zi, G. and Belytschko, T. (2003), 'New crack-tip elements for XFEM and applications to cohesive cracks', *International Journal for Numerical Methods in Engineering* **57**(15), 2221–40.

Zienkiewicz, O. C. and Taylor, R. L. (1989), *The finite element method: Basic formulation and linear problems*, Vol. 1, 4th edn, McGraw-Hill, London.

Zou, Z., Reid, S. R., Li, S. and Soden, P. D. (2002), 'General expressions for energy-release rates for delamination in composite laminates', *Proceedings of the Royal Society A* **458**(2019), 645–67.

Zou, Z., Reid, S. R., Soden, P. D. and Li, S. (2001), 'Mode separation of energy release rate for delamination in composite laminates using sublaminates', *International Journal of Solids and Structures* **38**(15), 2597–613.